polymers

Special Issue Reprint

Editorial Board Members' Collection Series

Polymer Physics and Theory

Edited by
Fahmi Zaïri, Matthias Ballauff, Ulrich Maschke and Rufina G. Alamo

mdpi.com/journal/polymers

MDPI

Editorial Board Members' Collection Series: Polymer Physics and Theory

Editorial Board Members' Collection Series: Polymer Physics and Theory

Editors

Fahmi Zaïri
Matthias Ballauff
Ulrich Maschke
Rufina G. Alamo

MDPI

Basel • Beijing • Wuhan • Barcelona • Belgrade • Novi Sad • Cluj • Manchester

Editors

Fahmi Zaïri
Lille University
Lille
France

Matthias Ballauff
Freie Universität Berlin
Berlin
Germany

Ulrich Maschke
Lille University
Lille
France

Rufina G. Alamo
FAMU-FSU College of
Engineering
Tallahassee, FL
USA

Editorial Office
MDPI AG
Grosspeteranlage 5
4052 Basel, Switzerland

This is a reprint of articles from the Special Issue published online in the open access journal *Polymers* (ISSN 2073-4360) (available at: https://www.mdpi.com/journal/polymers/special_issues/33N8WOI1F5).

For citation purposes, cite each article independently as indicated on the article page online and as indicated below:

Lastname, A.A.; Lastname, B.B. Article Title. *Journal Name* **Year**, *Volume Number*, Page Range.

ISBN 978-3-7258-1419-0 (Hbk)
ISBN 978-3-7258-1420-6 (PDF)
doi.org/10.3390/books978-3-7258-1420-6

© 2024 by the authors. Articles in this book are Open Access and distributed under the Creative Commons Attribution (CC BY) license. The book as a whole is distributed by MDPI under the terms and conditions of the Creative Commons Attribution-NonCommercial-NoDerivs (CC BY-NC-ND) license.

Contents

About the Editors . . . . . **vii**

Preface . . . . . **ix**

Arash Nikoubashman and Miho Yanagisawa
Confinement-Induced Fractionation and Liquid–Liquid Phase Separation of Polymer Mixtures
Reprinted from: *Polymers* **2023**, *15*, 511, doi:10.3390/polym15030511 . . . . . **1**

Emi Haladjova, Silvia Panseri, Monica Montesi, Arianna Rossi, Athanasios Skandalis, Stergios Pispas and Stanislav Rangelov
Influence of DNA Type on the Physicochemical and Biological Properties of Polyplexes Based on Star Polymers Bearing Different Amino Functionalities
Reprinted from: *Polymers* **2023**, *15*, 894, doi:10.3390/polym15040894 . . . . . **12**

Anita Białkowska, Mohamed Bakar, Wojciech Kucharczyk and Iwona Zarzyka
Hybrid Epoxy Nanocomposites: Improvement in Mechanical Properties and Toughening Mechanisms—A Review
Reprinted from: *Polymers* **2023**, *15*, 1398, doi:10.3390/polym15061398 . . . . . **28**

Wenqian Lin, Zhenna Li, Shanliang Zhang and Jianzhong Lin
Numerical Study on the Distribution of Rodlike Particles in Laminar Flows of Power Law Fluids Past a Cylinder
Reprinted from: *Polymers* **2023**, *15*, 1956, doi:10.3390/polym15081956 . . . . . **59**

Radu Claudiu Fierascu, Irina Fierascu, Roxana Ioana Matei (Brazdis) and Doina Manaila-Maximean
Natural and Natural-Based Polymers: Recent Developments in Management of Emerging Pollutants
Reprinted from: *Polymers* **2023**, *15*, 2063, doi:10.3390/polym15092063 . . . . . **75**

Cihan Aktas, Osman Polat, Mohamadreza Beitollahpoor, Melika Farzam, Noshir S. Pesika and Nurettin Sahiner
Force-Based Characterization of the Wetting Properties of LDPE Surfaces Treated with CF_4 and H_2 Plasmas
Reprinted from: *Polymers* **2023**, *15*, 2132, doi:10.3390/polym15092132 . . . . . **102**

Qiuyue Ding, Ning Ding, Xiangfeng Chen, Wenyue Guo and Fahmi Zaïri
Understanding the Effect of Grain Boundaries on the Mechanical Properties of Epoxy/Graphene Composites
Reprinted from: *Polymers* **2023**, *15*, 3218, doi:10.3390/polym15153218 . . . . . **113**

Ali Kassab, Dawood Al Nabhani, Pravansu Mohanty, Christopher Pannier and Georges Y. Ayoub
Advancing Plastic Recycling: Challenges and Opportunities in the Integration of 3D Printing and Distributed Recycling for a Circular Economy
Reprinted from: *Polymers* **2023**, *15*, 3881, doi:10.3390/polym15193881 . . . . . **129**

Jean Pierre Ibar
The Challenges Facing the Current Paradigm Describing Viscoelastic Interactions in Polymer Melts
Reprinted from: *Polymers* **2023**, *15*, 4309, doi:10.3390/polym15214309 . . . . . **174**

Gege Huang, Zhihao Chen, Jian Wu, Ange Lin, Qinxiu Liu, Shouyao Liu, et al.
Effect of Hydrothermal Aging on the Tribological Performance of Nitrile Butadiene Rubber Seals
Reprinted from: *Polymers* **2024**, *16*, 81, doi:10.3390/polym16010081 . . . . . **221**

About the Editors

Fahmi Zaïri

Fahmi Zaïri, currently serving as a Full Professor at the University of Lille in France since September 2014, is an expert in the mechanics of soft materials, including polymers and biological tissues. His expertise extends to the multiscale and multiphysics modeling of these materials. Professor Zaïri's research is particularly focused on establishing the structure–property relationships in soft materials through a synergistic approach that integrates experimental and modeling techniques. He completed his educational journey at the University of Lille, where he earned his Ph.D. in the Mechanics of Materials in 2004 and later achieved his Habilitation in the same field in 2012. His academic career at the University of Lille progressed from an Assistant Professor position starting in September 2005, to Associate Professor by mid-2012, before reaching his current full professorship. Over the course of his career, Professor Zaïri has published more than 140 papers in international peer-reviewed journals. He has also been instrumental in mentoring and guiding the academic and professional paths of over 30 Ph.D. students. His contributions have been repeatedly recognized, earning him multiple awards for doctoral supervision and research. Professor Zaïri has played a key role in establishing international bilateral research programs and maintains a broad network of international collaborations that spans the United States, China, Japan, the Maghreb countries, Qatar, and Europe, enhancing the global impact of his research. Professor Zaïri collaborates with academic and industrial partners to advance the mechanics of materials, leading to joint publications and practical applications of his research.

Matthias Ballauff

Professor Matthias Ballauff received his doctorate from the University in Mainz in 1981. He then joined the group of Prof. P.J. Flory at Stanford University. In 1984, he became a research associate at the Max Planck Institute for Polymer Research in Mainz, working with liquid crystal polymers. In 1990, he moved to the University of Karlsruhe as a full professor of polymer science. From 2003 to 2009, he was a professor of physical chemistry at the University of Bayreuth. In 2009, he became a professor of experimental physics at the Humboldt University in Berlin. Since his retirement in 2019, he works as a visiting professor at the Freie Universität Berlin. His main field is colloid science as applied to polymeric and biochemical systems. Moreover, he has worked a lot on scattering methods for the characterization of polymeric and colloidal systems. He is an expert on biological polyelectrolytes and their interaction with proteins. He is the author of more than 400 original papers and has received numerous invitations to international conferences.

Ulrich Maschke

Ulrich Maschke studied chemistry at the University of Mainz, Germany, where he received his DEA in 1989 with a thesis on the phase behavior of polymer blends (PMPS/PS). In 1992, he completed his Ph.D. thesis at the Physics Department of the Max Planck Institute for Polymer Research (MPI-P, Mainz) on the "Static and dynamic properties of polymer melts studied by neutron scattering". In 1992, he joined the University of Lille (France) as Chargé de Recherche at the Centre National de la Recherche Scientifique (CNRS). In 2001, he obtained the accreditation of the University of Lille for research supervision (HDR). He is now CNRS Research Director at UMET, in charge of a group working mainly on polymers and material recycling. His main areas of scientific activity include the photochemistry and radiochemistry of mainly organic materials (ultraviolet irradiation, electron beam bombardment, polymerization/crosslinking processes, grafting, surface treatment, polymer

coatings...); the deactivation of halogenated toxic substances by radiation treatment and adsorption; chemically cross-linked polymer networks (synthesis, characterization, swelling/deswelling studies); and nano- and micron-sized liquid crystal dispersions in polymers. His scientific output refers to more than 200 international publications, referenced in Web of Science; 7 national and international patents; about 500 presentations (invited, oral, posters); the supervisor/co-director of 30 Ph.D. theses; and numerous academic and industrial collaborations at national and international level. He has also been the leader of several PHC projects (Dnipro, Tassili, Al Maqdisi) and other collaborative projects (exchange agreements, PICS, LIA...), as well having academic responsibility for several projects with academic and industrial partners (Interreg FWVL, FUI OSEO, ADEME, ANR...).

Rufina G. Alamo

Professor R. G. Alamo received a Doctorate in Chemistry/Polymers from the Complutense University of Madrid and the Institute of Science and Technology of Polymers (CSIC) of Spain. After a Fulbright postdoctoral stay at Florida State University, and two years with Dow Chemical Ibérica, in 1995, she joined the Department of Chemical and Biomedical Engineering of the jointly managed FAMU-FSU College of Engineering where she is presently the Simon Ostrach Professor of Engineering. She is a Fellow of the American Association for the Advancement of Sciences (AAAS), a Fellow of the American Physical Society, and has received the NSF Research Creativity Award and the Mettler Award of the North American Thermal Analysis Society for outstanding contributions to thermal analysis in crystalline polymers. Her major research interest is to advance the knowledge of the interplay between chain microstructure, phase structure, crystallization kinetics, and the morphology of non-oriented bulk crystallized polymers. Her vision is to understand this interplay using well-characterized crystalline polymers that serve as models to understand or predict the behavior of more complex commercial systems. She has published over 165 peer-reviewed journal papers and 15 book chapters, and has delivered numerous invited presentations.

Preface

It is with great pleasure and deep appreciation that we present to you this Special Issue of the Special Collection entitled "Editorial Board Members' Collection Series: Polymer Physics and Theory". This publication represents an outstanding collaborative effort, orchestrated by the distinguished members of our Editorial Board, with the aim of highlighting significant advances and key discoveries in the field of polymer science.

This initiative was conceived with the ambition of compiling high-quality research papers solicited and invited by the members of our Editorial Board. The aim was to provide a platform for the exchange of comprehensive reviews and original articles that address the diverse topics covered by *Polymers*. This Special Issue covers a wide range of topics. These include the pioneering development of multiscale methodologies and groundbreaking theories, as well as the implementation of efficient algorithms and machine learning schemes that elucidate structure–property relationships with new clarity. In addition, we have placed a special emphasis on experimental studies devoted to the formulation and characterization of novel polymeric materials, not to mention innovations in instrumentation.

This collection is enriched by articles that navigate the frontiers of polymer science, from investigating the behavior of polymer blends to biomedical applications, particularly drug delivery via star polymer-based polyplexes. It explores the mechanical properties of epoxy-based nanocomposites and the fluid dynamics of rod-like particles, paving the way for industrial optimization. Sustainability is a focus, with studies of natural polymers against pollutants and advanced plastic recycling, including 3D printing. Research concerning low-density polyethylene films and epoxy/graphene composites rethinks material strength and resilience. Finally, critical analyses of viscoelastic interactions and the tribological performance of nitrile-butadiene rubber seals under hydrothermal aging challenge established knowledge. Each piece contributes a vital thread to the state of the art of polymer research, highlighting innovations ranging from improvements in mechanical properties to the environmental and sustainability challenges facing the industry.

We would like to express our deepest gratitude to all the authors for their significant contributions that have broadened the horizons of polymer science. We are also grateful to the reviewers for their expertise and dedication in ensuring the scientific quality and rigor of the published papers. Special thanks go to Mr. Alan Cui and the entire *Polymers* staff for their invaluable support and dedication throughout the publication process.

Under the wise leadership of Prof. Dr. Fahmi Zaïri, Prof. Dr. Matthias Ballauff, Prof. Dr. Ulrich Maschke, and Prof. Dr. Rufina G. Alamo, this Special Issue aims to be not only a testament to the current state of research in the field of polymer science, but also a source of inspiration for future innovations.

As you open this Special Issue, we invite you to explore the depths of polymer science, an ever-evolving field that continues to shape the world around us. Let this collection inspire your next steps in research and innovation, and foster the ongoing pursuit of knowledge and breakthroughs.

Fahmi Zaïri, Matthias Ballauff, Ulrich Maschke, and Rufina G. Alamo
Editors

polymers

MDPI

Article

Confinement-Induced Fractionation and Liquid–Liquid Phase Separation of Polymer Mixtures

Arash Nikoubashman [1,2,*] and Miho Yanagisawa [3,4]

[1] Institute of Physics, Johannes Gutenberg University Mainz, Staudingerweg 7, 55128 Mainz, Germany
[2] Department of Mechanical Engineering, Keio University, Yokohama 223-8522, Japan
[3] Komaba Institute for Science, Graduate School of Arts and Sciences and Center for Complex Systems Biology, Universal Biology Institute, The University of Tokyo, Meguro, Tokyo 153-8902, Japan
[4] Graduate School of Science, The University of Tokyo, Bunkyo, Tokyo 113-0033, Japan
* Correspondence: anikouba@uni-mainz.de

Abstract: The formation of (bio)molecular condensates via liquid–liquid phase separation in cells has received increasing attention, as these aggregates play important functional and regulatory roles within biological systems. However, the majority of studies focused on the behavior of pure systems in bulk solutions, thus neglecting confinement effects and the interplay between the numerous molecules present in cells. To better understand the physical mechanisms driving condensation in cellular environments, we perform molecular simulations of binary polymer mixtures in spherical droplets, considering both monodisperse and polydisperse molecular weight distributions for the longer polymer species. We find that confinement induces a spatial separation of the polymers by length, with the longer ones moving to the droplet center. This partitioning causes a distinct increase in the local polymer concentration near the droplet center, which is more pronounced in polydisperse systems. Consequently, the confined systems exhibit liquid–liquid phase separation at average polymer concentrations where bulk systems are still in the one-phase regime.

Keywords: phase separation; polymer mixture; droplet; protocell; confinement; molecular simulation; PEG; Dextran

Citation: Nikoubashman, A.; Yanagisawa, M. Confinement-Induced Fractionation and Liquid–Liquid Phase Separation of Polymer Mixtures. *Polymers* **2023**, *15*, 511. https://doi.org/10.3390/polym15030511

Academic Editor: Fahmi Zaïri

Received: 9 December 2022
Revised: 13 January 2023
Accepted: 16 January 2023
Published: 18 January 2023

Copyright: © 2023 by the authors. Licensee MDPI, Basel, Switzerland. This article is an open access article distributed under the terms and conditions of the Creative Commons Attribution (CC BY) license (https://creativecommons.org/licenses/by/4.0/).

1. Introduction

The liquid–liquid phase separation (LLPS) of (bio)molecules in living cells has attracted much attention as a mechanism for intracellular organization via the formation of biomolecular condensates [1,2]. To elucidate the underlying mechanisms of LLPS, bulk solutions of purified biomolecules from cells have been analyzed extensively over the past decade. Although such in vitro studies facilitate the analysis of LLPS and comparisons with theoretical models [3], they systematically ignore confinement effects and the molecular diversity encountered in cellular environments [4]. For example, broad molecular weight distributions can have a profound impact on the phase behavior of polymers, e.g., leading to the self-assembly of monodisperse micelles from polydisperse surfactants [5] or the fractionation of polymer chains by molar mass in solutions near criticality [6,7]. Typically, the demixing of polymers becomes more pronounced in confinemenet due to the associated spatial inhomogeneity [8]. For example, simulations of binary polymer mixtures in spherical droplets have revealed an entropy-driven spatial segregation of the confined polymers based on their molecular weight, stiffness, and/or topology [9–11]. It is thus important to understand the phase behavior of confined systems for designing experiments and understanding the physical mechanisms driving LLPS in cellular environments.

Experimentally, confinement effects have been studied using DNA-based protocells [12,13] or water-in-oil droplets containing polymer mixtures such as polyethylene glycol (PEG) and bovine serum albumin, PEG and DNA, or PEG and Dextran, serving as a synthetic cytoplasm [14–17]. At sufficiently high concentrations, these polymer mixtures

separate into two coexisting aqueous compartments, which can be used to localize additional components such as proteins [14,15]. Recently, Watanabe et al. systematically studied the phase coexistence of PEG–Dextran mixtures in cell-sized droplets, discovering that the two-phase coexistence region in small droplets extends to much lower PEG and Dextran concentrations compared to bulk systems [18]. The bulk behavior was only recovered for rather large droplets with radii $R > 20\,\mu$m. They speculated that this R-dependent phase separation stemmed from a confinement-induced partitioning of the polymers. To elucidate the origin of this confinement-induced LLPS, we simulate PEG–Dextran mixtures in spherical confinement at two different droplet radii.

2. Simulation Model

We perform dissipative particle dynamics (DPD) simulations [19–21] using a coarse-grained polymer model in an explicit solvent. The simulations contain three different particle types, i.e., P (PEG), D (Dextran), and W (water), which are equal in their diameter a and mass m. To approach experimental length- and time-scales, we model each PEG chain as a single spherical bead of diameter a, as shown schematically in Figure 1. To facilitate a direct comparison with experiments, we have chosen polymer sizes similar to previously conducted experimental studies [18,22].

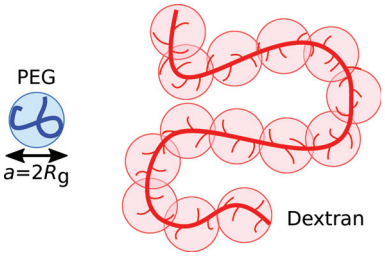

Figure 1. Schematic representation of the model, illustrating the coarse-graining of PEG and Dextran polymers.

To establish a mapping between experiments and simulations, we first estimated the characteristic size of a PEG chain in solution: the mass and length of a Kuhn segment of PEG are $m_K^P = 0.137\,\mathrm{kg/mol}$ and $b_K^P = 1.1\,\mathrm{nm}$, respectively, resulting in $N_K \equiv M_w/m_K \approx 44$ Kuhn segments for a PEG chain with molecular weight $M_w^P = 6\,\mathrm{kg/mol}$. At θ-conditions, the root-mean-square radius of gyration can be estimated as $R_g = b_K(N_K/6)^{1/2}$, resulting in a value of $R_g^P \approx 3.0\,\mathrm{nm}$. The DPD particles representing water have the same diameter a, and thus contain roughly 3700 water molecules. The Dextran chains are modeled as linear chains consisting of DPD particles with diameter a because the branches of Dextran are, on average, typically shorter than three glucose units [23] and therefore cannot be resolved at this level of coarse-graining (see Figure 1). We determined the number of DPD beads per Dextran chain, N_D, by matching R_g^D from single-chain simulations to experimental R_g measurements; in ref. [24], R_g was derived from self-diffusion coefficient measurements of Dextran chains in water at $T = 293\,\mathrm{K}$, with molecular weights ranging between 4 kg/mol and 464 kg/mol. By extrapolating their data, we estimated $R_g = 23.8\,\mathrm{nm}$ for a Dextran chain with 500 kg/mol, which leads to $N_D = 80$ for our simulation model. Hence, roughly 40 Dextran monomers are mapped to one DPD bead.

Thus, each DPD particle effectively represents a coil-like polymer segment, which typically interact with each other via soft and bounded pair potentials [25–27]. Therefore, we use the standard soft repulsion for the conservative forces acting between bonded and non-bonded DPD beads

$$\mathbf{f}_m(r) = \begin{cases} A_{ij}(1 - r/a)\hat{\mathbf{r}}, & r \leq a \\ 0, & r > a, \end{cases} \tag{1}$$

where r is the distance between the two particles, and $\hat{\mathbf{r}}$ is the unit vector connecting the two. The parameter A_{ij} controls the repulsion strength between particles of type i and j and has been set according to [21]

$$A_{ij} = A_{ii} + 3.497\chi_{ij}, \tag{2}$$

with $A_{ii} = 25\,k_\mathrm{B}T/a$ and Flory–Huggins interaction parameter χ_{ij} (the values for χ_{ij} are discussed in Section 3.1 below). This specific value for A_{ii} was originally determined by Groot and Warren to match the compressibility of water [21], but since then, this choice has been widely used to model other (incompressible) liquids and polymer melts [28–31].

Neighboring monomers within a Dextran chain are bonded through harmonic springs with force

$$\mathbf{f}_\mathrm{b}(r) = -k\mathbf{r}. \tag{3}$$

Note that the individual beads should not be regarded as single monomers, but rather as fluid elements containing several chain segments. Thus, the harmonic springs between DPD particles do not represent covalent bonds between monomers, but instead ensure the connectivity of the Dextran chains. We use a soft spring constant $k = 4\,k_\mathrm{B}T/a^2$ [28], which is consistent with the typical free energy associated with deforming a polymer in the blob model [32].

In addition to these two conservative forces, all particles are subjected to pairwise dissipative and random forces

$$\mathbf{f}_\mathrm{d}(r) = -\gamma_{ij}\omega(r)(\hat{\mathbf{r}}\cdot\Delta\mathbf{v})\hat{\mathbf{r}}, \tag{4}$$

$$\mathbf{f}_\mathrm{r}(r) = \sqrt{\gamma_{ij}\omega(r)}\xi\hat{\mathbf{r}}, \tag{5}$$

with drag coefficient γ_{ij}, and velocity difference between two particles $\Delta\mathbf{v}$. The parameter ξ is a uniformly distributed random number drawn for each particle pair, with zero mean $\langle\xi(t)\rangle = 0$ and variance $\langle\xi(t)\xi(t')\rangle = 2k_\mathrm{B}T\delta(t-t')$ to satisfy the fluctuation-dissipation theorem. For simplicity, we used the same drag coefficient $\gamma_{ij} = \gamma = 4.5\sqrt{mk_\mathrm{B}T}/a$ for all particles, and the standard DPD weight function [21]

$$\omega(r) = \begin{cases} (1-r/a)^2, & r \le a \\ 0, & r > a. \end{cases} \tag{6}$$

For the droplet simulations, all beads are confined to a spherical container with radius R by applying a purely repulsive Weeks–Chandler–Andersen (WCA) potential [33]

$$U_\mathrm{WCA}(r') = \begin{cases} 4k_\mathrm{B}T\left[\left(\frac{a}{r'}\right)^{12} - \left(\frac{a}{r'}\right)^{6} + \frac{1}{4}\right], & r' \le 2^{1/6}a \\ 0, & r' > 2^{1/6}a \end{cases}, \tag{7}$$

where r' is the distance between the droplet surface and the center of a bead. In all simulations, the particle number density was set to $\rho = 3\,a^{-3}$. The equations of motion were integrated using a time step of $\Delta t = 0.02\,\tau$, with the unit of time being τ. Each simulation was run for at least 10^7 time steps, and three independent simulations were performed for each parameter set to improve the statistics and determine measurement uncertainties.

3. Results

3.1. Parameterization and Bulk Phase Behavior

To faithfully reproduce experimental conditions, we first needed to determine the interaction parameters for the PEG (P), Dextran (D), and water (W) particles (see Section 2). Following previous simulation studies [34,35], we used a Flory–Huggins interaction parameter of $\chi_{\mathrm{P-W}} = 0.3$ for the PEG-water interactions, which was extracted from experimental

phase coexistence measurements by Saeki et al. [36]. We took $\chi_{D-W} = 0.50$ for the Dextran–water interactions, derived from experimental vapor-pressure measurements at $T = 298\,K$ conducted by Bercea et al. [37]. This value is in excellent agreement with previous findings by Clark [38], who applied a Flory–Huggins theory-based analysis to experimental tie line data of PEG–Dextran mixtures in water at $T = 298 - 300\,K$ [39,40]; Clark also extracted the PEG–Dextran interaction parameter from his analysis, i.e., $\chi_{P-D} = 0.031 \pm 0.007$. Note that the physically relevant quantity for a pair of polymers is the *combined* Flory–Huggins parameter χN [32], and thus a scaled interaction parameter $\chi^{\mathrm{eff}}_{P-D} \approx 1.23$ needs to be used in the simulations to reach the same $(\chi N)_{P-D} \approx 100$ as in the experiments, since we mapped about 40 Dextran monomers onto one DPD particle. Given the uncertainties in extracting χ_{ij} from experiments, and the high degree of coarse-graining of our model, it was, however, unclear whether this initial parameterization would faithfully reproduce the interactions between the PEG and Dextran chains in water.

To test (and tune, if necessary) the interaction parameters of our coarse-grained model, we first attempted to reproduce the experimentally known phase behavior [18,41] of aqueous PEG–Dextran mixtures in the bulk. The groups of Dimova [41] and Yanagisawa [18] determined the binodals of mixtures containing short PEG chains ($M^{P}_{w} = 6$ or $8\,kg/mol$) and long Dextran chains ($M^{D}_{w} \approx 500\,kg/mol$), finding a critical concentration of slightly below 4 wt% for PEG and 4 wt% for Dextran. Initially, we simulated bulk systems at two concentrations, i.e., $c_P = 3$ wt% for PEG and $c_D = 3$ wt% for Dextran, where we expected a single mixed phase, and at $c_P = 4$ wt% and $c_D = 4$ wt%, where the polymers should phase separate. We performed simulations in a cubic box with an edge length of $L \approx 360\,nm$ and applied periodic boundary conditions to all three Cartesian directions. The systems were initialized by placing all PEG particles and Dextran chains in opposite halves of the simulation box and were then run until the density profiles did not change anymore. For $\chi^{\mathrm{eff}}_{P-D} = 1.23$, we found a single phase at both concentrations, which indicates that the initially chosen $\chi^{\mathrm{eff}}_{P-D}$ value was too small. Therefore, we iteratively increased $\chi^{\mathrm{eff}}_{P-D}$ until we observed aggregation of the Dextran chains at the higher concentration and observed a fully mixed system at the lower concentration. This was achieved for $\chi^{\mathrm{eff}}_{P-D} = 18.6$ (Figure 2), which is about 15 times larger than our initial estimate for the PEG–Dextran interactions.

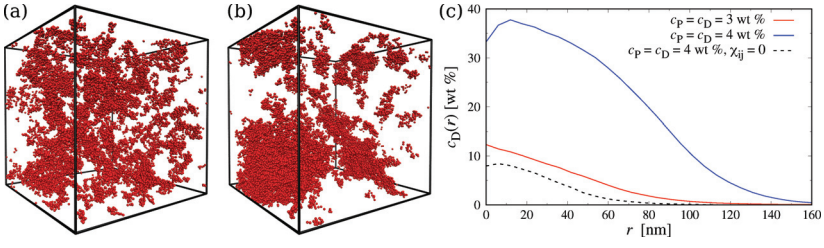

Figure 2. (**a**,**b**) Simulation snapshot of the bulk system at (**a**) $c_P = 3$ wt%, $c_D = 3$ wt%, and (**b**) $c_P = 4$ wt%, $c_D = 4$ wt%. Only Dextran beads shown for clarity. Snapshots rendered using Visual Molecular Dynamics (version 1.9.3) [42]. (**c**) Radial concentration profile of Dextran monomers $c_D(r)$ in the largest Dextran aggregate.

To quantify the size and concentration of the Dextran condensates, we performed a cluster analysis using the density-based spatial clustering of applications with noise (DBSCAN) algorithm [43]; here, Dextran monomers are assigned to the same aggregate if their distance is smaller than 7 nm, which roughly corresponds to the position of the first minimum of the radial distribution function $g(r)$ between Dextran particles and all other particle types. To establish a baseline, we performed additional simulations of ideal mixtures by setting $\chi_{ij} = 0$. Figure 2c shows the radial concentration profile $c_D(r)$ of Dextran monomers belonging to the largest cluster identified in the system. For the system at $c_P = 4$ wt% and $c_D = 4$ wt%, this analysis revealed one large droplet with a Dextran

concentration of about 35 wt% in its core. In contrast, the cluster identified at $c_P = 3$ wt% and $c_D = 3$ wt% was much smaller and more diluted, and the resulting concentration profile resembled that of an ideal Dextran chain in solution. To characterize the size of the aggregates in more detail, we also computed the average number of Dextran monomers in a cluster, $\langle M \rangle$. For the the ideal mixtures, this analysis yielded $\langle M \rangle_0 \approx 100$, which is comparable to the number of monomers per Dextran chain ($N_D = 80$). For the less concentrated system with $\chi_{ij} \neq 0$, we found $\langle M \rangle \approx 400$, which indicates the formation of small intermittent clusters. In contrast, at $c_P = 4$ wt% and $c_D = 4$ wt%, we found a much larger value of $\langle M \rangle \approx 4800$.

The discrepancy between the initial estimate and the final value of χ^{eff}_{P-D} is rather large, and we can only speculate about its origin: Clark extracted χ_{P-D} from experimental coexistence curves using Flory–Huggins solution theory [38], which ignores the polymer architecture and thus the branching of the Dextran chains. Further, a monodisperse molecular weight distribution is assumed in his treatment, although generally available Dextran polymers typically have a broad molecular weight distribution [7,17,18,22,44]. Finally, we used a rather coarse-grained description, which maps about 40 monomers onto a single bead, resulting in a larger entropy of mixing in the simulations compared to the experiments [32]. To compensate for these effects, we will use $\chi^{\text{eff}}_{P-D} = 18.6$ in the following. Figure 3 shows the resulting phase coexistence results from our simulations compared to experiments [18], which are in excellent agreement with each other, thus further corroborating the appropriate parameterization of our simulation model.

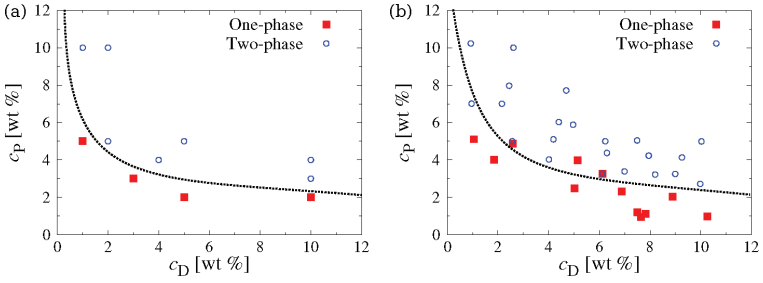

Figure 3. Phase diagram of PEG–Dextran blends in bulk from (**a**) simulations and (**b**) experiments [18]. The dotted lines indicate the estimated binodal. Simulation data are generated from monodisperse systems with $M_n^P = 6$ kg/mol and $M_n^D = 500$ kg/mol, while experimental data were gathered for blends with $M_w^P = 6$ kg/mol and $M_w^D = 500$ kg/mol.

3.2. Phase Behavior in Confinement

In recent experiments by Watanabe et al., the confinement-induced phase separation of PEG–Dextran mixtures was observed for droplets with radii $R < 20\,\mu$m [18]. Simulating such large droplets is computationally infeasible, even at the employed level of coarse-graining (see Methods section), as roughly 7×10^9 particles would already be needed to represent a droplet with $R = 5\,\mu$m. Therefore, we performed simulations at two smaller radii, i.e., $R \approx 260$ nm and $R \approx 380$ nm, which should still allow us to capture the effect of confinement on the phase behavior. Further, we considered mixtures containing either monodisperse or polydisperse Dextran chains, since high-molecular-weight Dextran usually has a broad molecular weight distribution; for example, the Dimova group used Dextran chains with $M_w \approx 380 - 490$ kg/mol and dispersities in the range of $Đ \equiv M_w/M_n \approx 1.8 - 2.2$ [7,41,44], while the Yanagisawa group used Dextran with $M_w \approx 500$ kg/mol and $Đ \approx 3.1$ [17,18]. In our simulations with polydisperse Dextran chains, we drew the molecular weight of each polymer from a Gaussian distribution, targeting $Đ \approx 1.5$ and $M_n \approx 500$ kg/mol. The PEG chains were kept monodisperse throughout, which is consistent with the rather small polydispersity of $Đ \approx 1.1$ reported in the experimental literature for low-molecular-weight PEG [7,17,44]. In all simulations, we selected

the number of PEG and Dextran chains so that $c_P = 3\,\text{wt\%}$ and $c_D = 3\,\text{wt\%}$, averaged over the entire droplet volume, which lies in the mixed one-phase regime of the bulk phase diagram (see Section 3.1).

To study the spatial distribution of the PEG and Dextran polymers in the droplet, we first calculated the radial monomer concentration profiles $c(r)$ of the two species (Figure 4), which reveal several important features: (i) in all cases, there is a local surplus and layering of PEG near the droplet surface, which is typical for short molecules close to hard walls [45]. In contrast, the long Dextran polymers are depleted from the droplet surface because of the associated loss in conformational entropy in that region [11]. In the monodisperse case, the width of this depletion zone is roughly $2\,R_g^D \approx 50\,\text{nm}$, with $R_g^D \approx 23.8\,\text{nm}$ being the radius of gyration of a Dextran chain at infinite dilution. In contrast, the excluded region is much wider for the polydisperse case due to the broader R_g^D spectrum; (ii) as a result, the Dextran concentration in the droplet center becomes distinctly larger than the average value (3 wt%), reaching almost 8 wt% for the polydisperse case in the small droplets (see Figure 4). By comparison, the concentration of PEG chains near the droplet center is only slightly below the average. (iii) As expected, the effect of confinement is significantly more pronounced in the smaller droplet, since the region close to the droplet surface occupies a larger volume fraction, i.e., $1 - (R - 2R_g^D)^3/R^3 \approx 0.45$ for $R = 260\,\text{nm}$ vs. ≈ 0.33 for $R = 380\,\text{nm}$.

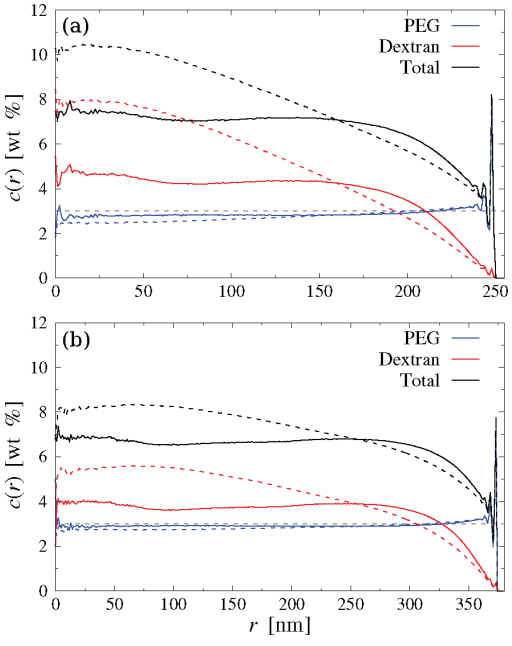

Figure 4. Radial monomer concentration profiles for droplets with (**a**) $R \approx 260\,\text{nm}$ and (**b**) $R \approx 380\,\text{nm}$. Solid and dashed lines show simulation results for monodisperse and polydisperse Dextran chains, respectively. The horizontal dashed grey line indicates the average polymer concentration of each species (3 wt%).

We analyzed the shape of the confined Dextran chains by computing their radius of gyration tensor

$$\mathbf{G} = \frac{1}{N_D} \sum_i^{N_D} \Delta\mathbf{r}_i \Delta\mathbf{r}_i^T, \tag{8}$$

with $\Delta \mathbf{r}_i$ being the position of monomer i relative to the polymer's center of mass. The root-mean-square radius of gyration is then $R_g \equiv \left\langle R_g^2 \right\rangle^{1/2} = \langle G_n + 2G_t \rangle^{1/2}$, where G_n and G_t are the components of $\mathbf{G}$ normal and tangential relative to the droplet surface, respectively. Figure 5 shows these components for monodisperse Dextran vs. the distance between the polymer's center of mass and the droplet surface. Polymers at distances larger than $\approx 2\,R_g$ have isotropic shapes, $\langle G_n \rangle^{1/2} = \langle G_t \rangle^{1/2} \approx 12\,\text{nm}$, whereas they become increasingly compressed along the normal direction as they approach the droplet surface (the tangential component is nearly constant). Further, chain conformations in the small and large droplets are almost indistinguishable.

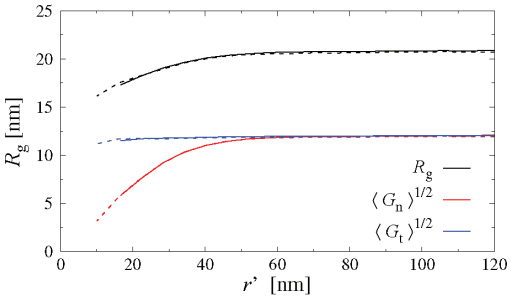

Figure 5. Radial profiles of the radius of gyration of monodisperse Dextran, R_g, and its normal ($\langle G_n \rangle^{1/2}$) and tangential ($\langle G_t \rangle^{1/2}$) components relative to the droplet surface. Data plotted against the distance between the droplet surface and the polymer's center of mass, r'. Solid and dashed lines show results for $R \approx 260\,\text{nm}$ and $R \approx 380\,\text{nm}$, respectively.

The confinement-induced increase in the polymer concentration near the droplet center could induce a phase separation of the PEG and Dextran chains there, as the local polymer concentration might cross the binodal of the mixtures (cf. Figure 3). Figure 6 shows simulation snapshots for the monodisperse and polydisperse systems confined in large droplets: while the monodisperse system appears to be still in the mixed one-phase regime, we can clearly see large Dextran aggregates in the polydisperse case, which is in excellent agreement with recent experiments by Watanabe et al. [18]. Looking more closely at the simulation snapshot, we can see that the aggregates in the polydisperse systems primarily consist of longer Dextran chains, whereas the shorter ones still remain well dispersed. Zhao et al. observed a similar molar mass fractionation in aqueous two-phase polymer solutions of PEG and Dextran [7], where the longer Dextran chains accumulated in the Dextran-rich phase, while the shorter Dextran chains were contained in the PEG-rich phase.

To better understand the distinct differences between the behavior of the monodisperse and polydisperse mixtures, we determined the probability $P(r)$ of finding Dextran chains at center-of-mass position r, itemized by their molecular weight. These results are shown in Figure 6b,c for both droplet sizes, revealing a distinct spatial fractionation of the Dextran chains: short polymers with $M_n < 250\,\text{kg/mol}$ are distributed almost homogeneously throughout the droplet and also come much closer to the droplet surface compared to the longer chains. In contrast, longer Dextran chains are moving to the droplet center to maximize their conformational entropy. These findings are consistent with recent experiments [18], where Watanabe et al. inferred from surface tension measurements that short Dextran chains ($M_w \ll 500\,\text{kg/mol}$) preferentially adsorbed to the droplet surface. This radial partitioning of short and long Dextran chains promotes their phase separation, as longer chains have a distinctly smaller entropy of mixing compared to their shorter counterparts [32].

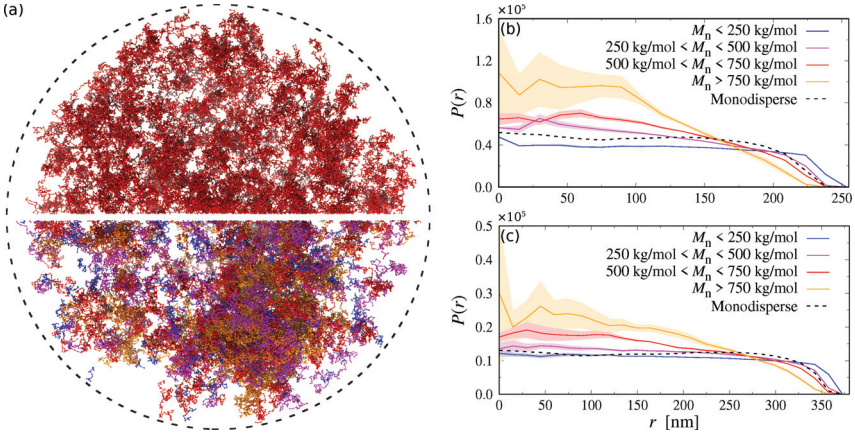

Figure 6. (**a**) Simulation snapshot of the confined systems ($R \approx 380$ nm, indicated by dashed circle). The top half shows the monodisperse case with Dextran chains colored in red. The bottom half shows the polydisperse case with Dextran chains colored according to their molecular weight as in panels (**b**,**c**). Water and PEG particles have been omitted for clarity. (**b**,**c**) Probability $P(r)$ to find a Dextran chain in the specified molecular weight range at center-of-mass position r in a droplet with (**b**) $R \approx 260$ nm and (**c**) $R \approx 380$ nm. The shaded area indicates the standard deviation from three independent runs. The dashed black line shows the distribution of the monodisperse case.

Finally, we quantified the size of the aggregates through the radial concentration profile $c_D(r)$ of Dextran monomers belonging to the largest cluster, and through the average number of Dextran monomers in a cluster, $\langle M \rangle$, as explained in Section 3.1 above. To establish a reference, we performed additional simulations of ideal mixtures by setting $\chi_{ij} = 0$ and determined the corresponding mean aggregation number $\langle M \rangle_0$. The concentration profiles are shown in Figure 7, revealing that the Dextran clusters in the polydisperse confined systems are much larger and more concentrated compared to the monodisperse systems in bulk as well as in confinement.

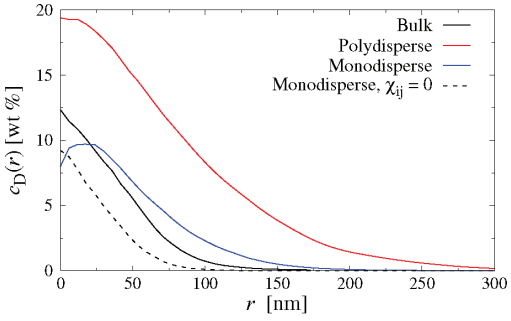

Figure 7. Radial concentration profile of Dextran monomers $c_D(r)$ in the largest Dextran aggregate in bulk and droplet systems ($R \approx 380$ nm) at overall average concentration $c_P = 3$ wt% and $c_D = 3$ wt%.

Table 1 summarizes the results of $\langle M \rangle$ for all droplet simulations, which will be discussed in the following: For ideal mixtures with monodisperse Dextran chains, we find $\langle M \rangle_0 \approx 100$, which is comparable to the number of monomers per Dextran chain ($N_D = 80$). This value is sensible given that $\chi_{ij} = 0$ and that the search radius of the clustering algorithm is slightly larger than the average segment length of our Dextran model ($b \approx 5.5$ nm). For polydisperse Dextran in the smaller droplets ($R = 260$ nm), the mean aggregation number increases to $\langle M \rangle_0 \approx 380$ due to an accumulation of longer

Dextran chains in the droplet center, even at ideal conditions. This effect is considerably less pronounced in the larger droplets (cf. Figure 6), where we find $\langle M \rangle_0 \approx 110$ instead. For the non-ideal mixtures with monodisperse Dextran, we find $\langle M \rangle \approx 1300 - 1600$, which indicates the existence of small aggregates consisting of $15 - 20$ Dextran chains (there are, in total, 348 and 1175 Dextran chains in the small and large droplets, respectively). The mean aggregation number becomes significantly larger in polydisperse PEG–Dextran mixtures, reaching values up to $\langle M \rangle \approx 10,000$. Interestingly, $\langle M \rangle$ is about two times smaller in the smaller droplets (see Table 1), which is likely a finite-size effect, as the smaller droplets contain about three times fewer Dextran chains compared to the large droplets. Nevertheless, both systems show clearly that the confinement-induced fractionation of short and long Dextran chains drives phase separation, as observed in recent experiments [18].

Table 1. Mean number $\langle M \rangle$ of Dextran segments in a Dextran aggregate ($\langle M \rangle_0$ corresponds to ideal mixtures with $\chi_{ij} = 0$).

	Monodisperse		**Polydisperse**	
R	$\langle M \rangle$	$\langle M \rangle_0$	$\langle M \rangle$	$\langle M \rangle_0$
260 nm	1600 ± 60	100 ± 5	5300 ± 1200	380 ± 20
380 nm	1300 ± 30	97 ± 4	9800 ± 1600	110 ± 3

4. Conclusions

To better understand the phase behavior and conformations of (bio)polymers in droplets, we have performed coarse-grained molecular simulations of binary polymer mixtures in spherical confinement. We have parameterized our model to closely mimic the behavior of aqueous PEG–Dextran mixtures and have considered both monodisperse and polydisperse molecular weight distributions for the Dextran chains. Simulations have been conducted for two droplet sizes at polymer concentrations lying in the mixed one-phase region in bulk. In spherical confinement, we have found a distinct spatial separation of the polymers by length, with the longer ones accumulating at the droplet center to maximize their conformational entropy. Furthermore, chains near the droplet surface became increasingly compressed along their normal direction. This confinement-induced partitioning was much more pronounced in the polydisperse systems and caused the phase separation of the two polymer species at average polymer concentrations where the bulk system was still in the one-phase regime.

Although we have chosen the model parameters to replicate PEG–Dextran mixtures, the rather generic nature of our coarse-grained model makes our results applicable to a wide range of different polymer mixtures. Our simulations demonstrate how the distribution of polymers is affected by confinement effects, even at good solvent conditions, with longer chains moving to the droplet center to maximize entropy. The resulting spatial inhomogeneity can drastically alter the phase behavior of the confined polymers, which is important for understanding, e.g., the liquid–liquid phase separation of biopolymers in cellular environments. Furthermore, our simulations provide useful guidelines for the fabrication of polymer-loaded droplets. For example, by tuning the interactions between the droplet surface and the different polymer species, one can either enhance or suppress their spatial separation and thus control the resulting phase behavior and surface tension.

Author Contributions: Conceptualization, A.N. and M.Y.; methodology, A.N.; software, A.N.; validation, A.N.; formal analysis, A.N.; investigation, A.N. and M.Y.; resources, A.N. and M.Y.; data curation, A.N.; writing—original draft preparation, A.N.; writing—review and editing, A.N. and M.Y.; visualization, A.N.; supervision, A.N. and M.Y.; project administration, A.N. and M.Y.; funding acquisition, A.N. All authors have read and agreed to the published version of the manuscript.

Funding: This work was supported by the Deutsche Forschungsgemeinschaft (DFG, German Research Foundation) through Project No. 470113688. M.Y. acknowledges funding by the Japan Society for the Promotion of Science (JSPS) KAKENHI (grant number 22H01188) and by the Japan Science and Technology Agency (JST) Program FOREST (grant number JPMJFR213Y).

Institutional Review Board Statement: Not applicable.

Informed Consent Statement: Not applicable.

Data Availability Statement: The data that support the findings of this study are available from the corresponding author upon reasonable request.

Acknowledgments: We thank Chiho Watanabe (Hiroshima University, Japan) for fruitful discussions.

Conflicts of Interest: The authors declare no conflict of interest.

References

1. Brangwynne, C.P.; Eckmann, C.R.; Courson, D.S.; Rybarska, A.; Hoege, C.; Gharakhani, J.; Jülicher, F.; Hyman, A.A. Germline P Granules Are Liquid Droplets That Localize by Controlled Dissolution/Condensation. *Science* **2009**, *324*, 1729–1732. [CrossRef] [PubMed]
2. Hyman, A.A.; Weber, C.A.; Jülicher, F. Liquid-Liquid Phase Separation in Biology. *Annu. Rev. Cell Dev. Biol.* **2014**, *30*, 39–58. [CrossRef] [PubMed]
3. Martin, E.W.; Holehouse, A.S.; Peran, I.; Farag, M.; Incicco, J.J.; Bremer, A.; Grace, C.R.; Soranno, A.; Pappu, R.V.; Mittag, T. Valence and patterning of aromatic residues determine the phase behavior of prion-like domains. *Science* **2020**, *367*, 694–699. [CrossRef] [PubMed]
4. Zimmermann, S.B.; Trach, S.O. Estimation of macromolecule concentrations and excluded volume effects for the cytoplasm of Escherichia coli. *J. Mol. Biol.* **1991**, *222*, 599. [CrossRef]
5. Matha, S.; Qi, S.; Barz, M.; Schmid, F. How ill-defined constituents produce well-defined nanoparticles: Effect of polymer dispersity on the uniformity of copolymeric micelles. *Phys. Rev. Materials* **2019**, *3*, 026002. [CrossRef]
6. van Heukelum, A.; Barkema, G.T.; Edelman, M.W.; van der Linden, E.; de Hoog, E.H.A.; Tromp, R.H. Fractionation in a Phase-Separated Polydisperse Polymer Mixture. *Macromolecules* **2003**, *36*, 6662–6667. [CrossRef]
7. Zhao, Z.; Li, Q.; Ji, X.; Dimova, R.; Lipowsky, R.; Liu, Y. Molar mass fractionation in aqueous two-phase polymer solutions of dextran and poly(ethylene glycol). *J. Chromatogr. A* **2016**, *1452*, 107–115. [CrossRef]
8. Nikoubashman, A. Ordering, phase behavior, and correlations of semiflexible polymers in confinement. *J. Chem. Phys.* **2021**, *154*, 090901. [CrossRef]
9. Zhou, X.; Guo, F.; Li, K.; He, L.; Zhang, L. Entropy-Induced Separation of Binary Semiflexible Ring Polymer Mixtures in Spherical Confinement. *Polymers* **2019**, *11*, 1992. [CrossRef]
10. Zhou, X.; Wu, J.; Zhang, L. Ordered aggregation of semiflexible ring-linear blends in ellipsoidal confinement. *Polymer* **2020**, *197*, 122494. [CrossRef]
11. Howard, M.P.; Nikoubashman, A. Stratification of polymer mixtures in drying droplets: Hydrodynamics and diffusion. *J. Chem. Phys.* **2020**, *153*, 054901. [CrossRef] [PubMed]
12. Merindol, R.; Loescher, S.; Samanta, A.; Walther, A. Pathway-controlled formation of mesostructured all-DNA colloids and superstructures. *Nat. Nanotechnol.* **2018**, *13*, 730–738. [CrossRef] [PubMed]
13. Samanta, A.; Sabatino, V.; Ward, T.R.; Walther, A. Functional and morphological adaptation in DNA protocells via signal processing prompted by artificial metalloenzymes. *Nat. Nanotechnol.* **2020**, *15*, 914–921. [CrossRef] [PubMed]
14. Dominak, L.M.; Gundermann, E.L.; Keating, C.D. Microcompartmentation in Artificial Cells: pH-Induced Conformational Changes Alter Protein Localization. *Langmuir* **2010**, *26*, 5697–5705. [CrossRef]
15. Monterroso, B.; Zorrilla, S.; Sobrinos-Sanguino, M.; Keating, C.D.; Rivas, G. Microenvironments created by liquid-liquid phase transition control the dynamic distribution of bacterial division FtsZ protein. *Sci. Rep.* **2016**, *6*, 35140. [CrossRef]
16. Yanagisawa, M.; Watanabe, C.; Yoshinaga, N.; Fujiwara, K. Cell-Size Space Regulates the Behavior of Confined Polymers: From Nano- and Micromaterials Science to Biology. *Langmuir* **2022**, *38*, 11811–11827. [CrossRef]
17. Yanagisawa, M. Cell-size space effects on phase separation of binary polymer blends. *Biophys. Rev.* **2022**, *22*, 1093–1103. [CrossRef]
18. Watanabe, C.; Furuki, T.; Kanakubo, Y.; Kanie, F.; Koyanagi, K.; Takeshita, J.; Yanagisawa, M. Cell-sized confinement initiates phase separation of polymer blends and promotes fractionation upon competitive membrane wetting. *ACS Materials Lett.* **2022**, *4*, 1742–1748. [CrossRef]
19. Hoogerbrugge, P.J.; Koelman, J.M.V.A. Simulating microscopic hydrodynamic phenomena with dissipative particle dynamics. *EPL* **1992**, *19*, 155. [CrossRef]
20. Español, P.; Warren, P.B. Statistical mechanics of dissipative particle dynamics. *EPL* **1995**, *30*, 191. [CrossRef]
21. Groot, R.D.; Warren, P.B. Dissipative particle dynamics: Bridging the gap between atomistic and mesoscopic simulation. *J. Chem. Phys.* **1997**, *107*, 4423. [CrossRef]
22. Liu, Y.; Lipowsky, R.; Dimova, R. Giant vesicles encapsulating aqueous two-phase systems: From phase diagrams to membrane shape transformations. *Front. Chem.* **2019**, *7*, 213. [CrossRef] [PubMed]
23. Larm, O.; Lindberg, B.; Svensson, S. Studies on the length of the side chains of the dextran elaborated by Leuconostoc mesenteroides NRRL B-512. *Carbohydr. Res.* **1971**, *20*, 39–48. [CrossRef] [PubMed]
24. Görisch, S.M.; Wachsmuth, M.; Tóth, K.F.; Lichter, P.; Rippe, K. Histone acetylation increases chromatin accessibility. *J. Cell Sci.* **2005**, *118*, 5825. [CrossRef]

25. Louis, A.A.; Bolhuis, P.G.; Hansen, J.P.; Meijer, E.J. Can Polymer Coils Be Modeled as "Soft Colloids"? *Phys. Rev. Lett.* **2000**, *85*, 2522. [CrossRef]
26. Likos, C.N. Effective interactions in soft condensed matter physics. *Phys. Rep.* **2001**, *348*, 267–439.
27. Berressem, F.; Scherer, C.; Andrienko, D.; Nikoubashman, A. Ultra-Coarse-Graining of Homopolymers in Inhomogeneous Systems. *J. Phys. Condens. Matter* **2021**, *33*, 254002. [CrossRef]
28. Groot, R.D.; Madden, T.J. Dynamic simulation of diblock copolymer microphase separation. *J. Chem. Phys.* **1998**, *108*, 8713. [CrossRef]
29. Petrus, P.; Lísal, M.; Brennan, J.K. Self-Assembly of Lamellar- and Cylinder-Forming Diblock Copolymers in Planar Slits: Insight from Dissipative Particle Dynamics Simulations. *Langmuir* **2010**, *26*, 14680–14693. [CrossRef]
30. Gavrilov, A.A.; Kudryavtsev, Y.V.; Chertovich, A.V. Phase diagrams of block copolymer melts by dissipative particle dynamics simulations. *J. Chem. Phys.* **2013**, *139*, 224901. [CrossRef]
31. Steinhaus, A.; Srivastva, D.; Nikoubashman, A.; Gröschel, A.H. Janus Nanostructures from ABC/B Triblock Terpolymer Blends. *Polymers* **2019**, *11*, 1107. [CrossRef] [PubMed]
32. Rubinstein, M.; Colby, R.H. *Polymer Physics*; Oxford University Press: Oxford, UK, 2003.
33. Weeks, J.D.; Chandler, D.; Andersen, H.C. Role of Repulsive Forces in Determining the Equilibrium Structure of Simple Liquids. *J. Chem. Phys.* **1971**, *54*, 5237. [CrossRef]
34. Groot, R.D.; Rabone, K.L. Mesoscopic simulation of cell membrane damage, morphology change and rupture by nonionic surfactants. *Biophys. J.* **2001**, *81*, 725–736. [CrossRef]
35. Luo, Z.; Jiang, J. pH-sensitive drug loading/releasing in amphiphilic copolymer PAE–PEG: Integrating molecular dynamics and dissipative particle dynamics simulations. *J. Control. Release* **2012**, *162*, 185–193. [CrossRef] [PubMed]
36. Saeki, S.; Kuwahara, N.; Nakata, M.; Kaneko, M. Upper and lower critical solution temperatures in poly(ethylene glycol) solutions. *Polymer* **1976**, *17*, 685. [CrossRef]
37. Bercea, M.; Nichifor, M.; Eckelt, J.; Wolf, B.A. Dextran-based polycations: Thermodynamic interaction with water as compared with unsubstituted Dextran, 2 – Flory/Huggins interaction parameter. *Macromol. Chem. Phys.* **2011**, *212*, 1932–1940. [CrossRef]
38. Clark, A.H. Direct analysis of experimental tie line data two polymer–one solvent systems) using Flory–Huggins theory. *Carbohydr. Polym.* **2000**, *42*, 337–351. [CrossRef]
39. Edmond, E.; Ogston, A.G. An approach to the study of phase separation in ternary aqueous systems. *Biochem. J.* **1968**, *109*, 569–576. [CrossRef]
40. King, R.S.; Blanch, H.W.; Prausnitz, J.M. Molecular thermodynamics of aqueous two-phase systems for bioseparations. *AIChE J.* **1988**, *34*, 1585–1594. [CrossRef]
41. Liu, Y.; Lipowsky, R.; Dimova, R. Concentration dependence of the interfacial tension for aqueous two-phase polymer solutions of Dextran and polyethylene glycol. *Langmuir* **2012**, *28*, 3831–3839. [CrossRef]
42. Humphrey, W.; Dalke, A.; Schulten, K. VMD - Visual Molecular Dynamics. *J. Molec. Graphics* **1996**, *14*, 33–38. [CrossRef] [PubMed]
43. Ester, M.; Kriegel, H.P.; Sander, J.; Xu, X. A density-based algorithm for discovering clusters in large spatial databases with noise. *Proc. Second Int. Conf. Knowl. Discov. Data Min.* **1996**, *96*, 226.
44. Li, Y.; Lipowsky, R.; Dimova, R. Transition from complete to partial wetting within membrane compartments. *J. Am. Chem. Soc.* **2008**, *130*, 12252–12253. [CrossRef] [PubMed]
45. Snook, I.K.; Henderson, D. Monte Carlo study of a hard-sphere fluid near a hard wall. *J. Chem. Phys.* **1978**, *68*, 2134. [CrossRef]

Disclaimer/Publisher's Note: The statements, opinions and data contained in all publications are solely those of the individual author(s) and contributor(s) and not of MDPI and/or the editor(s). MDPI and/or the editor(s) disclaim responsibility for any injury to people or property resulting from any ideas, methods, instructions or products referred to in the content.

polymers

MDPI

Article

Influence of DNA Type on the Physicochemical and Biological Properties of Polyplexes Based on Star Polymers Bearing Different Amino Functionalities

Emi Haladjova [1,*], Silvia Panseri [2], Monica Montesi [2], Arianna Rossi [2,3], Athanasios Skandalis [4], Stergios Pispas [4] and Stanislav Rangelov [1,*]

[1] Institute of Polymers, Bulgarian Academy of Sciences, Acad. G. Bonchev st. bl.103A, 1113 Sofia, Bulgaria
[2] Institute of Science, Technology and Sustainability for Ceramics, National Research Council of Italy, Via Granarolo 64, 48018 Faenza, Italy
[3] Department of Chemical, Biological, Pharmaceutical and Environmental Sciences, University of Messina, 98166 Messina, Italy
[4] Theoretical and Physical Chemistry Institute, National Hellenic Research Foundation, 48 Vass. Constantinou Ave., 116 35 Athens, Greece
* Correspondence: ehaladjova@polymer.bas.bg (E.H.); rangelov@polymer.bas.bg (S.R.)

Abstract: The interactions of two star polymers based on poly (2-(dimethylamino)ethyl methacrylate) with different types of nucleic acids are investigated. The star polymers differ only in their functionality to bear protonable amino or permanently charged quaternary ammonium groups, while DNAs of different molar masses, lengths and topologies are used. The main physicochemical parameters of the resulting polyplexes are determined. The influence of the polymer' functionality and length and topology of the DNA on the structure and properties of the polyelectrolyte complexes is established. The quaternized polymer is characterized by a high binding affinity to DNA and formed strongly positively charged, compact and tight polyplexes. The parent, non-quaternized polymer exhibits an enhanced buffering capacity and weakened polymer/DNA interactions, particularly upon the addition of NaCl, resulting in the formation of less compact and tight polyplexes. The cytotoxic evaluation of the systems indicates that they are sparing with respect to the cell lines studied including osteosarcoma, osteoblast and human adipose-derived mesenchymal stem cells and exhibit good biocompatibility. Transfection experiments reveal that the non-quaternized polymer is effective at transferring DNA into cells, which is attributed to its high buffering capacity, facilitating the endo-lysosomal escape of the polyplex, the loose structure of the latter one and weakened polymer/DNA interactions, benefitting the DNA release.

Keywords: gene delivery; star-shaped polymers; amino functionality; DNA structure; polycations; polyplexes; transfection

Citation: Haladjova, E.; Panseri, S.; Montesi, M.; Rossi, A.; Skandalis, A.; Pispas, S.; Rangelov, S. Influence of DNA Type on the Physicochemical and Biological Properties of Polyplexes Based on Star Polymers Bearing Different Amino Functionalities. *Polymers* **2023**, *15*, 894. https://doi.org/10.3390/polym15040894

Academic Editors: Fahmi Zaïri, Matthias Ballauff, Ulrich Maschke and Rufina G. Alamo

Received: 20 December 2022
Revised: 20 January 2023
Accepted: 7 February 2023
Published: 10 February 2023

Copyright: © 2023 by the authors. Licensee MDPI, Basel, Switzerland. This article is an open access article distributed under the terms and conditions of the Creative Commons Attribution (CC BY) license (https://creativecommons.org/licenses/by/4.0/).

1. Introduction

The delivery of nucleic acids is of great importance since it enables the development of modern therapeutic drugs and treatment strategies [1–4]. Nucleic acid transfer, however, is related to the use of vectors as vehicles to deliver the genetic material into the cells. Although approved therapies with viral vectors already exist [5], preference is currently given to non-viral carriers [6–8], since they display significant advantages and potential benefits including a controllable chemical diversity, possibilities for low costs, large-scale production in a more facile way, a larger payload capacity, better safety profiles and a reduced immunogenic response.

Cationic polymers are a major class of non-viral vectors for nucleic acids delivery [9–11]. Various polymer-based systems have been developed and studied as potential DNA carriers, though they have some limitations, which hinder their practical use [9–11]. The potential of cationic polymers containing amino or ammonium functionality

is due to their ability to bind and condense negatively charged nucleic acids through electrostatic interactions. In the resulting nanoparticulate structures, known as polyplexes, nucleic acids molecules are compacted and protected from enzymatic degradation. Such compact structures facilitate the uptake, but for efficient delivery, a successful release of the nucleic acids' cargo molecules is required. The polymer complexation ability is known to strongly depend on the amino functionality [7,9,11,12]. For example, quaternary ammonium groups and primary amine groups, most of which are protonated at the physiological pH, are permanently charged and characterized by a high binding affinity [13,14]. However, the nucleic acid release from the polyplexes is impeded by strong polymer/nucleic acid interactions. Polymers bearing secondary and tertiary amine groups form less strong complexes, but since these amine groups can be protonated, depending on pH of the medium, they are responsible for the successful endosomal escape of the polyplex and more efficient transfection [15,16]. The polymer/nucleic acid interactions are also known to depend on the molar mass of the two partners [17–22]. It has repeatedly been shown that the longer the polymer chain is, the stronger the nucleic acid binding affinity is [17–20]. The impact of the nucleic acid strands scale is significant as well [18,20–22]. Short linear DNA fragments (below 100 bp) are rigid and unable to bend spontaneously, whereas the longer molecules are flexible and capable of being shrunk and wrapped [23,24].

A number of physicochemical parameters of the resulting polyplexes, e.g., size, surface potential, colloidal stability in biological fluids, etc., are determinant factors for the biological performance of the systems [25]. However, a remaining challenge for the clinical utilization of such systems is the inherent cytotoxicity of the polyplexes due to the cationic character of the polymers utilized. Therefore, achieving a proper balance between a high transfection efficiency and a low toxicity profile is of significant importance. This relationship is known to strongly depend not only on the amino functionality (primary amino and quaternary ammonium groups are usually associated with high toxicity), but also on factors such as polymer composition, structure and topology, charge density, etc. [9,12,26]. Thus, polymers of branched topology were found to be more effective than the linear ones are, but they were also more toxic [27,28]. The molar mass is also known to strongly affect the efficiency/toxicity ratio, as high molar mass vectors are more effective, but they are associated with enhanced toxicity [26,29]. The type (RNA or DNA), structure (single or double stranded) and topology (linear or circular) of nucleic acids are also determinants of the behavior and physicochemical properties of the resulting vector systems [20–22].

We have previously evaluated and compared the physicochemical characteristics and biological performance of polyplexes based on linear copolymers composed of cationic blocks bearing tertiary amino and quaternary ammonium groups [30]. With the present study, we expand this work to investigate polymers of non-linear chain architecture, which, in general, exhibit a superior gene delivery ability, and to study the effects of the nucleic acid length and type. The aim of this work is to evaluate the interactions of two identical star-shaped polymers bearing tertiary amino or quaternary ammonium groups with nucleic acids of different molar mass and structure and to estimate how this relates to the physicochemical and biological behavior of the resulting systems. The polymers are based on poly(2-(dimethylamino)ethyl methacrylate) (PDMAEMA)—a highly promising cationic polymer with many desirable properties for developing efficient non-viral gene delivery systems. Polyplexes in a wide range of N/P ratios (N/P is the ratio of the positively charged polymer amine groups to negatively charged nucleic acid phosphate groups) were prepared using different types of nucleic acids: short linear segments, long linear molecules and circular/plasmid DNA. The effects of the length and topology of DNA and polymer amino functionality on the structure and properties of the resulting polyelectrolyte complexes were investigated by dynamic and electrophoretic light scattering. The cell viability and morphology, as well as in vitro transfection efficiency, of the investigated systems were evaluated using several representative human cell lines including osteosarcoma, osteoblast and human adipose-derived mesenchymal stem cells.

2. Materials and Methods

2.1. Materials

All of Sigma-Aldrich reagents were purchased from Merck-Bulgaria (Sofia, Bulgaria). Linear DNA sodium salt from salmon sperm (molar mass ~ 115 bp, denoted as lDNA 115) was purchased from Acros, linear DNA sodium salt from salmon testes (molar mass~2000 bp, denoted as lDNA 2000) was purchased from Sigma-Aldrich and plasmid DNA containing the gene encoding for the enhanced green fluorescent reporter protein (eGFP, molar mass~4730 bp, denoted as pDNA 4730) was purchased from Clontech (Palo Alto, CA, USA) and propagated in E. coli DH5 alpha strain (ThermoFisher Scientific, Walthman, MA, USA). For the preparation of DNA and polymer solutions, ultra-pure milliQ water (resistivity > 18 MΩ.cm) was used.

2.1.1. Synthesis and Quaternization of Star-Like PDMAEMA

The synthesis of star-like poly(2-(dimethylamino)ethyl methacrylate) (PDMAEMA) was achieved by RAFT polymerization using the "arm-first" method. At first, low molecular weight, linear PDMAEMA arms [31] were prepared by RAFT polymerization using 2,2′-azobis(2-methylpropionitrile) (AIBN) and 4-cyano-4-((dodecylsulfanylthiocarbonyl)-sulfanyl)pentanoic acid (CDTP) as the radical initiator and the chain transfer agent (CTA), respectively. The linear PDMAEMA homopolymers were used as macro-CTA for the synthesis of star-like PDMAEMA, with ethylene glycol dimethacrylate (EGDM) being the cross-linked core. The synthetic procedure has been described in detail elsewhere [32].

To impart permanent positive charges, the tertiary amine groups of the PDMAEMA arms were converted into quaternary ammonium groups via a quaternization reaction using methyl iodide (CH_3I). The conversion was analyzed quantitatively, and more details about this procedure can be found elsewhere [32].

2.1.2. Preparation of Polymer Solutions

The star-like PDMAEMA polymer was placed in an aqueous medium, followed by the addition of a weak acid (0.1 M HCl) until the full dissolution of the polymer. The quaternized polymer was spontaneously dissolved in pure water. The pH of all of the polymer solutions was adjusted to 7 by adding 0.1 M NaOH. The concentration of the stock polymer solutions was 1000 $\mu g.mL^{-1}$.

2.1.3. Polyplex Formation

The polyplexes were formed by mixing the polymer (100 $\mu g.mL^{-1}$) and DNA (100 $\mu g.mL^{-1}$ for lDNAs and 50 $\mu g.mL^{-1}$ for pDNA) aqueous solutions at ambient temperature during vortexing. The amounts of polymer and DNA solutions were selected to obtain amino-to-phosphate groups (N/P) ratios in the 0.5–10 range.

2.1.4. Cell Culture

Human osteosarcoma cell line (MG63, ATCC CRL-1427, ATCC, Manassas, VA, USA), human osteoblast cell line (hFOBs, ATCC CRL-11372, ATCC) and human adipose-derived mesenchymal stem cells (MSCs, ATCC PCS-500-011, ATCC) were used to test the materials. In detail, MG63 was cultured in DMEM/F-12 with GlutaMAX (Gibco, Langley, OK, USA), 10% Fetal Bovine Serum (FBS, Gibco) and 1% penicillin-streptomycin (pen/strep, 100 $U.mL^{-1}$–100 $\mu g.mL^{-1}$); hFOBs were cultured in DMEM/F-12 without phenol red (Gibco), with 10% Fetal Bovine Serum (FBS, Gibco) and 0.3 $mg.mL^{-1}$ Geneticin (G418, Gibco); MSCs were cultured in Alpha-MEM Glutamax (Gibco), 15% Fetal Bovine Serum (FBS, Gibco), 10 $ng.mL^{-1}$ recombinant human FGF-basic (Gibco) and 1% penicillin-streptomycin (pen/strep, 100 $U.mL^{-1}$–100 $\mu g.mL^{-1}$). The cell cultures were kept at 37 °C in an atmosphere of 5% CO_2. The cells were detached from culture flasks by trypsinization, centrifuged and re-suspended in fresh media. The cell number and viability were assessed using a trypan blue dye exclusion test; all of the cell handling procedures were performed in a sterile laminar flow hood.

2.2. Methods

2.2.1. Dynamic Light Scattering (DLS) and Electrophoretic Light Scattering (ELS)

The dynamic and electrophoretic light scattering measurements were performed on a 90Plus PALS instrument (Brookhaven Instruments Corporation) equipped with a 35 mW red diode laser (λ = 640 nm). The hydrodynamic diameter (D_h) was determined at a scattering angle (θ) of 90°, while the ζ potential was determined by phase analysis light scattering (PALS) method at a scattering angle (θ) of 15°. Each measurement was performed in triplicate.

2.2.2. Transmission Electron Microscopy (TEM)

The samples were examined using an high resolution TEM JEOL JEM-2100 electron microscope (JEOL, Tokyo, Japan) operating at 200 kV. They were prepared by depositing a drop of the solution onto a carbon grid.

2.2.3. Buffering Capacity

The buffering capacity of the PDMAEMA stars was determined by standard acid-base titration. Polymer aqueous solutions (c = 500 $\mu g.mL^{-1}$, V = 3 mL) were prepared, and the pH was adjusted to 10 by using 0.1 M NaOH. Then, titration with 0.1 M HCl to pH 3 was performed as 5 μL aliquots were added, and the pH was measured after each addition. Pure water was titrated as the control.

2.2.4. Stability of Polyplexes in Presence of Salt

To preformed polyplexes dispersions at N/P = 8, increasing amounts of NaCl solutions in the range from 0.01 to 0.25 M were added. The stability of the complexes was monitored by dynamic light scattering measurements.

2.2.5. Cell Viability Assay

Metabolically active cells were evaluated to assess the cell viability by performing an MTT assay. MSCs, hFOBs and MG63 cells were seeded in a 96-well plate (3.0×10^3 cells/well). After 24 h, polyplexes dispersions prepared with lDNAs at N/P = 8 and diluted to different concentrations (5 $\mu g.mL^{-1}$, 10 $\mu g.mL^{-1}$, 20 $\mu g.mL^{-1}$, 25 $\mu g.mL^{-1}$, 40 $\mu g.mL^{-1}$ and 50 $\mu g.mL^{-1}$) were added to the wells. Additional experiments were performed with hFOBs and MG63 cells in contact with the two star-like polymers complexed with the eGFP plasmid for 24 h. For the cell viability analysis, the cell culture in contact with the polplexes was analyzed after 24 h, 48 h and 72 h. In detail, the reagent 3-(4,5-dimethylthiazol-2-yl)-2,5-diphenyltetrazolium bromide (MTT) was dissolved in PBS 1X (5 $mg.mL^{-1}$) and incubated 1:10 for 2 h at 37 °C and 5% CO_2 at each time point. The medium was removed and dimethyl sulfoxide (DMSO) was added to dissolve formazan crystals produced by the metabolically active cells. After 15 min, the absorbance was read at λ_{max} 570 nm using the Multiskan FC Microplate Photometer (ThermoFisher Scientific, Walthman, MA, USA), and it is proportionally related to the number of metabolically active cells. For each time point, three samples were analyzed.

2.2.6. Cell Morphology Analysis

In a 24-well plate, 9.0×10^3 cells/well (hFOBs, MG63 and MSCs) were seeded, and the day after, 20 $\mu g.mL^{-1}$ of polyplexes dispersions prepared at N/P = 8 were added. The cell morphology was evaluated by observing the actin filaments after 24 h. The cells were washed two times with PBS 1X and fixed using 4% paraformaldehyde (Sigma) for 15 min at room temperature. Then, the fixed cells were permeabilized in PBS 1X with 0.1% (*v*/*v*) Triton X-100 (Sigma) for 5 min at room temperature. A PBS 1X wash was performed, and f-actin filaments were stained with FITC-conjugated fluorescein-phalloidin (LifeTechonologies, Carlsbad, CA, USA), followed by DAPI (600 nM, Invitrogen, Carlsbad, CA) counterstaining to identify the cell nuclei, following the manufacturer's instructions. The

samples were visualized using an inverted Ti-E Fluorescence Microscope (Nikon Corporation, Tokyo, Japan).

2.2.7. In Vitro Transfection

In a 96-well plate, 1.0×10^4 cells/well (hFOBs and MG63) were seeded. The following day, the media were removed, and the Opti-MEM Reduced Serum Medium (Gibco) with polyplex dispersions prepared with pDNA at N/P = 8 were added. The cells were transfected with 800 ng plasmid DNA. The polyplex dispersions were used at the final concentration of 20 $\mu g.mL^{-1}$. Lipofectamine 2000 Transfection Reagent (Invitrogen) was used as control. After 24 h, the transfection solution was removed and replaced with completed culture media. After 48 h, the cells were fixed and permeabilized as described above, then washed with PBS 1X, and DAPI (Invitrogen) staining was performed to reveal the cell nuclei. Fluorescence was derived from the transfection, and DAPI stains were detected, and images were acquired by using an Inverted Ti-E Fluorescent Microscope (Nikon Corporation, Tokyo, Japan). The transfection efficiency (% respect to Lipofectamine 2000) was calculated by counting the green fluorescence cells on the total cells number in a field; 8 fields for each condition were analyzed.

2.2.8. Statistical Analysis

A two-way analysis of variance (ANOVA) test was performed to elaborate the results of the MTT assay, and they were analyzed by using Tukey's multiple comparisons test as a post hoc test. The results are expressed as mean ± standard error of the mean (SEM) plotted on the graph. Statistical analyses were performed by GraphPad Prism software (version 8.0.1, GraphPad Software, San Diego, CA, USA).

3. Results and Discussion

3.1. Characterization and Aqueous Solution Properties of the Star-Shaped Polymers

The star-like PDMAEMA (hereinafter AF-P) was synthesized via RAFT polymerization using the "arm-first" method, which has been described in detail elsewhere [32]. The polymer consists of a cross-linked core to which an average of 25 PDMAEMA arms are attached; the average degree of polymerization of each arm is 23 [32]. The resulting molar mass (Table 1) is within the range of the molar masses of PDMAEMA-based polymers that is deemed to be optimal to achieve a decent transfection efficiency/toxicity ratio [26]. PDMAEMA polymers with larger molar mass exhibited an increased transfection efficiency, but at the same time, high toxicity [26]. In a wide range of concentration (100–1000 $\mu g.mL^{-1}$) in an aqueous solution, the AF-P polymer is characterized by a constant size and ζ potential (Table 1). AF-P exhibited strongly positive ζ-potential due to the partial protonation state of the tertiary amino groups in water [33,34]. The size distribution from DLS was narrow (Figure 1a, black curve), with a mean hydrodynamic diameter (D_h) of 11.4 nm. The later suggested molecularly dissolved state of the star-shaped polymer in the investigated concentration range.

Table 1. Molecular and physicochemical characteristics of PDMAEMA star-shaped polymers.

Sample	Code	M_w, [a] g/mol	M_w/M_n [a]	Number of Arms [b]	DP of Arm [b]	D_h, [c] nm (PDI [e])	ζ, [d] mV
Arm-first PDMAEMA	AF-P	89 000	1.37	25	23	11.4 (0.091)	24.1
Arm-first QPDMAEMA	AF-Q	169 000	1.37	25	23	15.8 (0.083)	31.6

[a] M_w, M_n and M_w/M_n are weight-averaged molar mass, number-averaged molar mass and molar mass distribution, respectively, from size exclusion chromatography [32]; [b] ^{1}H NMR [31]; [c] DLS; [d] ELS were performed in water at 25 °C and 100 $\mu g.mL^{-1}$; [e] the values of polydispersity index (PDI) are given in parenthesis.

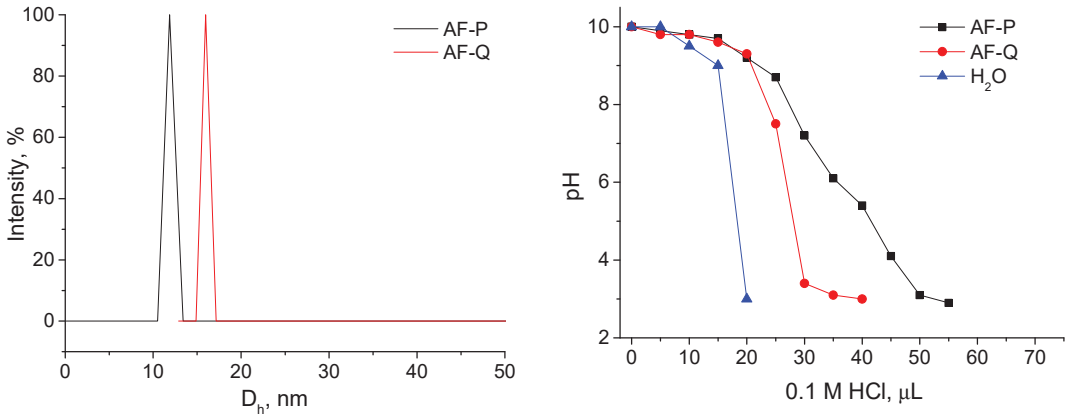

(**a**) (**b**)

Figure 1. Size distribution curves from DLS of star-shaped PDMAEMA polymers in water at 25 °C and 100 μg.mL^{-1} (**a**). pH versus volume of 0.1 M HCl curves for star-shaped PDMAEMA polymers (**b**). The titration was performed at 25 °C and initial concentration and volume of 500 μg.mL^{-1} and 3 mL, respectively.

The tertiary amines of AF-P polymer were converted into quaternary ammonium groups in order to impart permanent positive charges. This was achieved by a typical quaternization reaction using methyl iodide [32]. Thus, two identical star-like polymers bearing tertiary amino or quaternary ammonium groups and differing in their total molar masses (Table 1) were obtained. Their structure is schematically presented in Scheme 1. As expected, the quaternized polymer (hereafter, AF-Q) exhibited more positive ζ-potential than the parent AF-P polymer did (Table 1). The D_h of the AF-Q stars was slightly higher (15.8 nm), which is probably due to the presence of iodine counterion and the stronger electrostatic repulsion of the quaternized polymer chains. It is of note that the narrow size distribution was preserved, as evident from Figure 1a. The value of D_h suggested that AF-Q was also molecularly dissolved in the investigated concentration range.

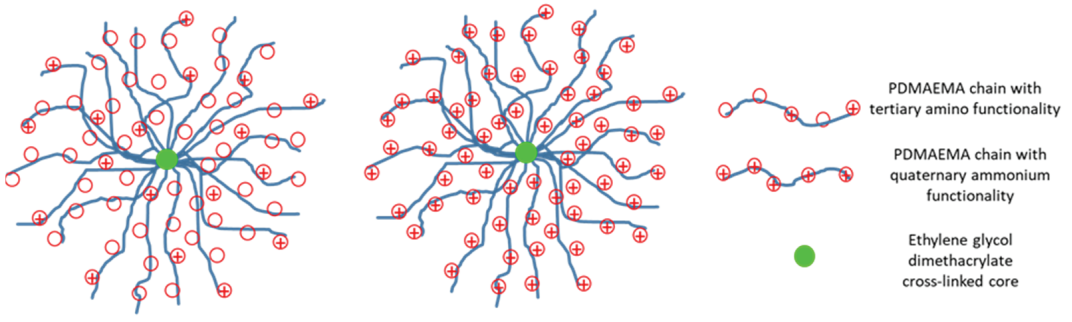

Scheme 1. Schematic presentation of the structure of the PDMAEMA-based star-like polymers.

Standard acid-base titration over a pH range from ten to three was employed to evaluate the buffering capacity of the two star-shaped polymers. The buffering capacity and the proton sponge effect are considered to be responsible for the endo-lysosomal escape of polyplexes, which is of paramount importance to avoid the enzymatic degradation of the polyplexes within the lysosomal compartments. The titration curves are presented in Figure 1b; pure water was titrated as a control. As is evident, the AF-P polymer is

characterized by a gradual change in the pH during titration due to the ability of protonable tertiary amino groups to trap protons. In contrast, the change in the pH for the quaternized AF-Q polymer was abrupt, owing to the lack of protonable moieties. In addition, an intrinsic buffering capability was calculated using the reciprocal value of the slope of curves, and the values are given in Table 2. The higher buffering capacity of the parent AF-P polymer revealed its potential to facilitate the endo-lysosomal escape.

Table 2. Buffering capacity of PDMAEMA star-shaped polymers given as reciprocal value of the slope of curves from Figure 1b over a pH range from 10 to 3.

Sample	Buffering Capacity, 1/Slope,
AF-P	6.76
AF-Q	4.54
H_2O	3.31

3.2. Interaction/Complexation of PDMAEMA Stars with Nucleic Acids

The interactions of the star-shaped PDMAEMA polymers with nucleic acids of different molar masses and structures were investigated by DLS, ELS and TEM. Polyplexes in a wide range of N/P ratios were prepared using short linear segments (115 bp, hereinafter, lDNA 115), long linear molecules (2000 bp, hereinafter, lDNA 2000) and circular/plasmid DNA (4730 bp, hereinafter, pDNA 4730). All of the complexes were spontaneously formed in water at room temperature.

The variations in the hydrodynamic diameter with the N/P ratio are shown in Figure 2. Areas of instability were entered at certain N/P ratios, in which strong data scattering, low reproducibility of results and occasional formation of very large particles and/or precipitates were detected. The instability areas, which are observable in the same N/P intervals for AF-P and AF-Q, gradually broadened and shifted to higher N/P ratios with increasing molar mass of DNA (Figure 2). Due to the star-like topology of the polymers, some of the amino or ammonium groups of the polymers were inaccessible, particularly for longer DNA molecules (lDNA 2000) and/or more rigid structure of the plasmid DNA (pDNA 4730) [22,35,36], which required larger amounts of polymer for neutralization and, hence, broadening and shifting of the instability areas to higher N/P ratios.

Outside the instability area, colloidally stable, narrowly distributed (PDI in the 0.075–0.105 range) and relatively small polyplex particles are observed (50–125 nm, Figure 2). Compared to the size of a single star-like macromolecule (Figure 1a, Table 1), they are considerably larger, implying that the polyplex particles consist of several polymer molecules. Beyond the instability areas, that is, in the excess of polymers, the size of the polyplex particles tends to increase with increasing DNA molar mass. Thus, the size of the polyplex particles that lDNA 115 formed with AF-P and AF-Q polymers was around 50 nm (Figure 2a). It was in the range from 50 to 85 nm for the polyplexes with lDNA 2000 (Figure 2b) to reach 50–125 nm for those with pDNA 4730 (Figure 2c).

The effects of tertiary amino vs. quaternary ammonium functionality are expressed in terms of the decreasing size of the polyplexes formed by AF-Q. This was pronounced for lDNA 2000 and pDNA 4730 (Figure 2b,c), whereas for the shortest DNA, the differences were insignificant (Figure 2a). The smaller sizes of the polyplexes that AF-Q formed may indicate the stronger binding affinity of the polymer bearing quaternary ammonium functionality and the formation of more compact and tighter particles, as previously observed [30,37,38].

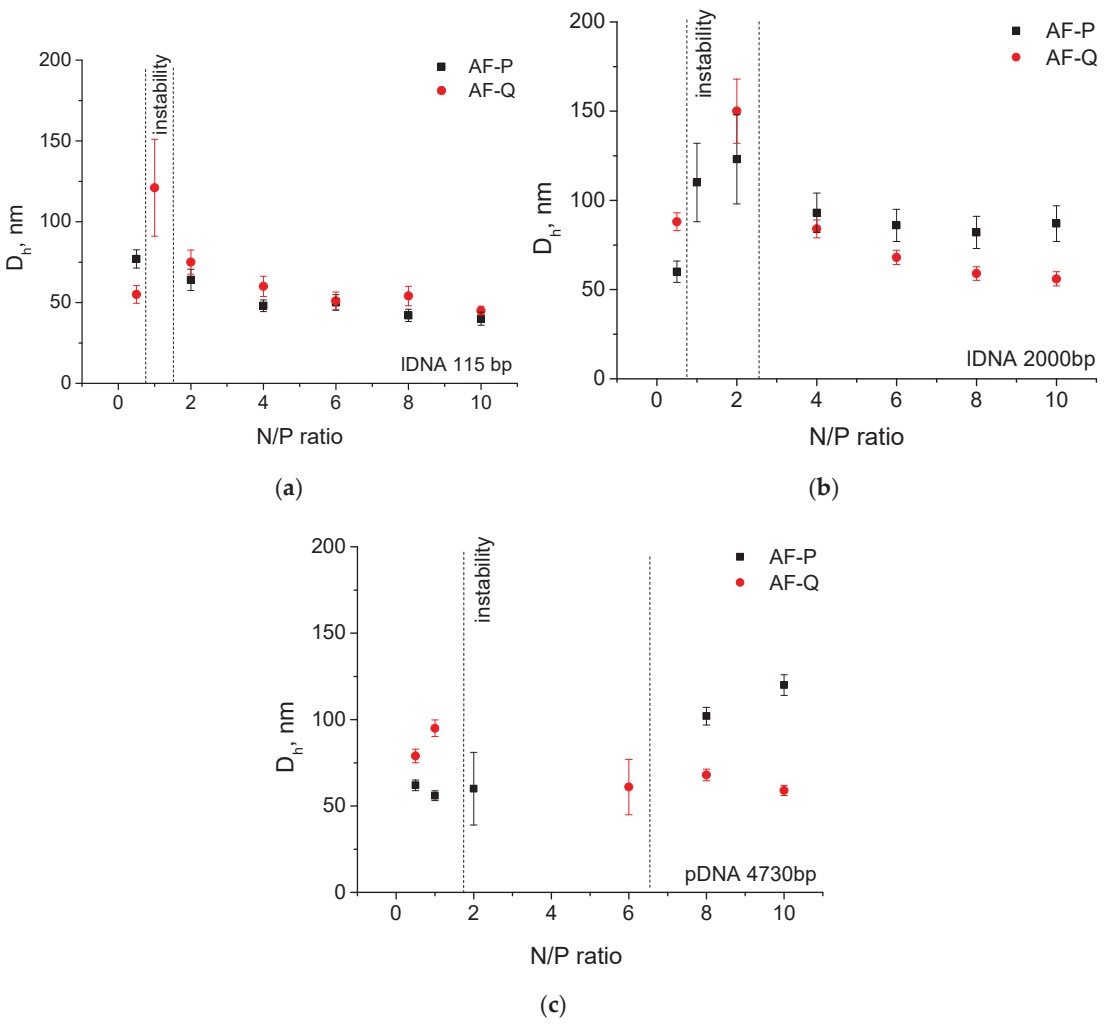

Figure 2. Variations of the hydrodynamic diameter, D_h, with the N/P ratio of polyplexes based on PDMAEMA star-shaped polymers prepared with (**a**) lDNA 115, (**b**) lDNA 2000 and (**c**) pDNA 4730.

The variations in the ζ potential of the polyplexes were also informative of the complexation of the investigated star-shaped polymers with DNA. A typical sigmoidal curve pattern with a transition from negative to positive values of the ζ potential with an increasing N/P ratio was identified in all of the polymer-to-nucleic acid formulations (Figure 3). Similarly to the instability areas of D_h variations, the transition intervals transformed from sharp and sudden to more gradual ones, whereas their positions shifted to higher N/P ratios with the molar mass (bp) and type (linear and plasmid) of DNA (cf. Figures 2 and 3). Besides the position and width of the transition intervals, the magnitude of the ζ potential beyond the transition was also influenced by the molar mass and type of DNA, being higher for the polyplexes of lDNA 115, which is most probably due to the easier access of its small molecules to the amino or ammonium groups of the star-like polymers than that of the larger molecules (lDNA 2000) and the more rigid plasmid structure (pDNA 4730). The effects of the polymer functionality (amino vs. ammonium) were more pronounced for the polyplexes with the plasmid DNA; beyond the transition, the AF-Q/pDNA 4730

complexes exhibited a more positive ζ potential than those of AF-P (Figure 3c). Referring to the smaller size of the former one (Figure 2c), the stronger complexation ability and the formation of more dense and tight complexes could be associated with the polymer bearing strongly positively charged quaternary ammonium groups.

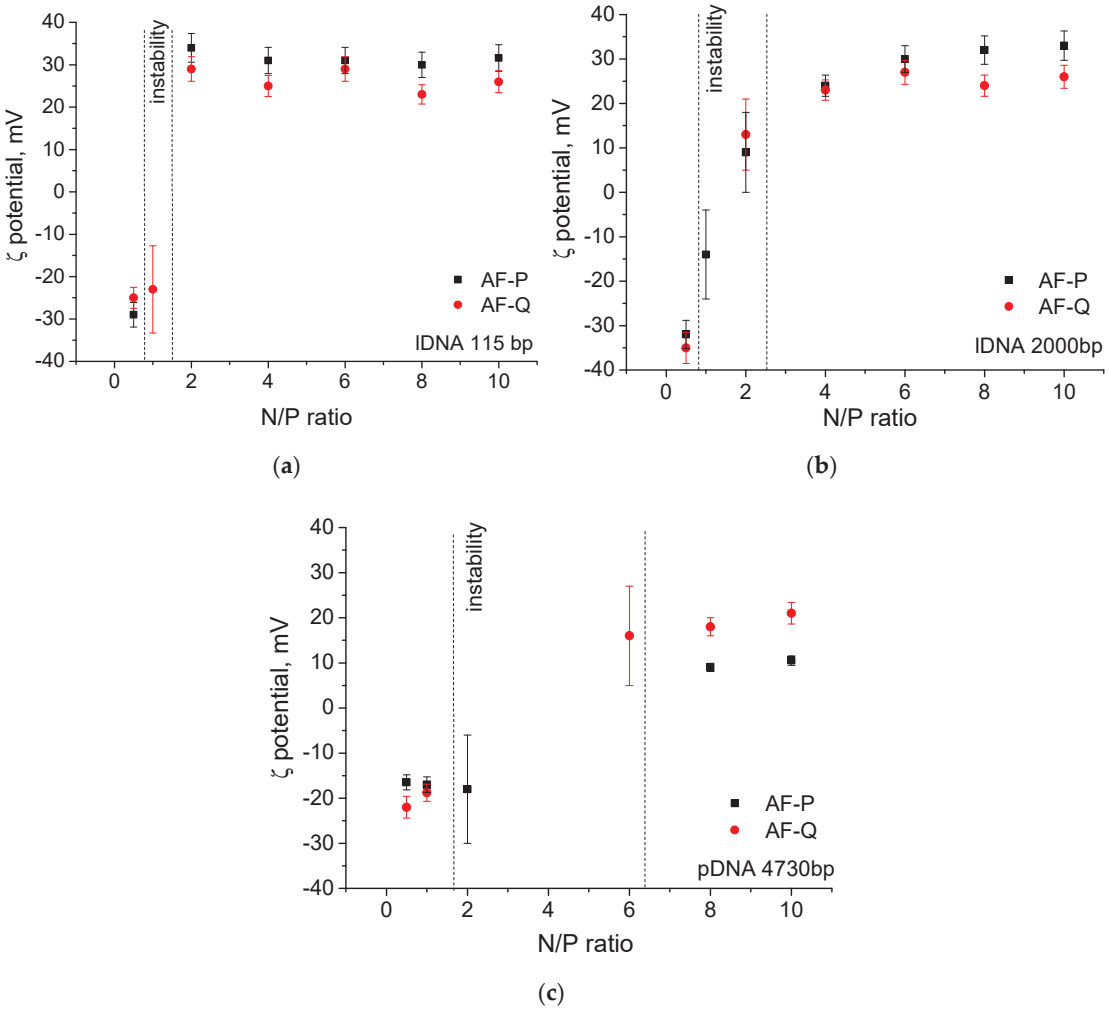

Figure 3. Variations of the ζ potential with the N/P ratio of polyplexes based on PDMAEMA star-shaped polymers prepared with (**a**) lDNA 115, (**b**) lDNA 2000 and (**c**) pDNA 4730.

The morphologies of the polyplexes were visualized by TEM. Representative micrographs are shown in Figure 4. An abundance of clusters composed of mostly spherical, individual particles was observed. The dimensions of the individual particles (inset pictures in Figure 4) were in good agreement with the results from the DLS, implying that the large clusters had been formed during the preparation of the samples for observation. The polyplex particles formed by the linear DNAs (lDNA 115 and lDNA 2000) were of a shape that somewhat deviates from sphericity. In addition, these objects were of high and homogeneous electron density, looking similar to coiled threads, inferring that the linear DNAs were probably condensed by the star-shaped polymers into compact and tight polyplex particles, as suggested above. In some aspects, the morphologies of the polyplexes

formed with pDNA 4730 were different. An interesting finding is depicted in the inset. It is composed of four individual spherical objects with dimensions that roughly correspond to the dimensions of the star-shaped polymers from Table 1. Supposedly, the whole structure is held together by the plasmid DNA molecules wrapping the individual polymer spheres. Interestingly, objects such as this were observed also for the formulations with lDNA 2000 (inset), but less frequently, and never for those with the shortest DNA.

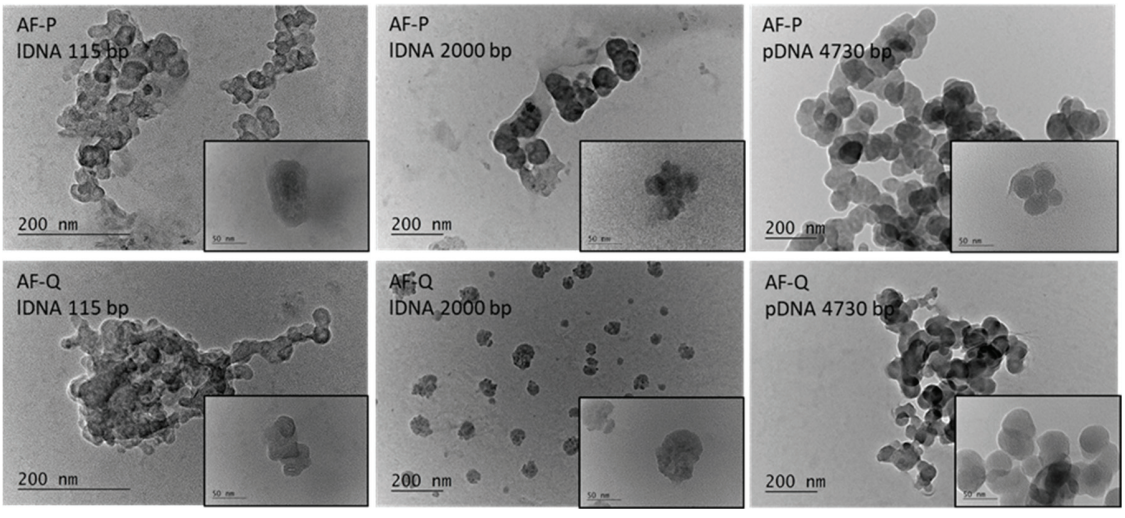

Figure 4. TEM micrographs of polyplexes based on PDMAEMA star–shaped polymers prepared at N/P ratio of 8. Scale bars of the insets 50 nm.

3.3. Salt-Induced Destabilization of Polyplexes

The release of DNA from the polyplexes' structures is a fundamental prerequisite for the efficiency of the systems. It is known that the addition of salt causes charge screening and may result in the weakening of the electrostatic interactions between the polymer and DNA phosphate groups, causing the destabilization of the complexes [30,37,39]. Furthermore, the interactions of a nucleic acid delivery system with biological fluids are ubiquitous in the delivery process. Therefore, the stability of the investigated polyplexes upon the addition of increasing amounts of salt to preformed polyplexes was investigated. N/P = 8 was selected for this study, as well as for the investigation of the biological performance of the polyplexes. As discussed in the previous section, N/P = 8 was positioned outside the instability areas, where a high reproducibility of results in terms of physiscochemical characteristics and properties of the polyplexes was exhibited. The further increase in the N/P ratio may negatively affect the biological tolerance of the polyplexes. The size variations were monitored by DLS (Figure 5). It is observable from Figure 5 that all of the polyplexes exhibited a gradual increase in size, indicating sensitivity to the addition of salt. The size increase is relatively small (up to 100 %) for the polyplexes of the quaternized polymer AF-Q with all the three types of DNA, as well as for the AF-P/lDNA 115, and it can be attributed to the loosening of the complexes resulting from the weakening of the electrostatic interactions and their swelling due to the insertion of water molecules in their structures. The size increase was considerably larger for the complexes of AF-P with the longer DNAs—lDNA 2000 and pDNA 4730—and revealed the impact of the DNA length. Particularly for the polyplex with the plasmid DNA, it reached 440%, which was too large to be attributed solely to swelling of the polyplex. The following scenario, which is supported by results from a previous study [30,40], is suggested: upon loosening of the polyplex structure, the segments of the long DNA chains can be partially dissociated, and thus, are

free to participate in complexation with other polyplexes. Thus, large superaggregates of loose polyplexes were formed.

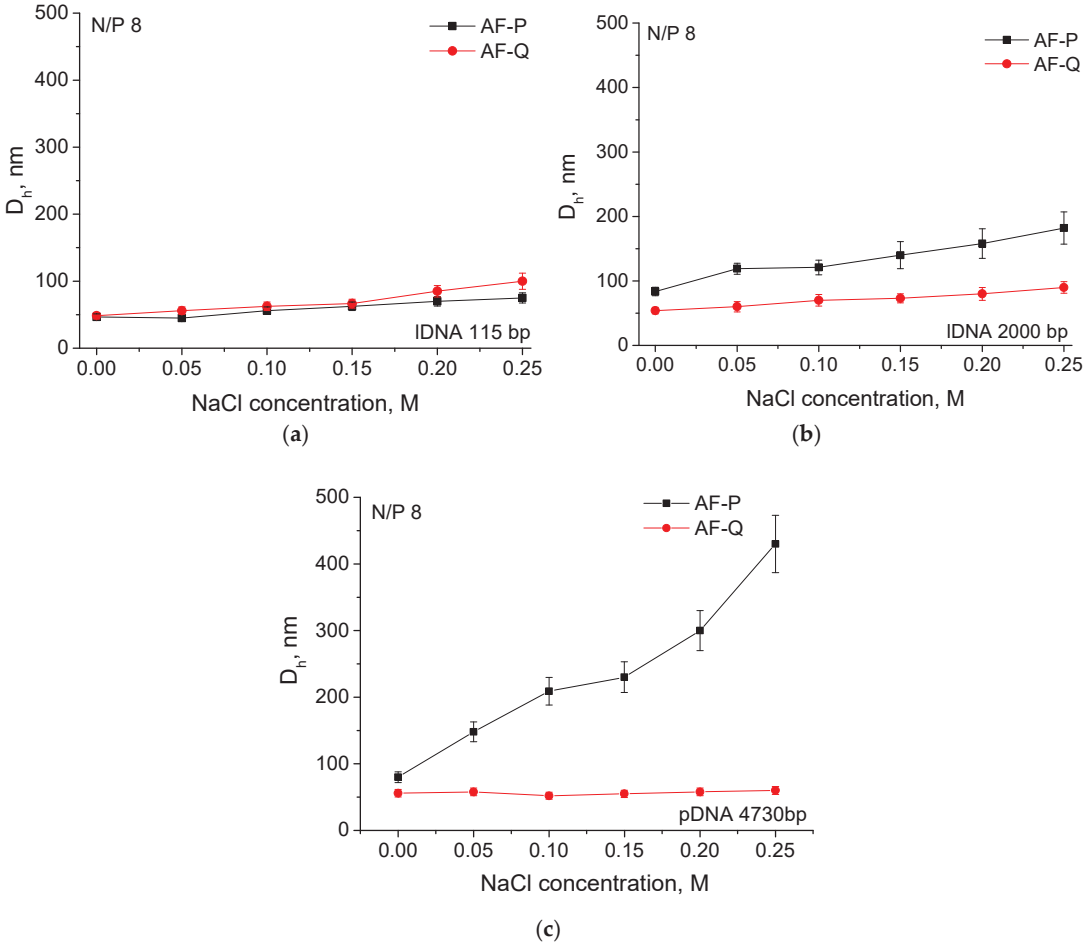

Figure 5. Variations of the hydrodynamic diameters, D_h, with NaCl concentration of polyplexes based on PDMAEMA star-shaped polymers prepared at N/P ratio of 8 with (**a**) lDNA 115, (**b**) lDNA 2000 and (**c**) pDNA 4730.

3.4. Biological Performance of Polyplexes

3.4.1. Cytotoxicity of Polyplexes Formed with lDNA

A detailed cytotoxic study of polyplexes formed with PDMAEMA star-shaped polymers and linear DNA was performed. Cell viability and morphology were evaluated after the cells were exposed to polyplexes formed from both AF-P and AF-Q polymers and lDNA 115 or lDNA 2000 at an N/P ratio of 8 to determine the cytotoxic effects. In detail, we checked the cell viability and proliferation over time of three human cell types in contact with several polyplex concentrations (5 μg.mL^{-1}, 10 μg.mL^{-1}, 20 μg.mL^{-1}, 25 μg.mL^{-1}, 40 μg.mL^{-1} and 50 μg.mL^{-1}). MG63, MSCs and hFOBs cells were selected as potential human cell targets for the development of new therapies based on nucleic acid delivery for the treatment of different pathologies (e.g., cancer) or to enhance tissue regeneration. The results showed a cell viability reduction after 24 h in the MSCs due to the presence of AF-P/lDNA 2000 and AF-Q/lDNA 2000 particles with respect to AF-P/lDNA 115

and AF-Q/lDNA 115, respectively, with a statistically significant difference starting from 20 $\mu g.mL^{-1}$ (Figure 6A). This initial difference disappeared after 48h and 72h, where only a significant decrease in cell viability is visible with the higher concentration of all of the polyplex dispersions (i.e., 50 $\mu g.mL^{-1}$) compared to the other concentrations, where the cells viability is about 80–70% with respect to the cells only (Figure 6A).

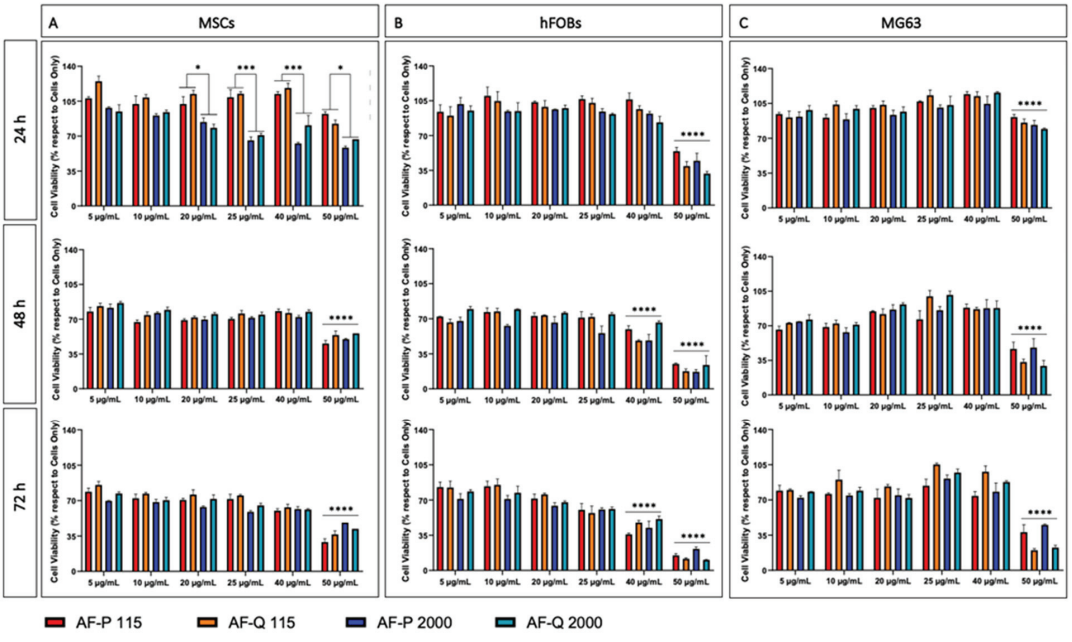

Figure 6. Cell viability analysis. MTT assay was performed after 24 h, 48 h and 72 h of being in the culture. MSCs (**A**), hFOBs (**B**) and MG63 (**C**) were cultured in contact with 5 concentrations of AF-P/lDNA 115, AF-Q/lDNA 115, AF-P/lDNA 2000 and AF-Q/lDNA 2000 (5 $\mu g.mL^{-1}$; 10 $\mu g.mL^{-1}$; 20 $\mu g.mL^{-1}$; 25 $\mu g.mL^{-1}$; 40 $\mu g.mL^{-1}$; 50 $\mu g.mL^{-1}$) at N/P of 8. The data show the percentage of viable cells as compared to cells only as the control, and the mean ± SEM are presented. * p value < 0.05, *** p value < 0.001, **** p value < 0.0001.

A different cell behavior was detected with the hFOBs. In fact, after 24 h, there were no significant differences among the groups, and all of the systems based on AF-P and AF-Q polymers with lDNA 115 and lDNA 2000 showed a cell viability that was comparable to the cells only group, except for the higher polyplex concentrations (Figure 6B). Over time and by increasing the polyplexes concentration, a remarkable reduction of cell viability without significant differences among the groups was observed, especially with the 40 and 50 $\mu g.mL^{-1}$ concentrations.

The MG63 cells were less sensitive to the presence of all of the polyplexes (Figure 6C). After 24 h, the cell viability was over 75–80% with respect to the cells only for all the concentrations. Only starting from 48 h, the 50 $\mu g.mL^{-1}$ polyplex solutions induced a strong cell viability reduction, but without any statistically significant differences among the groups (Figure 6C).

A qualitative cell morphology analysis was performed after 24 h with one concentration (20 $\mu g.mL^{-1}$) (Figure 7). The organization of the cytoskeletal structure of actin filaments is an essential element in maintaining and modulating the cellular morphology and cell structural integrity. The detection of actin filaments confirmed the cell viability data. In detail, a lower MSCs density was detected with AF-P/lDNA 2000 and AF-Q/lDNA 2000 compared to those of AF-P/lDNA 115 and AF-Q/lDNA 115. In addition, even the MSCs'

morphologies seemed to be compromised when the cells were cultured in the presence of AF-P/lDNA 2000 and AF-Q/lDNA 2000. In contrast, the polyplexes did not compromise the cytoplasmatic morphology in hFOBs and MG63. The cells were well spread, showing the typical cytoplasmic elongations without the presence of morphological cell damage markers (Figure 7).

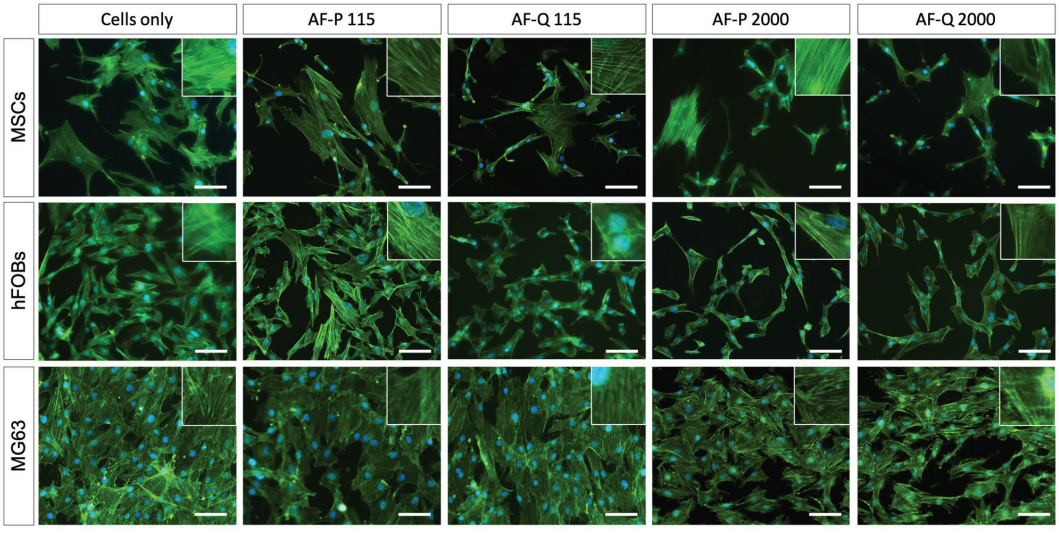

Figure 7. Morphological analysis of MSCs, hFOBs and MG63 cultured in presence of 20 μg.mL^{-1} of polyplexes at N/P of 8 for 24 h. Microspheres evaluated by phalloidin staining (green: actin filaments; blue: cell nuclei). Insets: details at higher magnification. Scale bars: 100 μm.

The observed deviation from the complexes formed with the AF-P and AF-Q polymers with lDNA 2000 could be due to their slightly larger size compared to those formed with lDNA 115. However, the cytotoxic evaluation of the systems revealed that they were sparing with respect to the cell lines studied. The polyplexes based on both the AF-P and AF-Q polymers exhibited good biocompatibility without disrupting the cytoskeletal structure of the actin filaments.

3.4.2. Cytotoxicity and Transfection Efficiency of Polyplexes Formed with pDNA

The cytotoxicity test of the polyplexes formed with pDNA 4730 was performed with the hFOBs and MG63 cell lines at an N/P ratio of 8. A single concentration of 20 μg.mL^{-1} was tested. AF-P/pDNA 4730 did not negatively affect the cell viability of both of the cell types after 24 h, whereas AF-Q/pDNA 4730 slightly decreased the cell viability (Figure 8a).

The ability of AF-P and AF-Q polymers to transfer pDNA 4730 into the cells was investigated as well. The transfection efficiency was analysed by the quantification of the eGFP positive cells by counting the number of green transfected cells in the total cell number, as assessed by DAPI staining. The results showed that the AF-Q/pDNA 4730 complexes did not transfect the cells, in fact, no eGFP positive cells were detected. The lack of transfected cells with the AF-Q polymer is probably due to the formed dense complexes and the resulting inability to release DNA. In contrast, AF-P/pDNA 4730 complexes promoted plasmid DNA internalization and expression, with a good fluorescence intensity level being detected in both of the cell types (Figure 8b). The transfection efficiencies of AF-P/pDNA 4730 and Lipofectamine, which was used in the control group, in the hFOBs and MG63 cells were 25.3 ± 6.2% and 19.4 ± 6.1%, respectively (Figure 8c). The positive results observed with AF-P polymer could be related to both the looser structure of these

polyplexes, enabling the release of DNA molecules and the presence of protonable tertiary amino groups, promoting the effective endo-lysosomal escape of the polyplex particles.

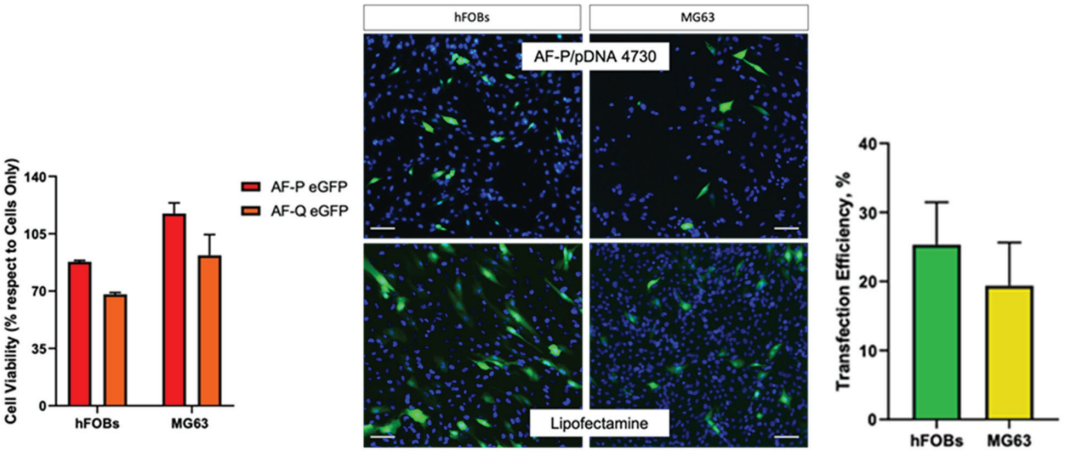

(**a**) (**b**) (**c**)

Figure 8. (**a**) Cells viability analysis. MTT assay was performed after 24 h of culture. hFOBs and MG63 were cultured in contact with 20 μg.mL^{-1} of AF-P eGFP and AF-Q eGFP at N/P of 8. The data show the percentage of viable cells as compared to cells only, as the control and the mean ± SEM are presented. (**b**) Qualitative transfection efficacy images. eGFP positive cells in green and cell nuclei in blue. Scale bars: 100 μm. (**c**) Transfection efficiency. % of transfection efficiency of AF-P eGFP complex at N/P of 8 compared to Lipofectamine used as control group.

4. Conclusions

Two identical star-like polymers bearing tertiary amino or quaternary ammonium groups were used in this study. They were prepared by RAFT polymerization of 2-(dimethylamino)ethyl methacrylate) using the "arm-first" approach and further modified via quaternization of the tertiary amino groups. The two polymers were of the same chain architecture (star-like), number and polymerization degree of the arms, and they differed only in the functionality—tertiary amino vs. quaternary ammonium. The polymers were molecularly dissolved in water and were characterized with a relatively small size (11.4 nm, 15.8 nm) and strongly positive (24.1 mV, 31.6 mV) ζ potential. Whereas the quaternized polymer exhibited a slightly larger size and a more positive ζ potential, the parent polymer was characterized by a higher buffering capacity due to the ability of the tertiary amino groups to absorb protons. Both polymers spontaneously formed polyelectrolyte complexes with nucleic acids of different lengths and types in a wide range of N/P ratios. The effects of the DNA length/type were expressed in the position and width of the instability areas/transition intervals (being wider and shifted to higher N/P ratios for the longer and plasmid DNA), the size of the polyplex particles (tended to increase with increasing molar mass/length of DNA), and the magnitude of the ζ potential (more positive for the polyplexes of the shorter DNA). The addition of NaCl contributed to weakening of the electrostatic interactions and loosening of the polyplexes, which were strongly pronounced for the polyplexes of the parent AF-P polymer with the longer (lDNA 2000) and plasmid (pDNA 4730) DNA. In general, the size was smaller and the ζ potential was more positive for the polyplex particles of the quaternized AF-Q polymer, particularly with the plasmid DNA, compared to those of the parent AF-P polymer due to the stronger binding and formation of more compact and tighter polyplex particles. The cytotoxicity of the polyplexes at N/P = 8 was evaluated for three human cell types—the osteosarcoma cell

line (MG63), the osteoblast cell line (hFOBs), and adipose-derived mesenchymal stem cells (MSCs). A remarkable reduction of the cell viability without significant differences among the groups was observed only at the highest polyplex concentrations (40 and/or 50 $\mu g.mL^{-1}$, depending on the cell type). The transfection efficiencies of the polyplexes of the two polymers were examined in the hFOBs and MG63 cell lines. The loose structure of the AF-P polyplexes and the presumed abilities to promote effective endo-lysosmal escape and the release of DNA appeared to be favorable features for the enhanced effectiveness of the parent, non-quaternized PDMAEMA star-like polymer to transfect the cells.

Author Contributions: Conceptualization, E.H., S.P. (Silvia Panseri), S.P. (Stergios Pispas) and S.R.; methodology, E.H., M.M., A.R. and A.S.; validation, E.H., M.M., A.R. and A.S.; formal analysis, E.H., M.M., A.R. and A.S.; investigation, E.H., S.P. (Silvia Panseri), M.M., A.R., A.S., S.P. (Stergios Pispas) and S.R.; writing—original draft preparation, E.H., S.P. (Silvia Panseri), M.M., A.R., A.S., S.P. (Stergios Pispas) and S.R.; writing—review and editing, E.H., S.P. (Silvia Panseri), S.P. (Stergios Pispas) and S.R.; visualization, E.H., M.M. and A.R.; supervision, S.P. (Silvia Panseri), S.P. (Stergios Pispas) and S.R.; project administration, E.H. All authors have read and agreed to the published version of the manuscript.

Funding: This research received no external funding.

Data Availability Statement: Data is contained within the article.

Acknowledgments: Research equipment from Distributed Research Infrastructure INFRAMAT, which is part of Bulgarian National Roadmap for Research Infrastructures, supported by Bulgarian Ministry of Education and Science was used in this investigation.

Conflicts of Interest: The authors declare no conflict of interest.

References

1. Shi, B.; Zheng, M.; Tao, W.; Chung, R.; Jin, D.; Ghaffari, D.; Farokhzad, O.C. Challenges in DNA delivery and recent advances in multifunctional polymeric DNA delivery system. *Biomacromolecules* **2017**, *18*, 2231–2246. [CrossRef] [PubMed]
2. Zhang, Y.; Satterlee, A.; Huang, L. In vivo gene delivery by nonviral vectors: Overcoming hurdles? *Mol. Ther.* **2012**, *20*, 1298–1304. [CrossRef] [PubMed]
3. Ibraheem, D.; Elaissari, A.; Fessi, H. Gene therapy and DNA delivery systems. *Int. J. Pharm.* **2014**, *459*, 70–83. [CrossRef] [PubMed]
4. Patil, S.D.; Rhodes, D.G.; Burgess, D.J. DNA-based therapeutics and DNA delivery systems: A comprehensive review. *AAPS J.* **2005**, *7*, E61–E77. [CrossRef] [PubMed]
5. Young, L.S.; Searle, P.F.; Onion, D.; Mautner, V. Viral gene therapy strategies: From basic science to clinical application. *J. Pathol.* **2006**, *208*, 299–318. [CrossRef]
6. Hill, A.; Chen, M.; Chen, C.-K.; Pfeifer, B.A.; Jones, C. Overcoming gene-delivery hurdles: Physiological considerations for nonviral vectors. *Trends Biotechnol.* **2016**, *34*, 91–105. [CrossRef]
7. Lai, W.F.; Wong, W.T. Design of polymeric gene carriers for effective intracellular delivery. *Trends Biotechnol.* **2018**, *36*, 713–728. [CrossRef]
8. Yin, H.; Kanasty, R.L.; Eltoukhy, A.A.; Vegas, A.J.; Dorkin, J.R.; Anderson, D.G. Non-viral vectors for gene-based therapy. *Nat. Rev. Genet.* **2014**, *15*, 541–555. [CrossRef]
9. Aied, A.; Greiser, U.; Pandit, A.; Wang, W. Polymer gene delivery: Overcoming the obstacles. *Drug Discov.* **2013**, *18*, 1090–1098. [CrossRef]
10. O'Rorke, S.; Keeney, M.; Pandit, A. Non-viral polyplexes: Scaffold mediated delivery for gene therapy. *Prog. Polym. Sci.* **2010**, *35*, 441–458. [CrossRef]
11. Eliyahu, H.; Barenholz, Y.; Domb, A.J. Polymers for DNA delivery. *Molecules* **2005**, *10*, 34–64. [CrossRef] [PubMed]
12. Jones, C.H.; Chen, C.-K.; Ravikrishnan, A.; Rane, S.; Pfeifer, B.A. Overcoming nonviral gene delivery barriers: Perspective and future. *Mol. Pharm.* **2013**, *10*, 4082–4098. [CrossRef] [PubMed]
13. Izumrudov, V.A.; Zhiryakova, M.V.; Kudaibergenov, S.E. Controllable stability of DNA-containing polyelectrolyte complexes in water-salt solutions. *Biopolymers* **1999**, *52*, 94–108. [CrossRef]
14. Varkouhi, A.K.; Mountrichas, G.; Schiffelers, R.M.; Lammers, T.; Storm, G.; Pispas, S.; Hennink, W.E. Polyplexes based on cationic polymers with strong nucleic acid binding properties. *Eur. J. Pharm. Sci.* **2012**, *45*, 459–466. [CrossRef] [PubMed]
15. Bus, T.; Traeger, A.; Schubert, U.S. The great escape: How cationic polyplexes overcome the endosomal barrier. *J. Mater. Chem. B* **2018**, *6*, 6904–6918. [CrossRef]
16. Warriner, L.W.; Duke III, J.R.; Pack, D.W.; DeRouchey, J.E. Succinylated polyethylenimine derivatives greatly enhance polyplex serum stability and gene delivery in vitro. *Biomacromolecules* **2018**, *19*, 4348–4357. [CrossRef]

17. Godbey, W.T.; Wu, K.K.; Mikos, A.G. Size matters: Molecular weight affects the efficiency of poly(ethylenimine) as a gene delivery vehicle. *J. Biomed. Mater. Res.* **1999**, *45*, 268–275. [CrossRef]
18. Blakney, A.K.; Yilmaz, G.; McKay, P.F.; Becer, C.R.; Shattock, R.J. One size does not fit all: The effect of chain length and charge density of poly(ethylene imine) based copolymers on delivery of pDNA, mRNA, and RepRNA polyplexes. *Biomacromolecules* **2018**, *19*, 2870–2879. [CrossRef]
19. Schaffer, D.V.; Fidelman, N.A.; Dan, N.; Lauffenburger, D.A. Vector unpacking as a potential barrier for receptor-mediated polyplex gene delivery. *Biotechnol. Bioeng.* **2000**, *67*, 598–606. [CrossRef]
20. Shen, Z.L.; Xia, Y.Q.; Yang, Q.S.; Tian, W.D.; Chen, K.; Ma, Y.Q. *Polymer–Nucleic Acid Interactions In Polymeric Gene Delivery Systems*; Topics in Current Chemistry Collections; Cheng, Y., Ed.; Springer: Cham, Switzerland, 2017.
21. Jiang, Y.; Reineke, T.M.; Lodge, T.P. Complexation of DNA with Cationic Copolymer Micelles: Effects of DNA Length and Topology. *Macromolecules* **2018**, *51*, 1150–1160. [CrossRef]
22. Tan, Z.; Jiang, Y.; Zhang, W.; Karls, L.; Lodge, T.P.; Reineke, T.M. Polycation Architecture and Assembly Direct Successful Gene Delivery: Micelleplexes Outperform Polyplexes via Optimal DNA Packaging. *J. Am. Chem. Soc.* **2019**, *141*, 15804–15817. [CrossRef] [PubMed]
23. Ugrinova, I.; Mitkova, E.; Moskalenko, C.; Pashev, I.; Pasheva, E. DNA Bending versus DNA End Joining Activity of HMGB1 Protein Is Modulated in Vitro by Acetylation. *Biochemistry* **2007**, *46*, 2111–2117. [CrossRef] [PubMed]
24. Kahn, J.D. DNA, Flexibly Flexible. *Biophys. J.* **2014**, *107*, 282–284. [CrossRef] [PubMed]
25. Yue, Y.; Wu, C. Progress and perspectives in developing polymeric vectors for in vitro gene delivery. *Biomater. Sci.* **2013**, *1*, 152–170. [CrossRef]
26. Agarwal, S.; Zhang, Y.; Maji, S.; Greiner, A. PDMAEMA based gene delivery materials. *Mater. Today* **2012**, *15*, 388–393. [CrossRef]
27. Dai, F.; Sun, P.; Liu, Y.; Liu, W. Redox-cleavable star cationic PDMAEMA by arm-first approach of ATRP as a nonviral vector for gene delivery. *Biomaterials* **2010**, *31*, 559–569. [CrossRef]
28. Mendrek, B.; Sieroń, Ł.; Libera, M.; Smet, M.; Trzebicka, B.; Sieroń, A.L.; Dworak, A.; Kowalczuk, A. Polycationic star polymers with hyperbranched cores for gene delivery. *Polymer* **2014**, *55*, 4551–4562. [CrossRef]
29. Eltoukhy, A.A.; Siegwart, D.J.; Alabi, C.A.; Rajan, J.S.; Langer, R.; Anderson, D.G. Effect of molecular weight of amine end-modified poly(β-amino ester)s on gene delivery efficiency and toxicity. *Biomaterials* **2012**, *33*, 3594–3603. [CrossRef]
30. Haladjova, E.; Chrysostomou, V.; Petrova, M.; Ugrinova, I.; Pispas, S.; Rangelov, S. Physicochemical Properties and Biological Performance of Polymethacrylate based Gene Delivery Vector Systems: Influence of Amino Functionalities. *Macromol. Biosci.* **2021**, *21*, 2000352. [CrossRef]
31. Skandalis, A.; Pispas, S. PDMAEMA-b-PLMA-b-POEGMA triblock terpolymers via RAFT polymerization and their self-assembly in aqueous solutions. *Polym. Chem.* **2017**, *8*, 4538–4547. [CrossRef]
32. Skandalis, A.; Pispas, S. Synthesis of (AB)n-, AnBn-, and AxBy-type amphiphilic and double-hydrophilic star copolymers by RAFT polymerization. *J. Polym. Sci. A Polym. Chem.* **2019**, *57*, 1771–1783. [CrossRef]
33. Van de Wetering, P.; Moret, E.E.; Schuurmans-Nieuwenbroek, N.M.; van Steenbergen, M.J.; Hennink, W.E. Structure-activity relationships of water-soluble cationic methacrylate/methacrylamide polymers for nonviral gene delivery. *Bioconjug. Chem.* **1999**, *10*, 589–597. [CrossRef] [PubMed]
34. Lee, H.; Son, S.H.; Sharma, R.; Won, Y.-Y. A discussion of the pH-dependent protonation behaviors of poly(2-(dimethylamino)ethyl methacrylate) (PDMAEMA) and poly(ethylenimine-ran-2-ethyl-2-oxazoline) (P(EI-r-EOz)). *J. Phys. Chem. B* **2011**, *115*, 844–860. [CrossRef] [PubMed]
35. Dhanoya, A.; Chain, B.M.; Keshavarz-Moore, E. The impact of DNA topology on polyplex uptake and transfection efficiency in mammalian cells. *J. Biotechnol.* **2011**, *10*, 377–386. [CrossRef]
36. Haladjova, E.; Halacheva, S.; Posheva, V.; Peycheva, E.; Moskova-Doumanova, V.; Topouzova-Hristova, T.; Doumanov, J.; Rangelov, S. Comb-like Polyethyleneimine-based Polyplexes: Balancing Toxicity, Cell Internalization, and Transfection Efficiency via Polymer Chain Topology. *Langmuir* **2015**, *31*, 10017–10025. [CrossRef]
37. Lee, J.H.; Lim, Y.B.; Choi, J.S.; Lee, Y.; Kim, T.I.; Kim, H.J.; Yoon, J.K.; Kim, K.; Park, J.S. Polyplexes assembled with internally quaternized PAMAM-OH dendrimer and plasmid DNA have a neutral surface and gene delivery potency. *Bioconjug. Chem.* **2003**, *14*, 1214–1221. [CrossRef]
38. Vader, P.; van der Aa, L.J.; Engbersen, J.F.J.; Storm, G.; Schiffelers, R.M. Physicochemical and Biological Evaluation of siRNA Polyplexes Based on PEGylated Poly(amido amine)s. *Pharm. Res.* **2012**, *29*, 352–361. [CrossRef]
39. Lai, E.; van Zanten, J.H. Monitoring DNA/Poly-l-Lysine Polyplex Formation with Time-Resolved Multiangle Laser Light Scattering. *Biophys. J.* **2001**, *80*, 864–873. [CrossRef]
40. Chrysostomou, V.; Katifelis, H.; Gazouli, M.; Dimas, K.; Demetzos, C.; Pispas, S. Hydrophilic random cationic copolymers as polyplex-formation vectors for DNA. *Materials* **2022**, *15*, 2650. [CrossRef]

Disclaimer/Publisher's Note: The statements, opinions and data contained in all publications are solely those of the individual author(s) and contributor(s) and not of MDPI and/or the editor(s). MDPI and/or the editor(s) disclaim responsibility for any injury to people or property resulting from any ideas, methods, instructions or products referred to in the content.

polymers

MDPI

Review

Hybrid Epoxy Nanocomposites: Improvement in Mechanical Properties and Toughening Mechanisms—A Review

Anita Białkowska [1,*], Mohamed Bakar [1,*], Wojciech Kucharczyk [2] and Iwona Zarzyka [3]

[1] Faculty of Chemical Engineering, University of Technology and Humanities, 26-600 Radom, Poland
[2] Faculty of Mechanical Engineering, University of Technology and Humanities, 26-600 Radom, Poland
[3] Faculty of Chemistry, Rzeszów University of Technology, 35-959 Rzeszów, Poland
* Correspondence: a.bialkowska@uthrad.pl (A.B.); mbakar@wp.pl (M.B.)

Abstract: This article presents a review on the recent advances in the field of ternary diglycidyl ether of bisphenol A epoxy nanocomposites containing nanoparticles and other modifiers. Particular attention is paid to their mechanical and thermal properties. The properties of epoxy resins were improved by incorporating various single toughening agents, in solid or liquid states. This latter process often resulted in the improvement in some properties at the expense of others. The use of two appropriate modifiers for the preparation of hybrid composites, possibly will show a synergistic effect on the performance properties of the composites. Due to the huge amount of modifiers that were used, the present paper will focus mainly on largely employed nanoclays with modifiers in a liquid and solid state. The former modifier contributes to an increase in the flexibility of the matrix, while the latter modifier is intended to improve other properties of the polymer depending on its structure. Various studies which were carried out on hybrid epoxy nanocomposites confirmed the occurrence of a synergistic effect within the tested performance properties of the epoxy matrix. Nevertheless, there are still ongoing research works using other nanoparticles and other modifiers aiming at enhancing the mechanical and thermal properties of epoxy resins. Despite numerous studies carried out so far to assess the fracture toughness of epoxy hybrid nanocomposites, some problems still remain unresolved. Many research groups are dealing with many aspects of the subject, namely the choice of modifiers and preparation methods, while taking into account the protection of the environment and the use of components from natural resources.

Keywords: epoxy resin; hybrid nanocomposites; mechanical properties; toughening; mechanisms

Citation: Białkowska, A.; Bakar, M.; Kucharczyk, W.; Zarzyka, I. Hybrid Epoxy Nanocomposites: Improvement in Mechanical Properties and Toughening Mechanisms—A Review. *Polymers* **2023**, *15*, 1398. https://doi.org/10.3390/polym15061398

Academic Editors: Fahmi Zaïri, Matthias Ballauff, Ulrich Maschke and Rufina G. Alamo

Received: 26 January 2023
Revised: 1 March 2023
Accepted: 6 March 2023
Published: 10 March 2023

Copyright: © 2023 by the authors. Licensee MDPI, Basel, Switzerland. This article is an open access article distributed under the terms and conditions of the Creative Commons Attribution (CC BY) license (https://creativecommons.org/licenses/by/4.0/).

1. Introduction

Epoxy resins are known for their excellent chemical resistance, high specific strength, good dimensional stability and adhesion properties [1–5]. Epoxy resins can be used as liquids or powders, which facilitate their mixing with reactive or non-reactive modifiers. They are used as paints, coatings, adhesives and matrices for structural composites [6]. However, once cured, epoxy resins exhibit a high crosslink density, which leads to increased brittleness, low strain at break, poor impact strength and low resistance to crack propagation. The inherent brittleness associated with the low toughness of epoxy resins constitutes serious limitations for their engineering applications. The structure of diglycidyl ether of bisphenol A epoxy resin is shown in Scheme 1.

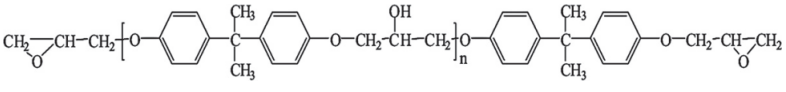

Scheme 1. Structure of diglycidyl ether of bisphenol A epoxy resin.

The modification of epoxy resins to improve the above-mentioned properties has been the subject of intense research interest in the last four decades [7–12]. They have been

successfully toughened using various suitable modifiers such as synthetic and natural fibers [13–19], thermoplastics [20–30], liquid rubbers [31–40], plasticizers [41–45], solid microparticles [46–53] and nanoparticles [54–65]. The toughening of epoxy resins was attributed to various mechanisms such as crack-pinning, phase separation, plastic deformation, interpenetrating polymer network formation and exfoliation of nanoparticles. The use of a single modifier for epoxy toughening has been known for many decades, but the preparation of hybrid ternary composites containing two different modifiers is a relatively new concept. It can take advantage of the possible existence of a synergistic effect, leading to a greater improvement in the performance properties of the composite. A correct selection of modifiers could lead to specific interactions between the components of the hybrid composite and therefore to a greater improvement in its properties. The simultaneous use of different reinforcing agents has recently been explored by various researchers as a useful and logical approach to improve the performance properties of epoxy resins and avoid negative side effects such as a reduction in stiffness, strength or temperature glass transition of the matrix.

Due to the very large number of potential modifiers to be used in the preparation of hybrid epoxy composites, this review focuses on nanofillers (such as graphene, carbon nanotubes, montmorillonite, silica, . . .) and other modifiers such as thermoplastics, liquid rubbers, thermosets, diluents. Very interesting reviews have already been published in recent years on hybrid epoxy nanocomposites [65–70]. The manuscript would provide a very significant contribution for industrialists and academics since it features the positive toughening of the DGEBA with two modifiers. This would lead to widening the field of application of reinforced materials or ensuring their safe use under severe conditions.

2. Hybrid Epoxy Nanocomposites

Nanoparticles can be classified into different categories depending on their shape, size, morphology and properties. Based on their shapes, nanofillers are classified into three categories [71,72]: nanoparticles with one nanoscale dimension (nanoplatelets), two nanoscale dimensions (nanofibers) and three nanoscale dimensions (nanoparticulates). Carbon nanotubes and halloysite nanotubes are considered as two-dimensional nanofillers, while clay and graphene nanoplatelets are examples of one-dimensional nanofillers. Two-dimensional nanofillers include nanotubes and nanofibers with a diameter lower than 0.1 μm. However, nanometric silica beads belong to the three-dimensional nanofiller group.

It is well known that the dispersion of nanoparticles plays a key role in improving the mechanical and thermal properties of polymer nanocomposites. This can be achieved by the intensive mixing of nanoparticles in the polymer matrix, aiming at the exfoliation and/or intercalation of the former, resulting in a higher contact surface between the constituents.

2.1. Hybrid Epoxy Nanocomposites Based on Liquid Rubbers

Epoxy resins were modified with different liquid modifiers such as liquid natural rubbers [73–78], epoxidized natural rubber, hydroxyl terminated polybutadiene, amine-terminated polybutadiene, epoxy-terminated polybutadiene and butadiene acrylonitrile rubbers terminated with carboxyl groups, amine groups or epoxy groups.

One of the most promising methods to toughen epoxy resin was the use of liquid rubbers in combination with nanoparticles. Rubber toughening of epoxy resin has been considered for over five decades to be one of the most effective methods for reducing brittleness and increasing other matrix properties. In general, epoxy resins modified with liquid rubbers exhibit improved flexibility and impact resistance. The inclusion of nanofillers in the epoxy matrix along with rubber is expected to improve its strength, stiffness and glass transition temperature, without, however, reducing the decrease in its stiffness, strength or glass transition temperature.

In fact, most of the conducted investigations using nanoparticles with liquid rubbers showed an improvement in epoxy performance properties. The epoxy/rubber nanocom-

posites have been used in various fields such as adhesives, coatings, transducers and in electromagnetic systems.

Hydroxyl-terminated polybutadiene (HTPB) is a telechelic, translucent liquid rubber which finds a wide range of applications. It is characterized by a low glass transition temperature of about −75 °C, an average molecular weight and a high level of reactive functionality, making it an excellent potential curing modifier for epoxy resin. Various researchers used both nanofillers and HTPB to improve the properties of diglycidyl ether of bisphenol A (DGEBA) epoxy resin [79–83]. Yi et al. [79] studied the properties of a prepared hybrid epoxy (EP) resin based on montmorillonite (MMT) and HTPB with different number average molecular weights. The advantage of using inorganic MMT clay as a reinforcement for a certain number of polymers is associated with their nanometric size and their ability to form intercalated and exfoliated structures (Scheme 2). It was shown that the tensile strength and elongation at break of EP/10 wt% HTPB/1 wt% MMT ternary composites were higher than those of epoxy binary blends. Moreover, HTPB with a higher molecular weight led to a more exfoliated nanostructure. It was also confirmed that 40 to 80 °C were the preferred temperatures to obtain nanostructured HTPB/MMT. The toughening of ternary epoxy nanocomposites was attributed to the slow and rapid growth of the cracks and the energy dissipated during the process of pulling out and debonding of nanoparticles from the matrix. The addition of microscale and nanoscale modifiers can lead to different interactions between the two kinds of particles and the matrix, which determine the final morphologies and properties of the hybrid polymer [80].

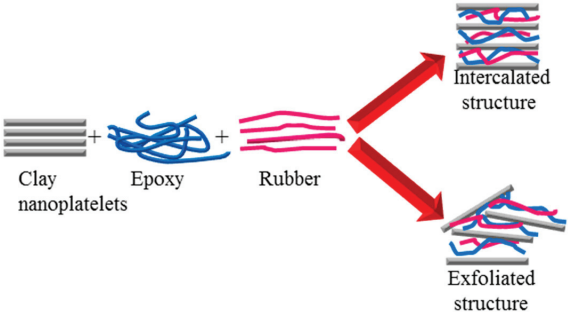

Scheme 2. Formation of intercalated and exfoliated structures with epoxy, rubber and MMT.

Marouf et al. [69] confirmed the "nano" effects of silica (<25 vol%) and rubber nanoparticles (>10 wt%) in toughening epoxy resin compared to silica and rubber microparticles at the same loading. Synergistic toughening effects were noted on the fracture toughness parameter G_C in epoxy/nanosilica/rubber microparticles, epoxy/nanosilica/rubber nanoparticle composites and epoxy/CNT/rubber nanoparticle composites. The simultaneous incorporation of microscale elastomers/thermoplastics and nanoscale fillers for the modification of epoxy systems was also investigated and confirmed the complicated interaction between the modifier at the micro- and nanoscales and the inherent problems of synergy [80].

Due to its good thermal oxidation resistance, oil resistance and damping properties, acrylic rubber (ACM) particles were combined with montmorillonite (MMT Na^+) to improve the mechanical and thermal properties of epoxy resin [81]. The tensile strength and modulus were shown to increase and the ductility to decrease with the increasing organic clay content, while rubber had the opposite effects on the epoxy resin properties. However, the ductility of the epoxy matrix was improved without compromising the modulus and strength when both modifiers were used. Relative elongation at break increased maximally in ternary epoxy nanocomposites. However, a synergistic effect was observed on the toughness and tensile modulus of ternary epoxy nanocomposites prepared by the solvent blending of acrylic rubber (ACM) and organomodified montmorillonite (Cloisite30B) [82].

The adhesive strength of an epoxy/ACM blend containing 3 wt% MMT also increased, due to a positive blending effect, resulting from the positive effect of crosslinking and the tearing energy of the adhesive film. The addition of liquid rubbers leads to a softening of the brittle epoxy matrix and decrease in stiffness, which results from the plasticization of the three-dimensional crosslinked network and the increase in the free volume, unlike solid montmorillonite nanoparticles which increase the rigidity of the epoxy matrix [69,82]. Fröhlich et al. [83] reported an improved toughness in hybrid epoxy nanocomposites, but decreased tensile strength, stiffness and glass transition temperature in epoxy composites containing both compatibilized liquid rubber and organophilic fluorohectorite, induced by rubber. Similar results were obtained by Ahmed et al. [84] in an epoxy matrix modified with both reactive rubber nanoparticles (RRNPs) and organically modified montmorillonite (Cloisite-30B). The addition of RRNPs led to a softening of the composites, with a lower stiffness and improved toughness compared to those of the neat resin. In contrast, the use of solid nanoparticles (MMTs) increased the stiffness and lowered the toughness of the nanocomposites. However, the combination of the two optimal percentages of RRNPs and nanoclay in the epoxy matrix improved the flexural stress–strain curve and storage modulus over the neat resin. Shayegan and Bagheri [85] reported, for the first time, a synergistic effect on the fracture toughness parameter (K_C) of the hybrid epoxy composite containing nanosilica and liquid rubber. The toughness of the ternary composite was higher than those of the binary epoxy systems, due to the obvious positive interactions between the epoxy hybrid constituents.

Graphene has attracted great interest over the past two decades due to its outstanding physical properties. With an excellent balance between their physical properties and low cost, graphene nanoplatelets (GnPs) have become one of the most attractive nanofillers for polymer matrices. They exhibit a very high mechanical strength with 1.0 TPa in Young's modulus, 130 GPa in ultimate strength, high thermal conductivity of about 5000 Wm^{-1} K^{-1}, an extremely high specific surface and non-toxicity. An epoxy resin modified with graphene nanoplatelets exhibited a significant improvement in the tensile modulus and tensile strength [86]. The tensile modulus of the nanocomposite containing 6 wt% of graphene increased by ~23% and its ultimate tensile strength decreased by ~54% compared to the pure matrix. The increase in epoxy stiffness was explained by a high tensile strength and high specific area of GnPs [87].

Still, with the aim of achieving an improvement in the mechanical properties of the matrix, another rubber, namely acrylonitrile butadiene terminated by carboxyl (CTBN), was used with graphene nanoplatelets (GnPs) with different diameters [88]. The addition of 3 wt% GnP with a diameter of 5 μm in 10 wt% CTBN has been shown to yield a ternary GnP/CTBN/epoxy nanocomposite with enhanced toughness and thermal conductivity, combined with a comparable stiffness to that of pure resin. The same mechanism as that of the work of [85] can be used to explain the increase in toughness of the epoxy resin.

A very successful approach that has been widely used by various researchers to toughen diglycidyl ether of Bisphenol A (DGEBA) modified with nanoparticles involved the addition of a liquid copolymer of acrylonitrile butadiene terminated by carboxyl (CTBN), amine (ATBN) and epoxy (ETBN) groups [89–98]. It is important to emphasize that the dispersion of nanoparticles in epoxy/rubber plays a crucial role in improving the properties of the material. However, it was found that well-dispersed organoclay (Cloisite 30B) in a CTBN/epoxy system with a suitable preparation method leads to an effective improvement in the tensile strength and modulus of an epoxy ternary composite [89]. The tensile strength of the hybrid nanocomposite was effectively improved when the MMT was first dispersed in the CTBN rubber phase. In addition, the degree of Cloisite–Na intercalation in the blend and with it, the performance properties of the composite were further increased by the compatibilizing effect of the curing agent.

Using high pressure and direct mixing methods, Liu et al. [90] showed that the fracture toughness parameters (K_C and G_C) maximally increased by 2.2 and 7.6 times, respectively, at 6 phr organoclay (Nanomer I.30E) and 20 phr CTBN loading compared to the pristine

resin. A positive superposition effect was obtained on the fracture toughness of the epoxy matrix modified with both rubber and organoclay. The ultimate strength, yield strength and glass transition temperature of the epoxy resin modified with rubber and organoclay have also been improved. Similar findings were obtained by Chonkaew et al. [91] regarding the improvement in the mechanical and tribological properties of epoxy resin using CTBN and organomodified MMT (Nanomer 1.31 PS). It should be noted that a small amount of 1 phr of nanoclay was sufficient to optimally improve both the mechanical and tribological properties of the epoxy matrix modified with 2.5 phr CTBN. It was also reported that epoxy/nanoclay/CTBN ternary nanocomposites prepared via sonication method exhibited the best tensile strength, due to a uniform and stable morphology as well as a good dispersion of nanoclay (Nanomer 1.28E) in the epoxy/CTBN system [92]. Cavitation of CTBN, connected with the formation of voids, debonding of nanoparticles and plastic deformation of the matrix are processes that require additional energy which will count in increased toughness [88,93].

Moreover, it was shown in a separate study that the fracture toughness parameters (K_C and G_C) of ternary epoxy/CTBN/SN composites were higher than those of epoxy/SN and epoxy/CTBN binary systems [94]. The K_C value of the hybrid composite containing 15 wt% CTBN and 5 wt% SN more than doubled compared to the virgin matrix with a distinct positive synergistic effect between the CTBN and SN nanofillers on the fracture energy, G_C. Liang and Pearson [95] confirmed the positive hybrid effect in their epoxy composites containing 3 wt% SN (20 nm in diameter) and 18 wt% CTBN. However, a negative hybrid effect on the fracture toughness parameter, G_C, was also obtained with more than 5 wt% SN in epoxy, most probably due to particle agglomeration.

Metal oxides such as Al_2O_3, ZnO and TiO_2 are generally used to solve the problems of corrosion resistance, stiffness, toughness and conductivity of epoxy systems [96]. Alumina nanoparticles (Al_2O_3) were also used in combination with CTBN liquid rubber to increase the fracture toughness of an epoxy resin. Hosseini and his research group [97] prepared hybrid epoxy nanocomposites with an optimum content of CTBN (15 phr) and different amounts of Al_2O_3 nanoparticles (0–10 phr). Hybrid nanocomposites containing 15 phr of CTBN and 7 phr of Al_2O_3 exhibited the maximum values of the critical stress intensity factor (K_C) and critical strain energy release rate (G_C).

In a comprehensive review, Kausar [98] compared the effects of various nanofillers such as graphene, carbon nanotube, carbon black, nanoclay, silica and other nanoparticles on the properties and structures of rubber-toughened epoxy resins. These nanofillers have enabled the development of rubber-reinforced epoxy nanocomposites with improved performance and their use in adhesives, coatings, anticorrosives and radiation shielding materials for military, aircraft and aerospace applications. The nanocomposite materials offer the advantages of light weight, high strength, high toughness and corrosion resistance. Zewde et al. [99] studied the effect of functionalized carbon nanotubes (fCNTs) and micron-sized rubber particles on the properties of epoxy resin. The nanotubes were mixed with carboxyl-terminated butadiene acrylonitrile-toughened epoxy (CTBNTE) by shear mixing and sonication. The fracture toughness of the epoxy/CTBN/fCNT ternary composites was higher by approximately 200% compared to the neat epoxy matrix, 20% and 110% compared to the epoxy/fCNT and epoxy/CTBN blends, respectively. The confirmed synergistic effect of fCNT nanofillers and rubber particles was attributed to plastic deformation, stress whitening and the overall rougher surface of the ternary composites compared to the pristine resin. Similar results were obtained by Hsieh et al. [100] with a significant improvement in the fracture toughness (G_C) of an epoxy matrix due to the synergistic effect of silica nanoparticles (SNs) and rubber particles. The critical strain energy release rate parameter, G_C, of the epoxy resin increased from 77 to 191 J/m^2 and 671 J/m^2 by adding 15 wt% SN and 9 wt% of rubber particles, respectively. However, it increased up to 965 J/m^2 for the ternary epoxy nanocomposites containing both SNs and rubber microparticles. The improvement in the toughness of the epoxy matrix containing soft and solid particles is explained by the same mechanism reported previously [85,88,93].

Similarly to CTBN, liquid butadiene acrylonitrile terminated with amine groups (ATBN) was also used to toughen epoxy nanocomposites [101–103]. It was shown that the addition of 1.5 wt% nanoclay to an epoxy composition modified with 5 wt% ATBN led to synergistic effects on the mechanical behavior [101]. A similar improvement in the epoxy resin mechanical properties was noted in the case of epoxy resin modified with a combination of ATBN and organomodified nanoclay (Nanobent ZW1) [102]. Ternary epoxy composites containing 1 wt% or 2 wt% Nanobent and ATBN showed improved mechanical properties in relation to the unmodified EP. The impact strength (IS) and the critical stress intensity factor (K_C) values of EP containing 1 wt% nanoclay increased approximately by 200% and 75%, respectively, in relation to the neat EP. In another study, the matrix was modified with Nanobent ZW1 and ATBN with different amine equivalent weights (ATBN-16 with 18% acrylonitrile and ATBN-21 containing 10 wt% acrylonitrile) [103]. A ternary composite containing 2 wt% nanoclay and 5 wt% ATBN exhibited a synergistic effect on the tensile adhesive strength toward the binary systems. The significant enhancement in the properties was explained by the reaction that took place between the amine groups of the modifier or hardener and the unreacted part of the cured epoxy matrix. Figure 1 shows how the incorporation of a rubber can change the morphology of a composite to a more elongated one with plastic deformation, thus explaining the increase in the mechanical properties of the matrix.

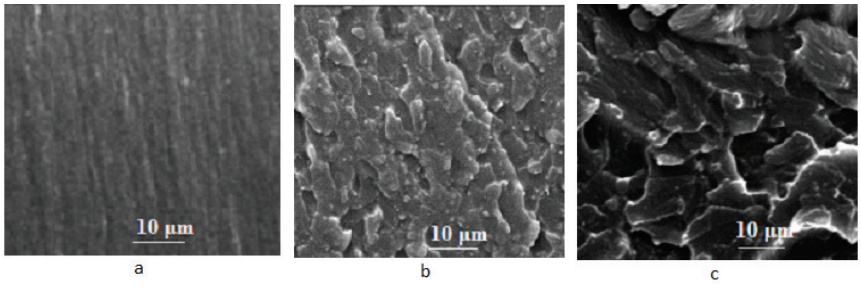

Figure 1. SEM micrographs of virgin epoxy matrix (**a**), epoxy resin with 1 wt% Nanobent ZR1 (**b**) and epoxy with 1 wt% Nanobent ZR1 and 10 wt% of reactive rubber (**c**).

Figure 2 shows the effect of the reactive rubber and Nanobent ZR1 content on the impact strength (IS) and critical stress intensity factor (K_C) of an epoxy composite. It is seen that the hybrid composite can be prepared by fixing the content of one modifier with the highest value and by varying the amount of the second modifier.

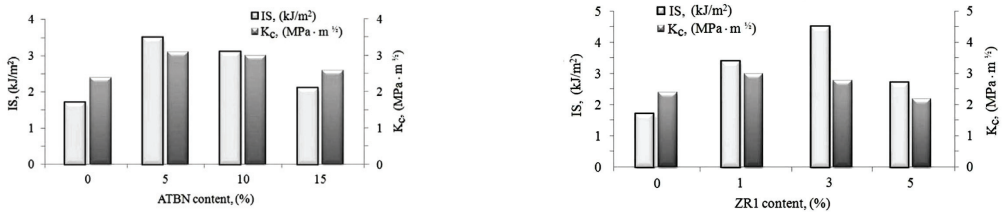

Figure 2. IS and K_C of epoxy nanocomposite containing 1 wt% of Nanobent ZR1 as a function of rubber content (**a**) and epoxy blend containing 5 wt% rubber and different nanoclay content (**b**); (our unpublished results).

Kong et al. [104] prepared a series of epoxy composites based on organomodified montmorillonite (oMMT) and epoxy-terminated acrylonitile butadiene copolymer (ETBN) and tested their mechanical performance. The addition of both oMMT and ETBN led

to a significant improvement in the epoxy matrix damping properties while maintaining the high tensile strength. The improvement in the damping performance due to the incorporation of ETBN-intercalating oMMT nanocomposites has been confirmed by Mao et al. [105].

Due to its reactive groups, polysulfide is considered, along with liquid rubbers such as CTBN, ATBN and hydroxyl-terminated polybutadiene, as the most effective toughening agent for epoxy resins. The reaction between the thiol and the epoxy groups is expected to enhance the flexibility and impact strength (IS) of the epoxy matrix but decrease certain properties such as the glass transition temperature (Tg) and modulus. Pristine and carboxyl-functionalized multiwalled carbon nanotubes (p-MWCNTs and f-MWCNTs) in addition to polysulfide were used to prepare an amine-cured epoxy resin with improved mechanical properties [106]. The incorporation of 0.1 wt% f-MWCNTs to the epoxy/polysulfide blend significantly improved the tensile and impact resistance of the epoxy nanocomposite. The Tg of the f-MWCNT/epoxy hybrid composites increased by 9.8 °C compared to the neat epoxy matrix. The improvement in the mechanical properties was attributed to the strong interfacial interactions between the f-MWCNTs and the epoxy matrix. The increase in the properties was explained by the plasticization of the cured epoxy by PSf, and most likely to increased matrix crosslinking [107].

Other liquid rubbers with specific physical properties have also been used in combination with nanoparticles to improve the properties of epoxy nanocomposites [108–111]. Tang et al. [108], for example, investigated the properties of epoxy resin modified with rigid silica nanoparticles (SNs) and phase-separated submicron soft rubber particles. Ternary epoxy composites showed a good balance between the stiffness, strength and fracture toughness compared to single-phase particle binary systems. The fracture toughness improvement in the ternary epoxy composites was attributed to the formation of a large plastic zone around the crack tip, resulting from the dual addition of rigid and soft particles.

Epoxidized natural rubber (ENR) has been used by various researchers to modify epoxy resins, for its polarity and good compatibility with several polar polymers [109–112]. Leelachai et al. [109] modified an epoxy resin cured with cycloaliphatic polyamine by using epoxidized natural rubber (ENR) with silica nanoparticles (SNs). The addition of ENR resulted in a significant improvement in the fracture toughness parameter (K_C) with a decrease in the glass transition temperature (T_g,) and Young's modulus. However, the addition of SNs led to a modest improvement in the toughness and T_g but a significant increase in the modulus. The ternary hybrid epoxy composites exhibited improvements in the K_C, stiffness and Tg. The maximum improvement in the fracture toughness, including a synergistic effect, was obtained with an epoxy matrix containing a defined amount of SNs and ENR. Morphology analysis revealed the existence of the cavitation of rubber particles together with matrix shear yielding, particle debonding and an increase in the damage zone size, which was associated with the dissipation of more energy during the crack propagation. Recently, Kam et al. [110] studied the effect of different vulcanized rubbers on the properties of epoxy resin filled with graphene nanoplatelets (GNPs). The epoxy matrix was modified with natural rubber (NR), liquid natural rubber (LNR) and recycled natural rubber (rNR). An epoxy/GNP nanocomposite filled with 5 vol% NR showed the highest values of flexural strength, flexural modulus and fracture toughness (K_C), as compared with LNR and rNR, due to better interfacial adhesion between the epoxy/NR/GNP system. Similar results were obtained on the properties of epoxy resin modified with natural rubber and graphene nanoplatelets [111].

The effect of preformed powdered rubber (PR) nanoparticles and chemically reduced graphene oxide (CRGO) was also evaluated on the mechanical and thermal properties of epoxy resin [112]. The inclusion of CRGO improved the fracture toughness, stiffness and thermal properties of epoxy resin, while the addition of PR resulted in a significant improvement in the fracture toughness but large reduction in the thermal stability and stiffness of the polymer matrix. The results confirmed the existence of a good balance between the stiffness, strength, fracture toughness, thermal stability and glass transition

temperature in ternary epoxy hybrid composites. The shear bands formed in the matrix most likely induced by the stress transfer, combined with the nanoparticle pull-out, can partly explain the improved properties of the hybrid epoxy nanocomposites [94,100,110].

A very interesting approach to toughen epoxy resin was the use of core–shell rubber (CSR) particles, which constitute the specific group of rubber of the effective toughening agent for epoxy resins. The particles are generally based on an elastomeric core such as a homopolymer of butadiene or a styrene–butadiene copolymer and a thin epoxy-compatible shell. The particular advantage of CSR particles compared to liquid rubbers is their compatibility with EPS. Tsang and Taylor [113] solved the brittleness problem of adhesives based on the anhydride cured epoxy thermosetting polymer by using CSR particles and silica nanoparticles (SNs). The fracture energy parameter, G_C, of the modified epoxy was measured at ambient and low temperatures (-40 °C and -80 °C). The results showed that hybrid composites with 10 wt% SN and 10 wt% CSR particles exhibited the maximum improvement in the G_C, but with no dual strengthening of the matrix, most probably due to the large size of the modifier particles. A similar study was performed with epoxy resin modified with CSR combined with SNs but different results improved the properties and mechanisms [114]. The soft shell was a copolymer synthesized from caprolactone and meso-lactide which was compatible with the epoxy system. The incorporation of 2 wt% of nanofillers resulted in a 40% increase in the impact resistance of the epoxy, while the glass transition temperature decreased slightly. Crazing, formation of microcracks and debonding of nanoparticles from the matrix were the main causes leading to the improved fracture toughness. Soft core–shell rubber (CSR) nanoparticles have also been used with multiwalled carbon nanotubes (MWCNTs) and SiO2 nanoparticles as rigid particles to toughen a bisphenol A-based epoxy cured with an amine hardener [115].

The MWCNT modifiers have attracted great interest as they generally lead to excellent mechanical, thermal and electrical properties in polymer composites. Furthermore, CSR particles have the ability to promote compatibility between incorporated modifiers with the matrix. Epoxy hybridization with CSR and SiO_2 resulted in a simultaneous improvement in the tensile and fracture properties. The fracture toughness parameter, K_C, and the fracture energy parameter, G_C, of hybrid systems containing 5 wt% CSR and 10 wt% SiO_2 increased to a maximum of about 220% and 900%, respectively, compared to the virgin polymer matrix. However, an increase of 165% was reported for the K_C of the epoxy hybrid based on 0.075 wt% MWCNTs and 10 wt% SiO_2. The so-called core–shell impact modifier particles (CSIMPs) were added with multiwalled carbon nanotubes (MWCNTs) to improve the toughness and tensile properties of the epoxy resin [116]. The soft particles consisted of a poly(butyl acrylate-allyl methacrylate) elastomeric core and a poly(methyl methacrylate-glycidyl methacrylate) shell. It was demonstrated that the highest fracture toughness of the ternary composite was achieved with the addition of 3 wt% MWCNTs and 3 wt% CSIMPs, while the maximum values of the tensile strength and modulus were obtained with same amount of MWCNTs and a lower content (only 1.03 wt%) of the CSIMPs. The improvement in the fracture toughness of the ternary epoxy composites was attributed to deflection/crack arrest as well as expanded plastic deformation around the crack tip induced by the combination of rigid and soft particles. In addition to the processes related to solid particle bridging, the crack deflection and increase in the crack path caused the observed reinforcement [117]. However, Zhu et al. [118] used core–shell rubber (CSR) with zinc oxide-functionalized multiwall carbon nanotubes (ZnO-MWCNTs) to improve the properties of epoxy resin. The functionalized multiwalled carbon nanotube is expected to further increase the properties of the matrix compared to the virgin modifier [106]. MWCNT modifiers have attracted great interest as they generally lead to excellent mechanical, thermal and electrical properties in composites. Additionally, CSR particles have the ability to promote compatibility between incorporated modifiers with the matrix. The obtained results confirmed that the fracture toughness parameter, K_C, of the hybrid epoxy nanocomposite was higher than those of the matrix binary systems, due to the synergistic effect associated with the shear band formation along with the crack deflection. Similar

impressive toughening was achieved by Mehrabi-Kooshki and Jalali-Arani [119] with hybrid epoxy nanocomposites based on CSR particles and graphene oxide (GO). As expected, the tensile strength and modulus of the epoxy systems modified with CSR decreased with the increasing CSR content, due to matrix flexibilization. With the incorporation of only 0.05 phr GO to the neat epoxy and epoxy/rubber blend, the hybrid epoxy composites exhibited a significant improvement in the tensile strain at break compared to the virgin matrix and binary systems. The strain at the break increase resulted mainly from the rubber particle cavitation and the reduction in the epoxy crosslinking density. However, when GO was replaced by silica nanoparticles (SNs), hybrid epoxy nanocomposites containing 4 vol% of SNs and 7 vol% CSR showed a fracture energy five times greater than that of the unmodified epoxy resin with no reduction in the tensile modulus [120]. The increase in the fracture energy of the matrix was explained by the shear yielding observed at the crack tips in the epoxy matrix and CSR cavitation and void growth. Interestingly, the observed lack of SN debonding acted as shear band stoppers. However, due to different constituents and their relevant possible interactions, it can be emphasized that there is no exclusive interpretation of the toughening mechanisms in epoxy composites based on CSR and SNs.

Most of the hybrid epoxy resin composites based on solid nanoparticles and liquid modifiers included nanoparticle debonding and void formation yielding of the polymer matrix. The created voids by the microparticles slow down the crack propagation and facilitate the plastic deformation of the epoxy matrix. Table 1 summarizes epoxy nanocomposites modified with rubbers and shows the synergistic effects on the matrix properties.

Table 1. Epoxy nanocomposites modified with rubber showing synergistic effect.

Modifiers	Improved Properties	References
CNT/rubber nanoparticles	G_C	[69]
HTPB/MMT	Tensile strength, strain break	[79]
Rubber/MMT	Tensile modulus	[82]
Rubber/SN	K_C	[85]
ATBN/Nanobent	Tensile adhesive strength	[103]
CTBN/Nanomer 130.E	G_c, K_C	[90]
CTBN/SN	G_c, K_C	[94]
fCNT/CTBNTE	Tensile fracture energy	[99]
ENR/SN	K_C	[110]
ZnO-MWCNT/CSR	K_C	[118]
GO/CSR	Tensile strain break	[119]

HTPB—hydroxyl terminated polybutadiene; ENR—epoxidized natural rubber; SN—silica nanoparticles; CTBNTE—carboxyl-terminated butadiene acrylonitrile; fCNT—functionalized carbon nanotubes; ATBN—amine-terminated butadiene-acrylonitrile; CTBN—carboxyl-terminated butadiene-acrylonitrile; ZnO-MWCNT—zinc oxide-functionalized multiwall carbon nanotubes; CSR—core–shell rubber; K_C—critical stress intensity factor (fracture toughness parameter); G_C—critical strain energy release rate.

2.2. Hybrid Epoxy Nanocomposites Based on Polyurethanes

Due to their specific mechanical, physical, biological and chemical properties, polyurethanes (PUs) are a class of versatile materials which can be used in different applications. Various studies concerned the toughening of epoxy resins by using polyurethanes and nanoparticles [121–129]. Jia et al. [121,122] demonstrated that the mechanical and thermal properties of interpenetrating epoxy/polyurethane polymer networks (IPNs) modified with organophilic montmorillonite (oMMT) were superior to those of pure PUs and PU/EP IPNs, due to an increased degree of exfoliation of the oMMT and better compatibility between PUs and EP. A strong interaction between the oMMT and the EP/PU IPNs was confirmed with an increase in hydrogen bonding at the interface between the oMMT and the EP/PU blend. In a separate work, it was shown that the effective dispersion of oMMT

in an EP/PU IPN system resulted in a synergistic effect in the tribological performance of EP/PU nanocomposites [123]. The obtained results also indicated that the thermal degradation temperature of the IPNs was attenuated by the addition of organically modified clay to the epoxy matrix. Polyurethanes with various structures and mechanical properties were also investigated by other researchers [124,125]. The maximum improvement in impact resistance was obtained with a composite containing 2 wt% nanoclay and 10 wt% PUs synthesized from polyethylene glycol with a molecular weight of 400 g/mol (PU400) and with 1 wt% nanoclay and 15 wt% PU400, corresponding, respectively, to 110% and 75% with respect to the unmodified epoxy resin [124]. However, a 10-fold increase in the flexural strain at break was observed for the composite containing 15 wt% polyoxypropylene diol-based PUs with a molecular weight of 1000 g/mole and 2 wt% nanoclay, including a synergistic effect. It is well known that the flexible polyurethane chains form interpenetrating polymer networks with the epoxy matrix with increased elasticity, while the solid nanoparticles increase the strength and rigidity of the matrix. Moreover, it is expected that chemical reactions occur between the hydroxyl groups of the EP and the isocyanate groups of the PUs (Scheme 3). Hybrid composites with improved mechanical properties will be obtained due to the increased yielding of EP and nanoclay exfoliation [125].

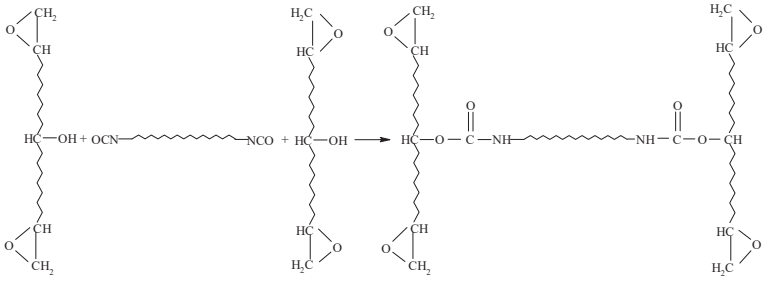

Scheme 3. Reaction between epoxy and polyurethane functional groups.

The impact strength (IS) and critical stress intensity factor (K_C) of the epoxy matrix containing 1 wt% and 2 wt% of nanoclay (Nanobent ZR1) are shown in Figure 3 as a function of commercial linear polyurethane (Desmocap 12). Although both parameters express the resistance to crack propagation, they show different trends as a function of the polyurethane content. The explanation would be related to the order of addition of the modifiers in the matrix.

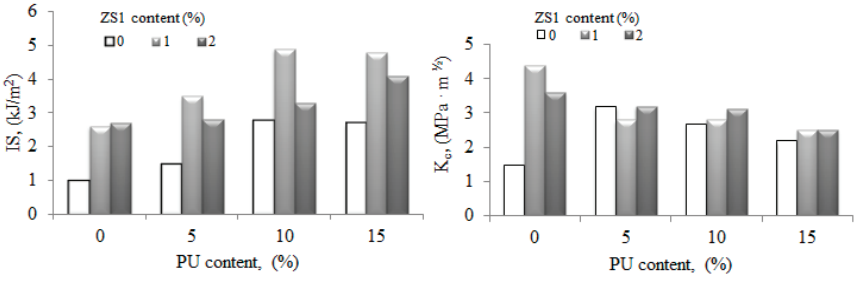

Figure 3. Effect of polyurethane content on IS and K_C of epoxy composites containing 1 wt% and 2 wt% nanoclay (of Nanobent ZR1); (*our unpublished results*).

Hydrogen bonds can also form at the interface between the organomodified montmorillonite (MMT) and the epoxy/polyurethane interpenetrating polymer network (EP/PU IPN), leading to a further improvement in the properties of the polymer blend and that of the epoxy matrix (Scheme 4).

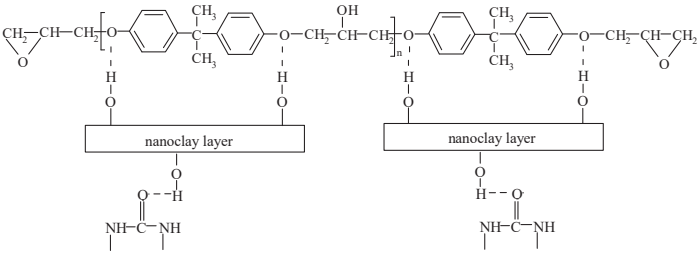

Scheme 4. Formation of hydrogen bonding at the interface between oMMT and EP/PU IPN.

Moreover, it should be remembered that modified montmorillonite (Cloisite 30B) contains quaternary ammonium ions with two hydroxyethyl groups which are able to react with the isocyanate groups of polyurethane, as shown in Scheme 5. This reaction can be confirmed by the FTIR measurement with a decrease in the peak height of the OH groups at 3300 cm^{-1}.

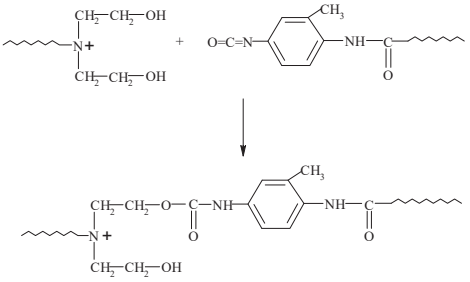

Scheme 5. Reaction between hydroxyl groups at surfaces of MMT platelets with isocyanate groups.

Recently, much attention has been paid to the toughening of epoxy resin using nanoparticles in combination with vegetable oil-based polyurethanes [126–129]. Due to their remarkable importance as an environmentally friendly component, vegetable oils have attracted considerable attention as a potential alternative to polyols for the synthesis of polyurethanes. Although some studies on polyurethane nanocomposites are available, works on vegetable oil-based polyurethane nanocomposites are currently limited. Polyurethanes based on vegetable oil are known for their very good corrosion resistance, good electrical insulation as well as their shape memory. They are also inexpensive, available in large quantities and biodegradable. Li [126] was one of the first to modify interpenetrating polymer networks (IPNs) prepared from epoxy (EP) resin and castor oil-polyurethane (PU) by using different amounts of organophilic montmorillonite (oMMT). Instrumental analysis of the nanocomposites confirmed a uniform dispersion of the nanoparticles in the IPNs with the formation of intercalated or exfoliated microstructures. Differential scanning calorimetry results showed that oMMT promoted the compatibility between the EP and PU phases accompanied by an improvement in the glass transition temperature of the oMMT/EP/PU ternary nanocomposites with the increasing oMMT content. The mechanical properties and thermal analysis indicated that oMMT and the IPN systems exhibited a synergistic effect on improving the mechanical and thermal properties of the pure EP. It appeared that the formation of cavitations and small cracks contributed to the improvement in the EP properties. However, it has been shown that the use of multiwalled carbon nanotubes (MWCNTs) to modify the properties of IPN castor oil-based PU/epoxy resin led to a significant improvement in the matrix properties [127]. The tensile strength of epoxy composites containing 0.1 wt% and 0.7 wt% MWCNTs increased by more than 30% relative to the matrix. The impact strength of the composite with 0.3 wt% MWCNT content increased by approximately 55% compared to the virgin epoxy resin, while the thermal decomposition temperature

decreased slightly, due most probably to the strong interaction between the nanoparticles and epoxy/PU matrix. Another vegetable oil (soybean oil) was used by Xu et al. [128] to prepare a polyurethane (PU) which was then mixed with an EP to form IPN structures. The ternary epoxy/PU composites containing oMMT exhibited an increased thermal stability as well as a synergically enhanced tensile strength and tensile modulus. The tensile strength and modulus of the PU/EP IPNs increased maximally by approximately 65% and 390% with 4 wt% and 6 wt% of oMMT, respectively. In a separate study, the tensile strength and scratch hardness of the epoxy resin were significantly improved, and the impact resistance increased slightly when the polyurethane based on *Mesua ferrea* L. seed oil (MFLSO) was used with organically modified bentonite to improve the matrix properties [129]. The thermal stability of the nanocomposites increased by about 40 °C.

The last decades have seen a very significant growth in interest in the use of bioderived products, which has been driven by the need to replace petroleum-based materials and produce eco-friendly materials. Recent research has focused on the use of environmentally friendly and non-toxic routes for the synthesis of polyurethanes, which avoid the use of diisocyanates. The procedure offers a number of advantages, including the use of environmentally friendly, inexpensive and biobased components. However, there remains a great challenge to produce epoxy hybrid nanocomposites based on renewable resources with improved performance properties and taking into account environmental protection. Despite the various studies conducted so far to assess the fracture resistance of epoxy nanocomposites, some issues still remain unclear.

Białkowska et al. [130] prepared and evaluated the mechanical properties of an epoxy resin by using condensation segmented nonisocyanate polyurethane (NIPU) and nanoclays (Nanobent) and analyzed the correlation between morphology and blend performance. The highest values of the impact strength, flexural strength and critical stress intensity factor were obtained with epoxy hybrid composites containing 10 wt% NIPU and 1 wt% nanoclay. As in the case of other studies on conventional isocyanate-based PUs [25,26], it was confirmed that the improvement in the mechanical properties of EP was due to the formation of an epoxy/NIPU network, an extensive matrix yielding with the formation of stretched morphology, but with no grafting reaction.

A green polyurethane (NIPU) was synthesized from sunflower oil via an environment-friendly and non-toxic route and used as a modifier for epoxy resin containing amine-functionalized graphene oxide (af-GO) [131]. The properties of the nanocomposites have been shown to increase with the increasing af-GO content, due to the strong hydrogen bonding and interactions between af-GO with the polymer network. The prepared hybrid epoxy nanocomposites exhibited a good balance between mechanical, chemical and thermal properties. These results highlight the potential of this environmentally friendly approach to prepare renewable NIPUs and high-performance nanocomposite materials.

The occurrence of chemical reactions between components in hybrid epoxy nanocomposites is possible due to the presence of urethane linkage in the polyurethane structure. Therefore, the order of the addition of components is expected to have a crucial effect on the properties of epoxy composites [132,133]. Cheng et al. [132] studied the component order of addition on selected properties of epoxy (EP) resin cured with triethylenetetramine (TETA) and modified with polyurethane (PU) synthesized by reacting polytetramethylene ether glycol (PTMG), isophorone diisocyanate (IPDI) in the presence of dibutyltin dilaurate (DBTDL). The results confirmed the role of the components in the mixing order, in that the best physical, mechanical and thermal properties were obtained when the epoxy matrix was first mixed with PTMG, IPDI, DBTDL, before adding TETA. Similar findings were obtained with two different mixing sequences and their effects on the properties of epoxy ternary nanocomposites [133]. The mechanical and thermal properties of epoxy/organoclay/polyether polyol ternary nanocomposites depended largely on the mixing sequence of the constituents. The results showed that the impact strength values of the ternary nanocomposites were higher when the polyether polyol was mixed with the curing agent followed by its incorporation into the EP/MMT mixture. This was explained by the

possible interactions between all the components of the prepared ternary nanocomposites. The importance of the order of the incorporation of the constituents was confirmed in our work on the properties of an epoxy resin modified with montmorillonite (MMT) and conventional polyurethane (PU) [134]. The best mechanical properties were exhibited by nanocomposites in which prepared PU was first mixed with EP before the incorporation of MMT (Cloisite 30B). Structural analysis indicated the formation of a non-grafted interpenetrating polymer network structure. The improvement in the properties was explained by the good interactions between the MMT and the polyurethane, possibly via hydrogen bonding, which, depending on the degree of dispersion of the stratified montmorillonite in the matrix, tends to improve its intercalation [122,124]. The order of the incorporation and mixing of the epoxy nanocomposite constituents are shown in Scheme 6.

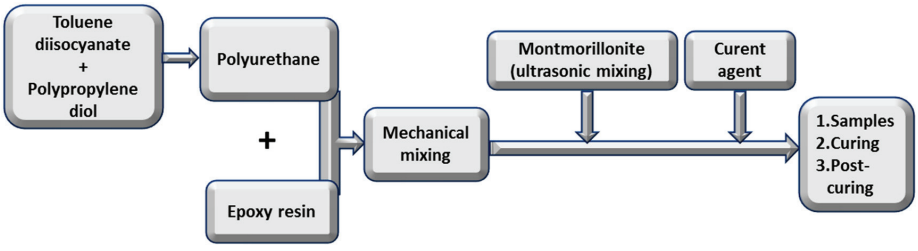

Scheme 6. Mixing order of epoxy nanocomposite constituents.

The addition of flexible polyurethane chains to an epoxy matrix has been shown to result in the formation of an interpenetrating polymer network (IPN) structure with improved ductility but also toughness with hydrogen bonding and grafting reactions. Moreover, the incorporation of solid nanoparticles to the IPN system contributes to the further reinforcement of the polymer matrix.

Table 2 presents epoxy nanocomposites modified with polyurethanes with a synergistic effect on the mechanical properties.

Table 2. Epoxy nanocomposites modified with polyurethanes with synergistic effects.

Nanoparticles	Improved Properties	References
oMMT	Wear loss, friction coefficient	[123]
oMMT	Flexural strain at break	[125]
Modified sodium bentonite	Tensile strength, K_c	[126]
oMMT Na^+	Tensile strength, tensile modulus	[127]
oMMT—Cloisite 30B	Tensile strength, flexural strain at break	[134]

2.3. Hybrid Epoxy Nanocomposites Based on Thermoplastics

The concept of incorporating both thermoplastic polymers and nanoclay in the epoxy matrix has been advanced as an efficient method to produce composites with improved mechanical and thermal properties. Thermoplastics have been intensively studied for about four decades as toughening agents because they generally do not cause a significant reduction in the modulus, yield strength and glass transition temperature, as in the case of liquid rubbers. Various ductile thermoplastics were investigated as an alternative to reactive rubber for improving the mechanical properties of the epoxy resins [135–156]. When mixed with an engineering polymer, the epoxy matrix can form an interpenetrating network which would prevent the agglomeration of the nanoparticles and thus allow their unform dispersion in the blend.

Although they have a lower strength and toughness than engineering plastics, commodity plastics have been employed in combination with nanoparticles to reinforce the

brittle thermosetting epoxy material. Park and Jana [135] were the first to study the modification of a diglycidyl ether of bisphenol A (DGEBA) epoxy resin with polymethyl methacrylate (PMMA) and nanoclay. Mixtures of aromatic and aliphatic DGEBA resins were prepared with organically modified montmorillonite (Cloisite 30B) and PMMA. The results confirmed that clay nanoparticles were fully exfoliated in the three-phase composites when the ratio of epoxy to clay was 10, resulting in a significant improvement in the tensile and impact strengths. However, Hernandez et al. [136] confirmed that the best dispersion of nanoparticles in ternary epoxy composites does not lead necessarily to the highest values of the mechanical properties. A synergistic effect was confirmed in a hybrid composite based on the same matrix and PMMA, but with a different nanoclay (Nanobent ZS1) using mechanical mixing followed by additional ultrasonic mixing [137]. The flexural strain at break and flexural energy to break of the composite containing 1 wt.% MMT and 5 wt% PMMA were higher compared to the epoxy binary systems. The same finding was obtained for the impact strength and brittle fracture energy of composites based on 2 wt% MMT and 5 wt% PMMA. The results demonstrated the formation of hydrogen bonding between PMMA and the epoxy matrix, according to Scheme 7. The improvement in the properties was explained by the specific interaction between the polymer modifier and the matrix but also with the uniformly dispersed and well-embedded nanoparticles in the polymer blend [138]. Rudresh et al. [139] used the same blending procedure and obtained an improved tensile strength and Young's modulus of hybrid epoxy nanocomposites containing 6 wt% PMMA and 4 wt% of modified halloysite nanoclay tubes (HNTs). The fracture toughness parameter, K_C, of the hybrid nanocomposite increased by approximately 95%, most probably due to the positive effects generated from the combination of two dissimilar toughening mechanisms, but also the prepared suspension of nanoparticles which is supposed to ensure the uniform dispersion and exfoliation of the latter.

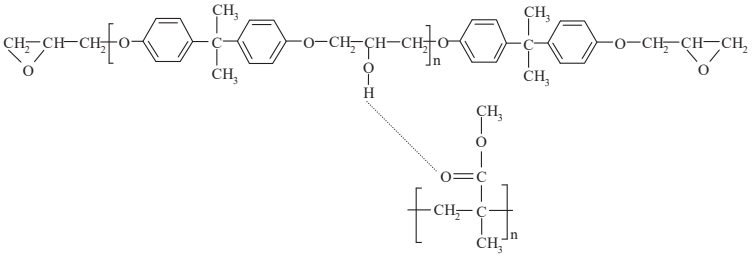

Scheme 7. Reaction between poly(methyl methacrylate) and the epoxy matrix.

Poly vinyl chloride (PVC), which belongs to the important group of commodity thermoplastics with interesting properties, was also used to toughen epoxy nanocomposites. Kaushal et al. [140] studied the properties of the nanocomposites of epoxy/PVC with different amounts of organomodified montmorillonite (oMMT) and found that the best mechanical properties were attributed to ternary epoxy composites with 5 phr PVC and 5 phr oMMT.

Another alternative to toughen epoxy resins was the use of tough engineering thermoplastics, such as polysulfone (PSU), polyethersulphone (PES), poly (ether ether ketone) (PEEK), polyetherimide (PEI), acrylonitrile–butadiene–styrene copolymer (ABS), polycarbonate (PC), poly(styrene-co-acrylonitrile) (SAN) and high impact polystyrene (HIPS) [141–147]. Wang et al. [141] used both polysulfone (PSU) and graphene oxide (GO) to toughen DEGBA epoxy resin. The resistance to crack propagation expressed by the fracture toughness parameter, K_C, and the elongation at break of epoxy ternary composites containing 5 phr PSU and 0.2 phr GO were maximally increased by 90% and 55%, respectively, compared to the pure matrix, while the tensile strength, Young's modulus and thermal stability were not affected. The current strategy of using both PSU and GO as dual toughening agents is promising for effectively toughening epoxy resins without sacrificing

mechanical and thermal properties. A similar improvement in mechanical properties was obtained by Rajasekaran et al. [142] with ternary epoxy composites based on oMMT and PSU. Introducing 5 wt% oMMT in the modified epoxy/PSU IPN system improved both the tensile and flexural strength compared to the virgin matrix. A maximum increase in the impact strength of 56% was exhibited by the hybrid composites containing 8 wt% PSU and 5 wt% oMMT. The improvement in the mechanical properties of the ternary composites was explained, on the one hand, by the formation of a flexible IPN structure within the system, but also by the effective interaction between the nanoclay, the PES and the epoxy matrix. Studies undertaken by Wang et al. [143,144] concerned the preparation of epoxy/polyethersulfone mixtures reinforced with organoclay montmorillonite (Nanocor 1.30E). Ternary composites prepared with the environmentally friendly melting method showed high tensile properties, a high fracture toughness, K_C, and good thermal performance compared to the solvent method. The dual addition of PES and organoclay resulted in a synergistic effect on the fracture toughness of the epoxy resin, regardless of the method used [143]. The K_C of the EP/PES blend modified with 1 wt.% organoclay increased by about 98% compared to the neat epoxy matrix, while it was higher by 49% and 58% compared to the EP/PES and EP/nanoclay systems, respectively. A different toughening mechanism has been proposed compared to the above studies, and which would involve the debonding of the exfoliated nanoparticles but also a bifurcation of the cracks as well as an induced plastic deformation of the matrix [144]. A similar improvement was obtained by Tangthana-umrung et al. [145] for the K_C of epoxy resin composites containing PES, graphene nanoplatelets (GNPs) and carbon nanotubes (CNTs). The addition of 5 wt% PES improved the mechanical properties and thermal stability including 35% and 40% increases in the tensile strength and fracture toughness, K_C, respectively. Hybrid epoxy nanocomposites based on 5 wt% PES, GNPs and CNTs showed a synergistic toughening on the K_C toward the binary matrix systems, with a remarkably higher Young's modulus in all epoxy/PES/CNT hybrid epoxy composites. The toughening of the GNP/PESU hybrid epoxy composites was attributed mainly to crack deflection by the PESU and GNP particles, as well as crack bifurcation by the GNP clusters.

If PSU and PES with similar molecular structures were used for their relatively high rigidity and glass transition temperatures, polyetherimide, poly(ether ether ketone) and acrylonitrile–butadiene–styrene terpolymer have been widely used due to the excellent combination of physical and mechanical properties including toughness, stiffness, chemical and solvent resistance as well as high glass transition temperature.

Studies on epoxy resin toughening using polyetherimide (PEI) combined with amino-grafted multiwalled carbon nanotubes (NH_2–MWCNTs) or carboxyl-functionalised (COOH–MWCNTs) have been carried out by Chen al. [146] and Ma et al. [147], respectively. The results indicated a significant improvement in the fracture toughness, impact strength and flexural strength of the epoxy composites by the simultaneous incorporation of a low content of PEI and NH_2–MWCNTs. Ternary composites with 5 phr PEI and 0.4 phr NH_2–MWCNTs showed the maximum improvement with a synergistic effect in the fracture toughness, K_C [146]. However, the critical strain energy release rate, G_C, referred to as the fracture toughness of composites based on (COOH–CNTs), significantly increased, while the glass transition temperature and the storage modulus remained unaffected [147]. The interactions between the nano- and microscale toughening under appropriate mixing conditions led to a synergistic improvement in the G_C of the matrix. The debonding of the nanotubes and the resulting increase in the crack path can explain the toughening of the epoxy matrix. Hydroxyl-terminated poly (ether ether ketone) oligomer with pendant methyl groups (PEEKMOH) was used by Asif et al. [148] to toughen DGEBA epoxy resin modified with organically modified montmorillonite (oMMT). The fracture toughness, K_C, and strain at break of epoxy composites based on 1 phr oMMT and 5 phr PEEKMOH increased by 65% and 85%, respectively, compared to the neat matrix, without synergistic reinforcement. This could be related to gel formation during the curing of the matrix.

Acrylonitrile–butadiene–styrene terpolymer (ABS) is a high-performance commercial thermoplastic with a specific structure, a rubbery polybutadiene dispersed in a rigid styrene–acrylonitrile copolymer system. Due to its excellent mechanical and thermal properties, ABS was used with nanoparticles to improve the properties of epoxy resin by several authors [149,150]. Mirmohseni and Zavareh [149] confirmed the increase in the tensile strength, strain at break and impact strength of a DGEBA resin with the addition of ABS and organically modified clay (Cloisite 30B). Adding 2.5 wt% clay and 4 phr ABS into the epoxy matrix resulted in a 133% increase in the impact strength. The impact and tensile strengths of the ternary composite were higher than the values of the binary systems, due to a good dispersion of the exfoliated clay platelets in the epoxy/ABS blend and crack blocking by ABS nanoparticles. A similar improvement in the same mechanical properties and associated mechanisms was observed in another study with hybrid epoxy composites containing ABS combined with multiwalled carbon nanotubes (MWCNTs) and diaminodiphenylsulfone as the matrix curing agent [150]. The impact strength (IS) and tensile strength (TS) increased significantly by 110% compared to the binary matrix system and 400% compared to the virgin matrix, while the TS was 165% higher than the binary system. The detachment of microparticles and nanoparticles can be used with the resulting energy to explain the improvement in the properties of the hybrid composites, as shown in Scheme 8.

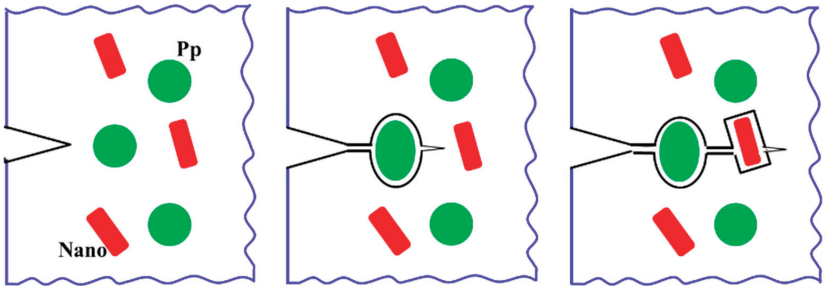

Scheme 8. Crack propagation in epoxy matrix containing microparticles and nanoparticles (Pp—polymer microparticles, Nano—nanoparticles).

To further improve the properties, the epoxy resin was modified with methyl phenyl silicone (MPS), before the incorporation of ABS and graphene oxide (GO) [151]. The tensile strength of the grafted epoxy resin containing 5 wt% MPS, 2 wt% ABS and 0.1wt% GO increased by approximately 35% compared to the sample containing 5 wt% MPS and 2 wt% ABS, and up to 50% compared to the pure matrix. Morphology analysis of the samples revealed the presence of micro-sized domains which were obtained by phase separation, thus explaining the improvement in the properties.

Polycarbonate (PC) is an amorphous engineering thermoplastic which has good thermal stability, outstanding impact resistance and good transparency. The maximum improvement in the impact strength (IS), fracture toughness (K_C) and flexural strength was obtained with an epoxy composite based on 1 wt% montmorillonite (Cloisite 30B) and 5 wt% by weight of PC [152]. An increase of 100% was obtained for the IS and K_C, while the flexural strength was slightly improved compared to the unmodified epoxy resin. Hybrid composites containing nanofillers in combination with another thermoplastic not only showed a higher impact strength and resistance to crack propagation, but also showed a synergistic effect with respect to the fracture energy [24]. From analysis of the morphology and structure, it appeared that the toughening resulted in part from the extensive yielding of the matrix and the chemical reactions that took place between the epoxy resin and the polymeric modifier, which was partially solubilized in the resin (Scheme 9).

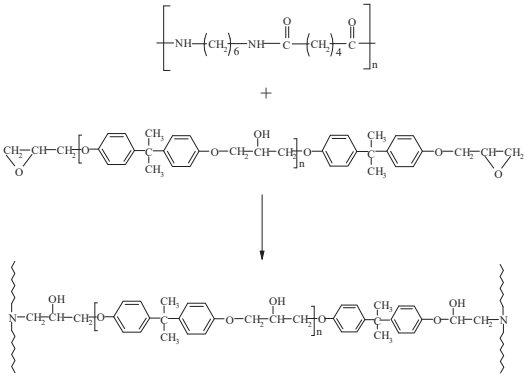

Scheme 9. Reactions between polyamide and the epoxy resin.

Although polyamide (PA) is of great interest as a compatible thermoplastic reinforcing agent for brittle epoxy resin and because of the possible formation of chemical bonds, there have not been enough research studies of its use in hybrid epoxy nanocomposites. Gul et al. [153] conducted an extensive review on epoxy/polyamide modified with nanofillers, including their application and future trends. It has been shown that the properties of epoxy/polyamide nanocomposites depend on the type of components as well as on the level of dispersion of the inorganic nanoparticles. White and Sue [154] evaluated the mechanical and electrical properties of a successfully prepared epoxy/MWCNT composite reinforced with preformed PA particles and using an ultrasonic and solvent evaporation method. The ternary composite showed significant improvements in the mechanical properties of the matrix, including a synergistic effect on the tensile strain at break, the fracture toughness parameters, K_C and G_C. This was attributed mainly to crack pinning and crack deflection in the vicinity of the large aggregates. However, the synergistic effect was not obtained with the composite of epoxy resin modified with polyamide 6 (PA6) and graphene oxide (GO) nanosheets grafted with PA6 [155]. The fracture toughness of the EP/PA6/GO increased by 52.6% compared to the neat epoxy resin, due to a better particle/matrix interface and rougher surface. A similar increase was obtained for the tensile strength and stiffness of an epoxy composite containing 5 phr of poly(styrene-co-acrylonitrile) and 1 wt% of MMT (Cloisite 20A), due to a good dispersion and reinforcement of nanoparticles [156]. High impact polystyrene (HIPS), as a standard thermoplastic material with a high impact strength, was combined with Cloisite 30B to improve the properties of the epoxy resin [157]. A significant improvement was reached in the tensile, compression and impact resistance of 60%, 65% and 400%, respectively, at the optimized modifier content. In addition, the tensile, flexural and strain at break under compression were improved by up to 55%, 40%, and 25% compared to the neat matrix, respectively, while the flexural strength remained unchanged. Fereidoon et al. [158] obtained a similar improvement in the previously mentioned properties when using multiwalled carbon nanotubes (MWCNTs) simultaneously with HIPS. The tensile, compressive and impact strength of the epoxy resin increased by 52%, 43% and 334%, respectively, while the tensile, flexural and compressive strain at break increased by 223%, 36% and 26%, respectively. Concurrent use of HIPS and MWCNTs resulted in synergistic effects on the ultimate tensile strength and tensile and flexural strain at break, most likely due to the homogeneous dispersion of the modifiers which act as crack stoppers and reinforcements of the matrix. Due to its high mechanical and thermal resistance, polyethylene terephthalate (PET) was combined with nanoparticles to toughen the epoxy resins. Prepared epoxy/PET/Al_2O_3 nanocomposites showed an improved tensile and impact strength combined with an excellent dielectric and heat resistance [159]. The improved properties of the ternary composites were remarkably superior to those of both the binary systems and the unmodified epoxy matrix. Sánchez-Cabezudo et al. [160] used polyvinyl acetate (PVA) for its miscibility with diglycidyl ether of bisphenol

A resin (DGEBA) and two organomodified montmorillonites (Cloisite 30B and Cloisite 93A) to strengthen the polymer matrix. The ternary epoxy nanocomposites developed different morphologies depending on the PVAc content. As expected, the inclusion of solid nanoparticles in the epoxy matrix improved the stiffness but decreased the ductility, while PVA improved the toughness and reduced the stiffness. The tensile strength in the epoxy composites with Cloisite 30B was higher than with Cloisite 93A due to the stronger adhesion between the components. Ternary composites containing 10 wt% Cloisite 30B and 10 wt% PVAc exhibited a good balance between the tensile modulus and toughness. The most dominant toughening mechanism in hybrid epoxy/thermoplastic nanocomposites remains particle debonding from the matrix as well as crack deflection and matrix plastic deformations. Table 3 shows epoxy nanocomposites modified with thermoplastics showing the synergistic effects on selected matrix properties.

Table 3. Epoxy nanocomposites modified with thermoplastics showing synergistic effects on selected matrix properties.

Thermoplastics	Nanoparticles	Improved Properties	References
PMMA	Nanobent ZS1	Flexural energy at break, flexural strain at break, impact strength, fracture energy	[137]
PMMA	HNT	Tensile strength, Young's modulus	[139]
PES	Nanocor 1.30E	K_C	[143,144]
PES	CNTs, GNTs	K_C	[145]
PEI	COOH-CNTs	G_C	[146]
PEI	NH_2-MWCNTs	K_C	[147]
ABS	Cloisite 30B	Impact strength, tensile strength	[149]
ABS	MWCNT	Impact strength, tensile strength	[150]
PA	MWCNT	Tensile strain at break, K_C, G_C	[154]
HIPS	MWCNT	Tensile strength, tensile and flexural strain at break	[158]
PET	Nano-Al_2O_3	Impact strength, tensile strength	[159]
PC	Bentone 34	Fracture energy	[24]

PES—polyethersulfone; PC—polycarbonate; PMMA—poly(methyl methacrylate); PET—polyethylene terephthalate; ABS—acrylonitrile butadiene styrene; PA6—polyamide 6; oMMT—organomodified montmorillonite; Nanocor 1.30E—montmorillonite; GO—graphene oxide; MWCNT—multiwalled carbon nanotubes; NH2-MWCNTs—amine terminated multiwalled carbon nanotubes; COOH—CNTs carboxyl terminated carbon nanotubes; HNT—halloysite nanoclay tubes.

2.4. Hybrid Epoxy Nanocomposites Based on Block Copolymers

Block copolymers offer several advantages over other copolymers due to their specific structures which consist of blocks of chemically dissimilar homopolymers linked together by covalent bonds. The effectiveness of a small amount of block copolymers as toughening agents for epoxy resins has been confirmed by various researchers [161–163]. They have also been considered as potential reinforcing agents in combination with solid nanoparticles for epoxy resins. Block copolymers such as polystyrene–polybutadiene–polymethylmethacrylate (SBM) and polymethylmethacrylate–polybutylmethacrylate– polymethylmethacrylate (MAM) have been used as effective soft toughening agents of bisphenol A (DGEBA) epoxy resin [162,163]. Tao et al. [162] demonstrated that the fracture toughness parameter, K_C, and impact strength of an epoxy resin containing 10 phr poly(methyl methacrylate)-*b*-poly(butyl acrylate)-*b*-poly(methyl methacrylate) triblock copolymer increased by 91.5% and 83.5%, respectively. They explained the increase in the mentioned properties by the nanophase structure obtained by self-assembly during the curing process. It was further confirmed that the toughness was improved to a large extent without significantly decreasing the glass transition temperature of the blends. In another work, the addition of 5 wt% poly(ethylene-*alt*-propylene)-*b*-poly(ethylene oxide) (PEP-PEO) (BCP)

block copolymer to a DGEBA epoxy resin led to a 100% improvement in the fracture toughness (K_C), without affecting the modulus and Tg [163]. The self-assembly of BCP molecules into well-dispersed wormlike micelles, which are more efficient than spherical micelles, also contributes to the K_C increase. As in most of the works previously described [85,94,110,139,144,145], the improvement in the properties was explained by the crack tip blunting, crack bridging, particle debonding and shear yielding of the matrix. When this BCP was incorporated with silica nanoparticles in the epoxy formulation, the BCP micelles were fixed on the surfaces of the nanoparticles, thus limiting the agglomeration of the latter [164]. The addition of 10 wt% nanosilica resulted in an increase in the critical stress intensity factor, K_C, by 20% and the critical strain energy release rate, G_C, by 25%, while the use of only 5 wt% BCP resulted in a significant improvement in the K_C (115%) and G_C (∼400%), compared to the virgin epoxy matrix. Moreover, the K_C and G_C parameters were further improved when simultaneously incorporating 10 wt% nanosilica and 5 wt% BCP into the epoxy resin, beyond those obtained with the EP/nanosilica systems and EP/BCP, individually. However, various investigations have confirmed that a synergistic improvement is obtained in the properties of hybrid epoxy nanocomposites when specific conditions are met. Jojibabu et al. [165] investigated the effect of functionalized carbon nanotubes (fCNTs) with two different triblock copolymers designated as SBM and MAM on the lap shear strength (LSS) of an epoxy resin. The LSS of composites based on 1 wt% fCNTs and 10 wt% MAM or 1 wt% fCNTs with 10 wt% SBM was 81% and 137% higher than that of the pure matrix. However, the highest LSS with a positive contribution of both modifiers was obtained when 0.5 wt% fCNTs were used in the ternary composite. It has been established that the increase in the LSS was caused by the excessive plastic deformation of the matrix in addition to the formation of voids and nanoparticle pull-out.

The addition of 5 phr polystyrene–polybutadiene–poly(methyl methacrylate) triblock copolymers with unfunctionalized carbon nanotubes (CNTs) resulted in an increase in the fracture toughness, K_C, of 115% and critical energy release rate, G_C, of 410% compared to the unmodified matrix [166]. Interestingly, the incorporation of a small amount, 0.25 phr, of CNTs also increased the fracture toughness parameters but only by 14.5%. Nevertheless, the combination of copolymers and CNTs did not further increase the fracture toughness of the rubber-modified epoxy, due to the small contribution of crack deformation and matrix yielding, which are considered along with particle pull-out as processes leading to polymer toughening. Schuster and Coelho [167] were also unable to obtain a positive toughening effect from the addition of a block copolymer (BCP), carbon nanotubes (CNT) and graphene nanoplatelets (GNP) on the properties of the epoxy resin. The results showed that a hybrid composite based on 0.5 wt% BCP, 0.25 w% CNT and 0.25 wt% GNP showed an increase in the K_C of 34% compared to the neat epoxy. The fracture toughness of the hybrid composite was not significantly improved compared to the binary epoxy systems, due to the difference in the mechanisms for the improvement in the properties and the inadequate proportion of the hybrid composite constituents. It seemed that the proportion of nanoparticles in the composite was not optimal to achieve a synergistic reinforcement of the matrix.

A similar trend was observed when a functionalized PMMA-bloc-PbuA-bloc-PMMA copolymer was used in combination with MWCNT nanofillers to develop hybrid epoxy nanocomposites [168]. The fracture toughness parameters, K_C and G_C, of the epoxy composite containing 6 wt% copolymer and 0.075 wt% MWCNTs increased from 0.57 to 1.41 MPa.m$^{1/2}$ and 0.096 to 0.59 kJ/m^2, respectively, but with no synergistic toughening effect. On the other hand, the tensile strength, strain at yield and modulus decreased with the increasing amount of copolymer particles, due to the softness of the particles. On the other hand, Zhang et al. [169] have recently demonstrated that the simultaneous addition of block copolymers based on polyethylene glycol and polypropylene glycol and multiwalled carbon nanotubes (MWCNTs) to an epoxy matrix resulted in a synergistic effect on the critical stress intensity factor (K_C). The fracture parameter maximally increased with the introduction of 5 wt% copolymer or 0.25 wt% MWCNTs, compared to the neat matrix. With the simultaneous incorporation of 5 wt% copolymer and 0.25 wt% MWCNTs, the K_C value

was significantly increased and was much higher than the binary system EP/copolymer and EP/MWCNTs. This was generated by a very good dispersion of the MWCNTs in the matrix, favored by the presence of the block copolymer, but also by the pull-out of MWCNT particles, crack bridging and matrix shear yielding. This is consistent with the positive results of Li et al. [170], who prepared ternary epoxy composites by using amine-terminated poly(butadiene−acrylonitrile)-functionalized graphene oxide (fGO) and a poly(ethylene oxide)-b-poly(ethylene-alt-propylene) diblock copolymer (BCP). The toughening efficiency of fGO alone was found to be highly dependent on the modifier concentration and the crosslink density of the matrix. The addition of 0.04 wt% GO with a lightly crosslinked density resulted in a 1.7-fold increase in the fracture energy, G_C, over the neat epoxy, while the incorporation of 5 wt% BCP enhanced the parameter, G_C, of the epoxy resin by a factor of 12. The combination of the rigid fGO and soft BCP particles at 0.04 wt% and 5 wt%, respectively, led to an 18 times increase in the G_C over the unmodified matrix and a 31% improvement over the binary systems.

A synergistic effect was also confirmed in the study on epoxy toughening by the simultaneous inclusion of block copolymers (BCPs) and core–shell particles (CSPs). It was shown that the epoxy/BCP/CSP flexural strength and fracture toughness (K_C) were significantly enhanced compared to the neat epoxy, BCP/epoxy and CSP/epoxy systems, while the thermal stability was maintained almost unchanged [171]. The morphological analysis of the epoxy composites indicated that the BCP micelles were deformed and pulled out from the matrix, thus creating voids in the composites. These successive processes were considered responsible for the drastic improvement in the fracture toughness. Epoxy nanocomposites modified with block copolymers showing synergistic effects are shown in Table 4.

Table 4. Epoxy nanocomposites modified with block copolymers showing synergistic effects.

Nanoparticles	Improved Properties	References
Nanosilica	K_C	[164]
fCNT	Lap shear strength	[165]
MWCNT	K_C	[169]
fGO	G_C	[170]
CSP	Flexural strength, K_C	[171]

CSP—core–shell particles (core—Poly Butadiene, shell—PMMA); MWCNT—multiwalled carbon nanotubes; fGO—amine-terminated poly(butadiene−acrylonitrile)-functionalized graphene oxide; fCNT—functionalized carbon nanotubes.

2.5. Hybrid Epoxy Nanocomposites Based on Diluents

It was reported that the inclusion of soft modifiers such as plasticizers or reactive diluents to epoxy resin generally deteriorate the mechanical properties, including the yield strength, stiffness and glass transition temperature. Plasticization of the epoxy matrix has also been considered as a possible method to increase some properties of epoxy resin by the flexibilization resulting from the increased free volume. Recently, reactive diluents have been considered as a potential modifier to improve the elasticity and impact strength of brittle epoxy resins. Rahman et al. [172] showed that the flexural strength, flexural modulus and energy to break of DGEBA epoxy resin increased maximally with 0.3 wt% NH_2-MWCNTs (amino-functionalized multiwalled carbon nanotubes) and 10 phr polyether polyol. Furthermore, the hybrid nanocomposite showed a synergistic effect on the K_C and the flexural fracture energy of the epoxy matrix. The crack deflection, void formation with particle cavitation, nanoparticle debonding and induced shear yielding result in a drastic increase in the properties of the matrix [173]. A study carried out by Yi et al. [174] confirmed a positive toughening on the properties of an epoxy resin modified with oxidized multiwalled carbon nanotubes (oCNTs) and NCO-terminated reactive oligomer. The highest impact strength was obtained for the epoxy composite containing 10 wt% of

oligomer and 0.5 wt% of oCNTs at room temperature (RT) and cryogenic temperature (CT), compared to the unmodified matrix as well as binary epoxy systems. The epoxy was toughened at RT and CT by the introduction of the flexible oligomer and was further reinforced by the addition of the oCNTs, without altering its tensile strength, due to positive interactions between the nanoclay and epoxy matrix as facilitated by the oligomer. In the case of the use of oxidized and amine-functionalized multiwalled carbon nanotubes (MWCNTs) with 5.0 wt% of reactive diluent, the IS of the epoxy resin was improved by up to 260% compared to the pure matrix, but no synergism [175]. However, a different result was obtained with the addition of oMMT (Cloisite 30B) and 7 wt% of polyether polyol which caused a decrease in the tensile and impact strength of the epoxy matrix with an increasing amount of nanoparticles [176].

Due to the presence of flexible ether linkages, polyethylene glycol (PEG) is expected to increase the toughness of epoxy resin. Chozhan et al. [177] reported that epoxy nanocomposites modified with PEG and/or octanediol (OCT) exhibited improved mechanical properties. The impact and tensile strengths of epoxy composites containing 3 wt% organoclay and 20 wt% PEG or 3 wt% organoclay and 10 wt% OCT were increased by 95% and 30%, respectively, compared to the neat epoxy. However, a considerable improvement was noted in the fracture toughness parameter, K_C, of 255% and 334%, respectively, compared to the neat matrix when the epoxy matrix was modified with 0.1 wt% graphene oxide (GO) or 0.1% wt% of (PEG-grafted GO (GO-g-PEG). Moreover, the thermal degradation temperatures of epoxy nanocomposites based on GO and PEG-grafted GO have been increased by 50 °C [178].

Furthermore, Chang et al. [179] studied the effects of different processing conditions, diluent and nanosilica content on the properties of epoxy nanocomposites. As expected, the addition of a diluent reduced the hardness of the composites, while the impact strength of composites containing 1 wt% of nanopowders without a diluent increased compared to the neat epoxy matrix. Although the addition of a diluent made mixing processes easier and more efficient, it reduced the impact strength value of the nanocomposites. Diluents are also used to provide a uniform dispersion of nanoparticles in the polymer matrix and therefore contribute to improved epoxy performance properties [180].

The effect of hexanediol diglycidylether as a reactive diluent for an epoxy resin cured with an anhydride hardener and modified with silica nanoparticles (SNs) and core–shell rubber (CSR) nanoparticles was studied by Carolan et al. [181]. The addition of 25 wt% of a reactive diluent to the epoxy matrix resulted in a 38% increase in the fracture energy compared to a six-fold increase with the incorporation of 20 wt% of CSR nanoparticles without a diluent. However, the fracture energy (G_C) improvement was much more significant with 25 wt% of a reactive diluent and 16 wt% CSR nanoparticles with a synergistic effect on the G_C. The hybrid epoxy nanocomposites with both SNs and CSR showed only a modest increase in the G_C. The increase in the toughness of the hybrid materials was related to the good dispersion of the nanoparticles in the epoxy polymer matrix. Another study concerned the contribution of 1,6-hexanediol diglycidyl ether (reactive diluent) in the toughening of DGEBA epoxy resin modified with graphene nanoplatelets (GNPs) and carboxyl-terminated acrylonitrile butadiene rubber (CTBN) or core–shell rubber (CSR) [182]. The fracture toughness parameter, K_C, of the matrix increased by approximately 430% with the incorporation of 9 wt% CTBN and 12.5% of the reactive diluent. In addition, the incorporation of a reactive diluent has been shown to improve the toughness of the epoxy polymer modified with CSR particles, due to the increased ductility of the epoxy matrix. The corresponding toughening mechanisms are those described previously [172,173]. In the work undertaken by Sarafrazi et al. [183], thermoplastic polyester urethane (PU) was used to toughen a DGEBA epoxy resin containing copper chromite CuCr2O4 nanoparticles, castor oil (ECO) and montmorillonite (Cloisite 30B). A diminution in the tensile strength and rigidity was reported for the DGEBA/ECO system as a result of the decrease in the crosslinking density. Moreover, optimization of the properties revealed a synergistic toughening with the fracture toughness parameter (K_C) and fracture energy (G_C) of the

DGEBA/ECO/Cloisite (at a ratio of 8:2:0.1) system which were found to be higher than the other epoxy systems. The improved hybrid properties have been explained mainly by the good dispersion of the nanoparticles as well as their interactions with the matrix, with the respective reactive groups. However, it was found that the use of epoxidized vegetable oil from *Mesua ferrea* L. seeds in an epoxy resin containing nanoparticles decreased the viscosity as expected but improved the mechanical and adhesive properties of the cured resin [184]. A significant enhancement in the adhesive strength was reached with 2.5 wt% nanoclay.

Liquid modifiers and solid nanoparticles are known to affect the properties of brittle epoxy resins differently, by flexibilization and strengthening, respectively. However, their simultaneous incorporation in the epoxy matrix can lead to positive toughening [71,73,81,83]. Table 5 summarizes the effects of nanoparticles and diluents on the properties of epoxy resins with relevant references.

Table 5. Improved epoxy resin properties as a function of the type of diluent and nanoparticles.

Diluent	Nanoparticles	Improved Properties	References
polyether polyol	NH_2-MWCNT	K_C, flexural energy to break	[172]
NCO terminated reactive oligomer	Oxidized CNTs	Impact strength	[174]
Reactive diluent	CSR	G_C	[181]
Castor oil	Cloisite 30B	K_C, G_C	[183]

NH_2-MWCNT—amino-functionalized multiwalled carbon nanotubes; oCNT—carbon nanotubes. CSR—core–shell rubber nanoparticles; Reactive diluent—hexanediol diglycidylether; G_C—fracture energy; K_C—critical stress intensity factor.

2.6. Hybrid Epoxy Nanocomposites Based on Thermosets

Unsaturated polyester (UP) resins, one of the most widely used thermosetting resins, have very good chemical and corrosion resistance, high thermal stability, good processability and low cost. Although cured UP resins are brittle with a low impact strength and poor resistance to crack propagation, they are expected to act as a toughening agent for epoxy resin. It has already been confirmed that oMMT improves the mechanical properties of the epoxy matrix through the exfoliation/intercalation processes [57,59]. Moreover, the introduction of unsaturated polyester into epoxy resin has been shown to improve its mechanical properties due to chain entanglement and network formation [185].

Various researchers used organomodified montmorillonite (oMMT) in combination with UP to toughen epoxy resins [186–188]. Chozhan et al. [186] modified epoxy resin (EP) with oMMT clays and unsaturated polyester (UP). The impact strength of an EP reinforced with 5 wt% oMMT and 10 wt% UP was maximally increased by more than 35% over that of the unmodified matrix. The tensile and flexural properties of the cited hybrid nanocomposites were also enhanced, due to the formation of intercalated nanocomposites and the formation of chain entanglements between UP and the epoxy matrix. The contribution of two types of oMMT nanoclays, namely Cloisite 30B and Nanomer, on the toughening of epoxy resin modified with UP was reported in another study [187]. The UP-toughened epoxy composite containing 1 wt% Cloisite 30B showed the optimum increase in the tensile strength (15%), tensile modulus (20%), flexural strength (10%) and flexural modulus (20%) compared to the epoxy/UP blend. In addition, the mechanical properties of Cloisite-based nanocomposites were superior to those of nanocomposites with Nanomer and the adhesion between the epoxy/UP and Cloisite was superior to that between the epoxy/UP and Nanomer. The very good dispersion and exfoliation of the nanoparticles within the epoxy/UP system, in addition to the creation of an IPN structure, lead to an increase in the mechanical properties. Similar property enhancements have been reported in another study [186]. Other researchers have reported similar results [188]. The use of mechanical mixing followed by an ultra-sonication process resulted in a significant improvement in the tensile, impact and shear strengths of an epoxy/UP blend modified

with bentonite [188]. However, manual mixing alone led to a reduction in the tensile strength and tensile modulus of an epoxy/UP/oMMT hybrid composite [189].

Studies have demonstrated that the increase in properties can be achieved by an optimum mixing of composite constituents [190,191]. In the work on UP/EP systems containing amine-modified silica nanoparticles (SNs), the decrease in the tensile and flexural strengths of the epoxy matrix due to the addition of UP was overcome by adding nanoparticles [190]. The combination of high shear mechanical mixing followed by an ultra-sonication process led to improved properties through the formation of crosslinked networks. Furthermore, hybrid epoxy composites containing UP and amine-functionalized multiwalled carbon nanotubes (NH2-MWCNTs), which were prepared using ball milling and sonication processes for the efficient dispersion of the nanoparticles in the epoxy matrix, exhibited improved tensile and flexural properties [191]. Tg values were also increased to an appreciable level with the incorporation of nanoparticles into the UP/EP system. The obtained positive results were explained by the homogeneous morphologies of the EP//UP blend and the chemical reactions between the reactive groups of EP and nanoparticles. However, Le and Huang [192] compared the effects of multiwalled carbon nanotubes (MWCNTs) and graphene nanoplatelets (GNPs) on the mechanical properties of an epoxy/unsaturated polyester mixture at different ratios. As in previous investigations, it was confirmed that a small amount of added MWCNTs (1 wt%) or GNPs (0.2 wt%) resulted in a significant increase of about 85% in the tensile strength of the epoxy/polyester blend.

Vinyl ester and phenolic resins have also been tested as potential toughening agents for epoxy/nanoclay composites [193,194]. Vinyl ester resin was used by Chozhan et al. [193] for its improved strength and chemical resistance to prepare composites with an epoxy resin (EP) and montmorillonite (oMMT). The obtained results showed that the addition of 10 wt% vinyl ester oligomer (VEO) and 5 wt% oMMT to the EP improved the tensile, flexural and impact strengths by more than 30% compared to the unmodified EP. The tensile modulus and flexural modulus values followed the same trend. The improvement in the mechanical properties was attributed to the formation of chain entanglements between EP and VEO, by the exfoliation of nanoclays as well as the homogeneous dispersion of montmorillonite in the epoxy system. Due to the acceptable mechanical properties already reported on phenolic–epoxy networks [194], the incorporation of both phenolic resin and nanoclay should improve the properties of the epoxy matrix. The epoxy/phenolic blend modified with 2.5 wt% montmorillonite (Cloisite 30B) showed a maximum increase in the fracture toughness (70%) and Young's modulus (30%) compared to the virgin matrix [195]. The improvement in the toughness was attributed to the crack pinning and deflection as well as the formation of the shear band in the matrix.

As in the case of unsaturated polyester, cyanate ester resin possesses attractive performance properties but exhibits poor flexibility and high brittleness, which limits its use in many areas. It is expected that a mixture of epoxy resin (EP) and cyanate ester (CE) reinforced with selected nanoparticles would result in improved mechanical properties. EP/CE blends reinforced with functionalized multiwalled carbon nanotubes (MWCNTs) have been prepared by Li et al. [196] and their properties evaluated at room temperature (RT) and liquid nitrogen temperature (77 K). The functionalization of the MWCNTs improved their dispersion in the matrix as well as the interfacial bonding with the blend. The mechanical properties were greatly improved compared to nanocomposites based on non-functionalized MWCNTs. The tensile strength of the nanocomposites at 0.5 wt% of MWCNT loading increased by 11.6% at RT and 18.3% at 77 K, relative to the neat matrix. This increase was attributed to the good dispersion and strong interfacial bonding between the functionalized MWCNTs and the cyanate ester/epoxy system. The tensile modulus of the nanocomposites followed the same trend as the tensile strength. All presented studies showed an improved but without the expected synergistic effect which is the main goal of each hybrid composite.

The studies indicated that the introduction of unsaturated polyester resin into the epoxy resin and further reinforcement with nanoparticles improved the mechanical and

damping properties to an appreciable extent but with no reported positive toughening and synergistic effect.

3. Applications of Epoxy Hybrid Nanocomposites

Depending on the improved properties, the prepared hybrid epoxy nanocomposites can be used in various fields. Epoxy/rubber nanocomposites can used as adhesives, while those based on engineering thermoplastics can be intended for the fabrication of advanced composite materials in the building, automotive and aerospace industries. Epoxy/unsaturated polyester systems are employed as a matrix for high-performance composites for engineering applications. The mentioned hybrid epoxy nanocomposites can also be used in existing fields but under severe conditions.

4. Future Trends and Challenges

This review presents advances on the improvement in the properties of epoxy nanocomposites modified with different types of modifiers. It focused on the toughening of diglycidyl ether of bisphenol A (DGEBA) epoxy resin by using solid nanoparticles with other modifiers such as rubbers, thermoplastics, thermosetting resins and diluents. It has been demonstrated that the performance properties of hybrid nanocomposites depend not only on the type and amount of components, and their eventual interactions, but also on the processing conditions [197–199].

The major challenges to be met in the context of obtaining hybrid polymer composites with high-performance properties remain in the choice of compatible polymers and nanofillers, the appropriate processing method of the constituents as well as the appropriate functionalization and dispersion of the nanofillers. The search for eco-friendly or green polymer nanocomposites is of great importance for researchers because of the necessary protection of the environment. The use of biobased and/or biodegradable modifiers seems to be a logical path toward reducing the problems of recycling ever-increasing quantities of plastic products.

Nevertheless, due to the very convincing results recorded during the last decade with remarkable synergies on the mechanical properties of epoxy resin, it would be wise to explore the method of reinforcing epoxy resin with only nanofillers such as montmorillonite, graphene platelets and multiwalled carbon nanotubes [200–203].

Author Contributions: Conceptualization, M.B. and A.B.; Draft preparation, M.B., A.B., W.K. and I.Z.; Writing, review and editing, M.B., A.B., W.K. and I.Z. All authors have read and agreed to the published version of the manuscript.

Funding: This research received no external funding.

Institutional Review Board Statement: Not applicable.

Informed Consent Statement: Not applicable.

Data Availability Statement: Not applicable.

Conflicts of Interest: The authors declare no conflict of interest.

References

1. May, C. (Ed.) *Epoxy Resins: Chemistry and Technology*, 2nd ed.; Routledge: New York, NY, USA, 2018.
2. Jin, F.L.; Li, X.; Park, S.J. Synthesis and application of epoxy resins. A review. *J. Ind. Eng. Chem.* **2015**, *29*, 1–11. [CrossRef]
3. Ellis, B. (Ed.) *Chemistry and Technology of Epoxy Resins*; Springer Science + Business Media: Dordrecht, The Netherlands, 1993.
4. Kumar, S.; Krishnan, S.; Mohanty, S.; Nayak, S.K. Synthesis and characterization of petroleum and biobased epoxy resins: A review. *Polym. Int.* **2018**, *67*, 815–839. [CrossRef]
5. Capricho, J.C.; Fox, B.; Hameed, N. Multifunctionality in epoxy resins. *Polym. Rev.* **2020**, *60*, 1–41. [CrossRef]
6. Czub, P.; Bończa-Tomaszewski, Z.; Penczek, P.; Pielichowski, J. *Chemia I Technologia Żywic Epoksydowych*; Wydawnictwa Naukowo-Techniczne: Warsaw, Poland, 2002. (In Polish)
7. Unnikrishnan, K.P.; Thachil, E.T. Toughening of epoxy resins. *Des. Monomers Polym.* **2006**, *9*, 129–152. [CrossRef]

8. Mohan, P. A critical review: The modification, properties, and applications of epoxy resins. *Polym.-Plast. Technol.* **2013**, *52*, 107–125. [CrossRef]
9. Paluvai, N.R.; Mohanty, S.; Nayak, S.K. Synthesis and modifications of epoxy resins and their composites: A review. *Polym.-Plast. Technol.* **2014**, *53*, 1723–1758. [CrossRef]
10. Ratna, D. Modification of epoxy resins for improvement of adhesion: A critical review. *J. Adhes. Sci. Technol.* **2003**, *17*, 1655–1668. [CrossRef]
11. Ligon-Auer, S.C.; Schwentenwein, M.; Gorsche, C.; Stampfl, J.; Liska, R. Toughening of photo-curable polymer networks: A review. *Polym. Chem.* **2016**, *7*, 257–286. [CrossRef]
12. Auvergne, R.; Caillol, S.; David, G.; Boutevin, B.; Pascault, J.P. Biobased thermosetting epoxy: Present and future. *Chem. Rev.* **2014**, *114*, 1082–1115. [CrossRef]
13. Mittal, V.; Saini, R.; Sinha, S. Natural fiber-mediated epoxy composites—A review. *Compos. Part B—Eng.* **2016**, *99*, 425–435. [CrossRef]
14. Fiore, V.; Valenza, A. Epoxy resins as a matrix material in advanced fiber-reinforced polymer (FRP) composites. In *Advanced Fibre-Reinforced Polymer (FRP) Composites for Structural Applications*; Bai, J., Ed.; Woodhead Publishing: Cambridge, UK, 2013; pp. 88–121.
15. Lu, T.; Jiang, M.; Jiang, Z.; Hui, D.; Wang, Z.; Zhou, Z. Effect of surface modification of bamboo cellulose fibers on mechanical properties of cellulose/epoxy composites. *Compos. Part B—Eng.* **2013**, *51*, 28–34. [CrossRef]
16. Saba, N.; Jawaid, M.; Alothman, O.Y.; Paridah, M.T.; Hassan, A. Recent advances in epoxy resin, natural fiber-reinforced epoxy composites and their applications. *J. Reinf. Plast. Compos.* **2016**, *35*, 447–470. [CrossRef]
17. Datta, J.; Włoch, M. Selected biotrends in development of epoxy resins and their composites. *Polym. Bull.* **2014**, *71*, 3035–3049. [CrossRef]
18. Krishna, K.V.; Kanny, K. The effect of treatment on kenaf fiber using green approach and their reinforced epoxy composites. *Compos. Part B—Eng.* **2016**, *104*, 111–117. [CrossRef]
19. del Borrello, M.; Mele, M.; Campana, G.; Secchi, M. Manufacturing and characterization of hemp-reinforced epoxy composites. *Polym. Compos.* **2020**, *41*, 2316–2329. [CrossRef]
20. Hodgkin, J.H.; Simon, G.P.; Varley, R.J. Thermoplastic toughening of epoxy resins: A critical review. *Polym. Adv. Technol.* **1998**, *9*, 3–10. [CrossRef]
21. Pearson, R.A. Toughening Epoxies Using Rigid Thermoplastic Particles: A Review. *Adv. Chem. Ser.* **1993**, *233*, 405–425.
22. Bucknall, C.B.; Partridge, I.K. Phase separation in epoxy resins containing polyethersulphone. *Polymer* **1983**, *24*, 639–644. [CrossRef]
23. Kinloch, A.J.; Yuen, M.L.; Jenkins, S.D. Thermoplastic-toughened epoxy polymers. *J. Mater. Sci.* **1994**, *29*, 3781–3790. [CrossRef]
24. Bakar, M.; Wojtania, I.; Legocka, I.; Gospodarczyk, J. Property enhancement of epoxy resins by using a combination of polyamide and montmorillonite. *Adv. Polym. Technol.* **2007**, *26*, 223–231. [CrossRef]
25. Gilbert, A.H.; Bucknall, C.B. Epoxy resin toughened with thermoplastic. *Makromol. Chem. Macromol. Symp.* **1991**, *45*, 289–298. [CrossRef]
26. Hourston, D.J.; Lane, J.M.; Zhang, H.X. Toughening of epoxy resins with thermoplastics: 3. An investigation into the effects of composition on the properties of epoxy resin blends. *Polym. Int.* **1997**, *42*, 349–355. [CrossRef]
27. Brooker, R.D.; Kinloch, A.J.; Taylor, A.C. The morphology and fracture properties of thermoplastic-toughened epoxy polymers. *J. Adhes.* **2010**, *86*, 726–741. [CrossRef]
28. Frigione, M.E.; Mascia, L.; Acierno, D. Oligomeric and polymeric modifiers for toughening of epoxy resins. *Eur. Polym. J.* **1995**, *31*, 1021–1029. [CrossRef]
29. Rong, M.; Zeng, H. Polycarbonate-epoxy semi-interpenetrating polymer network: 2. Phase separation and morphology. *Polymer* **1997**, *38*, 269–277. [CrossRef]
30. Remiro, P.M.; Riccardi, C.C.; Corcuera, M.A.; Mondragon, I. Design of morphology in PMMA-modified epoxy resins by control of curing conditions. I. Phase behavior. *J. Appl. Polym. Sci.* **1999**, *74*, 772–780. [CrossRef]
31. Bagheri, R.; Marouf, B.T.; Pearson, R.A. Rubber-toughened epoxies: A critical review. *Polym. Rev.* **2009**, *49*, 201–225. [CrossRef]
32. Kong, J.; Ning, R.; Tang, Y. Study on modification of epoxy resins with acrylate liquid rubber containing pendant epoxy groups. *J. Mater. Sci.* **2006**, *41*, 1639–1641. [CrossRef]
33. Saadati, P.; Baharvand, H.E.; Rahimi, A.; Morshedian, J. Effect of modified liquid rubber on increasing toughness of epoxy resins. *Iran. Polym. J.* **2005**, *14*, 637–646.
34. Maazouz, A.; Sautereau, H.; Gerard, J.F. Toughening of epoxy networks using pre-formed core-shell particles or reactive rubbers. *Polym. Bull.* **1994**, *33*, 67–74. [CrossRef]
35. Akbari, R.; Beheshty, M.H.; Shervin, M. Toughening of dicyandiamide-cured DGEBA-based epoxy resins by CTBN liquid rubber. *Iran. Polym. J.* **2013**, *22*, 313–324. [CrossRef]
36. Wise, C.W.; Cook, W.D.; Goodwin, A.A. CTBN rubber phase precipitation in model epoxy resins. *Polymer* **2000**, *41*, 4625–4633. [CrossRef]
37. Ratna, D.; Banthia, A.K. Rubber toughened epoxy. *Macromol. Res.* **2004**, *12*, 11–21. [CrossRef]
38. Chikhi, N.; Fellahi, S.; Bakar, M. Modification of epoxy resin using reactive liquid (ATBN) rubber. *Eur. Polym. J.* **2002**, *38*, 251–264. [CrossRef]

39. Ozturk, A.; Kaynak, C.; Tincer, T. Effects of liquid rubber modification on the behaviour of epoxy resin. *Eur. Polym. J.* **2001**, *37*, 2353–2363. [CrossRef]
40. Grishchuk, S.; Sorochynska, L.; Vorster, O.C.; Karger-Kocsis, J. Structure, thermal, and mechanical properties of DDM-hardened epoxy/benzoxazine hybrids: Effects of epoxy resin functionality and ETBN toughening. *J. Appl. Polym. Sci.* **2013**, *127*, 5082–5093. [CrossRef]
41. Mostovoy, A.S.; Nurtazina, A.S.; Kadykova, Y.A.; Bekeshev, A.Z. Highly efficient plasticizers-antipirenes for epoxy polymers. *Inorg. Mater. Appl. Res.* **2019**, *10*, 1135–1139. [CrossRef]
42. Rodrıguez, M.T.; Gracenea, J.J.; Garcıa, S.J.; Saura, J.J.; Suay, J.J. Testing the influence of the plasticizers addition on the anticorrosive properties of an epoxy primer by means of electrochemical techniques. *Prog. Org. Coat.* **2004**, *50*, 123–131. [CrossRef]
43. Rodríguez, M.T.; Garcia, S.J.; Cabello, R.; Suay, J.J.; Gracenea, J.J. Effect of plasticizer on the thermal, mechanical, and anticorrosion properties of an epoxy primer. *J. Coat. Technol. Res.* **2005**, *2*, 557–564. [CrossRef]
44. Núñez-Regueira, L.; Villanueva, M.; Fraga-Rivas, I. Effect of a reactive diluent on the curing and dynamomechanical properties of an epoxy-diamine system. *J. Therm. Anal. Calorim.* **2006**, *86*, 463–468. [CrossRef]
45. Sarwono, A.; Man, Z.; Bustam, M.A. Blending of epoxidised palm oil with epoxy resin: The effect on morphology, thermal and mechanical properties. *J. Polym. Environ.* **2012**, *20*, 540–549. [CrossRef]
46. Fellahi, S.; Chikhi, N.; Bakar, M. Modification of epoxy resin with kaolin as a toughening agent. *J. Appl. Polym. Sci.* **2001**, *82*, 861–878. [CrossRef]
47. Park, S.J.; Jin, F.L.; Lee, C. Preparation and physical properties of hollow glass microspheres-reinforced epoxy matrix resins. *Mater. Sci. Eng. A* **2005**, *402*, 335–340. [CrossRef]
48. Ahmad, Z.; Ansell, M.P.; Smedley, D. Epoxy adhesives modified with nano-and micro-particles for in-situ timber bonding: Effect of microstructure on bond integrity. *Int. J. Mech. Mater. Eng.* **2010**, *5*, 59–67.
49. Bello, S.A.; Agunsoye, J.O.; Adebisi, J.A.; Hassan, S.B. Effect of aluminium particles on mechanical and morphological properties of epoxy nanocomposites. *Acta Period. Technol.* **2017**, *48*, 25–38. [CrossRef]
50. Lange, F.F.; Radford, K.C. Fracture energy of an epoxy composite system. *J. Mater. Sci.* **1971**, *6*, 1197–1203. [CrossRef]
51. Spanoudakis, J.; Young, R.J. Crack propagation in a glass particle-filled epoxy resin. *J. Mater. Sci.* **1984**, *19*, 473–486. [CrossRef]
52. Nakamura, Y.; Yamaguchi, M.; Okubo, M.; Matsumoto, T. Effect of particle size on the fracture toughness of epoxy resin filled with spherical silica. *Polymer* **1992**, *33*, 3415–3426. [CrossRef]
53. Kochetov, R.; Andritsch, T.; Morshuis, P.H.; Smit, J.J. Thermal and electrical behaviour of epoxy-based microcomposites filled with Al_2O_3 and SiO_2 particles. In Proceedings of the 2010 IEEE International Symposium on Electrical Insulation, San Diego, CA, USA, 6–9 June 2010; IEEE: Piscataway, NJ, USA, 2010; pp. 1–5.
54. Liu, H.Y.; Wang, G.T.; Mai, Y.W.; Zeng, Y. On fracture toughness of nano-particle modified epoxy. *Compos. Part B—Eng.* **2011**, *42*, 2170–2175. [CrossRef]
55. Al-Turaif, H.A. Effect of nano TiO_2 particle size on mechanical properties of cured epoxy resin. *Prog. Org. Coat.* **2010**, *69*, 241–246. [CrossRef]
56. Wetzel, B.; Rosso, P.; Haupert, F.; Friedrich, K. Epoxy nanocomposites–fracture and toughening mechanisms. *Eng. Fract. Mech.* **2006**, *73*, 2375–2398. [CrossRef]
57. Messersmith, P.B.; Giannelis, E.P. Synthesis and characterization of layered silicate-epoxy nanocomposites. *Chem. Mater.* **1994**, *6*, 1719–1725. [CrossRef]
58. LeBaron, P.C.; Wang, Z.; Pinnavaia, T.J. Polymer-Layered Silicate Nanocomposites: An Overview. *Appl. Clay Sci.* **1999**, *15*, 11–29. [CrossRef]
59. Azeez, A.A.; Rhee, K.Y.; Park, S.J.; Hui, D. Epoxy clay nanocomposites–processing, properties and applications: A review. *Compos. Part B—Eng.* **2013**, *45*, 308–320. [CrossRef]
60. Nigam, V.; Setua, D.K.; Mathur, G.N.; Kar, K.K. Epoxy-montmorillonite clay nanocomposites: Synthesis and characterization. *J. Appl. Polym. Sci.* **2004**, *93*, 2201–2210. [CrossRef]
61. Zabihi, O.; Ahmadi, M.; Nikafshar, S.; Preyeswary, K.C.; Naebe, M. A technical review on epoxy-clay nanocomposites: Structure, properties, and their applications in fiber reinforced composites. *Compos. Part B—Eng.* **2018**, *135*, 1–24. [CrossRef]
62. Rana, S.; Alagirusamy, R.; Joshi, M. A review on carbon epoxy nanocomposites. *J. Reinf. Plast. Compos.* **2009**, *28*, 461–487. [CrossRef]
63. Wei, J.; Vo, T.; Inam, F. Epoxy/graphene nanocomposites–processing and properties: A review. *RSC Adv.* **2015**, *5*, 73510–73524. [CrossRef]
64. Sarathi, R.; Sahu, R.K.; Rajeshkumar, P. Understanding the thermal, mechanical and electrical properties of epoxy nanocomposites. *Mater. Sci. Eng. A* **2007**, *445*, 567–578. [CrossRef]
65. Neves, R.M.; Ornaghi, H.L., Jr.; Zattera, A.J.; Amico, S.C. Toughening epoxy resin with liquid rubber and its hybrid composites: A systematic review. *J. Polym. Res.* **2022**, *29*, 340. [CrossRef]
66. Sasidharan, S.; Anand, A. Epoxy-based hybrid structural composites with nanofillers: A Review. *Ind. Eng. Chem. Res.* **2020**, *59*, 12617–12631. [CrossRef]
67. Mi, X.; Liang, N.; Xu, H.; Wu, J.; Jiang, Y.; Nie, B.; Zhang, D. Toughness and mechanism of epoxy resins. *Prog. Mater. Sci.* **2022**, *130*, 100977. [CrossRef]

68. Shukla, M.K.; Sharma, K. Effect of carbon nanofillers on the mechanical and interfacial properties of epoxy based nanocomposites: A review. *Polym. Sci. Ser. A Polym. Phys.* **2019**, *61*, 439–460. [CrossRef]
69. Marouf, B.T.; Mai, Y.W.; Bagheri, R.; Pearson, R.A. Toughening of epoxy nanocomposites: Nano and hybrid effects. *Polym. Rev.* **2016**, *56*, 70–112. [CrossRef]
70. Nanda, T.; Singh, K.; Shelly, D.; Mehta, R. Advancements in multi-scale filler reinforced epoxy nanocomposites for improved impact strength: A review. *Crit. Rev. Solid State Mater. Sci.* **2021**, *46*, 281–329. [CrossRef]
71. Khan, I.; Saeed, K.; Khan, I. Nanoparticles: Properties, applications and toxicities. *Arab. J. Chem.* **2019**, *12*, 908–931. [CrossRef]
72. Strambeanu, N.; Demetrovici, L.; Dragos, D.; Lungu, M. Nanoparticles: Definition, classification and general physical properties. In *Nanoparticles' Promises and Risks*; Lungu, M., Neculae, A., Bunoiu, M., Biris, C., Eds.; Springer International Publishing: Wiesbaden, Germany, 2015; pp. 3–8.
73. Mathew, V.S.; George, S.C.; Parameswaranpillai, J.; Thomas, S. Epoxidized natural rubber/epoxy blends: Phase morphology and thermomechanical properties. *J. Appl. Polym. Sci.* **2014**, *131*. [CrossRef]
74. Kou, Y.; Zhou, W.; Li, B.; Dong, L.; Duan, Y.E.; Hou, Q.; Liu, X.; Cai, H.; Chen, Q.; Dang, Z.M. Enhanced mechanical and dielectric properties of an epoxy resin modified with hydroxyl-terminated polybutadiene. *Compos. Part A Appl. Sci. Manuf.* **2018**, *114*, 97–106. [CrossRef]
75. Kar, S.; Banthia, A.K. Synthesis and evaluation of liquid amine-terminated polybutadiene rubber and its role in epoxy toughening. *J. Appl. Polym. Sci.* **2005**, *96*, 2446–2453. [CrossRef]
76. Barcia, F.L.; Amaral, T.P.; Soares, B.G. Synthesis and properties of epoxy resin modified with epoxy-terminated liquid polybutadiene. *Polymer* **2003**, *44*, 5811–5819. [CrossRef]
77. Dong, L.; Zhou, W.; Sui, X.; Wang, Z.; Wu, P.; Zuo, J.; Cai, H.; Liu, X. Thermal, mechanical, and dielectric properties of epoxy resin modified using carboxyl-terminated polybutadiene liquid rubber. *J. Elastom. Plast.* **2017**, *49*, 281–297. [CrossRef]
78. Butta, E.; Levita, G.; Marchetti, A.; Lazzeri, A. Morphology and mechanical properties of amine-terminated butadiene-acrylonitrile/epoxy blends. *Polym. Eng. Sci.* **1986**, *26*, 63–73. [CrossRef]
79. Yi, H.; Wei, T.; Lin, H.; Zhou, J. Preparation and properties of hybrid epoxy/hydro-terminated polybutadiene/modified MMT nanocomposites. *J. Coat. Technol. Res.* **2018**, *15*, 1413–1422. [CrossRef]
80. Puglia, D.; Al-Maadeed, M.A.S.; Kenny, J.M.; Thomas, S. Elastomer/thermoplastic modified epoxy nanocomposites: The hybrid effect of 'micro'and 'nano'scale. *Mater. Sci. Eng. R Rep.* **2017**, *116*, 1–29.
81. Balakrishnan, S.; Start, P.R.; Raghavan, D.; Hudson, S.D. The influence of clay and elastomer concentration on the morphology and fracture energy of preformed acrylic rubber dispersed clay filled epoxy nanocomposites. *Polymer* **2005**, *46*, 11255–11262. [CrossRef]
82. Wang, L.; Shui, X.; Zheng, X.; You, J.; Li, Y. Investigations on the morphologies and properties of epoxy/acrylic rubber/nanoclay nanocomposites for adhesive films. *Compos. Sci. Technol.* **2014**, *93*, 46–53. [CrossRef]
83. Fröhlich, J.; Thomann, R.; Mülhaupt, R. Toughened epoxy hybrid nanocomposites containing both an organophilic layered silicate filler and a compatibilized liquid rubber. *Macromolecules* **2003**, *36*, 7205–7211.
84. Ahmed, M.A.; Kandil, U.F.; Shaker, N.O.; Hashem, A.I. The overall effect of reactive rubber nanoparticles and nano clay on the mechanical properties of epoxy resin. *J. Radiat. Res. Appl. Sci.* **2015**, *8*, 549–561. [CrossRef]
85. Shayegan, M.; Bagheri, R. The simultaneous effect of silica nanoparticles and rubber particles on the toughness of epoxy polymer. *Int. J. Nanomanuf.* **2010**, *5*, 232–244. [CrossRef]
86. Saberian, M.; Ghasemi, F.A.; Ghasemi, I.; Daneshpayeh, S. Investigation on tensile properties of epoxy/graphene nanoplatelets/carboxylated nitrile butadiene rubber ternary nanocomposites using response surface methodology. *Nanomater. Nanotechnol.* **2019**, *9*, 1847980419855842. [CrossRef]
87. King, J.A.; Klimek, D.R.; Miskioglu, I.; Odegard, G.M. Mechanical properties of graphene nanoplatelet/epoxy composites. *J. Appl. Polym. Sci.* **2013**, *128*, 4217–4223. [CrossRef]
88. Wang, F.; Drzal, L.T.; Qin, Y.; Huang, Z. Enhancement of fracture toughness, mechanical and thermal properties of rubber/epoxy composites by incorporation of graphene nanoplatelets. *Compos. Part A Appl. Sci. Manuf.* **2016**, *87*, 10–22. [CrossRef]
89. Lee, H.B.; Kim, H.G.; Yoon, K.B.; Lee, D.H.; Min, K.E. Preparation and properties of a carboxyl-terminated butadiene acrylonitrile toughened epoxy/montmorillonite nanocomposite. *J. Appl. Polym. Sci.* **2009**, *113*, 685–692. [CrossRef]
90. Liu, W.; Hoa, S.V.; Pugh, M. Morphology and performance of epoxy nanocomposites modified with organoclay and rubber. *Polym. Eng. Sci.* **2004**, *44*, 1178–1186. [CrossRef]
91. Chonkaew, W.; Sombatsompop, N.; Brostow, W. High impact strength and low wear of epoxy modified by a combination of liquid carboxyl terminated poly (butadiene-co-acrylonitrile) rubber and organoclay. *Eur. Polym. J.* **2013**, *49*, 1461–1470. [CrossRef]
92. Vijayan, P.P.; Puglia, D.; Pionteck, J.; Kenny, J.M.; Thomas, S. Liquid-rubber-modified epoxy/clay nanocomposites: Effect of dispersion methods on morphology and ultimate properties. *Polym. Bull.* **2015**, *72*, 1703–1722. [CrossRef]
93. Xu, S.A.; Wang, G.T.; Mai, Y.W. Effect of hybridization of liquid rubber and nanosilica particles on the morphology, mechanical properties, and fracture toughness of epoxy composites. *J. Mater. Sci.* **2013**, *48*, 3546–3556. [CrossRef]
94. Poonpipat, Y.; Leelachai, K.; Pearson, R.A.; Dittanet, P. Fracture behavior of silica nanoparticles reinforced rubber/epoxy composite. *J. Reinf. Plast. Compos.* **2017**, *36*, 1156–1167. [CrossRef]
95. Liang, Y.L.; Pearson, R.A. The toughening mechanism in hybrid epoxy-silica-rubber nanocomposites (HESRNs). *Polymer* **2010**, *51*, 4880–4890. [CrossRef]

96. Wetzel, B.; Haupert, F.; Zhang, M.Q. Epoxy nanocomposites with high mechanical and tribological performance. *Compos. Sci. Technol.* **2003**, *63*, 2055–2067. [CrossRef]
97. Hosseini, M.; Esfandeh, M.; Razavi-Nouri, M.; Rezadoust, A.M. Effect of Hybridization of Carboxyl-Terminated Acrylonitrile Butadiene Liquid Rubber and Alumina Nanoparticles on the Fracture Toughness of Epoxy Nanocomposites. *Polym. Compos.* **2019**, *40*, 2700–2711. [CrossRef]
98. Kausar, A. Rubber toughened epoxy-based nanocomposite: A promising pathway toward advanced materials. *J. Macromol. Sci. Part A Pure Appl. Chem.* **2020**, *57*, 499–511. [CrossRef]
99. Zewde, B.; Pitliya, P.; Karim, A.; Raghavan, D. Synergistic effect of functionalized carbon nanotubes and micron sized rubber particles on the mechanical properties of epoxy resin. *Macromol. Mater. Eng.* **2016**, *301*, 542–548. [CrossRef]
100. Hsieh, T.H.; Kinloch, A.J.; Masania, K.; Lee, J.S.; Taylor, A.C.; Sprenger, S. The toughness of epoxy polymers and fibre composites modified with rubber microparticles and silica nanoparticles. *J. Mater. Sci.* **2010**, *45*, 1193–1210. [CrossRef]
101. Kelnar, I.; Rotrekl, J.; Kaprálková, L.; Hromádková, J.; Strachota, A. Effect of amine-terminated butadiene-acrylonitrile/clay combinations on the structure and properties of epoxy nanocomposites. *J. Appl. Polym. Sci.* **2012**, *125*, 3477–3483. [CrossRef]
102. Bakar, M.; Szymańska, J. Property enhancement of epoxy resin using a combination of amine-terminated butadiene-acrylonitrile copolymer and nanoclay. *J. Thermoplast. Compos. Mater.* **2014**, *27*, 1239–1255. [CrossRef]
103. Szymańska, J.; Bakar, M.; Białkowska, A.; Kostrzewa, M. Study on the adhesive properties of reactive liquid rubber toughened epoxy-clay hybrid nanocomposites. *J. Polym. Eng.* **2018**, *38*, 231–238. [CrossRef]
104. Kong, Y.; Huang, Q.; Mao, D.; Chen, Y.; Zou, H.; Liang, M. Preparation and properties of epoxy-terminated butadiene acrylonitrile rubber-intercalating organic montmorillonite nanocomposites. *Polym. Bull.* **2019**, *76*, 3989–4002. [CrossRef]
105. Mao, D.; Zou, H.; Liang, M.; Zhou, S.; Chen, Y. Mechanical and damping properties of epoxy/liquid rubber intercalating organic montmorillonite integration nanocomposites. *J. Appl. Polym. Sci.* **2014**, *131*, 39797. [CrossRef]
106. Wu, Y.; Gu, Z.; Chen, M.; Zhu, C.; Liao, H. Effect of functionalization of multi-walled carbon nanotube on mechanical and viscoelastic properties of polysulfide-modified epoxy nanocomposites. *High Perform. Polym.* **2017**, *29*, 151–160. [CrossRef]
107. Nasab, M.G.; Kalaee, M. Epoxy/graphene oxide/liquid polysulfide ternary nano-composites: Rheological, thermal and mechanical, characterization. *RSC Adv.* **2016**, *6*, 45357–45368. [CrossRef]
108. Tang, L.C.; Zhang, H.; Sprenger, S.; Ye, L.; Zhang, Z. Fracture mechanisms of epoxy-based ternary composites filled with rigid-soft particles. *Compos. Sci. Technol.* **2012**, *72*, 558–565. [CrossRef]
109. Leelachai, K.; Kongkachuichay, P.; Dittanet, P. Toughening of epoxy hybrid nanocomposites modified with silica nanoparticles and epoxidized natural rubber. *J. Polym. Res.* **2017**, *24*, 41. [CrossRef]
110. Kam, K.W.; Teh, P.L.; Osman, H.; Yeoh, C.K. Characterization of different forms of vulcanized natural rubbers as elastomer spacer and toughening agent in two-matrix filled epoxy/natural rubber/graphene nano-platelets system. *J. Appl. Polym. Sci.* **2019**, *136*, 47198. [CrossRef]
111. Wei, K.K.; Leng, T.P.; Keat, Y.C.; Osman, H.; Rasidi, M.S.M. The potential of natural rubber (NR) in controlling morphology in two-matrix epoxy/NR/graphene nano-platelets (GNP) systems. *Polym. Test.* **2019**, *77*, 105905. [CrossRef]
112. Gong, L.X.; Zhao, L.; Tang, L.C.; Liu, H.Y.; Mai, Y.W. Balanced electrical, thermal and mechanical properties of epoxy composites filled with chemically reduced graphene oxide and rubber nanoparticles. *Compos. Sci. Technol.* **2015**, *121*, 104–114. [CrossRef]
113. Tsang, W.L.; Taylor, A.C. Fracture and toughening mechanisms of silica-and core-shell rubber-toughened epoxy at ambient and low temperature. *J. Mater. Sci.* **2019**, *54*, 13938–13958. [CrossRef]
114. Liu, S.; Fan, X.; He, C. Improving the fracture toughness of epoxy with nanosilica-rubber core-shell nanoparticles. *Compos. Sci. Technol.* **2016**, *125*, 132–140. [CrossRef]
115. Bajpai, A.; Carlotti, S. The effect of hybridized carbon nanotubes, silica nanoparticles, and core-shell rubber on tensile, fracture mechanics and electrical properties of epoxy nanocomposites. *Nanomaterials* **2019**, *9*, 1057. [CrossRef]
116. Gharieh, A.; Seyed Dorraji, M.S. A systematic study on the synergistic effects of MWCNTs and core-shell particles on the physicomechanical properties of epoxy resin. *Sci. Rep.* **2021**, *11*, 20789. [CrossRef]
117. Gam, K.T.; Miyamoto, M.; Nishimura, R.; Sue, H.J. Fracture behavior of core-shell rubber-modified clay-epoxy nanocomposites. *Polym. Eng. Sci.* **2003**, *43*, 1635–1645. [CrossRef]
118. Zhu, Z.; Chen, H.; Chen, Q.; Liu, C.; Noh, K.; Yao, H.; Kotaki, M.; Sue, H.-J. Fracture behavior of hybrid epoxy nanocomposites based on multi-walled carbon nanotube and core-shell rubber. *Nano Mater. Sci.* **2022**, *4*, 251–258. [CrossRef]
119. Mehrabi-Kooshki, M.; Jalali-Arani, A. Preparation of binary and hybrid epoxy nanocomposites containing graphene oxide and rubber nanoparticles: Fracture toughness and mechanical properties. *J. Appl. Polym. Sci.* **2019**, *136*, 46988. [CrossRef]
120. Quan, D.; Pearson, R.A.; Ivankovic, A. Interaction of toughening mechanisms in ternary nanocomposites. *Polym. Compos.* **2018**, *39*, 3482–3496. [CrossRef]
121. Jia, Q.M.; Zheng, M.S.; Chen, H.X.; Shen, R.J. Morphologies and properties of polyurethane/epoxy resin interpenetrating network nanocomposites modified with organoclay. *Mater. Lett.* **2006**, *60*, 1306–1309. [CrossRef]
122. Jia, Q.M.; Zheng, M.; Zhu, Y.C.; Li, J.B.; Xu, C.Z. Effects of organophilic montmorillonite on hydrogen bonding, free volume and glass transition temperature of epoxy resin/polyurethane interpenetrating polymer networks. *Eur. Polym. J.* **2007**, *43*, 35–42. [CrossRef]
123. Jia, Q.; Shan, S.; Wang, Y.; Gu, L.; Li, J. Tribological performance and thermal behavior of epoxy resin nanocomposites containing polyurethane and organoclay. *Polym. Adv. Technol.* **2008**, *19*, 859–864. [CrossRef]

124. Bakar, M.; Kostrzewa, M.; Hausnerová, B.; Sar, K. Preparation and property evaluation of nanocomposites based on polyurethane-modified epoxy/montmorillonite systems. *Adv. Polym. Technol.* **2010**, *29*, 237–248. [CrossRef]
125. Kostrzewa, M.; Hausnerova, B.; Bakar, M.; Pająk, K. Preparation and characterization of an epoxy resin modified by a combination of MDI-based polyurethane and montmorillonite. *J. Appl. Polym. Sci.* **2011**, *122*, 3237–3247. [CrossRef]
126. Li, J. High performance epoxy resin nanocomposites containing both organic montmorillonite and castor oil-polyurethane. *Polym. Bull.* **2006**, *56*, 377–384. [CrossRef]
127. Chen, S.; Wang, Q.; Wang, T. Damping, thermal, and mechanical properties of carbon nanotubes modified castor oil-based polyurethane/epoxy interpenetrating polymer network composites. *Mater. Des.* **2012**, *38*, 47–52. [CrossRef]
128. Xu, K.; Chen, R.; Wang, C.; Sun, Y.; Zhang, J.; Liu, Y.; Xie, H.; Cheng, R. Organomontmorillonite-modified soybean oil-based polyurethane/epoxy resin interpenetrating polymer networks (IPNs). *J. Therm. Anal. Calorim.* **2016**, *126*, 1253–1260. [CrossRef]
129. Dutta, S.; Karak, N.; Saikia, J.P.; Konwar, B.K. Biocompatible epoxy modified bio-based polyurethane nanocomposites: Mechanical property, cytotoxicity and biodegradation. *Bioresour. Technol.* **2009**, *100*, 6391–6397. [CrossRef]
130. Białkowska, A.; Bakar, M.; Przybyłek, M. Effect of nonisocyanate polyurethane and nanoclay on the mechanical properties of an epoxy resin. *Mech. Compos. Mater. Struct.* **2018**, *54*, 665–674. [CrossRef]
131. Doley, S.; Sarmah, A.; Sarkar, C.; Dolui, S.K. In situ development of bio-based polyurethane-blend-epoxy hybrid materials and their nanocomposites with modified graphene oxide via non-isocyanate route. *Polym. Int.* **2018**, *67*, 1062–1069. [CrossRef]
132. Cheng, H.T.; Lee, Y.S.; Liu, H.C.; Lee, W.J. The effect of component addition order on the properties of epoxy resin/polyurethane resin interpenetrating polymer network structure. *J. Appl. Polym. Sci.* **2021**, *138*, 49833. [CrossRef]
133. Isik-Gulsac, I.; Yilmazer, U.; Bayram, G. Effects of mixing sequence on epoxy/polyether polyol/organoclay ternary nanocomposites. *Plast. Rubber Compos.* **2020**, *49*, 368–377. [CrossRef]
134. Bakar, M.; Lavorgna, M.; Szymańska, J.; Dętkowska, A. Epoxy/polyurethane/clay ternary nanocomposites–Effect of components mixing sequence on the composites properties. *Polym.-Plast. Technol.* **2012**, *51*, 675–681. [CrossRef]
135. Park, J.H.; Jana, S.C. The relationship between nano-and micro-structures and mechanical properties in PMMA-epoxy-nanoclay composites. *Polymer* **2003**, *44*, 2091–2100. [CrossRef]
136. Hernandez, M.; Duchet-Rumeau, J.; Sautereau, H. Influence of processing conditions and physicochemical interactions on morphology and fracture behavior of a clay/thermoplastic/thermosetting ternary blend. *J. Appl. Polym. Sci.* **2010**, *118*, 3632–3642. [CrossRef]
137. Bakar, M.; Białkowska, A.; Kuřitka, I.; Hanuliková, B.; Masař, M. Synergistic effects of thermoplastic and nanoclay on the performance properties and morphology of epoxy resin. *Polym. Compos.* **2018**, *39*, E2540–E2551. [CrossRef]
138. Bakar, M.; Białkowska, A.; Molenda, J.; Piasek, J. Preparation and properties evaluation of thermoplastic modified epoxy nanocomposites. *J. Macromol. Sci. Part B Phys.* **2012**, *51*, 1159–1171. [CrossRef]
139. Rudresh, M.; Maruthi, B.H.; Channakeshavalu, K.; Nagaswarupa, H.P. Mechanical and thermal behavior of epoxy based halloysite nano clay/PMMA hybrid nanocomposites. *SN Appl. Sci.* **2019**, *1*, 687. [CrossRef]
140. Kaushal, P.; Singh, P.; Verma, V.; Pandey, K.N.; Kumar, V. Mechanical and thermal properties of epoxy/PVC/organo-modified clay nanocomposite. *Appl. Polym. Compos.* **2013**, *1*, 93–102.
141. Wang, T.T.; Huang, P.; Li, Y.Q.; Hu, N.; Fu, S.Y. Epoxy nanocomposites significantly toughened by both poly (sulfone) and graphene oxide. *Compos. Commun.* **2019**, *14*, 55–60. [CrossRef]
142. Rajasekaran, R.; Karikalchozhan, C.; Alagar, M. Synthesis, characterization and properties of organoclay-modified polysulfone/epoxy interpenetrating polymer network nanocomposites. *Chin. J. Polym. Sci.* **2008**, *26*, 669–678. [CrossRef]
143. Wang, Y.; Ma, X.; Zhang, B. Preparation and properties of organoclay/polyethersulphone/epoxy hybrid nanocomposites. *Polym. Compos.* **2015**, *36*, 767–774. [CrossRef]
144. Wang, Y.; Zhang, B.; Ye, J. Microstructures and toughening mechanisms of organoclay/polyethersulphone/epoxy hybrid nanocomposites. *Mater. Sci. Eng. A* **2011**, *528*, 7999–8005. [CrossRef]
145. Tangthana-umrung, K.; Zhang, X.; Gresil, M. Synergistic toughening on hybrid epoxy nanocomposites by introducing engineering thermoplastic and carbon-based nanomaterials. *Polymer* **2022**, *245*, 124703. [CrossRef]
146. Chen, Z.; Luo, J.; Huang, Z.; Cai, C.; Tusiime, R.; Li, Z.; Wang, H.; Cheng, C.; Liu, Y.; Sun, Z.; et al. Synergistic toughen epoxy resin by incorporation of polyetherimide and amino groups grafted MWCNTs. *Compos. Commun.* **2020**, *21*, 100377. [CrossRef]
147. Ma, H.; Aravand, M.A.; Falzon, B.G. Synergistic enhancement of fracture toughness in multiphase epoxy matrices modified by thermoplastic and carbon nanotubes. *Compos. Sci. Technol.* **2021**, *201*, 108523. [CrossRef]
148. Asif, A.; Rao, V.L.; Saseendran, V.; Ninan, K.N. Thermoplastic toughened layered silicate epoxy ternary nanocomposites—Preparation, morphology, and thermomechanical properties. *Polym. Eng. Sci.* **2009**, *49*, 756–767. [CrossRef]
149. Mirmohseni, A.; Zavareh, S. Epoxy/acrylonitrile-butadiene-styrene copolymer/clay ternary nanocomposite as impact toughened epoxy. *J. Polym. Res.* **2010**, *17*, 191–201. [CrossRef]
150. Jyotishkumar, P.; Abraham, E.; George, S.M.; Elias, E.; Pionteck, J.; Moldenaers, P.; Thomas, S. Preparation and properties of MWCNTs/poly (acrylonitrile-styrene-butadiene)/epoxy hybrid composites. *J. Appl. Polym. Sci.* **2013**, *127*, 3093–3103. [CrossRef]
151. Gholinezhad, F.; Golhosseini, R.; Moini Jazani, O. Synthesis, characterization, and properties of silicone grafted epoxy/acrylonitrile butadiene styrene/graphene oxide nanocomposite with high adhesion strength and thermal stability. *Polym. Compos.* **2022**, *43*, 1665–1684. [CrossRef]

152. Bakar, M.; Kostrzewa, M.; Okulska-Bożek, M.; Jacewicz, E. Mechanical and morphological properties of polycarbonate and montmorillonite filled epoxy hybrid composites. *J. Appl. Polym. Sci.* **2011**, *119*, 752–759. [CrossRef]
153. Gul, S.; Kausar, A.; Mehmood, M.; Muhammad, B.; Jabeen, S. Progress on epoxy/polyamide and inorganic nanofiller-based hybrids: Introduction, application, and future potential. *Polym.-Plast. Technol.* **2016**, *55*, 1842–1862. [CrossRef]
154. White, K.L.; Sue, H.J. Electrical conductivity and fracture behavior of epoxy/polyamide-12/multiwalled carbon nanotube composites. *Polym. Eng. Sci.* **2011**, *51*, 2245–2253. [CrossRef]
155. Zhao, X.; Li, Y.; Chen, W.; Li, S.; Zhao, Y.; Du, S. Improved fracture toughness of epoxy resin reinforced with polyamide 6/graphene oxide nanocomposites prepared via in situ polymerization. *Compos. Sci. Technol.* **2019**, *171*, 180–189. [CrossRef]
156. Surendran, A.; Geethamma, V.G.; Kalarikkal, N.; Thomas, S. Mechanical and Thermal Properties of Epoxy/Poly (Styrene-co-Acrylonitrile)(SAN)/Organoclay Nanocomposites. *Macromol. Symp.* **2021**, *398*, 2000184. [CrossRef]
157. Rostamiyan, Y.; Fereidoon, A.B.; Mashhadzadeh, A.H.; Khalili, M.A. Augmenting epoxy toughness by combination of both thermoplastic and nanolayered materials and using artificial intelligence techniques for modeling and optimization. *J. Polym. Res.* **2013**, *20*, 135. [CrossRef]
158. Fereidoon, A.; Mashhadzadeh, A.H.; Rostamiyan, Y. Experimental, modeling and optimization study on the mechanical properties of epoxy/high-impact polystyrene/multi-walled carbon nanotube ternary nanocomposite using artificial neural network and genetic algorithm. *Sci. Eng. Compos. Mater.* **2013**, *20*, 265–276. [CrossRef]
159. Cao, Y.M.; Sun, J.; Yu, D.H. Preparation and properties of nano-Al_2O_3 particles/polyester/epoxy resin ternary composites. *J. Appl. Polym. Sci.* **2002**, *83*, 70–77. [CrossRef]
160. Sánchez-Cabezudo, M.; Prolongo, M.G.; Salom, C.; García del Cid, M.A.; Masegosa, R.M. Ternary nanocomposites: Curing, morphology, and mechanical properties of epoxy/thermoplastic/organoclay systems. *Polym. Compos.* **2016**, *37*, 2184–2195. [CrossRef]
161. Hydro, R.M.; Pearson, R.A. Epoxies toughened with triblock copolymers. *J. Polym. Sci. Part B Polym. Phys.* **2007**, *45*, 1470–1481. [CrossRef]
162. Tao, L.; Sun, Z.; Min, W.; Ou, H.; Qi, L.; Yu, M. Improving the toughness of thermosetting epoxy resins via blending triblock copolymers. *RSC Adv.* **2020**, *10*, 1603–1612. [CrossRef]
163. Liu, J.; Thompson, Z.J.; Sue, H.-J.; Bates, F.S.; Hillmyer, M.A.; Dettloff, M.; Jacob, G.; Verghese, N.; Pham, H. Toughening of epoxies with block copolymer micelles of wormlike morphology. *Macromolecules* **2010**, *43*, 7238–7243. [CrossRef]
164. Pang, V.; Thompson, Z.J.; Joly, G.D.; Francis, L.F.; Bates, F.S. Block Copolymer and Nanosilica-Modified Epoxy Nanocomposites. *ACS Appl. Polym. Mater.* **2021**, *3*, 4156–4167. [CrossRef]
165. Jojibabu, P.; Zhang, Y.X.; Rider, A.N.; Wang, J.; Prusty, B.G. Synergetic effects of carbon nanotubes and triblock copolymer on the lap shear strength of epoxy adhesive joints. *Compos. Part B—Eng.* **2019**, *178*, 107457. [CrossRef]
166. Gómez-del Río, T.; Salazar, A.; Pearson, R.A.; Rodríguez, J. Fracture behaviour of epoxy nanocomposites modified with triblock copolymers and carbon nanotubes. *Compos. Part B—Eng.* **2016**, *87*, 343–349. [CrossRef]
167. Schuster, M.B.; Coelho, L.A. Toughness and roughness in hybrid nanocomposites of an epoxy matrix. *Polym. Eng. Sci.* **2019**, *59*, 1258–1269. [CrossRef]
168. Bajpai, A.; Alapati, A.K.; Wetzel, B. Toughening and mechanical properties of epoxy modified with block co-polymers and MWCNTs. *Procedia Struct. Integr.* **2016**, *2*, 104–111. [CrossRef]
169. Zhang, W.; Cui, H.; Lv, Y.; Yang, Q.; Huang, Y.; Li, G.; Kong, M. Synergistically enhanced performance of epoxy resin by block copolymer and multi-walled carbon nanotubes. *J. Appl. Polym. Sci.* **2022**, *139*, e52457. [CrossRef]
170. Li, T.; He, S.; Stein, A.; Francis, L.F.; Bates, F.S. Synergistic toughening of epoxy modified by graphene and block copolymer micelles. *Macromolecules* **2016**, *49*, 9507–9520. [CrossRef]
171. Wang, J.; Xue, Z.; Li, Y.; Li, G.; Wang, Y.; Zhong, W.H.; Yang, X. Synergistically effects of copolymer and core-shell particles for toughening epoxy. *Polymer* **2018**, *140*, 39–46. [CrossRef]
172. Rahman, M.M.; Hosur, M.; Zainuddin, S.; Jajam, K.C.; Tippur, H.V.; Jeelani, S. Mechanical characterization of epoxy composites modified with reactive polyol diluent and randomly-oriented amino-functionalized MWCNTs. *Polym. Test.* **2012**, *31*, 1083–1093. [CrossRef]
173. Jajam, K.C.; Rahman, M.M.; Hosur, M.V.; Tippur, H.V. Fracture behavior of epoxy nanocomposites modified with polyol diluent and amino-functionalized multi-walled carbon nanotubes: A loading rate study. *Compos. Part A Appl. Sci. Manuf.* **2014**, *59*, 57–69. [CrossRef]
174. Yi, X.F.; Mishra, A.K.; Kim, N.H.; Ku, B.C.; Lee, J.H. Synergistic effects of oxidized CNTs and reactive oligomer on the fracture toughness and mechanical properties of epoxy. *Compos. Part A Appl. Sci. Manuf.* **2013**, *49*, 58–67. [CrossRef]
175. da Silva, W.M.; Ribeiro, H.; Neves, J.C.; Sousa, A.R.; Silva, G.G. Improved impact strength of epoxy by the addition of functionalized multiwalled carbon nanotubes and dipropylene glycol diglycidyl ether-reactive diluent. *J. Appl. Polym. Sci.* **2015**, *132*, 42587. [CrossRef]
176. Isik, I.; Yilmazer, U.; Bayram, G. Impact modified epoxy/montmorillonite nanocomposites: Synthesis and characterization. *Polymer* **2003**, *44*, 6371–6377. [CrossRef]
177. Chozhan, C.K.; Elumalai, P.; Alagar, M. Studies on morphology and thermomechanical behavior of polyethylene glycol/1, 8-octanediol-modified epoxy-organoclay hybrid nanocomposites. *J. Compos. Mater.* **2009**, *43*, 2753–2770. [CrossRef]
178. Jayan, J.S.; Saritha, A.; Deeraj, B.D.S.; Joseph, K. Graphene oxide as a prospective graft in polyethylene glycol for enhancing the toughness of epoxy nanocomposites. *Polym. Eng. Sci.* **2020**, *60*, 773–781. [CrossRef]

179. Chang, H.L.; Chen, C.M.; Chen, C.H. Influences of nano-silica addition on diluent/epoxy mechanical properties. *Adv. Mater. Res.* **2014**, *853*, 34–39. [CrossRef]
180. Halder, S.; Goyat, M.S.; Ghosh, P.K. Morphological, structural, and thermophysical properties of zirconium dioxide-epoxy nanocomposites. *High Perform. Polym.* **2016**, *28*, 697–708. [CrossRef]
181. Carolan, D.; Ivankovic, A.; Kinloch, A.J.; Sprenger, S.; Taylor, A.C. Toughening of epoxy-based hybrid nanocomposites. *Polymer* **2016**, *97*, 179–190. [CrossRef]
182. Lim, Y.J.; Carolan, D.; Taylor, A.C. Simultaneously tough and conductive rubber-graphene-epoxy nanocomposites. *J. Mater. Sci.* **2016**, *51*, 8631–8644. [CrossRef]
183. Sarafrazi, M.; Ghasemi, A.R.; Hamadanian, M. Synergistic effect between $CuCr_2O_4$ nanoparticles and plasticizer on mechanical properties of EP/PU/CuCr2O4 nanocomposites: Experimental approach and molecular dynamics simulation. *J. Appl. Polym. Sci.* **2020**, *137*, 49425. [CrossRef]
184. Das, G.; Karak, N. Epoxidized *Mesua ferrea* L. seed oil-based reactive diluent for BPA epoxy resin and their green nanocomposites. *Prog. Org. Coat.* **2009**, *66*, 59–64. [CrossRef]
185. Dinakaran, K.; Alagar, M. Preparation and characterization of bismaleimide (*N*,*N*′-bismaleimido-4,4′-diphenyl methane)—Unsaturated polyester modified epoxy intercrosslinked matrices. *J. Appl. Polym. Sci.* **2002**, *85*, 2853–2861. [CrossRef]
186. Chozhan, C.K.; Alagar, M.; Sharmila, R.J.; Gnanasundaram, P. Thermomechanical behaviour of unsaturated polyester toughened epoxy-clay hybrid nanocomposites. *J. Polym. Res.* **2007**, *14*, 319–328. [CrossRef]
187. Paluvai, N.R.; Mohanty, S.; Nayak, S.K. Effect of nanoclay on the mechanical, thermal, and water absorption properties of an UP-toughened epoxy network. *J. Adhes.* **2016**, *92*, 840–861. [CrossRef]
188. Chakradhar, K.V.P.; Subbaiah, K.V.; Kumar, M.A.; Reddy, G.R. Blended epoxy/polyester polymer nanocomposites: Effect of "nano" on mechanical properties. *Polym.-Plast. Technol.* **2012**, *51*, 92–96. [CrossRef]
189. Sabu, M.; Ruban, Y.J.V.; Ginil, M.S. Effect of organoclay on contact angle, thermal and mechanical properties of filled epoxy composites. *Mater. Today Proc.* **2021**, *41*, 549–556. [CrossRef]
190. Jaya Vinse Ruban, Y.; Ginil Mon, S.; Vetha Roy, D. Mechanical and thermal studies of unsaturated polyester-toughened epoxy composites filled with amine-functionalized nanosilica. *Appl. Nanosci.* **2013**, *3*, 7–12. [CrossRef]
191. Ruban, Y.J.V.M.; Mon, S.G.; Roy, D.V. Processing and thermal/mechanical studies of unsaturated polyester toughened epoxy composites filled with amine functionalized carbon nanotubes. *Int. J. Plast. Technol.* **2011**, *15*, 133–149. [CrossRef]
192. Le, M.T.; Huang, S.C. Effect of nano-fillers on the strength reinforcement of novel hybrid polymer nanocomposites. *Mater. Manuf. Process.* **2016**, *31*, 1066–1072.
193. Chozhan, C.K.; Rajasekaran, R.; Alagar, M.; Gnanasundaram, P. Thermomechanical behavior of vinyl ester oligomer-toughened epoxy-clay hybrid nanocomposites. *Int. J. Polym. Mater.* **2008**, *57*, 319–337. [CrossRef]
194. Tyberg, C.S.; Bergeron, K.; Sankarapandian, M.; Shih, P.; Loos, A.C.; Dillard, D.A.; McGrath, J.E.; Riffle, J.S.; Sorathia, U. Structure-property relationships of void-free phenolic-epoxy matrix materials. *Polymer* **2000**, *41*, 5053–5062. [CrossRef]
195. Auad, M.L.; Nutt, S.R.; Pettarin, V.; Frontini, P.M. Synthesis and properties of epoxy-phenolic clay nanocomposites. *Express Polym. Lett.* **2007**, *9*, 629–639. [CrossRef]
196. Li, J.; Wu, Z.; Huang, C.; Liu, H.; Huang, R.; Li, L. Mechanical properties of cyanate ester/epoxy nanocomposites modified with plasma functionalized MWCNTs. *Compos. Sci. Technol.* **2014**, *90*, 166–173. [CrossRef]
197. Raja Othman, R.N.; Subramaniam, D.K.; Ezani, N.A.; Abdullah, M.F.; Ku Ahmad, K.Z. The synergistic effects of hybrid micro and nano silica in influencing the mechanical properties of epoxy composites—A new model. *Polymers* **2022**, *14*, 3969. [CrossRef] [PubMed]
198. de Oliveira, M.M.; Forsberg, S.; Selegård, L.; Carastan, D.J. The influence of sonication processing conditions on electrical and mechanical properties of single and hybrid epoxy nanocomposites filled with carbon nanoparticles. *Polymers* **2021**, *13*, 4128. [CrossRef] [PubMed]
199. Alsuwait, R.B.; Souiyah, M.; Momohjimoh, I.; Ganiyu, S.A.; Bakare, A.O. Recent development in the processing, properties, and applications of epoxy-based natural fiber polymer biocomposites. *Polymers* **2023**, *15*, 145. [CrossRef] [PubMed]
200. Zhang, M.; Zhai, Z.; Li, M.; Cheng, T.; Wang, C.; Jiang, D.; Chen, L.; Wu, Z.; Guo, Z. Epoxy nanocomposites with carbon nanotubes and montmorillonite: Mechanical properties and electrical insulation. *J. Compos. Mater.* **2016**, *50*, 3363–3372. [CrossRef]
201. Yang, S.Y.; Lin, W.N.; Huang, Y.L.; Tien, H.W.; Wang, J.Y.; Ma, C.C.M.; Li, S.M.; Wang, Y.S. Synergetic effects of graphene platelets and carbon nanotubes on the mechanical and thermal properties of epoxy composites. *Carbon* **2011**, *49*, 793–803. [CrossRef]
202. Bahari-Sambran, F.; Kazemi-Khasragh, E.; Orozco-Caballero, A.; Eslami-Farsani, R. Synergetic effects of graphene nanoplatelets/montmorillonite on their dispersion and mechanical properties of the epoxy-based nanocomposite: Modeling and experiments. *Polym. Compos.* **2022**, *43*, 6897–6911. [CrossRef]
203. Zhang, L.; Zhang, G.; Chang, L.; Wetzel, B.; Jim, B.; Wang, Q. Distinct tribological mechanisms of silica nanoparticles in epoxy composites reinforced with carbon nanotubes, carbon fibers and glass fibers. *Tribol. Int.* **2016**, *104*, 225–236.

Disclaimer/Publisher's Note: The statements, opinions and data contained in all publications are solely those of the individual author(s) and contributor(s) and not of MDPI and/or the editor(s). MDPI and/or the editor(s) disclaim responsibility for any injury to people or property resulting from any ideas, methods, instructions or products referred to in the content.

polymers

MDPI

Article

Numerical Study on the Distribution of Rodlike Particles in Laminar Flows of Power Law Fluids Past a Cylinder

Wenqian Lin [1], Zhenna Li [2], Shanliang Zhang [2] and Jianzhong Lin [2,*]

[1] School of Media and Design, Hangzhou Dianzi University, Hangzhou 310018, China
[2] State Key Laboratory of Fluid Power Transmission and Control, Zhejiang University, Hangzhou 310027, China
* Correspondence: mecjzlin@public.zju.edu.cn; Tel.: +86-571-87952882

Abstract: The contraction/expansion laminar flow containing rodlike particles in power-law fluid is studied numerically when the particles are in a dilute phase. The fluid velocity vector and streamline of flow are given at the finite Reynolds number (Re) region. The effects of Re, power index n and particle aspect ratio β on the spatial and orientation distributions of particles are analyzed. The results showed that for the shear-thickening fluid, particles are dispersed in the whole area in the contraction flow, while more particles are gathered near the two walls in the expansion flow. The spatial distribution of particles with small β is more regular. B has a significant, n has a moderate, but Re has a small impact on the spatial distribution of particles in the contraction and expansion flow. In the case of large Re, most particles are oriented in the flow direction. The particles near the wall show obvious orientation along the flow direction. In shear-thickening fluid, when the flow changes from contraction to expansion, the orientation distribution of particles becomes more dispersed; while in shear-thinning fluid, the opposite is true. More particles orient to the flow direction in expansion flow than that in contraction flow. The particles with a large β tend to align with the flow direction more obviously. Re, n and β have great influence on the orientation distribution of particles in the contraction and expansion flow. Whether the particles initially located at the inlet can bypass the cylinder depends on the transverse position and initial orientation of the particles at the inlet. The number of particles with $\theta_0 = 90°$ bypassing the cylinder is the largest, followed by $\theta_0 = 45°$ and $\theta_0 = 0°$. The conclusions obtained in this paper have reference value for practical engineering applications.

Keywords: rod-like particles; power-law fluid; spatial distribution; orientation; numerical simulation

Citation: Lin, W.; Li, Z.; Zhang, S.; Lin, J. Numerical Study on the Distribution of Rodlike Particles in Laminar Flows of Power Law Fluids Past a Cylinder. *Polymers* **2023**, *15*, 1956. https://doi.org/10.3390/polym15081956

Academic Editors: Fahmi Zaïri, Matthias Ballauff, Ulrich Maschke and Rufina G. Alamo

Received: 13 February 2023
Revised: 9 April 2023
Accepted: 19 April 2023
Published: 20 April 2023

Copyright: © 2023 by the authors. Licensee MDPI, Basel, Switzerland. This article is an open access article distributed under the terms and conditions of the Creative Commons Attribution (CC BY) license (https://creativecommons.org/licenses/by/4.0/).

1. Introduction

The flow containing rodlike particles is very common in chemical industry, materials, environmental protection and other industries. There are several important factors that determine the characteristics of such flow, and the most important factors are the spatial distribution and orientation of rodlike particles in the fluid.

The motion of rodlike particles in flows is complicated because the particle rotation and orientation are coupled with the translation motion. The particles will exhibit nonuniform spatial distribution and non-isotropic orientation distribution due to the difference of the flow velocity and shear rate in different region, which has aroused people's attention. Altan et al. [1] adopted the model of Dinh-Armstrog [2] and obtained the orientation distribution of particles by solving the equation of the direction tensor in a channel flow based on the assumption that the particles moved in a plane, and the rodlike particles are assumed to be rigid cylindrical bodies with negligible inertia. Chono and Makino [3] obtained the spatial and orientation distributions of particles by solving the equation of directional tensor combined with the equivalent strain tensor model and with considering the effect of particles on the fluid for the flow between two plates. Chiba and Nakamura [4] studied two-dimensional orientations of 1800 fibers in a Newtonian flow through a 1:4

backward-facing step channel, and found that the fibers with large aspect ratio (β = 10,000) are completely arranged along the streamline direction, while the fibers with small aspect ratio (β = 5) have a dominant orientation. Chiba et al. [5] solved the kinetic energy equation coupled with distribution function of fiber orientation for the flow between two plates, and the suspension consisted of high aspect-ratio 180 rigid fibers in a Newtonian fluid. They showed that the non-isotropic distribution of fiber orientation and stress occurred near the entrance, and the inlet region presented a significant non-Newtonian flow effect with the increase of fiber concentration and aspect ratio. Lin et al. [6] used three-dimensional vortex method to simulate the circular jet flow, and then calculated the fiber motion in flow by particle trajectory model without considering the effect of particle on the flow, finally obtained the spatial and orientation distributions of fibers under different Reynolds number, Stokes number and fiber aspect ratio. Lin et al. [7] compared various forces exerted on a moving rod-like particle in an incompressible elongational-shear flow, and indicated that the Stokes resistance, Basset force and added mass were much larger than the Magnus force, Saffman force and pressure gradient force.

Cai et al. [8] studied the gas-solid two-phase turbulent flow of rod-like particles with two-way coupling approach, and showed that the volume fraction of particles in central region was higher than that in near-wall region, the velocity and pressure of the flow decreased evidently in the region where the volume fraction of particles was high. They also obtained the distributions of pressure, velocity and turbulent kinetics along the axis of the riser [9]. Hao et al. [10] simulated numerically the frictional rod-like particle shear flows with different size distributions (monodisperse, binary, Gaussian, uniform), it was found that stress fluctuation reached the maximum, and stress rate increased with the increase of volume fraction at the jamming volume fraction. The jamming volume fraction presented obvious dependences on the fraction of longer particles and particle size in the case of polydisperse particles. They also indicated that no segregation appeared in the absence of gravity and interstitial fluid medium. The minimum stress difference due to the change in volume fraction of a particle species was observed at volume fraction of 0.2 [11].

The investigations as shown above are related to the case of rod-like particles flowing in the Newtonian fluids. However, in many industrial applications, the fluid containing rodlike particles is non-Newtonian fluid. The scenario is even more complex when rodlike particles are suspended in non-Newtonian fluids due to the fluids itself show the rheological properties, so the dynamics of rodlike particles in non-Newtonian fluids has been becoming the focus which people greatly concern for. Leal [12] studied the translation of a slender axisymmetric rodlike particle through a quiescent second-order fluid and rotation in a simple shear flow of the same material, and the results showed that freely translating particles with fore-aft symmetry presented a single stable orientation. The rheological property caused a particle drift through Jeffery orbit to equilibrium orbit at small and moderate shear rates. The rate of orbit drift could be employed to determine the second normal stress difference which also controlled the drifting rate. Brunn [13] studied the motion of rigid particles in a homogeneous shear flow of a viscoelastic fluid with a creeping-motion equation, and indicated that rod-like particles moved towards a vorticity alignment in the flow plane and tumble around the vorticity axis. Cohen et al. [14] studied the particle orientation in a dilute suspension of rod-like particles in a second-order fluid and found that most particles oriented close to the vorticity axis when the fluid elasticity was strong enough to restrain the rotational diffusion of the particles. Iso et al. [15,16] showed that a single rodlike particle rotated towards the vorticity axis in weakly elastic fluids (100 ppm polyacrylamide), but aligned rapidly along the flow direction in highly elastic fluids (1000 and 2000 ppm polyacrylamide). In intermediate elastic fluids (200 and 500 ppm polyacrylamide), the particle had an orientation in between the flow and the vorticity direction. Gunes et al. [17] studied the flow-induced orientation of spheroidal particles in viscoelastic fluids with a wide range of rotational Peclet and Weissenberg numbers, and indicated that particle changed orientation from a random state to spinning in Jeffery orbits with increasing shear rate. At higher elasticity, particles reoriented again to the flow

direction with the exception in Boger fluids. With suitable flow histories bimodal flow-vorticity orientation distributions could be generated. De Borzacchiello et al. [18] proposed simplified modeling of short rodlike particles in second-order fluids from microscopic to macroscopic scales, which could be used in industrial simulation software. Phan-Thien's group [19,20] extended the complete double layer boundary integral equation formulation for Stokes flows to viscoelastic fluids to solve the mobility problem for a particle in an unbounded body of fluid, and showed that viscoelastic stresses slowed down rotation of prolate spheroid in a shear flow of Oldroyd-B fluid at a relatively small Deborah number. Lin et al. [21] studied the dynamics of rod-like particles in the contraction flow of a second-order fluid when the particles were in a dilute phase, and showed that the spatial and orientation distributions of particles were dependent on the inertia, viscoelasticity and effect of confined wall. High shear rate of the fluid made the particles align with the flow direction. Particle spatial distribution became more non-uniform, andmore particles tended to align with theflowdirection with increasing Deborah number and contraction ratio. Particle aspect ratio had a weaker effect on the particle distribution than Deborah number, Stokes number and contraction ratio. Lin et al. [22] explored the effect of various factors on the orientation distributions of rod-like particlesin a mixing layer of an Oldroyd-B fluid in the range of Stokes number (St) from 0.005 to 1.0, Weissenberg number (Wi) from 5 to 15, particle aspect ratio (α) from 5 to 25, and indicated that the particles with a small St were distributed homogenously. More particles aligned on the flow-gradient plane with the increase of Wi, and the decrease of St and α. Wi had a stronger effect on the orientation distribution than St and α. Stover and Cohen [23] studied the motion of suspended rodlike particles in the flow between two flat plates of at low Reynolds numbers, and obtained the data for rodlike particles with aspect ratios of 12.0 suspended in a Newtonian fluid; and for rodlike particles with aspect ratios between 5 and 8 in a non-Newtonian fluid. The results showed that, for the Newtonian fluid, particles aligned with the flow direction and less than a particle half-length from a wall interacted irreversibly with the wall; for the non-Newtonian fluid, particles that were aligned with the flow direction and were near walls did not rotate. Domurath et al. [24] studied numerically the properties of power-law fluids filled with rigid rods of different aspect ratios, and found that there was no similarity between the rheological coefficients for these particles at large aspect ratios; there were negligible differences in the angular velocities between the Newtonian and power-law matrix fluids, especially for large aspect ratios.

As mentioned above, the dynamics of rodlike particles in some kind of non-Newtonian fluids were investigated, but the study in power-law fluid with shear-dependent viscosity is rare. Power-law fluid is very common, for example, low solid mud, polymer drilling fluid, high concentration starch paste, pulp and paint with high solid content. In addition, most of the flows mentioned above are unbounded flow or parallel flow. However, in practical applications, many cases are contraction and expansion flow [25,26], i.e., the flow first passes through a contraction channel and then enters an expansion channel. So far, the authors have not seen any research report on the contraction and expansion flow of power-law fluid containing rodlike particles, although this kind of flow has strong application background. Therefore, in this paper, a set of equations for the contraction and expansion flow of power-law fluid containing rodlike particles are established and solved by numerical simulation, aiming to illustrate the influence of Reynolds number, power-index and particle aspect ratio on the spatial and orientation distributions of particles.

2. Model and Equation

2.1. Particle and Flow Model

Figure 1 shows a rigid rodlike particle without Brown motion. The particle size is much smaller than the geometric size of the flow (the ratio of particle length to cylinder radius is $l/R = 0.13$). Let the particles be a dilute phase, ignoring the interaction between particles, and the effect of particles on the fluid. The effect of fluid on particles is reflected in the Stokes force caused by the velocity difference between the fluid and particles.

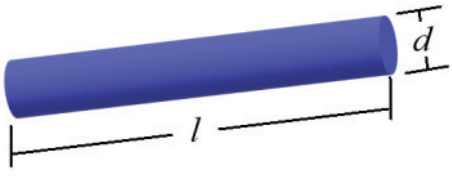

Figure 1. Schematic of a particle.

Figure 2 shows the flow and grid division. The power-law fluid containing rodlike particles enters from the left and flows out from the right. The upper and lower sides are solid walls, and there is a cylinder in the middle between the two walls.

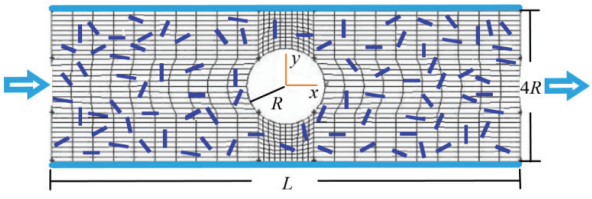

Figure 2. Schematic of a flow and grid division.

2.2. Equation for Particle Motion

When particles move in the flow, they are affected by Stokes force, Basset force, additional mass force and oscillation, but the Stokes force $\boldsymbol{F}$ dominates in the case of present study by comparing the effects of these factors [7], and can be expressed as:

$$\boldsymbol{F} = \mu a \boldsymbol{D} \cdot \boldsymbol{U}, \tag{1}$$

where μ is the fluid viscosity, a is the particle radius, $\boldsymbol{U}$ is the difference between the fluid and particles, $\boldsymbol{D}$ is the resistance coefficient and can be expressed as:

$$\boldsymbol{D} = \begin{bmatrix} D_{//} & 0 \\ 0 & D_{\perp} \end{bmatrix}, \tag{2}$$

where $D_{//}$ and $D_{\perp}$ are the resistance coefficients parallel to and perpendicular to the principal axis of particles, respectively, Loewenberg [27] presented the fitting curves of two resistance coefficients varying with the particle aspect ratio by experimental data:

$$\left.\begin{aligned} D_{//} &= 2.78715 + \frac{27.2277}{\beta} - \frac{8.26673}{\beta^2} \\ D_{\perp} &= 4.78194 + \frac{28.0349}{\beta} - \frac{10.0182}{\beta^2} \end{aligned}\right\} \beta \in (1, 100), \tag{3}$$

where β is the particle aspect ratio. Dividing both sides of Equation (1) by the mass of particles $m_p = \rho_p \pi l a^2$, we have:

$$\ddot{\boldsymbol{r}} = \frac{C_1}{\mathrm{St}} \boldsymbol{A}^{-1} \boldsymbol{D} \boldsymbol{A} \left(\boldsymbol{U}_f - \dot{\boldsymbol{r}} \right). \tag{4}$$

where $\ddot{\boldsymbol{r}}$ is the particle acceleration, $\dot{\boldsymbol{r}}$ is the particle velocity, $\boldsymbol{U}_f$ is the fluid velocity at particle center, $C_1 = U/\pi\beta L$ with L and U being the characteristic length and velocity of the flow, respectively, $\boldsymbol{A}$ is transition matrix for changing particle from body coordinate to rectangular coordinate:

$$\boldsymbol{A} = \begin{bmatrix} \cos\theta & \sin\theta \\ -\sin\theta & \cos\theta \end{bmatrix}, \tag{5}$$

where θ is the angle between particle principal axis and horizontal direction. St in Equation (4) is Stokes number:

$$\mathrm{St} = \rho_p a^2 U/\mu L, \tag{6}$$

where ρ_p is the particle density.

The moment acting on particles can be obtained from the slender body theory [28]:

$$\boldsymbol{M} = \frac{8}{3}\pi\mu\sigma L^3(C - \dot{\theta})[1 - \sigma(\ln 2 - 1.8333)], \tag{7}$$

where $\sigma = \ln^{-1}(2\beta)$, $C = -\sin\theta\cos\theta\left(\frac{\partial u_p}{\partial x} - \frac{\partial v_p}{\partial y}\right) + \cos^2\theta\frac{\partial v_p}{\partial x} - \sin^2\theta\frac{\partial u_p}{\partial y}$ with u_p and v_p being the velocity component of particle along the x and y direction, respectively. Dividing both sides of Equation (7) by the rotational inertia of particles $J_p = m_p(a^2 + l^2/6)/2$, we have:

$$\ddot{\theta} = 4\left(C - \dot{\theta}\right)\sigma[1 - \sigma(\ln 2 - 1.8333)]/(\mathrm{St}\cdot\mathrm{fst}), \tag{8}$$

where $\dot{\theta}$ and $\ddot{\theta}$ are the angular velocity and angular acceleration of particles, respectively, fst is a parameter with time dimension:

$$\mathrm{fst} = \frac{3L}{4U}\left(\frac{1}{\beta^2} + \frac{1}{6}\right). \tag{9}$$

When particle aspect ratio β is larger than 10, Equation (9) can be approximated as $\mathrm{fst} = L/8U$ and the rotational inertia of particles is $J_p = m_p l^2/12$.

2.3. Equations for Fluid

Equation (4) contains the fluid velocity $\boldsymbol{U}_f$, so the fluid velocity should be first given by solving equations for fluid before solving the equations for particles.

The continuity and momentum equations of the fluid are:

$$\nabla\cdot\boldsymbol{U}_f = 0, \tag{10}$$

$$\rho\frac{D\boldsymbol{U}_f}{Dt} = -\nabla p + \nabla\cdot\tau, \tag{11}$$

where $\boldsymbol{U}_f$ is the fluid velocity, ρ is the fluid density, p is the pressure, τ is the shear stress $\tau = \mu\dot{\gamma}$ with μ the dynamic viscosity and $\dot{\gamma}$ the rate of shearing tensor:

$$\dot{\gamma} = \frac{1}{2}\left[\left(\nabla U_f\right) + \left(\nabla U_f\right)^T\right]. \tag{12}$$

For the power-law fluid, the shear stress can be expressed as:

$$\tau = m\left|\dot{\gamma}\right|^{n-1}\dot{\gamma}, \tag{13}$$

then the effective viscosity is:

$$\mu = m\left|\dot{\gamma}\right|^{n-1}, \tag{14}$$

where m is the flow consistency coefficient; n is the power-law index; $n < 1$, $n = 1$ and $n > 1$ correspond to shear-thinning, Newtonian and shear-thickening fluids, respectively; $\left|\dot{\gamma}\right|$ is the local shear rate:

$$\left|\dot{\gamma}\right| = \sqrt{2\left(\frac{\partial u_f}{\partial x}\right)^2 + 2\left(\frac{\partial v_f}{\partial y}\right)^2 + \left(\frac{\partial u_f}{\partial x} + \frac{\partial v_f}{\partial y}\right)^2}, \tag{15}$$

with u_f and v_f are the velocity component of fluid along the x and y direction, respectively.

3. Numerical Simulation

The one-way coupling method is used for numerical solution here, i.e., considering only the effect of fluid on particles and ignoring the effect of particles on fluid. First solving the velocity of the fluid through Equations (10)–(15), then calculating the force and moment exerted by the fluid on the particles through Equations (1)–(3) and (7), and finally obtaining the acceleration, angular acceleration, velocity, angular velocity, trajectory and orientation of the particles through solving Equations (4) and (8).

3.1. Distribution of Fluid Velocity

A finite volume method is used to solve Equations (10)–(15). The grid division of the flow is generated using Gambit 2.0 as shown in Figure 2 where quadrilateral grid is selected. Gambit 2.0 will automatically generate the grid in Figure 2 when the number of grids and grid shape are determined. The SIMPLE and power-law scheme are used to deal with the term of velocity–pressure coupling and the convection term. A staggered mesh system and an alternating direction implicit method are used to solve the discretized equations.

3.2. Boundary Conditions

The no-slip condition is used on the walls. The condition of fully developed flow is used at the outlet. In Figure 2 it is assumed that the inlet is sufficiently far from the cylinder in the middle between the two walls, the presence of the cylinder has no effect on the fluid velocity distribution at the inlet. Therefore, the velocity distribution in a channel flow is used as the boundary condition at the inlet.

By solving Equations (10)–(15) in a channel flow, the analytical solution of fluid velocity along the x direction at the inlet can be obtained:

$$u_f = \frac{n}{n+1}\left(\frac{\Delta p}{2mL}\right)^{1/n}\left[(2R)^{\frac{n+1}{n}} - y^{\frac{n+1}{n}}\right], \tag{16}$$

where n is the power index of the fluid; Δp is the pressure drop; m is the flow consistency coefficient; L is the channel length and $2R$ is the half width of channel as shown in Figure 2. The corresponding mean velocity is:

$$\overline{u}_f = \frac{n}{(3n+1)}\left(\frac{\Delta p}{2mL}\right)^{\frac{1}{n}}(2R)^{\frac{n+1}{n}}. \tag{17}$$

3.3. Velocity, Angular Velocity and Spatial Position of Particles

30 randomly oriented particles are initially evenly distributed along the y-direction at the inlet. Every other time step, 30 particles enter the flow, and these particles pass through the flow and then exit the flow from the outlet. After the particles entering the flow and exiting the flow have stabilized, the statistics of the particles in the computational domain are performed to provide the spatial and orientation distribution characteristics of the particles. Therefore, the number of particles in the computational domain is not constant, and its value depends on the relevant parameters of the flow (Reynolds number) and particles (aspect ratio and initial orientation). The acceleration and angular acceleration of particles are calculated with Equations (4) and (8), and then the particle velocity, angular velocity, position and orientation angle at the next moment are calculated with the following formula:

$$\begin{gathered} \dot{x}_{i+1} = \dot{x}_i + \ddot{x}_i dt, \quad \dot{y}_{i+1} = \dot{y}_i + \ddot{y}_i dt, \\ x_{i+1} = \frac{x_i + \left(\dot{x}_{i-1} + \dot{x}_{i+1}\right)dt}{2},\ y_{i+1} = \frac{y_i + \left(\dot{y}_{i-1} + \dot{y}_{i+1}\right)dt}{2}, \\ \theta_{i+1} = \dot{\theta}_i + \ddot{\theta}_{i+1} dt,\ \theta_{i+1} = \frac{\theta_i + \left(\dot{\theta}_{i-1} + \dot{\theta}_{i+1}\right)dt}{2}. \end{gathered} \tag{18}$$

Equation (18) is numerically solved by the fourth-order Runge-Kutta method. The orientation distribution of particles can be obtained by statistically averaging the orientation angle of particles.

4. Results and Discussion

4.1. Fluid Velocity Vector and Streamline of Flow

Figures 3 and 4 show the fluid velocity vector and streamline distribution of the flow for Re = 2, 200 and n = 0.7. The Reynolds number is defined as Re $= 4R\overline{u}_f/\nu$ (4R is the channel width as shown in Figure 2, $\overline{u}_f$ is the mean velocity, and ν is the viscosity). We can see that when Re is small (Re = 2) as shown in Figure 3, the distributions of velocity vector and streamline are almost symmetrical about the center of the cylinder, which is consistent with the flow characteristics of small Re. When Re is large (Re = 200) as shown in Figure 4, the distributions of velocity vector and streamline in front of the cylinder are similar to those in Figure 3, but the difference is that there is obvious wake in the flow behind the cylinder because there is zero values in the velocity vector distribution in Figure 4a and vortex in the streamline distribution in Figure 4b.

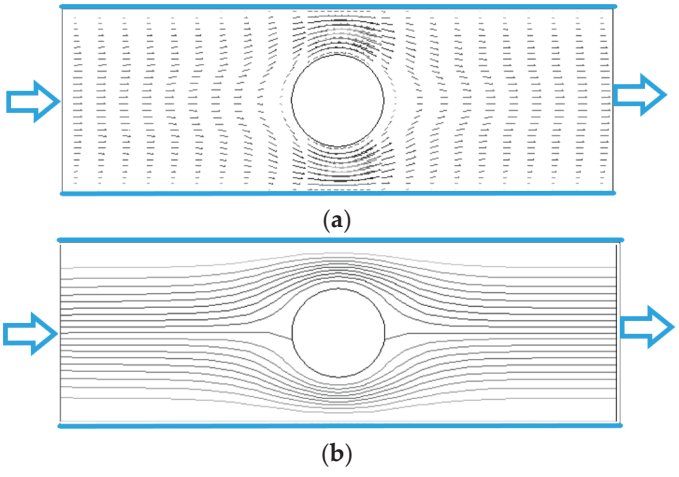

Figure 3. Fluid velocity vector and streamline of flow (Re = 2, n = 0.7). (**a**) velocity vector. (**b**) streamline.

In the unbounded flow around a cylinder of Newtonian fluid, there will be a Karman vortex street behind the cylinder when Re > 40. In Figure 4b, the Karman vortex street does not appear even if Re = 200. The reasons may be attributed to two aspects. One is that the existence of the upper and lower walls inhibits the generation of Karman vortex behind the cylinder because the walls have a large shear force on the fluid, and its direction is opposite to the shear force generated by the cylinder, which reduces the rotation of the flow behind the cylinder. Another reason is that the fluid in Figure 4 is shear-thinning fluid, and the fluid after thinning also reduces the rotation of the flow behind the cylinder.

Figure 5 shows the fluid velocity vector and streamline distribution of the flow for Re = 200 and n = 1.3. Compared to the shear-thinning situation in Figure 4b, the wake behind the cylinder becomes smaller. This is attributed to that the increased viscosity results in the reduction of the local Reynolds number.

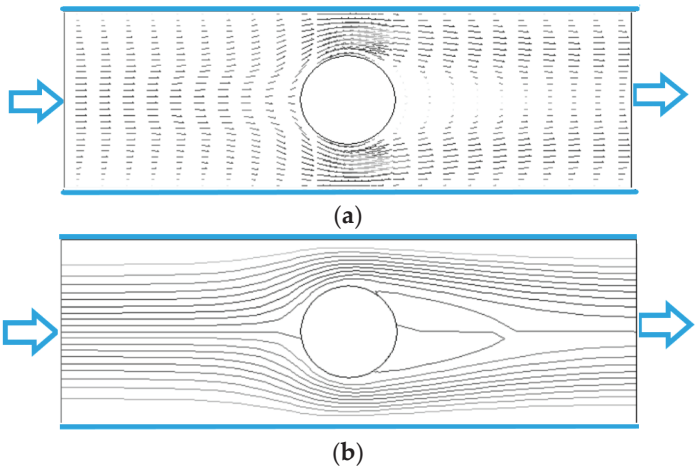

Figure 4. Fluid velocity vector and streamline of flow (Re = 200, n = 0.7). (**a**) velocity vector. (**b**) streamline.

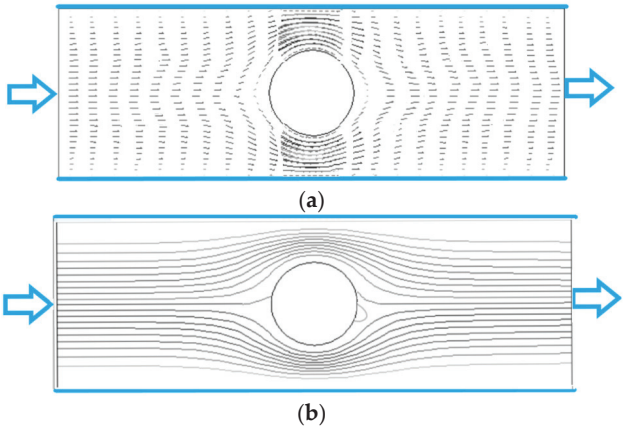

Figure 5. Fluid velocity vector and streamline of flow (Re = 200, n = 1.3). (**a**) velocity vector. (**b**) streamline.

4.2. Effect of Initial Orientation of Particles on the Distribution of Particles

When the rodlike particles flow through the cylinder between two planes, the flow goes through the process of contraction and expansion. For a particle initially located at the inlet, not all particles in the transverse position y can bypass the cylinder, and some particles will stay in the detention area in front of the cylinder. As shown in Figure 6a, the transverse position of the inlet where particles can bypass the cylinder is defined as y_p (if transverse position $y_0 < y_p$, the particles cannot bypass the cylinder), then y_p depends on the initial orientation θ_0 of particles at the inlet.

Figure 6a shows the spatial and orientation distributions of particles with $\theta_0 = 0^\circ$, we can see that $y_p \approx 0.3\ (2R)$, i.e., the particles with $y_0 < 0.3\ (2R)$ cannot bypass the cylinder. The spatial and orientation distributions of particles with $\theta_0 = 45^\circ$ are shown in Figure 6b where the particles, after entering the flow, first move towards the center, and the orientation angle θ decreases. When the particle approaches the cylinder, the values of θ increase, and the transverse velocity component of the particle becomes positive and gradually increases. At this time, $y_p \approx 0.25(2R)$, i.e., the particle with $y_0 < 0.25\ (2R)$ cannot bypass the

cylinder. Comparing with Figure 6a, more particles with $\theta_0 = 45°$ can bypass the cylinder than the particles with $\theta_0 = 0°$. Figure 6c shows the case for the particles with $\theta_0 = 90°$, it can be seen that the particles, after entering the flow, exhibit obvious rotation, and $y_p \approx 0.15$ ($2R$) in this case, indicating more particles can bypass the cylinder compared with the above two situations. Therefore, the initial orientation of particles has a great influence on whether particles can bypass the cylinder.

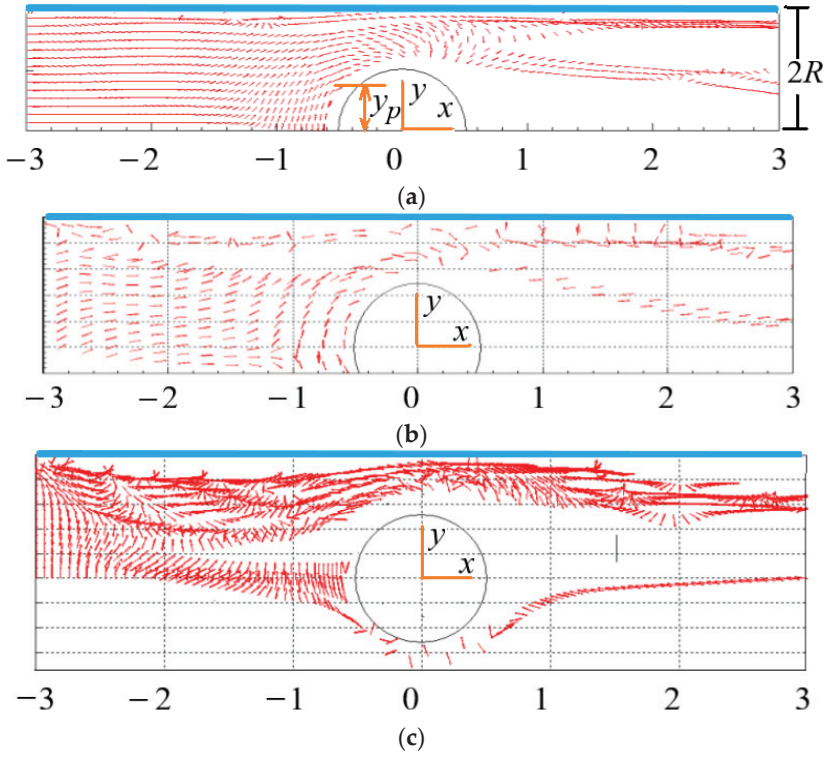

Figure 6. Spatial and orientation distributions of particles with different initial orientation (Re = 2, $n = 1.3$, $\beta = 8$). (**a**) initial orientation $\theta_0 = 0°$. (**b**) initial orientation $\theta_0 = 45°$. (**c**) initial orientation $\theta_0 = 90°$.

4.3. Effect of Re on the Distribution of Particles

The spatial and orientation distributions of particles for different Re are shown in Figures 7 and 8 where θ is the included angle between particle principal axis and horizontal direction, N is the number of particles. In Figures 7a and 8a, the number of particles around the cylinder, especially at the tail of the cylinder, is small, i.e., the existence of the cylinder leads to the uneven spatial distribution of particles. The reasons for the phenomenon that only some particles present in the wake are: on the one hand, when particles flow through the cylinder, they are squeezed near the wall, and cannot quickly enter the central region after passing through the cylinder. On the other hand, the rotation of the vortex in the wake of the cylinder throws the particles to the area near the walls. Comparing the two figures, it can be seen that Re has no obvious effect on the spatial distribution of particles. Figures 7a and 8a are the cases for Newtonian fluids ($n = 1$). However, the same trend is observed for non-Newtonian fluids ($n = 1.3$) as shown in Figure 9a (Re = 200) and Section 4.5.

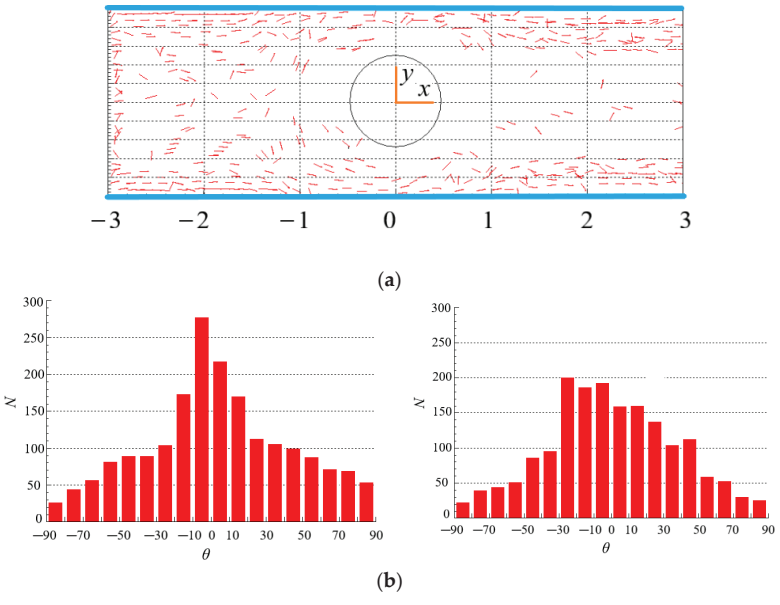

Figure 7. Spatial and orientation distributions of particles at Re = 2 (n = 1, β = 8). (**a**) spatial distribution. (**b**) orientation distribution: (**left**): contraction flow (x < 0); (**right**): expansion flow (x > 0).

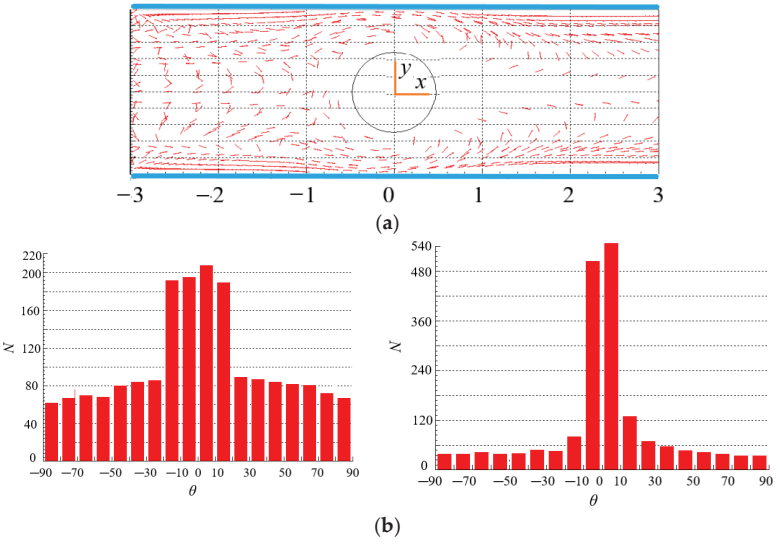

Figure 8. Spatial and orientation distributions of particles at Re = 200 (n = 1, β = 8). (**a**) spatial distribution. (**b**) orientation distribution: (**left**): contraction flow (x < 0); (**right**): expansion flow (x > 0).

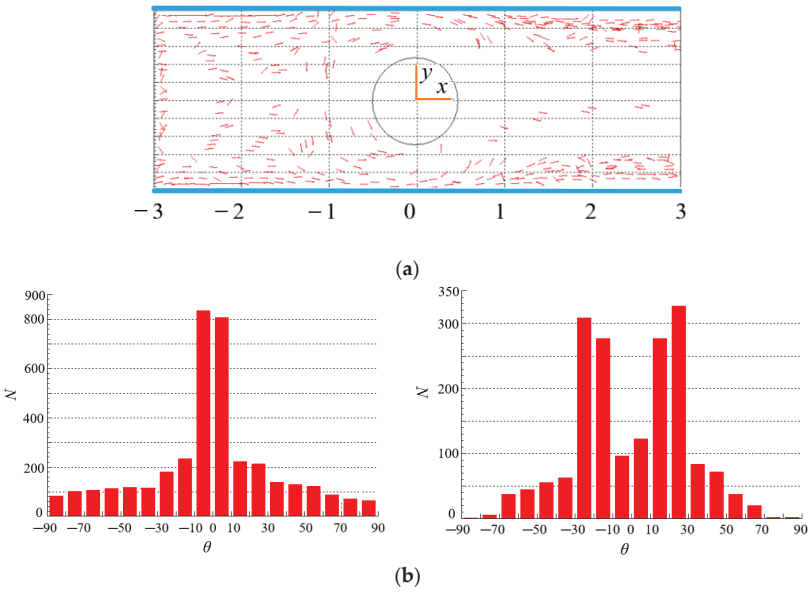

Figure 9. Spatial and orientation distributions of particles at n = 1.3 (Re = 200, β = 8). (**a**) spatial distribution. (**b**) orientation distribution: (**left**): contraction flow ($x < 0$); (**right**): expansion flow ($x > 0$).

Figures 7b and 8b show the number of particles with different θ for different Re. In the contraction flow ($x < 0$), more particles have a small θ value, indicating that the orientation of more particles points to the flow direction. However, the contraction flow changes the velocity gradient and shear rate of the flow, so there are many particles with different orientations. Moreover, there is little difference in particle spatial distribution under different Re. In the expansion flow ($x > 0$), the orientation distribution of particles is different with that in the contraction flow, and the difference is more obvious at large Re. The reason is that a wake is formed behind the cylinder when the flow bypasses the cylinder, resulting in changes in the velocity distribution and velocity gradient of the flow that affect the particle orientation. In the case of large Re as shown in Figure 8b, most particles are oriented in the flow direction (small θ), which can be attributed to that the wake area behind the cylinder is larger at large Re, while there exist large velocity gradient and strong shear force in wake area. The strong shear makes the torque acting on the particles larger and the rotation of the particles faster. The result of the torque action makes the particle orientation point to the flow direction. In addition, the particles near the wall show obvious orientation along the flow direction under strong shear force in Figure 8b. From this, we can draw the conclusion that Re has a great influence on the orientation distribution of rodlike particles in the contraction and expansion flow.

4.4. Effect of n on the Distribution of Particles

Figures 9 and 10 show the spatial and orientation distributions of particles for different power index n. Under the same velocity gradient and fluid shear rate, the force and torque of fluid with high viscosity acting on particles are also large as shown in Equations (1) and (7). The higher the shear-thickening degree, the larger the viscosity. In Figure 9a, particles are dispersed in the whole area in the contraction flow, while in the expansion flow, more particles are gathered near the two walls, and less particles are in the center area, which is caused by the rotation of the vortex in the wake of the cylinder, and the rotation throws the particles to the walls. Comparing Figures 9a and 10a, we can see that the power index n has an effect on the spatial distribution of particles. It is worth pointing out that the different streamlines as shown in Figures 4b and 5b do not affect

the spatial distribution significantly. The reason may be that although there are different streamlines between the two scenarios, the difference in velocity is not as obvious as the difference in streamline, and the particle motion is mainly influenced by velocity.

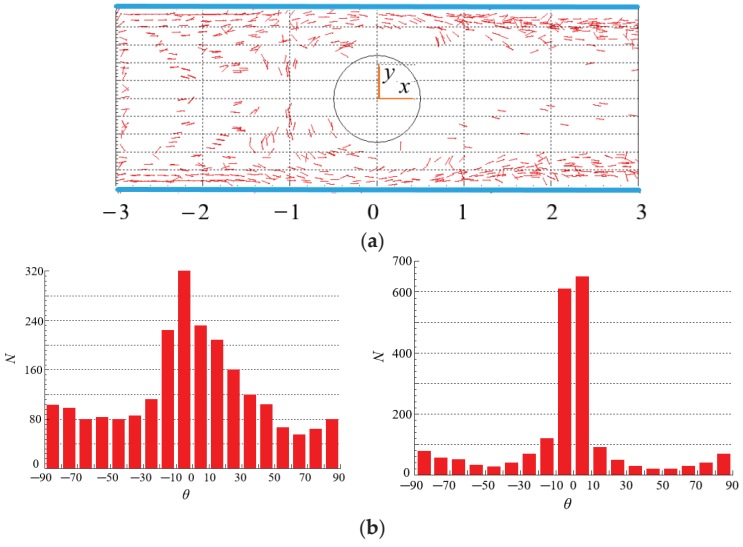

Figure 10. Spatial and orientation distributions of particles at $n = 0.7$ (Re = 200, $\beta = 8$). (**a**) spatial distribution. (**b**) orientation distribution: (**left**): contraction flow ($x < 0$); (**right**): expansion flow ($x > 0$).

As for the orientation distribution of particles, for the case of shear-thickening fluid in Figure 9b, more particles orient to the flow direction in the contraction flow ($x < 0$) because of high viscosity and even large force and torque acting on particles as shown in Equations (13) and (14), while viscosity and force are related to the velocity gradient as shown in Equation (15). By comparison, the orientation distribution of particles is more dispersed in the contraction flow for the shear-thinning fluid as shown in Figure 10b. However, more particles orient to the flow direction in the expansion flow ($x > 0$) for the case of shear-thinning fluid in Figure 10b, while the orientation distribution of particles exhibits two peaks in $-30°$~$-10°$ and $10°$~$30°$ in the expansion flow for the shear-thickening fluid as shown in Figure 9b. The reason is that the velocity distributions of shear-thinning fluid and shear-thickening fluid are different after fluid passing through the cylinder, the velocity distribution of the shear-thinning fluid produces larger shear rate as well as viscosity and force as shown in Equations (13)–(15), so that making more particles orient to the flow direction, but the velocity distribution of the shear-thinning make the orientation distribution exhibit two peaks. As a consequence, the power index n has a significant effect on the orientation distribution of particles in the contraction and expansion flow. In shear-thickening fluid, when the flow changes from contraction to expansion, the orientation distribution of particles becomes more dispersed; while in shear-thinning fluid, the opposite is true.

Comparing Figures 9b and 10b, we can see that there are more particles with an orientation of $90°$ in shear-thinning fluids than that in shear-thickening fluids. This is because the force and torque exerted by the shear-thinning fluid on the particles are relatively small, and the initial orientation of the particles at the inlet is randomly distributed.

4.5. Effect of Particle Aspect Ratio on the Distribution of Particles

The spatial distribution of particles for $\beta = 4$ in Figure 11a is more regular compared with the spatial distribution of particles for $\beta = 8$ in Figure 12a, even there is a symmetric distribution about $x = 0$ in the vicinity of the central line. This is because the particles

with small aspect ratio follow the fluid better, and their distribution can better reflect the symmetry characteristics of the flow around the cylinder at Re = 2. Therefore, particle aspect ratio has a significant impact on the spatial distribution of particles in contraction flow and expansion flow.

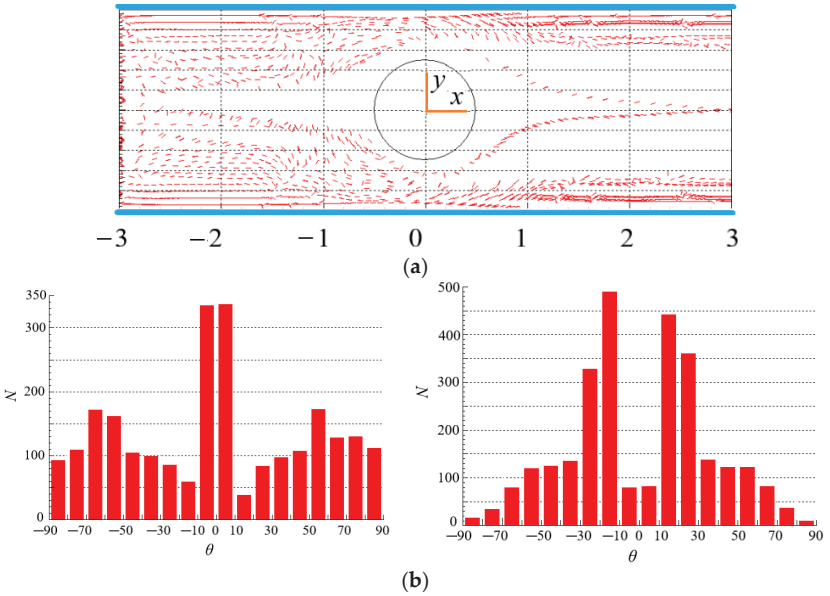

Figure 11. Spatial and orientation distributions of particles at $\beta = 4$ (Re = 2, $n = 1.3$). (**a**) spatial distribution. (**b**) orientation distribution: (**left**): contraction flow ($x < 0$); (**right**): expansion flow ($x > 0$).

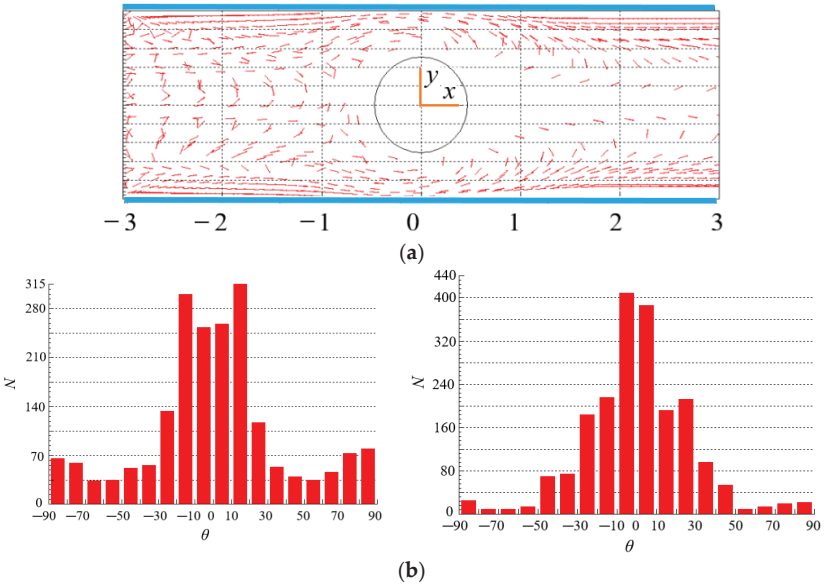

Figure 12. Spatial and orientation distributions of particles at $\beta = 8$ (Re = 2, $n = 1.3$). (**a**) spatial distribution. (**b**) orientation distribution: (**left**): contraction flow ($x < 0$); (**right**): expansion flow ($x > 0$).

In Figure 11b, the orientation angles of more particles are at $\theta = -10$~10, i.e., the orientation points to the flow direction in the contraction flow. The reason is that, in addition to shearing, there exists a strong extension effect in the contraction flow, which makes the particles align with the flow direction. However, the extension effect does not exist in the expansion flow, the orientation angles of more particles are at $\theta = -10$~-30 and 10~30, i.e., the orientation is close to the flow direction. The orientation distributions of particles with large aspect ratio ($\beta = 8$) are shown in Figure 12b. It can be seen that there are more particles orient to the flow direction in expansion flow than that in contraction flow. Comparing with Figure 11b, more particles point to the flow direction for $\beta = 8$ than that for $\beta = 4$. The reason may be that, as shown in Equations (1)–(3) and (7)–(10), the forces and moments acting on particles are directly related to the particle aspect ratioβ, in particular, the angular acceleration of particles is directly proportional to theβ, large torque and even large angular acceleration make the orientation of particles easier to point to the flow direction, thus the particles with a large aspect ratio tend to align with the flow direction more obviously. Moreover, particle aspect ratio has a stronger effect on the orientation distribution than spatial distribution by comparing Figures 11 and 12.

5. Conclusions

The contraction and expansion flow containing rodlike particles in power-law fluid is studied numerically. The movement, spatial and orientation distribution of particles are described by the equations of force and moment exerted on the particles. The fluid velocity vector and streamline of flow are given at different Reynolds number. The effects of Re, power index n and particle aspect ratio β on the spatial and orientation distributions of particles are analyzed. The main conclusions can be summarized as follows.

Distributions of velocity vector and streamline are almost symmetrical about the center of the cylinder when Re = 2. When Re = 200, the distributions of velocity vector and streamline in front of the cylinder are similar to those when Re = 2, but the difference is that there is obvious wake in the flow behind the cylinder. There is no Karman vortex street like Newtonian fluid in the power-law fluid even if Re = 200.

Te number of particles around the cylinder, especially at the tail of the cylinder is small. The existence of the cylinder leads to the uneven spatial distribution of particles. For the shear-thickening fluid, particles are dispersed in the whole area in the contraction flow, while more particles are gathered near the two walls in the expansion flow. The spatial distribution of particles with small β is more regular. B has a significant, n has a moderate, but Re has a small impact on the spatial distribution of particles in the contraction and expansion flow.

The orientation distributions of particles in the contraction flow and expansion flow are different, and the difference degree is more obvious at large Re. In the case of large Re, most particles are oriented in the flow direction. The particles near the wall show obvious orientation along the flow direction. In shear-thickening fluid, when the flow changes from contraction to expansion, the orientation distribution of particles becomes more dispersed; while in shear-thinning fluid, the opposite is true. The orientation of more particles points to the flow direction in the contraction flow, while is close to the direction of flow in the expansion flow. More particles orient to the flow direction in expansion flow than that in contraction flow. The particles with a large β tend to align with the flow direction more obviously. Re, n and β have great influence on the orientation distribution of particles in the contraction and expansion flow.

Whether the particles initially located at the inlet can bypass the cylinder depends on the transverse position and initial orientation of the particles at the inlet. The number of particles with $\theta_0 = 90^\circ$ bypassing the cylinder is the largest, followed by $\theta_0 = 45^\circ$ and $\theta_0 = 0^\circ$. The conclusions obtained in this paper have reference value for practical engineering applications.

Author Contributions: Conceptualization, J.L. and W.L.; methodology, W.L. and Z.L.; software, W.L., Z.L. and S.Z.; writing, W.L. and Z.L.; resources W.L., S.Z. and J.L.; review, J.L. All authors have read and agreed to the published version of the manuscript.

Funding: This work was supported by the National Natural Science Foundation of China (Grant no.12132015).

Conflicts of Interest: There are no conflicts of interest regarding the publication of this paper.

References

1. Altan, M.C.; Guceri, S.I.; Pipes, R.P. Anisotropic channel flow of fiber suspensions. *J. Non-Newton. Fluid Mech.* **1992**, *42*, 65–81. [CrossRef]
2. Dinh, S.M.; Armstrong, R.C. A rheological equation of state for semi-concentrated fiber suspensions. *J. Rheol.* **1984**, *28*, 207–221. [CrossRef]
3. Chono, S.; Makino, M. Numerical simulation of fiber suspension flow between parallel plates. *Trans. B Mach. Soc. Jpn.* **1995**, *61*, 3190–3205. [CrossRef]
4. Chiba, K.; Nakamura, K. Numerical solution of fiber suspension flow through a complex channel. *J. Non-Newton. Fluid Mech.* **1998**, *78*, 167–182. [CrossRef]
5. Chiba, K.; Yasuda, K.; Nakamura, K. Numerical solution of fiber suspension flow through a parallel plate channel by coupling flow field with fiber orientation distribution. *J. Non-Newton. Fluid Mech.* **2001**, *99*, 145–157. [CrossRef]
6. Lin, J.Z.; Wang, Y.L.; Wang, C.B. Research on the motion of suspended cylindrical particles in round jets. *J. Zhejiang Univ. Eng. Sci.* **2003**, *37*, 82–86.
7. Lin, J.Z.; Li, J.; Zhang, W.F. The forces exerted on a cylindrical particle in the elongational-shear flows. *Int. J. Nonlinear Sci. Numer. Simul.* **2004**, *5*, 9–16. [CrossRef]
8. Cai, J.; Yuan, Z.L.; Zhao, X.B. Study on two-way coupling of gas-solid two-phase flow of cylindrical particles. *Powder Technol.* **2016**, *300*, 136–145. [CrossRef]
9. Cai, J.; Yuan, Z.L.; Zhao, X.B.; Gu, Z.Z. Numerical research on flow features of gas-solid flow of cylindrical particles. *Int. J. Hydrogen Energy* **2016**, *41*, 15859–15867. [CrossRef]
10. Hao, J.H.; Li, Y.J.; Liu, Y.; Curtis, J.S.; Guo, Y. Jamming in granular shear flows of frictional, polydisperse cylindrical particle. *Adv. Powder Technol.* **2021**, *32*, 3746–3759. [CrossRef]
11. Hao, J.H.; Li, Y.J.; Guo, Y.; Jin, H.H.; Curtis, J.S. The effect of polydispersity on the stresses of cylindrical particle flows. *Powder Technol.* **2020**, *361*, 943–956. [CrossRef]
12. Leal, L.G. Slow motion of slender rod-like particles in a second-order fluid. *J. Fluid Mech.* **1975**, *69*, 305–337. [CrossRef]
13. Brunn, P. Slow motion of a rigid particle in a second-order fluid. *J. Fluid Mech.* **1977**, *82*, 529–547. [CrossRef]
14. Cohen, C.; Chung, B.; Stasiak, W. Orientation and rheology of rodlike particles with weak Brownian diffusion in a second-order fluid under simple shear flow. *Rheol. Acta* **1987**, *26*, 217–232. [CrossRef]
15. Iso, Y.; Koch, D.L.; Cohen, C. Orientation in simple shear flow of semi-dilute fiber suspensions 1. Weakly elastic fluids. *J. Non-Newton. Fluid Mech.* **1996**, *62*, 115–134. [CrossRef]
16. Iso, Y.; Koch, D.L.; Cohen, C. Orientation in simple shear flow of semi-dilute fiber suspensions 2. Highly elastic fluids. *J. Non-Newton. Fluid Mech.* **1996**, *62*, 135–153. [CrossRef]
17. Gunes, D.Z.; Scirocco, R.; Mewis, J.; Vermant, J. Flow-induced orientation of non-spherical particles: Effect of aspect ratio and medium rheology. *J. Non-Newton. Fluid Mech.* **2008**, *155*, 39–50. [CrossRef]
18. Borzacchiello, D.; Abisset-Chavanne, E.; Chinesta, F.; Keunings, R. Orientation kinematics of short fibers in a second-order viscoelastic fluid. *Rheol. Acta* **2016**, *55*, 397–409. [CrossRef]
19. Phan-Thien, N.; Fan, X.J. Viscoelastic mobility problem using a boundary element method. *J. Non-Newton. Fluid Mech.* **2002**, *105*, 131–152. [CrossRef]
20. Nguyen-Hoang, H.; Phan-Thien, N.; Khoo, B.C.; Fan, X.J.; Dou, H.S. Completed double layer boundary element method for periodic fibre suspension in viscoelastic fluid. *Chem. Eng. Sci.* **2008**, *63*, 3898–3908. [CrossRef]
21. Lin, J.Z.; Ouyang, Z.Y.; Ku, X.K. Dynamics of cylindrical particles in the contraction flow of a second-order fluid. *J. Non-Newton. Fluid Mech.* **2018**, *257*, 1–12. [CrossRef]
22. Lin, J.Z.; Wang, Y.L.; Zhang, P.J.; Ku, X.K. Mixing and orientation behaviors of cylindrical particles in a mixing layer of an Oldroyd-B fluid. *Chem. Eng. Sci.* **2018**, *176*, 270–284. [CrossRef]
23. Stover, C.A.; Cohen, C. The motion of rodlike particles in the pressure-driven flow between two flat plates. *Rheol. Acta* **1990**, *29*, 192–203. [CrossRef]
24. Domurath, J.; Ausias, G.; Ferec, J.; Saphiannikova, M. Numerical investigation of dilute suspensions of rigid rods in power-law fluids. *J. Non-Newton. Fluid Mech.* **2020**, *280*, 104280. [CrossRef]
25. Lin, J.Z.; Jiang, R.J.; Chen, Z.L.; Ku, X.K. Poiseuille flow-induced vibrations of two cylinders in tandem arrangement. *J. Fluids Struct.* **2013**, *40*, 70–85. [CrossRef]
26. Bao, F.B.; Lin, J.Z. Burnett simulation of gas flow and heat transfer in micro Poiseuille flow. *Int. J. Heat Mass Transf.* **2008**, *51*, 4139–4144. [CrossRef]

27. Loevenberg, M. Stokes resistance, added mass and Basset force for arbitrarily oriented, finite-length cylinders. *Phys. Fluids* **1993**, *A5*, 8199–8213.
28. Batchelor, G.K. Slender-body theory for particles of arbitrary cross-section in Stokes flow. *J. Fluid Mech.* **1970**, *44*, 419–440. [CrossRef]

Disclaimer/Publisher's Note: The statements, opinions and data contained in all publications are solely those of the individual author(s) and contributor(s) and not of MDPI and/or the editor(s). MDPI and/or the editor(s) disclaim responsibility for any injury to people or property resulting from any ideas, methods, instructions or products referred to in the content.

polymers

MDPI

Review

Natural and Natural-Based Polymers: Recent Developments in Management of Emerging Pollutants

Radu Claudiu Fierascu [1,2,†], Irina Fierascu [1,3,†], Roxana Ioana Matei (Brazdis) [1,2,†] and Doina Manaila-Maximean [4,5,*,†]

[1] National Institute for Research & Development in Chemistry and Petrochemistry-ICECHIM–Bucharest, 060021 Bucharest, Romania; fierascu.radu@icechim.ro (R.C.F.); irina.fierascu@icechim.ro (I.F.); roxana.brazdis@icechim.ro (R.I.M.)
[2] Faculty of Chemical Engineering and Biotechnologies, University "Politehnica" of Bucharest, 060042 Bucharest, Romania
[3] Faculty of Horticulture, University of Agronomic Sciences and Veterinary Medicine of Bucharest, 011464 Bucharest, Romania
[4] Faculty of Applied Sciences, University "Politehnica" of Bucharest, 060042 Bucharest, Romania
[5] Academy of Romanian Scientists, 3 Ilfov, 050044 Bucharest, Romania
* Correspondence: doina.manaila@upb.ro
† These authors contributed equally to this work.

Abstract: Anthropogenic activities lead to the issue of new classes of pollutants in the environment that are not currently monitored in environmental studies. This category of pollutants (known as emerging contaminants) includes a very wide range of target substances, such as pharmaceuticals, plant protection products, personal care products, dyes, toxins, microplastics and many other industrially important intermediaries. Together with an increasing demand for clean water (both for agricultural necessities and for the increasing population consumption), the need for the removal of emerging pollutants, simultaneously with the current "green chemistry" approach, opens the door for the industrial application of natural polymers in the area of environmental protection. Recent developments in this area are presented in this paper, as well as the application of these particular natural materials for the removal of other contaminants of interest (such as radioisotopes and nanoparticles). The current knowledge regarding the processes' kinetics is briefly presented, as well as the future development perspectives in this area.

Keywords: natural polymers; emerging pollutants; adsorption; catalytic oxidation; perspectives

Citation: Fierascu, R.C.; Fierascu, I.; Matei (Brazdis), R.I.; Manaila-Maximean, D. Natural and Natural-Based Polymers: Recent Developments in Management of Emerging Pollutants. *Polymers* **2023**, *15*, 2063. https://doi.org/10.3390/polym15092063

Academic Editors: Fahmi Zaïri, Matthias Ballauff, Ulrich Maschke and Rufina G. Alamo

Received: 6 April 2023
Revised: 19 April 2023
Accepted: 25 April 2023
Published: 26 April 2023

Copyright: © 2023 by the authors. Licensee MDPI, Basel, Switzerland. This article is an open access article distributed under the terms and conditions of the Creative Commons Attribution (CC BY) license (https://creativecommons.org/licenses/by/4.0/).

1. Introduction

Nowadays, water resources are an asset which must be protected, due to the increasing imbalance between the availability and consumption of freshwater. Water pollution is a global problem affecting the lives of millions of people around the world, being a risk factor for disease and death, but also a source of life. Alongside the growth of the population and global industrialization, which contribute to high pollution in organic and inorganic compounds, climate change is another important factor that affects water resources [1]. Persistent and emerging pollutants and their degradation products are released continuously into the environment, representing a serious and global issue that has sometimes irreversible effects on human health and ecosystems. Emerging pollutants include pharmaceuticals for human or veterinary uses, products for daily care, products of industrial and household origins and pesticides, which are used in larger amounts than several decades ago, due to the increased demand for food (a consequence of the increased population).

Dealing with the difficulties of providing clean water, regardless of whether we are dealing with organic or inorganic contaminants, many current studies and technologies are being developed in order to offer reliable solutions and minimize malignant and

detrimental water-borne diseases [2,3]. Classical methods, such as adsorption, precipitation, solvent extraction, co-precipitation, flocculation and coagulation, can be improved by the use of modern materials with bioactivity, biodegradability, biocompatibility and tunable physicochemical properties and morphology [4]. Activated carbon, clays, layered double hydroxide hybrids, metal or metal oxide nanoparticles (NPs) are just a few which can be nominated as good candidates for environmental applications [5–8]. Among them, biopolymers have the advantages offered by biodegradability (important from a "green chemistry" approach, although this aspect represents a subject of debate, fine-tuning of this property being necessary [9,10]) and biocompatibility, being used with success in potable and wastewater treatment [11]. The nature of the biopolymers represents one of the key parameters of an efficient treatment [12]. They are suitable for removing both types of pollutants (organic and inorganic) even if they are used as such, or in combination with other materials [13]. In addition, they offer high performance and good selectivity, and the process is cost-effective and eco-friendly [14].

In this context, the present paper aims to address the recent developments in the application of natural polymers for the management of emerging and hazardous contaminants, as well as the development perspectives in this area.

2. Emerging Pollutants—A New Threat to the Environment with Natural Solutions?

When addressing the issue of emerging pollutants, one would usually think of newly synthesized chemicals or compounds. However, the term relates more to the difficulties encountered in their monitoring, due to technological drawbacks or legal oversights, and less to the nature of these pollutants. As a generally accepted definition, emerging pollutants (EPs) are considered chemicals (natural or synthetic) **not commonly monitored** in the environment, having the potential to cause detrimental effects on ecosystems or human health [15]. As can be seen, the classification of a particular substance as an emerging pollutant is more related to the lack of routine monitoring and less to their nature. Although many of these pollutants are indeed newly synthesized chemicals, there are different types of EPs naturally occurring and already present in the environment, their potential effects being only recently evaluated.

According to the NORMAN network [16], EPs can be classified into 21 groups, covering very different types of substances, from biocides and plant protection chemicals to drugs, pharmaceutical and personal care products, and from smoke compounds to surfactants and human metabolites. Their origins are also very different depending on their nature. Most of these pollutants originate from industrial processes or human activities (not being addressed by urban or industrial treatment plants), but can also be traced to diffuse sources, such as atmospheric deposition or crop/animal production [15]. For the present work, the NORMAN emerging pollutants database was used as a reference [16].

The area of EPs has represented a domain of interest for over a decade now, with a series of very interesting opinions, review works and books being published on this topic, which we recommend for future reading [17–23].

One of the interesting approaches regarding the removal of emerging pollutants is represented by the use of natural polymers. In a world where the continuous diminishing of resources and environmental pollution have become critical issues, the use of easily recyclable or available materials becomes vital.

To have clear insight into polymers, their constituents and properties, polymers have been classified according to several points of view [24]. One of these criteria is represented by their origins [25]. According to this classification, *natural polymers* (formed by proteins, nucleic acids, polysaccharides or polyhydrocarbons), *artificial polymers* (obtained by modifying natural ones; for example, viscose and cellophane) and *synthetic polymers* can be found, obtained by chemical reactions starting from monomers.

The main EU law to protect human health and the environment from the risks that can be posed by chemicals is the **"Registration, evaluation, authorization and restriction of chemicals"** (REACH) [26]. In accordance with REACH (Article 3(5)), a polymer is defined

as a substance meeting the following criteria: more than 50% of the weight of that substance consists of polymer molecules, and the amount of polymer molecules presenting the same molecular weight must be less than 50% of the weight of the substance. According to ECHA, natural polymers are polymers that are the result of a polymerization process that has taken place in nature, independently of the extraction process. It results that natural polymers are not necessarily "substances which occur in nature". Considering these differences, some authors are introducing in their research the term of "naturally occurring polymers" [27].

In [25], Doppalapudi, considering the origin of natural polymers, systematizes them into three main classes: natural polymers of plant origin, of animal origin and of microbial origin, with polysaccharides being present in each class mentioned.

Polysaccharides of plant origin are cellulose, hemicellulose, cyclodextrins, starch, inulin, pectin, glucomannan, guar gum, arabinogalactan and carrageenan. Animal-origin polysaccharides include chitosan, hyaluronan and chondroitin sulfate. Microbial-origin polysaccharides comprise alginate and dextran.

Proteins are mainly of animal origin, such as collagen, gelatin, albumin, fibrin and silk fibroin; there are also proteins of vegetable origin, such as soy. Of plant origin are shellac resin and some esters; other esters (polyhydroxyalkanoate) have a microbial genesis, together with polyamides (polyglutamate) and polyanhydrides (polyphosphate).

The naturally occurring polymers have also been classified into six main categories [27,28]: polysaccharides (starch, cellulose, chitin, pectin, alginic acid, natural gums, etc.), one of the most studied groups of natural polymers [29–31]; proteins or naturally occurring polyamides found in animal and vegetable sources; polyisoprenes or natural rubbers and similar materials isolated from saps of plants; polynucleotides, which comprise DNA and RNA found in all living organisms; lignin or polymeric materials of coniferyl alcohol and related substances; naturally occurring miscellaneous polymers, such as shellac, a resin secreted by the lac insect.

Polysaccharides are of various types depending on their structure or function [32,33]. In terms of function, there are three main types: storage polysaccharides such as starch and glycogen, structural polysaccharides such as cellulose and chitin, and gel-forming polysaccharides such as alginic acid and mucopolysaccharides [32].

The following sections present the possible applications of natural polymers for the removal of emerging pollutants, the information being grouped considering the targeted pollutant. In addition, we chose to include in the current review examples of the use of chitosan. Although not technically a natural polymer (according to the definitions provided above), chitosan, due to its easy production (simple deacetylation of natural chitin), non-toxic characteristics, as well as its wide application in different important areas, chitosan is often included in the class of "natural polymers" [34–36].

3. Methodology

For the selection of the studies to be included in the present review, we followed the recommendations of Preferred Reporting Items for Systematic Reviews and Meta-Analyses 2020 (PRISMA) [37]. The research strategy was formulated according to the PICO (Problem, Intervention, Comparison, Outcome) approach (Table 1).

Table 1. Definition of PICO strategy applied in the present work.

P (Problem)	Presence of emerging pollutants in water streams
I (Intervention)	Application of innovative, natural polymeric materials for emerging pollutants' removal
C (Comparison)	Materials with known properties in environment protection or singular components, in the case of composite materials
O (Outcome)	Improvement of pollutant uptake and the use of natural polymers

The research was conducted based on the PICO question: "Can natural polymers be successfully used in the management of emerging pollutants?" As such, the following inclusion/exclusion criteria were defined.

Inclusion criteria:

- Research articles published from 2012 to the present, full text;
- Articles published or available in English;
- Removal of emerging pollutants—for the automatic screening, only the term "pollutant" was used;
- Evaluation of natural polymers' application in the management of emerging pollutants (as defined in Section 2)—manual screening;
- Relevance to the review topic (new information provided).

Exclusion criteria:

- Articles published before 2012;
- Book chapters or book;
- Review or systematic review articles;
- Conference papers, notes, letters, short surveys, errata or conference reviews;
- Articles published in languages other than English;
- Articles presenting the removal of pollutants monitored in routine studies (such as commonly encountered heavy metals).

The literature search was conducted using the database SCOPUS (as an exhaustive literature database), using "natural polymer" as the primary search term. A further selection of the articles was performed automatically, using the inclusion/exclusion criteria defined above, and inclusion in the present review was decided after a full reading of the manuscript.

4. Results

After applying the entire set of exclusion/inclusion criteria, followed by title, abstract and full-text reading, a total of 52 articles (and one correction article) were selected for inclusion in the present review (Figure 1), covering the removal of emerging pollutants using natural polymers. To the selected articles, other works were added for providing the necessary context. These articles were retrieved by a "search and find"/manual selection approach using the SCOPUS database (by searching using specific keywords), or were suggested by the reviewers during the peer review process. For the purpose of the current review, studies presenting the removal of heavy metals (already routinely monitored) and water remediation studies (i.e., turbidity remediation, sterilization, oil adsorption, etc.) were not considered for inclusion.

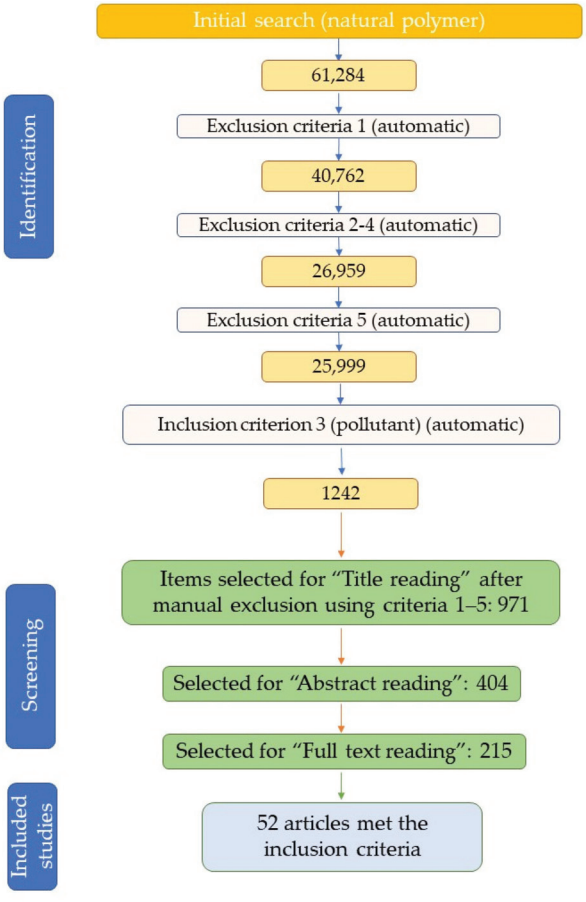

Figure 1. Article selection process flowchart.

The works selected for screening present the application of natural (and one natural-based) polymers for the management of emerging pollutants and some other emerging substances (potentially hazardous). Figure 2 presents the natural polymers reviewed and the major pollutant categories considered for the literature study.

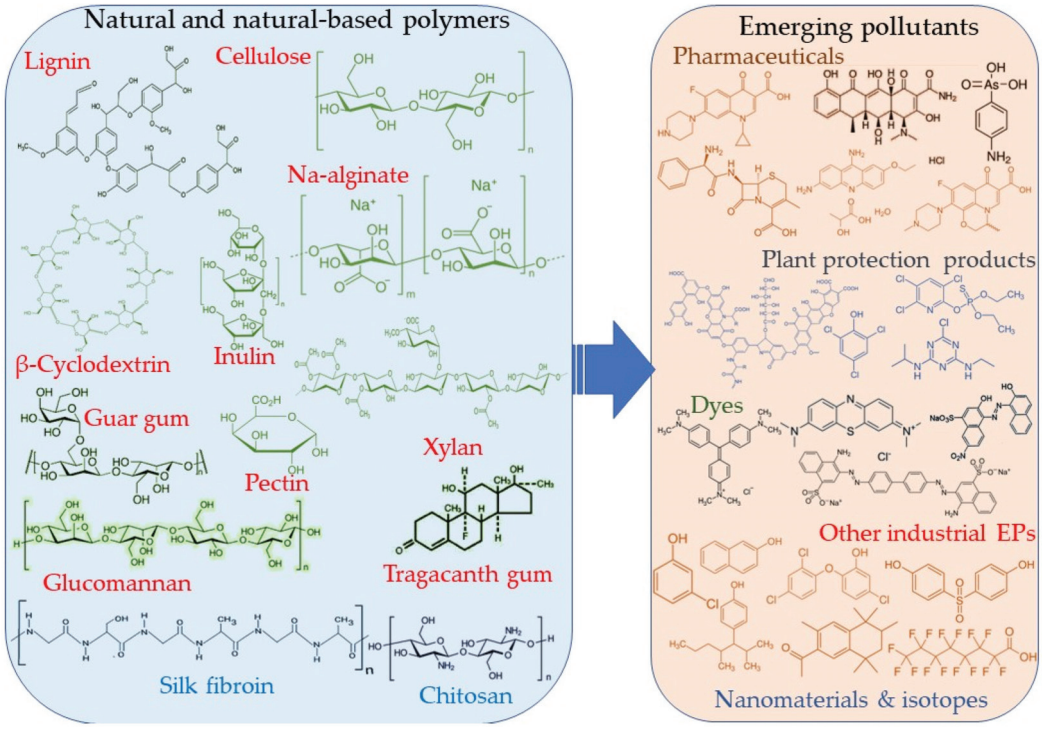

Figure 2. Natural and natural-based polymers and main contaminants discussed in the present review work.

5. Natural Polymers for the Management of Emerging Pollutants

5.1. Management of Pharmaceuticals Using Natural Polymers

One of the most diverse groups of EPs is represented by pharmaceutical substances. Most often originating from patient excretion, the presence of pharmaceutical substances as an environmental pollutant can also be related to emissions during production processes, as well as from the incorrect disposal of unneeded substances [38]. As the pharmaceutical industry represents an ever-growing industry, it can be expected that pharmaceutical pollution will follow a similar trend. At the same time, the pandemic conditions in the past few years led to a spike in the use of over-the-counter and prescription drugs, causing an increase in their presence in the environment, as well as the appearance of some new substances [39]. The pharmaceuticals present in the environment can cause a wide range of health issues; i.e., some of them act as endocrine disruptors (some being used as intentional endocrine disruptors), while others can contribute to the development of antimicrobial resistance [40]. Due to the varied nature of pharmaceutical compounds, there is a correspondingly high number of studies regarding their management. Among them, the literature survey identified several using natural polymers, presented in Table 2.

Table 2. Management of pharmaceutical EPs using natural polymers (in chronological order).

Natural Polymer	Targeted Application	Application Form	Obtained Results	Process Parameters	Ref.
Guar gum	Ciprofloxacin (fluoroquinolone antibiotic) adsorption, 15 mg/L	Zerovalent iron-guar gum nanocomposite, spherical, particle size of ~60–70 nm (0.5 g/L)	94% removal after 60 min	Superior adsorption at pH 4, compared with pH 2.6 (41%), superior to zerovalent ion by itself (69%); removal efficiency over 85% after 2 recycling cycles	[41]
Lignin	Adsorption of doxycycline hydrochloride (tetracycline antibiotic), 30 mg/L	Lignin xanthate resin–bentonite clay composite, porous structure	Adsorption capacity 438.75 mg/g	Superior to bentonite (119.93 mg/g); isotherm—Langmuir model (monolayer and uniform adsorption); kinetics—pseudo-second-order model (multilayer adsorption on heterogeneous surfaces, adsorption through electrostatic interaction, hydrogen bonding and π–π interactions—chemisorption)	[42]
Cellulose	p-arsanilic acid (veterinary use)	Ionic liquid-modified cellulose	Adsorption capacity 216.9 mg/g	Comparable results with other works, fast adsorption rate 3.21×10^{-3} g/(mg × min), process conformed to Freundlich (multi-layer adsorption on heterogenous surfaces) and pseudo-second-order kinetics model; 77% of initial capacity after six recycling cycles	[43]
Sodium alginate	Cephalexin (beta-lactam antibiotic), 30 mg/L	*Saccharomyces cerevisiae*/calcium alginate composite beads, 3.32 mm diameter	Adsorption capacity 94.34 mg/g	Superior to literature biosorbents; isotherm—Langmuir model; kinetics—pseudo-second-order model	[44]
Inulin	Adsorption and heterogenous catalysis of ofloxacin (fluoroquinolone-type antibiotic), 25 mM	Immobilization of laccase onto dialdehyde inulin -coated silica-capped magnetite nanoparticles, 90% of the particles with diameters 1–10 nm	63% removal capacity	Superior results to laccase alone. Ofloxacin removal—through adsorption and biodegradation mechanisms; kinetics—pseudo-second-order model; 50% of initial activity after 6 reuse cycles	[45]
Chitosan, sodium alginate	Adsorption and catalytic oxidation of naproxen, diclofenac (nonsteroidal anti-inflammatory drugs—NSAID), 25 mg/L, individually or simultaneously	Magnetite or Fe/Cu nanoparticles, on alginate or chitosan beads	84/92% removal of naproxen/ diclofenac, using Fe/Cu on alginate or chitosan, respectively, after 9 min	Good removal capacity in short reaction time (9 min); kinetics—pseudo-first-order model (reaction more inclined towards physisorption); slight decrease in removal efficiencies after three recycling cycles	[46]
Sodium alginate	Biosorption of ethacridine lactate (aromatic organic compound, antiseptic, trade name Rivanol), 50 mg/L	Encapsulation of *Saccharomyces pastorianus* residual biomass in calcium alginate, irregular and elongated shape, 1.89 mm diameter	Maximum capacity 21.39 mg/g, batch study	Kinetics—pseudo-second-order and intraparticle diffusion (adsorption controlled by one of the following: film diffusion/adsorbate diffusion into the pores/ surface adsorption); equilibrium isotherms—Freundlich and Dubinin–Radushkevich (adsorption is related to pores volume filling).	[47]
Sodium alginate	Biosorption of ethacridine lactate (aromatic organic compound, antiseptic, trade name Rivanol), 20/40 mg/L	Encapsulation of *Saccharomyces pastorianus* residual biomass in calcium alginate; spherical, whitish beads, 3.218 mm diameter	Biosorption capacity 138.584 mg/g, fixed-bed column study	Biosorption capacity variable with bed height, pollutant concentration and flow rate. Experimental data best fit the Yoon–Nelson (premise—decreasing adsorption rate directly proportional to adsorbate adsorption), Clark (premise—adsorption is mass-transfer concept combined with Freundlich isotherm, piston type behavior of flow in column), and, to a lesser extent, Yan model (dose–response model)	[48]

The examples above provide a good glimpse of the potential applications of natural polymers for the removal of pharmaceuticals. From the examples presented, a natural trend to use easily available resources for the removal of hazardous pollutants can be observed. For instance, two of the most common and often used natural polymers (in different applications), chitosan and sodium alginate, were evaluated by Sahin et al. [46] for the development of composite beads with magnetic nanoparticles (also synthesized by green routes—phytosynthesis using *Lathyrus brachypterus* extract). The resulting composites, providing a mixture of beneficial properties of magnetic nanoparticles (high catalyst

loading capacities, dispersion properties, stability, recyclability, surface area and separability) and natural polymers' up-take capacity, showed high efficiency for the removal of two nonsteroidal anti-inflammatory drugs (naproxen and diclofenac), both in individual and simultaneous experiments. The best results were obtained by the authors using the bimetallic nanoparticles deposited on chitosan (for diclofenac removal) and alginate (for naproxen removal). The results obtained were comparable with literature data but obtained using much shorter reaction times (9 min compared with over 60 min in other studies). Additionally, the conclusion of the authors was that the process was more inclined towards physisorption (kinetics respecting the pseudo-first-order model). A physical adsorption (explained by Van der Waals forces) was described by the authors as the primary adsorption mechanism. Rusu et al. evaluated the removal of acrinol (also known by the trade name Rivanol) using composites obtained from residual microbial biomass (*Saccharomyces pastorianus*) and a natural polymer (sodium alginate, modified by the addition of calcium chloride), both in batch [47] and in fixed-bed column studies [48]. The authors proved that the developed composites can be successfully applied for theoretical studies (using batch experiments) and can also be practically applied in scaled-up installations, as the fixed-bed column experiments would suggest.

Some of the cited authors also provide some insights into the mechanisms involved in the contaminants' management, as well as in the interaction between natural polymers and contaminants. For example, Balachandramohan and Sivasankar [41] attribute the efficiency of ciprofloxacin adsorption to the electrostatic interaction between the negative surface of the natural polymer composite and the positively charged compound, while the adsorption of doxycycline hydrochloride on a lignin xanthate resin–bentonite clay composite was attributed by Kong et al. [42] to the interactions between the benzene ring in the contaminant and lignin moieties, as well as to hydrogen bonds appearing between the two compounds, suggesting the apparition of a macromolecular complex, as also observed by Peng et al. [43] for the adsorption of p-arsanilic acid on ionic liquid-modified cellulose, and by Rusu et al. [44] for the adsorption of cephalexin on *Saccharomyces cerevisiae* calcium alginate beads.

Generally, pharmaceutical removal using natural polymer processes is governed by the pseudo-second-order model (the process being more inclined towards physisorption), while the best-fitting models for the equilibrium isotherms were the Freundlich and Langmuir models, supporting the authors' claims towards multi-layer adsorption on heterogenous surfaces and monolayer adsorption, respectively. Another relevant aspect that arises from literature data is that natural polymers are not commonly used as single adsorbents, but are more likely to be used in composites, with either other organic or inorganic compounds (which could act either as adsorbents or catalysts), as is the case for all the examples presented in Table 2.

5.2. Management of Plant Protection Product Pollutants Using Natural Polymers

With the increase in the global human population and the rising food demand, the use of pesticides and fungicides has seen an unprecedented spread. Although very useful in providing food in the quantities and at the quality required, pesticides and fungicides can have different adverse effects on water quality, and, consequently, on ecosystems and human health [49]. Although the effects of pesticides and fungicides are under continuous scrutiny, their use is majorly based on industry-performed studies, as other authors noticed [50]. Furthermore, their long-term effects on ecosystems and human health still represent a subject of debate. As such, there is a continuous need to develop appropriate technologies and materials for the removal of pesticides and fungicides from the environment. Some of the pesticides and fungicides cannot be defined as "emerging pollutants", strictly speaking, as there are national and/or international regulations requiring their monitoring. However, some examples are presented that can represent the basis for the development of new technologies for other compounds that are not currently regulated (i.e., phosphate).

Recently, the use of so-called "biostimulants" raised the interest of both the scientific community and farmers, leading to an increase in their practical use. Biostimulants can be defined as "a product stimulating plant nutrition processes independently of the product's nutrient content with the sole aim of improving one or more of the following characteristics of the plant or the plant rhizosphere: nutrient use efficiency; tolerance to abiotic stress; quality traits; availability of confined nutrients in soil or rhizosphere" [51,52]. Obviously, such a comprehensive definition leads to a very wide range of substances and compounds, their classification in this group being based on their final effect on plants and not their nature and/or composition. The class is currently under scrutiny for regulation at the European level, with an EU regulation recently being adopted covering this aspect [52].

Table 3 summarizes some examples of natural polymers applied for the removal of pesticides, fungicides and biostimulants from the environment.

Table 3. Management of plant protection products using natural polymers (in chronological order).

Natural Polymer	Pollutant	Pollutant Class	Application Form	Obtained Results	Process Parameters	Ref.
Cellulose	Humic acid, 1 g/L	Biostimulant	Cellulose nanofibers obtained by addition of epoxypropyl trimethyl ammonium chloride at 65 °C, 8 h	Adsorption rate 184×10^{-3} min^{-1}	Composite (1 mL, 0.2–0.4 wt%) added to different amounts of humic acid solution, shaken for 2 days; best results at pH 4.5; at pH = 6.2, adsorption rate = 49×10^{-3} min^{-1}; isotherms—Langmuir model	[53]
Chitosan	Humic acid	Biostimulant	Polyacrylamide/chitosan semi-interpenetrating network hydrogels	Maximum adsorption 166.30 mg/g	0.025 g of composite dispersed in 50 mL of 60 mg/mL pollutant; pH = 3 to 11; results superior to other organic and inorganic adsorbents in literature; isotherm—Sips model (multilayer adsorption on heterogeneous surfaces at low concentrations and monolayer adsorption at higher pollutant concentrations)	[54]
Chitosan	Phosphate	Fungicide	Iron oxide nanoparticle-loaded chitosan composites	Removal capacity of 0.059 mgP/g	Pilot plant: adsorption tower (height = 100 cm, inner diameter = 45 cm, flow rate = 7.05 ± 0.18 L/min), composite volume = 80 L, composite weight = 85.74 kg; constant adsorption capacity after six recycling cycles	[55]
Sodium alginate	Phosphate	Fungicide	Iron crosslinked alginate beads	Maximum adsorption capacity 79 mg/g	Experiments conducted with synthetic water; kinetics—pseudo-second-order model, isotherm—Freundlich model; experiments with real eutrophic lake water—81–100% removal in 24 h (11–69 µg/L initial concentration).	[56]

Table 3. *Cont.*

Natural Polymer	Pollutant	Pollutant Class	Application Form	Obtained Results	Process Parameters	Ref.
β-Cyclodextrin β-Cyclodextrin β-Cyclodextrin	Humic acid, 10 mg/L Fluvic acid, 30 mg/L 2,4,6-trichlorophenol, 0.1 mmol/L	Biostimulant Biostimulant Fungicide, herbicide, insecticide	β-cyclodextrin polymer synthesized in the aqueous phase using tetrafluoroterephthalonitrile as a rigid crosslinker, epichlorohydrin as a flexible crosslinker and 2,3-epoxypropyltrimethylammonium chloride as a quaternization reagent	Maximum adsorption 40 mg/g Maximum adsorption 166 mg/g Maximum adsorption 108 mg/g	Solid/liquid ratio = 1 mg/mL; adsorption superior to commercial materials; kinetics—pseudo-second-order model and Elovich model (solute adsorption rate decreases with the increase of adsorbed solute); isotherm—Freundlich model; no significant adsorption decrease after five recycling cycles	[57]
Chitosan, gelatin	Atrazine (20 mg/L), fenitrothion (20 mg/L)	Pesticides	Polymeric composite prepared by inotropic gelation at room temperature	Adsorption capacity 75.19 mg/g (atrazine), 36.23 mg/g (fenitrothion)	Composite (0.3 g/L) added to 50 mL pollutant solution; adsorption time 180 min. Isotherm—Langmuir model	[58]
Cellulose	Chlorpyrifos, 100 μg/L	Insecticide	Polymeric films developed by incorporating dibutyl sebacate, bis(2-ethylhexyl) sebacate, bis(2-ethylhexyl) phthalate, bis(1-butylpentyl) adipate, 2-nitrophenyl octyl ether or 2-fluorophenyl 2-nitrophenyl ether in cellulose triacetate, by solvent casting	Extraction efficiency from synthetic water 71–87% (after 8 h)	Best results obtained for composite with bis(2-ethylhexyl) sebacate; water samples maintained in contact with the film having area of 2.89 cm^2, under orbital agitation	[59]
β-cyclodextrin	Humic acid	Biostimulant	Friedel–Crafts alkylation reaction between modified β-cyclodextrin and 4,4′ -bis(chloromethyl)-1,1′—biphenyl in a homogeneous ionic liquid system	Maximum adsorption 142 mg/g	0.015 g of composite dispersed in 15 mL of 20 mg/L pollutant; results superior to activated carbon; isotherm—Freundlich model; over 90% efficiency after six recycling cycles	[60]

One interesting approach on this topic is presented by Attallah et al. [58]. Using natural and natural-based polymers (gelatin and chitosan), the authors developed a polymer composite with a removal efficiency of 87.13% to 94.48% for atrazine and 82.65% to 96.45% for fenitrothion after 120 min, superior to organic and inorganic adsorbents, as presented by literature data. The authors also proposed adsorption mechanisms, in which atrazine is removed by adsorption onto the composite pores and to the hydrophilic sites of oxygen-containing groups by hydrogen bonding, while fenitrothion is adsorbed on the surface of the composite and to the hydrophobic sites' interactions through π–π stacking. The mechanisms would allow the use of the developed composites in real conditions (in the presence of multiple target pollutants).

Humic acid's adsorption was attributed to the electrostatic interactions between the contaminant and the natural polymer part of the composites [53,54] and by ion exchange [57], a mechanism also involved in the adsorption of fluvic acid. Ion exchange was also described as the main mechanism in the adsorption of phosphate ions [55,56].

5.3. Management of Industrial Dyes and Dye Models Using Natural Polymers

The development of the textile industry has led to the extensive use of synthetic dyes, which could reach water sources as industrial effluents. Generally speaking, dyes are non-biodegradable organic compounds that have coloring properties towards a given substrate (due to the presence of chromophoric groups in their structure) [61]. As in many developing countries, the effluents (often insufficiently treated) are present in agricultural irrigation water [61], the dyes often reach water sources [62,63], having toxic, mutagenic and carcinogenic effects, while also impairing the photosynthesis process by preventing light penetration through water. The dyes have the tendency to bioaccumulate in superior organisms by crossing the food chain [61]. Of specific interest are azo-dyes, which have a relatively low binding yield during the industrial process (with up to 50% being released as wastewater). Other types of dyes can emerge from different industrial applications, including histological applications, biotechnology or the food and beverage industry). In practice, studies often use model dyes, i.e., methylene blue, a cationic and primary thiazine dye. Although it has high toxicity and a wide range of applications [64], methylene blue (MB) is easily photocatalyzed. As such, in the present work, MB is presented as a model for the removal of similar dyes, and not as a pollutant.

Considering their extensive use and potentially harmful effects, the removal of dyes from water streams represents a current subject of interest. An overview of the current applications of natural polymers for the removal of dyes and dye models is presented in Table 4.

Table 4. Management of industrial dyes and dye models using natural polymers (in chronological order).

Natural Polymer	Targeted Application	Application Form	Obtained Results	Process Parameters	Ref.
Cellulose	Adsorption of crystal violet (dye with practical applications), 11.1 mg/L	Freeze-dried foams consisting of cellulose nanofibers (obtained by addition of epoxypropyl trimethyl ammonium chloride at 65 °C, 8 h) with adsorbed humic acid	55% adsorption	Porous foam with density of 25 kg/m^3, porosity 98% (20 mg) added to 45 mL of dye solution	[53]
Chitosan	Reduction of methylene blue (model dye), 10 ppm	Silver nitrate mixed with chitosan/polyethylene glycol solution, various concentrations of TiO_2 added at 80 °C	63.48% degradation	Direct sunlight photocatalysis; Langmuir–Hinshelwood mechanism	[65]
Xylan	Adsorption of methylene blue (model dye), 400 mg/L	Xylan/poly(acrylic acid) magnetite nanoparticles nanocomposite hydrogel	Maximum adsorption capacity—438.60 mg/g	Removal rate >90% for 3 g/L adsorbent; isotherm—Langmuir model; kinetics—pseudo-second-order model	[66]
Cellulose and chitosan	Adsorption of Congo red (histological staining agent), 30 mg/L	Cellulose/chitosan hydrogel prepared by extruding and regenerating from ionic liquid 1-ethyl-3-methylimidazolium acetate in ethanol	Maximum adsorption capacity—40 mg/g	For adsorbent dosage of 2.0 g/L, equilibrium was reached within 115 min, removal rate was 89.6%; isotherms—Langmuir model; kinetics—pseudo-second-order model	[67]

Table 4. *Cont.*

Natural Polymer	Targeted Application	Application Form	Obtained Results	Process Parameters	Ref.
Silk	Filtration of dyes with industrial and biotechnology applications	Membranes prepared by vacuum filtration of exfoliated degummed *Bombyx mori* silk fibers	>90% rejection	Vacuum filtration device, best results obtained for Alcian Blue 8GX (100%, initial concentration 185 μM), Brilliant Blue G (100%, initial concentration 398 μM), Rhodamine B (91%, initial concentration 5 mM)	[68]
Chitosan	Photodegradation of Ponceau BS (staining agent)	Polyaniline-grafted chitosan prepared by chemical using ammonium per sulfate; Ag nanoparticles incorporated into the polymer matrix	Complete degradation after 40 min	Photodegradation under visible light; kinetic—pseudo-first-order model	[69]
Chitosan, lignin	Removal of acid black-172 (dye with industrial applications), 100 mg/L	Ternary graft copolymer (chitosan–acrylamide–lignin), synthesized using microwave irradiation and chemical-free radical initiator technique	Removal efficiency—97.1%	Dosage 200 mg/L; possible mechanisms—charge neutralization, bridging and sweeping effects	[70]
Guar gum	Catalytic oxidation of methyl orange (100 ppm)	Zerovalent iron–guar gum nanocomposite, spherical, particle size of ∼60–70 nm (0.5 g/L)	99% after 60 min, pH 7	Superior oxidation to zerovalent ion by itself (39%)	[41]
β-cyclodextrin	Adsorption of methylene blue (model dye), 100 mg/L	Citric acid-crosslinked β-cyclodextrin	Maximum adsorption capacity—0.9229 mmol/g	0.4 g in 200 mL pollutant, pH = 1–10; kinetics—pseudo-second-order model; isotherm—Sips model; no decrease in performance after five recycling cycles	[71]
Lignin	Adsorption of methylene blue (model dye), 1 mg/mL	Hydrogels obtained by crosslinking poly(methyl vinyl ether co-maleic acid) and lignin in ammonium and sodium hydroxide solutions	Adsorption capacity—629 mg/g	Dry hydrogels (20–30 mg) placed in 20 mL pollutant solution, stirred for 48 h at room temperature; maximum removal efficiency—96%, superior results to control hydrogels (without lignin)	[72]
Pectin	Adsorption of methylene blue (model dye), 100–1000 mg/L	Pectin microgel particles	Adsorption capacity—284.09 mg/g	Different uptake times (2–310 min), pH 1–7; isotherm—Langmuir model; kinetics—pseudo-second-order model; recovery efficiency higher than 80% after three cycles	[73]
Chitosan	Adsorption of CI Basic Red 14 (dye with industrial applications), 100 ppm	Polymeric beads containing chitosan, *Arundo donax* L. cells, gelatin and poly(vinyl)pyrrolidone	Maximum adsorption capacity—41.322 mg/g	Removal efficiency of 92.2% (at 2 g. adsorbent); isotherms—Langmuir model; kinetics—pseudo-first-order model	[74]
(Konjac) gluco-mannan	Adsorption of malachite green (common dye with industrial applications)	Konjac glucomannan/graphene oxide sponges prepared by ice template method	Maximum adsorption capacity—189.96 mg/g	Isotherms—Langmuir model; kinetics—pseudo-first-order model; adsorption capacity relatively high after five recycling cycles	[75]

Table 4. *Cont.*

Natural Polymer	Targeted Application	Application Form	Obtained Results	Process Parameters	Ref.
Sodium alginate	Adsorption and photocatalytic degradation of crystal violet (dye with practical applications)	Grafted sodium alginate/ZnO/graphene oxide composite	Maximum adsorption capacity—13.85 mg/g	Maximum capacity at pH = 5; isotherm—Freundlich model; kinetics—pseudo-second-order model; photocatalytic degradation enhanced the removal efficiency by 10%	[76]
Tragacanth gum	Adsorption of methylene blue (model dye)	Hydrogel nanocomposite composed of tragacanth gum and modified $CaCO_3$ nanoparticles	Maximum adsorption capacity—476 mg/g	Isotherm—Langmuir model; kinetics—pseudo-first-order model; film diffusion—main mechanism of adsorption	[77]
Chitosan	Adsorption of Acid Blue-113 (industrial dye)	Chitosan-coated polyacrylonitrile nanofibrous mat	Maximum adsorption capacity—1708 mg/g	Superior results compared with control (without chitosan); superior capacity than commercial activated carbon; isotherm—Langmuir model; kinetics—pseudo-second-order model; film diffusion—main mechanism of adsorption; slight decrease in adsorption after four cycles	[78]
Silk	Adsorption of crystal violet (dye with practical applications)	3D porous network in a freeze-dried silk fibroin/soursop seed polymer composite	Maximum adsorption capacity—83.31 mg/g	Isotherms—Freundlich model; kinetics—pseudo-first-order model.	[79]
Sodium alginate,	Adsorption of crystal violet (cationic dye with practical applications), 200 mg/L	Hydrogel beads from rice bran combined with sodium alginate	Maximum adsorption capacity—454.55 mg/g	Isotherms—Freundlich model; kinetics—pseudo-second-order model; no adsorption decrease after five regeneration cycles	[80]
Chitosan	Adsorption of reactive blue 4 (anionic dye with practical applications), 200 mg/L	Hydrogel beads from rice bran combined with chitosan	Maximum adsorption capacity—212.77 mg/g	Isotherms—Langmuir model; kinetics—pseudo-first-order model; satisfactory adsorption (20% decrease) after five recycling cycles	
Sodium alginate	Degradation of methylene blue (model dye)	Ca-alginate/CuO beads	92% degradation in 8 min	100 mg composite added to 5 mL methylene blue solution in the presence of 1 mL $NaBH_4$ (0.08 mol/L); kinetics—pseudo-first-order model; degradation reduced when using recycled composites; slow decrease in degradation after ten recycling cycles	[81]
Chitosan	Adsorption of Arsenazo-III (staining, analytical reagent), 100 mg/L	Chitosan hydrogel polymer, initiator potassium persulphate	Maximum adsorption capacity—99.9 mg/g	pH = 6, shaking time of 120 min, polymer dose of 0.01 g, room temperature	[82]
Chitosan	Alizarin Red S (staining, analytical reagent), 100 mg/L		Maximum adsorption capacity—62.5 mg/g		

Table 4. *Cont.*

Natural Polymer	Targeted Application	Application Form	Obtained Results	Process Parameters	Ref.
Sodium alginate	Separation of Congo red (histological staining agent), 0.1 mg/L Separation of Alizarin red (staining, analytical reagent), 0.1 mg/L Separation of Sunset yellow (dye for food and beverage industry), 0.1 mg/L	Nacre-inspired multiple crosslinked polyvinyl alcohol/ calcium alginate/SiO_2 membrane	Rejection efficiency—99.5% Rejection efficiency—99.1% Rejection efficiency—98.3%	Long-term separation properties demonstrated by the membrane; over 99% of initial efficiency retained after three recycling cycles	[83]

One of the most encountered natural polymers (chitosan) was also demonstrated by Alshahrani et al. [84] to form heterostructures with hydroxyapatite and cerium oxide, which proved efficient (11–96% removal efficiencies) in the removal of different industrially important dyes (Brilliant blue, Congo red, crystal violet, methylene blue, methyl orange, Rhodamine B).

Unlike other types of pollutants, the dyes can be removed by different methods, including filtration, adsorption and (photo)degradation (as presented in Table 4). Among the presented examples, the most encountered natural polymers used are polysaccharides, not only of vegetal origin (including cellulose, xylan, lignin, guar gum, β-cyclodextrin, pectin, glucomannan, Tragacanth gum, sodium alginate) but also of animal origin (chitosan) and proteins (silk).

The materials developed for dye removal include foams and sponges, hydrogels and microgels, membranes, as well as polymeric beads and (nano)composites. As a general remark, the adsorption model for their use is found by most authors to follow the Langmuir model, but the Freundlich model is also presented (for hydrogels and composites containing alginate or silk). Additionally, Huang et al. [71] suggested the Sips model for the adsorption of MB on citric acid-crosslinked β-cyclodextrin. Regarding the kinetics of the processes, the examples presented equally support pseudo-first-order and pseudo-second-order kinetics. However, it can be observed that for protein and natural polymers of animal origin (chitosan), the predominant model is represented by the pseudo-first-order model (reaction rate depending only on one reactant concentration), while for the natural polymers of vegetal origin, the predominant kinetic model proposed by the authors is the pseudo-second-order model (a model which proposes chemisorption as the rate-limiting step [85]). The exceptions to this model are represented by the adsorption of malachite green and MB on Konjac glucomannan/graphene oxide sponges and on hydrogel tragacanth gum/$CaCO_3$ nanoparticles, respectively [75], and the degradation of MB using Ca-alginate/CuO beads [81]. Several of the presented studies (see Table 4) demonstrate the positive influence of the natural polymer used on the removal efficiency of the final composite, as well as a superior removal capacity, compared with traditional materials.

The removal of the dyes by adsorption is usually achieved by electrostatic interactions (as demonstrated in several studies [66,71–73,78–80,82]), as well as the adsorption on both the surface and in the mesopores/macropores of composites [75,76]. On the other hand, the photodegradation of dyes using the proposed composites involves the use of active materials (such as TiO_2, Fe^0, ZnO), which leads to the formation of active species (reactive oxygen species •OH, electrons) involved in the photodegradation mechanisms [41,65,76], while flocculation is achieved by the charge neutralization mechanism [70]. The general mechanisms (and the interaction between the contaminants and the composites) are strongly

dependent on the nature of the dyes used in the studies, as well as on the contaminant removal method selected (adsorption, photodegradation, flocculation).

5.4. Management of Other Types of Industrial Emerging Pollutants Using Natural Polymers

Other types of emerging pollutants currently under scrutiny are represented by personal care products, plasticizers, surfactants and other types of industrially important chemical materials. Some examples of their removal are presented in Table 5.

Table 5. Management of other types of EPs from industrial sources using natural polymers (in chronological order).

Natural Polymer	Targeted Application	Pollutant Class	Application Form	Obtained Results	Process Parameters	Ref.
Chitosan	Adsorption of chlorophenol (50 mg/kg) and phthalic anhydride (70 mg/kg)	industrial precursor/plasticizer	Poly(N,N-diethylacrylamide), poly(N-isopropylacrylamide) and poly(N-vinylcaprolactum) grafted on chitosan/derivatives	100% removal of organic impurities	Best results obtained for poly(N-isopropylacrylamide) graft carboxymethyl-chitosan at 6 mg/mL; materials can be used for at least 5 cycles	[86]
Cellulose	Flocculation of nonylphenol, 100 μg/L	Precursor for antioxidants, lubricating oil additives, laundry, dish detergents, emulsifiers, solubilizers, surfactants	(poly N-isopropyl acrylamide)-co-(poly diallyl dimethyl ammonium chloride) grafted on carboxymethylcellulose	Flocculation, nonylphenol removal = 79%	Optimized conditions: pH = 4; T = 35 °C; dosage = 40 mg/L	[87]
β-cyclodextrin	Adsorption of perfluorooctanoic acid	surfactant, industrial importance	β-cyclodextrin decafluorobiphenyl polymer (DFB-CDP, 1:β-CD feed ratio = 3)	Adsorption capacity = 34 mg/g, superior to sieved coconut shell-activated carbon	Freundlich model best fit the adsorption isotherm; no significant differences after four recycling cycles	[88]
β-cyclodextrin	Adsorption of bisphenol A, 100 mg/L	Plastics industry	Citric acid-crosslinked β-cyclodextrin	Maximum adsorption capacity = 0.3636 mmol/g	0.4 g in 200 mL pollutant, pH = 1–10; kinetics—pseudo-second-order model; isotherm—Langmuir model; 80% adsorption capacity after five recycling cycles	[71]

Table 5. *Cont.*

Natural Polymer	Targeted Application	Pollutant Class	Application Form	Obtained Results	Process Parameters	Ref.
β-Cyclodextrin	Adsorption of 2-naphthol, 0.1 mmol/L	Intermediate in dyes production	β-cyclodextrin polymer synthesized in the aqueous phase using tetrafluoroterephthalonitrile as a rigid crosslinker, epichlorohydrin as a flexible crosslinker and 2,3-epoxypropyltrimethylammonium chloride as a quaternization reagent	Maximum adsorption = 74 mg/g	Solid/liquid ratio = 1 mg/mL; adsorption superior to commercial materials; kinetics—pseudo-second-order and Elovich (solute adsorption rate decreases with the increase of adsorbed solute) models; isotherm—Freundlich model	[57]
β-Cyclodextrin	Adsorption of 3-phenylphenol, 0.1 mmol/L	Colorimetric reagent		Maximum adsorption = 101 mg/g		
β-Cyclodextrin	Adsorption of bisphenol A, 0.1 mmol/L	Plastics industry		Maximum adsorption = 103 mg/g		
β-Cyclodextrin	Adsorption of bisphenol S, 0.1 mmol/L	Industrial application in epoxy resins		Maximum adsorption = 117 mg/g		
Chitosan	Catalytic reduction of p-nitrophenol, 5 mM	Industrial intermediate	Chitosan/reduced graphene oxide-based composite hydrogel, with glutaraldehyde crosslinking agent, loaded with Pd nanoparticles	Catalytic reduction, rate constant = 0.0348 min^{-1}	Hydrogel mixed with 1 mL pollutant solution, added 10 mL $NaBH_4$ solution (0.01 M); results superior to literature data, better for 2-nitroaniline	[89]
Chitosan	Catalytic reduction 2-nitroaniline, 5 mM	Industrial intermediate		Catalytic reduction, rate constant = 0.125 min^{-1}		
Chitosan	Degradation of phenol, 100 mg/L	Industrial intermediate	Recombination of chitosan and polyvinyl alcohol, with microorganisms added	Biodegradation, 99%, degradation rate increasing after several uses	Best results obtained at 30 °C, pH = 7, higher compared with microorganism alone; over 95% degradation rates after 90 recycling cycles	[90]
Chitosan	Degradation of p-cresol, 100 mg/L	Industrial intermediate		Degradation in the presence of 1600 mg/L phenol, concentration decreased to 0.4 mg/L		
Chitosan	Degradation of catechol, 100 mg/L	Industrial intermediate		Degradation in the presence of 1600 mg/L phenol, concentration decreased to 0.6 mg/L		
Chitosan	Degradation of 2-aminophenol, 100 mg/L	Industrial intermediate		Degradation in the presence of 1600 mg/L phenol, concentration decreased to 4.7 mg/L		

Table 5. *Cont.*

Natural Polymer	Targeted Application	Pollutant Class	Application Form	Obtained Results	Process Parameters	Ref.
Chitosan	Degradation of p-nitrophenol, 10 mg/L	Industrial intermediate	Bi-functional ternary nanocomposite constructed using chitosan-wrapped carbon nanofibers, embedded with Ag-doped Co_3O_4	Degradation constant = 0.0186 min^{-1}; degradation efficiency = 97.39% for 40 mg catalyst	10–40 mg catalyst immersed in 100 mL pollutant solution; solution irradiated with visible light; degradation rate higher than carbon nanofibers and metal oxide alone; over 90% degradation after five recycling cycles	[91]
β-cyclodextrin	Adsorption of bisphenol A, 20 mg/L	Plastics industry	Friedel–Crafts alkylation reaction between modified β-cyclodextrin and 4,4′-bis(chloromethyl)-1,1′-biphenyl in a homogeneous ionic liquid system	Maximum adsorption = 257.75 mg/g	0.015 g of composite dispersed in 15 mL pollutant; results superior to activated carbon; isotherm—Freundlich model; over 90% efficiency after six recycling cycles	[60]
Sodium alginate	Degradation of p-nitrophenol, 10^{-4} M	Industrial intermediate	Ca-alginate/CuO beads	Degradation constant = 0.202 min^{-1}; degradation efficiency = 97–98%	100 mg of composite, in the presence of 0.08 mol/L $NaBH_4$. Degradation efficiency higher than Ca-alginate alone; kinetics—pseudo-first-order model; 75% reduction after 60 min, after 10 recycling cycles	[81]
Chitosan	Degradation of p-nitrophenol, 20 mg/L	Industrial intermediate	Chitosan/Ag nanoparticles/layered double-hydroxide nanocatalyst	Apparent rate constant = 1.65×10^{-2} s^{-1}	20 mg nanocatalyst added to 4 mL $NaBH_4$ (0.54 g/L) and 6 mL of pollutant solution; kinetics—pseudo-first-order model; performance unchanged by 5 recycling cycles	[92]
Cellulose	Extraction of triclosan, tonalide, 100 μg/L	Personal care products	Polymeric films developed by incorporating dibutyl sebacate, bis(2-ethylhexyl) sebacate, bis(2-ethylhexyl) phthalate, bis(1-butylpentyl) adipate, 2-nitrophenyl octyl ether or 2-fluorophenyl 2-nitrophenyl ether in cellulose triacetate, by solvent casting	Extraction efficiency from synthetic water = 68–93%/ 44–94% (after 8 h)	Best results for composite with 2-nitrophenyl octyl ether/dibutyl sebacate; water samples maintained in contact with the film having area of 2.89 cm^2, under orbital agitation	[59]

A particular case is represented by the very interesting study of Ling et al. [93]. In their study, the authors evaluated the capacity of porous β-cyclodextrin polymers for the removal of 90 micropollutants (ranging from pesticides and industrial compounds to pharmaceuticals and personal care products, at 10 mg/L concentration), compared with a known adsorbent, coconut shell-activated carbon, in batch and flow-through experiments. The main conclusion of the batch experiments was that compared with the activated carbon process, the adsorption using the natural polymer was faster, but selective (for some of the pollutants, complete uptake was realized in 5 min). The authors correlated the selectivity of the natural polymer with the McGowan volume (bulk size of 1 mol of molecules) and the charge state of the target compounds. Overall, the natural polymer seemed to be a very good alternative to activated carbon, especially for pollutants with higher McGowan volume and positive charge (although for neutral and negatively charged pollutants with McGowan volumes > 1.7 (cm^3/mol) × 100, the adsorbent also had very good results).

Similar results were obtained by Topuz et al. [94] in the removal of several dyes and polycyclic aromatic hydrocarbons using nanofibrous hyper-crosslinked cyclodextrin network membranes produced by electrospinning, 460 nm in diameter. The results obtained for most of the micropollutants are superior to literature data, and the membranes exhibited very good reusability after acidic methanol treatment.

A widely encountered class of chemicals (personal care products, defined as products used to increase the quality of life), often associated with pharmaceuticals in the wider class of pharmaceuticals and personal care products (PPCP), is currently being defined as one of the most harmful chemicals to ecosystems, being encountered all over the world [95]. Examples of such contaminants related to PCPs include triclosan (antimicrobial agent) and tonalide (fragrance), commonly used in cosmetics. Merlo et al. [59] presented their extraction using polymeric films developed by incorporating different plasticizers in cellulose triacetate by solvent casting, with 93–94% efficiency after 8 h, a higher efficiency than the one recorded for the insecticide chlorpyrifos (see Table 2).

Another industry from which a significant class of emerging pollutants (surfactants) are discharged is the cleaning products industry. An example of a surfactant that was successfully eliminated using natural polymers is perfluorooctanoic acid, adsorbed using β-cyclodextrin-based polymers [88].

The plastics industry is also one of the industries to which hazardous emerging pollutants can be traced. Plasticizers (such as phthalic anhydride), intermediaries or additives (such as bisphenol A) or curing agents in the epoxy industry (such as bisphenol S) were successfully removed using chitosan or β-cyclodextrin composites. Other examples of industrial emerging pollutant management presented in Table 5 include the industrial intermediates chlorophenol (adsorbed using chitosan-based composites), nonylphenol (removed by flocculation using carboxymethylcellulose composites), 2-naphthol, 3-phenylphenol (adsorbed using β-cyclodextrin polymeric composites), 2-nitroaniline, p-nitrophenol (removed by catalytic reduction using chitosan-based hydrogels or composites, as well as calcium alginate/inorganic beads), phenol, p-cresol, catechol and 2-aminophenol (biodegradation using a mixture of chitosan-based composites and microorganisms). In degradation studies, the kinetics followed a pseudo-first-order model, and the results were superior to the literature data. Kinetic studies were also performed for the adsorption of different emerging pollutants on β-cyclodextrin-based polymers, with the two evaluated studies revealing a pseudo-second-order model. Composites based on the same natural polymer exhibited adsorption isotherms fitting the Freundlich model (for the adsorption of perfluorooctanoic acid, bisphenol A, 2-naphthol, 3-phenylphenol and bisphenol S) and the Langmuir model for the adsorption of bisphenol A on citric acid-crosslinked β-cyclodextrin [71].

Regarding the mechanisms involved in the contaminants' management, Hu et al. [57] attributed the removal of bisphenol A on β-cyclodextrin composites to the adsorption in the polymer's cavities and other hydrophobic sites by hydrophobic interactions; a similar mechanism was proposed by Huang et al. [71] and Sun et al. [60]. For the flocculation removal of nonylphenol, Yang et al. [87] proposed a mechanism in which charge attraction

and hydrophobic interaction play key roles. As previously presented for industrial dyes, the degradation of the contaminants presented in Table 5 was achieved via electron transfer [89,91]. The general mechanisms proposed for the degradation of phenolic compounds involve the adsorption of contaminants on the surface of the composite, electron transfer and adsorption of degradation products on the surface of the composite [81,92].

5.5. Management of Other Hazardous Emerging Pollutants Using Natural Polymers

Besides the examples discussed in the previous sections (not intended as an exhaustive presentation), there are numerous other types of chemicals belonging to the class of emerging contaminants. For example, polycyclic aromatic hydrocarbons (PAHs) are encountered across the world, caused especially by long-term anthropogenic sources. PAHs are continuously considered a major concern, as their properties (structural, hydrophobicity, thermostability, among others) are correlated with toxic, mutagenic or carcinogenic effects [92]. Some very interesting review works were recently published on this topic, which we suggest for further reading [96–98].

In the same category of hazardous EPs, microplastics, toxins or radionuclides can also be included. Table 6 presents some examples of the use of natural polymers for the management of such pollutants.

Table 6. Management of other hazardous EPs using natural polymers (in chronological order).

Natural Polymer	Targeted Application	Pollutant Class	Application Form	Obtained Results	Process Parameters	Ref.
Silk	Filtration of gold nanoparticles, 5 nm, 5.5×10^{13} unit per mL CdSeS/ZnS quantum dots, 6 nm, 1 mg/mL	Nanoparticles	Membranes prepared by vacuum filtration of exfoliated degummed *Bombyx mori* silk fibers	Rejection 99% Rejection 100%	Vacuum filtration device	[68]
Cellulose	Removal of pyrene (25, 100 ppb) from water	Polycyclic aromatic hydrocarbon	Cellulose fibers grafted with poly(lauryl acrylate) and poly(octadecyl acrylate	Adsorption capacity 38 mg/g	Higher capacity for octadecyl acrylate grafted cellulose	[99]
(Konjac) glucomannan	Adsorption of U (VI)	Radionuclides	Konjac glucomannan/graphene oxide sponges prepared by ice template method	Maximum adsorption capacity—266.97 mg/g	Selectivity in multi-ions system; isotherms—Langmuir model; kinetics—pseudo-first-order model; adsorption capacity relatively high after five recycling cycles	[75]
Cellulose	Removal of fluorene, 20 μg/L Removal of anthracene, 20 μg/L Removal of fluoranthene, 20 μg/L Removal of pyrene, 20 μg/L	Polycyclic aromatic hydrocarbon	Polystyrene–cotton composites, obtained by dipping pretreated cotton in 2% polystyrene solution in chloroform	Extraction recovery after two elution = 65% Extraction recovery after two elution = 71% Extraction recovery after two elution = 85% Extraction recovery after two elution = 93%	Recovery increased at the second elution	[100]

Table 6. *Cont.*

Natural Polymer	Targeted Application	Pollutant Class	Application Form	Obtained Results	Process Parameters	Ref.
Cellulose	Removal of polycyclic aromatic hydrocarbons from mainstream cigarette smoke	Polycyclic aromatic hydrocarbon	Cellulose cigarette filter with porous structure, pore size controlled by polyvinylpyrrolidone using a dip–dry method	Removal efficiency 61.79%	Higher than conventional cellulose acetate filter (39.22% removal)	[101]
Cellulose	Plastic micro/nanoparticles stained with neutral red dye	Microplastic particles from commercial body scrub	Cellulose surface functionalized with polyethylenimine	Maximum adsorption efficiency of 97%, 98% and 99% for polymethyl methacrylate, polyvinyl chloride and polyvinyl acetate nanoparticles	Kinetics—pseudo-second-order model	[102]
Cellulose, β-cyclodextrin	Adsorption of microcystin-LR, 1.5, 0.8 µg/mL	Cyanotoxin	Aerogels from cellulose nanofibril grafted with β-cyclodextrin	Adsorption capacity 0.078 mg/g	Aerogels placed in 20 mL of toxin solutions at room temperature and constant stirring; kinetics—pseudo-second-order model	[103]
Sodium alginate	Adsorption of U (VI), 5 mmol/L	Radionuclides	Granulated resin obtained by crosslinking sodium alginate with 1,6-hexamethylene diisocyanate in benzene	Maximum adsorption capacity—269.80 mg/g	Replacement of Na^+ ions by H^+ (using dilute mineral acids); replacement of hydrogen ions with metal ions by ion exchange. Higher capacity for U ions compared to other metals	[104]
Polysaccharides	Coagulation and removal of TiO_2 nanoparticles in the form of TiO_2–humic acid complex	Nanoparticles	*Enteromorpha prolifera* polysaccharide together with poly aluminum chloride	Removal efficiency 87.12%	Highest efficiency for 1 mg/L polysaccharides; in the presence of poly aluminum chloride 95.68%; isotherm—Langmuir model; faster growing, larger and stronger flocs	[105]

The use of cellulose-based compounds, as presented in Table 6, is a viable approach for the removal of PAHs from water sources (as demonstrated by Mehmandost et al. [100], who suggested a removal mechanism based on PAHs/polymer π–π interactions), as well as from mainstream cigarette smoke. The second application would be of particular importance for avoiding smoke-related illnesses [101].

A potential application of a granulated resin obtained using natrium alginate as a natural polymer precursor is represented by the chelation of radioisotope models, such as U(VI) ions, as presented by Hassan [104]. As in the case of the composite sponges made of Konjac glucomannan/graphene oxide, presented by Chen et al. [75], the polysaccharide composites exhibited high affinity for the isotope model, with a similar adsorption capacity. The proposed mechanism was chelation using the attraction forces between the opposite charges of the natural compound and the cationic metal.

With the unprecedented development of nanotechnology, nanoparticles will soon become emerging pollutants of high interest. Although the potentially detrimental effects of nanoparticles are, in most cases, a subject of debate, their particularities (small dimensions, non-biodegradability, mobility, high surface areas, etc.), differentiate them from the corresponding ions (which are in some cases currently monitored), making them a preventive subject for environmental management studies. Natural polymers can be used in this area, as demonstrated for the rejection of gold nanoparticles using silk membranes or the removal of TiO_2 nanoparticles by flocculation using polysaccharide composites.

More recently included in the category of emerging pollutants [106,107], microplastics and toxins can also be successfully managed by the use of natural polymers. Present in a large variety of products or resulting from the breakdown of larger materials, microplastics became a global issue due to their easy crossing through the food chain, ultimately affecting human health (although currently, their effects are poorly understood) [108]. Asma and Valiyaveettil [102] demonstrated the adsorption by electrostatic interactions of different types of micro- and nanoplastics using cellulose surface functionalized with polyethylenimine with more than 97% efficiency, the adsorption kinetics following a pseudo-second-order model.

Naturally occurring (being produced by cyanobacteria) hepatotoxic cyanotoxin microcystins (MCs) are currently considered emerging contaminants, with a poorly understood ecological role. The cyanotoxins were proven to have toxic effects on ecosystems [109] and human health [110]. In this context, Gomez-Maldonado et al. [103] evaluated the adsorption of microcystin-LR (the most toxic microcystin) at different concentrations (1.5 and 0.8 μg/mL) using cellulose–β-cyclodextrin aerogels. The aerogels revealed a good adsorption capacity (0.078 mg/g) and the kinetics studied revealed that the process fit a pseudo-second-order model, allowing the proposal of a viable alternative for the improvement of water quality. According to the authors, the adsorption process targets the hydrophobic Adda groups in the microcystin.

Another very useful potential application of natural polymers is the detection of hazardous phenolic compounds, as demonstrated by Balram et al. [91]. Besides the efficient degradation of p-nitrophenol, the nanocomposite, comprising chitosan-wrapped carbon nanofibers embedded with Ag-doped Co_3O_4 deposited onto a carbon electrode, also proved efficient in the detection of the same phenolic compound by electrochemical methods. The sensor developed with the composite revealed a sensitivity of 55.98 $\mu A \mu M^{-1} cm^{-2}$ and a detection limit of 0.4 nM; its application was demonstrated using sewage, underground water and tomatoes.

6. Concluding Remarks and Future Perspectives

The use of natural polymers for the management of emerging pollutants represents a topic of interest worldwide. Their availability in renewable resources, ease of manufacturing composites, as well as the possibilities to develop truly "green" materials with minimum environmental impact make them very good candidates for developing alternative de-pollution technologies. At the same time, their recyclability and stability also represent tremendous advantages.

According to the literature data, there are some steps necessary before the industrial development of these technologies. Unlike other newly proposed technologies, the reaction mechanisms are rather well established. For example, the adsorption mechanisms of β-cyclodextrin (one of the most encountered materials among the natural polymers applied in

environmental studies) are presented in many studies. For model dyes (such as methylene blue), the adsorption most probably occurs primarily by surface binding, while for a non-polar molecule (such as bisphenol A), the removal is achieved by host–guest inclusion in the hydrophobic cavities [71]. Another non-competitive adsorption process was observed by Hu et al. [57] for the removal of humic acid and bisphenol A using a β-cyclodextrin polymer (humic acid being removed by ion exchange with the quaternary ammonium groups of the polymer, while bisphenol A adsorbed in the cyclodextrin cavities by hydrophobic interactions). The different mechanisms would allow the independent removal of both types of pollutants from complex matrices. The use of this particular heptasaccharide in de-pollution studies proved to be efficient at a laboratory scale, and has several advantages such as the ease of preparation (performed by the action of cycloglycosyltransferase enzyme on partially hydrolyzed starch [111]) and low production costs. However, the upscaling to industrial applications is complicated by relatively complex functionalization steps, which are often required in order to reach appropriate decontamination properties [112]. A possible response to this issue could be represented by the use of citric acid-crosslinked β-cyclodextrin, demonstrated to have adsorptive properties towards dyes and phenolic compounds [71]. More widespread materials (including sodium alginate in its modified calcium form, cellulose or chitosan) could be viable alternatives, as they possess adsorptive properties, even in unmodified form or with basic alteration of their native form [43,80,81]. Such materials (iron oxide nanoparticle-loaded chitosan composites) proved successful, e.g., in the pilot-scale adsorption of phosphate [51].

On the other hand, when functionalized with different types of other compounds, all natural polymers proved effective in the removal of pollutants, either by adsorption, catalytic oxidation or flocculation. The efficiency of the process usually depends on other constituents of the composites, although the polymers were proven to contribute to the final effect (as demonstrated for lignin and chitosan in the adsorption of methylene blue, and Acid Blue-113, respectively [72,78], by comparing the results obtained with and without the natural polymer). However, in many of the presented studies, the natural polymer is used as a support material. This raises some questions regarding whose responses actually could constitute the future of this particular removal method: can the natural polymers be used, with as little as possible modification from their native state for the industrial-scale removal of emerging contaminants? This remains a question to be answered in future studies, as the field of emerging contaminants will unfortunately provide continuous research topics.

In our opinion, future studies should focus on the aspect of practical, industrial application, considering all involved factors: associated costs to produce the active material, energetic costs or costs related to the regeneration of the active materials, alongside the efficiency of the developed technologies, compared to the current state of the art (i.e., the use of activated carbon, clays, etc.) [113,114].

Author Contributions: Conceptualization, R.C.F. and D.M.-M.; methodology, R.C.F., I.F. and D.M.-M.; validation, R.C.F. and R.I.M.; investigation, R.C.F., I.F., R.I.M. and D.M.-M.; resources, R.C.F.; data curation, R.C.F. and D.M.-M.; writing—original draft preparation, R.C.F. and D.M.-M.; writing—review and editing, R.C.F. and D.M.-M.; supervision, R.C.F.; project administration, R.C.F.; funding acquisition, R.C.F. All authors have read and agreed to the published version of the manuscript.

Funding: R.C.F., I.F., and R.I.M. gratefully acknowledge the financial support provided by a grant of the Ministry of Research, Innovation and Digitization, CCCDI—UEFISCDI, project number PN-III-PN-III-P2-2.1-PTE-2021-0309, within PNCDI III. The authors also acknowledge the support provided by the Ministry of Research, Innovation and Digitization through INCDCP-ICECHIM Core Program PN 23.06.01.01 (AQUAMAT) and through Program 1—Development of the national research and development system, Subprogram 1.2-Institutional Performance—Projects to finance excellence in RDI, contract no. 15PFE/2021.

Institutional Review Board Statement: Not applicable.

Data Availability Statement: Not applicable.

Conflicts of Interest: The authors declare no conflict of interest. The funders had no role in the design of the study; in the collection, analyses, or interpretation of data; in the writing of the manuscript; or in the decision to publish the results.

References

1. Bolisetty, S.; Peydayesh, M.; Mezzenga, R. Sustainable technologies for water purification from heavy metals: Review and analysis. *Chem. Soc. Rev.* **2019**, *48*, 463–487. [CrossRef] [PubMed]
2. Srivastava, R.K.; Shetti, N.P.; Reddy, K.R.; Nadagouda, M.N.; Badawi, M.; Bonilla-Petriciolet, A.; Aminabhavi, T.M. Valorization of biowastes for clean energy production, environmental depollution and soil fertility. *J. Environ. Manag.* **2023**, *332*, 117410. [CrossRef] [PubMed]
3. Subash, A.; Naebe, M.; Wang, X.; Kandasubramanian, B. Biopolymer—A sustainable and efficacious material system for effluent removal. *J. Hazard. Mater.* **2023**, *443*, 130168. [CrossRef] [PubMed]
4. Pandi, K.; Prabhu, S.M.; Ahn, Y.; Park, C.M.; Choi, J. Design and synthesis of biopolymer-derived porous graphitic carbon covered iron-organic frameworks for depollution of arsenic from waters. *Chemosphere* **2020**, *254*, 126769. [CrossRef] [PubMed]
5. Köse, K.; Mavlan, M.; Youngblood, J.P. Applications and impact of nanocellulose based adsorbents. *Cellulose* **2020**, *27*, 2967–2990. [CrossRef]
6. Mallakpour, S.; Naghadi, M. Design and identification of poly(vinyl chloride)/layered double hydroxide@MnO_2 nanocomposite films and evaluation of the methyl orange uptake: Linear and non-linear isotherm and kinetic adsorption models. *New J. Chem.* **2020**, *44*, 6510–6523. [CrossRef]
7. Dai, K.; Liu, G.; Xu, W.; Deng, Z.; Wu, Y.; Zhao, C.; Zhang, Z. Judicious fabrication of bifunctionalized graphene oxide/$MnFe_2O_4$ magnetic nanohybrids for enhanced removal of Pb(II) from water. *J. Colloid Interface Sci.* **2020**, *579*, 815–822. [CrossRef] [PubMed]
8. Morin-Crini, N.; Lichtfouse, E.; Fourmentin, M.; Ribeiro, A.R.L.; Noutsopoulos, C.; Mapelli, F.; Fenyvesi, É.; Vieira, M.G.A.; Picos-Corrales, L.A.; Moreno-Piraján, J.C.; et al. Remediation of emerging contaminants. In *Environmental Chemistry for a Sustainable World; Emerging Contaminants*; Morin-Crini, N., Lichtfouse, E., Crini, G., Eds.; Springer International Publishing: Cham, Switzerland, 2021; Volume 2, pp. 1–106.
9. Rahaman, H.; Islam, A.; Islam, M.; Rahman, A.; Nur Alam, S.M. Biodegradable composite adsorbent of modified cellulose and chitosan to remove heavy metal ions from aqueous solution. *Curr. Res. Green Sustain. Chem.* **2021**, *4*, 100119. [CrossRef]
10. Mudhoo, A.; Sharma, G.; Mohan, D.; Pittman, C.U., Jr.; Sillanpää, M. Can 'biodegradability' of adsorbents constitute an 'Achilles' heel' in real-world water purification? Perspectives and opportunities. *J. Environ. Chem. Eng.* **2022**, *10*, 107321. [CrossRef]
11. Udayakumar, G.P.; Muthusamy, S.; Selvaganesh, B.; Sivarajasekar, N.; Rambabu, K.; Sivamani, S.; Sivakumar, N.; Maran, J.P.; Hosseini-Bandegharaei, A. Ecofriendly biopolymers and composites: Preparation and their applications in water-treatment. *Biotechnol. Adv.* **2021**, *52*, 107815. [CrossRef]
12. Deyris, P.A.; Pelissier, F.; Grison, C.M.; Hesemann, P.; Petit, E.; Grison, C. Efficient removal of persistent and emerging organic pollutants by biosorption using abundant biomass wastes. *Chemosphere* **2023**, *313*, 137307. [CrossRef] [PubMed]
13. Joseph, L.; Jun, B.M.; Flora, J.R.V.; Park, C.M.; Yoon, Y. Removal of heavy metals from water sources in the developing world using low-cost materials: A review. *Chemosphere* **2019**, *229*, 142–159. [CrossRef]
14. Liu, D.; Gu, W.; Zhou, L.; Wang, L.; Zhang, J.; Liu, Y.; Lei, J. Recent advances in MOF-derived carbon-based nanomaterials for environmental applications in adsorption and catalytic degradation. *Chem. Eng. J.* **2022**, *427*, 131503. [CrossRef]
15. Geissen, V.; Mol, H.; Klumpp, E.; Umlauf, G.; Nadal, M.; van der Ploeg, M.; van de Zee, S.E.A.T.M.; Ritsema, C.J. Emerging pollutants in the environment: A challenge for water resource management. *Int. Soil Water Conserv. Res.* **2015**, *3*, 57–65. [CrossRef]
16. NORMAN Network. Available online: https://www.norman-network.com/nds/susdat/susdatSearchShow.php# (accessed on 21 March 2023).
17. Deblonde, T.; Cossu-Leguille, C.; Hartemann, P. Emerging pollutants in wastewater: A review of the literature. *Int. J. Hyg. Environ. Health* **2011**, *214*, 442–448. [CrossRef] [PubMed]
18. Gavrilescu, M.; Demnerová, K.; Aamand, J.; Agathos, S.; Fava, F. Emerging pollutants in the environment: Present and future challenges in biomonitoring, ecological risks and bioremediation. *New Biotechnol.* **2015**, *25*, 147–156. [CrossRef]
19. Tang, Y.; Yin, M.; Yang, W.; Li, H.; Zhong, Y.; Mo, L.; Liang, Y.; Ma, X.; Sun, X. Emerging pollutants in water environment: Occurrence, monitoring, fate, and risk assessment. *Water Environ. Res.* **2019**, *91*, 984–991. [CrossRef]
20. Peña-Guzmán, C.; Ulloa-Sánchez, S.; Mora, K.; Helena-Bustos, R.; Lopez-Barrera, E.; Alvarez, J.; Rodriguez-Pinzón, M. Emerging pollutants in the urban water cycle in Latin America: A review of the current literature. *J. Environ. Manag.* **2019**, *237*, 408–423. [CrossRef]
21. Arman, N.Z.; Salmiati, S.; Aris, A.; Salim, M.R.; Nazifa, T.H.; Muhamad, M.S.; Marpongahtun, M. A Review on Emerging Pollutants in the Water Environment: Existences, Health Effects and Treatment Processes. *Water* **2021**, *13*, 3258. [CrossRef]
22. Krishnakumar, S.; Singh, D.S.H.; Godson, P.S.; Thanga, S.G. Emerging pollutants: Impact on environment, management, and challenges. *Environ. Sci. Pollut. Res.* **2022**, *29*, 72309–72311. [CrossRef]
23. Dalu, T.; Tavengwa, N. *Emerging Freshwater Pollutants. Analysis, Fate and Regulations*; Elsevier: Amsterdam, The Netherlands, 2022; pp. 1–6.
24. Desidery, L.; Lanotte, M. Polymers and plastics: Types, properties, and manufacturing. In *Plastic Waste for Sustainable Asphalt Roads*; Giustozzi, F., Nizamuddin, S., Eds.; Woodhead Publishing: Cambridge, MS, USA, 2022; pp. 3–28.

25. Doppalapudi, S.; Katiyar, S.; Domb, A.J.; Khan, W. Biodegradable natural polymers. In *Advanced Polymers in Medicine*; Puoci, F., Ed.; Springer Cham: Cham, Switzerland, 2015; pp. 33–66.
26. Guidance for Monomers and Polymers. Available online: Echa.europa.eu/guidance-documents/guidance-on-reach (accessed on 29 March 2023).
27. Ravve, A. *Naturally Occurring Polymers. Principles of Polymer Chemistry*; Springer: New York, NY, USA, 2000; pp. 449–475.
28. Olatunji, O. Classification of Natural Polymers. In *Natural Polymers*; Olatunji, O., Ed.; Springer: Cham, Switzerland, 2016; pp. 1–17.
29. Manaila-Maximean, D.; Danila, O.; Almeida, P.L.; Ganea, C.P. Electrical properties of a liquid crystal dispersed in an electrospun cellulose acetate network. *Beilstein J. Nanotechnol.* **2018**, *9*, 155–163. [CrossRef] [PubMed]
30. Manaila-Maximean, D.; Danila, O.; Ganea, C.P.; Almeida, P.L. Filling in the voids of electrospun hydroxypropyl cellulose network: Dielectric investigations. *Europ. Phys. J. Plus* **2018**, *133*, 159. [CrossRef]
31. Rosu, C.; Manaila-Maximean, D.; Kundu, S.; Almeida, P.L.; Danila, O. Perspectives on the electrically induced properties of electrospun cellulose/liquid crystal devices. *J. Electrostat.* **2011**, *69*, 623–630. [CrossRef]
32. Dumitriu, S. *Polysaccharides: Structural Diversity and Functional Versatility*, 2nd ed.; CRC Press: Boca Raton, FL, USA, 2004.
33. Ogawa, K.; Yui, T. *X-Ray Diffraction Study of Polysaccharides*; Marcel Dekker: New York, NY, USA, 1998; pp. 101–130.
34. Talebi, N.; Lopes, D.; Lopes, J.; Macário-Soares, A.; Dan, A.K.; Ghanbari, R.; Kahkesh, K.H.; Peixoto, D.; Giram, P.S.; Raza, F.; et al. Natural polymeric nanofibers in transdermal drug delivery. *Appl. Mater. Today* **2023**, *30*, 101726. [CrossRef]
35. Jiménez-Gómez, C.P.; Cecilia, J.A. Chitosan: A Natural Biopolymer with a Wide and Varied Range of Applications. *Molecules* **2020**, *25*, 3981. [CrossRef]
36. Lee, M.; Chen, B.-Y.; Den, W. Chitosan as a Natural Polymer for Heterogeneous Catalysts Support: A Short Review on Its Applications. *Appl. Sci.* **2015**, *5*, 1272–1283. [CrossRef]
37. Page, M.J.; McKenzie, J.E.; Bossuyt, P.M.; Boutron, I.; Hoffmann, T.C.; Mulrow, C.D.; Shamseer, L.; Tetzlaff, J.M.; Akl, E.A.; Brennan, S.E.; et al. The Prisma 2020 statement: An updated guideline for reporting systematic reviews. *PLoS Med.* **2021**, *18*, e1003583. [CrossRef]
38. Paut Kusturica, M.; Jevtic, M.; Ristovski, J.T. Minimizing the environmental impact of unused pharmaceuticals: Review focused on prevention. *Front. Environ. Sci.* **2022**, *10*, 1077974. [CrossRef]
39. Nippes, R.P.; Macruz, P.D.; da Silva, G.N.; Neves Olsen Scaliante, M.H. A critical review on environmental presence of pharmaceutical drugs tested for the COVID-19 treatment. *Process Saf. Environ. Prot.* **2021**, *152*, 568–582. [CrossRef]
40. Global Chemicals Outlook II, from Legacies to Innovative Solutions: Implementing the 2030 Agenda for Sustainable Development—Synthesis Report. Copyright © United Nations Environment Programme. 2019. Available online: https://wedocs.unep.org/bitstream/handle/20.500.11822/27651/GCOII_synth.pdf?sequence=1&isAllowed=y (accessed on 10 March 2023).
41. Balachandramohan, J.; Sivasankar, T. Ultrasound assisted synthesis of guar gum-zero valent iron nanocomposites as a novel catalyst for the treatment of pollutants. *Carbohydr. Polym.* **2018**, *199*, 41–50. [CrossRef]
42. Kong, Y.; Wang, L.; Ge, Y.; Su, H.; Li, Z. Lignin xanthate resin–bentonite clay composite as a highly effective and low-cost adsorbent for the removal of doxycycline hydrochloride antibiotic and mercury ions in water. *J. Hazard. Mater.* **2019**, *368*, 33–41. [CrossRef] [PubMed]
43. Peng, X.; Chen, L.; Liu, S.; Hu, L.; Zhang, J.; Wang, A.; Yu, X.; Yan, Z. Insights into the interfacial interaction mechanisms of p-arsanilic acid adsorption on ionic liquid modified porous cellulose. *J. Environ. Chem. Eng.* **2021**, *9*, 105225. [CrossRef]
44. Rusu, L.; Grigoraș, C.-G.; Simion, A.-I.; Suceveanu, E.M.; Șuteu, D.; Harja, M. Application of *Saccharomyces cerevisiae*/Calcium Alginate Composite Beads for Cephalexin Antibiotic Biosorption from Aqueous Solutions. *Materials* **2021**, *14*, 4728. [CrossRef]
45. Shokri, M.; Mojtabavi, S.; Jafari-Nodoushan, H.; Vojdanitalab, K.; Golshani, S.; Jahandar, H.; Faramarzi, M.A. Laccase-loaded magnetic dialdehyde inulin nanoparticles as an efficient heterogeneous natural polymer-based biocatalyst for removal and detoxification of ofloxacin. *Biodegradation* **2022**, *33*, 489–508. [CrossRef] [PubMed]
46. Şahin, M.; Arslan, Y.; Tomul, F. Removal of naproxen and diclofenac using magnetic nanoparticles/nanocomposites. *Res. Chem. Intermed.* **2022**, *48*, 5209–5226. [CrossRef]
47. Rusu, L.; Grigoraș, C.-G.; Simion, A.-I.; Suceveanu, E.-M.; Blaga, A.-C.; Harja, M. Encapsulation of *Saccharomyces pastorianus* Residual Biomass in Calcium Alginate Matrix with Insights in Ethacridine Lactate Biosorption. *Polymers* **2022**, *14*, 170. [CrossRef] [PubMed]
48. Rusu, L.; Grigoraș, C.-G.; Simion, A.-I.; Suceveanu, E.-M.; Dediu Botezatu, A.V.; Harja, M. Biosorptive Removal of Ethacridine Lactate from Aqueous Solutions by *Saccharomyces pastorianus* Residual Biomass/Calcium Alginate Composite Beads: Fixed-Bed Column Study. *Materials* **2022**, *15*, 4657. [CrossRef]
49. Tang, F.H.M.; Lenzen, M.; McBratney, A.; Maggi, F. Risk of pesticide pollution at the global scale. *Nat. Geosci.* **2021**, *14*, 206–210. [CrossRef]
50. Mie, A.; Rudén, C. What you don't know can still hurt you-underreporting in EU pesticide regulation. *Environ. Health* **2022**, *21*, 79. [CrossRef]
51. du Jardin, P. Plant biostimulants: Definition, concept, main categories and regulation. *Sci. Hortic.* **2015**, *196*, 3–14. [CrossRef]

52. European Parliament. Regulation (EU) 2019/1009 of the European Parliament and of the Council of 5 June 2019 Laying down Rules on the Making Available on the Market of EU Fertilising Products and Amending Regulations (EC) No 1069/2009 and (EC) No 1107/2009 and Repealing Regulation (EC) No 2003/2003. Available online: https://eur-lex.europa.eu/legal-content/EN/TXT/?uri=CELEX%3A02019R1009-20230316 (accessed on 21 March 2023).
53. Sehaqui, H.; de Larraya, U.P.; Tingaut, P.; Zimmermann, T. Humic acid adsorption onto cationic cellulose nanofibers for bioinspired removal of copper(II) and a positively charged dye. *Soft Matter* **2015**, *11*, 5294–5300. [CrossRef]
54. Liu, Z.; Zhou, S. Removal of humic acid from aqueous solution using polyacrylamide/chitosan semi-IPN hydrogel. *Water Sci. Technol.* **2018**, *2017*, 16–26. [CrossRef] [PubMed]
55. Kim, J.H.; Kim, S.B.; Lee, S.H.; Choi, J.W. Laboratory and pilot-scale field experiments for application of iron oxide nanoparticle-loaded chitosan composites to phosphate removal from natural water. *Environ. Technol.* **2018**, *39*, 770–779. [CrossRef]
56. Hossain, M.E.; Ritt, C.L.; Almeelbi, T.B.; Bezbaruah, A.N. Biopolymer Beads for Aqueous Phosphate Removal: Possible Applications in Eutrophic Lakes. *J. Environ. Eng.* **2018**, *144*, 04018030. [CrossRef]
57. Hu, X.; Xu, G.; Zhang, H.; Li, M.; Tu, Y.; Xie, X.; Zhu, Y.; Jiang, L.; Zhu, X.; Ji, X.; et al. Multifunctional β-Cyclodextrin Polymer for Simultaneous Removal of Natural Organic Matter and Organic Micropollutants and Detrimental Microorganisms from Water. *ACS Appl. Mater. Interfaces* **2020**, *12*, 12165–12175. [CrossRef]
58. Attallah, O.A.; Wafa, M.M.A.; Al-Ghobashy, M.A.; Nebsen, M.; Monir, H.H. Adsorptive removal of pesticides from aqueous solutions using chitosan/gelatin polymeric composite: Process monitoring and optimization. *Int. J. Environ. Sci. Technol.* **2022**, *19*, 8183–8194. [CrossRef]
59. Merlo, F.; Profumo, A.; Fontàs, C.; Anticó, E. Preparation of new polymeric phases for thin-film liquid phase microextraction (TF-LPME) of selected organic pollutants. *Microchem. J.* **2022**, *175*, 107120. [CrossRef]
60. Sun, L.; Xu, G.; Tu, Y.; Zhang, W.; Hu, X.; Yang, P.; Wu, D.; Liang, Y.; Wei, D.; Li, A.; et al. Multifunctional porous β-cyclodextrin polymer for water purification. *Water Res.* **2022**, *222*, 118917. [CrossRef]
61. Lellis, B.; Fávaro-Polonio, C.Z.; Pamphile, J.A.; Polonio, J.C. Effects of textile dyes on health and the environment and bioremediation potential of living organisms. *Biotechnol. Res. Innov.* **2019**, *3*, 275–290. [CrossRef]
62. Khan, S.; Naushad, M.; Govarthanan, M.; Iqbal, J.; Alfadul, S.M. Emerging contaminants of high concern for the environment: Current trends and future research. *Environ. Res.* **2022**, *207*, 112609. [CrossRef]
63. Singh, J.; Gupta, P.; Das, A. Dyes from Textile Industry Wastewater as Emerging Contaminants in Agricultural Fields. In *Sustainable Agriculture Reviews 50*; Kumar Singh, V., Singh, R., Lichtfouse, E., Eds.; Springer: Cham, Switzerland, 2021; Volume 50, pp. 109–129.
64. Khan, I.; Saeed, K.; Zekker, I.; Zhang, B.; Hendi, A.H.; Ahmad, A.; Ahmad, S.; Zada, N.; Ahmad, H.; Shah, L.A.; et al. Review on Methylene Blue: Its Properties, Uses, Toxicity and Photodegradation. *Water* **2022**, *14*, 242. [CrossRef]
65. Geetha, D.; Kavitha, S.; Ramesh, P.S. A novel bio-degradable polymer stabilized Ag/TiO_2 nanocomposites and their catalytic activity on reduction of methylene blue under natural sun light. *Ecotoxicol. Environ. Saf.* **2015**, *121*, 126–134. [CrossRef]
66. Sun, X.F.; Liu, B.; Jing, Z.; Wang, H. Preparation and adsorption property of xylan/poly(acrylic acid) magnetic nanocomposite hydrogel adsorbent. *Carbohydr. Polym.* **2015**, *118*, 16–23. [CrossRef]
67. Li, M.; Wang, Z.; Li, B. Adsorption behaviour of congo red by cellulose/chitosan hydrogel beads regenerated from ionic liquid. *Desalin. Water Treat.* **2016**, *57*, 16970–16980. [CrossRef]
68. Ling, S.; Jin, K.; Kaplan, D.L.; Buehler, M.J. Ultrathin Free-Standing Bombyx mori Silk Nanofibril Membranes. *Nano Lett.* **2016**, *16*, 3795–3800. [CrossRef]
69. Sultana, S.; Ahmad, N.; Faisal, S.M.; Owais, M.; Sabir, S. Synthesis, characterisation and potential applications of polyaniline/chitosan-Ag-nanobiocomposite. *IET Nanobiotechnol.* **2017**, *11*, 835–842. [CrossRef]
70. Cui, G.; Wang, X.; Xun, J.; Lou, T. Microwave assisted synthesis and characterization of a ternary flocculant from chitosan, acrylamide and lignin. *Int. Biodeter. Biodegrad.* **2017**, *123*, 269–275. [CrossRef]
71. Huang, W.; Hu, Y.; Li, Y.; Zhou, Y.; Niu, D.; Lei, Z.; Zhang, Z. Citric acid-crosslinked β-cyclodextrin for simultaneous removal of bisphenol A, methylene blue and copper: The roles of cavity and surface functional groups. *J. Taiwan Inst. Chem. Eng.* **2018**, *82*, 189–197. [CrossRef]
72. Domínguez-Robles, J.; Peresin, M.S.; Tamminen, T.; Rodríguez, A.; Larrañeta, E.; Jääskeläinen, A.S. Lignin-based hydrogels with "super-swelling" capacities for dye removal. *Int. J. Biol. Macromol.* **2018**, *115*, 1249–1259. [CrossRef] [PubMed]
73. Yu, L.L.; Jiang, L.N.; Wang, S.Y.; Sun, M.M.; Li, D.Q.; Du, G.M. Pectin microgel particles as high adsorption rate material for methylene blue: Performance, equilibrium, kinetic, mechanism and regeneration studies. *Int. J. Biol. Macromol.* **2018**, *112*, 383–389. [CrossRef] [PubMed]
74. El-Aassar, M.R.; Fakhry, H.; Elzain, A.A.; Farouk, H.; Hafez, E.E. Rhizofiltration system consists of chitosan and natural Arundo donax L. for removal of basic red dye. *Int. J. Biol. Macromol.* **2018**, *120*, 1508–1514. [CrossRef] [PubMed]
75. Chen, T.; Shi, P.; Zhang, J.; Li, Y.; Duan, T.; Dai, L.; Wang, L.; Yu, X.; Zhu, W. Natural polymer konjac glucomannan mediated assembly of graphene oxide as versatile sponges for water pollution control. *Carbohydr. Polym.* **2018**, *202*, 425–433. [CrossRef] [PubMed]
76. Mohamed, S.K.; Hegazy, S.H.; Abdelwahab, N.A.; Ramadan, A.M. Coupled adsorption-photocatalytic degradation of crystal violet under sunlight using chemically synthesized grafted sodium alginate/ZnO/graphene oxide composite. *Int. J. Biol. Macromol.* **2018**, *108*, 1185–1198. [CrossRef] [PubMed]

77. Mallakpour, S.; Tabesh, F. Tragacanth gum based hydrogel nanocomposites for the adsorption of methylene blue: Comparison of linear and non-linear forms of different adsorption isotherm and kinetics models. *Int. J. Biol. Macromol.* **2019**, *133*, 754–766. [CrossRef] [PubMed]
78. Lou, T.; Yan, X.; Wang, X. Chitosan coated polyacrylonitrile nanofibrous mat for dye adsorption. *Int. J. Biol. Macromol.* **2019**, *135*, 919–925. [CrossRef]
79. Ernawati, L.; Wahyuono, R.A.; Halim, A.; Noorain, R.; Widiyastuti, W.; Dewi, R.T.; Enomae, T. Hierarchically 3-D Porous Structure of Silk Fibroin-Based Biocomposite Adsorbent for Water Pollutant Removal. *Environments* **2021**, *8*, 127. [CrossRef]
80. Hong, G.-B.; Yu, T.-J.; Lee, H.-C.; Ma, C.-M. Using Rice Bran Hydrogel Beads to Remove Dye from Aqueous Solutions. *Sustainability* **2021**, *13*, 5640. [CrossRef]
81. Mallakpour, S.; Azadi, E.; Dinari, M. Novel mesoporous cupric oxide-based biomaterial: An efficient nanocatalyst toward catalytic reduction of emerging contaminants in the wastewater. *J. Clean. Prod.* **2022**, *378*, 134527. [CrossRef]
82. El Sayed, A.A.; Ali, M.M.S.; Helal, A.A. Synthesis of chitosan hydrogel polymer for removal of radioactive organic research waste prior to treatment. *Int. J. Environ. Analyt. Chem.* **2023**, *103*, 454–468. [CrossRef]
83. Ma, S.; Shi, W.; Li, H.; Zhang, Y. Biomimetic mineralization of nacre-inspired multiple crosslinked PVA/CaAlg/SiO_2 membrane with simultaneously enhanced mechanical and separation properties. *Int. J. Biol. Macromol.* **2023**, *234*, 123650. [CrossRef]
84. Alshahrani, A.A.; Alorabi, A.Q.; Hassan, M.S.; Amna, T.; Azizi, M. Chitosan-Functionalized Hydroxyapatite-Cerium Oxide Heterostructure: An Efficient Adsorbent for Dyes Removal and Antimicrobial Agent. *Nanomaterials* **2022**, *12*, 2713. [CrossRef]
85. Robati, D. Pseudo-second-order kinetic equations for modeling adsorption systems for removal of lead ions using multi-walled carbon nanotube. *J. Nanostructure Chem.* **2013**, *3*, 55. [CrossRef]
86. Paneysar, J.S.; Barton, S.; Chandra, S.; Ambre, P.; Coutinho, E. Novel thermoresponsive assemblies of co-grafted natural and synthetic polymers for water purification. *Water Sci. Technol.* **2017**, *75*, 1084–1097. [CrossRef] [PubMed]
87. Yang, Z.; Ren, K.; Guibal, E.; Jia, S.; Shen, J.; Zhang, X.; Yang, W. Removal of trace nonylphenol from water in the coexistence of suspended inorganic particles and NOMs by using a cellulose-based flocculant. *Chemosphere* **2016**, *161*, 482–490. [CrossRef]
88. Xiao, L.; Ling, Y.; Alsbaiee, A.; Li, C.; Helbling, D.E.; Dichtel, W.R. β-Cyclodextrin Polymer Network Sequesters Perfluorooctanoic Acid at Environmentally Relevant Concentrations. *J. Am. Chem. Soc.* **2017**, *139*, 7689–7692, correction to *J. Am. Chem. Soc.* **2017**, *139*, 10585. [CrossRef]
89. Ge, L.; Zhang, M.; Wang, R.; Li, N.; Zhang, L.; Liu, S.; Jiao, T. Fabrication of CS/GA/RGO/Pd composite hydrogels for highly efficient catalytic reduction of organic pollutants. *RSC Adv.* **2020**, *10*, 15091–15097. [CrossRef] [PubMed]
90. Liu, X.; Xue, P.; Jia, F.; Qiu, D.; Shi, K.; Zhang, W. Tailoring polymeric composite gel beads-encapsulated microorganism for efficient degradation of phenolic compounds. *Chinese J. Chem. Eng.* **2021**, *32*, 301–306. [CrossRef]
91. Balram, D.; Lian, K.Y.; Sebastian, N.; Al-Mubaddel, F.S.; Noman, M.T. Bi-functional renewable biopolymer wrapped CNFs/Ag doped spinel cobalt oxide as a sensitive platform for highly toxic nitroaromatic compound detection and degradation. *Chemosphere* **2022**, *291*, 132998. [CrossRef]
92. Mallakpour, S.; Amini, Z. Green synthesis of Ag ultra-fine nano-catalyst supported on layered double oxide and chitosan: Accelerated reduction of 4-nitrophenol to 4-aminophenol. *J. Clean. Prod.* **2022**, *381*, 135154. [CrossRef]
93. Ling, Y.; Klemes, M.J.; Xiao, L.; Alsbaiee, A.; Dichtel, W.R.; Helbling, D.E. Benchmarking Micropollutant Removal by Activated Carbon and Porous β-Cyclodextrin Polymers under Environmentally Relevant Scenarios. *Environ. Sci. Technol.* **2017**, *51*, 7590–7598. [CrossRef]
94. Topuz, F.; Holtzl, T.; Szekely, G. Scavenging organic micropollutants from water with nanofibrous hypercrosslinked cyclodextrin membranes derived from green resources. *Chem. Eng. J.* **2021**, *419*, 129443. [CrossRef]
95. Ebele, A.J.; Abdallah, M.A.E.; Harrad, S. Pharmaceuticals and personal care products (PPCPs) in the freshwater aquatic environment. *Emerg. Contam.* **2017**, *3*, 1–16. [CrossRef]
96. Patel, A.B.; Shaikh, S.; Jain, K.R.; Desai, C.; Madamwar, D. Polycyclic Aromatic Hydrocarbons: Sources, Toxicity, and Remediation Approaches. *Front. Microbiol.* **2020**, *11*, 562813. [CrossRef]
97. Låg, M.; Øvrevik, J.; Refsnes, M.; Holme, J.A. Potential role of polycyclic aromatic hydrocarbons in air pollution-induced non-malignant respiratory diseases. *Respir. Res* **2020**, *21*, 299. [CrossRef]
98. Honda, M.; Suzuki, N. Toxicities of Polycyclic Aromatic Hydrocarbons for Aquatic Animals. *Int. J. Environ. Res. Public Health* **2020**, *17*, 1363. [CrossRef] [PubMed]
99. Arteta, S.M.; Vera, R.; Pérez, L.D. Hydrophobic cellulose fibers via ATRP and their performance in the removal of pyrene from water. *J. Appl. Polym. Sci.* **2017**, *134*, 44482. [CrossRef]
100. Mehmandost, N.; Soriano, M.L.; Lucena, R.; Goudarzi, N.; Chamjangali, M.A.; Cardenas, S. Recycled polystyrene-cotton composites, giving a second life to plastic residues for environmental remediation. *J. Environ. Chem. Eng.* **2019**, *7*, 103424. [CrossRef]
101. Fu, Z.; Zhou, S.; Xia, L.; Mao, Y.; Zhu, L.; Cheng, Y.; Wang, A.; Zhang, C.; Xu, W. *Juncus effusus* fiber-based cellulose cigarette filter with 3D hierarchically porous structure for removal of PAHs from mainstream smoke. *Carbohydr. Polym.* **2020**, *241*, 116308. [CrossRef] [PubMed]
102. Batool, A.; Valiyaveettil, S. Surface functionalized cellulose fibers—A renewable adsorbent for removal of plastic nanoparticles from water. *J. Hazard. Mater.* **2021**, *413*, 125301. [CrossRef] [PubMed]

103. Gomez-Maldonado, D.; Reynolds, A.M.; Johansson, L.S.; Burnett, D.J.; Ramapuram, J.B.; Waters, M.N.; Erramuspe, I.B.V.; Peresin, M.S. Fabrication of aerogels from cellulose nanofibril grafted with β-cyclodextrin for capture of water pollutants. *J. Porous Mater.* **2021**, *28*, 1725–1736. [CrossRef]
104. Hassan (El-Moushy), R.M. Novel synthesis of natural cation exchange resin by crosslinking the sodium alginate as a natural polymer with 1,6-hexamethylene diisocyanate in inert solvents: Characteristics and applications. *Int. J. Biol. Macromol.* **2021**, *184*, 926–935. [CrossRef] [PubMed]
105. Zhang, J.; Jia, W.; Yan, Y.; Zhao, S. Coagulation removal and recycling strategy of TiO_2 nanoparticles based on *Enteromorpha prolifera* polysaccharide application. *J. Water Proc. Eng.* **2022**, *49*, 103083. [CrossRef]
106. Campo, J.; Picó, Y. Emerging contaminants and toxins. In *Chemical Analysis of Food. Techniques and Applications*, 2nd ed.; Pico, Y., Ed.; Academic Press: London, UK, 2020; pp. 729–758.
107. Lambert, S.; Wagner, M. Microplastics Are Contaminants of Emerging Concern in Freshwater Environments: An Overview. In *Freshwater Microplastics. The Handbook of Environmental Chemistry*; Wagner, M., Lambert, S., Eds.; Springer: Cham, Switzerland, 2018; Volume 58, pp. 1–23.
108. Bhuyan, M.S. Effects of Microplastics on Fish and in Human Health. *Front. Environ. Sci.* **2022**, *10*, 827289. [CrossRef]
109. González-Pleiter, M.; Cirés, S.; Wörmer, L.; Agha, R.; Pulido-Reyes, G.; Martín-Betancor, K.; Rico, A.; Leganés, F.; Quesada, A.; Fernández-Piñas, F. Ecotoxicity assessment of microcystins from freshwater samples using a bioluminescent cyanobacterial bioassay. *Chemosphere* **2020**, *240*, 124966. [CrossRef]
110. Lad, A.; Breidenbach, J.D.; Su, R.C.; Murray, J.; Kuang, R.; Mascarenhas, A.; Najjar, J.; Patel, S.; Hegde, P.; Youssef, M.; et al. As We Drink and Breathe: Adverse Health Effects of Microcystins and Other Harmful Algal Bloom Toxins in the Liver, Gut, Lungs and Beyond. *Life* **2022**, *12*, 418. [CrossRef]
111. Commission Regulation (EU) No 231/2012 of 9 March 2012 Laying down Specifications for Food Additives Listed in Annexes II and III to Regulation (EC) No 1333/2008 of the European Parliament and of the Council. Available online: https://eur-lex.europa.eu/legal-content/EN/ALL/?uri=CELEX%3A32012R0231 (accessed on 1 April 2023).
112. Przybyla, M.A.; Yilmaza, G.; Becer, C.R. Natural cyclodextrins and their derivatives for polymer synthesis. *Polym. Chem.* **2020**, *11*, 7582–7602. [CrossRef]
113. Kunwar, B.; Mondal, S.; Saini, V.K.; Bahukhandi, K.D.; Kumar, A. Utilization of barks of *Araucaria columnaris*: Preparation of activated carbon/clay composite beads and adsorptive treatment of phenolic wastewater. *Ind. Crop. Prod.* **2023**, *197*, 116534. [CrossRef]
114. Hussain, O.A.; Hathout, A.S.; Abdel-Mobdy, Y.E.; Rashed, M.M.; Abdel Rahim, E.A.; Fouzy, A.S.M. Preparation and characterization of activated carbon from agricultural wastes and their ability to remove chlorpyrifos from water. *Toxicol. Rep.* **2023**, *10*, 146–154. [CrossRef]

Disclaimer/Publisher's Note: The statements, opinions and data contained in all publications are solely those of the individual author(s) and contributor(s) and not of MDPI and/or the editor(s). MDPI and/or the editor(s) disclaim responsibility for any injury to people or property resulting from any ideas, methods, instructions or products referred to in the content.

polymers

MDPI

Article

Force-Based Characterization of the Wetting Properties of LDPE Surfaces Treated with CF_4 and H_2 Plasmas

Cihan Aktas [1], Osman Polat [1], Mohamadreza Beitollahpoor [2], Melika Farzam [2], Noshir S. Pesika [2] and Nurettin Sahiner [1,3,4,*]

[1] Department of Chemical, Biomolecular and Materials Engineering, University of South Florida, Tampa, FL 33620, USA
[2] Chemical and Biomolecular Engineering Department, Tulane University, New Orleans, LA 70118, USA
[3] Department of Ophthalmology, Morsani College of Medicine, University of South Florida, 12901 Bruce B. Downs Blvd, MDC21, Tampa, FL 33612, USA
[4] Department of Chemistry, Faculty of Science and Arts & Nanoscience, Technology Research and Application Center (NANORAC), Canakkale Onsekiz Mart University, Terzioglu Campus, 17100 Canakkale, Turkey
* Correspondence: sahiner71@gmail.com or nsahiner@usf.edu

Abstract: Low-density polyethylene (LDPE) films are widely used in packaging, insulation and many other commodity applications due to their excellent mechanical and chemical properties. However, the water-wetting and water-repellant properties of these films are insufficient for certain applications. In this study, bare LDPE and textured LDPE (T-LDPE) films were subjected to low-pressure plasmas, such as carbon tetrafluoride (CF_4) and hydrogen (H_2), to see the effect of plasma treatment on the wetting properties of LDPE films. In addition, the surface of the LDPE film was textured to improve the hydrophobicity through the lotus effect. The LDPE and T-LDPE films had contact angle (θ) values of 98.6° ± 0.6 and 143.6° ± 1.0, respectively. After CF_4 plasma treatments, the θ values of the surfaces increased for both surfaces, albeit within the standard deviation for the T-LDPE film. On the other hand, the contact angle values after H_2 plasma treatment decreased for both surfaces. The surface energy measurements supported the changes in the contact angle values: exposure to H_2 plasma decreased the contact angle, while exposure to CF_4 plasma increased the contact angle. Kinetic friction force measurements of water drops on LDPE and T-LDPE films showed a decrease in friction after the CF4 plasma treatment, consistent with the contact angle and surface energy measurements. Notably, the kinetic friction force measurements proved to be more sensitive compared to the contact angle measurements in differentiating the wetting properties of the T-LDPE versus 3× CF_4-plasma-treated LDPE films. Based on Atomic Force Microscopy (AFM) images of the flat LDPE samples, the 3× CF4 plasma treatment did not significantly change the surface morphology or roughness. However, in the case of the T-LDPE samples, Scanning Electron Microscopy (SEM) images showed noticeable morphological changes, which were more significant at sharp edges of the surface structures.

Keywords: LDPE; plasma modification; surface texture; wetting properties of LDPE; lotus effect

Citation: Aktas, C.; Polat, O.; Beitollahpoor, M.; Farzam, M.; Pesika, N.S.; Sahiner, N. Force-Based Characterization of the Wetting Properties of LDPE Surfaces Treated with CF_4 and H_2 Plasmas. *Polymers* **2023**, *15*, 2132. https://doi.org/10.3390/polym15092132

Academic Editors: Fahmi Zaïri, Matthias Ballauff, Ulrich Maschke, Rufina G. Alamo and Martin Kröger

Received: 2 April 2023
Revised: 21 April 2023
Accepted: 27 April 2023
Published: 29 April 2023

Copyright: © 2023 by the authors. Licensee MDPI, Basel, Switzerland. This article is an open access article distributed under the terms and conditions of the Creative Commons Attribution (CC BY) license (https://creativecommons.org/licenses/by/4.0/).

1. Introduction

Polymers are crucial materials in various fields, such as packaging, adhesives, automotive and even the biomedical field [1]. Because of their inert nature and desired mechanical properties with tunable functional properties, polymers have replaced traditional engineering materials, such as metals and wood, and have been used in many forms and shapes, such as films, disk, plates, wire, foams, etc. [2,3]. Low-density polyethylene (LDPE) is one of the most widely used polymers in several industries, and its production is well established, easy and cheap [4,5]. Although LDPE has superior thermal, electrical and mechanical properties, it possesses a low surface free energy that affects its wettability and adhesion. LDPE similar to most of the commodity polymers are inert, and there are

several contamination layers on the surface, e.g., low-molecular-weight oligomers, additives, release agents, oil, etc. [6–8]. Those contaminations make the bonding on the surface of LDPE even more challenging [9]. Most of the industrial and biomedical applications require additional modifications of the polymer surfaces [9,10]. By changing the surface properties, it is possible to improve the wettability, printability and biocompatibility and, hence, enhance the applications of the polymers [11,12].

There are several methods available for the surface modifications of polymers. For example, Shenton et al. used atmospheric pressure plasma to increase the adhesive property of LDPE and polyethylene terephthalate (PET) [9]. Cheng et al. used the vapor phase deposition-initiated roll-to-roll method to modify cellulose chromatography paper [13]. Nejati et al. reported using lasers to functionalize the surface of carbon to attach silver nanoparticles on it [14]. Strobel and his coworkers exposed polypropylene (PP) to flames to improve its wettability [15]. Netravali and his colleagues used pulsed argon ion beams to increase the hydrophilicity of ultra-high-strength polyethylene fibers [16]. Further, even wet chemical techniques are available to functionalize the surface of crystals, such as gallium phosphide crystalline [17].

The low-pressure, cold plasma technique has many advantages for the surface modification of polymers [18–21]. Plasma treatment alters only a few tens to hundred angstroms of the samples' surface, while the bulk material remains unchanged [22]. Plasma gas treatment shows better homogeneity on surface modifications of polymers than corona discharge or flame exposure methods [18,23]. The treatments after the plasma process show better uniformity on the treated sample [24,25]. Furthermore, the exposure time can be kept noticeably short [26], and the parameters can be adjusted well and tuned with variable plasma gases and do not require any drying processes, such as wet chemical processes and solvent removal [27]. The plasma gas technique is ecological when the absence of chemical waste is considered [28]. Since it is a dry process, plasma treatment affords significant advantages for industrial applications.

In this study, commercially available LDPE and physically altered LDPE films (i.e., microtextured, as shown in Figure S1) were treated with CF_4 and H_2 plasmas. The plasma treatments were performed multiple times, e.g., up to three times, and the changes in the surface energy, water contact angle and roll-of angle were measured. The surface topography of textured LDPE (T-LDPE) samples was examined with the help of scanning electron microscopy (SEM, Hitachi 3400 electron microscope, Santa Clara, CA, USA), and the wetting properties of the surfaces were characterized by contact angle and sliding angle measurements, as well as by force-based friction measurements between a water drop and the films. This study shows the combined effects of the low-pressure plasma treatment and the surface texturing method on LDPE films.

2. Materials and Methods

2.1. Plasma Treatment

All the experiments for the capacitively coupled plasma gas treatments were conducted via a low-pressure radio frequency (RF,13.56 MHz) plasma generator instrument (Femto AR-PC, Diener Electronic, Ebhausen, Germany). The low-pressure chamber of the plasma generator was evacuated by a rotary vane pump (16 m^3/h, Trivac D16BCS, Leybold Vakuum GmbH, Köln, Germany), and the pressure was monitored using a Pirani sensor. The inlet gas was introduced into the chamber at a flow rate of 1 mL/min by the mass flow controller of the plasma generator. The optimal working conditions of the plasma generator were set at 0.3 mbar, and the pressure was kept constant at that value during the plasma gas exposure. In the treatments of LDPE, H_2 and CF_4 gas plasmas were used. To dispose of the undesired gases from previous runs and the accumulated air from the waiting time, the plasma generator ran empty for 15 min prior to each plasma treatment. To determine the optimum parameters for the employed plasma gases, the LDPE samples were exposed to plasma gases for 2, 4, 6, 8, 10 and 15 min. For each time duration, the plasma power was varied as 30, 90 and 150 W values. After treatments, the water contact angles (CAs) were

measured via an optical tensiometer (Biolin Scientific, Attention Theta Flex, Phoenix, AZ, USA). A 150 W, 15 min exposure resulting in the highest CA value for the CF_4 treatment was chosen, whereas the lowest-CA-value resulting treatment from H_2 treatments was set with the optimum parameters of 30 W and 8 min.

To see the difference in single and multiple plasma gas treatments, samples were treated one time and three times with the same plasma gas. After treatments, the wetting properties, such as surface free energy, CA, sliding angle and water drop friction, were measured.

2.2. Surface Texturing of LDPE

Laser machining (CAJO, Technologies, New Orleans, LA, USA) was used to create a square lattice of circular holes (100 μm in diameter with 150 μm center-to-center spacing) on stainless steel. The latter served as a mold to create the textured LDPE films. In a typical molding step, the stainless-steel mold was preheated on a hotplate to 140 °C. A smooth LDPE film was placed on the mold and allowed to melt. Once the LDPE film turned translucent, a Teflon roller (McMaster-Carr, Douglasville, GA, USA) was used to compress the film so as to ensure that the liquid LDPE entered the holes in the stainless-steel mold. The latter was then cooled to room temperature, and the LDPE film was peeled off the surface, resulting in the textured LDPE film.

2.3. Measurements of Wetting Properties Using Contact Angles

The effect of functionalization via plasma treatment was assessed by the change in the wetting properties of the LDPE plate. The characterization of the plasma-treated samples' CA values was measured via an optical tensiometer. For the CA and surface free energy measurements, the sessile drop method was utilized. A 6 μL volume of liquid dropped on the surface of the sample was used, and 332 frames were recorded in 10 s.

In the sliding angle measurements, a volume of 100 μL distilled (DI) water was used. The sample holder was tilted at a rate of 90° per minute until the droplet slid off the sample surface. During the tilting, the droplets were captured at 5.5 frames per second (FPS), and the changes in CA on both sides of the drop were also recorded to measure the contact angle hysteresis (CAH). The CA, surface free energy and sliding angle CAH results were presented as the average of three different measurements. For the analysis of wetting properties, a software (One Attention from Biolin Scientific, Phoenix, AZ, USA, version 4.2.0) was used.

The OWRK (Owen, Wendt, Rabel and Kaelble) Model was utilized to evaluate the surface free energy of the polymer [29–32]. This model uses dispersive and polar force components of the material to calculate the surface free energy. The following equation, Equation (1), was used to determine the samples surface tensions.

$$\left(\gamma_{sv}^{d}\gamma_{lv}^{d}\right)^{\frac{1}{2}} + \left(\gamma_{sv}^{p}\gamma_{lv}^{p}\right)^{\frac{1}{2}} = 0.5 + \gamma_{lv}(1+\cos(\theta_Y)) \quad (1)$$

where γ_{sv} and γ_{lv} are the surface tensions of the solids and liquids, respectively; superscripts "d" and "p" are the dispersive and polar force components; and, finally, θ_Y is the contact angle of the liquid. Previous studies show using water and diiodomethane produces the most accurate results [31,33]. For that reason, DI water and diiodomethane were used for the calculation of dispersive and polar force components.

2.4. Measurements of Wetting Properties using Force-Based Friction Measurements

A nanotribometer (UMT Multi-specimen Test system, Bruker (formally CETR), San Jose, CA, USA) with a sensitivity of ± 1 μN and a force range of ±10 mN was used to measure normal and lateral friction forces. The protocol developed by Beitollahpoor et al. [34] was followed. A total of 20 μL water drops were placed on a copper ring probe, with an inside diameter of 2.3 mm, and covered by a PDMS layer on the top so as to prevent each water drop from passing through the probe during compression of the drop on the

surfaces (Figure S2). In a typical run, the water drop held by the ring probe was brought into contact with the SH surface at the velocity of 2 mm/s. Once the drop touched the surface, a predetermined preload was applied on the drop for 20 s to allow the solid/liquid interface to equilibrate (resting time) within the static regime. In the next step, the ring probe began to move laterally, thereby sliding the drop on the surface under a constant load, at a velocity of 0.1 mm/s for 30 s. The feedback controller of the instruments ensured that the load was maintained at the desired value throughout this step. In the transition step, while the ring was moving, the water drop remained pinned on the SH surface, and the static friction increased. Typically, the highest friction force was obtained at the very moment the receding edge of the water drop began to slide, i.e., the static friction force, $F_{\parallel}^{static}$, or the threshold force. The transition regime was followed by the kinetic regime, in which the water drop slid while overcoming the dynamic friction force, $F_{\parallel}^{kinetic}$, on the SH surface. The drop was finally pulled off of the surface in the last step. Generally, if the surface is homogenous and void of defects, $F_{\parallel}^{static}$ is greater than $F_{\parallel}^{kinetic}$. Each run was repeated at least five times, and the error bars correspond to the standard deviations.

3. Results

3.1. Contact Angle and Surface Free Energy Measurements

The effect of two different plasmas, CF_4 and H_2, on the surface of LDPE was studied. For these two different LDPE surfaces, smooth and textured with microstructures were employed. Plasma treatment of the surfaces with either H_2 or CF_4 rendered the LDPE surfaces more hydrophilic or hydrophobic with respect to a virgin LDPE surface. The effect of multiple plasma treatments (1× or 3×) was also investigated to determine whether further modification after the first plasma treatments was possible.

The CA measurements were determined right after the plasma treatment of LDPE with CF_4 and H_2 plasma gases. Figure 1 shows the change in the CA of H_2- and CF_4-plasma-gas-treated samples.

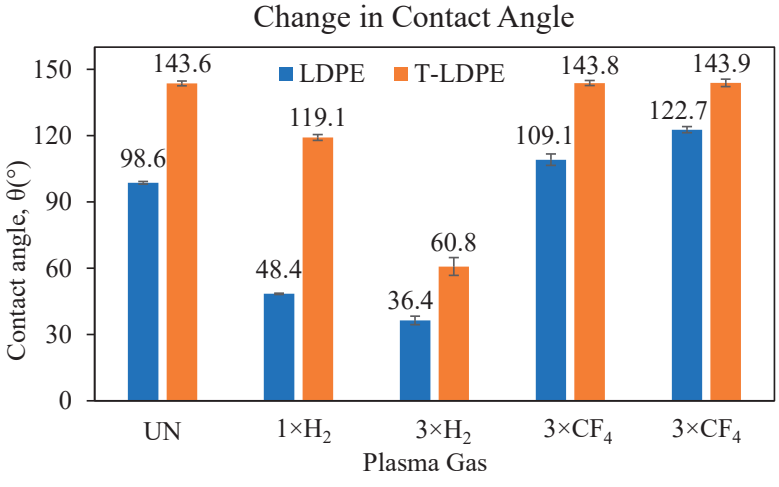

Figure 1. Contact angle (CA) values of LDPE and T-LDPE samples upon multiple H_2 and CF_4 plasma treatments.

After texturing the LDPE films, T-LDPE, the CA values increased drastically from 98.6° ± 0.6 to 143.6° ± 1.0. Since LDPE is inherently hydrophobic, the addition of surface roughness and texture is expected to increase the CA value. In this case, the surface texturing traps air pockets, and water drops remain in the Cassie–Baxter state [35]. After functionalization via CF_4 and H_2 plasma treatments, the wetting behavior of the smooth LDPE films showed a higher change than the T-LDPE samples. Upon H_2 plasma treatment,

the generation of radicals and species, such as H^+, H_2^+ and H_3^+, the functional groups on the surface of LDPE, reacts with air molecules and gases upon exposure to the atmospheric gases after the plasma treatment [36,37]. This can lead to the formation of more polar groups, such as double carbon bonds, hydroxyl, carboxyl, carbonyl, peroxide, ester and ether on the surface of the LDPE samples, which resulted in lower CA values, e.g., from 98.6° ± 0.6 to 36.4° ± 2.0 after the 3rd H_2 plasma treatment. This hydrophilicity is attributed to the increased interaction of the newly formed functional groups on the surface of LDPE with water molecules [38–40]. The T-LDPE samples followed a similar behavior, and their CA values changed from 143.6° ± 1.0 to 60.80° ± 4.0 after the 3rd H_2 plasma treatment. A reason for this could be the functionalization of additional surface groups after repeated H_2 plasma treatments. These results show that the chemical composition of the surfaces also plays a significant role in the surface wetting behavior, in addition to the surface morphology, emphasizing the availability of appropriate functional groups [41–43].

It was reported that the surface of the LDPE samples could be fluorinated upon CF_4 plasma treatment [41]. After introducing the C–CF, CF, CF_2 and CF_3 groups by means of CF_4 plasma treatments, the hydrophobicity of the materials increased [44–46]. The main reason for the increased hydrophobicity of fluorinated surfaces is the lower-density packing of fluorocarbons on those surfaces, which causes weaker van der Waals interactions with water [47]. Upon three consecutive CF_4 plasma treatments, the contact angle values for LDPE samples increased from 98.6° ± 0.6 up to 122.7° ± 1.4. On the other hand, the hydrophobicity of T-LDPE samples did not change significantly, as it was found to change 143.6° ± 1.0 to 143.9° ± 1.6 after the 3rd CF_4 plasma treatment. These results indicate that the polar force component of T-LDPE samples was almost unchanged after the CF_4 plasma treatment. The surface area of the T-LDPE in contact with the DI water droplet was much smaller in the Cassie–Baxter state in comparison to the LDPE with smooth surfaces, hence the adhesive forces, and this could be a reason for the unchanged contact angle values. Since the CA measurements were not sufficiently sensitive to detect changes in the wetting properties of the T-LDPE samples before and after CF_4 plasma treatment, a force-based measurement developed by Beitollahpoor et al. [34] was used and is presented in Section 3.3.

The surface free energies of the samples were also measured. Figure 2 depicts the changes of the surface free energies of LDPE samples after plasma treatments.

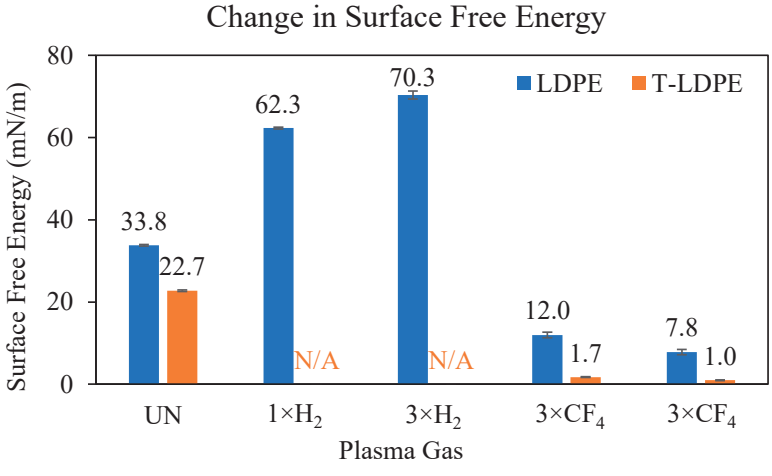

Figure 2. Change in surface free energies of LDPE samples and T-LDPE samples.

Since the measurements were determined with DI water and diiodomethane, the surface energy measurements can provide insight not only into the change in the polar force component, but also the change in the dispersive force component of the plasma-

treated LDPE and T-LDPE samples. The CA measurements resulted in an increase in hydrophilicity after H_2 plasma treatments for LDPE and T-LDPE. Therefore, the increase in the surface free energies was expected after H_2 plasma treatments. The surface free energy of LDPE increased from 33.8 ± 0.2 mN/m to 70.3 ± 1.0 mN/m after the 3rd H_2 plasma treatment. Unfortunately, the diiodomethane drops formed unmeasurable shapes on the surface of T-LDPE samples after H_2 plasma treatments; therefore, the surface free energy of these samples could not be measured.

CF_4 plasma treatments of both the LDPE and T-LDPE samples showed a decrease in surface free energies. These results were expected for LDPE samples, since the fluorination increased the hydrophobicity of the surface of the LDPE samples. The surface free energies of LDPE samples dropped from 33.8 ± 0.2 mN/m to 7.8 ± 0.7 mN/m after being treated 3 times with CF_4 plasma. Similarly, T-LDPE samples also dropped from 22.7 ± 0.2 mN/m to 1.0 ± 0.1 mN/m after the 3rd CF_4 plasma treatment. The surface free energy measurements show that the attraction from dispersive force component of both LDPE and T-LDPE surfaces decreased after the CF_4 plasma treatments.

3.2. Sliding Angle Measurements

Any chemical modifications on the sample surface also affects the necessary incline in the tilting angle to slide the droplets off the surface of LDPE and T-LDPE films. The tilting angle of the stage is referred to as the cradle angle, θ_c. Besides the sliding angles, the contact angle hysteresis (CAH) was also measured. During the tilting of the stage, gravitational force cause deformation in the shape of the droplets. This deformation leads to two results: (1) an increase in CA on one side of the droplets, which is called the advancing contact angle, θ_a, and (2) a decrease in CA on the other side of the droplets, known as the receding contact angle, θ_r. The difference between the advancing and the receding contact angle is the CAH [32,48,49]. On hydrophobic surfaces, the sliding occurs at low θ_C values, and the deformation in the shape of the droplets is usually very low. When the CA of a surface results in a value greater than 150°, the surface is called super hydrophobic. The CAH values of super-hydrophobic surfaces are close to 0°. The CAH measurements are summarized in Table 1, along with the values of various angles: the sliding angle (α), advancing contact angle (θ_a) and receding contact angle (θ_r) for LDPE and T-LDPE films after plasma gas treatments.

Table 1. Change in sliding angle (α), advancing contact angle (θ_a), receding contact angle (θ_r) and contact angle hysteresis (CAH) after plasma treatment of LDPE and T-LDPE samples.

Sample	Sliding Angle, α (°)	Advancing Contact Angle, θ_a (°)	Receding Contact Angle, θ_r (°)	Contact Angle Hysteresis, CAH = $\theta_a - \theta_r$ (°)
LDPE	12.5 ± 0.4	102.0 ± 0.8	80.1 ± 2.7	21.9
T-LDPE	6.9 ± 0.3	130.2 ± 3.5	110.5 ± 4.8	19.7
LDPE, 3× H_2	14.7 ± 1.9	47.6 ± 0.6	7.6 ± 0.5	40
T-LDPE, 3× H_2	38.2 ± 2.5	107.1 ± 3.5	23.2 ± 3.8	83.9
LDPE, 3× CF_4	27.2 ± 2.7	141.1 ± 1.0	81.1 ± 2.1	59.9
T-LDPE, 3× CF_4	1.7 ± 0.1	121.2 ± 0.7	118.3 ± 0.9	2.8

H_2-plasma-treated LDPE and T-LDPE samples show higher CAH values because of increased hydrophilicity. The sliding angle (α) for H_2-treated LDPE samples increased from 12.5° ± 0.4 to 14.7° ± 1.9. However, H_2 plasma treatment resulted in a much greater increase for T-LDPE samples. The surface roughness of T-LDPE samples can affect the droplets' grip on the surface. That effect can increase the droplet resistance against sliding off the T-LDPE surface. For CF_4-treated samples, on the other hand, the sliding angles of LDPE samples increased from 12.5° ± 0.4 to 27.2° ± 2.7. One reason for that could be the increased nanoscale roughness with the plasma etching, which can lead to drop pinning [41,50,51]. The increased roughness can make the droplets less prone to slide off

the surface of LDPE samples. The T-LDPE samples show almost perfect super-hydrophobic behavior after three consecutive CF_4 plasma treatments. The sliding angle drops from $6.9^\circ \pm 0.3$ down to $1.7^\circ \pm 0.1$, and the deformation on droplets is very low when compared to the other samples.

3.3. Force-Based Friction Measurements on T-LDPE Surfaces

Figure 3a compares the $F_{\parallel}^{kinetic}$ between a water drop and four surfaces: unmodified smooth LDPE, 3× CF_4-treated smooth LDPE, unmodified T-LDPE and 3× CF_4-treated T-LDPE. The force-based measurement could not be performed on the H_2 plasma-treated samples because the samples were too hydrophilic. As a result of the strong interaction between the water drop and the surface, the ring drop holder was unable to drag the water drop (i.e., the water drop remained pinned on the surface until it detached from the ring drop holder). An applied load equal to the weight of the 20 μL drop (i.e., 200 μN) was maintained during the measurement. The effect of the CF_4 treatment was apparent on both smooth and T-LDPE surfaces. In the case of the smooth LDPE surface, the $F_{\parallel}^{kinetic}$ dropped from an average value of 102 μN to 81.3 μN after the CF_4 treatment. The drop was even more significant on the T-LDPE surface, starting at an average value of 14.4 μN and decreasing to 3.17 μN after the CF_4 treatment. As demonstrated previously, CA measurements did not show significant differences between the unmodified and CF_4-plasma-treated T-LDPE samples, even after 3× treatments. Using the nanotribometer, loads ranging from 100 to 1000 μN were applied and maintained on 20 μL drops during shearing against the unmodified and CF_4-plasma-treated T-LDPE samples. Figure 3b shows a plot of $F_{\parallel}^{kinetic}$ as a function of the applied preload on a water drop as it is sheared on the T-LDPE surfaces. Under the entire load range of 100–1000 μN, the $F_{\parallel}^{kinetic}$ on the unmodified T-LDPE (yellow dashed lines) was greater than the $F_{\parallel}^{kinetic}$ on the CF_4-plasma-treated T-LDPE (blue dashed lines). The lower $F_{\parallel}^{kinetic}$ on the CF_4-plasma-treated T-LDPE is attributed to the lower surface energy provided by the CF_4 modification (See Figure 2). The water drop remained in the Cassie–Baxter state for both surfaces over the entire applied load range (i.e., the drop did not enter the Wenzel state).

3.4. SEM and AFM Images of Altered LDPE Samples

To see the effect of plasma treatment on surface morphology and roughness, AFM (Bruker Dimension ICON, San Jose, CA, USA) images of the 3× CF_4-plasma-treated flat LPDE were acquired, and the corresponding images are shown in Figure S3. As can be seen from the AFM images, the surface roughness did not change significantly. However, the SEM images of the T-LDPE samples presented in Figure 4a show significant surface morphological changes, as presented in Figure 4b at the tips of the surface structures, i.e., developing sharp edges after 3× CF_4 treatments. The plasma process only affects a few tens of nm, maybe up to 50 nm [52,53] of the surface layer of the polymers, depending on the nature of the polymers, such as the crystallinity, glass transition temperature, MW and the extent and the nature of the functional groups. Upon comparison of the SEM images of the T-LDPE samples before and after 3× CF_4, there is some morphological change in the surface of the T-LDPE samples that occurred due to the 3× CF_4 treatments.

The low-pressure plasma process plays a very limited role in the physical alteration of the T-LDPE, depending on the plasma parameters, such as exposure time, power, etc.; however, it is possible to induce some slight alteration in the surface morphology of T-LDPE with plasma exposure, while maintaining the main features. As plasma parameters, e.g., power, exposure time, etc., can be controlled, it is possible to find appropriate parameters that do not induce recognizable changes on the surface features of T-LDPE. However, it may be necessary to make chemical modifications on the surface of LDPE, e.g., generation of C-F groups so that the chemical modification is achieved, and this can somehow change the surface morphology. Moreover, etching could play an important role in the surface modification of T-LDPE samples [54–56].

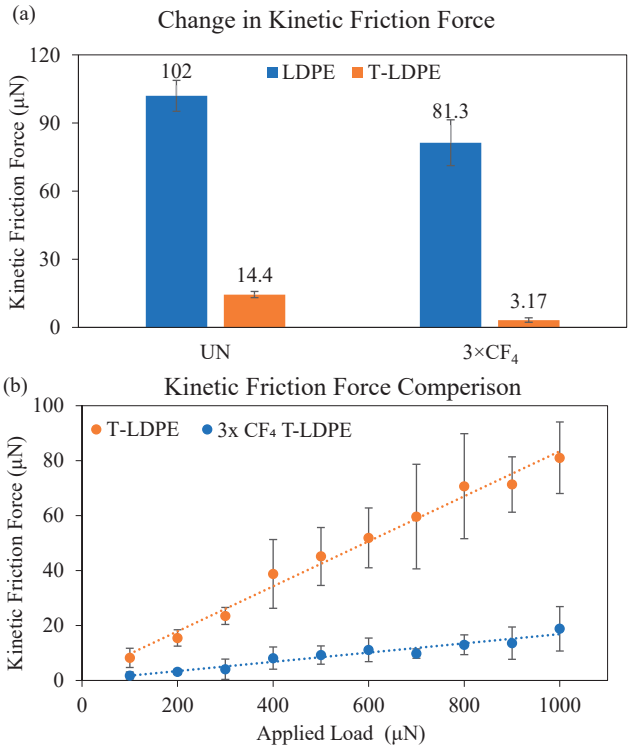

Figure 3. (**a**) Change in the $F_{\parallel}^{kinetic}$ of LDPE samples and T-LDPE samples after 3× CF_4 plasma treatment. The applied load on the water drop was maintained at 200 μN. (**b**) Plot of the $F_{\parallel}^{kinetic}$ versus applied normal load of a 20 μL water drop sheared against an unmodified (red data) and 3× CF_4-plasma-treated textured LPDE. The shear velocity is 0.1 mm/s. Each experiment was repeated at least 3 times, and error bars represent the standard deviations.

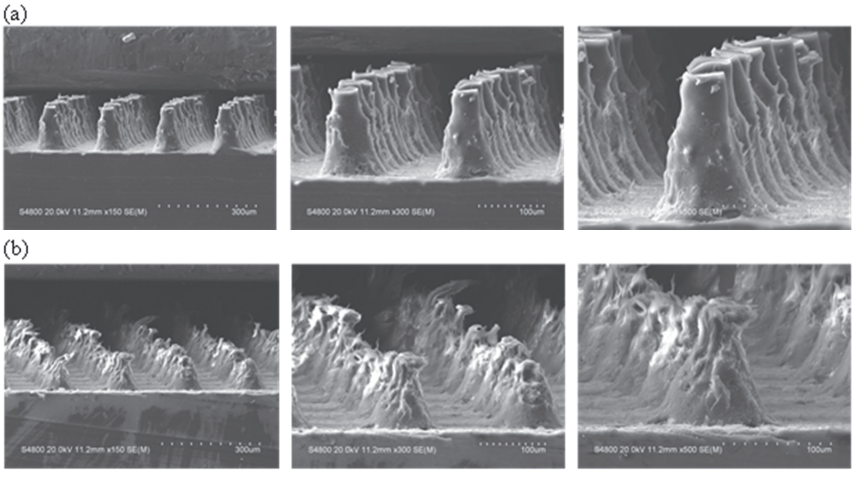

Figure 4. SEM images of (**a**) untreated T-LDPE and (**b**) after three times treatment with CF_4 (3× CF_4 T-LDPE) at 3 magnifications.

4. Conclusions

LDPE and T-LDPE samples were treated with successive H_2 and CF_4 plasmas. H_2 plasma treatments caused a decrease in water CA measurements, while CF_4 plasma treatments resulted in an increase in water CA measurements. After a 3rd H_2 plasma treatment, the surface free energy value of LDPE increased to 70.3 ± 1.0 mN/m from 33.8 ± 0.2 mN/m, and after a 3rd CF_4 treatment, the surface free energy value decreased to 7.8 ± 0.7 mN/m. The sliding angle α value of LDPE samples increased from $12.5^\circ \pm 0.4$ to $14.7^\circ \pm 1.9$ after the 3rd H_2 plasma treatment and to $27.2^\circ \pm 2.7$ after the 3rd CF_4 treatment. The CA of T-LDPE decreased from $143.6^\circ \pm 1.0$ to $60.8^\circ \pm 4.0$ after the 3rd H_2 plasma treatment and increased to $143.9^\circ \pm 1.6$ after the 3rd CF_4 plasma treatment. The surface free energy of T-LDPE decreased from 22.74 ± 0.2 mN/m to 1.0 ± 0.1 mN/m after the 3rd consecutive CF_4 plasma treatment. The sliding angle of T-LDPE samples increased to $38.2^\circ \pm 2.5$ from $6.9^\circ \pm 0.3$ after the 3rd H_2 plasma treatment and decreased to $1.7^\circ \pm 0.1$ after the 3rd CF_4 plasma treatment. The CAH values of the samples increased based on the increases of the hydrophilicity of the surfaces, regardless of the treatment. However, samples with surface features, e.g., T-LDPE, had a lower CAS than their non-textured surfaces, e.g., LDPE with smooth surfaces. After the 3rd consecutive CF_4 plasma treatment, the friction force between water drops, and LDPE and T-LDPE films dropped from 102 μN to 81.3 μN and from 14.4 μN to 3.17 μN, respectively. These results suggest that the combinatory effect of surface texturing and plasma gas treatments of LDPE provide significant changes in the wetting properties of surfaces, which are potentially advantageous in many applications using this material. The area of application of textured and plasma-treated samples not only include tubing, piping, packing and food and beverage, but also cover biomedical applications.

Supplementary Materials: The following supporting information can be downloaded at: https://www.mdpi.com/article/10.3390/polym15092132/s1, Figure S1: LDPE (top left) and T-LDPE (top right) samples. DI water forms different shapes on LDPE (bottom left) and on T-LDPE (bottom right); Figure S2: Optical image of the experimental setup used to measure the kinetic friction between a water drop and a textured LDPE sample. The water drop is 20 μL. The copper ring drop holder is connected to a dual-axis force sensor which allows for simultaneous normal and lateral force measurements.; Figure S3: AFM images using tapping mode of flat LDPE samples (a) before, (b) after 3× CF4 plasma treatment. The surface roughness (Rq) changes from 9.22 ± 3.73 nm to 10.28 ± 3.73 nm. The surface roughness values were obtained by averaging the roughness of 3 random locations on each sample.

Author Contributions: Conceptualization, N.S.P. and N.S.; methodology, C.A., O.P., M.B. and M.F.; software, N.S.P.; validation, C.A., N.S.P. and N.S.; formal analysis, N.S.P. and N.S.; investigation, C.A., O.P., M.B. and M.F.; resources, N.S.P. and N.S.; data curation, C.A., O.P., M.B. and M.F.; writing—original draft preparation, C.A., O.P., M.B. and M.F.; writing—review and editing, N.S.P. and N.S.; visualization, N.S.P. and N.S.; supervision, N.S.; project administration, N.S.; funding acquisition, N.S.P. and N.S. All authors have read and agreed to the published version of the manuscript.

Funding: Partial financial support from the startup fund (N. Sahiner) from Ophthalmology Department, Morsani College of Medicine at USF, is greatly appreciated. In addition, N. Pesika acknowledges support from the Louisiana Board of Regents and Intralox L.L.C. (LEQSF (2019-22)-RD-B-04).

Data Availability Statement: The data presented in this study are available on request from the corresponding author.

Acknowledgments: We also thank Roya Gadimli from the Albert group (Chemical and Biomolecular Engineering, Tulane, New Orleans, LA, USA) for the AFM imaging of samples.

Conflicts of Interest: The authors declare no conflict of interest.

References

1. Švorčík, V.; Kotál, V.; Slepička, P.; Bláhová, O.; Špírková, M.; Sajdl, P.; Hnatowicz, V. Modification of Surface Properties of Polyethylene by Ar Plasma Discharge. *Nucl. Instrum. Methods Phys. Res. B* **2006**, *244*, 365–372. [CrossRef]
2. Ataeefard, M.; Moradian, S.; Mirabedini, M.; Ebrahimi, M.; Asiaban, S. Investigating the Effect of Power/Time in the Wettability of Ar and O2 Gas Plasma-Treated Low-Density Polyethylene. *Prog. Org. Coat.* **2009**, *64*, 482–488. [CrossRef]
3. Sanchis, M.R.; Blanes, V.; Blanes, M.; Garcia, D.; Balart, R. Surface Modification of Low Density Polyethylene (LDPE) Film by Low Pressure O2 Plasma Treatment. *Eur. Polym. J.* **2006**, *42*, 1558–1568. [CrossRef]
4. Olifirenko, A.S.; Novak, I.; Rozova, E.Y.; Saprykina, N.N.; Mitilineos, A.G.; Elyashevich, G.K. Hydrophilization of Porous Polyethylene Films by Cold Plasma of Different Types. *Polym. Sci. Ser. B* **2009**, *51*, 247–255. [CrossRef]
5. Drnovská, H.; Lapčík, L.; Buršíková, V.; Zemek, J.; Barros-Timmons, A.M. Surface Properties of Polyethylene after Low-Temperature Plasma Treatment. *Colloid. Polym. Sci.* **2003**, *281*, 1025–1033. [CrossRef]
6. Xie, T.; McAuley, K.B.; Hsu, J.C.C.; Bacon, D.W. Gas Phase Ethylene Polymerization: Production Processes, Polymer Properties, and Reactor Modeling. *Ind. Eng. Chem. Res.* **1994**, *33*, 449–479. [CrossRef]
7. Nowlin, T.E. Low Pressure Manufacture of Polyethylene. *Prog. Polym. Sci.* **1985**, *11*, 29–55. [CrossRef]
8. Dilks, A. Polymer Surfaces. *Anal. Chem.* **1981**, *53*, 802A–816A. [CrossRef]
9. Shenton, M.J.; Lovell-Hoare, M.C.; Stevens, G.C. Adhesion Enhancement of Polymer Surfaces by Atmospheric Plasma Treatment. *J. Phys. D Appl. Phys.* **2001**, *34*, 2754–2760. [CrossRef]
10. Patra, N.; Hladik, J.; Pavlatová, M.; Militký, J.; Martinová, L. Investigation of Plasma-Induced Thermal, Structural and Wettability Changes on Low Density Polyethylene Powder. *Polym. Degrad. Stab.* **2013**, *98*, 1489–1494. [CrossRef]
11. Popelka, A.; Kronek, J.; Novák, I.; Kleinová, A.; Mičušík, M.; Špírková, M.; Omastová, M. Surface Modification of Low-Density Polyethylene with Poly(2-Ethyl-2-Oxazoline) Using a Low-Pressure Plasma Treatment. *Vacuum* **2014**, *100*, 53–56. [CrossRef]
12. Farzam, M.; Beitollahpoor, M.; Solomon, S.E.; Ashbaugh, H.S.; Pesika, N.S. Advances in the Fabrication and Characterization of Superhydrophobic Surfaces Inspired by the Lotus Leaf. *Biomimetics* **2022**, *7*, 196. [CrossRef] [PubMed]
13. Cheng, C.; Gupta, M. Roll-to-Roll Surface Modification of Cellulose Paper via Initiated Chemical Vapor Deposition. *Ind. Eng. Chem. Res.* **2018**, *57*, 11675–11680. [CrossRef]
14. Nejati, S.; Mirbagheri, S.A.; Waimin, J.; Grubb, M.E.; Peana, S.; Warsinger, D.M.; Rahimi, R. Laser Functionalization of Carbon Membranes for Effective Immobilization of Antimicrobial Silver Nanoparticles. *J. Environ. Chem. Eng.* **2020**, *8*, 104109. [CrossRef]
15. Strobel, M.; Branch, M.C.; Ulsh, M.; Kapaun, R.S.; Kirk, S.; Lyons, C.S. Flame Surface Modification of Polypropylene Film. *J. Adhes. Sci. Technol.* **1996**, *10*, 515–539. [CrossRef]
16. Netravali, A.N.; Caceres, J.M.; Thompson, M.O.; Renk, T.J. Surface Modification of Ultra-High Strength Polyethylene Fibers for Enhanced Adhesion to Epoxy Resins Using Intense Pulsed High-Power Ion Beam. *J. Adhes. Sci. Technol.* **1999**, *13*, 1331–1342. [CrossRef]
17. Mukherjee, J.; Peczonczyk, S.; Maldonado, S. Wet Chemical Functionalization of III−V Semiconductor Surfaces: Alkylation of Gallium Phosphide Using a Grignard Reaction Sequence. *Langmuir* **2010**, *26*, 10890–10896. [CrossRef]
18. Liston, E.M.; Martinu, L.; Wertheimer, M.R. Plasma Surface Modification of Polymers for Improved Adhesion: A Critical Review. *J. Adhes. Sci. Technol.* **1993**, *7*, 1091–1127. [CrossRef]
19. Primc, G. Surface Modification of Polyamides by Gaseous Plasma—Review and Scientific Challenges. *Polymers* **2020**, *12*, 3020. [CrossRef]
20. Liu, Y.-X.; Zhang, Q.-Z.; Zhao, K.; Zhang, Y.-R.; Gao, F.; Song, Y.-H.; Wang, Y.-N. Fundamental Study towards a Better Understanding of Low Pressure Radio-Frequency Plasmas for Industrial Applications. *Chin. Phys. B* **2022**, *31*, 085202. [CrossRef]
21. Desmet, T.; Morent, R.; De Geyter, N.; Leys, C.; Schacht, E.; Dubruel, P. Nonthermal Plasma Technology as a Versatile Strategy for Polymeric Biomaterials Surface Modification: A Review. *Biomacromolecules* **2009**, *10*, 2351–2378. [CrossRef] [PubMed]
22. Chan, C.-M.; Ko, T.-M.; Hiraoka, H. Polymer Surface Modification by Plasmas and Photons. *Surf. Sci. Rep.* **1996**, *24*, 1–54. [CrossRef]
23. Friedrich, J.F.; Geng, S.; Unger, W.; Lippitz, A.; Erdmann, J.; Gorsler, H.-V.; Wöll, C.; Schertel, A.; Bierbaum, K. Plasma Functionalization and Reorientation of Macromolecules at Polymer Surfaces. *Surf. Coat. Technol.* **1995**, *74–75*, 664–669. [CrossRef]
24. Nuzzo, R.G.; Smolinsky, G. Preparation and Characterization of Functionalized Polyethylene Surfaces. *Macromolecules* **1984**, *17*, 1013–1019. [CrossRef]
25. Harth, K.; Hibst, H. Surface Modification of Polypropylene in Oxygen and Nitrogen Plasmas. *Surf. Coat. Technol.* **1993**, *59*, 350–355. [CrossRef]
26. Mühlhan, C.; Weidner, S.; Friedrich, J.; Nowack, H. Improvement of Bonding Properties of Polypropylene by Low-Pressure Plasma Treatment. *Surf. Coat. Technol.* **1999**, *116–119*, 783–787. [CrossRef]
27. Bhowmik, S.; Bonin, H.W.; Bui, V.T.; Chaki, T.K. Physicochemical and Adhesion Characteristics of High-Density Polyethylene When Treated in a Low-Pressure Plasma under Different Electrodes. *J. Adhes.* **2006**, *82*, 1–18. [CrossRef]
28. Sanchis, R.; Fenollar, O.; García, D.; Sánchez, L.; Balart, R. Improved Adhesion of LDPE Films to Polyolefin Foams for Automotive Industry Using Low-Pressure Plasma. *Int. J. Adhes. Adhes.* **2008**, *28*, 445–451. [CrossRef]
29. Owens, D.K.; Wendt, R.C. Estimation of the Surface Free Energy of Polymers. *J. Appl. Polym. Sci.* **1969**, *13*, 1741–1747. [CrossRef]
30. Kaelble, D.H. Dispersion-Polar Surface Tension Properties of Organic Solids. *J. Adhes.* **1970**, *2*, 66–81. [CrossRef]

31. Yu, X.; Hörst, S.M.; He, C.; McGuiggan, P.; Kristiansen, K.; Zhang, X. Surface Energy of the Titan Aerosol Analog "Tholin. " *Astrophys. J.* **2020**, *905*, 88. [CrossRef]
32. de Gennes, P.G. Wetting: Statics and Dynamics. *Rev. Mod. Phys.* **1985**, *57*, 827–863. [CrossRef]
33. Hejda, F.; Solar, P.; Kousal, J. Surface Free Energy Determination by Contact Angle Measurements—A Comparison of Various Approaches. In Proceedings of the 19th Annual Conference of Doctoral Students, WDS'10 "Week of Doctoral Students 2010", Charles University, Faculty of Mathematics and Physics, Prague, Czech Republic, 1–4 June 2010; Volume 19, pp. 25–30.
34. Beitollahpoor, M.; Farzam, M.; Pesika, N.S. Determination of the Sliding Angle of Water Drops on Surfaces from Friction Force Measurements. *Langmuir* **2022**, *38*, 2132–2136. [CrossRef] [PubMed]
35. Cassie, A.B.D.; Baxter, S. Wettability of Porous Surfaces. *Trans. Faraday Soc.* **1944**, *40*, 546. [CrossRef]
36. Lamichhane, P.; Acharya, T.R.; Kaushik, N.; Nguyen, L.N.; Lim, J.S.; Hessel, V.; Kaushik, N.K.; Choi, E.H. Non-Thermal Argon Plasma Jets of Various Lengths for Selective Reactive Oxygen and Nitrogen Species Production. *J. Environ. Chem. Eng.* **2022**, *10*, 107782. [CrossRef]
37. Sode, M.; Jacob, W.; Schwarz-Selinger, T.; Kersten, H. Measurement and Modeling of Neutral, Radical, and Ion Densities in H_2 -N_2 -Ar Plasmas. *J. Appl. Phys.* **2015**, *117*, 083303. [CrossRef]
38. Chu, P. Plasma-Surface Modification of Biomaterials. *Mater. Sci. Eng. R Rep.* **2002**, *36*, 143–206. [CrossRef]
39. Švorčík, V.; Kolářová, K.; Dvořánková, B.; Michálek, J.; Krumbholcová, E.; Hnatowicz, V. Plasma Modification of HEMA and EOEMA Surface Properties. *Radiat. Eff. Defects Solids* **2006**, *161*, 15–19. [CrossRef]
40. Švorčík, V.; Kolářová, K.; Slepička, P.; Macková, A.; Novotná, M.; Hnatowicz, V. Modification of Surface Properties of High and Low Density Polyethylene by Ar Plasma Discharge. *Polym. Degrad. Stab.* **2006**, *91*, 1219–1225. [CrossRef]
41. Polat, O.; Bhethanabotla, V.R.; Ayyala, R.S.; Sahiner, N. Carbon Tetrafluoride, Oxygen, and Air RF Plasma Modified Low-Density Polyethylene and Polydimethylsiloxane. *Plasma Chem. Plasma Process.* **2023**, *43*, 737–756. [CrossRef]
42. Gizer, S.G.; Bhethanabotla, V.R.; Ayyala, R.S.; Sahiner, N. Low-Pressure Plasma Treated Polycarbonate and Polymethyl Methacrylate (PMMA) Sheets with Different Surface Patterns to Change Their Surface Properties. *Surf. Interfaces* **2023**, *37*, 102646. [CrossRef]
43. Cordeiro, A.L.; Nitschke, M.; Janke, A.; Helbig, R.; D'Souza, F.; Donnelly, G.T.; Willemsen, P.R.; Werner, C. Fluorination of Poly(Dimethylsiloxane) Surfaces by Low Pressure CF4 Plasma—Physicochemical and Antifouling Properties. *Express Polym. Lett.* **2009**, *3*, 70–83. [CrossRef]
44. Nitschke, M.; König, U.; Lappan, U.; Minko, S.; Simon, F.; Zschoche, S.; Werner, C. Low Pressure Plasma-Based Approaches to Fluorocarbon Polymer Surface Modification. *J. Appl. Polym. Sci.* **2007**, *103*, 100–109. [CrossRef]
45. Sawada, Y.; Kogama, M. Plasma-Polymerized Tetrafluoroethylene Coatings on Silica Particles by Atmospheric-Pressure Glow Discharge. *Powder Technol.* **1997**, *90*, 245–250. [CrossRef]
46. Zisman, W.A. Relation of the Equilibrium Contact Angle to Liquid and Solid Constitution. In *Contact Angle, Wettability, and Adhesion*; American Chemical Society: Washington, DC, USA, 1964; pp. 1–51.
47. Dalvi, V.H.; Rossky, P.J. Molecular Origins of Fluorocarbon Hydrophobicity. *Proc. Natl. Acad. Sci. USA* **2010**, *107*, 13603–13607. [CrossRef] [PubMed]
48. Dussan, V.E.B.; Chow, R.T.-P. On the Ability of Drops or Bubbles to Stick to Non-Horizontal Surfaces of Solids. *J. Fluid. Mech.* **1983**, *137*, 1–29. [CrossRef]
49. Joanny, J.F.; de Gennes, P.G. A Model for Contact Angle Hysteresis. *J. Chem. Phys.* **1984**, *81*, 552–562. [CrossRef]
50. Olde Riekerink, M.B.; Terlingen, J.G.A.; Engbers, G.H.M.; Feijen, J. Selective Etching of Semicrystalline Polymers: CF_4 Gas Plasma Treatment of Poly(Ethylene). *Langmuir* **1999**, *15*, 4847–4856. [CrossRef]
51. Acharya, T.R.; Chaudhary, D.K.; Gautam, S.; Singh, A.K.; Shrestha, R.; Adhikari, B.C.; Lamichhane, P.; Paudyal, B.; Kaushik, N.K.; Choi, E.H. Influence of Nanoparticle Size on the Characterization of ZnO Thin Films for Formaldehyde Sensing at Room Temperature. *Sens. Actuators A Phys.* **2023**, *351*, 114175. [CrossRef]
52. Nitschke, M.; Meichsner, J. Low-Pressure Plasma Polymer Modification from the FTIR Point of View. *J. Appl. Polym. Sci.* **1997**, *65*, 381–390. [CrossRef]
53. Grace, J.M.; Gerenser, L.J. Plasma Treatment of Polymers. *J. Dispers. Sci. Technol.* **2003**, *24*, 305–341. [CrossRef]
54. Liu, N.; Li, Z.; Chen, G.; Chen, Q.; Li, S. Space Charge Dynamics of CF_4 Fluorinated LDPE Samples from Different Fluorination Conditions and Their DC Conductivities. *Mater. Res. Express* **2017**, *4*, 075308. [CrossRef]
55. Egitto, F.D. Plasma Etching and Modification of Organic Polymers. *Pure Appl. Chem.* **1990**, *62*, 1699–1708. [CrossRef]
56. Riekerink, M.B.O. *Structural and Chemical Modification of Polymer Surfaces by Gas Plasma Etching*; Printpartners Ipskamp: Enschede, The Netherlands, 2001; ISBN 9789036516433.

Disclaimer/Publisher's Note: The statements, opinions and data contained in all publications are solely those of the individual author(s) and contributor(s) and not of MDPI and/or the editor(s). MDPI and/or the editor(s) disclaim responsibility for any injury to people or property resulting from any ideas, methods, instructions or products referred to in the content.

polymers

MDPI

Article

Understanding the Effect of Grain Boundaries on the Mechanical Properties of Epoxy/Graphene Composites

Qiuyue Ding [1,2], Ning Ding [1,2,*], Xiangfeng Chen [1], Wenyue Guo [2,*] and Fahmi Zaïri [3]

[1] Engineering Research Center of Failure Analysis and Safety Assessment, Shandong Analysis and Test Center, Qilu University of Technology (Shandong Academy of Sciences), Jinan 250014, China
[2] School of Materials Science and Engineering, China University of Petroleum (East China), Qingdao 266580, China
[3] Civil Engineering and Geo-Environmental Laboratory (ULR 4515 LGCgE), Lille University, 59000 Lille, France
* Correspondence: nding3-c@my.cityu.edu.hk (N.D.); wyguo@upc.edu.cn (W.G.)

Abstract: This work presents a molecular dynamics (MD) simulation study on the effect of grain boundaries (GBs) on the mechanical properties of epoxy/graphene composites. Ten types of GB models were constructed and comparisons were made for epoxy/graphene composites containing graphene with GBs. The results showed that the tensile and compressive behaviors, the glass transition temperature (T_g), and the configurations of epoxy/graphene composites were significantly affected by GBs. The tensile yield strength of epoxy/graphene composites could be either enhanced or weakened by GBs under a tensile load parallel to the graphene sheet. The underlying mechanisms may be attributed to multi-factor coupling, including the tensile strength of the reinforcements, the interfacial interaction energy, and the inflection degree of reinforcements. A balance exists among these effect factors, resulting in the diversity in the tensile yield strength of epoxy/graphene composites. The compressive yield strength for epoxy/graphene composites is higher than their counterpart in tension. The tensile/compressive yield strength for the same configuration presents diversity in different directions. Both an excellent interfacial interaction and the appropriate inflection degree of wrinkles for GB configurations restrict the translational and rotational movements of epoxy chains during volume expansion, which eventually improves the overall T_g. Understanding the reinforcing mechanism for graphene with GBs from the atomistic level provides new physical insights to material design for epoxy-based composites containing defective reinforcements.

Keywords: epoxy resin; graphene; grain boundary; mechanical property; glass transition temperature; molecular dynamics

Citation: Ding, Q.; Ding, N.; Chen, X.; Guo, W.; Zaïri, F. Understanding the Effect of Grain Boundaries on the Mechanical Properties of Epoxy/Graphene Composites. *Polymers* **2023**, *15*, 3218. https://doi.org/10.3390/polym15153218

Academic Editor: Brian J. Edwards

Received: 13 June 2023
Revised: 21 July 2023
Accepted: 24 July 2023
Published: 28 July 2023

Copyright: © 2023 by the authors. Licensee MDPI, Basel, Switzerland. This article is an open access article distributed under the terms and conditions of the Creative Commons Attribution (CC BY) license (https://creativecommons.org/licenses/by/4.0/).

1. Introduction

Epoxy with a cross-linked network structure is the most promising high-performance thermosetting polymer for multifunctional composites due to its excellent mechanical properties, good chemical stability, and durability. These characteristics make epoxy widely used in aerospace, coating, adhesives, electronics, automotive, and biotechnology fields [1–6]. However, due to its high cross-linking degree, epoxy exhibits low toughness and impact and crack resistance, which limits its application in high-end fields [7]. Previous studies showed that these limitations can be overcome by embedding nanofillers inside epoxy [8–10]. Among the various types of nanofillers, graphene has emerged as a potential reinforcement for epoxy matrix due to its superior mechanical, thermal, and electrical properties [11–13].

Extensive experimental and computational studies were carried out on epoxy/graphene systems, highlighting significant improvements in their mechanical and thermal properties with the incorporation of graphene into epoxy [14–22]. Rafiee et al. [14] experimentally illustrated that embedding graphene platelets at a low concentration can enhance a variety of the mechanical properties of epoxy resins, including the tensile strength, stiffness, fracture toughness, fracture energy, and resistance to fatigue crack growth. Wang et al. [23] tested

the shear properties of epoxy construction adhesive reinforced with graphene nanoplatelets through a thick adherend shear test (TAST). Their results showed that the shear strength of the epoxy/graphene composites with a graphene content of 0.75 wt% was 22.7 MPa, which was about a 102% improvement compared with neat epoxy adhesive (11.2 MPa). Bian et al. [24] systematically investigated the mechanical properties of graphene-reinforced cross-linked epoxy using a multiscale simulation framework, including the molecular dynamics (MD) method and the finite element method (FEM). Their simulations predicted that the higher compatibility of the graphene orientation simultaneously increases the stiffness, strength, and toughness of composites. In addition, the mechanical properties of composites can be improved by increasing the waviness of graphene, which mainly results from blocking the debonding region at the interface between graphene and epoxy. Sun et al. [25] also performed MD simulations to investigate the effect of hydrogen-functionalized graphene on the tensile properties of epoxy composites. An overall enhancement in the modulus and strength of hydrogen-functionalized graphene-reinforced composites was predicted due to the improved interfacial bonding between the functionalized graphene sheet and epoxy matrix which provides much better load transfer capability.

Although a significant amount of research has been performed to study the effect of graphene as reinforcement on the mechanical and thermal properties of epoxy, the reports are mostly focused on the effect of pristine and functionalized graphene. In fact, due to the limitations of synthetic techniques, the crystal growth of large-size graphene during the chemical vapor deposition (CVD) method leads to the formation of geometrical defects such as vacancies, dislocations, and grain boundaries (GBs) [26,27]. The existence of GBs always affects the mechanical properties of graphene sheets [28–31]. Xu et al. [29] reported that the existence of GBs can decrease the Young's modulus and the ultimate strength of graphene. Wei et al. [30] found that GB defects can either strengthen or weaken graphene, which relies on the detailed arrangement of GBs, not just the density of GBs. In addition, the strengths of graphene GBs increase as the GB tilt angles increase only if the pentagon–heptagon defects are evenly spaced. Grantab et al. [31] demonstrated that graphene sheets with large-angle tilt boundaries that have a high density of defects are as strong as the pristine material and much stronger than those with low-angle boundaries having fewer defects. Regulating the properties of graphene by controlling GB growth is an important means to expand the application of graphene. Recently, some progress has been experimentally made in the controllable formation of GBs. Dong et al. [32] synthesized graphene containing only 30° titled GBs on a liquid Cu surface, offering more insightful guidelines for the design and controlled synthesis of graphene. Meanwhile, their results provided feasibility for the application of graphene-containing GBs in composite materials. Thus, it is also an important technology for regulating the properties of such composites [33,34].

Although these research works have made progress on the effect of GBs on the mechanical properties of graphene, there is a lack of research related to the effect of GBs on the mechanical and thermal properties of polymer/graphene composites. Verma et al. [34] evaluated the reinforcing capabilities of bi-crystalline graphene and pristine graphene on the mechanical properties of polyethylene (PE) composites. Their results showed that, compared with pristine graphene, bi-crystalline graphene can significantly improve the tensile, interfacial shear, and normal cohesive strength of PE composites. This observation can be explained by more adhesion points and a better non-bonding interaction at the interface in bi-crystalline graphene containing higher misorientation angle GBs. The above study provided meaningful information about the effect of bi-crystalline graphene on the mechanical properties of thermoplastic polymer (PE) composites. Nevertheless, to the best of the authors' knowledge, the effect of bi-crystalline graphene on the mechanical properties and the thermal stability of thermosetting polymer (epoxy) composites has not yet been investigated systematically and comprehensively. As we all know, compared with PE, a complex cross-linked process exists in epoxy. The interface between the graphene and epoxy matrix is different from that between graphene and PE as the fluidity of epoxy molecules is affected by the cross-linking structure. Moreover, how the GBs affect the thermal stability of epoxy/graphene composites

is still unclear. Hence, it is necessary to further explore the effect mechanism behind the enhancement in mechanical properties and thermal stability of epoxy composites reinforced with bi-crystalline graphene-containing GBs.

In this work, using the MD method, we investigated in detail the effect of 10 types of GBs on the tensile/compressive behaviors and the glass transition temperature (T_g) of bi-crystalline graphene-reinforced epoxy composites. The stress–strain response, yield strength, elastic moduli (including Young's modulus and compressive modulus), interfacial interaction energy, and T_g of epoxy composites reinforced by pristine graphene and graphene with GBs are also estimated. The mechanism associated with the GB parameters on the mechanical properties and the thermal stability properties is proposed as well. Therefore, this work provides a theoretical basis for the industrialization of nano-reinforced graphene composites.

2. Computational Details

2.1. Atomistic Models

The polymer matrix was composed of di-glycidyl ether of bisphenol A (DGEBA) as the resin matrix and triethylenetetramine (TETA) as the hardener. To reduce the computational cost, the polymerization degree of the initial DGEBA prior to cross-linking was set to 0 (i.e., n = 0). The atomistic models for the DGEBA and TETA segments are shown in Figure 1a. To study the effect of GBs on the mechanical properties and the thermal stability of epoxy/graphene composites, pristine graphene and graphene containing ten different sets of GB configurations along the zigzag (ZZ) and armchair (AM) directions were constructed. According to previous work [29], GB is the one-dimensional interface between single-crystalline domains with different lattice orientations for two-dimensional graphene. As shown in Figure 1e, GBs can be denoted by pairs of translation vectors (n_L, m_L) and (n_R, m_R) of the left and right crystalline domains. The constructions of GBs along the ZZ and AM directions are shown in Figures 1c and 1d, respectively. One can see that all GBs are spaced evenly and the misorientation angles of GBs along the ZZ and AM directions are 27.8°/21.8°/13.2°/9.4°/8.9° and 27.8°/21.8°/17.9°/15.2°/13.2°, respectively. Furthermore, eleven different composite models were considered that included (a) epoxy reinforced with pristine graphene (referred as Epoxy/GRP); (b–f) epoxy reinforced with graphene containing GB along the ZZ direction with a misorientation angle of 27.8°/21.8°/13.2°/9.4°/8.9° (referred as Epoxy/ZZ 27.8°, Epoxy/ZZ 21.8°, Epoxy/ZZ 13.2°, Epoxy/ZZ 9.4°, and Epoxy/ZZ 8.9°, respectively); and (g–k) epoxy reinforced with graphene containing GB along the AM direction with a misorientation angle of 27.8°/21.8°/17.9°/15.2°/13.2° (referred as Epoxy/AM 27.8°, Epoxy/AM 21.8°, Epoxy/AM 17.9°, Epoxy/AM 15.2°, and Epoxy/AM 13.2°, respectively). This kind of classification and nomenclature has been used in previous literature [34].

In the modeling process, graphene nanosheets were inserted in the cubical supercell, with a size of 57 Å × 57 Å × 57 Å, and the monomers and the hardeners were randomly packed in the available space based on a ratio of 3:1. The density of the uncross-linked composite was 1.15 g/cm^3, which was reported to be an average density for an epoxy [35,36]. Also, the epoxy/graphene composites contained about 16,734 atoms, including 16,014 atoms of epoxy and about 720 atoms of either pristine graphene or graphene with GBs (as shown in Figure 1b).

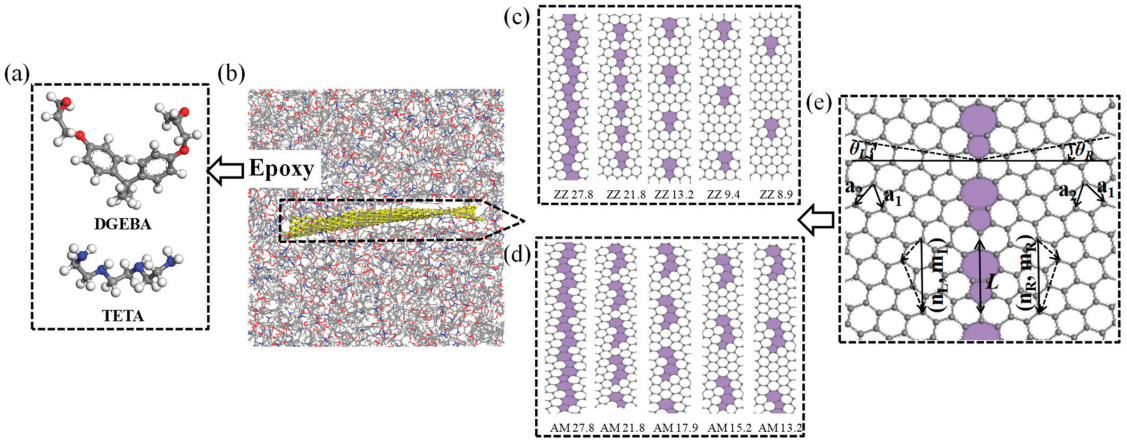

Figure 1. Diagram of the epoxy/graphene composite model. (**a**) Molecular structures of the DGEBA and TETA molecules (carbon, oxygen, nitride, and hydrogen atoms are shown in gray, red, blue, and white, respectively); (**b**) Epoxy/GRP composite system; structures of graphene nanosheets with (**c**) the zigzag tilt GBs and (**d**) the armchair tilt GBs; and (**e**) diagram of the GB model with misorientation angle θ ($\theta = \theta_L + \theta_R$) in which GB is formed by two evenly spaced disclinations.

2.2. Simulation Methods

All the MD simulations were performed using the large-scale atomic/molecular massively parallel simulator (LAMMPS) package [37]. The atomistic interactions within the composite systems were described by the polymer consistent forcefield (PCFF) [38], which has been used successfully in previous studies on epoxy composites [33,35,39,40]. The van der Waals interaction and the Coulombic interactions for the non-bonded part were calculated with a cutoff distance of 12.5 Å. To avoid the effect of size, periodic boundary conditions were applied in all three dimensions.

During the analysis, models with cross-linking degrees of around 84% were considered. The initial uncross-linked models were minimized using the conjugate gradient method with an energy convergence criterion of 0.0001 kcal mol^{-1}, followed by another 100 ps equilibration under an isothermal-isobaric (NPT) ensemble at 300 K and 1 atm. Then, a series of cross-linked reactions were performed using a cross-linking algorithm [39,41]. No atom of the composites was fixed during the cross-linked process. The cross-linked process mainly involved the following steps: (1) recognize the C atom of the epoxide and the N atom of the amine groups as reactive atoms; (2) define the initial and final cross-linked cutoff radius, which are set to be 3.5 to 8.5 Å with an increment of 0.5 Å. The reaction temperature and the target cross-linked degree were set as 500 K [42] and 100%, respectively; (3) if the distances of the reaction atoms C and N are within the reaction radius, the rings of epoxide groups are opened and connect with the N atoms on the hardeners, removing the hydrogen atom of the amine group to the oxygen atom of epoxide group; and (4) if there is no unreacted atom within the reaction cutoff radius, the cutoff radius is increased by steps of 0.5 Å, and the cross-linked structure is optimized and relaxed for the next reaction. The cross-linking process stops when all the potential reactive atoms within the cutoff radius are reacted.

After the initial cross-linked models were established, the mechanical properties of the epoxy/graphene composites were investigated by uniaxial tension and compression deformation using MD simulations. Three independent samples for each individual epoxy/graphene model were utilized for statistical analysis to quantify the errors. The final value of the mechanical properties was the average of three independent results and the error bars were determined by standard deviation. Before deformation, the initial cross-linked structures were minimized with the help of the conjugate gradient algo-

rithm. Subsequently, the systems were relaxed with multi-step equilibration processes with an isothermal-isochoric (NVT) ensemble at 300 K for 1 ns, NPT (P = 1 atm, T = 300 K) ensemble for 1ns, and an additional NVT (T = 300 K) ensemble for 1ns. The integration time step during the equilibration process was set to 0.25 fs. The root–mean–square displacement (RMSD) was examined to confirm the full equilibrium state. After the equilibration process, a constant uniaxial strain was applied along the x, y, or z directions at a strain rate of 0.0005 ps^{-1}. The tensile and compressive deformation processes were performed under an NPT (P = 1 atm, T = 300 K) ensemble with an integration time step of 1 fs. The atomic stress was calculated using the virial theorem [33,34,43]:

$$\sigma_{ij}^{\alpha} = \frac{1}{V_f^{\alpha}} \sum_{\alpha \neq \beta} \left(-m^{\alpha} v_i^{\alpha} v_j^{\alpha} + \frac{1}{2} r_i^{\alpha\beta} f_j^{\alpha\beta} \right) \quad (1)$$

where V_f^{α} is the volume of atom α post deformation; m^{α} and v^{α} are the mass and the velocity of atom α; $r_i^{\alpha\beta}$ is the distance between the atom α and atom β in the *i* direction; and $f_j^{\alpha\beta}$ is the *j* component of the interatomic force on atom α from atom β.

3. Results and Discussion

3.1. Tensile Behavior of Epoxy/Graphene Composites

In this section, uniaxial tensile tests parallel to the graphene sheets (perpendicular to the GB lines) and perpendicular to the graphene sheets were performed for all epoxy/graphene composites to investigate the effect of GBs on the mechanical properties of epoxy/graphene composites. Because it can directly influence the GB normal strength for graphene sheets, the stress component perpendicular to GBs can better reflect the effect of GBs on the properties of graphene [30]. Thus, the stress component perpendicular to GBs, when the tensile load is parallel to the graphene surface was mainly considered in this work. The composite tensile response for different types of graphene containing GBs is plotted in Figure 2. The stress–strain curves show three distinct regions, including the initial linear response, the yielding, and the strain hardening. The elastic and plastic deformation stages can be captured from the stress–strain curves to estimate Young's modulus and the yield strength of the composites. Young's modulus is determined from the slope of the elastic region and the yield strength is determined from the plateau stress, which is also considered as the yielding state of the materials [44–46]. The mechanical properties of the epoxy/graphene composites including Young's modulus and yield strength are collected in Table 1. From Table 1, one can see that the Young's modulus of Epoxy/GRP along the x, y, or z directions is 2.36 GPa, 2.48 GPa, and 2.25 GPa, respectively. The average Young's modulus of Epoxy/GRP is 2.36 GPa. Table 2 displays the Young's modulus of epoxy/graphene composites obtained from previous experiments or simulations. It can be seen that the calculated results in this work are within a reasonable range compared with the existing experimental or simulation results.

Figure 2a presents the stress–strain curves of pristine graphene and graphene with ZZ types of GB-reinforced epoxy composites with the load direction parallel to the graphene sheets and perpendicular to the GB lines (along the x axial direction). The result shows that the existence of GBs along the ZZ direction can either enhance or weaken the tensile yield strength of epoxy/graphene composites. From Table 1, one can see that, compared with Epoxy/ZZ GRP, the Epoxy/ZZ 27.8 and Epoxy/ZZ 8.9 configurations weaken the tensile yield strength of the epoxy/graphene composites, and are about 77.2% and 95.0% that of Epoxy/ZZ GRP, respectively. However, the other three GB configurations along the ZZ direction enhance the tensile yield strength of the epoxy/graphene composites. Epoxy/ZZ 9.4 shows the highest tensile yield strength compared with all other ZZ configurations, and an overall enhancement in tensile yield strength of 10.4% is predicted for Epoxy/ZZ 9.4 as compared to Epoxy/ZZ GRP. Figure 2b shows the stress–strain curves of pristine graphene and graphene with AM types of GB-reinforced epoxy composites with the load direction parallel to the graphene sheets and perpendicular to the GB lines (along the y-

axial direction). The result indicates that, except for the Epoxy/AM 13.2 configuration, the tensile yield strengths of other GB configurations along the AM direction are higher than that of Epoxy/AM GRP. Epoxy/AM 21.8 shows the highest tensile yield strength among all the AM configurations under the tensile load parallel to the graphene sheet, which is about 142.6% of that of Epoxy/AM GRP. The Young's modulus of pristine graphene and graphene with GB-reinforced epoxy composites were calculated from the slope of the stress–strain curve with a strain of up to 3% and are tabulated in Table 1. With the tensile load parallel to the graphene sheet, the Young's modulus of Epoxy/ZZ GRP and Epoxy/AM GRP is calculated to be 2.36 GPa and 2.48 GPa, respectively. Epoxy/AM 13.2 shows the highest Young's modulus (2.86 GPa) among all the GB configurations, which is improved by about 15.3% compared with that of Epoxy/AM GRP.

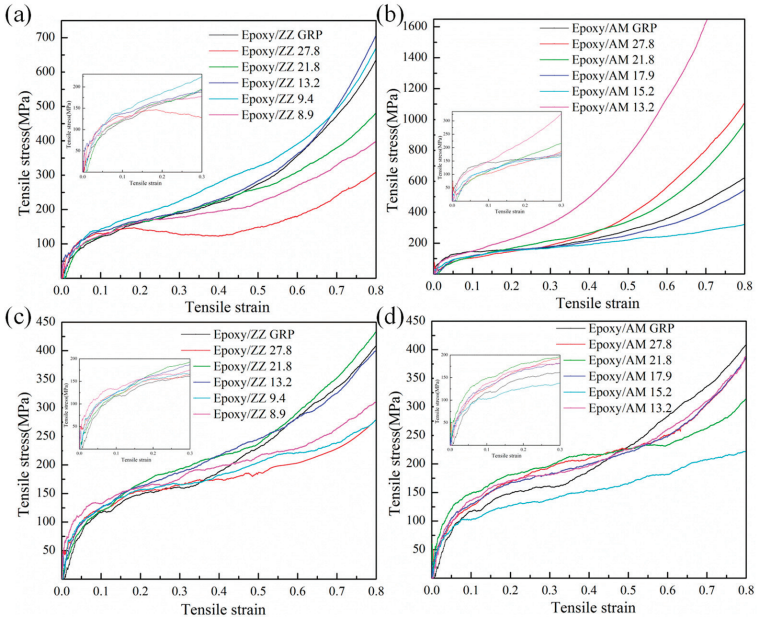

Figure 2. Stress–strain response of (**a**) Epoxy/ZZ systems and (**b**) Epoxy/AM systems subjected to a uniaxial tensile load parallel to the graphene sheet and perpendicular to the GB lines; (**c**) Epoxy/ZZ systems and (**d**) Epoxy/AM systems subjected to a uniaxial tensile load perpendicular to the graphene sheet.

Figures 2c and 2d show the stress–strain curves of the ZZ and AM configurations with a tensile load perpendicular to the graphene sheets (along the z-axial direction), respectively. It shows a similar trend with the tensile curves and the load direction parallel to the graphene sheet. As shown in Table 1, except for Epoxy/AM 15.2, the tensile yield strength of all the other GB configurations is higher than that of pristine graphene-reinforced epoxy as the tensile loading is perpendicular to the graphene sheets. In addition, Epoxy/ZZ 9.4 (Epoxy/AM 21.8) shows the highest tensile yield strength among the ZZ (AM) configurations. The tensile yield strength along the z direction of Epoxy/ZZ 9.4 and Epoxy/AM 21.8 were improved by about 37.4% and 34.8% compared with the pristine epoxy/graphene composites, respectively. The results above suggest that Epoxy/ZZ 9.4 and Epoxy/AM 21.8 are considered to be the superlative configurations, as they showcase the highest yield strength with a tensile direction parallel or perpendicular to the graphene sheets. As shown in Table 1, under a tensile load perpendicular to the graphene sheets, the Young's modulus of Epoxy/GRP is calculated to be 2.25 GPa. Epoxy/ZZ 27.8 and Epoxy/AM 13.2 show the lowest and highest Young's modulus, which are about 67.1% and 126.2% of Epoxy/GRP, respectively.

Table 1. Model parameters for the epoxy/graphene composites including the yield strength, elastic moduli (Young's modulus and compressive modulus), glass transition temperature T_g, interaction energy, inflection angle θ, and tensile strength of the graphene sheet.

Configurations	Parallel to Graphene		Perpendicular to Graphene		Parallel to Graphene		Perpendicular to Graphene		T_g (K)	Interaction Energy {Kcal/mol}	Inflection Angle θ	Tensile Strength of Graphene Sheet {GPa}
	Tensile Yield Strength {MPa}	Young's Modulus {GPa}	Tensile Yield Strength {MPa}	Young's Modulus {GPa}	Compressive Yield Strength {MPa}	Compressive Modulus {GPa}	Compressive Yield Strength {MPa}	Compressive Modulus {GPa}				
Epoxy/ZZ GRP	188.07 ± 2.65	2.36 ± 0.31	160.56 ± 4.45	2.25 ± 0.04	290.96 ± 4.29	2.58 ± 0.06	262.62 ± 5.61	1.72 ± 0.20	422.8	−1044.32	14	146.29
Epoxy/AM GRP	158.76 ± 5.18	2.48 ± 0.46	160.56 ± 4.45	2.25 ± 0.04	256.62 ± 2.13	3.19 ± 0.23	262.62 ± 5.61	1.72 ± 0.20				126.67
Epoxy/ZZ 27.8	145.26 ± 2.34	2.61 ± 0.17	174.32 ± 5.87	1.51 ± 0.31	246.54 ± 3.31	2.94 ± 0.11	231.94 ± 5.19	2.78 ± 0.25	423.7	−992.78	20	127.39
Epoxy/ZZ 21.8	194.23 ± 6.40	2.65 ± 0.19	194.27 ± 7.16	2.22 ± 0.27	296.85 ± 6.43	3.15 ± 0.20	314.83 ± 3.18	2.98 ± 0.43	427.2	−1026.56	46	130.01
Epoxy/ZZ 13.2	191.81 ± 4.11	1.90 ± 0.15	175.30 ± 6.98	2.45 ± 0.35	311.18 ± 6.80	2.67 ± 0.16	239.75 ± 4.00	2.76 ± 0.25	437.9	−1041.51	48	122.04
Epoxy/ZZ 9.4	207.58 ± 4.00	2.58 ± 0.12	220.62 ± 5.30	2.23 ± 0.17	320.95 ± 4.16	3.92 ± 0.27	334.13 ± 4.51	2.91 ± 0.27	462.1	−1044.55	41	122.86
Epoxy/ZZ 8.9	178.58 ± 2.51	2.02 ± 0.06	165.85 ± 1.09	2.46 ± 0.53	300.74 ± 7.75	3.39 ± 0.52	283.99 ± 5.32	3.05 ± 0.14	456.2	−1013.91	25	119.98
Epoxy/AM 27.8	159.29 ± 7.49	1.91 ± 0.15	209.47 ± 4.20	1.88 ± 0.11	277.94 ± 4.54	2.34 ± 0.14	265.35 ± 3.23	2.74 ± 0.16	409.9	−1018.11	15	127.67
Epoxy/AM 21.8	226.47 ± 1.86	2.45 ± 0.35	216.36 ± 3.86	2.63 ± 0.30	291.25 ± 2.31	3.96 ± 0.12	272.67 ± 3.51	3.47 ± 0.18	427.2	−1017.33	35	118.96
Epoxy/AM 17.9	161.20 ± 2.78	2.16 ± 0.09	176.53 ± 2.61	2.24 ± 0.07	259.33 ± 2.13	2.25 ± 0.52	277.71 ± 1.35	2.46 ± 0.17	428.7	−998.02	60	109.85
Epoxy/AM 15.2	163.78 ± 7.19	1.98 ± 0.08	154.14 ± 3.24	1.99 ± 0.18	251.21 ± 6.74	3.08 ± 0.42	252.02 ± 4.30	2.43 ± 0.13	455.6	−1002.46	52	115.52
Epoxy/AM 13.2	135.91 ± 7.91	2.86 ± 0.70	183.28 ± 3.79	2.84 ± 0.36	286.21 ± 2.59	2.42 ± 0.16	282.26 ± 5.55	3.76 ± 0.27	455.9	−1038.25	62	95.93

Table 2. Calculated Young's modulus of epoxy/GRP and the values obtained from previous experiments or simulations.

References	Method	Young's Modulus {GPa}
Shen et al. [16]	Experiment	2.66
Zakaria et al. [47]	Experiment	1.65
Yu et al. [48]	MD	3.35
Moeini et al. [49]	MD	3.20
This work	MD	2.36

To further investigate the mechanism of GBs affecting the tensile mechanical properties of epoxy/graphene composites, the effect of the misorientation angle, the tensile strength of graphene sheets, the interaction energy, and the inflection angle on the tensile yield strength of epoxy/graphene composites with a tensile direction parallel to the graphene sheet were analyzed. Figure 3a shows the relationship between the misorientation angle of GBs and the yield strength of the epoxy/graphene composites. Results show that with increasing misorientation angle, the yield strength shows no obvious trend. This indicates that the lattice orientation of the GBs in the plane is not the main factor affecting the mechanical properties of epoxy/graphene composites. In addition, the effect of the tensile strength of graphene sheets on the yield strength of epoxy/graphene composites was analyzed. From Figure 3b, one can see that the yield strength of the epoxy/graphene composites basically increases as the tensile strength of graphene sheets increases. The stronger the strength of reinforcements, the better the mechanical properties of the composites. However, the relative scattering suggests that there are other factors affecting the yield strength of composites besides the strength of graphene sheets.

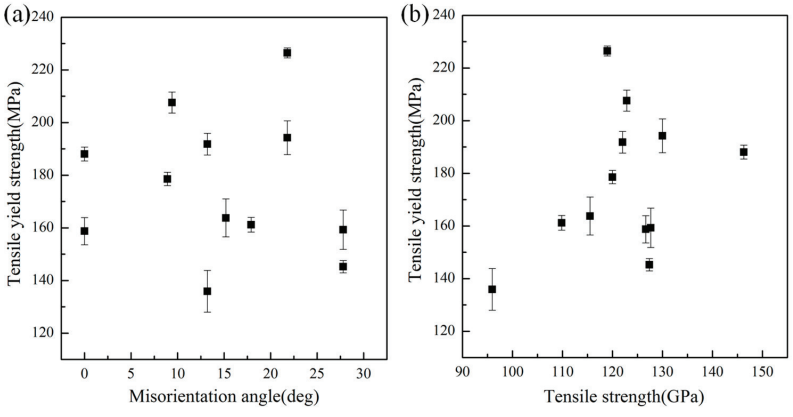

Figure 3. Effect of (**a**) the misorientation angle of GBs and (**b**) the tensile strength of graphene sheets on the tensile yield strength of composites under a uniaxial tensile load parallel to the graphene sheet.

In order to further comprehend the factors affecting the yield strength of epoxy/graphene composites, the interaction energy between the epoxy matrix and graphene with GBs was calculated using the following expression [50,51].

$$\Delta E = E_{total} - E_{epoxy} - E_{graphene} \quad (2)$$

where E_{total}, E_{epoxy}, and $E_{graphene}$ represent the total potential energies of the composite system, epoxy matrix, and graphene, respectively. The interaction energy between the epoxy matrix and the graphene is basically in association with the van der Waals interactions.

As shown in Table 1, the interfacial interaction energy affects the tensile yield strength of composites. However, the configuration with the highest interaction energy does not

exhibit the strongest tensile yield strength. This can be explained by the fact that the tensile yield strength of composites is affected by multi-factors simultaneously. The introduction of GBs would induce structural changes in the graphene sheets. The most obvious phenomenon is the appearance of different degrees of wrinkles on the surface of the graphene sheet, which results in the change of the three-dimensional conformation of graphene. Actually, the change of the three-dimensional plane conformation of reinforcements has a regular effect on the mechanical properties of composites. The inflection degree of graphene sheets can be described by the inflection angle θ [52]. Figures 4a and 4b analyze the synergistic influence of the interaction energy and inflection angle on the yield strength of composites under a uniaxial tensile load parallel and perpendicular to the graphene sheet, respectively. With increasing interaction energy and inflection angle, the yield strength of epoxy/graphene composites increases at first and then decreases. The highest yield strength of composites occurs in the middle of the analyzed data range, which indicates that the yield strength is governed by both the interaction energy between the epoxy matrix and reinforcement and the structural conformation of the reinforcement. Figures 5a and 5b show the local microstructures of composites containing graphene with small and large inflection angles, respectively. The introduction of appropriate wrinkles in graphene surfaces can enhance the mechanical properties of composites because the wrinkle structure inhibits the movement of epoxy chains. However, when the inflection degree of a wrinkle increases to a certain degree, the distance between epoxy and graphene increases, as shown in Figure 5b. This mainly results from the cross-linked structure of epoxy resin. The epoxy chain cannot move to the areas where graphene has heavy wrinkles, which further leads to a decrease in the load transfer capability between the epoxy matrix and the reinforcement. Moreover, the existence of GBs can lead to the redistribution of stress in the graphene sheet [30], which further affects the load transfer between the epoxy and graphene. Simultaneously, high-energy sites can be created in graphene-containing GBs [34]. Different types of GBs can result in different distribution forms of high-energy sites, inducing changes in the local interaction between epoxy and graphene that may affect the mechanical properties of epoxy/graphene composites.

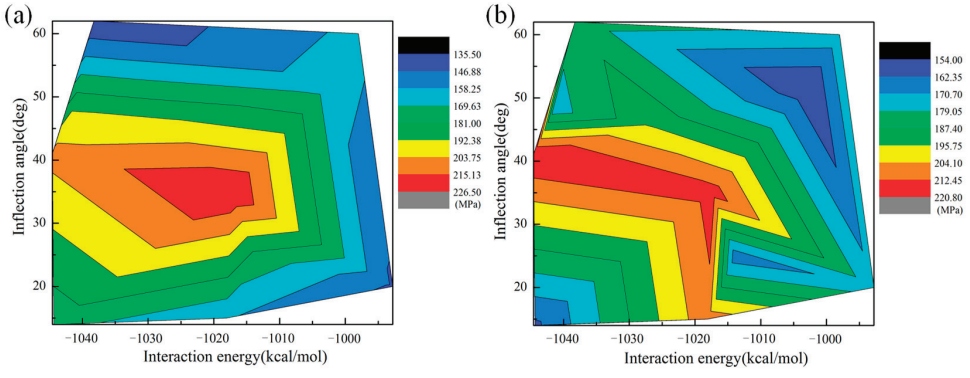

Figure 4. The influence of the interaction energy and inflection angle on the tensile yield strength of composites under a uniaxial tensile load (**a**) parallel to the graphene sheet and (**b**) perpendicular to the graphene sheet.

In a word, the tensile yield strength of epoxy/graphene composites is affected by multi-factors simultaneously, including the tensile strength of the reinforcement, the interaction energy, and the structure of the reinforcement. The physics behind the enhancement in the mechanical properties of composites reinforced with graphene is complicated; a balance exists among these factors leading to a great difference in the tensile yield strength of all the GBs configurations.

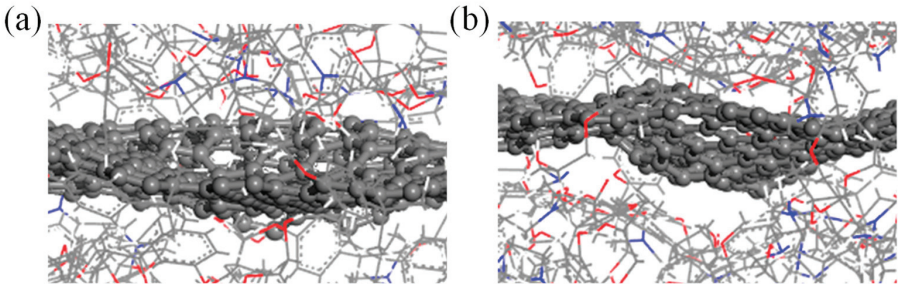

Figure 5. Schematic view of the composite local microstructures containing graphene with (**a**) slight wrinkles and (**b**) heavy wrinkles (carbon, oxygen, nitride, and hydrogen atoms are shown in gray, red, blue, and white, respectively).

3.2. Compressive Behavior of Epoxy/Graphene Composites

To further investigate the effect of GBs on the mechanical properties of epoxy/graphene composites, uniaxial compression along parallel and perpendicular directions to the interface was performed for different configurations of epoxy/graphene composites. The composite compression responses for pristine graphene and graphene with GB-reinforced epoxy composites are plotted in Figure 6. Similar to the tensile process, the compressive stress–strain curves include three distinct regions: the initial linear response, the yielding, and the strain hardening. The compressive yield strength and the compressive modulus are reported in Table 1.

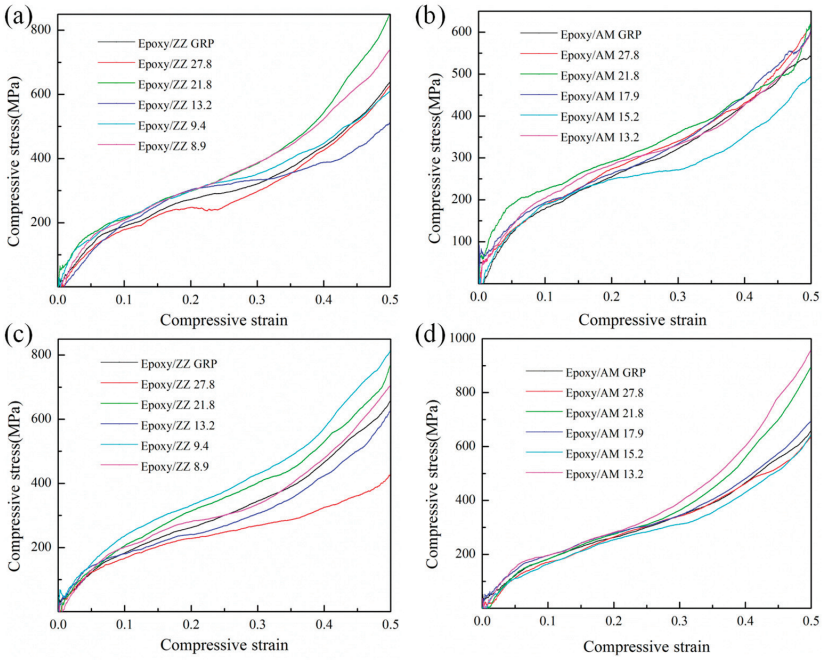

Figure 6. Stress-strain response of (**a**) Epoxy/ZZ systems and (**b**) Epoxy/AM systems subjected to a uniaxial compressive load parallel to the graphene sheet and perpendicular to the GB lines; (**c**) Epoxy/ZZ systems and (**d**) Epoxy/AM systems subjected to a uniaxial compressive load perpendicular to the graphene sheet.

A uniaxial compressive simulation for the ZZ and AM configurations was performed with a compressive load parallel to the interface and perpendicular to the GB lines, as illustrated in Figures 6a and 6b, respectively. As shown in Figure 6a and Table 1, the existence of GBs along the ZZ direction significantly affects the compressive mechanical properties of epoxy/graphene composites. Except for Epoxy/ZZ 27.8, the compressive yield strengths of the other ZZ configurations are higher than that of the Epoxy/ZZ GRP composite. Among all the ZZ configurations, the Epoxy/ZZ 9.4 system presents the highest compressive yield strength (320.95 MPa) and compressive modulus (3.92 GPa), which are improved by about 10.3% and 51.9% compared with those of Epoxy/ZZ GRP (290.96 MPa and 2.58 GPa), respectively. As illustrated in Figure 6b, among all the AM configurations, only the compressive yield strength of Epoxy/AM 15.2 is lower than that of the Epoxy/AM GRP composite. The compressive yield strength (291.25 MPa) and the compressive modulus (3.96 GPa) of Epoxy/AM 21.8 are the highest, with about a 13.5% and 24.1% improvement compared with those of Epoxy/AM GRP (256.62 MPa and 3.19 GPa), respectively.

From Table 1 and Figure 7a, one can see that the compressive yield strength of epoxy/graphene composites is mainly related to the interfacial interaction energy. With increasing interfacial interaction energy, the compressive yield strength of the epoxy/graphene composites basically exhibits a rising trend. However, it is interesting to note that some points deviate significantly from the curve, which indicates that there are other factors affecting the compressive yield strength of composites besides the interfacial interaction energy. To further capture the underlying mechanism, the effect of the three-dimensional conformational changes of graphene sheets on the compressive yield strength of epoxy/graphene composites was analyzed. Figure 7b shows the relationship between the inflection angle of GBs and the compressive yield strength of epoxy/graphene composites under a load parallel to the interface. With increasing inflection angle, the compressive yield strength of the epoxy/graphene composites increases at first and then decreases. The results indicate that the introduction of appropriate wrinkles in graphene surfaces can increase the resistance to compression force during the compressive process and further enhance the compressive yield strength of composites, as it can block the compressive movement of epoxy chains in a three-dimensional space.

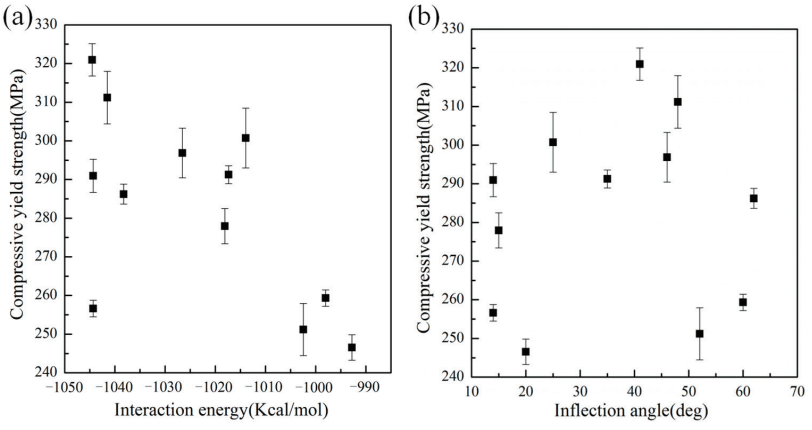

Figure 7. Effect of (**a**) the interaction energy and (**b**) the inflection angle of graphene sheets on the compressive yield strength of composites under a uniaxial compressive load parallel to graphene sheet.

Figures 6c and 6d show the stress–strain curves for ZZ and AM configurations subjected to a uniaxial compression load perpendicular to the graphene sheet, respectively. The mechanical parameters are tabulated in Table 1. As shown in Figure 6c and Table 1, the Epoxy/ZZ 27.8 configuration shows the lowest compressive yield strength, with about an 11.7% reduction compared with that of Epoxy/ZZ GRP. Epoxy/ZZ 9.4 shows the high-

est compressive yield strength, with about a 27.2% improvement compared with that of Epoxy/ZZ GRP. This enhancement is mainly due to the strong interaction energy and appropriate inflection angle of Epoxy/ZZ 9.4 which helps in establishing strong mechanical interlocking and transferring loads more efficiently. The compressive modulus of Epoxy/ZZ 8.9 is the highest among all the ZZ configurations, which is about a 77.3% improvement compared with that of Epoxy/ZZ GRP. For the AM configurations (see Figure 6d and Table 1), Epoxy/AM 13.2 possesses the highest compressive yield strength and compressive modulus, with about a 7.5% and 118.6% improvement compared with those of Epoxy/AM GRP, respectively. Epoxy/AM 15.2 shows the lowest compressive yield strength, with about 4.0% reduction compared with that of Epoxy/AM GRP.

Figures 8a and 8b show a comparison of the tensile and compressive yield strength for each configuration. The results indicate that the obtained compressive yield strength for all the models is not equal to the tensile yield strength. In fact, the compressive yield strength of any epoxy/graphene configuration is significantly higher than its tensile yield strength. For the superlative configuration, Epoxy/ZZ 9.4, the compressive yield strength is about 54.6% (51.5%) higher than the tensile yield strength with a load parallel (perpendicular) to the interface. This phenomenon may be mainly caused by the inherent rigid properties of the epoxy material. Moreover, from Figures 8a and 8b, one can see that a certain degree of difference exists between the tensile yield strength (or compressive yield strength) parallel and perpendicular to the interface. For the Epoxy/AM 13.2 configuration, the tensile yield strength parallel to the interface is 135.91 MPa, which is about 74.2% of that perpendicular to the interface. For the Epoxy/ZZ 13.2 configuration, the compressive yield strength perpendicular to the interface is about 77.0% of that parallel to the interface. This indicates that the tensile and compressive yield strengths are dependent to some extent on the loading direction, i.e., the capacity of reinforced graphene to alter the mechanical properties of epoxy is variable in different directions.

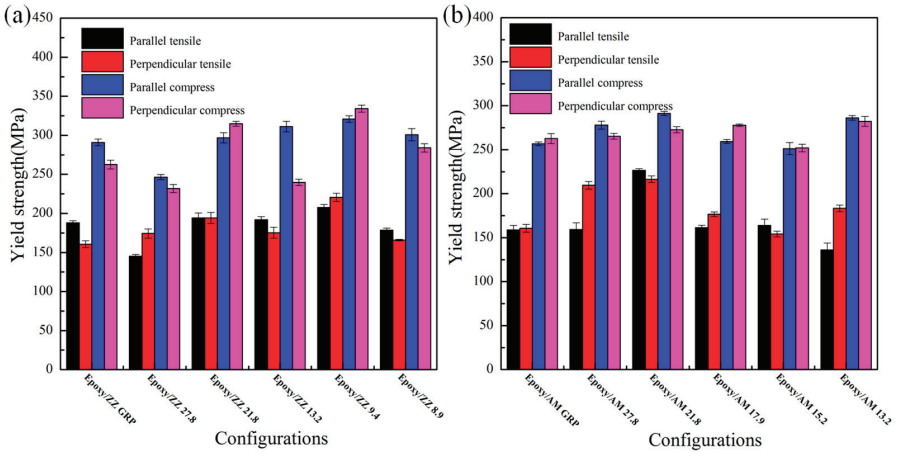

Figure 8. The yield strength of (**a**) Epoxy/ZZ systems and (**b**) Epoxy/AM systems subjected to a uniaxial tensile (compressive) load parallel and perpendicular to the graphene sheet.

3.3. Glass Transition Temperature of Epoxy/Graphene Composites

To understand the effect of GBs on the thermal stability of epoxy/graphene composites, T_g was calculated for all models. Note that it is a key thermal property affecting the mechanical properties, chemorheology, and internal stresses of thermosetting polymers [53–55].

The T_g of all epoxy/graphene composites was determined by measuring the density of the composites while the NPT equilibration temperature levels gradually decreased from 600 to 300 K in increments of 20 K. During the cooling process, the structures were equilibrated for 500 ps under NPT ensemble (P = 1 atm) at each temperature with a density

tolerance of 0.02 g/cm^3. After fitting the data with a straight line, the value of T_g could be obtained by searching for the intersection point of the density–temperature curves. In addition, the epoxy composite goes through a transition from a rubbery state, which is identified with a large slope, to a glassy state, which is identified with a small slope, during the cooling process [56].

Figures 9a and 9b show the density-temperature curves for the ZZ and AM configurations, respectively. The values of T_g calculated by density-temperature curves are tabulated in Table 1. The T_g of pristine graphene-reinforced epoxy composite is about 422.8 K, which is in good agreement with the value of 418.0 K from previous results [56]. Additionally, it is noteworthy that graphene sheets with GBs along the ZZ direction are better than pristine graphene sheets at improving the T_g of epoxy composites. The T_g of Epoxy/ZZ 8.9 and Epoxy/ZZ 9.4 are shown to be 456.2 K and 462.1 K, which are about a 7.9% and 9.3% improvement compared with that of epoxy/ZZ GRP, respectively. From Figure 9b and Table 1, one can see that, except for Epoxy/AM 27.8, the T_g of the other AM configurations is higher than that of Epoxy/AM GRP. The T_g of Epoxy/AM 13.2 and Epoxy/AM 15.2 are shown to be 455.9 K and 455.6 K, which are about 33.1 K and 32.8 K higher than that of Epoxy/AM GRP, respectively.

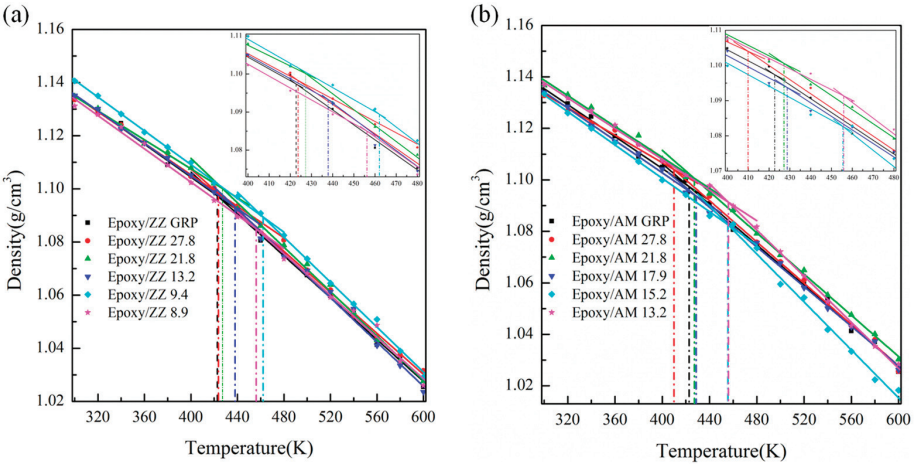

Figure 9. The density-temperature relationship of (**a**) Epoxy/ZZ systems and (**b**) Epoxy/AM systems.

The improvement of T_g in pristine graphene and graphene containing GB reinforced epoxy composites is mainly related to the excellent interfacial interaction and the inflection degree of the wrinkles in graphene sheets. The strong interfacial interaction between the epoxy matrix and reinforcement can help to restrict the translational and rotational movements of epoxy chains during volume expansion. Moreover, the wrinkle structure of graphene with GBs increases the surface roughness, which is also conducive to blocking the slippage of epoxy chains. It also allows the composites to be heated evenly, avoiding heat concentration in the materials. However, the heavy wrinkle structure weakens the interfacial interaction energy to a certain degree, which creates a complex balance in influencing the T_g of the epoxy/graphene composites. The T_g of Epoxy/AM 27.8 is lower than that of epoxy/AM GRP, which is mainly due to its relatively weak interfacial interaction (−1018.11 Kcal/mol) and the low inflection angle of the graphene sheet (about 15°). The higher T_g of Epoxy/ZZ 9.4 is related to its relatively strong interfacial interaction (−1044.55 Kcal/mol) and the appropriate inflection angle of the graphene sheet (about 41°). The improvement in T_g indicates that the epoxy/graphene composites need a higher temperature to change from a glassy state to a rubbery state and that the strength of epoxy/graphene composites can remain stable at a higher temperature.

4. Conclusions

In summary, the effect of pristine graphene and graphene with GBs on the mechanical properties of epoxy composites was investigated using MD simulations. The results show that the yield strength, elastic moduli (Young's modulus and compressive modulus), and T_g of epoxy/graphene composites are significantly affected by GBs. When the tensile load is parallel to the graphene sheet and perpendicular to the GB lines, the existence of GBs can either enhance or weaken the tensile yield strength of epoxy/graphene composites. The Epoxy/ZZ 9.4 and Epoxy/AM 21.8 configurations present stronger tensile yield strengths, which are considered to be superlative configurations. Multiple factors affect the tensile yield strength of epoxy/graphene composites, including the tensile strength of the reinforcement, the interfacial interaction energy, and the inflection degree of reinforcement. There is a complex balance of these influencing factors which leads to the difference in the tensile yield strength of all the GB configurations. The compressive yield strength for all GB configurations is stronger than the tensile yield strength, and diversity exists for the tensile (compressive) yield strength due to different loading directions. Graphene-containing GB-reinforced epoxy composites obtain a higher T_g compared with pristine graphene-reinforced epoxy. The enhancement mechanism can be attributed to the excellent interfacial interaction and appropriate inflection degree of wrinkles in the graphene sheets with GBs. This work will shed light, from the molecular level, on the material design for epoxy composites containing defective reinforcements for practical applications.

Author Contributions: Investigation, Q.D.; Software, Q.D.; Conceptualization, Q.D.; Validation, X.C.; Data curation, X.C. and F.Z.; Writing—original draft, Q.D.; Writing—review & editing, N.D., W.G. and F.Z.; Supervision, N.D and W.G. All authors have read and agreed to the published version of the manuscript.

Funding: This research was funded by the National Natural Science Foundation of China (Grant No. 11404192), the Key Research and Development Project of Shandong Province, China (Grant No. 2017GSF220004), the Shandong Province Special Grant for High-Level Talents, and the research fund of Qilu University of Technology (Shandong Academy of Sciences).

Institutional Review Board Statement: Not applicable.

Data Availability Statement: The data presented in this study are available on request from the corresponding authors.

Conflicts of Interest: The authors declare no conflict of interest.

References

1. Kang, H.J.; Shao, Q.; Guo, X.K.; Galaska, A.; Liu, Y.Y.; Guo, Z.H. Separation and recovery of copper foil and fabric from waste printed circuit boards by decomposing brominated epoxy resin using near critical water. *Eng. Sci.* **2018**, *1*, 78–85. [CrossRef]
2. Zhang, Y.X.; Zhao, M.; Zhang, J.X.; Shao, Q.; Li, J.F.; Li, H.; Lin, B.; Yu, M.Y.; Chen, S.G.; Guo, Z.H. Excellent corrosion protection performance of epoxy composite coatings filled with silane functionalized silicon nitride. *J. Polym. Res.* **2018**, *25*, 130. [CrossRef]
3. Jiang, Y.; Li, M.; Chen, C.; Xue, Z.; Xie, X.; Zhou, X.; Mai, Y.W. Effect of elastic modulus mismatch of epoxy/titanium dioxide coated silver nanowire composites on the performance of thermal conductivity. *Compos. Sci. Technol.* **2018**, *165*, 206–213. [CrossRef]
4. Li, M.; Zhou, H.; Zhang, Y.; Liao, Y.; Zhou, H. Effect of defects on thermal conductivity of graphene/epoxy nanocomposites. *Carbon* **2018**, *130*, 295–303. [CrossRef]
5. Shokuhfar, A.; Arab, B. The effect of cross linking density on the mechanical properties and structure of the epoxy polymers: Molecular dynamics simulation. *J. Mol. Model.* **2013**, *19*, 3719–3731. [CrossRef] [PubMed]
6. Aghadavoudi, F.; Golestanian, H.; Beni, Y.T. Investigating the effects of resin crosslinking ratio on mechanical properties of epoxy-based nanocomposites using molecular dynamics. *Polym. Compos.* **2017**, *38*, 433–442. [CrossRef]
7. Domun, N.; Hadavinia, H.; Zhang, T.; Sainsbury, T.; Liaghat, G.; Vahid, S. Improving the fracture toughness and the strength of epoxy using nanomaterials—A review of the current status. *Nanoscale* **2015**, *7*, 10294–10329. [CrossRef]
8. Kulkarni, H.B.; Tambe, P.; Joshi, G.M. Influence of covalent and non-covalent modification of graphene on the mechanical, thermal and electrical properties of epoxy/graphene nanocomposites: A review. *Compos. Interfaces* **2018**, *25*, 381–414. [CrossRef]
9. Rahman, A.; Deshpande, P.; Radue, M.S.; Odegard, G.M.; Gowtham, S.; Ghosh, S.; Spear, A.D. A machine learning framework for predicting the shear strength of carbon nanotube-polymer interfaces based on molecular dynamics simulation data. *Compos. Sci. Technol.* **2021**, *207*, 108627. [CrossRef]

10. Jian, W.; Wang, X.; Lu, H.; Lau, D. Molecular dynamics simulations of thermodynamics and shape memory effect in CNT-epoxy nanocomposites. *Compos. Sci. Technol.* **2021**, *211*, 108849. [CrossRef]
11. Lee, C.; Wei, X.; Kysar, J.W.; Hone, J. Measurement of the elastic properties and intrinsic strength of monolayer graphene. *Science* **2008**, *321*, 385–388. [CrossRef] [PubMed]
12. Tang, L.C.; Wan, Y.J.; Yan, D.; Pei, Y.B.; Zhao, L.; Li, Y.B.; Wu, L.B.; Jiang, J.X.; Lai, G.Q. The effect of graphene dispersion on the mechanical properties of graphene/epoxy composites. *Carbon* **2013**, *60*, 16–27. [CrossRef]
13. Xie, W.H.; Wei, Y.J. Roughening for strengthening and toughening in monolayer carbon based composites. *Nano Lett.* **2021**, *21*, 4823–4829. [CrossRef] [PubMed]
14. Rafiee, M.A.; Rafiee, J.; Wang, Z.; Song, H.; Yu, Z.Z.; Koratkar, N. Enhanced mechanical properties of nanocomposites at low graphene content. *ACS Nano* **2009**, *3*, 3884–3890. [CrossRef]
15. Idowu, A.; Boesl, B.; Agarwal, A. 3D graphene foam-reinforced polymer composites—A review. *Carbon* **2018**, *135*, 52–71. [CrossRef]
16. Shen, X.J.; Liu, Y.; Xiao, H.M.; Feng, Q.P.; Yu, Z.Z.; Fu, S.Y. The reinforcing effect of graphene nanosheets on the cryogenic mechanical properties of epoxy resins. *Compos. Sci. Technol.* **2012**, *72*, 1581–1587. [CrossRef]
17. Yang, S.Y.; Lin, W.N.; Huang, Y.L.; Tien, H.W.; Wang, J.Y.; Ma, C.C.M.; Li, S.M.; Wang, Y.S. Synergetic effects of graphene platelets and carbon nanotubes on the mechanical and thermal properties of epoxy composites. *Carbon* **2011**, *49*, 793–803. [CrossRef]
18. Saha, M.; Tambe, P.; Pal, S. Thermodynamic approach to enhance the dispersion of graphene in epoxy matrix and its effect on mechanical and thermal properties of epoxy nanocomposites. *Compos. Interfaces* **2016**, *23*, 255–272. [CrossRef]
19. Chandrasekaran, S.; Sato, N.; Tölle, F.; Mülhaupt, R.; Fiedler, B.; Schulte, K. Fracture toughness and failure mechanism of graphene based epoxy composites. *Compos. Sci. Technol.* **2014**, *97*, 90–99. [CrossRef]
20. Teng, C.C.; Ma, C.C.M.; Lu, C.H.; Yang, S.Y.; Lee, S.H.; Hsiao, M.C.; Yen, M.Y.; Chiou, K.C.; Lee, T.M. Thermal conductivity and structure of non-covalent functionalized graphene/epoxy composites. *Carbon* **2011**, *49*, 5107–5116.
21. Fu, Y.X.; He, Z.X.; Mo, D.C.; Lu, S.S. Thermal conductivity enhancement of epoxy adhesive using graphene sheets as additives. *Int. J. Therm. Sci.* **2014**, *86*, 276–283. [CrossRef]
22. Li, Y.L.; Wang, Q.; Jie, W.S. A review on enhancement of mechanical and tribological properties of polymer composites reinforced by carbon nanotubes and graphene sheet: Molecular dynamics simulations. *Compos. Part B Eng.* **2019**, *160*, 348–361. [CrossRef]
23. Wang, Z.Y.; Jia, Z.M.; Feng, X.P.; Zou, Y. Graphene nanoplatelets/epoxy composites with excellent shear properties for construction adhesives. *Compos. Part B Eng.* **2018**, *152*, 311–315. [CrossRef]
24. Bian, P.L.; Verestek, W.; Yan, S.; Xu, X.; Qing, H.; Schmauder, S. A multiscale modeling on fracture and strength of graphene platelets reinforced epoxy. *Eng. Fract. Mech.* **2020**, *235*, 107197. [CrossRef]
25. Sun, R.; Li, L.; Feng, C.; Kitipornchai, S.; Yang, J. Tensile property enhancement of defective graphene/epoxy nanocomposite by hydrogen functionalization. *Compos. Struct.* **2019**, *224*, 111079. [CrossRef]
26. Biró, L.P.; Lambin, P. Grain boundaries in graphene grown by chemical vapor deposition. *New J. Phys.* **2013**, *15*, 035024. [CrossRef]
27. Duong, D.L.; Han, G.H.; Lee, S.M.; Gunes, F.; Kim, E.S.; Kim, S.T.; Kim, H.; Ta, Q.H.; So, K.P.; Yoon, S.J.; et al. Probing graphene grain boundaries with optical microscopy. *Nature* **2012**, *490*, 235–239. [CrossRef]
28. Zhang, J.F.; Zhao, J.J.; Lu, J.P. Intrinsic strenth and failure behaviors of graphene grain boundaries. *ACS Nano* **2012**, *6*, 2704–2711. [CrossRef]
29. Xu, N.; Guo, J.; Cui, Z. The influence of tilt grain boundaries on the mechanical properties of bicrystalline graphene nanoribbons. *Phys. E Low-Dimens. Syst. Nanostruct.* **2016**, *84*, 168–174. [CrossRef]
30. Wei, Y.J.; Wu, J.T.; Yin, H.Q.; Shi, X.H.; Yang, R.G.; Dresselhaus, M. The nature of strength enhancement and weakening by pentagon-heptagon defects in graphene. *Nat. Mater.* **2012**, *11*, 759–763. [CrossRef]
31. Grantab, R.; Shenoy, V.B.; Ruoff, R.S. Anomalous strength characteristics of tilt grain boundaries in graphene. *Science* **2010**, *330*, 946–948. [CrossRef] [PubMed]
32. Dong, J.C.; Geng, D.C.; Liu, F.N.; Ding, F. Formation of twinned graphene polycrystals. *Angew. Chem. Int. Ed.* **2019**, *58*, 7723–7727. [CrossRef] [PubMed]
33. Li, M.Y.; Chen, P.; Zheng, B.; Deng, T.; Zhang, Y.; Liao, Y.; Zhou, H. Effect of stone-wales defect on mechanical properties of Gr/epoxy nanocomposites. *Polymers* **2019**, *11*, 1116. [CrossRef] [PubMed]
34. Verma, A.; Parashar, A.; Packirisamy, M. Effect of grain boundaries on the interfacial behaviour of graphene-polyethylene nanocomposite. *Appl. Surf. Sci.* **2019**, *470*, 1085–1092. [CrossRef]
35. Sahraei, A.A.; Mokarizadeh, A.H.; George, D.; Rodrigue, D.; Baniassadi, M.; Foroutan, M. Insights into interphase thickness characterization for graphene/epoxy nanocomposites: A molecular dynamics simulation. *Phys. Chem. Chem. Phys.* **2019**, *21*, 19890–19903. [CrossRef]
36. Brandrup, J.; Immergut, E.H.; Grulke, E.A. *Polymer Handbook*, 4th ed.; Wiley: Hoboken, NJ, USA, 2004.
37. Plimpton, S. Fast parallel algorithms for short-range molecular dynamics. *J. Comput. Phys.* **1995**, *117*, 1–19. [CrossRef]
38. Sun, H.; Mumby, S.J.; Maple, J.R.; Hagler, A.T. An ab Initio CFF93 all-atom force field for polycarbonates. *J. Am. Chem. Soc.* **1994**, *116*, 2978–2987. [CrossRef]
39. Wei, J.; Denvid, L. Understanding the effect of functionalization in CNT-epoxy nanocomposite from molecular level. *Compos. Sci. Technol.* **2020**, *191*, 108076.

40. Li, M.Y.; Zhou, H.; Zhang, Y.; Liao, Y.G.; Zhou, H.M. The effect of defects on the interfacial mechanical properties of graphene/epoxy composites. *RSC Adv.* **2017**, *7*, 46101–46108. [CrossRef]
41. Tam, L.H.; Lau, D. A molecular dynamics investigation on the cross-linking and physical properties of epoxy-based materials. *RSC Adv.* **2014**, *4*, 33074–33081. [CrossRef]
42. Fankhänel, J.; Arash, B.; Rolfes, R. Elastic interphase properties of nanoparticle/epoxy nanocomposites: A molecular dynamics study. *Compos. Part B Eng.* **2019**, *176*, 107211.
43. Meng, F.; Chen, C.; Song, J. Lattice trapping and crack decohesion in graphene. *Carbon* **2017**, *116*, 33–39. [CrossRef]
44. Tamrakar, S.; Ganesh, R.; Sockalingam, S.; Haque, B.Z.; Gillespie, J.W. Experimental investigation of strain rate and temperature dependent response of an epoxy resin undergoing large deformation. *J. Dyn. Behav. Mater.* **2018**, *4*, 114–128. [CrossRef]
45. Elder, R.M.; Knorr, J.D.B.; Andzelm, J.W.; Lenhart, J.L.; Sirk, T.W. Nanovoid formation and mechanics: A comparison of poly(dicyclopentadiene) and epoxy networks from molecular dynamics simulations. *Soft Matter* **2016**, *12*, 4418–4434. [CrossRef]
46. Chowdhury, S.C.; Elder, R.M.; Sirk, T.W.; Gillespie, J.W. Epoxy resin thermo-mechanics and failure modes: Effects of cure and cross-linker length. *Compos. Part B Eng.* **2020**, *186*, 107814. [CrossRef]
47. Zakaria, M.R.; Kudus, M.H.A.; Akil, H.M.; Thirmizir, M.Z.M. Comparative study of graphene nanoparticle and multiwall carbon nanotube filled epoxy nanocomposites based on mechanical, thermal and dielectric properties. *Compos. Part B Eng.* **2017**, *119*, 57–66. [CrossRef]
48. Yu, H.P.; Tong, Z.H.; Chen, P.; Cai, A.W.; Qin, F. Effects of different parameters on thermal and mechanical properties of aminated graphene/epoxy nanocomposites connected by covalent: A molecular dynamics study. *Curr. Appl. Phys.* **2020**, *20*, 510–518. [CrossRef]
49. Moeini, M.; Isfahani, R.B.; Saber-Samandari, S.; Aghdam, M.M. Molecular dynamics simulations of the effect of temperature and strain rate on mechanical properties of graphene-epoxy nanocomposites. *Mol. Simul.* **2020**, *46*, 476–486. [CrossRef]
50. Zheng, Q.; Xue, Q.; Yan, K.; Gao, X.; Li, Q.; Hao, L. Effect of chemisorption on the interfacial bonding characteristics of carbon nanotube-polymer composites. *Polymer* **2008**, *49*, 800–808. [CrossRef]
51. Hasheminejad, K.; Montazeri, A. Enhanced interfacial characteristics in PLA/graphene composites through numerically-designed interface treatment. *Appl. Surf. Sci.* **2020**, *502*, 144150. [CrossRef]
52. Ding, Q.Y.; Ding, N.; Liu, L.; Li, N.; Wu, C.-M.L. Investigation on mechanical performances of grain boundaries in hexagonal boron nitride sheets. *Int. J. Mech. Sci.* **2018**, *149*, 262–272. [CrossRef]
53. Fan, J.; Anastassiou, A.; Macosko, C.W.; Tadmor, E.B. Molecular dynamics predictions of thermomechanical properties of an epoxy thermosetting polymer. *Polymer* **2020**, *196*, 122477. [CrossRef]
54. Hale, A.; Macosko, C.W.; Bair, H.E. Glass transition temperature as a function of conversion in thermosetting polymers. *Macromolecules* **1991**, *24*, 2610–2621. [CrossRef]
55. Schichtel, J.J.; Chattopadhyay, A. Modeling thermoset polymers using an improved molecular dynamics crosslinking methodology. *Comp. Mater. Sci.* **2020**, *174*, 109469. [CrossRef]
56. Ji, W.M.; Zhang, L.W.; Liew, K.M. Understanding interfacial interaction characteristics of carbon nitride reinforced epoxy composites from atomistic insights. *Carbon* **2021**, *171*, 45–54. [CrossRef]

Disclaimer/Publisher's Note: The statements, opinions and data contained in all publications are solely those of the individual author(s) and contributor(s) and not of MDPI and/or the editor(s). MDPI and/or the editor(s) disclaim responsibility for any injury to people or property resulting from any ideas, methods, instructions or products referred to in the content.

polymers

MDPI

Review

Advancing Plastic Recycling: Challenges and Opportunities in the Integration of 3D Printing and Distributed Recycling for a Circular Economy

Ali Kassab [1], Dawood Al Nabhani [2], Pravansu Mohanty [2], Christopher Pannier [2] and Georges Y. Ayoub [1,*]

[1] Department of Industrial and Manufacturing Systems, University of Michigan-Dearborn, Dearborn, MI 48128, USA; akassab@umich.edu
[2] Department of Mechanical Engineering, University of Michigan-Dearborn, Dearborn, MI 48128, USA; dalnabha@umich.edu (D.A.N.); pannier@umich.edu (C.P.)
* Correspondence: gayoub@umich.edu

Abstract: The concept of the circular economy has emerged as a promising solution to address the mounting concerns surrounding plastic waste and the urgent need for sustainable resource management. While conventional centralized recycling remains a common practice for plastic waste, centralized facilities may prove inadequate in handling the ever-increasing volumes of plastic waste generated globally. Consequently, exploring alternative recycling methods, such as distributed recycling by additive manufacturing, becomes paramount. This innovative approach encompasses actively involving communities in recycling practices and promotes a circular economy. This comprehensive review paper aims to explore the critical aspects necessary to realize the potential of distributed recycling by additive manufacturing. In this paper, our focus lies on proposing schemes that leverage existing literature to harness the potential of distributed recycling by additive manufacturing as an effective approach to plastic waste management. We explore the intricacies of the recycling process, optimize 3D printing parameters, address potential challenges, and evaluate the mechanical properties of recycled materials. Our investigation draws heavily from the literature of the last five years, as we conduct a thorough critical assessment of DRAM implementation and its influence on the properties of 3D printing structures. Through comprehensive analysis, we reveal the potential of recycled materials in delivering functional components, with insights into their performance, strengths, and weaknesses. This review serves as a comprehensive guide for those interested in embracing distributed recycling by additive manufacturing as a transformative approach to plastic recycling. By fostering community engagement, optimizing 3D printing processes, and incorporating suitable additives, it is possible to collectively contribute to a more sustainable future while combatting the plastic waste crisis. As progress is made, it becomes essential to further delve into the complexities of material behavior, recycling techniques, and the long-term durability of recycled 3D printed components. By addressing these challenges head-on, it is feasible to refine and advance distributed recycling by additive manufacturing as a viable pathway to minimize plastic waste, fostering a circular economy and cultivating a cleaner planet for generations to come.

Keywords: thermoplastics; mechanical recycling; circular economy; distributed recycling; additive manufacturing

Citation: Kassab, A.; Al Nabhani, D.; Mohanty, P.; Pannier, C.; Ayoub, G.Y. Advancing Plastic Recycling: Challenges and Opportunities in the Integration of 3D Printing and Distributed Recycling for a Circular Economy. *Polymers* **2023**, *15*, 3881. https://doi.org/10.3390/polym15193881

Academic Editors: Ulrich Maschke, Matthias Ballauff, Rufina G. Alamo and Fahmi Zaïri

Received: 20 August 2023
Revised: 12 September 2023
Accepted: 20 September 2023
Published: 25 September 2023

Copyright: © 2023 by the authors. Licensee MDPI, Basel, Switzerland. This article is an open access article distributed under the terms and conditions of the Creative Commons Attribution (CC BY) license (https://creativecommons.org/licenses/by/4.0/).

1. Introduction

The utilization of plastic materials in various structural and non-structural applications has witnessed significant growth over the past 70 years, attracting interest across multiple industries. However, a major concern arises from the fact that most plastic produced in the last 60 years is not biodegradable and, consequently, can take decades to decompose [1–3]. With a staggering 86% of plastic ending up in landfills [4], a substantial volume of plastic waste has accumulated over the last few decades, resulting in waste-management issues as

well as the environmental crises of microplastics in marine environments and microplastic ingestion by humans and animals [5,6]. One key issue contributing to this problem is the prevalence of plastics intended to be discarded after a single use. Instead of single-use, plastics could be given new life through recycling to make use of the embodied energy already spent in production and distribution of the plastic [7,8]. Therefore, it becomes crucial for designers to consider in their material selection and product design, the recycling of the material for use in applications different from the initial application. As a note to the reader, it is important to clarify that in this manuscript, the terms "thermoplastics" and "plastics" will be used interchangeably to refer only to the polymers that can be reprocessed by melting.

Plastic waste poses significant challenges for effective recycling. Plastic materials constitute a substantial portion, approximately 12.9%, of total US municipal solid waste [9]. Unlike metals, which are relatively easier to recycle, plastic waste presents unique difficulties. The production of plastic materials encompasses a wide range of applications, with packaging and single-use products accounting for approximately 50% of its usage. In contrast, only a modest proportion, between 20% and 25%, of produced plastics are employed in long-term infrastructure, primarily in the construction and building sectors. The remaining plastic production caters to intermediate lifespan products including electrical and electronic goods, furniture, vehicles, and agriculture [2,10,11]. Plastic production is distributed across various types of polymers: polyethylene (PE)-based products constitute 24% of plastic production, followed by polypropylene (PP) products at 16.6%, polyvinyl chloride (PVC) products at 11.4%, polyurethane (PU) products at 5.5%, polystyrene (PS) products at 6.1%, and polyethylene terephthalate (PET) products at 5.3% [12]. The combination of different polymers and the potential contamination by food particles, metal, paper, pigment, and ink further complicates the recycling of polymers. The challenges in plastic recycling are exacerbated by a shortage of collection and sorting facilities, the difficulty in effectively sorting different types of plastic, and the high cost associated with collecting and processing plastic waste. The higher costs associated with plastic recycling act as a deterrent for manufacturers and investors alike. This issue presents a significant barrier that hinders the widespread adoption of plastic recycling initiatives. Recycling and remanufacturing plastic can save between 30% to 80% of carbon emissions compared to processing and manufacturing of virgin plastics [13]. As governments implement carbon pricing, the economics of plastic recycling will improve compared to virgin plastic production. To enhance the quality of recycled polymers and increase their economic viability as alternatives to virgin materials, significant investment in recycling technologies is necessary.

The degradation rates of polymers are significantly influenced by environmental factors such as ultraviolet light, oxygen, and temperature. These environmental influences pose challenges to recycling efforts and contribute to the overall decrease in the quality of recycled plastic material. Compared to their non-recycled counterparts, recycled plastics often exhibit lower quality, characterized by color variation and decreased strength. These quality issues pose barriers to their utilization in the manufacturing sector, as they may be less appealing to manufacturers and hinder their incorporation into new products [2]. The compromised quality of recycled plastics necessitates further attention and research to address these limitations and enhance the desirability and applicability of recycled materials in various industries.

Plastic recycling encompasses various methods, classified into four categories: primary recycling, secondary recycling, tertiary recycling, and quaternary recycling. Each category involves distinct processes and objectives. Primary recycling, also known as closed-loop recycling, entails mechanically reprocessing plastic scrap to produce a product with properties equal to those of the original material. Secondary recycling, referred to as downgrading recycling, involves mechanically reprocessing plastic scrap to produce a product with altered properties. Tertiary recycling focuses on the recovery of chemical constituents from plastic scrap, while quaternary recycling harnesses the energy content of scrap plastic to generate steam and electricity [2]. Mechanical recycling is used in both

primary and secondary recycling. While most thermoplastics, including PET, PE, and PP, have high potential for mechanical recycling, thermosets such as unsaturated polyester and epoxy resin cannot be mechanically recycled due to their molecular structure. The varying processing requirements and molecular incompatibility of different plastic types present challenges in the production of recycled plastic from plastic waste. The mechanical recycling process comprises several key stages, including collection, sorting, cleaning, size reduction, and compatibilization or separation. Typically, these stages occur at centralized recycling facilities strategically located near industrial areas or urban centers. These large-scale recycling centers are equipped with specialized machinery and technologies capable of handling significant volumes of plastic waste, enabling efficient processing.

However, despite the existing infrastructure and centralized recycling facilities, the traditional recycling model faces certain challenges that limit its effectiveness. These challenges include the scarcity of collection and sorting facilities, difficulties in separating different plastic types, and the high costs associated with collecting and processing plastic waste. Furthermore, the low weight-to-volume ratio of plastic waste exacerbates the economic feasibility of the traditional recycling process. As an illustration, Craighill and Powell [14] highlight that PET plastics generated in Britain are often exported to centralized recycling facilities in the Netherlands and Ireland for recycling, reflecting the challenges posed by transporting lightweight plastic waste over long distances. The reliance on centralized facilities and the associated logistics of transporting waste materials from individual consumers to recycling centers and back to manufacturers are increasingly considered impractical and environmentally burdensome. Despite comprising less than 5 percent of the worldwide population in 2016, North America was responsible for producing 14 percent of the planet's total waste, amounting to 289 million tons, translating to a daily rate of 2.21 kg per person. The high collection rate of waste in North America, at 99.7 percent, is attributed to sufficient funding for waste management. Nevertheless, 12 percent of this waste is incinerated, over half ends up in landfills, and only about one-third is subjected to recycling. Part of this challenge is not solely driven by costs but rather by the complexities within the logistics network [15]. To establish an efficient and sustainable plastic recycling ecosystem, it is imperative to adopt a comprehensive approach that integrates localized recycling solutions alongside centralized facilities. This approach aims to reduce the reliance on new resources and minimize waste production, while simultaneously improving energy efficiency and promoting environmental sustainability. These objectives align with the principles of a circular economy, which seeks to protect the environment, foster social justice, and encourage sustainable economic growth. By embracing a comprehensive approach, the plastic recycling ecosystem can transition from a linear model to a circular one, in which materials are kept in use for as long as possible and waste is minimized. Further, this transformation requires localized recycling solutions that are close to the point of waste generation to reduce the need for extensive transportation and logistics. The integration of localized recycling into the existing network of centralized facilities offers the potential to create a more resilient and adaptable system that is responsive to the unique needs of different communities and regions. A promising localized approach that promotes resource efficiency, minimizes environmental impacts, and fosters a more sustainable and inclusive future for plastic recycling is the concept of distributed recycling, illustrated in Figure 1. Figure 1 presents two distinct recycling models. The first model represents the existing centralized recycling facilities, wherein plastic waste is collected from across a large area and transported to a central facility for processing. While this model has been effective to date, it faces limitations from transportation costs and the commensurate energy expended and carbon emissions. In contrast, the second model shows distributed recycling. Operating on a smaller scale, this system runs in parallel with the established centralized system, contributing to a more decentralized and locally driven recycling process. In this distributed model, recycling takes place closer to the source of waste generation, reducing the need for extensive transportation and allowing for greater community involvement.

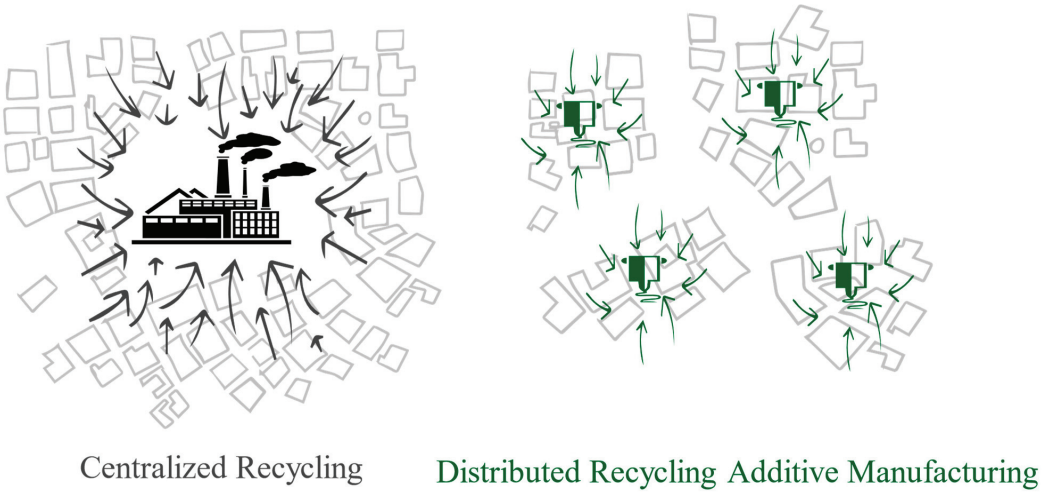

Figure 1. Comparing Centralized Recycling to Distributed Recycling by Additive Manufacturing.

Defining the circular economy in precise terms can be challenging due to the many facets of the concept [16,17]. However, at its core, the circular economy seeks to provide an alternative to the linear economic model, which is inherently unsustainable. The circular economy prioritizes the circularity of resource flow and aims to prevent the loss of materials from the system [18]. While recycling is often associated with circularity efforts, it is just one aspect of the broader circular economy framework. The circular economy takes a systemic approach that integrates economic, environmental, and social sustainability principles. It aims to maintain the highest value of products and materials within the system for as long as possible, reduce reliance on non-renewable resources, minimize waste generation from the outset, and prevent contamination, toxicity, and pollution. Unlike traditional recycling, which primarily focuses on mitigating environmental damage and pollution, the circular economy aims to address the underlying causes of environmental degradation [19]. To achieve a more sustainable and effective approach to plastic recycling, it is crucial to prioritize local or regional solutions over the global waste trade. This entails implementing circularity strategies that limit the geographic reach of end-of-life plastic products. By doing so, the negative environmental impacts associated with long-distance transportation of plastic waste can be minimized. Additionally, this approach fosters the development of robust and transparent local recycling systems that are better equipped to meet the unique needs of individual communities [20]. Embracing the principles of the circular economy in the context of plastic recycling can lead to substantial benefits. It decreases the dependence on virgin resources, reduces waste generation, promotes resource efficiency, and contributes to the creation of a more sustainable and resilient recycling ecosystem. By prioritizing local solutions and integrating circularity strategies, it is achievable to strive towards a future in which plastic waste is minimized, and materials are continually circulated within the economy, aligning with the principles of environmental preservation and social well-being.

A promising development in polymer recycling involves the integration of additive manufacturing facilities with relatively smaller-sized plastic extruders [21]. Additive manufacturing, commonly known as 3D printing, is a transformative technology that constructs structures layer by layer to create three-dimensional objects. This process has gained significant attention for its ability to create complex structures with high precision and customization. In the context of plastic recycling, additive manufacturing can be integrated with recycling processes, giving rise to a novel approach known as distributed recycling by additive manufacturing (DRAM). DRAM represents a paradigm shift in traditional recycling practices by combining the benefits of additive manufacturing with recycling prin-

ciples, offering the potential to make recycling more accessible and participatory. DRAM enables decentralized recycling schemes that operate closer to the point of use, offering numerous advantages over centralized recycling systems. One key advantage of DRAM is the elimination of the need to manage and operate a centralized system with physical inventories, along with the associated transportation costs of shipping waste to a central recycling facility. By enabling recycling to occur locally, DRAM simplifies supply chain systems and logistics [21,22]. Moreover, the integration of additive manufacturing in DRAM opens up possibilities for producing complex structures, enabling innovative approaches to open-loop recycling [23]. This integration facilitates the engagement of a broader community in the recycling process, resulting in a larger volume of waste being reutilized. While the distributed recycling initiative remains a dynamic project with its exact metrics yet to be fully determined, it surely complements and addresses the shortcomings of a centralized system aimed at achieving economies of scale and harnessing advanced technology. In conjunction with the existing approach, this scheme fosters community involvement, minimizes transportation needs, and fortifies the resilience of the recycling system against potential disruptions.

The practice of open-loop recycling plays a crucial role in maintaining resource flow and advancing the establishment of a circular economy [7]. Utilizing recycled plastic waste as 3D printing materials is an option that is financially viable and easily achievable. As a consequence, the cost of 3D printing materials will decrease, and the wide adoption of this recycling practice has a ripple effect on reducing the prices of 3D printers themselves. Recent years have seen a significant decline in the prices of 3D printers, providing clear evidence of the cost reduction associated with their widespread use. In 2014, a typical consumer-grade 3D printer cost approximately $1000. However, just two years later, in 2016, due to a remarkable compound annual growth rate of 30%, equivalent to a billion-dollar increase each year, the average price of budget-friendly 3D printers plummeted to less than $400 [24,25]. At present, affordable 3D printers designed for home use, while possibly lacking certain advanced features such as enhanced printing precision sensors and automation, are ideally suited for recycling purposes and are available within the price range of $100 to $400. It is reasonable to assume that an increased demand for 3D printers, driven in part by recycling efforts, could further contribute to reducing their prices. This substantial decrease in price effectively eliminates barriers for using 3D printing technology, making it accessible to a broader audience, including individuals, businesses, schools, community centers, and households. These communities are becoming essential participants in the effort to incorporate recycled waste into their printing materials [26]. Moreover, sectors such as the military can benefit from 3D printing by reducing their dependence on complex supply chains and avoiding operational delays. The US military, for instance, has shown interest in using recycled plastic bottles collected in camps to create replacement supplies for soldiers on the battlefield, providing a sustainable and conservation-focused alternative [27].

The integration of additive manufacturing and distributed recycling not only offers environmental benefits but also fosters local empowerment and engagement in the recycling system. By decentralizing the recycling process and involving a broader range of stakeholders, it is possible to unlock the potential for increased waste reutilization, resource conservation, and the establishment of a more circular economy.

However, achieving high-quality structures with 3D printing requires tuning process settings [28]. Factors such as wall thickness, infill density, and temperature control play crucial roles in determining the strength and durability of the printed parts. Moreover, the polymeric waste used for recycling often undergoes various forms of degradation, including contamination, exposure to environmental elements, and the application of shear forces and high temperatures, which can significantly affect the quality of the recycled materials. Therefore, it is imperative to conduct further research to comprehensively understand the mechanical properties of recycled thermoplastic polymers when employed in additive manufacturing [29]. This knowledge can inform the development of guidelines and best

practices for 3D printing with recycled materials, ensuring that the resulting structures meet necessary quality standards. By educating local communities on the use of 3D printing in recycling and fostering their active involvement in the process, it is possible to create a more inclusive and sustainable recycling ecosystem. Empowering communities with knowledge and skills related to additive manufacturing and recycled materials will not only drive local economic development but also contribute to global efforts in promoting environmental sustainability. Through collaborative efforts and informed practices, there is potential to harness the potential of 3D printing in recycling to advance towards a more resource-efficient and environmentally conscious future.

To gain a broader understanding of the existing body of research on plastic recycling, Table 1 offers a comprehensive summary of published review articles that have extensively explored this topic. Additionally, it highlights the key findings and conclusions derived from these previous reviews. Previous research has explored the integration of 3D printing in plastic recycling, considering various approaches and examining economic and environmental aspects. However, these studies have only provided a cursory overview of the challenges and opportunities associated with this method. Conversely, other research has focused on the broader challenges of recycling without specifically addressing 3D printing. To fully understand and integrate 3D printing as a complementary approach within the circular economy of plastics, a comprehensive investigation of the distinct challenges and opportunities of 3D printing recycling is necessary. Given the limited available sources on this topic, this review paper aims to bridge this knowledge gap by discussing the current challenges and insights from other mechanical recycling methods. It then delves into a more detailed examination of 3D printing recycling. Furthermore, the paper intends to explore the mechanical properties of recycled polymers by drawing upon existing literature on 3D printing and injection molding. This comprehensive approach will enhance our understanding of these properties and enable the identification of necessary conditions for successful 3D printing recycling experiments. To achieve these goals, the paper is structured as follows: Section 2 addresses the challenges encountered throughout the multiple stages of recycling commonly conducted in centralized facilities. This discussion provides an understanding of the existing obstacles in traditional recycling practices. Section 3 introduces the concept of 3D printing and distributed recycling within the context of the circular economy, establishing a connection between the challenges outlined in the previous section and the potential issues that may arise in this alternative approach. By exploring the implications of adopting 3D printing for distributed recycling, it is possible to identify how it addresses or introduces new challenges in the recycling process. Section 4 examines potential strategies to enhance the mechanical properties of recycled polymers. While previous research has predominantly focused on such improvements in relation to injection molding, this exploration opens new avenues for investigating chemicals and agents specifically applicable to 3D printing recycling. Finally, the paper concludes with a summary that outlines the research areas that should be prioritized to effectively implement 3D printing recycling in the circular economy of plastics, emphasizing the need for further investigation and development. By following this structured approach, this review paper aims to provide a comprehensive understanding of the challenges, opportunities, and potential improvements in 3D printing recycling. It serves as a foundation for future research and development, guiding efforts to advance the integration of 3D printing in the circular economy of plastics.

Table 1. Comprehensive Summary of Published Review Articles.

Study Title	Aim/Objective	Comments/Key Findings	Reference
Mechanical recycling of packaging plastics: A review.	This review summarizes current methods and challenges in mechanically recycling five main packaging plastics. It also discusses ways to improve polymer blending in mixed plastic waste streams and uses for lower quality recyclate.	Across the five common types of plastic, changes in polymer chain length and mechanical properties remain a persistent challenge despite differences in the degradation mechanisms.	[30]
Recycling of waste from polymer materials: An overview of the recent works.	This study involves comparing the mechanical and chemical recycling techniques for various types of plastics, as well as analyzing the properties of polymers that have been mechanically recycled.	Mechanical recycling is the preferred and commonly used method of recycling compared to chemical recycling, which involves complex chemical treatments of the waste.	[31]
Mechanical recycling: Compatibilization of mixed thermoplastic wastes.	Approaches employed to achieve compatibility in blends of various thermoplastic waste.	Mechanical recycling of mixed plastic wastes can be viable if their properties are enhanced through compatibilization, but the stability behavior of the resulting materials must be considered before they can be utilized in the production of new goods.	[32]
Mechanical recycling of polylactide, upgrading trends and combination of valorization techniques.	This report provides an overview of the current state of mechanical recycling for PLA, with particular focus on a multi-scale comparison of various studies.	Out of all the recovery methods, mechanical recycling is the most cost-effective approach for PLA, but the recycled materials are typically used for lower-value applications due to inherent thermo-mechanical degradation.	[33]
Quality concepts for the improved use of recycled polymeric materials: A review.	This review explores new methods of mechanically recycling plastics to produce quality materials from waste streams.	Introducing a quality standard is crucial in plastic recycling. The biggest obstacle is finding a way to merge scientific understanding of the degradation and quality properties of recyclates with the design of an efficient upgrading process for each waste stream.	[34]
Mechanical and chemical recycling of solid plastic waste.	The current methods of polymer recycling, encompassing both mechanical and chemical recycling, are thoroughly described in this review.	Mechanical and chemical recycling are promising industrial techniques that can complement each other in closing the polymer loop.	[35]
Polymer recycling in additive manufacturing: An opportunity for the circular economy.	This short review focuses on the circular economy of materials and the recycling methods utilized in the polymer additive manufacturing process.	The development of recycled composites thorough fused deposition modeling (FDM) can lead to increased strength compared to that of the printed recycled polymer.	[36]
3D printing filament as a second life of waste plastics a review.	The main objective of this paper is to examine the existing literature concerning the use of recycled polymers in filament production for 3D printing, as an alternative to the current method of central selective plastic collection.	Traditional recycling methods have involved the use of large, centralized plants that produce low-value commodities, which results in high transportation costs. However, 3D printing presents new opportunities for recycling.	[37]

Table 1. *Cont.*

Study Title	Aim/Objective	Comments/Key Findings	Reference
Plastic recycling in additive manufacturing: A systematic literature review and opportunities for the circular economy.	The focus of this study is to explore key themes within the six stages (recovery, preparation, compounding, feedstock, printing, and quality) of the distributed recycling by additive manufacturing chain proposed.	Limited efforts have been made regarding the recovery and preparation stages, whereas significant advancements have been made in the other stages to assess the technical feasibility, environmental impact, and economic viability.	[21]
Plastics recycling: challenges and opportunities.	The challenges that may arise during various stages of the recycling process were discussed, along with potential opportunities for enhancing recycling efforts.	Expanding the scope of recycling to include post-consumer plastic packaging, as well as waste plastics from consumer goods and end-of-life vehicles, can enhance the recovery rates of plastic waste and reduce the amount that ends up in landfills.	[2]
Fused deposition modelling approach using 3D printing and recycled industrial materials for a sustainable environment: a review.	This paper examines the sustainability of extrusion-based 3D printing materials, with a particular emphasis on the potential use of reusable and biodegradable materials.	Desktop 3D printing has the potential to advance plastic recycling through 3D printing.	[38]

2. Plastic Mechanical Recycling: Processes and Challenges

Mechanical recycling is a multi-step process that involves several key stages, including collection, sorting, cleaning, shredding, and compatibilization or separation. However, the ease of recycling varies depending on the types of plastic, with some posing greater challenges than others. While closed-loop recycling is theoretically possible for most thermoplastics, practical implementation presents financial and technical difficulties. The complexities arising from different processing requirements and molecular incompatibilities between plastic types make the production of recycled resins from plastic waste a complex task. Despite these challenges, mechanical recycling plays a vital role in waste management by conserving natural resources, reducing greenhouse gas emissions, and diverting waste from landfills. To enhance the effectiveness of mechanical recycling, ongoing research and development efforts focus on developing new technologies, improving sorting methods, and enhancing compatibility among different plastic types. Furthermore, consumer education and the implementation of effective recycling programs and policies are crucial to advancing mechanical recycling efforts.

Mechanical recycling encompasses both primary and secondary recycling approaches. Closed-loop recycling, also known as primary recycling, involves the repurposing of post-consumer plastic materials, such as industrial parts or single-use plastic, to create new products with similar properties. This recycling process aims to achieve a closed loop, where the recovered material is reintroduced into its original application, maintaining a circular flow of resources (e.g., recycling post-consumer PET bottles into new bottles). However, closed-loop recycling isn't extensively embraced by recyclers due to the need for partially clean scrap plastics. On the other hand, secondary recycling focuses on the mechanical reprocessing of more complex or contaminated plastics than those encountered in closed-loop recycling. The resulting recovered plastic is typically used in products with lower performance requirements compared to the original application. These products do not need to meet the same stringent standards or undergo the same level of usage as those made from virgin materials.

Mechanical recycling presents significant challenges at various stages, demanding effective collection, efficient sorting, and a thorough understanding of properties and behavior of diverse plastic types. The presence of contaminants or different types of plastics, especially in multi-layer plastics, further complicate sorting and reprocessing.

Hence, there is an urgent need to tackle these challenges by increasing recycling efficiency and recycled end-product quality. Figure 2 illustrates the stages involved in standard recycling procedures. Table 2 provides a comprehensive overview of recent studies (within the past 5 years) that investigated the various stages of plastic recycling, with a specific emphasis on the challenges encountered at each stage.

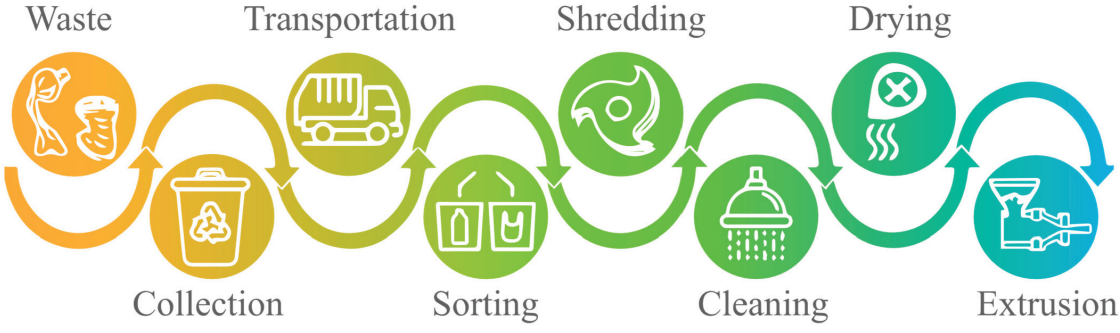

Figure 2. Stages of Plastic Mechanical Recycling Process.

Table 2. Recent Studies Investigating the Stages and Challenges of Plastic Recycling.

Recycling Stages	Management and Logistics	Waste Management	[39–48]
		Collection	[49,50]
		Supply Chain Modelling	[51–57]
	Mechanical Sorting	Sink-Float	[58–62]
		Froth Flotation	[63–71]
		Spectroscopy	[72–79]
		Magnetic Density Separation	[80,81]
	Shredding	Design and Modelling	[82–87]

2.1. Waste Collection and Sorting for Recycling

The initial stage of the mechanical recycling process involves the collection of post-consumer materials from households, commercial establishments, and institutions. Effective management of plastic waste requires tailored waste collection methods based on different types of waste and population densities [88]. In densely populated areas where a significant volume of waste is generated, daily household waste collection using specialized vehicles has proven to be an effective method [89]. These vehicles are equipped with specialized equipment to collect, compact, and transport waste to designated waste management facilities. This approach is particularly suitable for densely populated areas where waste accumulates rapidly. Conversely, in areas with lower population densities, cost-effective solutions involve placing bins in the locality that are emptied regularly. This method is suitable for areas where the waste volume does not justify daily waste collection using vehicles. Drop-off recycling is another effective method for managing plastic waste [90]. It involves providing large bins or machines in easily accessible areas such as community centers or nearby residential areas. Residents can conveniently drop off their plastic waste into the designated bins. This method works well for recycling specific types of plastic waste, such as bottles or packaging. Buy-back centers offer fixed or mobile options for exchanging waste for useful items. These centers incentivize residents to recycle their plastic waste by providing rewards in the form of useful items, household goods, or vouchers for local stores [91]. This approach encourages community participation in

recycling efforts. Another noteworthy collection method is the deposit or refund system, where waste packaging can be returned for recycling in exchange for credits, cash, or tax returns. This method provides residents with financial incentives to recycle their plastic waste and is particularly effective in countries with low recycling rates, as it offers tangible benefits that encourage participation. By employing diverse collection methods tailored to specific contexts, communities can enhance waste management and recycling practices, promoting a more sustainable approach to plastic waste.

The last two methods of plastic waste collection mentioned above rely on providing incentives to individuals, recognizing the significant obstacle of raising community awareness and motivation. Insufficient knowledge on proper plastic waste sorting further compounds this challenge, stemming from a lack of clear guidance and readily available information on recyclable plastics. Moreover, the process of sorting plastic waste can be time-consuming and inconvenient, discouraging individuals from engaging in proper waste sorting practices. Additionally, the lack of infrastructure for managing plastic waste presents a significant obstacle in numerous countries worldwide, particularly those in developing regions. In these areas, the collection and disposal of plastic waste is further complicated by weak policies and a shortage of resources [92].

Following the waste collection process, the next crucial step in the recycling process is the "End-of-Waste" phase [35], where waste materials are transformed into new raw materials before being reprocessed into new products. The initial stage of this phase involves the separation and categorization of recyclable materials, which is particularly important due to the immiscibility of thermoplastic polymers, causing different plastic types to be incompatible with one another [2]. Sorting plastics is a critical step in the recycling process and requires various complementary methods. One such method is manual sorting, where skilled operators sort materials according to their type. Despite its high effectiveness, the manual approach can be expensive. Several density separation methods are employed in sorting, including float–sink separation. This technique involves using water to float shredded flakes of polymers with densities below 1 g/cm^3, allowing for their separation. Froth flotation is a particle separation technique based on differences in surface properties. The process includes introducing bubbles into a mixture of particles and water, where specific particles adhere to the bubbles and ascend to the surface, resulting in the formation of a froth layer. Optical sorting of plastics relies on the use of lasers, cameras, and sensors to identify and sort plastics based on their physical properties, such as color, transparency, and reflectivity. X-ray technology is also utilized to sort plastics based on their elemental composition, which is particularly useful for identifying and separating PVC containers due to their high chlorine content [35,93,94]. However, this method may not be suitable for sorting large quantities of plastic, as it can lead to potential misclassification. Spectroscopy is commonly employed for sorting bottles in commercial industries, but has limitations when used for sorting other plastic products. This is due to the incompatibility of the radiation technologies used to identify the plastic's chemical structure. For instance, durable goods such as automobiles and appliances exhibit significant variations in shape, size, and thickness, making it challenging to find a suitable orientation that accurately identifies the plastic and transmits the energy through its thick walls [95].

The presence of certain additives, pigments, and reinforcements in plastic products further complicates the sorting process. Carbon black pigments, for example, can block spectroscopic scanning and reduce the efficiency of sorting [96]. Black plastics have been identified as a hindrance to efficient sorting [97,98]. Additionally, reclaimers have reported that other colors of plastics can result in up to 35% of plastics being classified incorrectly. Furthermore, the variety of additives in durable products, such as automobiles and appliances, increases the complexity of sorting and reduces the accuracy of identification systems. Moreover, sorting contaminated waste presents an added layer of difficulty, not only due to its detrimental impact on the material's properties but, more importantly, because of the health hazards it poses.

Addressing chemical contamination is crucial for achieving high-quality recycled plastics. Strategies such as improved sorting and separation techniques, proper cleaning methods, and careful consideration of plastic compatibility during recycling can significantly mitigate the adverse effects of chemical contamination. By focusing on these aspects, it is feasible to foster the development of a more sustainable and effective plastic recycling process.

Chemical contamination poses a significant threat to the microstructural and chemical properties of post-consumer plastics. The quality of plastics can vary depending on their specific applications and intended uses [99]. Plastics used in food packaging, for example, are subject to stringent regulations regarding their chemical composition and the potential release of harmful substances. Conversely, plastics not utilized in the food industry may contain a range of chemical additives in varying concentrations. Moreover, unintended substances, such as residues from catalysts or metal impurities from non-metal additives, can be introduced during the production process. The challenge is further exacerbated as some contaminants become chemically embedded in the plastic matrix, making simple washing insufficient to remove them, resulting in their retention even after recycling [100]. Additionally, most plastic types are incompatible with one another at a molecular level and have diverse processing requirements. Consequently, contamination may arise when different plastics chemically react with elements present in the other's matrix. According to Hopewell et al. [2], even a small quantity of PVC contaminant in a PET recycling process can result in the degradation of the recycled PET. This degradation occurs due to the release of hydrochloric acid gas from the PVC at the higher temperature needed to melt and reprocess PET. Consequently, the recycled PET may exhibit issues such as brittleness, yellowing, and diminished adhesive properties.

Ink and coatings (such as paint) are significant chemical substances that can be found on plastics. Ink, when present, can reduce the transparency and may result in chemical reactions that weaken the plastic's mechanical properties. On the other hand, coatings on plastics create a twofold problem during the recycling process. Firstly, certain coatings can act as stress risers in specific applications. Secondly, the degradation of the coating itself adds to the deterioration of the plastic material [98].

Contamination has far-reaching consequences beyond just impacting the quality of plastic; it can cause serious health hazards. For instance, PET plastics may contain acetaldehyde, and detergents can contain toxic metals, both of which can be harmful if inhaled or ingested. Eriksen et al. [100] explored the presence of metals in recycled plastic waste and found that metal concentrations increased after the recycling process, although they remained within acceptable limits for food safety [100]. However, the long-term effects of repeated recycling cycles on metal contamination requires further investigation. If metal contamination continues to rise, plastics that undergo numerous reprocessing cycles might no longer meet safety standards.

Furthermore, the economic viability of sorting plastics can be compromised by the high costs associated with the sorting technologies. While these technologies may offer precise sorting capabilities, the expenses involved in implementing and maintaining them can render the process uneconomical. An example is the biodegradability of poly(lactic acid) (PLA), a bio-based plastic often made from corn. Although PLA can be composted or recycled, the market for PLA does not currently justify extensive sorting efforts. As a result, PLA can contaminate high-value and durable plastics, compromising their recyclability.

Despite the ongoing efforts to address the challenges of sorting plastic waste, the continuous development of new additives and polymer mixtures introduces additional complexities to the recycling process. As the plastic industry evolves and new types of plastics emerge, material recovery facilities face the challenge of effectively sorting and processing these novel materials. The dynamic nature of the industry necessitates that sorting technologies adapt and keep pace with these changes to ensure efficient separation and recycling of plastic waste. Failure to effectively sort plastic waste can have detrimental consequences. Even small amounts of contaminants present in the sorted waste stream can

lead to cross-contamination of otherwise pure waste streams. This cross-contamination compromises the quality of the recycled material, rendering it less valuable and limiting its potential applications [101]. Furthermore, the presence of contaminants in the recycling process can cause damage to machinery during reprocessing, leading to additional costs and operational disruptions for recycling facilities. Addressing the issue of contamination requires a comprehensive approach. Material recovery facilities need to implement robust sorting systems that can identify and separate different types of plastics accurately, taking into account the evolving landscape of plastic compositions and additives. Additionally, initiatives should focus on improving the infrastructure and logistics of the recycling industry to enable the proper treatment of contaminated recyclables. This includes investing in advanced sorting technologies, enhancing collection and transportation systems, and establishing efficient waste management networks.

2.2. Shredding and Extrusion

Shredding is a critical step in reducing the volume of plastic waste and facilitating its processing in mechanical recycling extruders. This process involves breaking down plastic into smaller pieces, making it easier to handle and feed into the extruder. In addition to volume reduction, shredding improves storage and transportation efficiency. Preliminary shredding is often necessary before employing sorting techniques such as flotation. During the shredding process, plastic is fragmented using a circular saw (shredder) or bandsaw. A shredder equipped with rotating blades, driven by an electric motor, is employed for this purpose. The shredded plastic is transformed into flakes measuring between 5 and 10 mm, with smaller sizes resulting in more uniform shapes [102].

From an environmental perspective, grinding plastic waste consumes a significant amount of energy due to the viscoelastic nature of plastic polymers [103]. The energy required for grinding depends on the cuttability of the material. As a result, the different strengths and cuttability of various polymers pose a challenge in achieving a uniform shredding process. Inefficiencies and entanglement can occur during shredding due to the varying mechanical and physicochemical properties of the plastics. Another consideration when recycling plastic films, bags, and sheets is the use of an agglomerator for pre-processing. The agglomerator is a device that consists of a cylinder equipped with several stationary blades and two rotating blades positioned at the base. This configuration induces friction and generates heat. Utilizing agglomeration machines proves to be a highly economical approach to recycle thin-walled polymers. These machines are instrumental in converting loose plastic materials into suitable flakes or chips, which can then be effortlessly fed into an extruder's hopper for further processing. The agglomerator cuts, preheats, and dries the plastic, increasing its density and quality. Even when the resulting agglomerates or crumbs may not be suitable for direct further processing, they can be mixed with plastic flakes for extrusion [85].

Extrusion is the most widely used method for recycling plastic. In this process, the plastic is blended and fed into an extruder through a hopper. Inside the extruder, the plastic encounters a rotating screw that pushes it into a heated barrel. Gradually, the pressure and heat melt and mix the plastic until it reaches the desired temperature. The molten plastic is then forced through a die, creating a continuous strand or pellet that can be cooled and cut to the desired shape or size. However, concerns arise regarding the mechanical degradation caused by shearing forces and heat during shredding and extrusion. These factors can lead to a reduction in the average molecular weight and mechanical properties of the polymer [104].

Efficient shredding and extrusion processes are crucial for maintaining the quality and properties of recycled plastics. Optimizing these steps can help minimize degradation and ensure the production of high-quality recycled materials. Ongoing research and development efforts focus on improving shredding techniques, enhancing extrusion parameters, and exploring additives or compatibilizers to mitigate the adverse effects of shearing forces

and heat. By advancing these technologies, the recycling industry can achieve higher-quality recycled plastics that meet the performance requirements for various applications.

2.3. Thermoplastic Blends in Recycling

Polymer blends play a significant role in recycling processes, as they offer the opportunity to create materials with tailored properties by combining different polymers. These blends are physical mixtures of two or more polymers without covalent bonds between them. The interactions between the components can lead to desired property combinations and improved overall performance [105]. Polymer blends are commonly formulated to achieve specific properties or enhance certain aspects of the materials. By combining different polymers, a balance of mechanical strength, flexibility, durability, heat resistance, or chemical resistance can be achieved. However, one challenge that arises in polymer blends is the occurrence of immiscibility and incompatibility. In such cases, the blends may exhibit the presence of large particles from the less abundant component, uneven distribution, and poor adhesion to the surrounding matrix [106]. This challenge is more pronounced in the recycling process, where the original structure of the polymer blend needs to be restored, and the desired arrangement and distribution of the polymer phases must be re-established. Restoring the structure and stabilizing the system during recycling requires appropriate mixing techniques and re-compatibilization. Re-compatibilization involves the addition of chemical additives to improve the interfacial bonding between the polymers [107]. While there are common and readily available compatibilizers, it is important to note that each compatibilizer is designed to address the specific needs of a particular polymer blend. However, considering the vast number of possible polymer blend combinations, the current range of available compatibilizer options is limited from an economic perspective. Developing more cost-effective compatibilizers requires a comprehensive understanding of the interfacial behavior exhibited by different polymers. Such an understanding is crucial for the development of effective and affordable compatibilizers [108]. However, the costs associated with research and experimentation in the development of new compatibilizers pose a challenge. The limited economic feasibility often discourages extensive exploration in this field. Balancing the costs and benefits of developing and implementing compatibilizers is crucial to foster the recycling of polymer blends and maximize their potential in the circular economy of plastics. Ongoing research and innovation in this area can lead to the discovery of cost-effective and efficient compatibilization strategies, enabling the utilization of a broader range of polymer blends in recycling processes.

One of the significant challenges in recycling polymer blends is the potential degradation that the original blend may have undergone, which adds complexity to the recycling process. The degradation behavior of individual polymers within the blend can be influenced by the presence of fillers and other components, further complicating the recycling of polymer blends. Even when compatibilizers are employed, challenges persist, especially in blends containing polymers with different degradation rates. The varying degradation rates among the constituent polymers can impact the overall degradation behavior during recycling [109]. Numerous research studies have focused on investigating the degradation of polymer blends to better understand and address these challenges. For instance, Mistretta et al. [110] demonstrated the positive impact of specific compatibilizers in enhancing the photo-resistance of polymer blends. These studies provide valuable insights into the degradation mechanisms and offer potential strategies for improving the recycling of polymer blends. Continued research and innovation in this area will contribute to advancing the recycling technologies for polymer blends and optimizing their use in the circular economy of plastics.

Research papers have explored various aspects related to polymer blends, extending beyond degradation. For example, Taufiq et al. [111] conducted a study investigating the mechanical properties and morphology of a polymer blend derived from rejected disposable diapers. The study specifically examined the influence of processing temperature on the blend. The results indicated that increasing the compounding temperature led to

improved microstructural homogeneity, resulting in enhanced mechanical performance and morphology. In addition to understanding the mechanical properties of polymer blends, researchers have also focused on investigating the impact of recycling on the properties of these blends. One study investigated the reprocessability of high-density polyethylene (HDPE) blends through extrusion molding for multiple cycles [112]. The findings revealed a gradual decline in mechanical performance with each recycling stage, with the most significant drop occurring after the initial recycling step. Another study examined the rheological and mechanical properties of a polymer blend consisting of PLA and PS, prepared using a single screw extruder [113]. The study observed a decrease in the apparent viscosity of the blend with increasing processing cycles, and the flow behavior became more sensitive to shear rate and temperature after recycling. Furthermore, the mechanical properties of the blend deteriorated as the number of processing cycles increased. Although these studies examined different polymer blends, they collectively highlight the negative effects of recycling on the mechanical properties and processability of blends. The decrease in mechanical performance and alterations in rheological behavior after recycling underscore the challenges associated with the recyclability of polymer blends. Consequently, it is essential to develop innovative approaches and technologies that address these challenges, allowing for improved recyclability and the utilization of polymer blends in a sustainable manner.

2.4. Degradation of Recycled Plastics

Polymers undergo degradation by various mechanisms throughout their lifecycle and are influenced by factors such as the application environment, operational conditions, and inherent polymer properties. Degradation can occur through processes such as mechanical breakdown, moisture-related damage, heat-induced deterioration, and oxidation due to light exposure. Each degradation mechanism presents unique challenges and can significantly affect the performance and lifespan of polymers. Understanding the diverse ways in which polymers degrade is crucial for optimizing their durability and facilitating effective recycling efforts. During the degradation process, two fundamental mechanisms, chain scission and crosslinking, play a significant role. Polymers consist of interconnected chains of monomers held together by chemical bonds. Chain scission involves the breaking of these bonds within the polymer chain, while crosslinking refers to the formation of chemical bonds that connect different polymer chains. These two mechanisms are in competition with each other, and their prevalence is influenced by factors such as polymer structure, composition, initial molecular weight, and processing temperature [35,114]. By comprehending the mechanisms of polymer degradation, researchers and practitioners can develop strategies to mitigate degradation effects and enhance the recyclability of polymers. This knowledge can guide the selection of suitable recycling processes and conditions that minimize further degradation during recycling. Furthermore, this knowledge aids in the identification of polymers and polymer blends that are more resistant to degradation, thus ensuring the production of high-quality recycled materials. Continued research in understanding and controlling polymer degradation is essential for advancing the circular economy of plastics and promoting sustainable recycling practices.

Mechanical degradation is a prominent phenomenon that occurs during the processing of polymers, primarily during shredding and extrusion. These processes subject the polymer to various forms of mechanical stress, which can result in degradation and alterations in its physical and mechanical properties. The intense shear forces exerted on the polymeric chains can lead to their breakdown, causing a decrease in the average molecular weight. This mechanical shear generates significant forces in regions where the polymeric chains are entangled, leading to chain scission [115]. While mechanical forces are not the sole catalysts, they greatly accelerate the degradation process, collaborating with other environmental factors such as temperature, UV radiation, and humidity [116]. Different terms are often used to describe these degradation mechanisms based on their underlying causes. For instance, when temperature and mechanical stress act in combination, this is

called thermomechanical degradation. Degradation resulting from UV exposure during processing is known as photodegradation. If oxygen is present alongside UV exposure, it leads to a specific type of degradation called photooxidative degradation. Similarly, degradation caused by moisture during reprocessing is commonly referred to as moisture-induced degradation. Figure 3 depicts the key environmental factors that contribute to material degradation, including heat, UV radiation, humidity, oxygen, and microorganisms. Some of these factors have been discussed earlier. Thermoplastic degradation can occur when any of these factors act independently. However, when two or more of these factors combine, the degradation rate significantly accelerates.

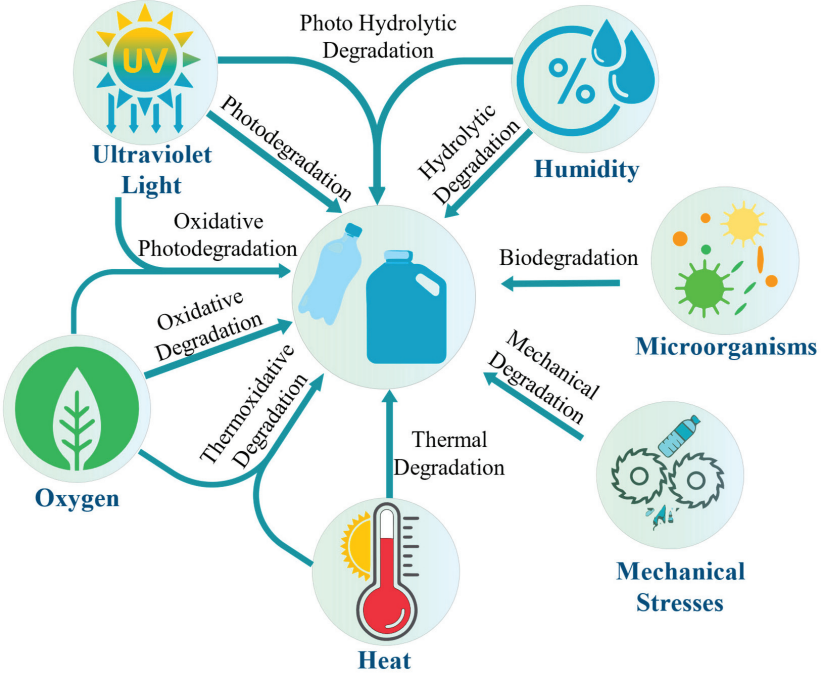

Figure 3. Environmental Factors Leading to Thermoplastic Degradation.

Recognizing the importance of mechanical degradation is essential before delving into the significance of other degradation factors. Extensive research has been conducted to investigate the effects of reprocessing polymers, focusing specifically on the mechanical aspects and the impact of shear forces. These studies aim to understand the behavior of polymers under controlled mechanical stresses while considering other degradation factors. One notable study examined the thermal stability of polystyrene (PS) and revealed its remarkable stability, even at high temperatures of up to 230 degrees Celsius. However, the study highlighted that mechanical stresses encountered during material processing can lead to a reduction in molecular weight, even at lower temperatures. By subjecting the material to similar processing conditions in terms of temperature and duration, but varying the mechanical stresses, distinct variations in molecular weight were observed, which were detected through changes in melt viscosity [117]. This study underscored the influence of mechanical stresses on the degradation of PS, emphasizing the need to carefully consider these factors during processing. Furthermore, a study conducted by Schweighuber et al. [118] provided significant insights into the degradation mechanisms of polyolefins during multiple extrusions using a twin-screw compounder. The investigation revealed that the degradation process is strongly linked to the screw speed employed during extrusion. At lower speeds, chain scission was found to be the predominant degradation mechanism,

whereas oxidation processes dominated at higher speeds. These findings highlight the importance of controlling processing conditions to gain a comprehensive understanding of the observed behaviors and their implications for polymer degradation.

As previously mentioned, mechanical degradation alone is not the primary accelerator of polymer degradation. It is the concurrent occurrence of thermal, moisture, or other degradation processes during processing that accelerates the degradation. Moreover, certain degradation factors can amplify the other's effects, further hastening the degradation process. Thermal degradation plays a significant role in influencing the mechanical properties of processed polymers. When plastics are exposed to higher temperatures during the melting process, thermal degradation can occur, leading to the breaking of the polymeric chain's weakest bonds and causing a reduction in the compound's molecular weight [119]. The thermal stability of a polymer is determined by the strength of its weakest bonds [120]. In addition to thermal degradation, the presence of aggressive chemical substances can significantly impact the polymer when exposed to heat. For instance, the interaction between oxygen and the polymer can result in a specific type of degradation known as thermal oxidation [121]. This occurs when oxygen reacts with the polymer, causing further deterioration. Excessive thermal degradation is particularly relevant in the recycling process, especially when dealing with polymer blends. Due to the varying melting temperatures of different plastics, recyclers often encounter challenges in reprocessing plastics based solely on the melting temperature of a single component. As a result, some elements may not melt at all, while others experience excessive thermal degradation.

Numerous research studies have investigated the process of thermal degradation, particularly focusing on the kinetics of thermal and thermo-oxidative degradation in various polymers such as PS, PE, PP, and PET. Peterson et al. [122] conducted a study that revealed the initiation of thermal degradation through random chain scission in the absence of oxygen. However, when heat and oxygen are both present, thermo-oxidative degradation occurs, leading to changes in the degradation characteristics of the polymers. Thermal degradation in PET has also been observed [123,124]. In a recent attempt to prevent degradation, Phanthong et al. introduced an innovative approach that involves attaching a molten resin reservoir unit to extruders. This method facilitates the relaxation and elimination of shear history from the molten state of polymer chains, effectively reducing degradation. As a result, the lamellar structure and morphology can be rejuvenated to closely resemble that of the original virgin materials [125].

During the reprocessing of polymers, moisture is another factor that contributes to degradation and leads to a decrease in molecular weight and durability [126]. Usually, the removal of contaminants and impurities requires mechanical cleaning of the polymers by washing them with water and then drying them. However, insufficient drying may lead to the plastics retaining moisture. Moisture can also be present due to the humidity in the environment. Moisture causes swelling in the amorphous phase, leading to residual hygroscopic stresses and degradation through hydrolysis [127]. The effects of moisture degradation on polycarbonate molding were studied in [128]. Moisture absorption can occur rapidly, with dried pellets exposed to 49% relative humidity at 75 °F reaching the permissible moisture level for molding within 30 min.

The degradation mechanisms discussed earlier primarily focus on factors occurring during processing. However, it is important to recognize that environmental factors such as UV irradiation, moisture, and oxygen also play significant roles in the degradation of polymers. When polymers are exposed to the environment, their degradation occurs gradually over time. Prolonged exposure leads to significant deterioration, a process known as weathering. Weathering is a natural degradation process resulting from the combined effects of UV radiation, atmospheric oxygen, and water. UV radiation, through photophysical and photochemical processes, along with the presence of oxygen and water, causes oxidative and hydrolytic effects on the polymers [129]. Oxygen reacts with polymer chains, forming oxygenated groups in a phenomenon known as photo-oxidation, resulting in the gradual degradation of polymers [130]. Additionally, water absorption by synthetic materials and

coatings from humidity and wetness can lead to hydration of surface layers and mechanical stress on the dry subsurface layers. Simultaneously, UV rays from sunlight can accelerate the degradation process by initiating photo-degradation, breaking down chemical bonds in the polymer material and leading to a gradual loss of physical properties [131]. Numerous research papers have examined the impact of UV aging on the mechanical and fracture characteristics of thermoplastic polymers.

The impact of degradation on the mechanical recycling process is evident, and the quality of the waste material before recycling plays a crucial role in determining the overall success of the process. While the direct influence of polymer degradation on technical stages such as sorting or cleaning remains inconclusive, chemically degraded waste materials require stricter controls and greater precision to achieve the desired results. Handling lower quality waste materials necessitates heightened attention and control throughout the recycling process.

In summary, environmental factors such as UV irradiation, moisture, and oxygen contribute to the degradation of polymers in the environment, leading to weathering and gradual deterioration. UV radiation causes photo-oxidation and initiates photo-degradation, while moisture absorption and exposure to oxygen contribute to hydrolytic and oxidative effects on the polymers. Research studies have highlighted the impact of UV aging on the mechanical properties of polymers, revealing the competition between chain scission and crosslinking mechanisms. Understanding the degradation caused by environmental factors is essential in managing the quality of waste materials and implementing effective recycling processes. By considering the effects of degradation, greater attention can be given to controlling and improving the recycling of lower quality waste materials.

3. Integrating Plastics into a Circular Economy through the 3D Printing Process

Addressing the urgency of global challenges requires a transition from lifestyles solely centered on consumption, towards more sustainable activities. The shift is driven by the aim of meeting the present needs, while safeguarding the well-being of future generations. To achieve sustainability, it is crucial to seek a balance between environmental, social, and economic considerations [132]. Environmental sustainability involves protecting natural resources, reducing carbon emissions, and minimizing pollution. This requires adopting renewable energy, sustainable land management approaches, and eco-friendly practices across industries. Social sustainability focuses on promoting social justice, equity, and inclusion [133]. Economic sustainability involves maintaining a thriving economy while ensuring it is not at the expense of the environment or society. It involves creating economic systems that promote sustainable development, job creation, and a fair distribution of wealth and resources [134]. Achieving sustainability requires collaboration among governments, businesses, and individuals to develop and implement sustainable policies, technologies, and practices [135]. This includes investing in renewable energy, sustainable agriculture, eco-friendly transportation, and circular economy principles to achieve a more sustainable future [136,137].

The concept of a circular economy is important for achieving sustainability, as it focuses on reducing waste and maximizing resource efficiency, leading to a more robust and sustainable future [138]. A circular economy model aims to keep materials, products, and waste in use for as long as possible through reuse, repair, and recycling. The objective is to minimize waste and its environmental impact by reducing the demand for virgin materials and lowering energy consumption. This model replaces the linear economy approach known as the "take-make-dispose" model [134,139]. The linear economy relies on unlimited resources to produce, use, and dispose of products, which is unsustainable and disregards the negative environmental consequences and the finite nature of natural resources [140]. To transition to a circular economy, industries must adopt strategies for extending the life of products and materials, creating a sustainable and resilient circular economy. Recycling plastic within the circular economy is a solution for sustainability as it promotes resource efficiency and waste reduction. Plastic waste poses a significant environmental threat due to

its slow biodegradability and persistent presence in the ecosystem [141]. A circular economy aims to extend the useful life of plastic through the utilization of various frameworks, such as the 6 Rs or 9 Rs [142].

The sustainability framework, developed by multiple industries, provides an outline for waste reduction and the promotion of sustainable practices. The 6 Rs framework shown in Figure 4 includes Reduce, Reuse, Recycle, Repair, Refuse, and Rethink, while the 9 Rs framework expands to include Rs such as Refurbish, Remanufacture, Repurpose, or Recover [142–144]. While the first three Rs are widely known and promoted, all the Rs are important for achieving a sustainable future. Repairing and reusing products extends their lifespan and reduces the need for new materials and energy in manufacturing. Refusing single-use products is a critical step for filtering out items that harm the environment. By incorporating all the Rs into the circular economy, society can significantly reduce its environmental impact and promote sustainable practices for future generations [145]. Replacing single-use plastics with environmentally friendly alternatives, such as reusable metal or bamboo straws and refillable glass or stainless-steel water bottles, can significantly reduce waste [146]. Governments and businesses are implementing policies and offering incentives to encourage the use of reusable alternatives to single-use plastics, fostering a shift towards sustainability [147,148]. Integrating plastic recycling into the circular economy is vital for reducing plastic waste, conserving resources, and promoting sustainable practices [147]. These efforts aim to close the loop on plastic waste reduction within the circular economy.

Figure 4. Six Rs of Sustainability.

Establishing plastic recycling as part of the circular economy requires the creation of a closed-loop system that prioritizes waste management frameworks. It begins with product design in which designers prioritize recyclability by using fewer complex parts and a higher percentage of the same plastic to enhance recycling efficiency and effectiveness [149]. Establishing a supply chain that prioritizes recycling is also crucial for a circular economy of plastics. This involves partnerships with waste management companies and specialized recycling facilities capable of handling different types of plastic, as well as localized platforms to facilitate recycling and eliminate the need for long-distance transportation to centralized recycling facilities [150]. Policymakers and businesses must prioritize sustainability concerns and integrate circular economy principles into their strategies to support the shift towards a circular economy for plastic [151]. By integrating these strategies, it

is possible to reduce waste, conserve resources, mitigate the negative impacts of plastic production and disposal on the environment and human health, and gain a competitive advantage in the marketplace through improved efficiency and reduced costs [142]. As described in Section 1, thermoplastics, given their widespread use in various applications, are a major focus for recycling efforts [32].

3.1. Recycling of Thermoplastics

Thermoplastic polymers are widely used in various products, such as packaging, consumer goods, and industrial applications, due to their unique properties, including durability, flexibility, and relative resistance to degradation [152]. However, the linear model of polymer consumption and disposal has resulted in significant environmental challenges [32]. According to the report "What a Waste 2.0" [15], the world generated 242 million tons of plastic waste in 2016, and this figure is predicted to increase to 460 million tons per year by 2030 if the current trend continues. The accumulation of plastic waste and its disposal in landfills or incineration contribute to environmental pollution and greenhouse gas emissions, exacerbating climate change [153]. To address this issue, it is crucial to integrate polymers into the circular economy, which involves reducing production and consumption, promoting reuse, recycling, and recovery cycles [154]. In the context of mechanical recycling, significant efforts have been made to recycle thermoplastics using injection molding, thermoforming, and 3D printing technologies as described in the next three subsections.

3.1.1. Recycling Thermoplastics through Injection Molding

Injection molding is a manufacturing method for producing a wide range of plastic products, including those made from recycled materials [155]. The process of recycling by injection molding typically involves a series of steps including collection, sorting, cleaning, and size reduction to create plastic pellets. These pellets are then dried to remove moisture as it affects the production process. Next, pellets are melted and injected into a mold, where they form the desired product [156]. However, there are several advantages to using injection molding with recycled plastic. Firstly, it is a cost-effective solution for plastic recycling, as shredded recycled plastic makes a pellet form feedstock to the injection molding and the process can be repeated multiple times. Additionally, injection molding reduces waste by reusing plastic that would otherwise end up in landfills or oceans [157]. The flexibility of injection molding enables the production of complex shapes and sizes, making it suitable for a wide range of plastic products. Through the utilization of recycled plastic and injection molding, this approach has the potential to make a significant difference in waste reduction and promote a more sustainable environment [158].

An example of plastic recycling involves the use of recycled polyethylene terephthalate (rPET) in injection-molded products, sourced from post-consumer PET bottle recycling. This practice not only reduces plastic waste, but also lowers raw material costs. Studies have explored various additives, processing parameters, and types of rPET waste to enhance the properties of injection-molded rPET, demonstrating the potential for sustainable solutions and value-added product creation in addressing the plastic waste issue [159]. Another effort in injection molding has been extended to plastic waste collected from marine environments. Utilizing different manufacturing technologies, including injection molding, 3D printing, and thermoforming, researchers have examined the recyclability of PET, HDPE, and PP plastic waste retrieved from the ocean. Comparative analysis with virgin plastics indicates that recycled plastic products exhibit comparable properties, highlighting the potential for effective recycling of marine plastic waste and the significance of improved waste management strategies in marine environments [160]. Thermoforming represents another method employed in the recycling of thermoplastics and is covered in the next subsection.

3.1.2. Recycling Thermoplastic through Thermoforming

Thermoforming is a manufacturing process used in plastic recycling. The technique starts by heating a plastic sheet to its softening point, stretching it over a mold, and then vacuum-forming it into the desired shape. This method has found extensive use in recycling applications, facilitating the creation of diverse products from recycled plastic, such as food packaging, automotive parts, and consumer goods. One noteworthy application of thermoforming is its role in producing high-stiffness trays. The tray's inherent structural integrity and rigidity makes it ideal for tasks demanding stability and resistance to deformation. A key advantage lies in the ability to carefully select appropriate materials and optimize the thermoforming process, thereby yielding trays with superior stiffness tailored to meet specific requirements [161].

While injection molding and thermoforming are commonly used technologies in plastic recycling, additive manufacturing through 3D printing provides an innovative approach. Unlike injection molding and thermoforming, which involve heating and molding plastic into predetermined shapes, 3D printing allows for the creation of complex and customizable objects using recycled plastic materials [156]. Therefore, this section will explore 3D printing as a novel approach to plastic recycling.

3.2. Recycling of Thermoplastics through Additive Manufacturing: Opportunities and Challenges

Additive manufacturing, commonly known as 3D printing, presents a promising solution for integrating plastics into the circular economy and recycling plastic waste [162]. This technology allows for the creation of complex objects while optimizing material use and reducing waste during the manufacturing process [21]. One of the widely used additive manufacturing processes is fused filament fabrication (FFF), in which polymer material is deposited layer by layer over a heated bed, as depicted in Figure 5a. This approach results in efficient material utilization and minimizes waste generation. Another technology employed in additive manufacturing is fused granule fabrication (FGF). In this method, illustrated in Figure 5b, feedstock for 3D printing is provided in the form of granules. The granules are heated and melted by passing through a screw extruder, after which the molten material is extruded through an extrusion nozzle to build the desired object [163]. FGF offers an alternative approach to incorporate recycled polymers into the additive manufacturing process, promoting the reuse of plastic waste and contributing to a more sustainable production cycle. By harnessing the potential of 3D printing, the circular economy can be further advanced, leading to reduced material wastage and improved environmental impact.

The utilization of additive manufacturing and 3D printing technology in recycling polymers presents numerous environmental benefits. It enables the transformation of plastic waste into new products, reducing the amount of waste generated and the reliance on raw materials, energy, and water typically required in traditional manufacturing processes [164]. Recycling plastic materials through 3D printing can significantly reduce waste, diverting plastic from landfills. It also helps conserve resources by reusing plastic, reducing the need for new plastic production and the associated energy consumption [165]. The recycling process itself typically requires less energy and a reduced carbon footprint compared to producing new plastic from raw materials. Furthermore, recycling can create new markets for recycled plastic materials, promoting economic diversification and generating new business opportunities [166]. Moreover, 3D printing allows for the creation of customized and complex designs as well as minimizing material waste during production [167]. While additive manufacturing offers valuable advantages, it also presents challenges that need to be addressed.

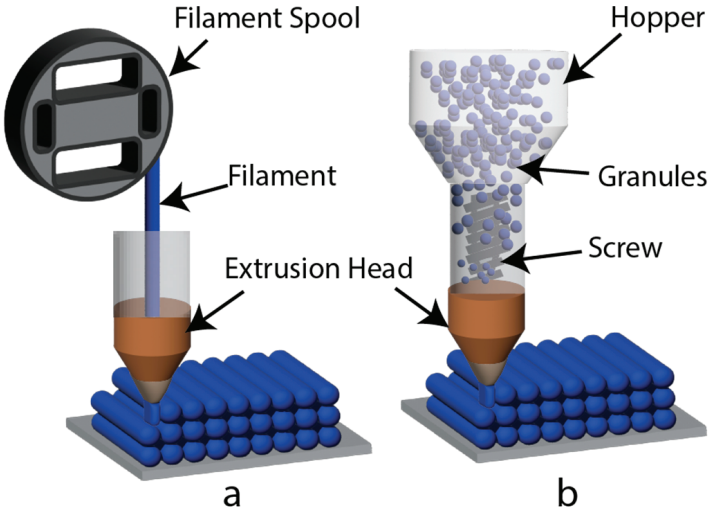

Figure 5. Illustration of Additive Manufacturing Techniques: (**a**) Fused Filament Fabrication and (**b**) Fused Granule Fabrication.

Effectively recycling polymers for 3D printing presents a significant challenge, requiring a thorough understanding of which materials can be recycled without compromising mechanical properties [54]. Based on the reviewed literature, research studies have explored the recyclability of various polymers, with a focus on acrylonitrile butadiene styrene (ABS), polylactic acid (PLA), polyethylene terephthalate (PET), and polypropylene (PP). However, fewer studies have investigated the recycling potential of polystyrene (PS), high-density polyethylene (HDPE), and low-density polyethylene (LDPE) polymers [168]. To address this challenge, researchers are dedicated to comprehending the mechanical properties of recycled materials and developing strategies to mitigate degradation. Techniques such as incorporating additives or blending multiple polymers to enhance filament flexibility will be further discussed in Section 4 [169,170].

A significant challenge in thermoplastic recycling in general and for 3D printing in particular is the collection and sorting of plastic materials, as discussed in Section 2.1. Ensuring the proper sorting of plastics becomes critical due to the variation in melting points among different polymers. This discrepancy can present a major difficulty during the 3D printing process. Proper sorting of plastics becomes a crucial step that greatly influences the success of 3D printing with recycled materials [171].

It is widely acknowledged that not all materials are suitable for recycling by 3D printing. Consequently, various methods were explored involving specialized equipment to address the challenges associated with printing these materials. It was often concluded that recycling such materials may not be feasible or would be financially irrelevant. For example, let's examine the recycling of composite materials commonly used in packaging, which consist of both polymers and aluminum [172]. While it is technically possible to recycle these materials, the process demands substantial resources for effective processing. Furthermore, some of these difficult-to-recycle plastics can present safety and regulatory concerns, particularly if they release hazardous fumes or byproducts during the recycling and printing processes [173]. Hence, it is important to approach these materials with caution and implement appropriate mitigation strategies.

Ensuring that recycled plastics meet the required specifications for 3D printing can be difficult. Moreover, recycled thermoplastic materials may exhibit different physical characteristics compared to virgin materials, potentially influencing the performance of the printed object. Variations in melting points, viscosities, and flow characteristics can affect printability, leading to issues such as warping, poor layer adhesion, and surface finish

problems [174]. This can lead to issues such as inadequate layer adhesion, stringing, and clogging, which can compromise the quality of the print [175]. Furthermore, achieving proper adhesion of the material to the print bed can be challenging, especially when using recycled polymer materials that may have different surface qualities compared to virgin materials. This can result in problems such as warping and poor layer adhesion, affecting the overall print quality. Additionally, factors such as print speed, layer height, and cooling settings can have a significant impact on printing quality and may contribute to failed prints [176], which will be discussed in Section 3.4.

When considering the use of recycled plastic materials, the factor of cost plays a crucial role. While it has been argued that recycled plastics can be more expensive than their virgin counterparts due to additional processing and quality control requirements [2], a deeper examination of this cost dynamic is essential. Choosing between virgin and recycled plastic involves a complex decision-making process that extends beyond mere cost considerations. Recycled plastic undoubtedly offers substantial environmental benefits in terms of sustainability, but it may entail additional processing stages, leading to increased expenses. The higher cost associated with recycled plastics typically stems from various stages, including collection, sorting, cleaning, and transportation. However, the adoption of a distributed recycling approach can help offset these added costs by eliminating the need for transportation to centralized recycling facilities. Moreover, it is important to note that the cost of the raw material itself is effectively eliminated during the recycling process. This holistic perspective underscores that the choice between virgin and recycled plastics involves a nuanced evaluation of multiple factors beyond cost alone.

Nonetheless, it is imperative for the recycling community to acknowledge the multi-faceted benefits that recycling offers, extending beyond its environmental advantages to encompass economic gains. In order to establish a tangible benchmark for quantifying the costs associated with the implementation of a DRAM approach, a meticulous estimation has been undertaken. This estimation stands as a foundational point for comparison, particularly against commercially available recycled PET (rPET) sourced from re3D, Houston, TX, USA. The principal objective of this model is to foster community engagement, with a significant portion of the endeavor relying on the dedicated efforts of volunteers. Additionally, the intent is to manufacture pellets from plastic products collected within the community, procured at no cost. However, there exist other essential cost considerations in the process. These encompass various expenditures, including water bills associated with cleaning and electricity bills for operations such as shredding and drying. To provide a comprehensive overview, Table 3 outlines the projected expenses associated with the production of 1 kg of PET using conventional equipment.

Table 3. Cost Breakdown of the Operation of a Distributed Recycling Center.

Stage	Resource	Quantity	Time (Hours)	Cost ($)
Collection	Labor	N/A	N/A	Volunteer
Sorting	Labor	N/A	N/A	Volunteer
Cleaning	Water	10 Gallons	0.5	$0.02
Drying	Oven	1.88 kWh	6	$0.45
Shredding	Shredder	0.75 kWh	8	$0.14
		Total		**$0.61**

The initial estimate points suggest significant cost savings for the community when compared to the price of rPET, which stands at $19.64 per kilogram. Consistent with our calculations, Alexandre et al., have indicated that the production costs of fused granular fabrication pellets can be efficiently reduced to less than $1 per kilogram of material [177]. While we acknowledge the potential presence of supplementary costs, notably labor and equipment expenses, it is imperative to assess the broader financial implications. An optimally staffed recycling center would ideally involve three to five skilled individuals responsible for sorting, cleaning, and shredding operations, complemented by one individual overseeing the collection and the team. Our data were collected using equipment available in our laboratory, a Filabot Reclaimer (Filabot, Barre, Vermont, USA), valued at $8190, and the drying ovens, akin to the Thermo Scientific 3488M-1 Imperial V model, ranged in price from $2000 to $5000. Additionally, prudent financial planning should encompass an annual maintenance cost, equivalent to 1–3% of the machine's assessed value, to ensure sustained operational efficiency and longevity.

In devising a simplified model for these recycling centers, let's assume each center is equipped with a single industrial shredding machine capable of processing 50 kg of plastic material in an 8-h shift. This limitation would mean that each center could handle up to 50 kg of material every 8 h, constrained by the shredding process. In the United States, the average per capita daily plastic consumption stands at approximately 0.605 kg/day. Based on this, a single shredder can effectively serve and process materials from around 83 recyclers. Now, let's consider that roughly 20% of the community members are inclined towards distributed recycling. In such a scenario, each center would need to meet the daily demands of a population comprising approximately 415 individuals within its vicinity. Applying this model to Michigan, it becomes apparent that recycling centers would need to be strategically located within an approximate radius of 2.8 km to efficiently serve the community. For instance, in Saginaw County, this would necessitate the establishment of approximately 24 recycling centers to accommodate the local population's recycling needs. Larger communities may require additional equipment and centers for effective recycling management.

However, in the context of additive manufacturing, the fused granule fabrication (FGF) process offers a more direct route for using recycled materials [178]. Instead of creating a spool of filament for the fused filament fabrication (FFF) process, which requires additional steps in processing, the FGF process allows the utilization of recycled material promptly after chopping and cleaning. This streamlined approach not only simplifies the production process but also has the potential to lower overall costs, making recycled plastics a viable and sustainable option for additive manufacturing.

Overall, FFF and FGF provide a promising pathway for recycling thermoplastics and integrating polymers into the circular economy. By addressing the challenges associated with polymer recycling, such as material selection, printability optimization, and cost considerations, the environmental impact of plastic production and disposal can be significantly reduced. Table 4 highlights additional initiatives complementing those discussed in Section 3.1, with a focus on injection molding, thermoforming, and 3D printing processes. These ongoing efforts are dedicated to further advancing the recycling of plastic materials, demonstrating the versatility and potential of various recycling techniques in creating sustainable solutions.

Table 4. Efforts of Recycling Thermoplastic.

Topic	Material/Composite	Reference
Injection Molding	PP/Composite	[179]
	PP/Composite	[180]
	SEBS/PP	[181]
	ASA	[174]
	Composite	[182]
	Composite	[183]
	Nylon 12	[184]
	PP/Composite	[185]
3D Printing	HDPE	[186]
	PET	[187]
	Nylon 6	[188]
	Composites	[164]
	PP	[189]
	HDPE	[190]
	ABS	[191]
	PET/Rubber	[192]
	PLA + Glass Fiber	[193]
	LPDE	[194]
	PET, PP, PS	[195]
	PET	[196]
	PP/Composite	[197]
	PLA	[29]
Thermoforming	PP	[161]
	PET/Glass Fiber	[198]
	Composite	[199]

3.3. Pathway to Community-Scale Recycling through Additive Manufacturing

Over the past decade, the concept of distributed recycling by additive manufacturing (DRAM) has garnered considerable attention in academic literature [200]. DRAM has been explored not only as an individual or household practice but also as a viable community-based solution [162]. Individual DRAM practice demands substantial skill, effort, and capital, so it may result in low machine utilization. Therefore, our focus lies on the broader implementation of DRAM at the community scale, where it can be adopted by small enterprises, non-profits, or volunteer initiatives. In this review, we outline the essential steps for establishing DRAM at the community level, paving the way for a more accessible and sustainable approach to recycling and additive manufacturing.

To prepare plastic waste for 3D printing, a series of essential steps are undertaken to transform discarded materials into usable feedstock. The process commences with the collection and sorting of plastic waste, followed by thorough cleaning and shredding into smaller pieces. Subsequently, the shredded plastic undergoes extrusion or other processing techniques to create filament or pellets suitable for 3D printing, as depicted in Figure 6. This transformation is a key factor in converting plastic waste into a valuable resource, promoting sustainability and circularity by reducing environmental impact and maximizing material reuse. Advocating a decentralized approach to waste recycling, our review paper proposes the concept of distributed recycling within the community. This approach eliminates the need for transportation to a centralized recycling center, promoting greater efficiency and reduced logistics. Consequently, our review focuses on the process of establishing a distributed recycling unit consisting of five stages, as depicted in Figure 7. The five stages are: plastic waste collection, material recovery, material storage, 3D printing, and community use. By highlighting these stages, our review aims to promote the implementation of an effective distributed recycling unit, fostering community involvement and contributing to a more sustainable and responsible waste management system.

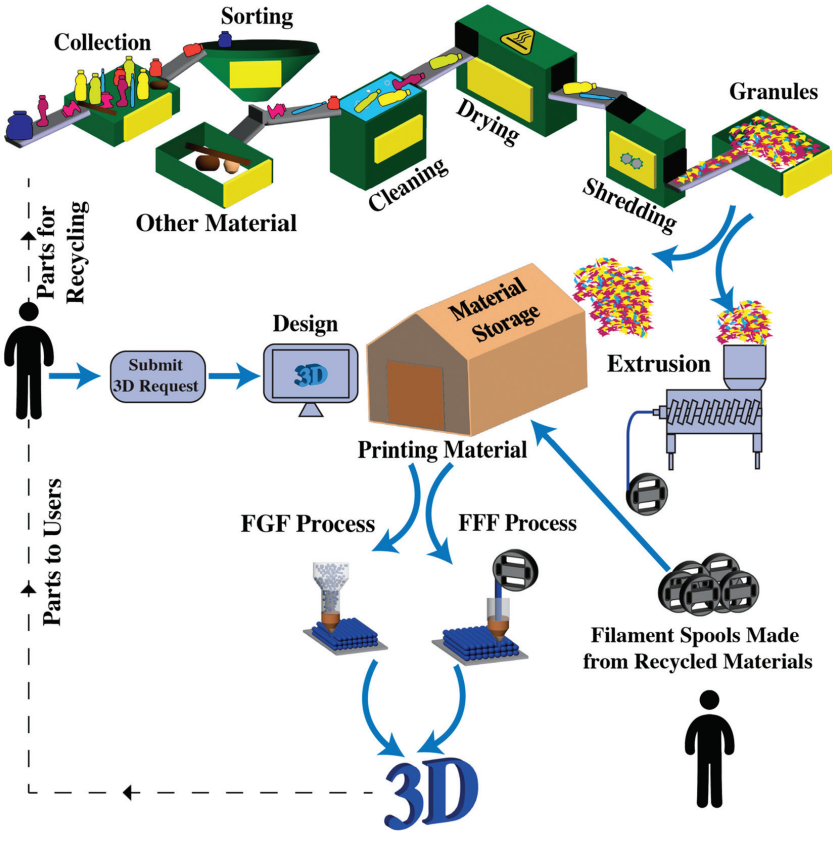

Figure 6. Transformation of plastic waste into a 3D printing feedstock through a local recycling process.

Figure 7. Stages of Distributed Recycling for 3D Printing: From Waste Collection to Community Use.

Pathway to Decentralized Recycling

Sorting waste and ensuring its proper recycling has always been a challenge due to contamination issues [29,188]. However, communities can overcome this challenge by establishing efficient sorting systems and educating residents on proper recycling practices. Initiating a recycling program, as illustrated in Figure 6, allows communities to determine the procedures for sorting and collection while developing clear policies on what can be recycled. To involve the local community in the waste collection process, collection containers can be placed in public spaces, schools, and at community events [201]. Additionally, setting up drop-off locations enables community members to contribute by bringing their already recycled plastic.

Once the plastic waste is collected, the next crucial step is shredding and preparing the recycled plastic for 3D printing. Mechanical shredders are used to downsize the plastic into desired sizes, typically flakes or granules. Proper sizing is essential, whether producing filaments or directly 3D printing using a fused granule fabrication (FGF) 3D printer. Community-scale recycling centers can benefit from cost-effective and accessible shredding systems, such as the open-source plastic granulator, which can be built by members of the local community with expertise in mechanical and electrical fabrication [202]. Alternatively, the concept of the "Green Fab Lab" can be adopted, focusing on establishing local recycling facilities [203].

Before 3D printing, all recycled materials must be thoroughly cleaned and dried to avoid moisture-related issues during the printing process. Common methods for drying include air and vacuum drying at temperatures below the glass transition temperature [204]. Communities can invest in a drying oven or dehumidifier to ensure proper drying of materials. By implementing community-based waste recycling and 3D printing, communities can take significant steps towards sustainability, reducing environmental impact, and promoting the circular economy. Through collective efforts, waste can be transformed into valuable resources, fostering a more sustainable and eco-friendly future for generations to come.

The Process of Filament Fabrication

In the recycling and 3D printing process, as depicted in Figure 6, the dried and stored plastic material undergoes extrusion to create filament suitable for 3D printing. In the reviewed literature, the most common filament diameter used for 3D printers is 1.75 mm, with tolerance levels ranging from $+/-0.04$ [194] to 0.1 mm [192]. Maintaining the filament diameter within an acceptable range of tolerance is critical as it directly impacts the printing quality and the outcome of the print. To ensure smooth and consistent extrusion during printing, it is essential for the filament diameter to be consistent throughout the spool. Any variations in diameter can lead to issues such as clogging or under-extrusion, compromising the quality of the 3D printed object. Therefore, stringent quality control measures should be in place during filament fabrication to guarantee uniformity in diameter. Therefore, [193] used a laser micrometer with an accuracy of ± 2 µm to monitor the filament diameter during extrusion. Moreover, the filament must be free of contaminants such as dust and particles [205]. Contaminants can lead to clogging in the 3D printer nozzle or poor adhesion between layers, resulting in flawed prints. Properly cleaning and filtering the recycled material before extrusion is crucial to eliminate any potential contaminants. A mesh filter is often used inside the extruder nozzle as well.

Direct Printing Using Granules

An alternative method for 3D printing with recycled polymers involves the direct use of granules as feedstock, eliminating the need for intermediate steps such as filament production. In this approach, plastic waste is processed into granules of a specific size and then directly fed into a 3D printer equipped with a hopper, bypassing the step of filament production. Table 5 is an example of printing parameters using an open-source 3D printer Gigabot X 2 XLT (re3d, Texas, USA) to print a recycled polymer (PLA) [206]. While direct printing using granules shows potential for sustainable 3D printing, it may require modifications to the 3D printer to prevent clogging of granules in the hopper.

Advancements in open-source technology and the availability of pelletizer choppers or open-source granulators offer feasible solutions for the local community to create granules of the appropriate size without the need to produce filament for 3D printers [207].

Table 5. Examples of Printing Parameters for FGF process Using the Gigabot X 2 XLT Printer.

Parameter	Value	Unit
Nozzle Diameter	2.85	mm
Layer Height	1.5	mm
Skirt Outlines	5	count
Bottom Heat Zone (T0)	185	°C
Middle Heat Zone (T1)	180	°C
Top Heat Zone (T2)	165	°C
Bed Temperature	60	°C
Printing Speed	900	mm/min
Travel Speed	6000	mm/min
3D Printer	Gigabot X 2 XLT	

3.4. Controlling the Printing Quality of the Recycling Plastic

To ensure accurate and reliable 3D printing of the recycled plastic, process control is crucial. With the growing popularity of 3D printing technology, understanding and optimizing printing process parameters is key. The process control aspects of FFF and FGF 3D printing encompass various factors, including printing material selection, printing temperature, layer thickness, and print speed. Wu and Chen conducted an analysis using cause-and-effect analysis [208] to identify factors contributing to poor print quality, which are summarized in Figure 8. By monitoring and controlling these factors, it is possible to reduce failed prints and improve overall printing performance. These factors are divided into two main categories: before printing (process planning) and during printing.

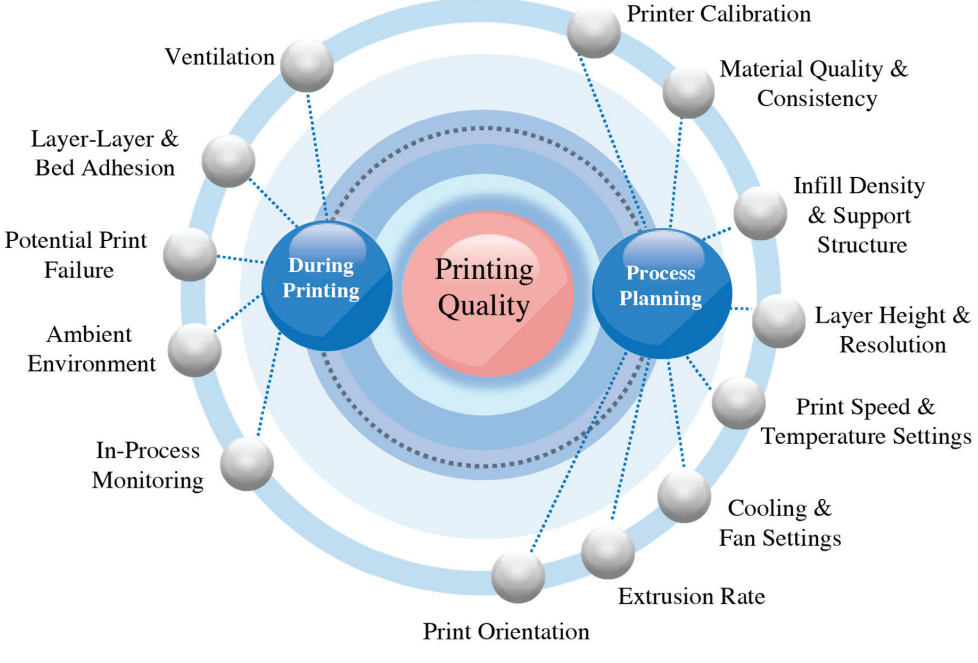

Figure 8. Printing Quality Control for 3D Printing.

3.4.1. Process Planning

Several important 3D printing parameters have a big impact on the success of the printing process. Figure 8 illustrates the important elements of control that must be considered during the process planning phase. Layer height, printing speed, extrusion rate, and temperature settings are important factors in 3D printing [209]. Lower layer heights produce finer vertical details but lengthen print time. Additionally, the material's adhesion to the prior layer depends on the extrusion rate and temperature. Therefore, consistent print quality is ensured by using correct and optimized settings [210].

Other factors that affect print quality are settings in software used for slicing a 3D design into machine instructions for printing. These important slicer settings include support settings, infill density, and print orientation. The creation of support structures that stabilize overhanging components while printing is controlled by support material parameters. Better support for complex geometries is ensured by higher support density, but it also requires more material and post-processing work. The infill density parameter determines how much material is used to fill the inside of the part, which affects the print's strength and weight. Greater structural integrity is achieved with higher infill densities, but at the cost of increased printing time and material usage. Another factor that needs to be considered is the print orientation, which affects the object's structural integrity and surface finish [210,211].

3.4.2. Control during Printing

Once the printing instructions are sent to the 3D printer, the print begins. Most of the print monitoring tasks are left to the human operator, with typical printers using closed loop control of only heated bed and extruder temperatures. The operator must monitor the bed adhesion and layer-to-layer adhesion to detect failures that require nozzle or bed cleaning and a material reset. Additionally, print chamber air temperature plays an important role in cooling and thus part shrinkage and residual stress-driven warpage. The chamber temperature requirements vary based on the specific plastic being printed. In particular, PLA requires an open printer enclosure for rapid cooling below its approximately 60 °C glass transition temperature, while other plastics demand a closed chamber or even a heated chamber for optimal results. Moreover, controlling the ambient humidity is also important to ensure the print quality and success [212].

3.4.3. In-Process Monitoring

Nevertheless, advancements are continuously being made to enhance the process control of 3D printing. In-process monitoring systems incorporating sensors and machine learning algorithms have emerged as a modern technique. These systems provide real-time feedback and enable modification of process parameters during printing. A study has proposed the use of sensors and machine learning algorithms to prevent nozzle clogging, achieving an impressive prediction accuracy rate of 97.2% for the future state of the 3D print [213]. Such systems aim to eliminate the need for operator monitoring and enhance print success. Based on the specific requirements of the application, the community can develop a similar system tailored to their needs, further improving the process control of 3D printing within a community recycling center and enhancing the reliability and efficiency of their printing operations [214].

3.4.4. Empowering Local Communities through Self-Sustaining Recycling Centers

Extrapolating the idea of DRAM to the context of a local community, we envision the concept of a self-sustaining recycling center in the local community practicing collection, sorting, cleaning, processing, and 3D printing of plastics for applications in the local community. Several essential pieces to this center are the trained operators, the machines, the education and engagement of potential customers or users of the parts to be produced by DRAM. This idea is similar to the Precious Plastics initiative for local centers to collect and recycle plastics and then use the manufacturing processes of die

extrusion, injection molding, and thermoforming. To those processes, we add additive manufacturing processes. Precious Plastics fosters the sustainment of such local centers with participating machine shops and marketplaces distributed regionally and with knowledge sharing online. By taking ownership of the recycling process and developing expertise within the community, the center becomes more self-reliant and fosters local economic growth and learning. With trained operators, the proposed DRAM center can operate efficiently, producing high-quality recycled materials and products through 3D printing. This not only promotes environmental sustainability by reducing plastic waste but also encourages active community participation in recycling initiatives. By involving the local community in the process, 3D printing with recycled materials becomes a collaborative effort that fosters environmental consciousness and community engagement. As a result, the community benefits from a self-sustaining recycling center that contributes to a cleaner and more sustainable environment while promoting economic and social growth within the community itself.

In the context of a local self-sustaining recycling center, the application of 3D printing technology offers a multipurpose and sustainable approach to addressing various household needs and the promotion of community empowerment. Through 3D printing, communities can produce many household items that might eliminate the need to purchase from the market, ranging from replacement parts such as vacuum attachments, gardening tools, home accessories and many others. This approach encourages the utilization of the resources within the local community, which can help in community engagement and innovation. Such combined efforts align with the vision of sustainability and circular economy, contributing to a more self-reliant community model.

4. Mechanical Properties of Recycled Polymers

The successful integration of plastics into a circular economy requires maintaining the mechanical properties of recycled thermoplastic structures to a high standard. This emphasis ensures that the recycled materials retain their strength and reliability, enabling them to endure repeated use without any compromise in performance. By prioritizing the quality of recycled thermoplastics, it is possible to create a closed-loop system in which materials are continuously reused, minimizing waste and reducing the demand for virgin resources. To achieve this objective, it is essential to understand the mechanical behavior of thermoplastics before and after recycling and to uncover the underlying mechanisms involved in their property changes. Polymers are composed of large chain molecules, with carbon atoms forming the backbone of the chain. Polymerization is the process of linking monomers, the building blocks of polymers, to create these chains. Thermoplastic polymers are characterized by linear chains that are connected to side groups, and in some cases, these chains may have branches, forming branched structures [215]. This unique feature distinguishes thermoplastics from other polymers because their chains are not crosslinked. As a result, they can be easily melted at relatively low temperatures, which contributes to their excellent recyclability potential. Furthermore, the arrangement of these linear chains can vary, and these structural characteristics significantly affect the mechanical behavior and performance of the polymer under different conditions. Many thermoplastics display a semicrystalline morphology, with a molecular structure comprising amorphous regions of randomly oriented molecular chains and crystalline regions that exhibit a highly ordered and repetitive chain arrangement with hydrogen bonding between chains. However, it is essential to note that thermoplastics can also exist in an entirely amorphous state such as polystyrene (PS), polycarbonate (PC), and polymethyl methacrylate (PMMA), also known as acrylic. The mechanisms of deformation as well as mechanisms of degradation are tightly linked to the macromolecular structure of the thermoplastic.

The amorphous thermoplastics featuring a network of randomly organized and entangled polymer chains [216], exhibit an isotropic behavior. When a semicrystalline thermoplastic is subjected to mechanical forces, the amorphous phase experiences initial elongation, leading to the stretching and unraveling of some polymer chains, and the breaking of

weaker intermolecular bonds [216]. As the deformation progresses, the load is primarily borne by the crystalline region of the thermoplastic. This causes the crystalline lamellae to align in the direction of the first principal stress. This point coincides with the macroscopic plastic yielding, characterized by localized narrowing and uneven deformation, leading to a concentrated area of strain [217]. With further applied force, the crystalline phase starts to separate into distinct crystalline blocks [218]. As the deformation continues, both the crystalline blocks and the chains of the amorphous region that connect them become highly elongated, resulting in the formation of a fibrillar-like structure. Both these crystalline block segments and the interlinking amorphous regions adjust their orientation to align with the direction of maximum stretch, known as the principal stretch direction [219]. However, this hardening is constrained by the macromolecular chains' ability to stretch. Once their extensibility limit is reached, fracture occurs. This intricate fibrillar arrangement contributes to the thermoplastic's ability to withstand deformation and maintain its mechanical integrity under stress. Figure 9 illustrates the described deformation mechanisms occurring within the crystalline and amorphous regions associated with the semicrystalline polymer's mechanical response. The interplay between the amorphous and crystalline regions within thermoplastics enables a complex mechanical response to external forces. The amorphous phase provides resilience and flexibility, allowing the material to absorb impacts and recover its shape, while the crystalline phase offers strength and rigidity.

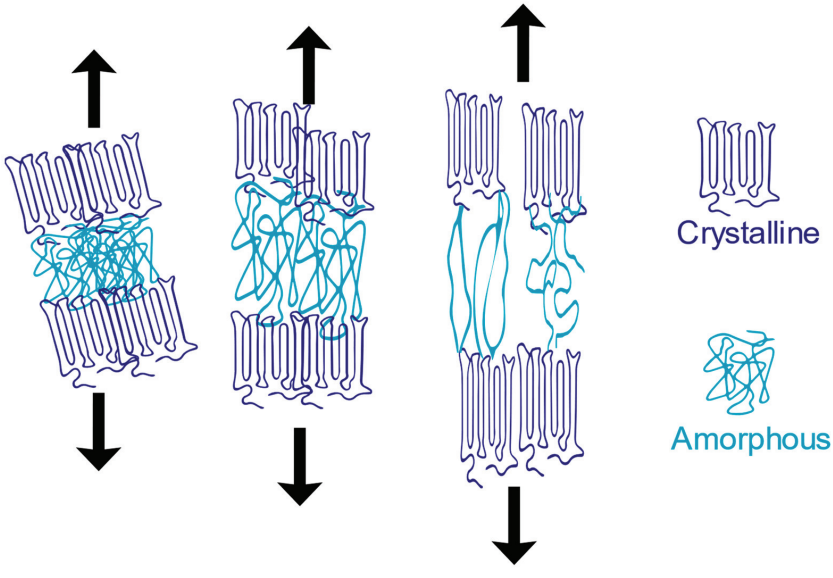

Figure 9. Microstructural Evolution under Deformation in a Semicrystalline Polymer.

4.1. Mechanical Properties of Recycled Plastics

Extensive research has been conducted to investigate the impact of recycling through injection molding, on the physical, chemical, and structural properties of plastics. However, when it comes to recycling by 3D printing, there is a notable scarcity of comprehensive literature in this domain. As a result, this section seeks to bridge the gap by drawing upon the insights and conclusions derived from the injection molding research. By extrapolating and adapting these findings, it is possible to gain valuable understanding and guidance for the effective recycling of plastics by 3D printing.

Section 2.4 highlights the impact of environmental factors and processing conditions on the mechanical properties of thermoplastics. Recycling involves heat and shear stresses that lead to degradation, while oxygen and moisture act as catalysts during processing, affecting the material's properties. In injection molding, polymer degradation occurs

through three primary process mechanisms: high temperatures required for melting, shear stresses during flow, and the residence time within the heated barrel. These parameters significantly influence the degradation kinetics of molten polymers. While reprocessing at high temperatures leads to significant thermal degradation, even lower reprocessing temperatures can induce degradation in polymers susceptible to mechanical degradation [220]. The processing conditions can alter the molecular structure of polymers through chain scission, crosslinking, and branching of polymer chains. High temperatures and shear stresses cause chain scission, reducing polymer chain length [221,222]. Additionally, crosslinking of polymer chains can occur in the presence of free radicals formed at elevated temperatures [30], which tends to decrease the mobility of polymer chains, making the material more brittle. The crosslinking in elastomers can be different from the crosslinking in thermosets or thermoplastics. While the crosslinks in elastomers are typically fewer and more flexible, the crosslinks in thermosets/thermoplastics are often numerous and highly rigid. With each successive recycling cycle, these changes become more pronounced as degradation accumulates. A higher number of reprocessing cycles results in increased brittleness, while an acceleration in chain scission contributes to earlier fracture occurrences after each cycle. Numerous studies have investigated the effects of mechanical recycling on the physicochemical and microstructural characteristics of thermoplastics [31,223–227]. Many of these studies have examined the impact of multiple recycling cycles on rheological and mechanical properties, consistently finding a decline in tensile strength, impact resistance, and elongation at break, indicating reduced strength, energy absorption capability, and stretchability of the polymer.

Additionally, an increasing number of recycling process cycles have been found to decrease the average molecular weight of the polymer chains, affecting their behavior, and influencing the melt flow properties of the recycled material [228–232]. Moreover, particularly in scenarios involving contaminants and microparticles, only a limited number of studies have delved into the implications of recycling on thermoplastics [233]. The presence of contaminants and microparticles has been reported to contribute to a reduction in creep resistance and fatigue properties of the recycled plastics [234].

4.2. Mechanical Properties of Recycled Plastics with Additive Manufacturing

Before delving into the evolution of recycled polymers through 3D printing, it is crucial to recognize that, in general, the mechanical properties of 3D printed parts are inferior to those produced through injection molding. Notably, the tensile strength, elastic modulus, elongation at break, and impact strength of 3D printed samples are significantly lower than those of injection molded samples [235].

In injection molding, a seamless and continuous structure is achieved, ensuring uniformity in both material composition and structural integrity. This process results in plastic parts with consistent properties throughout. On the other hand, 3D printing operates by building objects layer by layer, with the quality of adhesion between these layers governing the characteristics of the end product. The layering nature of 3D printing can introduce porosities and imperfections, leading to variations in structural properties. Consequently, mechanical testing often highlights the inferior properties of these dominant structural aspects rather than the material's properties. Therefore, factors such as print speed, print orientation, sample size, layer dimensions and nozzle size might not have a direct impact on the fundamental material properties of the plastic being used in 3D printing [236–238]. However, they can still manifest differences in the overall properties of the printed parts during subsequent mechanical testing. The interplay of these factors can affect the bonding between layers, leading to variations in strength, durability, and other mechanical attributes. Therefore, establishing standards for the mechanical testing of 3D printed materials becomes significant for research literature comparison.

However, a significant factor governing the decline in mechanical properties due to recycling, as compared to using pristine materials, is degradation. In the field of 3D printing, based on our research, we have not come across any investigations that specifically analyze

degradation mechanisms. Nevertheless, we can hypothesize that degradation mechanisms akin to those identified in injection molding components might also be operational in recycled 3D printed components. Consequently, our focus will be on investigating these mechanisms, aiming to enhance our comprehension of the potential degradation processes that could occur in recycled 3D printed components [239]. These processes involve a combination of thermomechanical degradation and thermal oxidation, with varying degrees of impact for each process. Moreover, even within the domain of 3D printing, two distinct processes exhibit differing levels of degradation: fused granular fabrication (FGF) and fused filament fabrication (FFF).

In FGF (fused granular fabrication) 3D printing, the process involves three key mechanisms. First, thermo-oxidative degradation occurs due to the polymer undergoing melting at elevated temperatures. As a result, the material can experience chain scission. Secondly, during printing, the polymer is subjected to high shear forces in the screw extruder and nozzle, leading to additional mechanical degradation. The third mechanism involves residence time. Unlike injection molding, FGF 3D printing has a shorter residence time in the molten state. This is because the heating and melting process is localized to the immediate area where material is being deposited. Quantifying the exact contribution of each factor remains challenging. This complexity arises primarily from the interdependence of these variables, making it difficult to isolate their individual effects. Figure 10 illustrates a modification in one aspect, revealing the complex interconnection among these variables.

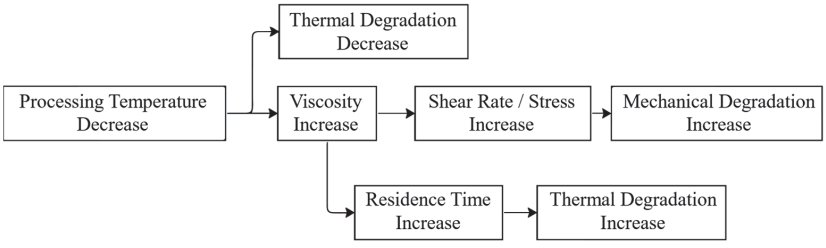

Figure 10. Effects of Decreasing Temperature on Viscosity and Residence Time: Relationship and Interactions.

In comparison, FFF (fused filament fabrication) has similar degradation mechanisms to FGF, including thermo-oxidative degradation, shear forces during printing, and residence time considerations. However, FFF involves an additional step prior to printing—filament extrusion. This preliminary step demands dedicated heating and extrusion processes, which introduces further thermal and mechanical stresses to the material.

The study of the mechanical behavior of recycled polymers, specifically for 3D printing applications, is relatively limited. Anderson conducted a comparative study on 3D printed parts using virgin polylactic acid (PLA) and recycled PLA [240]. The mechanical testing results indicated that using recycled PLA for 3D printing is feasible, although certain mechanical properties exhibited variations. For instance, there was a reduction in tensile strength, an increase in shear strength, and a decrease in hardness. However, the tensile modulus of elasticity remained statistically unchanged. Notably, the recycled filament showed higher variability in the obtained results. In another study, the mechanical properties of 3D printed specimens using recycled PLA were investigated. The focus was on understanding the effect of interlaminar properties and short-beam strength. The findings revealed that the short-beam strength of specimens recycled once and twice was similar to that of virgin specimens. However, a third recycling process had a negative impact on the short-beam strength, leading to decreased strength and increased variability in the results [241]. Vidakis et al. explored various recycling approaches for acrylonitrile-butadiene-styrene [191], polyamide [165], polypropylene [189], high-density polyethylene [190], and polyethylene terephthalate glycol [242]. These investigations examined the impact of thermomechanical processing on the mechanical, thermal, and structural properties through multiple recycling

cycles. The findings indicated that the materials exhibited increased stiffness and strength after the third and fourth round of recycling, but this effect was not observed after the fifth and sixth cycle. Furthermore, thermal analysis revealed no significant degradation until the fifth round of recycling. The results also showed that the crystallinity of high-density polyethylene and polyamide polymers decreased with an increasing number of extrusion cycles, while multiple extrusions predominantly resulted in crosslinking and branching, leading to an increase in mechanical properties.

4.3. Recycled Plastics Using Compatibilizers and Stabilizers

Additives play a pivotal role in plastic formulations, as they help maintain and modify the properties of polymers, enhance overall performance, and ensure long-term usability. Commonly employed additives effectively fulfill basic commercial requirements, primarily aimed at preserving the properties of plastics. In some cases, the implementation of specialized additives such as antioxidants, heat stabilizers, and light stabilizers becomes necessary to enhance durability, particularly in scenarios involving outdoor usage [243]. Moreover, in the context of recycling plastic waste, effective management of pre-damaged plastic is essential. This involves gaining insights into the material's past, including the extent of degradation that has taken place, as well as identifying and quantifying any prior additives present. By strategically selecting and utilizing appropriate additives, the properties of recycled polymers can be optimized, promoting their effective reuse and contributing to a more sustainable approach to plastic waste management [244]. Table 6 outlines the primary advantages and disadvantages associated with each of the additives.

Table 6. Key Attributes of Additives in Polymer Research.

Additive	Benefit	Drawback
Stabilizer	Prevents Degradation	Infeasible
Compatibilizer	Enhances Blend Compatibility	Infeasible
Chain Extender	Increases Molecular Weight	Thermal Instability

Stabilizers are intentional additives incorporated into plastics to protect the polymer against environmental factors such as heat, UV light, and mechanical stress. This ensures smooth processing and extends the service life of the recycled material in its intended application. Failure to evaluate the stability of used plastics before recycling can lead to a decline in their properties, resulting in the production of poor-quality products. In some cases, the substandard properties are mistakenly attributed to the recycled material alone, when the lack of proper stabilization is the actual root cause [244].

Stabilizers play a vital role in enhancing the properties and longevity of plastics, but their utilization in the recycling industry is not as widespread. Cost considerations often dissuade the recycling industry from incorporating stabilizers into their recycling processes, assuming that the virgin material already contains a sufficient amount of stabilizers. However, it should be acknowledged that the concentration of stabilizers in virgin plastics may decrease over time, especially during reprocessing [245]. This decrease can compromise their effectiveness, making it essential to consider adding stabilizers for recycled polymers. Unfortunately, a lack of information regarding the quantity of stabilizers in the plastic from its previous use poses a challenge for the recycling industry, particularly when repurposing the material for different applications. For instance, using plastic intended for indoor use in outdoor settings without weather-resistant stabilizers may lead to performance and appearance issues over time. Addressing these challenges and recognizing the importance of stabilizers in recycled plastics can greatly improve the overall quality and usability of recycled materials.

A recent review examined the importance of stabilizers in relation to the level of aging and oxidation in polymers, known as predamage [245]. Polymers that have undergone substantial damage during their previous use may necessitate higher concentrations of

stabilizers compared to pristine materials. It becomes crucial to ensure the effective stabilization of polymers during their initial application to minimize degradation and ensure high-quality recycling outcomes. Although re-stabilization may incur additional costs, the benefits are manifold, including consistent processing, reduced downtime, improved material properties, and the ability to provide high-quality recycled grades suitable for a wide range of applications. Thus, the use of stabilizers is essential, even if the plastic's next intended purpose does not demand top-tier quality. This practice maintains product quality for future recycling processes, contributing to a circular economy with high-quality materials. Moreover, the optimal stabilizer package for recycled plastics, in terms of both cost and performance, differs from that used for corresponding virgin plastics. This difference arises due to structural variations in the plastic, the presence of stabilizer residues from the initial application, and loose policies and standards [243].

In another recent investigation [246], the incorporation of a stabilizing additive into recycled polypropylene greatly enhanced its performance. The study utilized various characterization techniques such as spectroscopy, rheology, optics, and mechanical testing to assess the effects of recycling and additive incorporation. After subjecting polypropylene to 20 recycling cycles of mechanical processing, the study identified chain scission and oxidation of polymer chains as the main degradation processes. However, the addition of a small amount of a stabilizing additive proved to be highly beneficial. The properties of the recycled polypropylene significantly improved throughout the 20 reprocessing cycles. The additive acted as a hardener and facilitated crosslinking of the recycled polymer chains, resulting in enhanced performance.

Compatibilizers: Compatibilization involves the addition of a component which promotes physical or chemical bonds between the phases of a polymer blend. Compatibilizers are particularly important in polymer blends to enhance compatibility between different polymers. When two or more polymers with differences in chemical composition, polarity, and molecular weight are combined to achieve specific properties or characteristics, their blending can be hindered, leading to phase separation or weak interfacial bonding. Compatibilizers address this issue by having a unique chemical structure that allows them to interact and bond with both polymers. This interaction promotes molecular-level mixing and improves the adhesion between the polymer phases. When recycling polymer blends, it is often necessary to restore the original structure and stability of the material. This can be achieved through appropriate mixing processes and re-compatibilization of the blend. Similar to the initial preparation of the blend, it is crucial to create blends with consistent and stable properties during recycling and operation. Re-compatibilization plays a key role in achieving this objective as it helps to restore the original blend morphology and promote strong interfacial bonding between the different constituents. By employing re-compatibilization techniques, the recycled blend can maintain its desired characteristics and ensure reliable performance [107]. Furthermore, the use of compatibilizers presents potential opportunities for recycling mixed plastic waste, where sorting may be impractical. Compatibilization techniques can enhance the properties of mixed plastic waste, making mechanical recycling feasible [32].

The widespread adoption of polymer blend compatibilization is currently limited by cost-effectiveness concerns when compared to conventional waste management methods. Conventional approaches of diblock copolymers or in situ generated graft copolymers have a strong historical track record of effectiveness, but they may not be economically competitive with other waste management alternatives. Block copolymer structures are outside the scope of the present paper. For a thorough understanding, interested readers can refer to [247]. Nonetheless, there is considerable promise in using multiblock copolymer compatibilizers. Recent advancements in this area suggest that they could offer a viable solution to enhance the cost competitiveness of polymer blend compatibilization. Promising advancements have demonstrated that specially designed multiblock copolymers can significantly improve the blend compatibility of polymers, even when present in extremely small amounts, such as around 0.2 weight percent (wt%). This discovery

presents an opportunity for a cost-effective option that may be feasibly integrated into industrial processes.

In the context of 3D printing, Zander et al. [195] processed blends of waste PET, PP, and polystyrene (PS) into filaments for 3D printing. They investigated the effects of compatibilization with SEBS elastomers on the properties of the filaments. Although the addition of SEBS elastomers did not significantly enhance the tensile strength, morphological analysis revealed improved bonding between the different phases of the blend. SEBS elastomers are thermoplastic materials with rubber-like behavior and full recyclability. Furthermore, the compatibilization process resulted in an increase in the glass transition temperature of the materials. This expanded the performance window of the filaments, making them more suitable for various applications.

Furthermore, despite the ongoing challenges, the use of compatibilizers presents potential opportunities for recycling mixed plastic waste. Where sorting is technically or economically impractical, the mechanical recycling of incompatible mixed plastic waste may become feasible through the use of compatibilization additives.

Chain Extenders are valuable additives, primarily used in polycondensation polymers such as polyesters or polyamides, to enhance the molecular weight of degraded polymers by reacting with their functional end-groups. This process, known as chain extension, involves linking low molecular weight materials with two or more functional groups to the carboxyl and/or hydroxyl end-groups of the polymer. The aim is to mend the polymer chains that may have broken during melt processing due to chain scissions [195].

In an ideal scenario with two end-groups per chain, difunctional additives can linearly increase the molecular weight. However, higher functionalities may lead to branching and cross-linking, depending on the concentration and functionality of the additive [245]. It is important to consider that some chain extenders might exhibit limited thermal stability, posing risks during multiple recycling cycles [248]. Furthermore, chain extension in certain cases may cause an excess of acid groups, accelerating degradation rates [30]. Careful selection of chain extenders is essential to maintain the desired properties of recycled polymers while mitigating potential issues during the recycling process.

5. Conclusions

The preceding sections cover the principles and steps of mechanical recycling of plastics and the recent idea of a more circular economy of plastics through distributed recycling by additive manufacturing (DRAM), and the mechanical properties of recycled polymers. Identified problems for plastic recycling generally stem from cost and quality as well as the highly technical nature of polymers and their applications. Plastic recycling often struggles to compete economically with the production of goods from virgin polymer sources. The problems of collection, sorting, and cleaning have all become more complicated, not less complicated, as more specialized plastics and applications were introduced in recent years. Problems also stem from polymer degradation due to environmental factors. As a solution to the recycling challenge, DRAM has emerged as a new approach with the benefits of decentralization, individual agency, and community participation. There remain questions to explore in establishing the feasibility of DRAM for various materials, scales, and contexts. The use of additives for stabilization and compatibilization are reviewed in this work and appear to be possible routes to enhance DRAM. Further study is needed on microstructural and mechanical property changes to plastics in DRAM systems and to optimize and control the fused filament and fused granule fabrication systems for maximum DRAM performance.

The centralized recycling facility has long been the adopted solution, but the current demands and complexities of logistics call for alternative approaches. The proposed DRAM approach, leveraging 3D printing and localized facilities, offers a promising solution by involving communities and addressing transportation challenges. Despite its potential, it is crucial to acknowledge that challenges will persist in the distributed approach. These challenges encompass various aspects such as technology access and knowledge, the

establishment of community-based infrastructure and logistics, ensuring quality control of 3D printed components, managing material contamination and degradation, as well as the allocation of financial resources. To overcome these challenges, a multifaceted strategy is required, involving collaboration between governments, industries, research institutions, and local communities. Enhancing technological literacy and providing adequate training will empower communities to effectively utilize 3D printing technology. Investment in building and maintaining community-based recycling facilities and optimizing waste collection logistics will be vital for a successful distributed recycling system. Implementing stringent quality control measures and utilizing advanced sorting and cleaning technologies will ensure the production of high-quality 3D printed products from recycled materials. Additionally, research and innovation in materials science can lead to the development of more robust and sustainable recycled materials for 3D printing.

Furthermore, the benefits of this approach extend beyond natural resource conservation. Embracing 3D printing for localized recycling can support local economies, create job opportunities, and promote technological development in underserved regions. As technology becomes more accessible and user-friendly, the difficulties faced by inexperienced communities will diminish, paving the way for increased adoption globally. The DRAM approach presents a transformative path towards a greener, more efficient, and community-driven recycling system. With continued research and collaboration, society can unlock the full potential of 3D printing in plastic waste management, contributing to a more sustainable future for generations to come.

Funding: This research received no external funding.

Conflicts of Interest: The authors declare no conflict of interest.

References

1. Khalid, M.Y.; Arif, Z.U.; Ahmed, W.; Arshad, H. Recent trends in recycling and reusing techniques of different plastic polymers and their composite materials. *Sustain. Mater. Technol.* **2021**, *31*, e00382. [CrossRef]
2. Hopewell, J.; Dvorak, R.; Kosior, E. Plastics recycling: Challenges and opportunities. *Philos. Trans. R. Soc. B Biol. Sci.* **2009**, *364*, 2115–2126. [CrossRef] [PubMed]
3. Andrady, A.L. Assessment of Environmental Biodegradation of Synthetic Polymers. *J. Macromol. Sci. Part C Polym. Rev.* **1994**, *34*, 25–76. [CrossRef]
4. Milbrandt, A.; Coney, K.; Badgett, A.; Beckham, G.T. Quantification and evaluation of plastic waste in the United States. *Resour. Conserv. Recycl.* **2022**, *183*, 106363. [CrossRef]
5. Barnes, D.K.A.; Galgani, F.; Thompson, R.C.; Barlaz, M. Accumulation and fragmentation of plastic debris in global environments. *Philos. Trans. R. Soc. Lond. B Biol. Sci.* **2009**, *364*, 1985–1998. [CrossRef]
6. Gregory, M.R. Environmental implications of plastic debris in marine settings—Entanglement, ingestion, smothering, hangers-on, hitch-hiking and alien invasions. *Philos. Trans. R. Soc. B Biol. Sci.* **2009**, *364*, 2013–2025. [CrossRef]
7. Giurco, D.; Littleboy, A.; Boyle, T.; Fyfe, J.; White, S. Circular Economy: Questions for Responsible Minerals, Additive Manufacturing and Recycling of Metals. *Resources* **2014**, *3*, 432–453. [CrossRef]
8. Kravchenko, M.; Pigosso, D.C.; McAloone, T.C. Circular economy enabled by additive manufacturing: Potential opportunities and key sustainability aspects. In Proceedings of the DS 101: Proceedings of NordDesign 2020, Lyngby, Denmark, 12–14 August 2020. [CrossRef]
9. Advancing Sustainable Materials Management: Facts and Figures Report | US EPA. Available online: https://www.epa.gov/facts-and-figures-about-materials-waste-and-recycling/advancing-sustainable-materials-management (accessed on 21 February 2023).
10. Livesey, S.M. The Discourse of the Middle Ground. *Manag. Commun. Q.* **2002**, *15*, 313–349. [CrossRef]
11. Political Negotiation and Co-Operation in the Shadow of Public Discourse: The Formation of the German Waste Management System DSD as a Case Study. Available online: https://www.ecolex.org/details/literature/political-negotiation-and-co-operation-in-the-shadow-of-public-discourse-the-formation-of-the-german-waste-management-system-dsd-as-a-case-study-ana-066391/ (accessed on 21 February 2023).
12. PlascticsEurope. Plastics-the Facts 2021 an Analysis of European Plastics Production, Demand and Waste Data. Available online: https://www.plasticseurope.org/en/resources/publications/1804-plastics-facts-2019 (accessed on 23 February 2023).
13. Voulvoulis, N.; Kirkman, R.; Giakoumis, T.; Metivier, P.; Kyle, P.; Midgley, C. *Examining Material Evidence: The Carbon Fingerprint*; Imperial College London: London, UK, 2020; Volume 7, pp. 1–15.
14. Craighill, A.L.; Powell, J.C. Lifecycle assessment and economic evaluation of recycling: A case study. *Resour. Conserv. Recycl.* **1996**, *17*, 75–96. [CrossRef]

15. Kaza, S.; Yao, L.; Bhada-Tata, P.; Van Woerden, F. *What a Waste 2.0: A Global Snapshot of Solid Waste Management to 2050*; World Bank: Washington, DC, USA, 2018.
16. Korhonen, J.; Nuur, C.; Feldmann, A.; Birkie, S.E. Circular economy as an essentially contested concept. *J. Clean. Prod.* **2018**, *175*, 544–552. [CrossRef]
17. Kirchherr, J.; Reike, D.; Hekkert, M. Conceptualizing the circular economy: An analysis of 114 definitions. *Resour. Conserv. Recycl.* **2017**, *127*, 221–232. [CrossRef]
18. Aurisano, N.; Weber, R.; Fantke, P. Enabling a circular economy for chemicals in plastics. *Curr. Opin. Green Sustain. Chem.* **2021**, *31*, 100513. [CrossRef]
19. Bucknall, D.G. Plastics as a materials system in a circular economy. *Philos. Trans. R. Soc. A* **2020**, *378*, 20190268. [CrossRef]
20. Havas, V.; Falk-Andersson, J.; Deshpande, P. Small circles: The role of physical distance in plastics recycling. *Sci. Total Environ.* **2022**, *831*, 154913. [CrossRef] [PubMed]
21. Sanchez, F.A.C.; Boudaoud, H.; Camargo, M.; Pearce, J.M. Plastic recycling in additive manufacturing: A systematic literature review and opportunities for the circular economy. *J. Clean. Prod.* **2020**, *264*, 121602. [CrossRef]
22. Ford, S.; Despeisse, M. Additive manufacturing and sustainability: An exploratory study of the advantages and challenges. *J. Clean. Prod.* **2016**, *137*, 1573–1587. [CrossRef]
23. Wu, H.; Mehrabi, H.; Karagiannidis, P.; Naveed, N. Additive manufacturing of recycled plastics: Strategies towards a more sustainable future. *J. Clean. Prod.* **2021**, *335*, 130236. [CrossRef]
24. D Printing Market: 10 Million 3D Printers to Sold by 2030. Available online: https://www.globenewswire.com/en/news-release/2022/08/08/2494063/0/en/3D-printing-Market-10-million-3D-Printers-to-Sold-by-2030-Thanks-to-Declining-Cost-and-Advancing-Technology.html (accessed on 31 August 2023).
25. Wohlers Report 2016 Published: Additive Manufacturing Industry Surpassed $5.1 Billion—Wohlers Associates. Available online: https://wohlersassociates.com/press-releases/wohlers-report-2016-published-additive-manufacturing-industry/ (accessed on 31 August 2023).
26. Stansbury, J.W.; Idacavage, M.J. 3D Printing with Polymers: Challenges among Expanding Options and Opportunities. *Dent. Mater.* **2016**, *32*, 54–64. [CrossRef]
27. Going Green: Eco-Friendly Plastic to Replace Soldier's Supplies in Battle | Article | The United States Army. Available online: https://www.army.mil/article/234840/going_green_eco_friendly_plastic_to_replace_soldiers_supplies_in_battle (accessed on 12 December 2022).
28. Reiter, M.; Miron, V.M.; Lämmermann, S.; Freudenthaler, P.J.; Jerabek, M.; Major, Z. Comparing the mechanical properties of additively manufactured post-consumer polypropylene to injection molded specimens. *Mater. Today Proc.* **2022**, *70*, 55–60. [CrossRef]
29. Sanchez, F.A.C.; Lanza, S.; Boudaoud, H.; Hoppe, S.; Camargo, M. Polymer Recycling and Additive Manufacturing in an Open Source Context: Optimization of Processes and Methods. 2017. Available online: https://www.researchgate.net/publication/318922042 (accessed on 30 November 2022).
30. Schyns, Z.O.G.; Shaver, M.P. Mechanical Recycling of Packaging Plastics: A Review. *Macromol. Rapid Commun.* **2020**, *42*, e2000415. [CrossRef]
31. Hamad, K.; Kaseem, M.; Deri, F. Recycling of waste from polymer materials: An overview of the recent works. *Polym. Degrad. Stab.* **2013**, *98*, 2801–2812. [CrossRef]
32. Maris, J.; Bourdon, S.; Brossard, J.-M.; Cauret, L.; Fontaine, L.; Montembault, V. Mechanical recycling: Compatibilization of mixed thermoplastic wastes. *Polym. Degrad. Stab.* **2018**, *147*, 245–266. [CrossRef]
33. Badia, J.; Ribes-Greus, A. Mechanical recycling of polylactide, upgrading trends and combination of valorization techniques. *Eur. Polym. J.* **2016**, *84*, 22–39. [CrossRef]
34. Vilaplana, F.; Karlsson, S. Quality Concepts for the Improved Use of Recycled Polymeric Materials: A Review. *Macromol. Mater. Eng.* **2008**, *293*, 274–297. [CrossRef]
35. Ragaert, K.; Delva, L.; Van Geem, K. Mechanical and chemical recycling of solid plastic waste. *Waste Manag.* **2017**, *69*, 24–58. [CrossRef]
36. Shanmugam, V.; Das, O.; Neisiany, R.E.; Babu, K.; Singh, S.; Hedenqvist, M.S.; Berto, F.; Ramakrishna, S. Polymer Recycling in Additive Manufacturing: An Opportunity for the Circular Economy. *Mater. Circ. Econ.* **2020**, *2*, 11. [CrossRef]
37. Mikula, K.; Skrzypczak, D.; Izydorczyk, G.; Warchoł, J.; Moustakas, K.; Chojnacka, K.; Witek-Krowiak, A. 3D printing filament as a second life of waste plastics—A review. *Environ. Sci. Pollut. Res.* **2020**, *28*, 12321–12333. [CrossRef]
38. Madhu, N.R.; Erfani, H.; Jadoun, S.; Amir, M.; Thiagarajan, Y.; Chauhan, N.P.S. Fused deposition modelling approach using 3D printing and recycled industrial materials for a sustainable environment: A review. *Int. J. Adv. Manuf. Technol.* **2022**, *122*, 2125–2138. [CrossRef]
39. Brouwer, M.; Picuno, C.; van Velzen, E.U.T.; Kuchta, K.; De Meester, S.; Ragaert, K. The impact of collection portfolio expansion on key performance indicators of the Dutch recycling system for Post-Consumer Plastic Packaging Waste, a comparison between 2014 and 2017. *Waste Manag.* **2019**, *100*, 112–121. [CrossRef]
40. Pan, D.; Su, F.; Liu, C.; Guo, Z. Research progress for plastic waste management and manufacture of value-added products. *Adv. Compos. Hybrid Mater.* **2020**, *3*, 443–461. [CrossRef]

41. Vanapalli, K.R.; Sharma, H.B.; Ranjan, V.P.; Samal, B.; Bhattacharya, J.; Dubey, B.K.; Goel, S. Challenges and strategies for effective plastic waste management during and post COVID-19 pandemic. *Sci. Total Environ.* **2020**, *750*, 141514. [CrossRef] [PubMed]
42. Idumah, C.I.; Nwuzor, I.C. Novel trends in plastic waste management. *SN Appl. Sci.* **2019**, *1*, 1402. [CrossRef]
43. Alhazmi, H.; Almansour, F.H.; Aldhafeeri, Z. Plastic Waste Management: A Review of Existing Life Cycle Assessment Studies. *Sustainability* **2021**, *13*, 5340. [CrossRef]
44. Silva, A.L.P.; Prata, J.C.; Walker, T.R.; Campos, D.; Duarte, A.C.; Soares, A.M.; Barcelò, D.; Rocha-Santos, T. Rethinking and optimising plastic waste management under COVID-19 pandemic: Policy solutions based on redesign and reduction of single-use plastics and personal protective equipment. *Sci. Total Environ.* **2020**, *742*, 140565. [CrossRef] [PubMed]
45. Mazhandu, Z.S.; Muzenda, E.; Mamvura, T.A.; Belaid, M.; Nhubu, T. Integrated and Consolidated Review of Plastic Waste Management and Bio-Based Biodegradable Plastics: Challenges and Opportunities. *Sustainability* **2020**, *12*, 8360. [CrossRef]
46. Horodytska, O.; Cabanes, A.; Fullana, A. Plastic Waste Management: Current Status and Weaknesses. In *Plastics in the Aquatic Environment-Part I: Current Status and Challenges*; Springer International Publishing: Cham, Switzerland, 2019; pp. 289–306. [CrossRef]
47. Drzyzga, O.; Prieto, A. Plastic waste management, a matter for the 'community'. *Microb. Biotechnol.* **2018**, *12*, 66–68. [CrossRef]
48. Payne, J.; McKeown, P.; Jones, M.D. A circular economy approach to plastic waste. *Polym. Degrad. Stab.* **2019**, *165*, 170–181. [CrossRef]
49. Gibovic, D.; Bikfalvi, A. Incentives for Plastic Recycling: How to Engage Citizens in Active Collection. Empirical Evidence from Spain. *Recycling* **2021**, *6*, 29. [CrossRef]
50. Huang, S.; Wang, H.; Ahmad, W.; Ahmad, A.; Vatin, N.I.; Mohamed, A.M.; Deifalla, A.F.; Mehmood, I. Plastic Waste Management Strategies and Their Environmental Aspects: A Scientometric Analysis and Comprehensive Review. *Int. J. Environ. Res. Public Health* **2022**, *19*, 4556. [CrossRef]
51. Santander, P.; Cruz Sanchez, F.A.; Boudaoud, H.; Camargo, M. Closed loop supply chain network for local and distributed plastic recycling for 3D printing: A MILP-based optimization approach. *Resour. Conserv. Recycl.* **2020**, *154*, 104531. [CrossRef]
52. Khadke, S.; Gupta, P.; Rachakunta, S.; Mahata, C.; Dawn, S.; Sharma, M.; Verma, D.; Pradhan, A.; Krishna, A.M.S.; Ramakrishna, S.; et al. Efficient Plastic Recycling and Remolding Circular Economy Using the Technology of Trust–Blockchain. *Sustainability* **2021**, *13*, 9142. [CrossRef]
53. Barford, A.; Ahmad, S.R. A Call for a Socially Restorative Circular Economy: Waste Pickers in the Recycled Plastics Supply Chain. *Circ. Econ. Sustain.* **2021**, *1*, 761–782. [CrossRef] [PubMed]
54. Chaudhari, U.S.; Lin, Y.; Thompson, V.S.; Handler, R.M.; Pearce, J.M.; Caneba, G.; Muhuri, P.; Watkins, D.; Shonnard, D.R. Systems Analysis Approach to Polyethylene Terephthalate and Olefin Plastics Supply Chains in the Circular Economy: A Review of Data Sets and Models. *ACS Sustain. Chem. Eng.* **2021**, *9*, 7403–7421. [CrossRef]
55. Gardas, B.B.; Raut, R.D.; Narkhede, B. Identifying critical success factors to facilitate reusable plastic packaging towards sustainable supply chain management. *J. Environ. Manag.* **2019**, *236*, 81–92. [CrossRef]
56. Russo, I.; Confente, I.; Scarpi, D.; Hazen, B.T. From trash to treasure: The impact of consumer perception of bio-waste products in closed-loop supply chains. *J. Clean. Prod.* **2019**, *218*, 966–974. [CrossRef]
57. Howson, P. Building trust and equity in marine conservation and fisheries supply chain management with blockchain. *Mar. Policy* **2020**, *115*, 103873. [CrossRef]
58. Mumbach, G.D.; Cunha, R.d.S.; Machado, R.A.F.; Bolzan, A. Dissolution of adhesive resins present in plastic waste to recover polyolefin by sink-float separation processes. *J. Environ. Manag.* **2019**, *243*, 453–462. [CrossRef]
59. Dimas, T.; Peeters, J.; Eggers, A.; Vanierschot, M. Development and Validation of a Computational Fluid Dynamics Model for the Optimization of a Sink-Float Separator for Plastics Recycling. *Procedia CIRP* **2022**, *105*, 116–121. [CrossRef]
60. Quelal, W.O.M.; Velázquez-Martí, B.; Gisbert, A.F. Separation of virgin plastic polymers and post-consumer mixed plastic waste by sinking-flotation technique. *Environ. Sci. Pollut. Res.* **2021**, *29*, 1364–1374. [CrossRef]
61. Hoseini, H.; Movahed, S.O.; Jourabchi, S. The Float-Sink Behavior of Selected Pre-microwave Irradiated Plastics by Surface Adsorption of Several Dual Depressants. *J. Polym. Environ.* **2022**, *30*, 2824–2836. [CrossRef]
62. Czarnecka-Komorowska, D.; Kanciak, W. Development of Sink-Float Density Separation Process of Mixed Automotive Plastics for Mechanical Recycling. In *EAI International Conference on Management of Manufacturing Systems*; Springer International Publishing: Cham, Switzerland, 2023; pp. 115–130. [CrossRef]
63. Kökkılıç, O.; Mohammadi-Jam, S.; Chu, P.; Marion, C.; Yang, Y.; Waters, K.E. Separation of plastic wastes using froth flotation—An overview. *Adv. Colloid Interface Sci.* **2022**, *308*, 102769. [CrossRef] [PubMed]
64. Zhang, Y.; Li, C.; Wang, L.; Wang, H. Application of froth flotation in the separation of polyvinyl chloride and polycarbonate for recycling of waste plastic based on a novel surface modification. *Waste Manag.* **2020**, *110*, 43–52. [CrossRef] [PubMed]
65. Chen, S.; Zhang, Y.; Guo, C.; Zhong, Y.; Wang, K.; Wang, H. Separation of polyvinyl chloride from waste plastic mixtures by froth flotation after surface modification with sodium persulfate. *J. Clean. Prod.* **2019**, *218*, 167–172. [CrossRef]
66. Du, Y.; Zhang, Y.; Jiang, H.; Li, T.; Luo, M.; Wang, L.; Wang, C.; Wang, H. Hydrophilic modification of polycarbonate surface with surface alkoxylation pretreatment for efficient separation of polycarbonate and polystyrene by froth flotation. *Waste Manag.* **2020**, *118*, 471–480. [CrossRef] [PubMed]
67. Zhang, Y.; Jiang, H.; Bian, K.; Wang, H.; Wang, C. Is froth flotation a potential scheme for microplastics removal? Analysis on flotation kinetics and surface characteristics. *Sci. Total Environ.* **2021**, *792*, 148345. [CrossRef]

68. Zhao, Y.; Mishra, P.; Han, F.; Liu, X.; Shen, Z. Surface micro-alcoholysis treatment: A novel approach towards froth flotation based separation for binary mixtures of polyethylene terephthalate and polyvinyl chloride. *J. Clean. Prod.* **2019**, *232*, 848–857. [CrossRef]
69. Jiang, H.; Zhang, Y.; Bian, K.; Wang, H.; Wang, C. Insight into the effect of aqueous species on microplastics removal by froth flotation: Kinetics and mechanism. *J. Environ. Chem. Eng.* **2022**, *10*, 107834. [CrossRef]
70. Utimura, S.K.; Chaves, A.P.; Tenório, J.A.S.; Espinosa, D.C.R. Selecting chemicals for separation of ABS and HIPS in WEEE by froth flotation. *Polímeros* **2019**, *29*. [CrossRef]
71. Saneie, R.; Abdollahi, H.; Ghassa, S.; Azizi, D.; Chelgani, S.C. Recovery of Copper and Aluminum from Spent Lithium-Ion Batteries by Froth Flotation: A Sustainable Approach. *J. Sustain. Met.* **2022**, *8*, 386–397. [CrossRef]
72. Neo, E.R.K.; Yeo, Z.; Low, J.S.C.; Goodship, V.; Debattista, K. A review on chemometric techniques with infrared, Raman and laser-induced breakdown spectroscopy for sorting plastic waste in the recycling industry. *Resour. Conserv. Recycl.* **2022**, *180*, 106217. [CrossRef]
73. Zeng, Q.; Sirven, J.-B.; Gabriel, J.-C.P.; Tay, C.Y.; Lee, J.-M. Laser induced breakdown spectroscopy for plastic analysis. *TrAC Trends Anal. Chem.* **2021**, *140*, 116280. [CrossRef]
74. Adarsh, U.; Kartha, V.; Santhosh, C.; Unnikrishnan, V. Spectroscopy: A promising tool for plastic waste management. *TrAC Trends Anal. Chem.* **2022**, *149*, 116534. [CrossRef]
75. Wu, X.; Li, J.; Yao, L.; Xu, Z. Auto-sorting commonly recovered plastics from waste household appliances and electronics using near-infrared spectroscopy. *J. Clean. Prod.* **2020**, *246*, 118732. [CrossRef]
76. Chen, X.; Kroell, N.; Wickel, J.; Feil, A. Determining the composition of post-consumer flexible multilayer plastic packaging with near-infrared spectroscopy. *Waste Manag.* **2021**, *123*, 33–41. [CrossRef]
77. Junjuri, R.; Gundawar, M.K. Femtosecond laser-induced breakdown spectroscopy studies for the identification of plastics. *J. Anal. At. Spectrom.* **2019**, *34*, 1683–1692. [CrossRef]
78. Junjuri, R.; Zhang, C.; Barman, I.; Gundawar, M.K. Identification of post-consumer plastics using laser-induced breakdown spectroscopy. *Polym. Test.* **2019**, *76*, 101–108. [CrossRef]
79. Liu, K.; Tian, D.; Li, C.; Li, Y.; Yang, G.; Ding, Y. A review of laser-induced breakdown spectroscopy for plastic analysis. *TrAC Trends Anal. Chem.* **2019**, *110*, 327–334. [CrossRef]
80. Zhang, X.; Gu, F.; Xie, J.; Zhang, C.; Fu, J.; Zhao, P. Magnetic projection: A novel separation method and its first application on separating mixed plastics. *Waste Manag.* **2019**, *87*, 805–813. [CrossRef]
81. Grbic, J.; Nguyen, B.; Guo, E.; You, J.B.; Sinton, D.; Rochman, C.M. Magnetic Extraction of Microplastics from Environmental Samples. *Environ. Sci. Technol. Lett.* **2019**, *6*, 68–72. [CrossRef]
82. Wong, J.H.; Gan, M.J.H.; Chua, B.L.; Gakim, M.; Siambun, N.J. Shredder machine for plastic recycling: A review paper. In *IOP Conference Series: Materials Science and Engineering*; IOP Publishing: Bristol, UK, 2022; Volume 1217. [CrossRef]
83. Jemy, A.N.Q.; Octary, A.V.; Saptaji, K.; Septiani, T.D.; Fauziyyah, S.M.; Mohammad, R.N.; Djamari, D.W. Design and Modeling of Shredding Machine for Recycling Plastic Waste. In Proceedings of the 2021 IEEE 7th International Conference on Computing, Engineering and Design (ICCED), Sukabumi, Indonesia, 5–6 August 2021; pp. 1–6. [CrossRef]
84. Mahule, S.; Nagpure, V.; Bhoyar, S.; Bhoyar, D. Design and Fabrication of Low Cost Plastic Shredder. *Int. J. Res. Eng. Sci. Manag.* **2021**, *4*, 4–5. Available online: https://journal.ijresm.com/index.php/ijresm/article/view/709 (accessed on 23 July 2023).
85. Flizikowski, J.; Kruszelnicka, W.; Macko, M. The Development of Efficient Contaminated Polymer Materials Shredding in Recycling Processes. *Polymers* **2021**, *13*, 713. [CrossRef]
86. Suliman, M.S.; Johar, M.A. Development of Shredding Machine for Plastic Recycling. *Res. Prog. Mech. Manuf. Eng.* **2022**, *3*, 160–169.
87. Kumaran, P.; Lakshminarayanan, N.; Martin, A.V.; George, R.; JoJo, J. Design and analysis of shredder machine for e-waste recycling using CATIA. In *IOP Conference Series: Materials Science and Engineering*; IOP Publishing: Bristol, UK, 2020; Volume 993, p. 012013. [CrossRef]
88. Balwada, J.; Samaiya, S.; Mishra, R.P. Packaging Plastic Waste Management for a Circular Economy and Identifying a better Waste Collection System using Analytical Hierarchy Process (AHP). *Procedia CIRP* **2021**, *98*, 270–275. [CrossRef]
89. Bing, X.; de Keizer, M.; Bloemhof-Ruwaard, J.M.; van der Vorst, J.G. Vehicle routing for the eco-efficient collection of household plastic waste. *Waste Manag.* **2014**, *34*, 719–729. [CrossRef]
90. Sidique, S.F.; Lupi, F.; Joshi, S.V. The effects of behavior and attitudes on drop-off recycling activities. *Resour. Conserv. Recycl.* **2010**, *54*, 163–170. [CrossRef]
91. Manomaivibool, P.; Vassanadumrongdee, S. Buying back household waste electrical and electronic equipment: Assessing Thailand's proposed policy in light of past disposal behavior and future preferences. *Resour. Conserv. Recycl.* **2012**, *68*, 117–125. [CrossRef]
92. Browning, S.; Beymer-Farris, B.; Seay, J.R. Addressing the challenges associated with plastic waste disposal and management in developing countries. *Curr. Opin. Chem. Eng.* **2021**, *32*, 100682. [CrossRef]
93. Lange, J.-P. Managing Plastic Waste-Sorting, Recycling, Disposal, and Product Redesign. *ACS Sustain. Chem. Eng.* **2021**, *9*, 15722–15738. [CrossRef]
94. Vogt, B.D.; Stokes, K.K.; Kumar, S.K. Why is Recycling of Postconsumer Plastics so Challenging? *ACS Appl. Polym. Mater.* **2021**, *3*, 4325–4346. [CrossRef]

95. Biddle, M.B.; Dinger, P. An Overview of Recycling Plastics from Durable Goods: Challenges and Opportunities. Available online: https://d1wqtxts1xzle7.cloudfront.net/74227110/46173-libre.pdf?1636121433=&response-content-disposition=inline%3B+filename%3DAn_Overview_of_Recycling_Plastics_from_D.pdf&Expires=1695092482&Signature=etZrtqEe-t9-ee5Nu~IAUVj0rEyYxGS~4C1hwbnWm50EpKgvODiPDjHMXQ~6d1WEQcilXizbzhXNHMBre2KeoTTdkAb2mu6tuUjYwVz1M3XAjH7w6ywvrJWdbGV0POxyufJ9TfHjuqerINABhMGMurDa8g1zN5aeTUw4eDwDGgPnwMyniOC4u4LzA8c5qQbfC8TO9lnUD4YD2hZNjQl4m87QCXlB7BF820pNbFUrroRu8VutddzCkSLErgs6WWyQUS5AfWPw6p1Fjq3aQc-lNEE~XfpMB98vjGuUSYq6z0hDmqCnxvweGeRFpnfQqloW2gMcjcxPghK5fomjL-YBdw__&Key-Pair-Id=APKAJLOHF5GGSLRBV4ZA (accessed on 26 January 2023).
96. Carey, J. On the brink of a recycling revolution?: We're awash in plastics, many of which are hard to recycle. Could innovations, girded by the right incentives, finally whittle down the piles of plastic waste? *Proc. Natl. Acad. Sci. USA* **2017**, *114*, 612–616. [CrossRef]
97. Lubongo, C.; Alexandridis, P. Assessment of Performance and Challenges in Use of Commercial Automated Sorting Technology for Plastic Waste. *Recycling* **2022**, *7*, 11. [CrossRef]
98. Awaja, F.; Pavel, D. Recycling of PET. *Eur. Polym. J.* **2005**, *41*, 1453–1477. [CrossRef]
99. Biron, M. Recycling Plastics: Advantages and Limitations of Use. In *A Practical Guide to Plastics Sustainability*; Elsevier BV: Amsterdam, The Netherlands, 2020; pp. 411–467.
100. Eriksen, M.; Pivnenko, K.; Olsson, M.; Astrup, T. Contamination in plastic recycling: Influence of metals on the quality of reprocessed plastic. *Waste Manag.* **2018**, *79*, 595–606. [CrossRef] [PubMed]
101. Iacovidou, E.; Velenturf, A.P.; Purnell, P. Quality of resources: A typology for supporting transitions towards resource efficiency using the single-use plastic bottle as an example. *Sci. Total Environ.* **2019**, *647*, 441–448. [CrossRef] [PubMed]
102. El-Haggar, S.M. Sustainability of Municipal Solid Waste Management. *Sustain. Ind. Des. Waste Manag.* **2007**, 149–196. [CrossRef]
103. Damanhuri, E. *Post-Consumer Waste Recycling and Optimal Production*; IntechOpen: London, UK, 2012. [CrossRef]
104. Shen, L.; Worrell, E. Chapter 13—Plastic Recycling. In *Handbook of Recycling*; Worrell, E., Reuter, M.A., Eds.; Elsevier: Amsterdam, The Netherlands, 2014; pp. 179–190. [CrossRef]
105. Ajitha, A.R.; Thomas, S. Chapter 1—Introduction: Polymer blends, thermodynamics, miscibility, phase separation, and compatibilization. *Compat. Polym. Blends* **2019**, 1–29. [CrossRef]
106. Utracki, L.A. Compatibilization of Polymer Blends. *Can. J. Chem. Eng.* **2002**, *80*, 1008–1016. [CrossRef]
107. Dorigato, A. Recycling of polymer blends. *Adv. Ind. Eng. Polym. Res.* **2021**, *4*, 53–69. [CrossRef]
108. Lyatskaya, Y.; Gersappe, D.; Gross, N.A.; Balazs, A.C. Designing Compatibilizers to Reduce Interfacial Tension in Polymer Blends. 1996. Available online: https://pubs.acs.org/sharingguidelines (accessed on 21 May 2023).
109. La Mantia, F.P.; Morreale, M.; Botta, L.; Mistretta, M.C.; Ceraulo, M.; Scaffaro, R. Degradation of polymer blends: A brief review. *Polym. Degrad. Stab.* **2017**, *145*, 79–92. [CrossRef]
110. Mistretta, M.; Fontana, P.; Ceraulo, M.; Morreale, M.; La Mantia, F. Effect of compatibilization on the photo-oxidation behaviour of polyethylene/polyamide 6 blends and their nanocomposites. *Polym. Degrad. Stab.* **2015**, *112*, 192–197. [CrossRef]
111. Taufiq, M.; Mustafa, Z.; Mansor, M. Utilisation of recycled thermoplastics sourced from rejected-unused disposable diapers as polymer blends. *J. Mech. Eng. Sci.* **2017**, *11*, 3137–3143. [CrossRef]
112. Mnif, R.; Elleuch, R. Effects of reprocessing cycles and ageing on the rheological and mechanical properties of virgin-recycled HDPE blends. *Matér. Tech.* **2015**, *103*, 704. [CrossRef]
113. Hamad, K.; Kaseem, M.; Deri, F. Effect of recycling on rheological and mechanical properties of poly(lactic acid)/polystyrene polymer blend. *J. Mater Sci.* **2011**, *46*, 3013–3019. [CrossRef]
114. Hahladakis, J.N.; Velis, C.A.; Weber, R.; Iacovidou, E.; Purnell, P. An overview of chemical additives present in plastics: Migration, release, fate and environmental impact during their use, disposal and recycling. *J. Hazard. Mater.* **2018**, *344*, 179–199. [CrossRef]
115. Zweifel, H. Principles of Oxidative Degradation. *Stab. Polym. Mater.* **1998**, 1–40. [CrossRef]
116. Niaounakis, M. Chapter 2—Properties. *Biopolym. Process. Prod.* **2015**, 79–116. [CrossRef]
117. Capone, C.; Di Landro, L.; Inzoli, F.; Penco, M.; Sartore, L. Thermal and mechanical degradation during polymer extrusion processing. *Polym. Eng. Sci.* **2007**, *47*, 1813–1819. [CrossRef]
118. Schweighuber, A.; Felgel-Farnholz, A.; Bögl, T.; Fischer, J.; Buchberger, W. Investigations on the influence of multiple extrusion on the degradation of polyolefins. *Polym. Degrad. Stab.* **2021**, *192*, 109689. [CrossRef]
119. Pielichowski, K.; Njuguna, J. Thermal Degradation of Polymeric Materials. Available online: http://www.rapra.net (accessed on 13 March 2023).
120. Lederer, K. Thermal degradation of polymeric materials. *Polimeri* **1993**, *14*, 253–257.
121. White, J.R. Polymer ageing: Physics, chemistry or engineering? Time to reflect. *Comptes Rendus Chim.* **2006**, *9*, 1396–1408. [CrossRef]
122. Peterson, J.D.; Vyazovkin, S.; Wight, C.A. Kinetics of the Thermal and Thermo-Oxidative Degradation of Polystyrene, Polyethylene and Poly(propylene). *Macromol. Chem. Phys.* **2001**, *202*, 775–784. [CrossRef]
123. Botelho, G.; Queiros, A.; Liberal, S.; Gijsman, P. Studies on thermal and thermo-oxidative degradation of poly(ethylene terephthalate) and poly(butylene terephthalate). *Polym. Degrad. Stab.* **2001**, *74*, 39–48. [CrossRef]
124. Romão, W.; Franco, M.F.; Corilo, Y.E.; Eberlin, M.N.; Spinacé, M.A.; De Paoli, M.-A. Poly (ethylene terephthalate) thermo-mechanical and thermo-oxidative degradation mechanisms. *Polym. Degrad. Stab.* **2009**, *94*, 1849–1859. [CrossRef]

125. Phanthong, P.; Yao, S. Revolutionary Plastic Mechanical Recycling Process: Regeneration of Mechanical Properties and Lamellar Structures. In *Recycling Strategy and Challenges Associated with Waste Management towards Sustaining the World*; IntechOpen: London, UK, 2023. [CrossRef]
126. Banjo, A.D.; Agrawal, V.; Auad, M.L.; Celestine, A.-D.N. Moisture-induced changes in the mechanical behavior of 3D printed polymers. *Compos. Part C Open Access* **2022**, *7*, 100243. [CrossRef]
127. Weitsman, Y.J.; Elahi, M. Effects of fluids on the deformation, strength and durability of polymeric composites—An overview. *Mech. Time-Depend. Mater.* **2000**, *4*, 107–126. [CrossRef]
128. Long, T.S.; Sokol, R.J. Molding polycarbonate: Moisture degradation effect on physical and chemical properties. *Polym. Eng. Sci.* **1974**, *14*, 817–822. [CrossRef]
129. Feldman, D. Polymer Weathering: Photo-Oxidation. *J. Polym. Environ.* **2002**, *10*, 163–173. [CrossRef]
130. Allara, D.L. Aging of polymers. *Environ. Health Perspect.* **1975**, *11*, 29–33. [CrossRef]
131. Hashim, U.R.; Jumahat, A.; Jawaid, M.; Dungani, R.; Alamery, S. Effects of Accelerated Weathering on Degradation Behavior of Basalt Fiber Reinforced Polymer Nanocomposites. *Polymers* **2020**, *12*, 2621. [CrossRef]
132. Geissdoerfer, M.; Savaget, P.; Bocken, N.M.P.; Hultink, E.J. The circular economy—A new sustainability paradigm? *J. Clean. Prod.* **2017**, *143*, 757–768. [CrossRef]
133. Barbier, E.B. The Concept of Sustainable Economic Development. *Environ. Conserv.* **1987**, *14*, 101–110. [CrossRef]
134. Ghisellini, P.; Cialani, C.; Ulgiati, S. A Review on Circular Economy: The Expected Transition to a Balanced Interplay of Environmental and Economic Systems. *J. Clean. Prod.* **2016**, *114*, 11–32. [CrossRef]
135. Elia, V.; Gnoni, M.G.; Tornese, F. Measuring circular economy strategies through index methods: A critical analysis. *J. Clean. Prod.* **2017**, *142*, 2741–2751. [CrossRef]
136. Korhonen, J.; Honkasalo, A.; Seppälä, J. Circular Economy: The Concept and its Limitations. *Ecol. Econ.* **2018**, *143*, 37–46. [CrossRef]
137. Murray, A.; Skene, K.; Haynes, K. The Circular Economy: An Interdisciplinary Exploration of the Concept and Application in a Global Context. *J. Bus. Ethics* **2017**, *140*, 369–380. [CrossRef]
138. Niyommaneerat, W.; Suwanteep, K.; Chavalparit, O. Sustainability indicators to achieve a circular economy: A case study of renewable energy and plastic waste recycling corporate social responsibility (CSR) projects in Thailand. *J. Clean. Prod.* **2023**, *391*, 136203. [CrossRef]
139. Schwarz, A.E.; Ligthart, T.N.; Bizarro, D.G.; De Wild, P.; Vreugdenhil, B.; van Harmelen, T. Plastic recycling in a circular economy; determining environmental performance through an LCA matrix model approach. *Waste Manag.* **2021**, *121*, 331–342. [CrossRef]
140. Shamsuyeva, M.; Endres, H.-J. Plastics in the context of the circular economy and sustainable plastics recycling: Comprehensive review on research development, standardization and market. *Compos. Part C Open Access* **2021**, *6*, 100168. [CrossRef]
141. Genovese, A.; Acquaye, A.A.; Figueroa, A.; Koh, S.C.L. Sustainable supply chain management and the transition towards a circular economy: Evidence and some applications. *Omega* **2017**, *66*, 344–357. [CrossRef]
142. Potting, J.; Hekkert, M.; Worrell, E.; Hanemaaijer, A. *Circular Economy: Measuring Innovation in the Product Chain Policy Report*; PBL Netherlands Environmental Assessment Agency: The Hague, Netherlands, 2017.
143. Valencia, M.; Bocken, N.; Loaiza, C.; De Jaeger, S. The social contribution of the circular economy. *J. Clean. Prod.* **2023**, *408*, 137082. [CrossRef]
144. Khan, A.A.; Abonyi, J. Simulation of Sustainable Manufacturing Solutions: Tools for Enabling Circular Economy. *Sustainability* **2022**, *14*, 9796. [CrossRef]
145. Figge, F.; Thorpe, A.S.; Gutberlet, M. Definitions of the circular economy: Circularity matters. *Ecol. Econ.* **2023**, *208*, 107823. [CrossRef]
146. Luan, Y.; Huang, B.; Chen, L.; Wang, X.; Ma, Y.; Yin, M.; Song, Y.; Liu, H.; Ma, X.; Zhang, X.; et al. High-performance, low-cost, chemical-free, and reusable bamboo drinking straw: An all-natural substitute for plastic straws. *Ind. Crop. Prod.* **2023**, *200*, 116829. [CrossRef]
147. Nicolau, J.L.; Stadlthanner, K.A.; Andreu, L.; Font, X. Explaining the willingness of consumers to bring their own reusable coffee cups under the condition of monetary incentives. *J. Retail. Consum. Serv.* **2022**, *66*, 102908. [CrossRef]
148. Krause, R.M. Why Are We Doing This? Issue Framing, Problem Proximity, and Cities' Rationale for Regulating Single-Use Plastics. *J. Environ. Policy Plan.* **2021**, *23*, 482–495. [CrossRef]
149. Lessard, J.-M.; Habert, G.; Tagnit-Hamou, A.; Amor, B. Tracking the Environmental Consequences of Circular Economy over Space and Time: The Case of Close- and Open-Loop Recovery of Postconsumer Glass. *Environ. Sci. Technol.* **2021**, *55*, 11521–11532. [CrossRef] [PubMed]
150. Nylén, E.-J.A.; Salminen, J.M. How does the circular economy discourse affect policy-making? The case of streamlining waste utilisation in Finnish earthworks. *Resour. Conserv. Recycl.* **2019**, *149*, 532–540. [CrossRef]
151. Hekkert, M.P.; Worrell, E. Sustainable Agriculture View Project Regional Economic and Environmental Impacts of Wind Power Developments: A Case Study of a German Region View Project José Potting. Available online: https://www.researchgate.net/publication/319314335 (accessed on 23 February 2023).
152. Taghavi, N.; Udugama, I.A.; Zhuang, W.-Q.; Baroutian, S. Challenges in biodegradation of non-degradable thermoplastic waste: From environmental impact to operational readiness. *Biotechnol. Adv.* **2021**, *49*, 107731. [CrossRef]

153. Kazemi, M.; Kabir, S.F.; Fini, E.H. State of the art in recycling waste thermoplastics and thermosets and their applications in construction. *Resour. Conserv. Recycl.* **2021**, *174*, 105776. [CrossRef]
154. Di, L.; Yang, Y. Towards closed-loop material flow in additive manufacturing: Recyclability analysis of thermoplastic waste. *J. Clean. Prod.* **2022**, *362*, 132427. [CrossRef]
155. Zainudin, S.; Shuaib, N.A.; Omar, N.W.Y.; Azmi, A.I. Using taguchi approach for investigating mechanical properties of recycled carbon fibre reinforced thermoplastics for injection moulding applications. *Int. J. Mod. Manuf. Technol.* **2021**, *13*, 149–154. [CrossRef]
156. Borkar, A.; Hendlmeier, A.; Simon, Z.; Randall, J.D.; Stojcevski, F.; Henderson, L.C. A comparison of mechanical properties of recycled high-density polyethylene/waste carbon fiber via injection molding and 3D printing. *Polym. Compos.* **2022**, *43*, 2408–2418. [CrossRef]
157. Huang, P.-W.; Peng, H.-S. Number of Times Recycled and Its Effect on the Recyclability, Fluidity and Tensile Properties of Polypropylene Injection Molded Parts. *Sustainability* **2021**, *13*, 11085. [CrossRef]
158. Romoaldo, C.H.; Francisquetti, E.L.; Simon, D.A.; Ernze, J.R.; Bischoff, E. Recycling Tetrafluoroethylene–Perfluoroalkyl Vinylether Copolymer (PFA) Using Extrusion Process. *Macromol. Mater. Eng.* **2022**, *308*, 2200458. [CrossRef]
159. Benyathiar, P.; Kumar, P.; Carpenter, G.; Brace, J.; Mishra, D.K. Polyethylene Terephthalate (PET) Bottle-to-Bottle Recycling for the Beverage Industry: A Review. *Polymers* **2022**, *14*, 2366. [CrossRef]
160. Ronkay, F.; Molnar, B.; Gere, D.; Czigany, T. Plastic waste from marine environment: Demonstration of possible routes for recycling by different manufacturing technologies. *Waste Manag.* **2020**, *119*, 101–110. [CrossRef]
161. Freudenthaler, P.J.; Fischer, J.; Liu, Y.; Lang, R.W. Polypropylene Post-Consumer Recyclate Compounds for Thermoforming Packaging Applications. *Polymers* **2023**, *15*, 345. [CrossRef]
162. Zhong, S.; Pearce, J.M. Tightening the loop on the circular economy: Coupled distributed recycling and manufacturing with recyclebot and RepRap 3-D printing. *Resour. Conserv. Recycl.* **2017**, *128*, 48–58. [CrossRef]
163. Woern, A.L.; Byard, D.J.; Oakley, R.B.; Fiedler, M.J.; Snabes, S.L.; Pearce, J.M. Fused Particle Fabrication 3-D Printing: Recycled Materials' Optimization and Mechanical Properties. *Materials* **2018**, *11*, 1413. [CrossRef]
164. Dertinger, S.C.; Gallup, N.; Tanikella, N.G.; Grasso, M.; Vahid, S.; Foot, P.J.S.; Pearce, J.M. Technical pathways for distributed recycling of polymer composites for distributed manufacturing: Windshield wiper blades. *Resour. Conserv. Recycl.* **2020**, *157*, 104810. [CrossRef]
165. Vidakis, N.; Petousis, M.; Tzounis, L.; Maniadi, A.; Velidakis, E.; Mountakis, N.; Kechagias, J.D. Sustainable Additive Manufacturing: Mechanical Response of Polyamide 12 over Multiple Recycling Processes. *Materials* **2021**, *14*, 466. [CrossRef] [PubMed]
166. Liu, W.; Huang, H.; Zhu, L.; Liu, Z. Integrating carbon fiber reclamation and additive manufacturing for recycling CFRP waste. *Compos. Part B Eng.* **2021**, *215*, 108808. [CrossRef]
167. Kreiger, M.; Pearce, J.M. Environmental Life Cycle Analysis of Distributed Three-Dimensional Printing and Conventional Manufacturing of Polymer Products. *ACS Sustain. Chem. Eng.* **2013**, *1*, 1511–1519. [CrossRef]
168. Dong, X.; Hu, D.; Wang, H.; Huang, Y.; Long, S.; Zhang, G.; Li, X. Mechanical characterizations, recyclability of thermoplastics through melt grafting a dynamic covalent network onto polyethylene. *Polym. Test.* **2023**, *122*, 108005. [CrossRef]
169. Domingues, J.; Marques, T.; Mateus, A.; Carreira, P.; Malça, C. An Additive Manufacturing Solution to Produce Big Green Parts from Tires and Recycled Plastics. *Procedia Manuf.* **2017**, *12*, 242–248. [CrossRef]
170. Schneevogt, H.; Stelzner, K.; Yilmaz, B.; Abali, B.E.; Klunker, A.; Völlmecke, C. Sustainability in additive manufacturing: Exploring the mechanical potential of recycled PET filaments. *Compos. Adv. Mater.* **2021**, *30*. [CrossRef]
171. Reich, M.J.; Woern, A.L.; Tanikella, N.G.; Pearce, J.M. Mechanical Properties and Applications of Recycled Polycarbonate Particle Material Extrusion-Based Additive Manufacturing. *Materials* **2019**, *12*, 1642. [CrossRef]
172. Wei, B.; Yang, S.; Wang, Q. Green recycling of aluminum plastic packaging waste by solid-state shear milling and 3D printing for thermal conductive composites. *Polym. Adv. Technol.* **2021**, *32*, 2576–2587. [CrossRef]
173. Rahmatabadi, D.; Soltanmohammadi, K.; Aberoumand, M.; Soleyman, E.; Ghasemi, I.; Baniassadi, M.; Abrinia, K.; Bodaghi, M.; Baghani, M. Development of Pure Poly Vinyl Chloride (PVC) with Excellent 3D Printability and Macro- and Micro-Structural Properties. *Macromol. Mater. Eng.* **2022**, *308*, 2200568. [CrossRef]
174. Meyer, T.K.; Tanikella, N.G.; Reich, M.J.; Pearce, J.M. Potential of distributed recycling from hybrid manufacturing of 3-D printing and injection molding of stamp sand and acrylonitrile styrene acrylate waste composite. *Sustain. Mater. Technol.* **2020**, *25*, e00169. [CrossRef]
175. Sasse, J.; Pelzer, L.; Schön, M.; Ghaddar, T.; Hopmann, C. Investigation of Recycled and Coextruded PLA Filament for Additive Manufacturing. *Polymers* **2022**, *14*, 2407. [CrossRef] [PubMed]
176. Patti, A.; Acierno, S.; Cicala, G.; Zarrelli, M.; Acierno, D. Assessment of Recycled PLA-Based Filament for 3D Printing. *Mater. Proc.* **2021**, *7*, 16. [CrossRef]
177. Alexandre, A.; Sanchez, F.A.C.; Boudaoud, H.; Camargo, M.; Pearce, J.M. Mechanical Properties of Direct Waste Printing of Polylactic Acid with Universal Pellets Extruder: Comparison to Fused Filament Fabrication on Open-Source Desktop Three-Dimensional Printers. *3D Print. Addit. Manuf.* **2020**, *7*, 237–247. [CrossRef]

178. Thompson, N.; Weaver, J.M. Closed Loop Recycling of Low Friction Polymers in Fused Granule Fabrication Additive Manufacturing Processes. Faculty Publications. 2022. Available online: https://scholarsarchive.byu.edu/facpubhttps://scholarsarchive.byu.edu/facpub/5871 (accessed on 18 August 2023).
179. van Straten, B.; van der Heiden, D.; Robertson, D.; Riekwel, C.; Jansen, F.; van der Elst, M.; Horeman, T. Surgical waste reprocessing: Injection molding using recycled blue wrapping paper from the operating room. *J. Clean. Prod.* **2021**, *322*, 129121. [CrossRef]
180. Othman, M.H. Recycled Clothes with Polypropylene-Nanoclay for Industrial Product via Injection Molding. *Mater. Sci. Mater. Eng.* **2019**, *1*, 713–716. [CrossRef]
181. He, W.; Yang, J.; Chen, Y.; Liu, P.; Li, C.; Xiong, M.; Niu, X.; Li, X. Study on co-injection molding of poly(styrene-ethylene-butylene-styrene) and polypropylene: Simulation and experiment. *Polym. Test.* **2022**, *108*, 107510. [CrossRef]
182. Myasoedova, V.V. Graded Recycled Polymers Modified by Thermoelastoplasts: Composite Materials to Be Used for Injection Molding. *Polym. Sci. Ser. D* **2021**, *14*, 462–466. [CrossRef]
183. Synyuk, O.; Musiał, J.; Zlotenko, B.; Kulik, T. Development of Equipment for Injection Molding of Polymer Products Filled with Recycled Polymer Waste. *Polymers* **2020**, *12*, 2725. [CrossRef]
184. Nur-A-Tomal, M.; Pahlevani, F.; Handoko, W.; Cholake, S.; Sahajwalla, V. Effect of cyclic reprocessing on nylon 12 under injection molding: Working toward more efficient recycling of plastic waste. *Mater. Today Sustain.* **2021**, *11–12*, 100056. [CrossRef]
185. Gu, F.; Hall, P.; Miles, N. Development of composites based on recycled polypropylene for injection moulding automobile parts using hierarchical clustering analysis and principal component estimate. *J. Clean. Prod.* **2016**, *137*, 632–643. [CrossRef]
186. Mejia, E.B.; Al-Maqdi, S.; Alkaabi, M.; Alhammadi, A. Upcycling of HDPE Waste using Additive Manufacturing: Feasibility and Challenges; Upcycling of HDPE Waste using Additive Manufacturing: Feasibility and Challenges. 2020. Available online: https://www.researchgate.net/publication/342221344_Upcycling_of_HDPE_Waste_using_Additive_Manufacturing_Feasibility_and_Challenges (accessed on 18 August 2023).
187. Patra, N.R.; Negi, Y.S. Thermal, structural, and rheological modifications in recycled polyethylene terephthalate for a sustainable alternative source for additive manufacturing. *Polym. Eng. Sci.* **2022**, *62*, 2486–2497. [CrossRef]
188. Boparai, K.S.; Singh, R.; Fabbrocino, F.; Fraternali, F. Thermal characterization of recycled polymer for additive manufacturing applications. *Compos. Part B Eng.* **2016**, *106*, 42–47. [CrossRef]
189. Vidakis, N.; Petousis, M.; Tzounis, L.; Maniadi, A.; Velidakis, E.; Mountakis, N.; Papageorgiou, D.; Liebscher, M.; Mechtcherine, V. Sustainable Additive Manufacturing: Mechanical Response of Polypropylene over Multiple Recycling Processes. *Sustainability* **2021**, *13*, 159. [CrossRef]
190. Vidakis, N.; Petousis, M.; Maniadi, A. Sustainable Additive Manufacturing: Mechanical Response of High-Density Polyethylene over Multiple Recycling Processes. *Recycling* **2021**, *6*, 4. [CrossRef]
191. Vidakis, N.; Petousis, M.; Maniadi, A.; Koudoumas, E.; Vairis, A.; Kechagias, J. Sustainable Additive Manufacturing: Mechanical Response of Acrylonitrile-Butadiene-Styrene over Multiple Recycling Processes. *Sustainability* **2020**, *12*, 3568. [CrossRef]
192. Zander, N.E.; Boelter, Z.R. Rubber toughened recycled polyethylene terephthalate for material extrusion additive manufacturing. *Polym. Int.* **2020**, *70*, 742–748. [CrossRef]
193. Rahimizadeh, A.; Kalman, J.; Fayazbakhsh, K.; Lessard, L. Recycling of fiberglass wind turbine blades into reinforced filaments for use in Additive Manufacturing. *Compos. Part B Eng.* **2019**, *175*, 107101. [CrossRef]
194. Hart, K.R.; Frketic, J.B.; Brown, J.R. Recycling meal-ready-to-eat (MRE) pouches into polymer filament for material extrusion additive manufacturing. *Addit. Manuf.* **2018**, *21*, 536–543. [CrossRef]
195. Zander, N.E.; Gillan, M.; Burckhard, Z.; Gardea, F. Recycled polypropylene blends as novel 3D printing materials. *Addit. Manuf.* **2018**, *25*, 122–130. [CrossRef]
196. Zander, N.E.; Gillan, M.; Lambeth, R.H. Recycled polyethylene terephthalate as a new FFF feedstock material. *Addit. Manuf.* **2018**, *21*, 174–182. [CrossRef]
197. Zander, N.E.; Park, J.H.; Boelter, Z.R.; Gillan, M.A. Recycled Cellulose Polypropylene Composite Feedstocks for Material Extrusion Additive Manufacturing. *ACS Omega* **2019**, *4*, 13879–13888. [CrossRef] [PubMed]
198. Kang, G.; Joung, C.; Kim, H.; Im, S.; Kang, S.; Ji, W.; Park, Y. Manufacturing, thermoforming, and recycling of glass fiber/PET/PET foam sandwich composites: DOE analysis of recycled materials. *Polym. Compos.* **2022**, *43*, 8807–8817. [CrossRef]
199. von Freeden, J.; Rodenwaldt, B.; Nebel, D. Investigation of the influence of multiple thermoforming processes on the properties of continuous fiber-reinforced thermoplastics to enable structural reuse. *SN Appl. Sci.* **2023**, *5*, 54. [CrossRef]
200. Kreiger, M.; Anzalone, G.C.; Mulder, M.L.; Glover, A.; Pearce, J.M. Distributed Recycling of Post-Consumer Plastic Waste in Rural Areas. In *MRS Proceedings*; Cambridge University Press (CUP): Cambridge, UK, 2013; Volume 1492, pp. 91–96.
201. Spekkink, W.; Rödl, M.; Charter, M. Repair Cafés and Precious Plastic as translocal networks for the circular economy. *J. Clean. Prod.* **2022**, *380*, 135125. [CrossRef]
202. Byard, D.J.; Woern, A.L.; Oakley, R.B.; Fiedler, M.J.; Snabes, S.L.; Pearce, J.M. Green fab lab applications of large-area waste polymer-based additive manufacturing. *Addit. Manuf.* **2019**, *27*, 515–525. [CrossRef]
203. Ravindran, A.; Scsavnicki, S.; Nelson, W.; Gorecki, P.; Franz, J.; Oberloier, S.; Meyer, T.K.; Barnard, A.R.; Pearce, J.M. Open Source Waste Plastic Granulator. *Technologies* **2019**, *7*, 74. [CrossRef]
204. Berkane, I.; Aracil, I.; Fullana, A. Evaluation of thermal drying for the recycling of flexible plastics. *Waste Manag.* **2023**, *168*, 116–125. [CrossRef]

205. Woern, A.L.; McCaslin, J.R.; Pringle, A.M.; Pearce, J.M. RepRapable Recyclebot: Open source 3-D printable extruder for converting plastic to 3-D printing filament. *HardwareX* **2018**, *4*, e00026. [CrossRef]
206. Al Nabhani, D.; Kassab, A.; Habbal, O.; Mohanty, P.; Ayoub, G.; Pannier, C. Benchmarking the Tensile Properties of Polylactic Acid (PLA) Recycled Through Fused Granule Fabrication Additive Manufacturing. In Proceedings of the Solid Freeform Fabrication Symposium, Austin, TX, USA, 14–16 August 2023.
207. Woern, A.L.; Pearce, J.M. 3-D Printable Polymer Pelletizer Chopper for Fused Granular Fabrication-Based Additive Manufacturing. *Inventions* **2018**, *3*, 78. [CrossRef]
208. Wu, H.-C.; Chen, T.-C.T. Quality control issues in 3D-printing manufacturing: A review. *Rapid Prototyp. J.* **2018**, *24*, 607–614. [CrossRef]
209. Vidakis, N.; David, C.; Petousis, M.; Sagris, D.; Mountakis, N. Optimization of key quality indicators in material extrusion 3D printing of acrylonitrile butadiene styrene: The impact of critical process control parameters on the surface roughness, dimensional accuracy, and porosity. *Mater. Today Commun.* **2023**, *34*, 105171. [CrossRef]
210. Patel, R.; Desai, C.; Kushwah, S.; Mangrola, M.H. A review article on FDM process parameters in 3D printing for composite materials. *Mater. Today Proc.* **2022**, *60 Pt 3*, 2162–2166. [CrossRef]
211. Ambade, V.V.; Rajurkar, S.W.; Awari, G.K. Optimization of process parameters affecting performance of part characteristics in fused deposition modeling (FDM) 3D printing: A critical review. *AIP Conf. Proc.* **2023**, *2800*, 020072.
212. Urbanic, R.J.; Hedrick, R.W.; Burford, C.G. A process planning framework and virtual representation for bead-based additive manufacturing processes. *Int. J. Adv. Manuf. Technol.* **2016**, *90*, 361–376. [CrossRef]
213. Sampedro, G.A.R.; Agron, D.J.S.; Amaizu, G.C.; Kim, D.-S.; Lee, J.-M. Design of an In-Process Quality Monitoring Strategy for FDM-Type 3D Printer Using Deep Learning. *Appl. Sci.* **2022**, *12*, 8753. [CrossRef]
214. Honarvar, F.; Varvani-Farahani, A. A review of ultrasonic testing applications in additive manufacturing: Defect evaluation, material characterization, and process control. *Ultrasonics* **2020**, *108*, 106227. [CrossRef]
215. Meyers, M.A.; Chawla, K.K. *Mechanical Behavior of Materials*; Cambridge University Press (CUP): Cambridge, UK, 2008.
216. Rozanski, A.; Galeski, A. Plastic yielding of semicrystalline polymers affected by amorphous phase. *Int. J. Plast.* **2013**, *41*, 14–29. [CrossRef]
217. Chudnovsky, A.; Preston, S. Configurational mechanics of necking phenomena in engineering thermoplastics. *Mech. Res. Commun.* **2002**, *29*, 465–475. [CrossRef]
218. Galeski, A.; Bartczak, Z.; Kazmierczak, T.; Slouf, M. Morphology of undeformed and deformed polyethylene lamellar crystals. *Polymer* **2010**, *51*, 5780–5787. [CrossRef]
219. Bartczak, Z.; Galeski, A. Plasticity of Semicrystalline Polymers. *Macromol. Symp.* **2010**, *294*, 67–90. [CrossRef]
220. La Mantia, F.P. Mechanical properties of recycled polymers. *Macromol. Symp.* **1999**, *147*, 167–172. [CrossRef]
221. Guyot, A. Recent developments in the thermal degradation of polystyrene—A review. *Polym. Degrad. Stab.* **1986**, *15*, 219–235. [CrossRef]
222. Cameron, G.; Kerr, G. Thermal degradation of polystyrene—I. Chain scission at low temperatures. *Eur. Polym. J.* **1968**, *4*, 709–717. [CrossRef]
223. Zahavich, A.T.P.; Latto, B.; Takacs, E.; Vlachopoulos, J. The Effect of Multiple Extrusion Passes During Recycling of High Density Polyethylene. *Adv. Polym. Technol. J. Polym. Process. Inst.* **1997**, *16*, 11–24. [CrossRef]
224. Oblak, P.; Gonzalez-Gutierrez, J.; Zupančič, B.; Aulova, A.; Emri, I. Processability and mechanical properties of extensively recycled high density polyethylene. *Polym. Degrad. Stab.* **2015**, *114*, 133–145. [CrossRef]
225. Yin, S.; Tuladhar, R.; Shi, F.; Shanks, R.A.; Combe, M.; Collister, T. Mechanical reprocessing of polyolefin waste: A review. *Polym. Eng. Sci.* **2015**, *55*, 2899–2909. [CrossRef]
226. Cusano, I.; Campagnolo, L.; Aurilia, M.; Costanzo, S.; Grizzuti, N. Rheology of Recycled PET. *Materials* **2023**, *16*, 3358. [CrossRef]
227. Takkalkar, P.; Jatoi, A.S.; Jadhav, A.; Jadhav, H.; Nizamuddin, S. Thermo-mechanical, rheological, and chemical properties of recycled plastics. *Plast. Waste Sustain. Asph. Roads* **2022**, 29–42. [CrossRef]
228. Gonzàlez, V.A.; Neira-Velázquez, G.; Angulo-Sánchez, J.L. Polypropylene chain scissions and molecular weight changes in multiple extrusion. *Polym. Degrad. Stab.* **1998**, *60*, 33–42. [CrossRef]
229. Scaffaro, R.; Maio, A.; Sutera, F.; Gulino, E.F.; Morreale, M. Degradation and Recycling of Films Based on Biodegradable Polymers: A Short Review. *Polymers* **2019**, *11*, 651. [CrossRef]
230. Vohlidal, J. Polymer degradation: A short review. *Chem. Teach. Int.* **2021**, *3*, 213–220. [CrossRef]
231. Zhou, J.; Hsu, T.; Wang, J. Mechanochemical Degradation and Recycling of Synthetic Polymers. *Angew. Chem. Int. Ed.* **2023**, *62*, e202300768. [CrossRef] [PubMed]
232. Itim, B.; Philip, M. Effect of multiple extrusions and influence of PP contamination on the thermal characteristics of bottle grade recycled PET. *Polym. Degrad. Stab.* **2015**, *117*, 84–89. [CrossRef]
233. Incarnato, L.; Scarfato, P.; Acierno, D.; Milana, M.R.; Feliciani, R. Influence of recycling and contamination on structure and transport properties of polypropylene. *J. Appl. Polym. Sci.* **2003**, *89*, 1768–1778. [CrossRef]
234. Alzerreca, M.; Paris, M.; Boyron, O.; Orditz, D.; Louarn, G.; Correc, O. Mechanical properties and molecular structures of virgin and recycled HDPE polymers used in gravity sewer systems. *Polym. Test.* **2015**, *46*, 1–8. [CrossRef]

235. Lay, M.; Thajudin, N.L.N.; Hamid, Z.A.A.; Rusli, A.; Abdullah, M.K.; Shuib, R.K. Comparison of physical and mechanical properties of PLA, ABS and nylon 6 fabricated using fused deposition modeling and injection molding. *Compos. Part B Eng.* **2019**, *176*, 107341. [CrossRef]
236. Giri, J.; Patil, A.; Prabhu, H. The Effect of Various Parameters on the Nozzle Diameter and 3D Printed Product in Fused Deposition Modelling: An Approach. In *Lecture Notes in Networks and Systems*; Springer: Berlin/Heidelberg, Germany, 2018; pp. 839–847. [CrossRef]
237. Doshi, M.; Mahale, A.; Singh, S.K.; Deshmukh, S. Printing parameters and materials affecting mechanical properties of FDM-3D printed Parts: Perspective and prospects. *Mater. Today Proc.* **2021**, *50*, 2269–2275. [CrossRef]
238. Podsiadły, B.; Skalski, A.; Rozpiórski, W.; Słoma, M. Are We Able to Print Components as Strong as Injection Molded?—Comparing the Properties of 3D Printed and Injection Molded Components Made from ABS Thermoplastic. *Appl. Sci.* **2021**, *11*, 6946. [CrossRef]
239. Vaes, D.; Van Puyvelde, P. Semi-crystalline feedstock for filament-based 3D printing of polymers. *Prog. Polym. Sci.* **2021**, *118*, 101411. [CrossRef]
240. Anderson, I.; Raza, I.; Iannucci, L.; Curtis, P.T.; Ruppert, D.S.; Harrysson, O.L.; Marcellin-Little, D.J.; Abumoussa, S.; Dahners, L.E.; Weinhold, P.S.; et al. Mechanical Properties of Specimens 3D Printed with Virgin and Recycled Polylactic Acid. *3D Print. Addit. Manuf.* **2017**, *4*, 110–115. [CrossRef]
241. Lanzotti, A.; Martorelli, M.; Maietta, S.; Gerbino, S.; Penta, F.; Gloria, A. A comparison between mechanical properties of specimens 3D printed with virgin and recycled PLA. *Proc. CIRP* **2019**, *79*, 143–146. [CrossRef]
242. Vidakis, N.; Petousis, M.; Tzounis, L.; Grammatikos, S.A.; Porfyrakis, E.; Maniadi, A.; Mountakis, N. Sustainable Additive Manufacturing: Mechanical Response of Polyethylene Terephthalate Glycol over Multiple Recycling Processes. *Materials* **2021**, *14*, 1162. [CrossRef] [PubMed]
243. Pfaendner, R. How will additives shape the future of plastics? *Polym. Degrad. Stab.* **2006**, *91*, 2249–2256. [CrossRef]
244. Pfaendner, R.; Herbst, H.; Hoffmann, K.; Sitek, F. Recycling and restabilization of polymers for high quality applications. An Overview. *Die Angew. Makromol. Chem.* **1995**, *232*, 193–227. [CrossRef]
245. Pfaendner, R. Restabilization—30 years of research for quality improvement of recycled plastics review. *Polym. Degrad. Stab.* **2022**, *203*, 110082. [CrossRef]
246. Mihelčič, M.; Oseli, A.; Huskić, M.; Perše, L.S. Influence of Stabilization Additive on Rheological, Thermal and Mechanical Properties of Recycled Polypropylene. *Polymers* **2022**, *14*, 5438. [CrossRef]
247. Self, J.L.; Zervoudakis, A.J.; Peng, X.; Lenart, W.R.; Macosko, C.W.; Ellison, C.J. Linear, Graft, and Beyond: Multiblock Copolymers as Next-Generation Compatibilizers. *JACS Au* **2022**, *2*, 310–321. [CrossRef]
248. Raffa, P.; Coltelli, M.-B.; Savi, S.; Bianchi, S.; Castelvetro, V. Chain extension and branching of poly(ethylene terephthalate) (PET) with di- and multifunctional epoxy or isocyanate additives: An experimental and modelling study. *React. Funct. Polym.* **2012**, *72*, 50–60. [CrossRef]

Disclaimer/Publisher's Note: The statements, opinions and data contained in all publications are solely those of the individual author(s) and contributor(s) and not of MDPI and/or the editor(s). MDPI and/or the editor(s) disclaim responsibility for any injury to people or property resulting from any ideas, methods, instructions or products referred to in the content.

polymers

MDPI

Review

The Challenges Facing the Current Paradigm Describing Viscoelastic Interactions in Polymer Melts

Jean Pierre Ibar †

Polymat Institute, University of the Basque Country (UPV/EHU), 48013 Donostia-San Sebastian, Euskadi, Spain; jpibar@alum.mit.edu

† Current address: Aurrera Center of Dissipative Interactions (ACDI), Irun, 20305 Gipuskoa, Spain.

Abstract: Staudinger taught us that macromolecules were made up of covalently bonded monomer repeat units chaining up as polymer chains. This paradigm is not challenged in this paper. The main question raised in polymer physics remains: how do these long chains interact and move as a group when submitted to shear deformation at high temperature when they are viscous liquids? The current consensus is that we need to distinguish two cases: the deformation of "un-entangled chains" for macromolecules with molecular weight, M, smaller than M_e, "the entanglement molecular weight", and the deformation of "entangled" chains for $M > M_e$. The current paradigm stipulates that the properties of polymers derive from the statistical characteristics of the macromolecule itself, the designated statistical system that defines the thermodynamic state of the polymer. The current paradigm claims that the viscoelasticity of un-entangled melts is well described by the Rouse model and that the entanglement issues raised when M > Me, are well understood by the reptation model introduced by de Gennes and colleagues. Both models can be classified in the category of "chain dynamics statistics". In this paper, we examine in detail the failures and the current challenges facing the current paradigm of polymer rheology: the Rouse model for un-entangled melts, the reptation model for entangled melts, the time–temperature superposition principle, the strain-induced time dependence of viscosity, shear-refinement and sustained-orientation. The basic failure of the current paradigm and its inherent inability to fully describe the experimental reality is documented in this paper. In the discussion and conclusion sections of the paper, we suggest that a different solution to explain the viscoelasticity of polymer chains and of their "entanglement" is needed. This requires a change in paradigm to describe the dynamics of the interactions within the chains and across the chains. A brief description of our currently proposed open dissipative statistical approach, "the Grain-Field Statistics", is presented.

Keywords: viscoelasticity; polymer physics; paradigm of polymer rheology; entanglements; Rouse model; reptation model; dual-phase model; grain-field statistics; sustained-orientation; shear-refinement

Citation: Ibar, J.P. The Challenges Facing the Current Paradigm Describing Viscoelastic Interactions in Polymer Melts. *Polymers* **2023**, *15*, 4309. https://doi.org/10.3390/polym15214309

Academic Editors: Ulrich Maschke, Matthias Ballauff, Rufina G. Alamo and Fahmi Zaïri

Received: 1 September 2023
Revised: 3 October 2023
Accepted: 9 October 2023
Published: 2 November 2023

Copyright: © 2023 by the author. Licensee MDPI, Basel, Switzerland. This article is an open access article distributed under the terms and conditions of the Creative Commons Attribution (CC BY) license (https://creativecommons.org/licenses/by/4.0/).

1. Introduction

Staudinger [1] taught us that macromolecules were made up of covalently bonded monomer repeat units chaining up as polymer chains. The chemical nature of the monomer directed the type of covalent bonds conferring most of the specific properties of the polymer. The greater the number of repeat units the longer the chains and the greater the possibility for the chains to assume a variety of shapes, from an extended elongated one to a more compact coiled one. Also, the chemical process that resulted in the synthesis of macromolecules produced many chains, often not with the same shape or size. The properties of the polymers improved when the chains became longer but it was more difficult to process them: their viscosity increased with molecular weight; viscosity was no longer an intensive property like it was for small liquids.

The main question raised in polymer physics was: how do these long chains interact and move as a group when submitted to shear deformation at high temperature when they

are viscous liquids? This question is debated in a field of polymer physics called rheology, whose purpose is to understand the viscoelastic aspects of polymer melts deformation [2].

The current consensus is that we need to distinguish two cases: the deformation of "un-entangled chains" for macromolecules with molecular weight, M, smaller than M_e, "the entanglement molecular weight", and the deformation of "entangled" chains for $M > M_e$.

Several eminent scientists have extensively studied these two cases over the last 70 years. Paul J. Flory, in 1974, and Pierre-Gilles de Gennes, in 1991, were awarded the Nobel prize in Chemistry and Physics, respectively, for their significant theoretical contribution to the understanding of these challenging problems [3,4]. For both these authors, the properties of polymers derive from the statistical characteristics of the macromolecule itself, the designated statistical system that defines the thermodynamic state of the polymer [5,6]. The molecular weight between entanglements, M_e, is defined from the rubber elasticity theory and known to be equal to $M_c/2$ where M_c is the molecular weight for the entanglements when viscosity measurements are carried out. The current paradigm is that the viscoelasticity of un-entangled melts ($M < M_c$) is well described by the Rouse model [7] and the entanglement issues raised by the impact of the increase in length of the macromolecules on the melt viscoelasticity, when $M > M_c$, are well understood by the reptation model introduced by de Gennes in 1971 [8]. Both models can be classified in the category of "chain dynamics statistics" [9–12].

In this paper, we examine in detail the failures and the current challenges facing the current paradigm of polymer rheology: the Rouse model [7] for $M < M_c$, the reptation model [4,6,8] for $M > M_c$, the time–temperature superposition principle [13], the strain-induced time dependence of viscosity [14], shear-refinement [15] and sustained-orientation [16]. The basic failure of the current paradigm and its inherent inability to fully describe the experimental reality [17] is reviewed in this paper.

We focus on re-examining some experimental facts, the most damaging, for these two models based on chain dynamics statistics, being their inability to explain the time dependence of viscosity under small shear strain conditions [14] and the observation of "Sustained-Orientation", i.e., the reversible triggering of the instability of the network of entanglement [2,16].

In the discussion and conclusion of the paper, we suggest that new concepts are needed to explain the viscoelasticity of polymer chains and of their "entanglement", also answering a question raised a long time ago [18] regarding their relaxation and thermal analysis behavior. These concepts represent a change of paradigm to describe the dynamics of the interactions within the chains and across the chains. A brief description of our currently proposed open dissipative statistical approach, "the Grain-Field Statistics of Open Dissipative Systems" [19–21], is introduced in the conclusion.

2. Development

2.1. The Great Myth of the Rouse Model: Its Failure to Describe the Rheology of Unentangled Melts ($M < M_c$)

2.1.1. (In)validation of the Rouse Model Using Dynamic Data $G'(\omega)$, $G''(\omega)$

A classical misconception, already emphasized in other instances ([13], ch. 3 of Ref. [2]), is the statement that polymer melts below Mc follow the predictions of the Rouse model [7]. The myth is so well established that the majority of the authors make this statement without fully verifying the accuracy of the allegation using their own data to validate it.

We give two examples of authors claiming that their data can be fitted by the Rouse model, and present good reasons to dispute such validation. The data both concern dynamic rheological results obtained on a series of monodispersed polystyrene (PS) samples [22,23]. The first set of dynamic data is from Matsumiya and Watanabe (The data were kindly provided by Prof. Watanabe, who also clarified some of the experimental issues by email) [22]. It applies to a monodispersed PS with M = 27,000 obtained at four temperatures T = 115 °C, 120 °C, 130 °C and 140 °C. The second set of dynamic data is from Majeste who studied in his thesis a series of monodispersed PS samples both unentangled and entangled [23].

Note that for Matsumiya and Watanabe's results the temperatures are all located below the T_{LL} temperature for this molecular weight (164.1 °C, see Equation (18) in [24]), whereas the temperature of T = 160 °C is the reference temperature chosen by Majeste to shift the other frequency sweep isotherms and obtain the mastercurves for eight unentangled PS samples. As we learn in [24], T_{LL} varies with M for PS like $T_g(M)$ + 70.44 °C, so the choice of T= 160 °C for the mastercurves in Majeste's data at various M positions the analysis of the data very near below or above T_{LL} for all the molecular weights below Mc. This contrasts with Matsumiya and Watanabe's data analysis.

The Rouse model is very simple to apply to a set of data: one needs the longest relaxation time, τ_R, at a given temperature, and the melt modulus G_N. The melt modulus, $G_N = \rho RT/M$, is calculated using the well-known modulus formula taken from rubber elastic theory, where ρ is the melt density, M the molecular weight, and T the value of the temperature (R is the gas constant). In other words, when the molecular weight and the temperature are given, the Rouse model only depends on one parameter, τ_R. The value of τ_R is linearly correlated to the Newtonian viscosity at that temperature, η^*_o; it is also the inverse of the cross-over frequency of $G'(\omega)$ and $G''(\omega)$, ω_x, also at the same temperature. The secondary relaxation times, τ_p are found from τ_R: $\tau_p = \tau_R/p^2$ with p= 1 to N= M/M_o where M_o is the mer molecular weight (For PS and M = 27,000 N = 257). A simple spreadsheet permits the calculation of $G'(\omega)$ and $G''(\omega)$ according to the following Equation.

$$\begin{aligned} G^*_{ROUSE}(\omega) &= \tfrac{\rho RT}{M}\sum_{p=1}^{N}\tfrac{\omega^2\tau_p^2+j\omega\tau_p}{1+\omega^2\tau_p^2} with \tau_p = \tfrac{\tau_R}{p^2} gives: \\ G'(\omega) &= \tfrac{\rho RT}{M}\sum_{p=1}^{N}\tfrac{\omega^2\tau_p^2}{1+\omega^2\tau_p^2} \\ G''(\omega) &= \tfrac{\rho RT}{M}\sum_{p=1}^{N}\tfrac{\omega\tau_p}{1+\omega^2\tau_p^2} \end{aligned} \quad . \tag{1}$$

The density ρ of the PS melts is given by Fox–Flory (Ref. 36 of [23]):

$$\frac{1}{\rho} = 0.767 + 5.510^{-4}T + \frac{6.4310^{-2}T}{M} \tag{2}$$

The Rouse time τ_R is given by:

$$\tau_R = \frac{6\eta_o}{\pi^2}\frac{M}{\rho RT} \tag{3}$$

The Newtonian viscosity η_o is determined at each temperature using the empirical Cole–Cole equation [25] to fit the data $\log(\eta^*(\omega))$ vs. $\log\omega$ and extrapolate to $\omega \to 0$. For PS M = 27,000, the temperature dependence of the Newtonian viscosity varies with temperature following the Vogel–Fulcher equation [26]:

$$\begin{gathered} \log(\eta_0(T)) = A + \tfrac{B}{T-T_\infty} \\ with\ A = -3.20583, B = 703.5571, T_\infty = 44.78°C = 317.93°K \end{gathered} \tag{4}$$

As already mentioned, the Rouse time can also be determined, $\tau_R = 1/\omega_x$, from the cross-over of the Maxwell straight lines passing through the low ω data points of $\log G'(\omega)$ and $\log G''(\omega)$ vs. $\log(\omega)$, by forcing their respective slopes to be two and one in the low ω line regressions, respectively, and calculating the coordinates of the intercepting straight lines.

Let us look at the match between the experimental results of Matsumiya and Watanabe, and the Rouse Equation (1). Figures 1–4 compare the results for T = 130 °C.

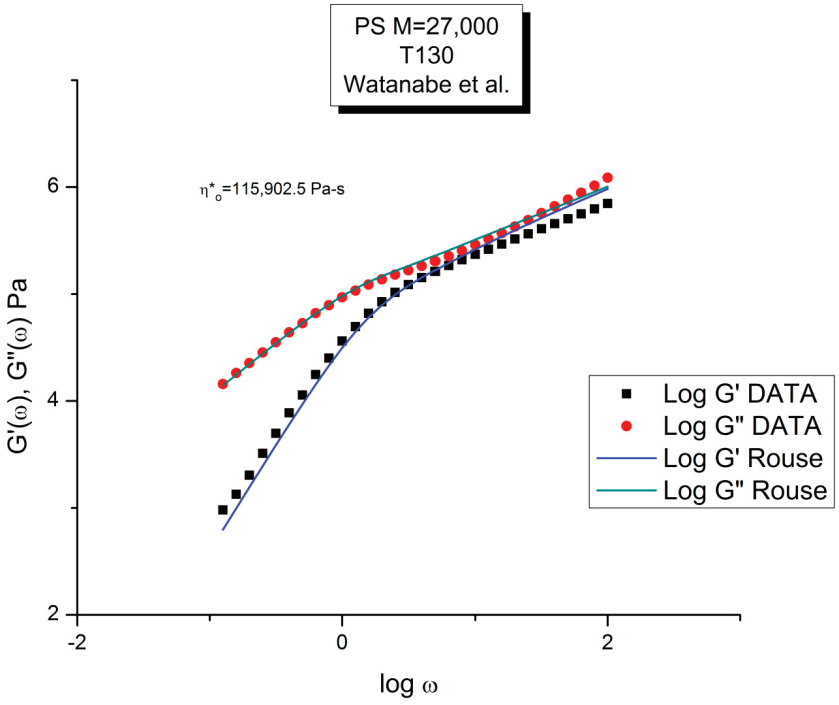

Figure 1. Comparison of log G′(ω), G″(ω) vs. logω for Data of Matsumiya and Watanabe [22] and the predictions of the Rouse model pursuant to Equations (1)–(4).

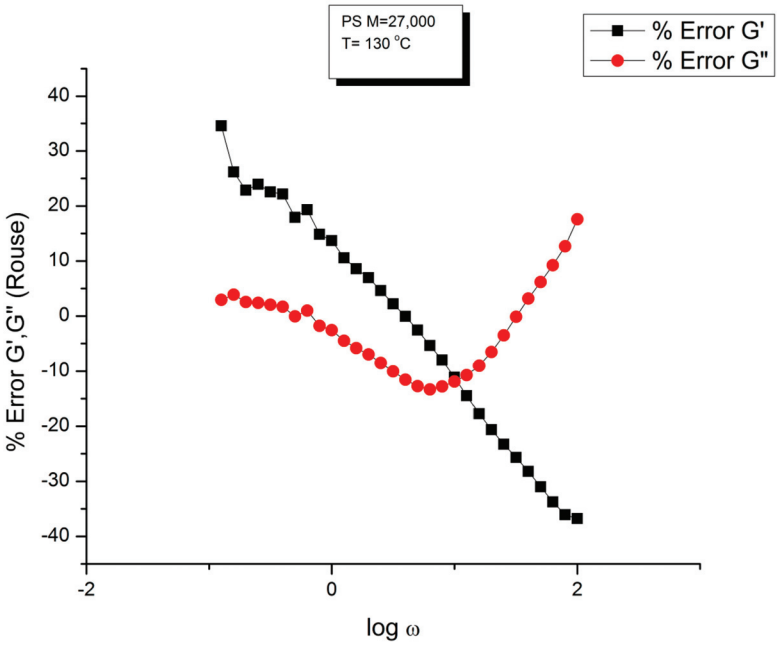

Figure 2. % error G′(ω) and G″(ω) with respect to Rouse simulation in Figure 1 plotted against ω.

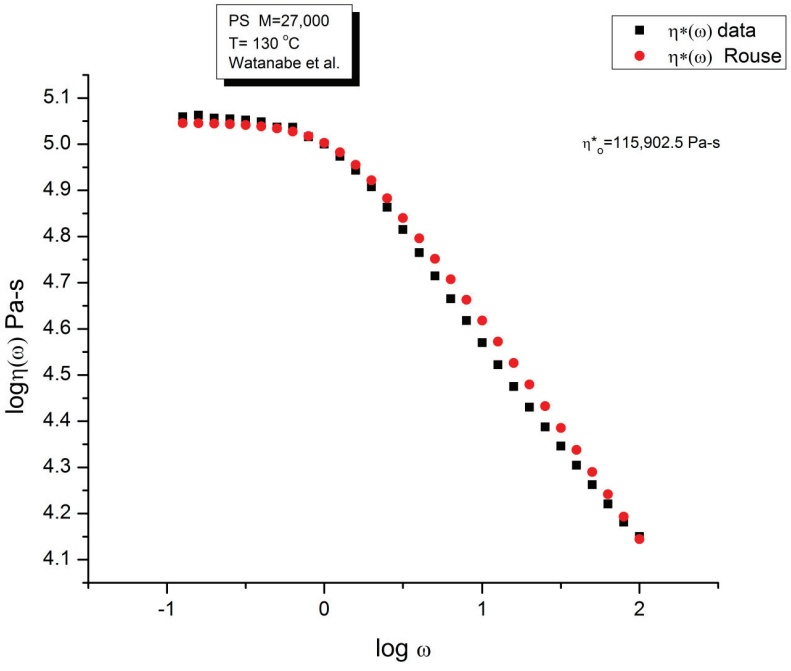

Figure 3. Comparison of the Rouse model prediction of log η*(ω) vs. logω and the data of Matsumiya and Watanabe [22] for PS (M = 27,000) at T = 130 °C (same data as in Figure 1).

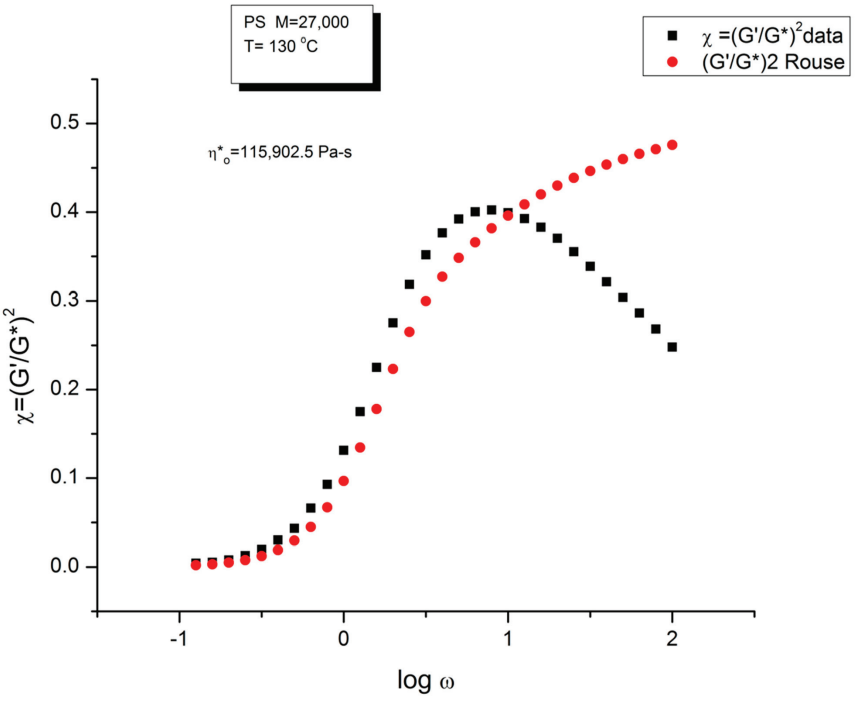

Figure 4. Comparison of $\chi = (G'/G^*)^2$ vs. logω for the data in Figures 1–3 and the predictions of the Rouse model pursuant to Equations (1)–(4).

Figure 1 displays the dynamic moduli $G'(\omega)$ and $G''(\omega)$ for the data (symbols) and the Rouse Equation (1) (red and blue lines). At first glance, one may say that the fit is remarkably good if one realizes that there is just one fitting constant involved, τ_R, the Rouse model providing a theoretical basis to determine the other constants G_N and τ_p. The fit is especially good for $G''(\omega)$ in the lower frequency region, explaining why the Rouse equation is often validated in the Newtonian range using the viscosity as the variable ($G''/\omega \rightarrow \eta^*_o$ at low ω). But, as we have expressed many times ([13], Ch. 3 of [2]), a close examination of the plot makes visible all the objective reasons to reject such a model, which turns out to provide an unacceptable fit of the data. Figure 2 provides the proof.

One of the reasons the apparent fitness of the Rouse model to the data in Figure 1 looked "good", is that we used log scales on both axes, which clearly compresses the resolution in order to display the overview picture. The log compression of the ω axis covers only three decades of variation of ω, from 0.1 to 100 rad/s. When the curves are mastercurves obtained by horizontal shifting, the log compression extends one-to-three more decades, which makes the appearance of a good fit even better because of the further data compression. Such is the case in the figures presented in Majeste's thesis, for instance, when they compare the data to the Rouse equation projections [23]. Even in Figure 1, which is not a mastercurve, one can see unacceptable discrepancies when comparing the results: the $G'(\omega)$ curves never seem to overlap, a fact proven in the next figure that shows that the residuals for the errors are totally curved when they should be random (i.e., with the points of the residual plot randomly disposed on both sides of the zero horizontal line). Figure 2 provides the % error between the data and its corresponding Rouse prediction. The verdict is crystal clear: there is no range where the fit can be considered acceptable, not even in the low frequency zone, in the terminal region, where Figure 1 gives the illusion of some relative success, especially for $G''(\omega)$ as we mentioned earlier. For all the values of ω the residuals are badly curved, the error is two-to-five times the accuracy for measuring the modulus: the Rouse model fails to fit the dynamic behavior for this $M < M_c$ melt. This is true for T = 130 °C in Figure 2, as well as for the three other temperatures chosen by Matsumiya and Watanabe (Data not shown). In fact, the errors become much worse for T = 120 and 115 °C. Only T = 140 °C shows a decrease in the magnitude of the errors, yet the residuals are still badly curved.

Figure 3 compares the data and the Rouse dynamic viscosity $\eta^*(\omega)$. As in Figure 1, the illusion of a good fit is what is apparent at first, perhaps even more so for the viscosity than for the moduli. All the features of shear-thinning are displayed by the Rouse model: the Newtonian plateau and the decrease in viscosity with strain rate at higher frequency. Yet, these are the same data that produced the unacceptable errors in the determination of $G'(\omega)$ and $G''(\omega)$ in Figure 2. One sees how the choice of the variables and the use of the log scale can easily mislead the conclusion.

As we said, the elegance of the Rouse model is its lack of fitting constants, being based on a molecular understanding of the motion of a macromolecule to produce flow. The Rouse equation that we have written above can even be further tuned down to include the expression of the radius of gyration of a single macromolecule, R_G, which can be measured by light or neutron scattering. However, if we desire to optimize the fit between the Rouse's predictions and the experimental data, we need to make "loose" the value of τ_R or G_N in Equation (1) and introduce them as regression parameters. The regression fits at low ω become much improved as we do that, yet it is at the expense of the physical Rouse reality: the value of τ_R and G_N values found by regression become 2000 to 5000% different from their respective values pursuant to the Rouse model ($G_N = \rho RT/M$). For instance, if the value of G_N is made different for the $G'(\omega)$ than for the $G''(\omega)$ equation in the Rouse formula (Equation (1)), the fits are considerably improved but the molecular explanation of the model goes down the drain. See below.

Figure 4 is a graph that displays an important apparent discrepancy between the prediction of the Rouse model and the data in the non-Newtonian range of ω. The graph compares the value of $\chi = (G'/G^*)^2$ at various ω either measured experimentally by

Matsumiya and Watanabe [22], the black squares, or calculated from the Rouse model (the red dots). What we mean by "discrepancy" is that the large departure between the Rouse model and the data seen in Figure 4 can be demonstrated (as shown below) to not be caused by a transitional high-frequency relaxation process that needs to be introduced to correct the data, it is the demonstration of the failure of the Rouse model to describe shear-thinning correctly. The range of the data investigated in Figure 4 is the lower and middle ω range for shear-thinning, a phenomenon expressing the shear dependence of viscosity, classically exhibited as a departure from the Newtonian range, itself only observed at very low frequency ($\omega < 10^0 = 1$ rad/s). The reason we bring this up is to differentiate our conclusions about the origin of the differences (observed at higher frequency in Figure 4) as a failure of the Rouse model, from the explanations by many other authors, such as Majeste in his thesis, who have claimed, that the Rouse model basic equations can be corrected to include the influence of the transitional high frequency relaxation terms on the dynamics of flow, thus would have attributed the differences in Figure 4 to the lack of corrections pursuant to the transitional high-frequency relaxation terms. We dedicate the following section to disprove the applicability of these authors' argument.

We have expressed in several previous publications [2,14,27] our interest in the variable $\chi = (G'/G^*)^2$, equal to $\cos^2\delta$, also equal to $1/(1 + \tan^2\delta)$, where δ is the phase angle between stress and strain. This parameter χ, we have suggested, is more appropriate than other traditional rheological variables (such as G'' or $\tan\delta$) to describe the viscoelastic character of the melt, especially when it is formulated in terms of the Dual-Phase and Cross-Dual-Phase parameters [20]. The maximum of $\chi(\omega)$, visible in Figure 4, corresponding to a minimum of $\tan\delta$, is known to occur for entangled ($M > M_c$) melts, and its frequency occurrence is attributed to the beginning of the rubbery plateau. In the case of unentangled melts, however, such as is the case for the sample of Watanabe and colleagues in Figure 4, the current paradigm understanding is that there is no rubbery plateau and therefore the phenomenon giving rise to the maximum in Figure 4 must have a different origin than the onset of entanglements. Since the absence of the rubbery plateau implies the juxtaposition of the terminal region and the T_α transitional region, many authors were led to attribute the departure they saw in their higher frequency data to the presence of the transitional high-frequency relaxation terms, the so-called T_α terms. Note that the Rouse model is not capable, on its own and without correction, of making χ exhibit a maximum (or a minimum of $\tan\delta$). The simple reason is that, in the Rouse mathematical formulation limited to τ_R, χ is equal to G'/G_N, (see Equation (16) of Ref. [13]). Since its $G'(\omega)$ never exhibits a maximum for all molecular weights and all values of the frequency ω, the Rouse model is doomed to fail to explain the maximum in Figure 4 without adding at least an extra term.

This failure is, indeed, recognized by the molecular models of the unentangled state which have considered correcting the Rouse modulus to include an extra term due to these high-frequency relaxations. Likewise, earlier models than the dynamic molecular Rouse's model that tackle viscoelastic network deformation by expressing the moduli in terms of a spectrum of relaxations have shown the need to correct the high-frequency terms. For instance, Gray, Harrison and Lamb [28] considered a continuous and dissymmetric distribution of the relaxation times of the type Davidson and Cole [29] resulting in the modification of the complex compliance to include three terms. This manipulation of the spectrum of relaxation did result in a very good fit between the data and the corrected deformation model, such as applied to Rouse [25], but amounts to modify-to-fit the spectrum of relaxation without a sound physical foundation to justify it. The use of mathematical patches to make failing models fit the results may be useful if they point to the right direction to what needs to be done theoretically to modify the initial assumptions of the model. In the case of models based on the spectrum of relaxation profile, the Gray et al.'s corrections of the spectrum of relaxation represents a real success. In the case of the Rouse model, we have quoted in Ref. [13] (Equation (18)) an expression due to Allal [30] that has been claimed to extend the range of fitness of the Rouse expression of $G'(\omega)$ and $G''(\omega)$ to higher frequencies. Majeste used Allal's method to correct his data and claimed that it

improved the fits to the Rouse model [23]. We evaluate in detail below the merit of such improvements and its relevance to explain the discrepancy in Figure 4.

Equation (5) explains the Allal's high-frequency correction which adds a new term, G^*_{HF}, to the complex modulus.

$$\begin{array}{c} \textit{Modulus according to Rouse}: \\ G^*_{ROUSE}(\omega) = \frac{\rho RT}{M}\sum_{p=1}^{N}\frac{\omega^2\tau_p^2 + j\omega\tau_p}{1+\omega^2\tau_p^2} \\ \tau_p = \frac{\tau_R}{p^2} \\ G^*(\omega) = G'(\omega) + jG''(\omega) \\ \textit{For the High Frequency terms}: \\ G^*_{HF}(\omega) = G_\infty\left[1 - \frac{1}{\sqrt{1+j\omega\tau'_o}}\right] \\ \tau'_o = \frac{1}{\pi^2}\frac{\xi_o b'^2}{kT} \\ \textit{Total Modulus}: \\ G^*(\omega) = G^*_{ROUSE}(\omega) + G^*_{HF}(\omega) \end{array} \quad (5)$$

In this equation, G_∞ is the glass modulus, ξ_o the monomeric friction coefficient, b′ the monomeric length, j the imaginary unity number ($j^2 = -1$) and k is the Boltzmann's constant (1.38065×10^{-23}). We have found two sets of values for the molecular parameters introduced in Equation (5): ξ_o, b′ and G_∞. Leonardi (Table II-1 of Ref. [31]) studied a PS with M_w = 326,000 and polydispersity I = 3.4 and gives the following values: $\xi_o = 6.3 \times 10^{-8}$ Kg/s, b′ = 7.4×10^{-10} m and G∞ = 6 × 109 Pa. This PS sample is entangled and polydispersed. For T = 130 °C (i.e., 403 °K in Equation (5)), the value of τ'_o is: 6.2823×10^{-7} s. Majeste [23] studied 8 monodispersed unentangled PS samples and provides for those grades the following values: $\xi_o = 2.7 \times 10^{-14}$ Kg/s, b′ = 3.7×10^{-10} m and $G_\infty = 1 \times 10^9$ Pa. For T = 130 °C we now find $\tau'_o = 6.7310 \times 10^{-14}$ s. This high-frequency relaxation time is one million times smaller than that found for the Leonardi's entangled PS. It is unclear why the fundamental molecular parameters entering the Allal's high-frequency relaxation correcting term would make τ'_o vary significantly with the length and the polydispersity of the chain. Could it be a new characteristic of entanglements? The physical reason for such a huge variation of τ'_o appears doubtful because the high-frequency component is supposed to represent the local relaxation at the monomeric level and should not depend, at least approximately, on the length of the chain, whether it is entangled or not. Such large differences in the values of ξ_o and b′ between the two PS samples of Majeste and Leonardi do not make sense. Additionally, assuming that the value of ξ_o and b′ tabulated by either Majeste or Leonardi are acceptable, we have found another reason to be concerned with the Allal's formulation of the Rouse's correction and it is exposed below.

G^*_{HF} is a complex number in Equation (5) that can be decomposed into an elastic and viscous component by way of the de Moivre's formula to remove the square root:

$$\begin{array}{c} G'_{HF} = G_\infty\left(1 - \sqrt{\rho_{HF}}\cos(\theta_{HF}/2)\right) \\ G''_{HF} = -G_\infty\sqrt{\rho_{HF}}\sin(\theta_{HF}/2) \\ \text{with}: \\ \rho_{HF} = \frac{1}{\sqrt{1+\omega^2\tau'^2_o}} \\ \tan(\theta_{HF}) = -\omega\tau'_o \end{array} \quad (6)$$

Figure 5 is a graph of $G'_{HF}(\omega)$ and $G''_{HF}(\omega)$ versus logω for T = 130 °C using the ξ_o, b′ and G_∞ constants of Leonardi plugged into Equations (5) and (6). The data range region covers the ω range between 0.1 and 100. The higher values of ω are added to show how Allal's formula works. In this figure, in the data range region, the magnitude of the value found for $G''_{HF}(\omega)$ is greater than its $G'_{HF}(\omega)$ counterpart by more than five decades! When we add these high-frequency correction moduli, $G'_{HF}(\omega)$ and $G''_{HF}(\omega)$, to the Rouse modulus $G'(\omega)$ and $G''(\omega)$, respectively, using the PS M = 27,000 sample, we

observe that $G'(\omega)$ remains unchanged because $G'_{HF}(\omega)$ is irrelevantly small, and that the corrected $G''(\omega)$ is worse than the uncorrected $G''(\omega)$ Rouse modulus in the low ω region, the very region where the fit to the real data was not so bad. This is shown in Figure 6, a plot of $G''(\omega) = G''_{ROUSE}(\omega) + G''_{HF}(\omega)$, using the Leonardi's parameters, versus $G''(\omega)$ data. The Rouse modulus corresponds to the red dots, the corrected Rouse modulus is represented by the black square, the perfect fit is the straight line y = x. One sees that the black squares are further away from the perfect fit. The conclusion is that the Allal's high-frequency correction appears to render the fit worse than the pure Rouse equation: the Rouse correction cannot be applied to the PS 27,000 data using Leonardi's PS molecular parameters. The other possibility is that only the molecular constants of a monodispersed unentangled PS should be used in the Allal's equations when applied to PS 27,000 which is also unentangled and monodispersed. Figure 7 is the same graph as Figure 5 but uses the molecular parameters assumed by Majeste, everything else being the same. One sees that the correction moduli, $G'_{HF}(\omega)$ and $G''_{HF}(\omega)$, are now both too small to add anything relevant to the values of the uncorrected Rouse moduli in the data range used to analyze this polymer. This is confirmed in Figure 8, similar to Figure 6 but now using the Majeste's constants in the Allal's equation. In Figure 8, the graphs before and after correction are identical and still very poorly fitting the data.

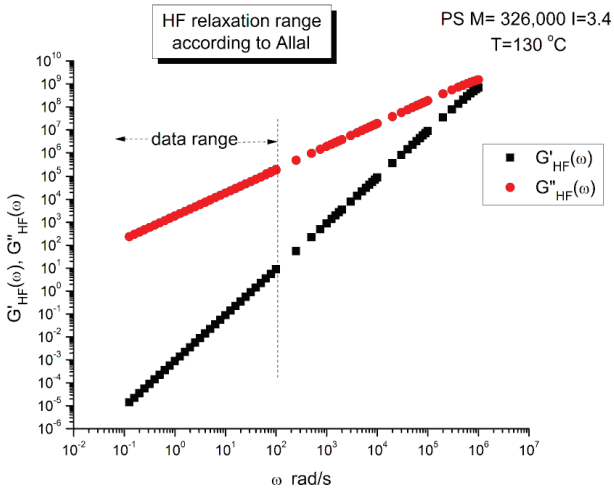

Figure 5. Calculated high frequency (HF) moduli, $G'_{HF}(\omega)$, $G''_{HF}(\omega)$ vs. logω, pursuant to Allal [30], Equations (5) and (6), using the molecular parameters provided by Leonardi in [31] for a PS specified in the graph.

In conclusion, the Allal's high-frequency terms added to the Rouse terms does not improve fitting the data. The use of the Rouse formulation should be limited to the Newtonian (terminal) region and is not adequate to describe shear-thinning of unentangled polymer melts.

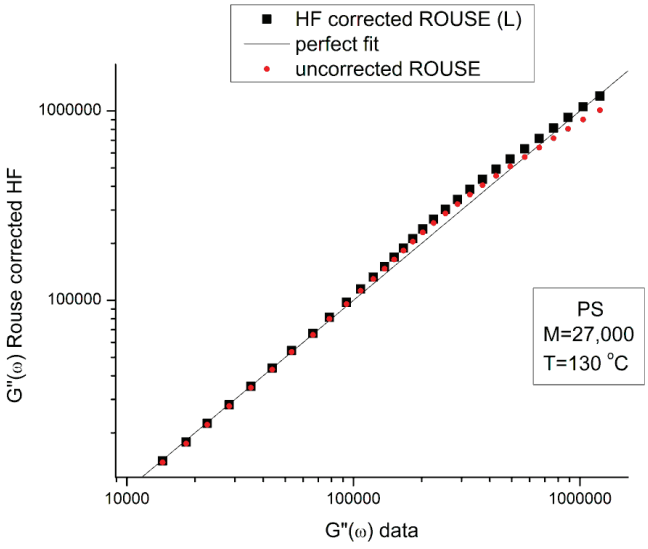

Figure 6. Plot of simulated G″(ω) using Rouse and the HF corrections from Figure 5 against G″(ω) for the data of Matsumiya and Watanabe, in Figure 1. The red dots apply to the uncorrected Rouse Equations (1)–(4) and the black squares to the corrected G″(ω) after adding $G''_{HF}(\omega)$ calculated from Equations (5) and (6). The straight line is Y = X, assuming a perfect fit.

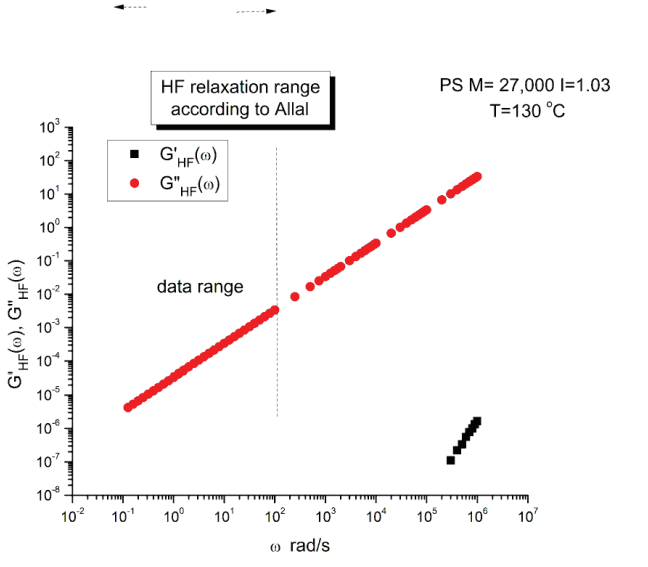

Figure 7. Calculated high frequency (HF) moduli, $G'_{HF}(\omega)$, $G''_{HF}(\omega)$ vs. log ω, pursuant to Allal [30], Equations (5) and (6), using the molecular parameters provided by Majeste in [23] for a PS with the specifications of the Matsumiya and Watanabe's sample.

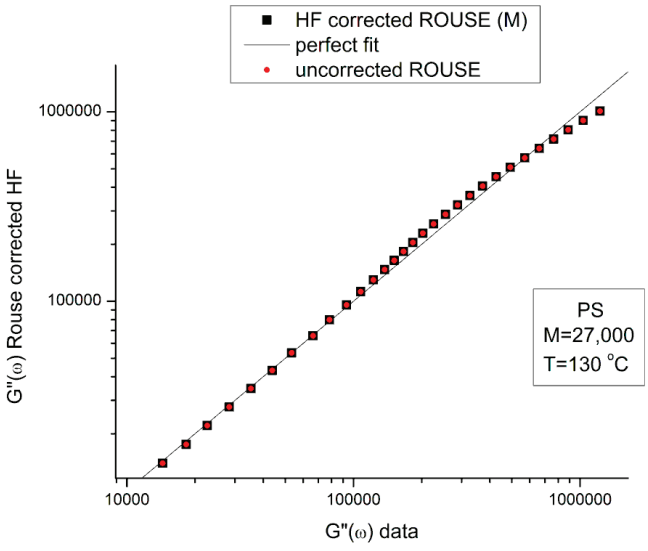

Figure 8. Plot of simulated $G''(\omega)$ using Rouse and the HF corrections from Figure 7 against $G''(\omega)$ for the data of Matsumiya and Watanabe. in Figure 1 The red dots apply to the uncorrected Rouse Equations (1)–(4) and the black squares to the corrected $G''(\omega)$ after adding $G''_{HF}(\omega)$ calculated from Equations (5) and (6). The straight line is Y = X, assuming a perfect fit.

Note that Majeste applied the Allal's corrections to the mastercurves obtained after shifting the isotherms to T = 160 °C. This shifting expands by a couple of decades the span of frequency toward the higher frequency region. Yet, looking at Figure 7 and expanding the data range to the right by two or three decades will not increase the values of $G'_{HF}(\omega)$ and $G''_{HF}(\omega)$ sufficiently to explain the large residuals observed in Figure 2. In addition, the time–temperature superposition principle needs to be validated over the data range analyzed in order to apply it with confidence, and, as will be shown below, the time–temperature shifting validity is limited for the Matsumiya and Watanabe's PS to the low ω range, below the maximum of χ vs. logω in Figure 3.

The reason we conclude that the Allal's high-frequency term has nothing to do with the maximum of χ observed in Figure 3, which occurs around ω = 10 rad/s, is the value of τ'_o in the expression of G^*_{HF} in Equation (5). With the values provided by Leonardi, τ'_o is around 10^{-6} to 10^{-7}, which, we agree, is "big enough" to start to have an impact in the ω = 0.1 to 100 rad/s range. However, we saw that the parameters provided for the Leonardi's PS made the Allal's corrections worse, not better. For the other option, with $\tau'_o \sim 10^{-14}$ to 10^{-13}, the values provided by Majeste, corresponding to the vibrational motions in the glassy state, it is clear that Allal's correction $G^*_{HF}(\omega)$ will practically remain equal to 0 until the frequency is near resonance, i.e., until $\omega \sim 1/\tau'_o$.

In conclusion, although the basic idea of adding a "glassy component" to the behavior in the terminal region makes sense to try to complement the Rouse's basic molecular dynamic contribution, it does not appear to be correctly addressed by Allal's formula. In addition, as we will show using the data of Matsumiya and Watanabe, the time–temperature superposition principle only applies satisfactorily within a limited range of temperature, which raises some questions regarding the accuracy of the shifted data at high frequency in the case of the Majeste's data.

In conclusion, the "satisfying improvement of the fitting of the data" claimed by Majeste to be the result of adding the high-frequency Allal's correction is definitely overstated, to say the least. For instance, Figure 1.88 (M = 8500) of Majeste's thesis (not reproduced here) clearly shows that the improvement is not satisfactory, according to our standards:

all the calculated G′(ω) values calculated after corrections are systematically off the data values, even in the terminal region, and using log–log axes. This seems to be the same type of fitting failure observed for G′(ω) in Figure 1 for the M = 27,000 PS.

2.1.2. (In)validity of the Rouse Formula to Predict the Molecular Dependency of τ_R below M_c

We said that the Rouse model was not capable of describing well the dynamics of shear-thinning for unentangled melts, but also added that its use could be limited to the Newtonian region. Does this mean that the Rouse model is correct/useful in the terminal regime of viscoelasticity? This is what we want to examine in this section.

Equation (3) is often used to validate the Rouse model. There are two ways to verify this formula, one at T constant, M variable, i.e., using the Majeste's data at T = 160 °C, and by working at M constant and varying T, i.e., using Matsumiya and Watanabe's data at M = 27,000 and T variable between 115 and 140 °C.

As we already mentioned before, the Maxwell lines cross-over, ω_x, can easily been found from fitting the low ω region where G′(ω) and G″(ω) can be forced to verify the Maxwell's slopes of 2 and 1 when plotted against ω on log–log axes. This provides an accurate way to determine $\tau_R = 1/\omega_x$.

Molecular Weight Dependence of the Rouse Time, τ_R from the M < M_c Majeste Data

The Rouse theory implies that τ_R is proportional to M^2, which is equivalent to predicting that η_o is proportional to M.

Figure 9 is a plot of log ω_x vs. logM for the 8 unentangled samples of Majeste at T = 160 °C. We expect to see a slope of −2 if the Rouse formula is validated.

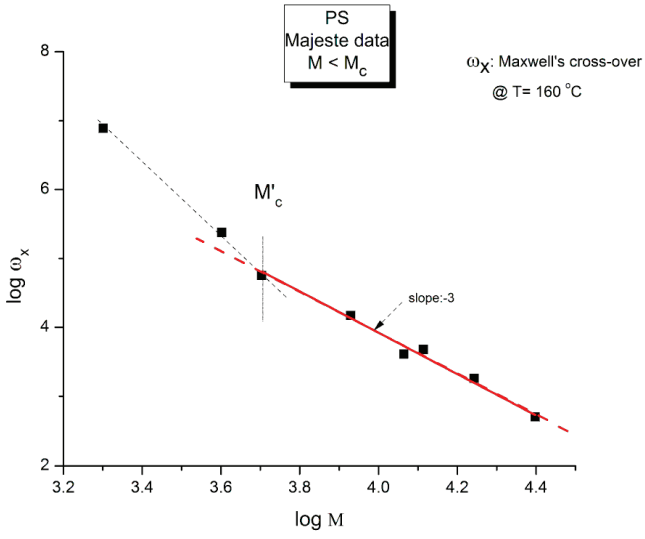

Figure 9. Logω_x vs. log M for un-entangled PS samples [23].

The graph in Figure 9 is better described by two straight lines than by just one. The crossing of these two lines occurs for log M~3.67 (M = 4700) that we have designated M'_c. The regression line passing through the points M > M'_c has a (forced) slope of −3.0 ± 0 and an intercept equal to 15.92 ± 0.033 (r^2 = 0.987, χ^2/DoF = 0.0067). This regression straight line is the red line drawn in Figure 9 passing randomly through six data points including M'_c. The unconstrained slope, −2.92 ± 0.16 (r^2 = 0.994), also points towards a slope of −3.

The conclusion is that the slope is not equal to −2 as it should be if the Rouse formula had been validated. It is clear that a slope of −3, although unexpected, is closer to what

is measured (−2.92). In such a case, η_o would vary against M^2 instead of M. The other observation concerns M'_c that we find at approximately $M = M_c/8$ (4375). This same M'_c "transition" in the log viscosity–logM curve is observed using viscometry data on the same monodispersed PS, but this is not the subject of this presentation. Needless to say, the Rouse model does not predict the presence of M'_c. We let the reader know, in that regard, that in our Dual-Phase model of polymer interactions to describe viscoelasticity [20], the transition M'_c is predicted and represents the molecular weight for the formation of stable macrocoils, the first rheological manifestation of the macromolecular aspect of the interactive systems of mers.

Temperature Dependence of τ_R at M Constant

Equation (3) involves the Newtonian viscosity, η_o, the shear elastic modulus of the melt, $G_N = \rho RT/M$, and τ_R computed from the cross-over frequency: $\omega_x = 1/\tau_R$. G_N is calculated by Equation (2) and the Newtonian viscosity by Equation (4). All these variables are temperature dependent and known. We can test its validity by plotting the product G_N $\tau_x(T)$ versus $\eta^*_o(T)$. The Rouse equation is validated if the slope is equal to $6/\pi^2 = 0.608$

A linear regression applied to the 3 upper isotherms, T = 140 to 120 °C, is represented by the red segment in Figure 10. It is a quasi-perfect linear fit with $r^2 = 1.0$; the slope, 0.6151, is almost exactly what is projected by the Rouse model (0.60935). The extrapolation is slightly off the T = 115 °C data point at the top of the figure, but this offset is expected and will be explained in the next section.

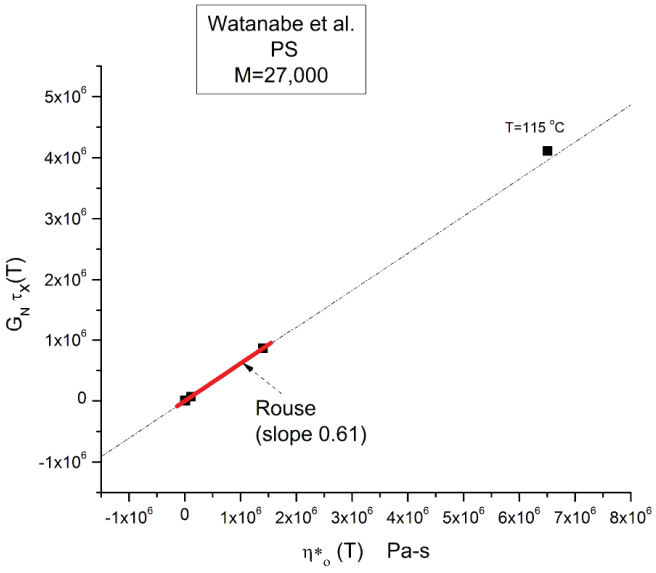

Figure 10. Validation of Rouse Equation (3) between G_N, τ_x and η^*_o in the Newtonian region using the data of Matsumiya and Watanabe [22] for PS with M = 27,000.

In other words, the Rouse model correctly describes the relationship between $\eta_o(T)$ and $\tau_R(T)$ at M constant and correctly assigns the ratio of the viscosity to the relaxation time (G^*/τ_R) to the melt modulus: $(6/\pi^2)$ G_N. **This result is not a minor achievement of the Rouse model.** This correct prediction of $G_N(T)$ may explain its popularity at a time when the relaxation processes in polymers were mainly described by networks of spring and dashpots placed in series (Maxwell network) or in parallel (Voigt network). In these networks, the relaxation time was equal to the ratio of the spring modulus to the dashpot viscosity ($\tau = G/\eta$).

Yet, the validation of Equation (3) provided by Figure 10 corresponds to validating G_N from $G''(\omega)$ in Equation (1) since $\eta^*_o = \lim (G''/\omega)$ when $\omega \to 0$. Equation (1) assumes that $G'(\omega)$ and $G''(\omega)$ have both the same terminal relaxation time, τ_R, and the same normalization modulus, G_N. Equation (3) can easily be derived from the $G''(\omega)/G_N$ side of the Rouse formula:

$$G''_{\text{ROUSE}}(\omega) = G_N \sum_{p=1}^{N} \frac{\omega\tau_p}{1+\omega^2\tau_p^2}$$

when $\omega \to 0$ the $G''_{\text{Rouse}}(\omega)$ simplifies to :

$$G''_{\text{ROUSE}}(\omega) = G_N \sum_{p=1}^{N} \frac{\omega\tau_p}{1} = \omega G_N \tau_R \sum_{p=1}^{N} \frac{1}{p^2}$$

from which we derive :

$$\frac{G''}{\omega} = \eta_o = G_N \tau_R \sum_{p=1}^{N} \frac{1}{p^2} \tag{7a}$$

For $M = 27{,}000$ g/ mole and $M_o = 105$ g/ mole $N = 259$

$$1 + \frac{1}{4} + \frac{1}{9} + \frac{1}{16} + \ldots + \frac{1}{259^2} = 1.6410805$$

For $N \to \infty$, *the sum equals* $\pi^2/6 = 1.644926 = 0.60793^{-1}$

Hence :

$$\tau_R = \frac{\eta_o}{G_N} \frac{1}{\sum_{p=1}^{N} \frac{1}{p^2}} = 0.60935 \frac{\eta_0}{G_N} \sim 0.61 \frac{\eta_0}{\frac{\rho RT}{M}}$$

The last line of Equation (7a) is Equation (3) verified by Figure 10. In other words, $G''(\omega)$ is correctly normalized by the rubber elasticity theory modulus G_N when ω is in the Newtonian range.

We now need to check that the $G'(\omega)/G_N$ part of the Rouse formula in Equation (1) is also validated in the Newtonian range at $\omega \to 0$.

$$G'_{\text{ROUSE}}(\omega) = G_N \sum_{p=1}^{N} \frac{\omega^2\tau_p^2}{1+\omega^2\tau_p^2} = \omega^2\tau_R^2 \left[\sum_{p=1}^{N} \frac{1}{p^2+\omega^2\tau_R^2}\right]$$

$$with\ G_N = \frac{\rho RT}{M}$$

$$when\ \omega \to 0 \sum_{p=1}^{N} \frac{1}{p^2+\omega^2\tau_R^2} \to 1.64108$$

$$and : \frac{G'_{\text{ROUSE}}(\omega, T)}{G_N} = 1.64108\omega^2{\tau_R}^2 \tag{7b}$$

Hence, in the Newtonian regime:

$$log(G') = 0.21513 + 2log(\tau_R) + log(G_N) + 2log(\omega)$$

Intercept of Maxwell straight line relative to G', I'_M :

$$I'_M = 0.21513 + 2\log(\tau_R) + \log(G_N)$$

$$\text{so: } \log(G_N)_{exp} = I'_M - 0.21513 + 2\log(\omega_X)$$

The testing of the Rouse equation in the Newtonian regime conducted from a $G'(\omega)$ point of view can be done by plotting first $\log G'(\omega)$ vs. $\log\omega$ and fitting the low ω range with a Maxwell's straight line of slope 2. This is shown in Figure 11 for the M = 27,000 PS of Matsumiya and Watanabe. at T = 130 °C. The intercept is $I'_M = 4.6973$. The value of ω_x to calculate τ_R, $\omega_x = 1/\tau_R$, imposes itself because τ_R is the same for $G'(\omega)$ and $G''(\omega)$ in the Rouse equation and thus ω_x must be at the cross-over point where $G'(\omega_x) = G''(\omega_x)$.

When ω_x and I'_M are known, Equation (7b) provides the value of G_{Nexp} calculated from $G'(\omega)$. We repeat the same operation for the other temperatures that show a Maxwell's behavior at low ω, i.e., for T = 120 °C and 140 °C. The T = 115 °C plot, similarly to what we saw in Figure 11, does not present a range of data points that could be fitted by a straight line with slope 2 in the low ω data range). For the Rouse model to be validated we should have $G_{Nexp} = G_N = \rho RT/M$: so, if we plot $G_{Nexp}(T)$ vs. $G_N(T)$, we should find all the points on the line Y = X. The values of ω_x, G_N, I'_M and G_{Nexp} are confined in Table 1.

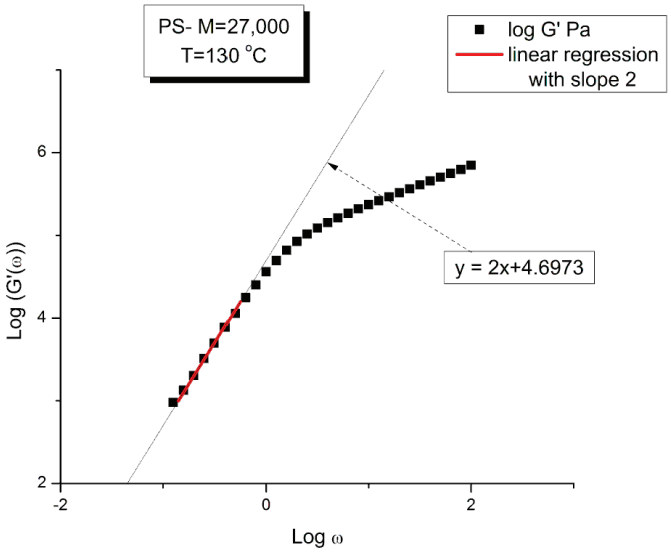

Figure 11. Testing the Rouse equation in the Newtonian regime from a $G'(\omega)$ point of view pursuant to Equation (7a): A plot of log $G'(\omega)$ vs. logω is fitted in the low ω range with a Maxwell's straight line of slope 2. The value of G_N is derived from the fit.

Table 1. Working variables to test the Rouse model (see text): "Rau" = ρ; "tau" = τ.

	T °C	Log τ_x $\tau_x = 1/\omega_x$	Log η^*_o Pa-s (Eq. (4))	ρ (g/cc) melt density	G_N (Pa) PS 27,000 $\rho RT/M$	G_N x τ_x	η^*_O Pa-s	I'_M See text	G_N calc. from $G'(\omega)$
1	115	1.52824	6.8135	1.01854	121,744.4	4.11×10^6	6.51×10^6		-
2	120	0.84678	6.14749	1.01568	122,966.2	864,105.4	1.40×10^6	6.78861	75,843.4
3	130	−0.27389	5.04994	1.01	125,389.1	66,736.86	112,187.5	4.6973	107,141.6
4	140	−1.15712	4.18292	1.00439	127,785.1	8899.472	15,237.84	3.02546	133,217.8

Figure 12 demonstrates the clear failure of the Rouse model to predict in the Newtonian region the correct G_N value that normalizes the $G'(\omega)$ moduli data of Matsumiya and Watanabe. We can draw a straight line passing through the three data points in Figure 12 and a linear regression gives: $G_{Nexp} = (-1.39 \times 10^6 + 11.9\, G_{NRouse})$ with $r^2 = 0.999$. One sees that G_N calculated from $G'(\omega)$ is not equal to G_N calculated from $G''(\omega)$ and, therefore, the validation of the Rouse model that emerged from Figure 10 based on the $G''(\omega)$ Newtonian branch of the Rouse Equation (1) is contradicted without ambiguity by Figure 12. The only temperature at which the two G_N values coincide is at the crossing of the Y = X and the red line in Figure 12, occurring for G_N = 127,500, which, according to $G_N(T)$ occurs at T = 137.5 °C. We cannot predict, without the necessary experimental data to test it, whether

the invalidation of the Rouse model persists at higher temperature, for instance above T_{LL}~164 °C for this polymer.

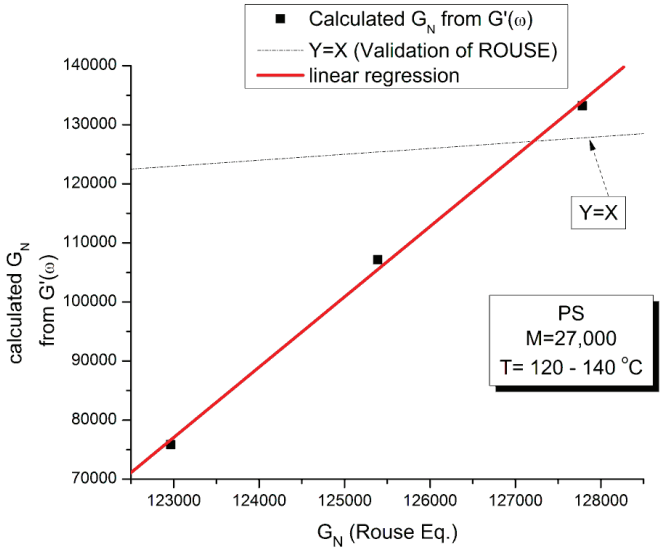

Figure 12. Invalidation of Rouse Equations (1)–(4) in the Newtonian regime from a G′(ω) point of view pursuant to Equation (7a): the value of G_N is totally different from the Rouse value determined from G″(ω).

We saw in Figure 9 that the Rouse model failed to describe the molecular dependence of ω_x when Equation (3) was applied to the Majeste data at T = 160 °C. This meant to say that the Rouse modulus, G_N, although good to predict $G_N(T)$ when calculated from G″(ω), was not good to predict $G_N(M)$. What about the value of $G_N(M)$ found from G′(ω): does it match the Rouse model molecular modulus, $G_N = \rho RT/M$ with ρ(M) given by Equation (2)?

Comparing the Calculations of G_N from the G′(ω) or G″(ω) Sides of the Rouse Equations and Invalidating the Rouse Approach

In order to proceed with this new (in)validation step, we find for each unentangled PS sample of Majeste's thesis the value of I'_M given by Equation (7b) by plotting log G′(ω) vs. logω. This is illustrated in Figure 13 for M = 13,000. We already know the values of ω_x for all these samples (Table 2) and thus can calculate the value of log G_{Nexp} (M) for each M and compare it with the corresponding value of G_N from the Rouse equation. This comparison is done in Figure 14. Finally, Figure 15 compares the log G_N vs. log M at T = 160 °C for the Majeste PS unentangled samples with G_N coming from three sources: from the Rouse Equation (black squares), from Equation (7a), i.e., the G″(ω) data based on ω_x and η_o (blue triangles), and from Equation (7b), i.e., the G′(ω) data based on ω_x and I'_M (red dots).

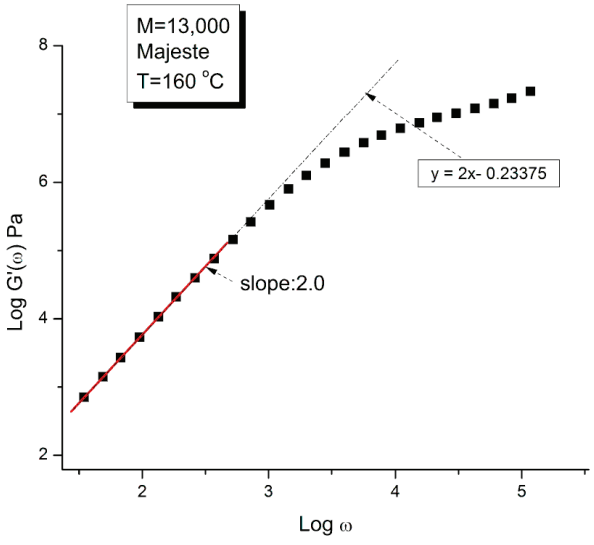

Figure 13. Same testing of the Rouse equation as in Figure 11, here applied to Majeste's data [23] at T = 160 °C, M = 13,000.

Table 2. Working variables to test the Rouse model (see text): "Rau" = ρ; "tau" = τ.

	M g/mole	ρ g/cm^3	Log G_N calc from ρRT/M	I'_M (see text)	ω_x(M) Maxwell rad/s	Log G_N calc from $G'(\omega)$	Log η^*_o (Pa-s) [23]	Log G_N calc from $G''(\omega)$
1	2000	0.98129	6.24709	−6	7.73×10^6	7.56106	−3.03205	3.6399
2	4000	0.98803	5.94903	−3.38286	238404.6	7.15664	−1.88678	3.27439
3	5050	0.98945	5.84842	−3.19938	56491.44	6.08946	−0.6361	3.89974
4	8500	0.99164	5.62326	−1.35373	14874.16	6.77601	−0.17089	3.78539
5	11600	0.99251	5.4886	−1.20429	4096.45	5.8054	0.36388	3.76014
6	13000	0.99276	5.43922	−0.23375	4769.655	6.90809	0.83051	4.29285
7	17500	0.9933	5.31037	0.53143	1815.841	6.83446	1.6037	4.64663
8	25000	0.99378	5.15567	1.42833	501.593	6.6139	2.38771	4.87192

2.1.3. Conclusion Regarding the Myth of the Applicability of the Rouse Equation to the Rheology of Unentangled Polymer Melts

The results of our investigation regarding the applicability of the Rouse model are provided in Tables 1 and 2. These results and the figures drawn from them are devastating for the Rouse model's validation to describe polymer melts. Its failure to describe experimental data is so flagrant and demonstrated in so many ways that it is almost incomprehensible that both authors of the data which we re-analyzed concluded that the Rouse model satisfactorily described their data. Take Figure 15 for instance, the black squares on the straight line are the points given by the Rouse formula for G_N, the melt modulus. The red dots and the blue triangles are calculated from the Rouse equation (Equation (1)) taking either the $G'(\omega)$ or the $G''(\omega)$ expressions in the Newtonian range to find G_N, respectively. These red dots and blue triangles should all be disposed on the black line if the Rouse theory was applicable to these data. What we observe, instead, is unambiguously different: the red dots are all located above the black line, shifted vertically by almost a decade and a half and the blue triangles are all scattered below the black line, almost forming a straight line

pattern. The myth of the Rouse model applicability to unentangled polymer melts is so anchored in the current paradigm that even the most reliable polymer scientists fail to test it fully on their own data.

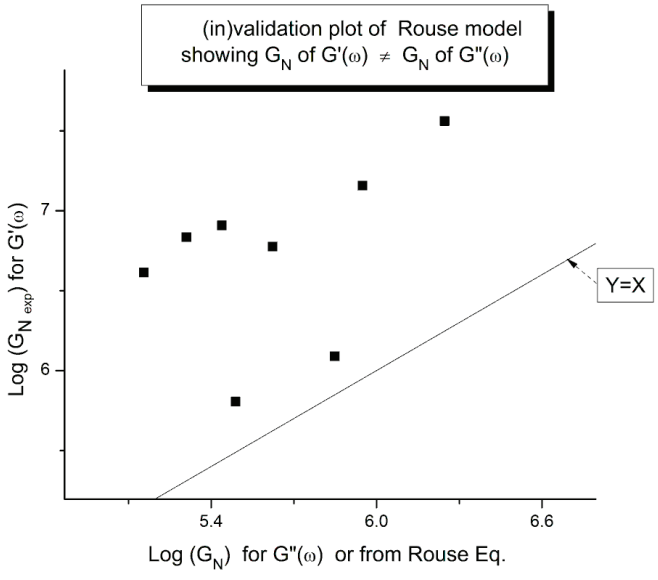

Figure 14. Comparison of the G_N values calculated from G′(ω) and G″(ω) in the Newtonian region using the Rouse Equations (1)–(6). The points should be on the Y = X line for validation of the Rouse model.

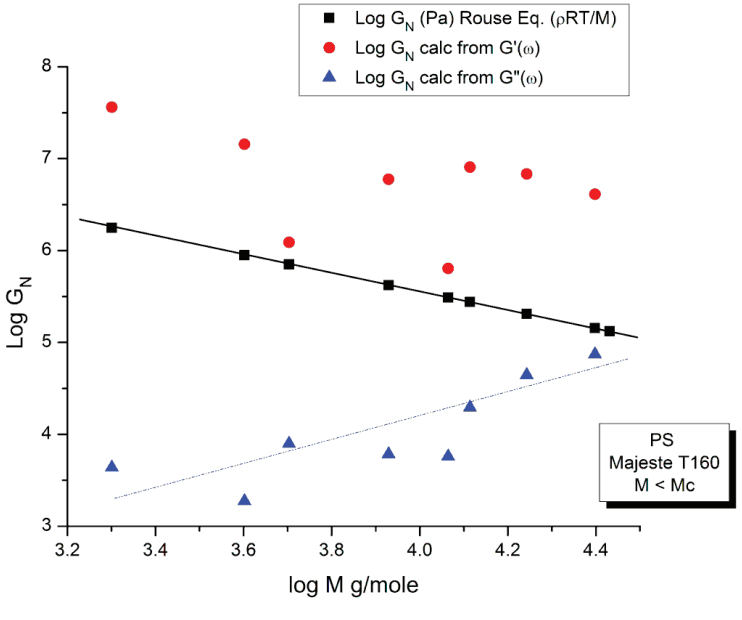

Figure 15. Comparing the value of G_N calculated from G′(ω), G″(ω) and from the Rouse's formula based on the rubber elastic theory.

An important conclusion of the failure of the Rouse model to satisfactorily describe rheological data for unentangled polymer melts is that the normalizing melt modulus, G_N, is different for the elastic and the viscous components, $G'(\omega)$ and $G''(\omega)$ of the complex modulus, $G^* = G' + jG''$. We can call them G'_N and G''_N, respectively. We could also push this exercise one step further and consider that the elastic and viscous components of G^* have different terminal times, say τ'_R and τ''_R, respectively. The Rouse equation remains the same, formerly, but we have made the real and the imaginary terms of the complex function G^* "independent". These two terms might still be coupled but in a way different than what is implied by the un-modified Rouse equation. We have already mentioned above that making the G_N and τ_R constants "loose" in the non-linear regression of the Rouse formula improved the fit of the data a great deal. We also added, however, that this bifurcation from the Rouse basic formula inevitably took us away from the Rouse molecular reality. But what is the real molecular reality? Is the modulus of the melt truly a complex entity with elastic and dissipative coordinates? The Rouse equation establishes very simply the viscoelastic nature of the melt by considering the formula of two functions $G'(\omega,T)$ and $G''(\omega,T)$ and stating that they are the real and imaginary coordinates of a complex function. This mathematical foundation—based on the coupling between a spring and a dashpot in a mechanical system—correctly led to the observed Maxwell slopes of 2 and 1 for the log $G'(\omega)$ or log $G''(\omega)$ when plotted against logω in the Newtonian region. The true appeal of the Rouse model is to have found a molecular basis for the "spring and dashpot" mathematical parameters, G_N and τ_R. The problem of the Rouse model is illustrated in Figure 15 that shows that beautiful and simple mathematics might be enough to create a myth but not enough to be validated through its confrontation with the data. We show in Chapter I.5 of Ref. [20] (simulation of the Dual-Phase model) that the attribution of the Maxwell slopes 2 and 1 is not necessarily derived from a Rouse type of mathematical formalism, and that the origin of and the coupling between $G'(\omega)$, that force proportional to ω^2, and $G''(\omega)$, that force proportional to ω, may be understood in a way fundamentally different than a complex dependence of the type: $G^* = G' + jG''$.

In conclusion, there is no merit to the Rouse model, in our opinion, in its present formulation, Equation (1). The Rouse model fails to describe the viscoelastic behavior of unentangled polymeric melts. The introduction of $G_N = \rho RT/M$, borrowed from the rubber elasticity theory, permits to normalize the dynamic moduli, $G'(T,\omega)$ and $G''(T,\omega)$, but it has no molecular meaning in the Rouse's physical reality (or if it does, the theory of rubber elasticity must be reconsidered). The introduction of τ_R, the Rouse time, since it is the inverse of the cross-over frequency, $\tau_R = 1/\omega_x$, is useful, practically: it permits the introduction of a "marker" of the state of the melt, more or less correlated to the end of the Newtonian range for ω. Of course we do not need a theoretical meaning to use τ_R, and there is none. The physical molecular modelization of flow proposed by the Rouse model is wrong: like any molecular model that considers the single chain as the system to explain the flow behavior it cannot predict the existence of any transition in the melt, neither the $T_g + 23$ °C transition [18,19] nor T_{LL} (see next section). The temperature and molecular weight dependence of $\tau_R = 1/\omega_x$ also provide useful information. However, τ_R is totally useless (theoretically) to quantify the "dynamics" of the viscoelastic behavior, i.e., shear-thinning, the effect of rate and temperature on the kinetics of molecular motion. The spectrum of relaxation generated by $\tau_p = \tau_R/p^2$ is simple but useless to correctly describe shear-thinning or to understand why $\chi(\omega) = (G'/G^*)^2$ presents a maximum. Likewise, we find the various attempts to modify the Rouse equation by either "truncating-to-fit" the spectrum of relaxation or by adding a high frequency term to the Rouse modulus (the Allal's approach) to be either empirical or not working according to the claims (despite of our best efforts to make these attempts work).

2.2. The Myth of the Extended Applicability of the Time–Temperature Superposition Principle

The "time–temperature superposition" principle is an extrapolation method that permits to extend the range of measurement of an experiment, in time or in frequency, by

operating at other temperatures and shifting the multi-T data to obtain a mastercurve, at a given chosen temperature, with the extended time/frequency range. This extrapolation method has been extensively used, for instance, to present the full view of the elastic modulus from the molten state temperature region to the glassy state region, a complete picture that no single instrument can provide. It is, therefore, of the utmost importance to trust the method of extrapolation in question, namely the validity of the Time–Temperature superposition claims.

The current paradigm of polymer physics teaches that the validity of the "time-temperature superposition principle" (tts) covers the range T_g to T_g + 100 °C, i.e., works approximately over a 100 degrees range above T_g [32]. The tts is also applicable to dynamic data obtained by frequency sweeps at constant temperature, i.e., under oscillation at various frequencies ω under given temperatures. The tts expresses the following: the rheological variables found at temperature T_1, using frequency ω_1, are the same as those found at T using frequency ω provided the time scale (here the frequency) is changed by a shift factor, $\log a_T = \log(\omega/\omega_1)$, which varies with temperature only; the Vogel-Fulcher equation (see Equation (4) can be re-arranged to describe $\log a_T$ as a function of T and T_1 (WLF equation, Ch. 11 of Ref. [32]). The moduli to superpose must be normalized by the Rouse modulus, $G_N = \rho RT/M$, before superposition. This amounts to say that there is a vertical shift factor $b_T = \rho_1 T_1/\rho T$ to be applied to the modulus variables to superpose in order to optimize the superposition. The data set at T_1, ω_1 is called the reference data set; the other data sets at T, ω are shifted by b_T on the vertical axis and a_T on the horizontal axis to produce a mastercurve at T_1. We have discussed the limitations of the tts and its status as a myth in Ch. 3, pp. 59–73 of Ref. [2] and we refer to that writing for more details. To summarize our findings:

- The superposition of curves by horizontal shifting on the log time or log frequency is a good approximation over a rather short temperature interval. There are 3 ranges of temperature within which the tts works well for polymer melts: the T_g to (T_g + 23 ± 2) region, the (T_g + 23) to T_{LL} region and the T > T_{LL} region. For each temperature region a new set of WLF constants (or Vogel Fulcher constants) must be established. Superposition across regions is physically improper according to the Dual-Phase model [20].
- The use of b_T pursuant to the normalization of the moduli by the Rouse modulus G_N is incorrect. The reason has been implicitly given in the previous section which showed the inadequacy of using G_N except for G″(ω) and thus viscosity (Figure 10). To find the correct value of b_T, a double-shifting regression is always required [33]. It has been shown, for instance, that the vertical shift factor, $\log b_T$, when it is obtained by regression-double-shifting, is not as predicted by the Rouse modulus G_N/G_{N1}, yet that its variation with T permits to detect the presence of transitions, such as the transition at T_g + 23 °C also visible from thermal stimulated depolarization data [19] or the T_{LL} transition [24,34].
- The temperature range of applicability of the tts varies with the strain imposed during the frequency sweeps ([2] "Effect of Strain" (Section 5.8, p. 322) and with the thermal-mechanical history of the melt prior to the frequency sweep ([2] "Thermal-Mechanical History to create out-of-equilibrium melt properties", Section 4.3.5.2 p. 206).
- The tts might be valid for a limited frequency range only or it might be valid on two or successive frequency ranges with different constants to express the 2 shift factors, $\log a_T$ and $\log b_T$. It is the case for the 3 temperature ranges delimited by T_g + 23 and T_{LL}.

In this section we want to illustrate the difficulty encountered applying the frequency-temperature superposition to the data of Matsumiya and Watanabe. already introduced in the previous section. These data on a well characterized monodispersed PS are within the range of temperature above T_g (T_g = 93.78 °C for M = 27,000) where the time–temperature superposition is claimed to apply, and, the range of temperature analyzed is only 25 °C (from T = 115 °C to 140 °C). The melt is located below its T_{LL} evaluated at 161.4 °C for M = 27,000. Also note that T_g + 23 °C = 116.78 °C, which positions T = 115 °C inside the

T_g + 23 range (barely though) and T = 120, 130 and 140 in a different range, the (T_g + 23) to T_{LL} range. Our intention is to show that the principle of superposition does not work well for these data because it needs to be perfected based on a better understanding of its origin and its limitations. The possible reasons for the need to modify and limit the time–temperature superposition naturally shift the light on the necessity to reconsider our understanding of the physics of the interactions in polymers. A quantitative explanation of the rheological results of Matsumiya and Watanabe. based on the concepts of the new paradigm is described in another publication (Ch. II.7 of Ref. [20]) and not in this paper.

The time–temperature principle is illustrated in Figures 16–25 using the data of Matsumiya and Watanabe which are obtained by dynamic rheometry. These authors have described their experimental procedure as follows: the frequency sweeps were "DOWN sweeps", from high to low frequency (100 to 0.1 rad/s). The temperature for the 1st sweep was 140 °C, followed by the other frequency sweeps done at the lower temperatures (130, 120, 115 °C in this order) using the same sample. The strain was chosen to keep the results in the linear viscoelastic region (2%). This procedure is not unusual but is different from the one used most often that consists of UP sweeps and changing the sample after each frequency sweep to avoid the slightest possibility of inducing a thermal-mechanical history in the sample when operating sequentially on the same sample even in the linear range.

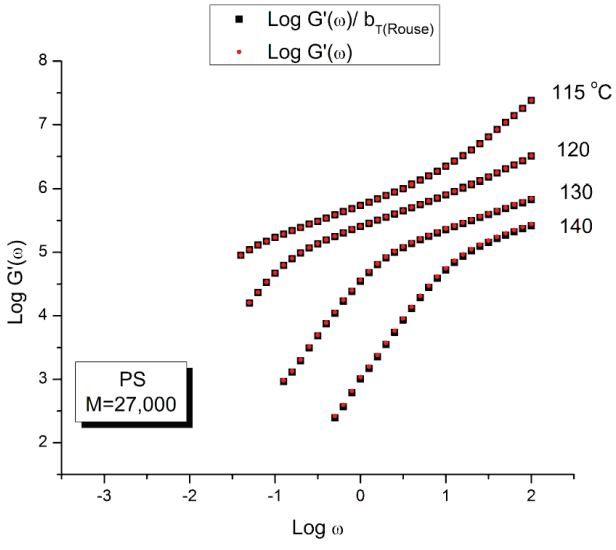

Figure 16. Comparison of log (G'/b_{TRouse}) and log (G') vs. log ω at various temperatures for Matsumiya and Watanabe PS = 27,000 [22].

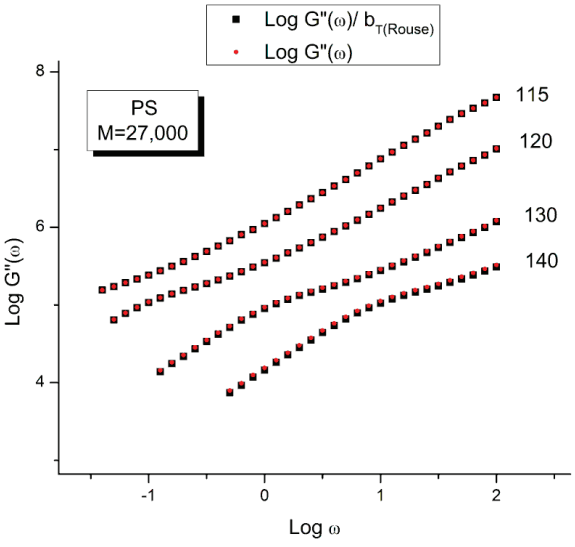

Figure 17. Comparison of log (G''/b_{TRouse}) and log (G'') vs. log ω at various temperatures for Matsumiya and Watanabe PS = 27,000 [22].

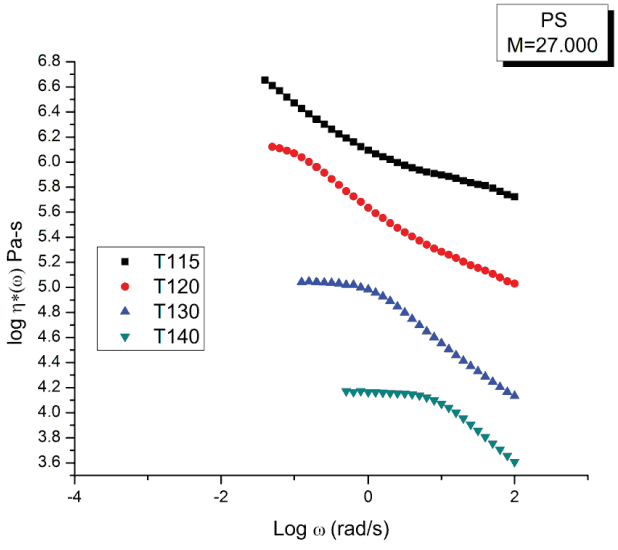

Figure 18. log η*(ω) vs. log ω at 4 temperatures for PS M = 27,000. Raw data [22].

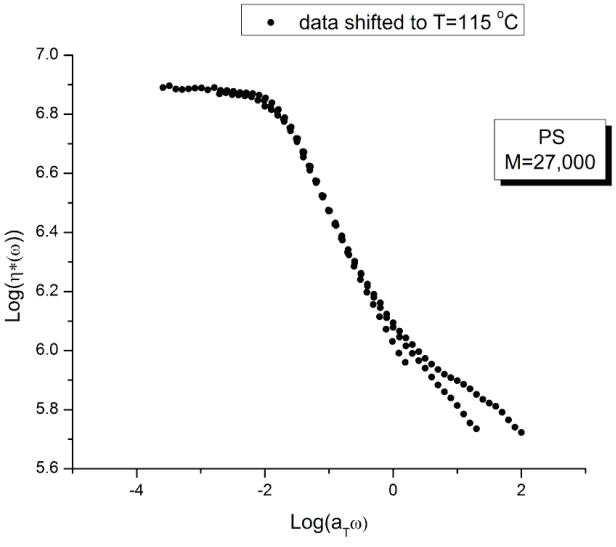

Figure 19. Viscosity mastercurve of log η*(ω) vs. log $a_T\omega$ after horizontal shifting of the curves of Figure 18 onto the T_1 = 115 °C curve.

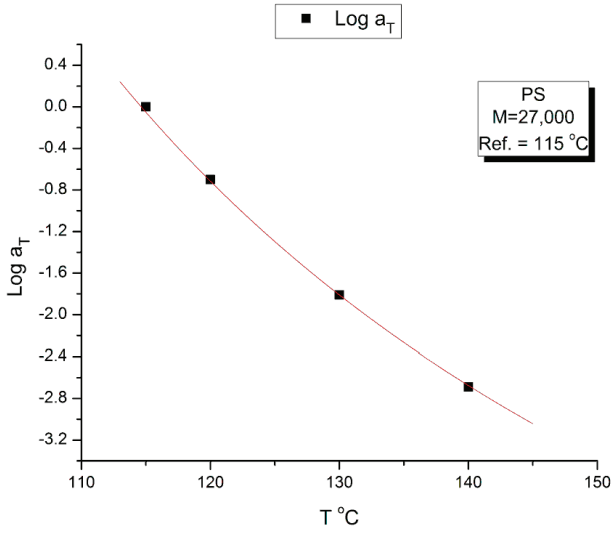

Figure 20. log a_T vs. T for shifting the curves of Figure 18 onto the reference temperature T_1 = 115 °C.

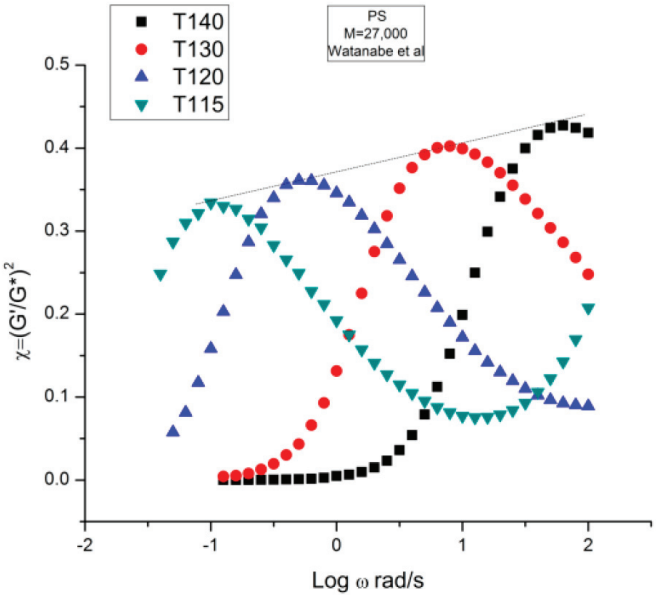

Figure 21. $\chi = (G'/G^*)^2$ vs. log ω for the Matsumiya and Watanabe [22] PS = 27,000 at 4 temperatures.

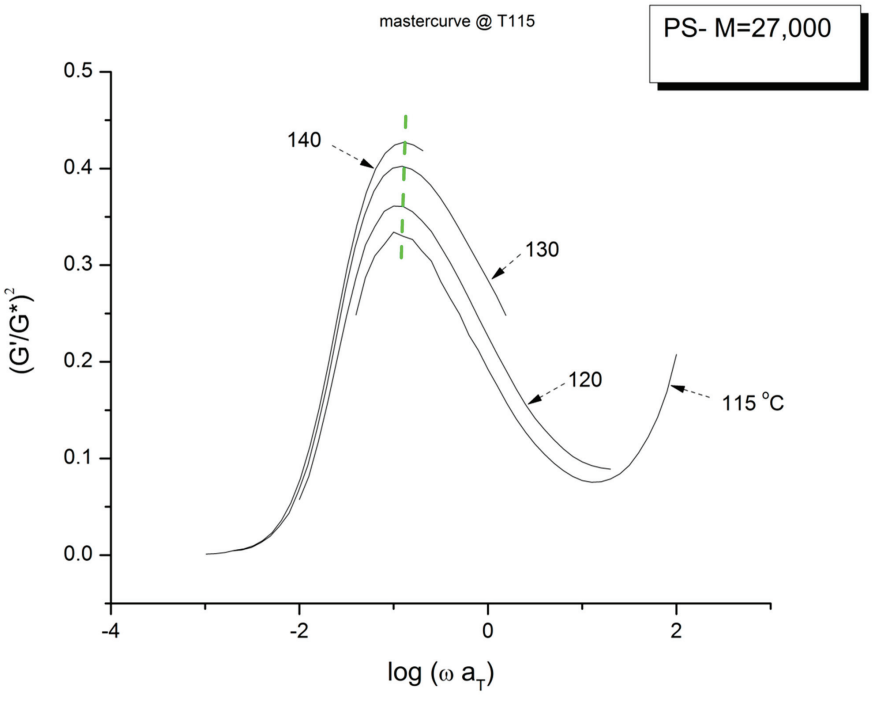

Figure 22. Mastercurve at T = 115 °C obtained after shifting horizontally the data of Figure 21 by the log a_T of Figure 20, i.e., the values that were used to shift the viscosity curves of Figure 18 to obtain the mastercurve of Figure 19.

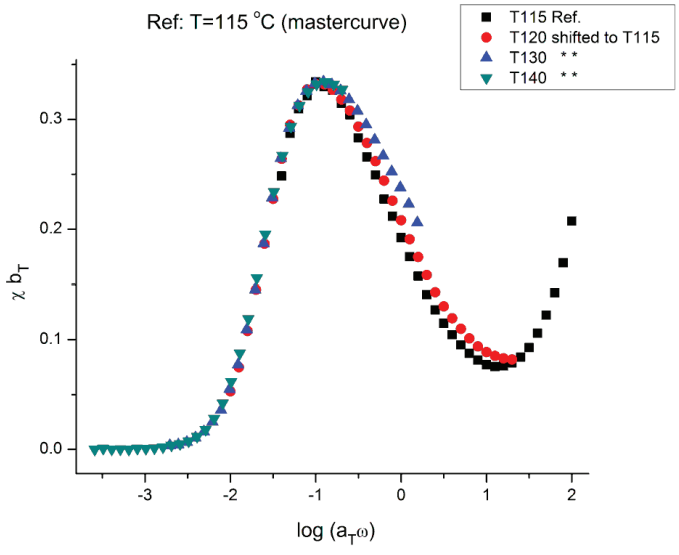

Figure 23. ($b_T\chi$) plotted against log (a_T ω) at $T_1 = T_{Ref}$ = 115 °C.

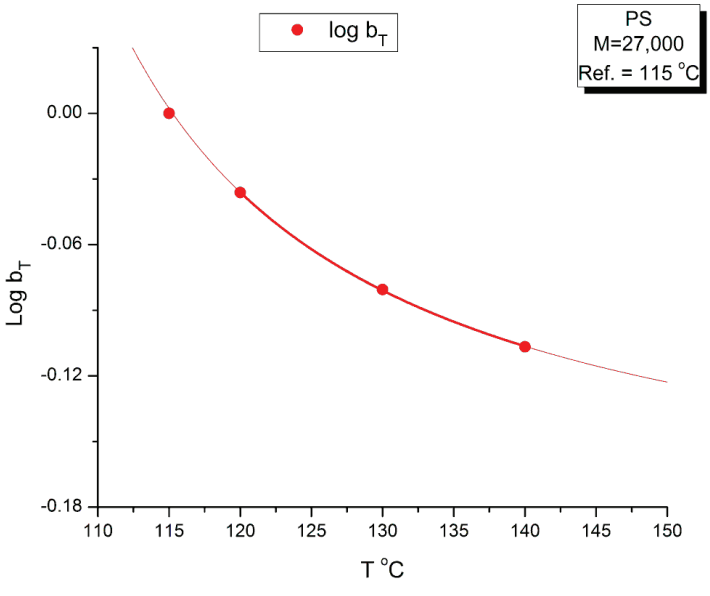

Figure 24. log b_T of the vertical shift factor in Figure 23 plotted against T showing an hyperbolic fit.

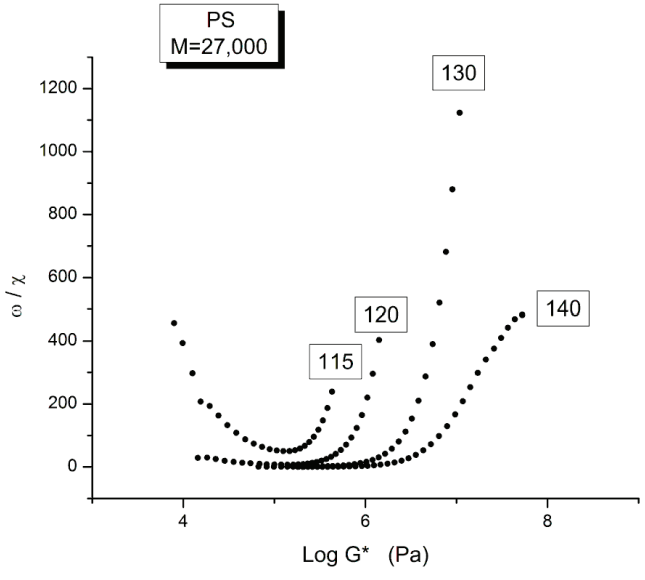

Figure 25. Plot of $\omega' = \omega/\chi$ against log G* at the 4 temperatures of the Matsumiya and Watanabe. data [22] demonstrates the presence of the T_g + 23 °C transition at T~115 °C. See text.

Figures 16 and 17 are plotted from the original data of Matsumiya and Watanabe which were kindly provided to this author. The black squares represent the "reduced" modulus values, i.e., G′ and G″ corrected by T_1/T where T_1 = 115 is the reference temperature and T is the temperature of the frequency sweep to shift, both converted to °K. This correction is induced by the adherence to the Rouse model for which the dynamic moduli are proportional to $G_N = \rho RT/M$ (Equation (1). The round red dots (reduced in size to avoid overlapping the black squares) are the data without any temperature correction. The difference between the red dots and the black squares is hardly visible. The small temperature interval (25°) renders the Rouse correction of the moduli negligible.

The complex viscosity, $\eta^*(\omega) = G^*/\omega$, is calculated from the values of $G'(\omega)$ and $G''(\omega)$ in Figures 16 and 17, with $G^* = (G'^2 + G''^2)^{0.5}$, and plotted in Figure 18 against the log of frequency ω. The tts can be used to superpose these curves into a mastercurve. We followed Matsumiya and Watanabe's choice of T_1 = 115 for the reference mastercurve to check that our values of the shift factors, log a_T, matched theirs [22]. Table 3 provides those values which were validated by us. Retrospectively, though, the choice of T_1 = 115 °C for the mastercurve was not the best one since this temperature is right on the transition between ranges mentioned earlier, the ($T < T_g + 25$) range and the ($(T_g + 25) < T < T_{LL}$) range (see Figure 25 above).

Table 3. Horizontal and vertical shift factors, a_T and b_T, respectively, for the superposition of the rheological data of Matsumiya and Watanabe [22].

Temperature °C	Log a_T T_{Ref} = 115	Log b_T (from χ) T_{Ref} = 115
115	0	0
120	−0.7	−0.03617
130	−1.81	−0.08049
140	−2.69	−0.10672

Figure 19 is the "viscosity mastercurve" at T= 115 °C obtained after shifting horizontally and vertically the data of Figure 18 by an amount log a_T and $-\log a_T$, respectively. The shift factors log a_T are given in Table 3. The shift by $-\log a_T$ on the viscosity axis is due to the definition of the viscosity: $\eta^*(\omega) = G^*/\omega$, which becomes after superposition: $G^*/(a_T\omega)$, so the shifted viscosity using the log scale is: $\log(G^*/\omega) - \log a_T$.

Our conclusion from Figure 19 is that the tts does not work, at least over the full range of $a_T\omega$. A closer observation permits to fine tune our conclusion. First, T = 115 °C seems to behave differently than the other 3 frequency sweeps. This is visible at both frequency ends. In the Newtonian region (the plateau region), although it is harder to see without zooming in, the "T115" (T = 115 °C) is the only curve not really merging with the rest (see later in Figure 25 for a more convincing perspective). Second, the overlapping of the 3 frequency sweeps, other than T115, is restricted to a range of frequency that extends from the Newtonian region to the inflective point of the shear-thinning drop off line (at which log $\eta^*(\omega)$~6.46). This restricted range is the only one where we can ascertain that the tts is validated.

Figure 20 plots the temperature variation of log a_T, the horizontal shift factor. As expected, a_T is equal to the ratio of the Newtonian viscosity at T and T_1:

$$\log a_T = \log \frac{\eta_o(T)}{\eta_o(T_1)} \tag{8}$$

The red curve in Figure 20 is calculated from Equation (8) using the values of $\log(\eta^*_o(T))$ in Equation (4) with T_1 = 115 °C.

Figure 21 displays the variation of χ vs. log ω with temperature for the PS27 of Matsumiya and Watanabe. $\chi = (G'/G^*)^2 = \cos^2 \delta$ was introduced in Section 1 (Figure 4). Both the position and the magnitude of the maximum vary with temperature. (G'/G^*) is the stored elastic energy, which is expected to increase as T decreases, but we observe the opposite trend: the peak maximum amplitude decreases as T decreases. One may think, for a reason, the fact that the modulus is proportional to G_N which increases with T. This explanation cannot stand, however, since (G'/G^*) is the ratio of two moduli, which cancels out the vertical correction due to the proportionality of the modulus to G_N according to the classical tts. In other words, the usual correction on the vertical axis for the temperature dependence of a modulus, T_1/T, is not required in Figure 21. In addition, as we mentioned before, the temperature span being small, the T_1/T correction is negligible. According to the current tts, based on the Rouse molecular background, one should not need a vertical shift factor to superpose $(G'/G^*)^2$ vs. log ω. Figure 21 visually contradicts such a statement: shifting only horizontally will not superpose the data.

Figure 22 is the mastercurve at T = 115 °C obtained after shifting horizontally the data of Figure 21 by the log a_T values that were used to shift the viscosity curves of Figure 18 to obtain the mastercurve of Figure 19. We already said that our log a_T values matched the values published by Matsumiya and Watanabe [22] for which these authors claimed that the tts works. We see in Figure 22 that when the elastic component of the viscoelastic modulus is used, the time–temperature superposition fails entirely, even in the restricted frequency range it was validated to superpose viscosity in Figure 19. In other words, we face the same dilemma as for the invalidation of the Rouse formula comparing the value of G_N from the viscosity side and the elastic side of G* to determine G_N. In Figure 22 we have drawn a dash straight line (green) joining the peak maxima that shows a tilt from the expected verticality of such a line if the horizontal shifting of the curves the way the tts works had been successful. In other words, if we want to be able to obtain a true mastercurve by shifting the curves in Figure 21, not only do we need to use a vertical shift b_T to address the issue of a peak magnitude which varies with T, but we also need to modify a_T on the horizontal shifting axis.

The values of b_T were found by plotting $\log(\eta^*(a_T\omega))$ vs. $\chi(\omega)$, not shown, for which we saw that all the maxima at the 4 temperatures lined up horizontally for $\log(\eta^*(\omega)) = 6.46$, the value found for the inflection of $\log(\eta^*(\omega a_T)$ vs. $\log(\omega a_T)$ in Figure 19; we then

determined the value of χ at the maximum of χ(ω) from which we determined b_T as the ratio of the χ values found at T and T_1, with T_1 = 115 °C. The values found for b_T are listed in Table 3 and the variation of log b_T with T is found in Figure 24. A couple of remarks regarding the procedure to find b_T: By plotting log(η*(a_Tω)) vs. χ(ω), the horizontality of the maxima of χ(ω) with T made it not necessary to find a new a_T, as suggested by the tilt of the green dash line in Figure 22. The choice for b_T to be the ratio of the values of χ at the maximum for T and T_1 was hinted by the considerations we expressed earlier on the possibility to define G'_N and G''_N in the section on the myth of the Rouse model. In effect, the Rouse model is not capable to understand the need of b_T to superpose the χ(ω) at various T, the way the Rouse equations stand (Equation (1). Yet, if we accept to modify the Rouse equations to have G'_N and G''_N different (with still $G''_N = G_N = \rho RT/M$)), then b_T can be an affine function of χ.

The mastercurve at T = 115 °C obtained by "double-shiftin_G" on both the horizontal and vertical axes by log a_T and log b_T, respectively, is shown in Figure 23. The y-axis scale remains linear in this figure and, therefore, the y coordinate is (χ b_T). The temperature dependence of b_T is in Figure 24.

We confirm in Figure 23 that the data of Figure 21 can be superposed, using two shift factors, a_T and b_T, yet the superposition is only valid in the range of frequency up to the maximum of χ(ω). This successful shifting of the data up to the maximum of χ matches what we observed for the successful shifting of the log(η*(ω)) vs. log(ω) up to the inflection point in the shear-thinning range. We know that the correspondence between the two ranges matches because the b_T data were obtained at log(η*(ω)) = 6.46, which was also the value obtained at the inflection of log(η*(ω)) vs. log(ωa_T) in Figure 19.

Figure 24 provides the temperature variation of log b_T. It is remarkable that log b_T vs. T can be fitted by an hyperbolic function of the Vogel-Fulcher type: A + B/(T − C), with the fitting constants A, B and C determined by non-linear regression: A = −0.19876; B = 4.26732; C = 93.78 °C (r^2 = 0.9999). The value of C was forced to equal the T_g of the M = 27,000 monodispersed PS. A loose regression, without forcing the value of C, provided a value of C = 91.00, B = 5.0138 and A = −0.209. The r^2 is not improved for the loose regression. Let us consider here that C is truly equal to T_g for the variation of log b_T. For the variation of log a_T (which can be expressed from the Vogel-Fulcher equation, Equation (4), where C is designated T_∞), we have shown in [35] how the value of T_g and T_∞ correlate with the isomeric state of the Dual-conformers and their dynamic free volume to determine the value of the T_{LL} transition of the melt. The value of T_{LL} plays an important dynamic role in the Dual-Phase theory of interactions ([2,19], Chs. I.4, II.7 of [20,34]); for our purpose in this section, let's just say that T_{LL} determines the upper temperature end of the tts applicability that starts at T_g + 23 °C, and the need to find a different set of shift factors log a_T and log b_T when T > T_{LL} to extrapolate the data correctly on the mastercurve for the data in that T region. In addition, T_{LL} also holds many important functions, for instance the end of the dynamism of the dual-phase dissipative statistics, (Ch. 3 of Ref. [19]).

Conclusion Regarding the Myth of the Time–Temperature Superposition Principle

The classical claim, e.g., by J.D. Ferry [34], that the Time–Temperature Superposition (tts) can be applied from T = T_g to T = T_g+100 °C to obtain the behavior over the full range of frequency or relaxation times by data shifting extrapolation, is perhaps true for certain polymers under certain circumstances, but we miss the original data to be able to validate the generality of that claim. What we know for certain is that many limitations and restrictions to the general sst must be added to establish it as a workable general rule and that these restrictions are as fundamental or even more fundamental than the sst principle itself to understand the behavior of polymer melts. The restrictions imply that the sst should only be applied over delimited temperature and frequency (time) intervals which depend on the chemical nature of the polymer and its thermal-mechanical history (its processing and thermal history). We have used the specific example of the data of Matsumiya and Watanabe on a classical polystyrene sample to prove the need for certain

restrictions that, we claim, should be the ones to be generalized. Here are the specific reservations concerning tts:

- The time–temperature superposition principle is not verified for the data we analyzed. Matsumiya and Watanabe recognized in their paper the shortcomings of the superposition applied to $G'(\omega)$ and $G''(\omega)$, yet they did not question why their data showed such a flagrant discrepancy. We believe that questioning why the tts does not work when performing super standard dynamic rheological experiments on a super standard polymer (PS) was worth the subsequent dedicated analysis time and effort it demands and triggers.
- Why do the rheological curves for a simple PS studied in the linear range of viscoelasticity fail to superpose over a classical range of frequency (0.1 to 100 rad/s) using a span of temperature of only 25 °C? Why do the users of the current paradigm of polymer science avoid reporting the failures of a full superposition of their data? Why is there the need to restrict the frequency range or the temperature range for the sst to work? Is there no fundamental requirement for the prevailing theory of viscoelasticity to answer the following questions:
  - Why is the tts valid only for the low (left) frequency side of the peak of χ vs. log ω?
  - Why does log $\eta^*(\omega)$ only needs <u>one</u> horizontal shift of the curves, log a_T, whereas the χ vs. log ω requires <u>two</u> shift factors, log a_T and log b_T when applying the tts,
  - Why are we systematically correcting vertically the rheological moduli by $(\rho T)^{-1}$ without checking if the Rouse modulus G_N does normalize <u>both</u> $G'(\omega)$ and $G''(\omega)$?
  - Why is the value of χ at the maximum increased and not decreased as T increases? This appears counter-intuitive with the explanation that glassy relaxation components are causing the maximum in the χ vs. log ω curve.
  - Why is the rheological behavior at T = 115 °C different than at T = 120 to 140 °C?

Figure 25 is another way to plot the data to make appear the T_g + 25 transition introduced earlier, explain that T = 115 °C is located at the T_g + 25 and thus belongs to a different rheological range, with its own shift factor characteristics.

Figure 25 is a graph of ω/χ plotted against log G* as the frequency decreases from left to right in the down sweep procedure used by Matsumiya and Watanabe [22]. As we explain in Ch. 5.4 of Ref. [2], $\omega' = \omega/\chi$ is the frequency of the elastic dissipative wave that maintains the collective coherence of the melt despite of the local density fluctuation due to the dual-phase interactions. The figure shows that the ω/χ values of the frequency sweeps at T = 140, 130 and 120 °C fuse and overlap at low ω, i.e., at lower values of G*, merging into a single curve like data do in a mastercurve. This is not the case for T = 115 °C which is singled out by showing a minimum and the curve starting to rise sharply at lower ω. This distinct behavior separates out the two regions of viscoelastic across the T_g + 23 transition. The presence of one of the isotherms very close to a transition made it impossible to consolidate the tts curves into a mastercurve for this narrow range of temperature interval explored by Matsumiya and Watanabe.

In conclusion, the myth of the time–temperature superposition is linked to the myth of the Rouse model which, we suggested, is in no way descriptive of the rheology of unentangled polymers. The use of the Rouse molecular model as the theoretical base to apply the tts creates huge confusion on the precise way to superpose the data, single or double-shifting, on what range of temperature and frequency, with what correction and depending on which rheological function. In addition, even when the limitations to the superposition are noted, the reason for the restrictions remain obscure and without explanation. As we will see in the next section, the same clueless response to basic fundamental results faces the reptation theory. The mathematical solutions proposed by the reptationist school follow the steps of the Rouse molecular dynamic model to focus on modeling the variations of the chain dimensions during deformation, which, as we have suggested, is the wrong statistical system to model. This fundamental assumption that the dimensions of a single chain are correlated to the macroscopic stresses can be tested experimentally using the Rheo-SANS

technique (defined below). As a matter of fact, despite the mathematical brilliance of the reptation work, some recent experimental results fail to agree with the predictions of the reptation theory. This is presented in our next section.

2.3. The Great Myth of Reptation. The Failure of the Reptation Model to Correctly Describe and Understand the Shear-Thinning Behavior of Entangled Polymeric Melts ($M > M_c$)

2.3.1. The Brilliance of the de Gennes's Reptation Ideas

The Rouse model was created to describe the viscoelastic behavior of polymer solutions, not polymer melts. The application of the Rouse model to unentangled polymer melts was the initiative of J.D Ferry [32]. It was clear immediately to polymer scientists that the Rouse model could not predict the distinct rheological behavior of entangled melts (or entangled solutions). However, the natural tendency is to start from what is known and to modify it, i.e., in the case of de Gennes, to keep certain basic assumptions of the Rouse formalism while adapting it to the case of reptiles moving within fixed obstacles, which is the title given by de Gennes when he published his first paper in 1971 [8]. De Gennes, who was not a polymer scientist by training, learned from the context of the thoughts on viscoelasticity established at the time. The theory of viscoelasticity of polymers considered then, which still serves as the ground foundation for the current paradigm describing viscoelastic interactions, assumed that the rheological deformation of polymer melts resulted from the behavior of singular chains embedded in a sea of interactions with other chains. In the existing theories of macromolecular physics, the emphasis is placed on determining the shape of the individual macromolecules, often called their chain conformation. The presence of neighboring and interpenetrating macromolecules is perceived as a disturbance to the ideal conformation of the chain. In the traditional texts, the field of interaction responsible for the disturbance is homogeneous. Therefore, de Gennes, like all his predecessors before him, considered the behavior of the melt as the consequences of what happens to a single chain after the effect of the interactions between the chains had been established. De Gennes had the idea of considering the interactions between the chains as a field of obstacles between which a single chain is oscillating through, the way reptiles move, when the chain is requested to move pursuant to an external deformation. De Gennes modeled the motion of the chain among the obstacles using the molecular dynamic language already established in the Rouse model, thus defining the reptation time of a single chain.

In the case of shear deformation, the Newtonian viscosity is classically considered to describe the local internal friction between the bonds of interacting macromolecules which assume a stable thermodynamics state, the equilibrium state at a given temperature and pressure. The non-Newtonian behavior, shear-thinning, is due to a modification by the flow of the dimensions of the macromolecules, i.e., of their conformation, which can be calculated from the effect of the shear rate on the rms end-to-end distance of the macromolecule and the amount of slippage (relax/retraction) occurring. Theoretical models predict that for a shear rate strong enough to overpower the ability of the chain to relax—and this happens at the reptation time—shear-thinning starts to be observed, corresponding to an increase in the rms end-to-end distance of the chain, leading to its orientation. In the classical formulas that describe the non-Newtonian dependence of viscosity with shear rate, the amount of shear-thinning is only a function of two parameters (in addition to the strain rate, of course): the Newtonian viscosity and the value of the reptation time. But these two parameters can be correlated to each other, as in the Rouse's formula , Equation (3), and to the dimensions and interactions between the chains, which simplifies the description of the flow deformation process to the description of the dependence of the reptation time with temperature, pressure, and chain length (the interactions between the macromolecules, defined by "their entanglement", is already incorporated in the definition of the reptation time).

In summary, the effect of strain rate, temperature, molecular weight, according to the accepted reptation model, could all be related to a simple explanation: the deformation

and relaxation of single macromolecular chains confined to move within the boundaries of a tube, the entanglement tube, whose lifetime was the reptation time. The whole process would continuously be happening, from very low strain rate to high shear-thinning producing strain rate. Additionally, the reptation model provided a new understanding of "entanglement" by quantifying the dimensions of the tube and correlating it to the reptation time. The interactions between the macromolecules could be described topologically, the tube serving as the new topological description of the environment of the bonds.

This was the brilliance, even the beauty, of the original reptation model of de Gennes [2], who succeeded in scaling the effect of all variables into the description of a single parameter, the reptation time. However, this extraordinary tour de force had to be refined over the years to account for a better description of the experimental data, in particular to improve the molecular weight dependence of the reptation time which did not follow the predicted M^3 variation by de Gennes [3]. The model of reptation in a tube has been significantly improved over the years, by incorporating additional molecular mechanisms such as contour length fluctuation [36–38], constraint release [9,39–42], and chain stretching [43–45]. Doi and Edwards [46] proposed to account for the nonlinear rheological behavior by asserting that the external deformation acted on the tube, instead of the polymer chain [47]. The non-affine evolution of chain conformation beyond the Rouse time would be caused by chain retraction within the affinely deformed tube. Other essential improvements to the tube reptation model were done by many contributors, notably Marrucci [9,10], Wagner [11], McLeish [12] but the state-of-the-art version of the tube theory is the GLaMM model (named after Graham, Likhtman, Milner, and McLeish) as it incorporates the effects of reptation, convective constraint release and chain stretch on the microscopic level [45].

It is fair to recognize that the tube model revolutionized the field of polymer dynamics, and stands at present on the highest step of the podium of the current paradigm for its predictions of the linear and nonlinear viscoelastic properties of entangled polymers.

Small-angle neutron scattering (SANS) studies on polymer melts under steady-state flow provide in situ information at a molecular scale on how the flow field is transmitted to the melt. Such experiments, called "Rheo-SANS", are difficult to set up and require special equipment but their results are fundamental to test experimentally the accepted claim by the reptation model [6,46] that the shear-thinning of entangled polymer chains is due to significant orientation of the segments between entanglements under the shear flow. We quote below two significant Rheo-SANS studies, one by Watanabe et al. in Japan, published in 2007 [48], and the other one by Noirez et al. in France, published in 2009 [49].

Both studies concluded that the chains remained largely un-deformed under steady-state shear flow conditions for which extensive shear-thinning was present. These results represent a formidable challenge to the reptation model of melt deformation [9,36–47].

Recently, in 2017, there was the new Rheo-SANS evidence published by Zhe Wang et al. [50], that demonstrates experimentally that the chain retraction step of the tube model does not occur, which led these authors to conclude that our current understanding of the flow and relaxation of entangled polymers, based on the reptation theoretical model of motions pioneered by de Gennes (1971) and Doi-Edwards (1979) is fundamentally wrong:

> *"...This result calls for a fundamental revision of the current theoretical picture for nonlinear rheological behavior of entangled polymeric liquids...the predictions by the tube model are not experimentally observed in a well-entangled polystyrene melt after a large uniaxial step deformation".*

2.3.2. Invalidation of Reptation by Rheo-SANS Results of Watanabe et al. (2007)

In order to examine the chain conformation changes under shear flow for a well-characterized monodispersed entangled polymer and the orientation distribution along the chain backbone, Watanabe et al. examined the Rheo-SANS behavior for an entangled polybutadiene sample dissolved in a deuterated oligomeric butadiene at the volume fraction of 0.28. The rheometer was a Couette apparatus, allowing high-flow shear rates at constant temperature [48]. The shear rate, normalized by the reptation time, was between

24 and 29 $s^{-1}$and at these shear rates the viscosity of the systems was significantly smaller than the zero-shear viscosity (by a factor of ~40). Despite this intense shear-thinning, Watanabe et al. observed that "*the I(q) data just moderately deviate from the Debye function (describing the data at equilibrium)... These SANS data allow us to examine the current molecular picture for the entangled chains under fast shear flow. This picture assumes that successive entanglement segments are not orientationally correlated and behave as independent stress sustaining units even under fast flow... Thus, the above assumption fails for the entangled chains under fast flow*".

In other words, at a shear rate that reduced the Newtonian viscosity by a factor of 40, i.e., under strong non-Newtonian conditions, the chain rms end-to-end distance hardly varied from its value under static (equilibrium) conditions: this result, if verified, was in full contradiction with the basic assumption of the reptation model regarding the deformation mechanism involving the singular macromolecules. Yet, this catastrophic contradiction was kept buried in the archives and was not brought forward by the authors; it remained an isolated research report which was not confirmed.

2.3.3. Invalidation of Reptation by Rheo-SANS Results of Noirez et al. (2009)

Noirez et al., apparently unaware of the results of Watanabe et al. [48], probably for the reasons evoked above, used a similar Quartz Couette rheometer set up and reported on in situ observations of polymer melts under steady-state shear flow using neutron scattering [49]. The amorphous melts studied by these authors were an entangled polybutadiene ($T_g = -110$ °C, $M_w = 29\ M_e$) characterized by a reptation time $\tau_d = 7 \times 10^{-3}$ s ($\omega_x = 143$ rad/s) and a low-molecular-weight (unentangled) polybutylacrylate ($T_g = -64$ °C, $M_w \sim M_e$), characterized by $\tau_d = 10^{-3}$ s ($\omega_x = 1000$ rad/s). Both melts were monodispersed and sheared at room temperature (i.e., far above their respective T_g). The melts were sheared with a range of strain rates spanning the zone from far below the reptation time to far above it (from 0.011 s^{-1} to 1000 s^{-1}) to determine the variation of the chain dimensions across the reptation time and test the admitted reptation theories claims regarding the onset of shear-thinning and of chain orientation/disentanglement [6,46].

Figure 1 of Noirez et al. [49] clearly demonstrates that the two components, azimuthal and longitudinal, of the radius of gyration (R_v and R_z) remained constant at 80 Å as the shear rate varied from the Newtonian range to a highly shear-thinned melt, and, besides, that no change of the radius of gyration occurred as the melt crossed τ_d. The authors concluded "*that the chains remain largely undeformed under steady-state shear flow... These observations are of prime importance; they reveal that the flow mechanism and its viscoelastic signature reflect a collective effect and not properties of individual chains*".

We emphasize the last sentence in the conclusion: "...the viscoelastic signature reflects a collective effect and not properties of individuals chains". This is the key sentence to remember from this experimental research. In summary, both Watanabe et al. and Noirez et al. concluded that the macromolecular dimensions remain quasi-unchanged as the melt is sheared in the non-Newtonian region, and this conflicts totally with the currently accepted understanding of shear-thinning. The failure of the existing models to interpret such a fundamental aspect of polymer rheology cannot remain unchallenged [13–21].

2.3.4. Invalidation of Reptation by Rheo-SANS Evidence That Chain Retraction Does Not Occur by Zhe Wang et al., 2017

This paper by Zhe Wang and 11 other co-authors [50] solves the problem of critically testing the chain retraction hypothesis of the tube theory for entangled polymers. In principle, these authors explain in their paper, one should be able to critically test the chain retraction hypothesis by performing SANS experiments on uniaxially stretched entangled polymer melts and comparing the measured R_g with theoretical predictions. "*In reality, experimentalists have encountered tremendous difficulty in following this approach...it is practically impossible to reliably determine the radius of gyration tensor through model independent Guinier analysis, because of the limited Q range and flux of existing SANS instruments and the large molecular size of entangled polymers*". These limitations of the analysis of the radius of gyration

tensor in step-strain relaxation Rheo-SANS investigations may represent arguments to question the results of Noirez et al. [49] or Watanabe et al. [48] above.

Zhe Wang et al. recently recognized the value of "spherical harmonic expansion" as a general approach for characterizing Q-dependent deformation anisotropy and chain conformation at different length scales. The idea of using spherical harmonic expansion of the orientation distribution function of statistical segments in deformed polymer networks was conceived by Roe and Kribaum who discussed the potential application of this technique to analyze the amorphous halo for stretched polymers [50]. A more formal treatment of the measured scattering intensity by Legendre expansion was developed by Mitchell [Refs. 84–86 of [50]] and applied to the tensile deformation mode. The originality of Zhe Wang et al.'s work is to have applied the spherical expansion analysis to test directly and unambiguously the chain retraction hypothesis, central to the theoretical picture of the tube model.

The stretching of the rectangular samples of PS to orient them before their SANS analysis was conducted by Zhe Wang et al. by uniaxial elongation at 130 °C to a stretch ratio $\lambda = 1.8$, with a constant crosshead velocity $v = 40\, l_0 / \tau_R$, where l_0 is the initial length of the sample, and τ_R the Rouse relaxation time (~600 s). The oriented samples were allowed to relax for different amounts of time (from 0 to $20\tau_R$) at 130 °C and then were immediately quenched by pumping cold air into the oven. The authors verified that they successfully froze the conformation of the polymer chain with negligible stress relaxation during the quenching procedure.

Zhe Wang et al unambiguously showed that:

> *"the two prominent spectral features associated with the chain retraction—peak shift of the leading anisotropic spherical harmonic expansion coefficient and anisotropy inversion in the intermediate wave number (Q) range around Rouse time—were not experimentally observed in a well-entangled polystyrene melt after a large uniaxial step deformation".*

They added:

> *"Unlike the previous investigations, there is no ambiguity associated with model fitting and no room for human bias. Therefore, our critical test clearly demonstrates that the chain retraction hypothesis of the tube model is not supported by small-angle neutron scattering experiments."*

> ***"This result calls for a fundamental revision of the current theoretical picture for nonlinear rheological behavior of entangled polymeric liquids."***

> *"Therefore, without an alternative mechanism for molecular relaxation, the idea of non-affine deformation alone does not seem to be able to explain the experimental observation."*

> *"Since the tube theory is of paramount importance for our current understanding of the flow and deformation behavior of entangled polymers, the invalidation of the chain retraction hypothesis has immense ramifications."*

2.3.5. Conclusion on the Great Myth of the Applicability of the Reptation Model to Entangled Polymer Melts (M > Mc)

Despite all its elegance, mathematical sophistication and quasi-general acceptation we conclude that the reptation model incorrectly describes the Rheo-SANS experiments of Watanebe et al. [48], Noirez et al. [49], and of Zhe Wang et al. [50] and **should be abandoned**. The reason for this radical proposition, in our view, is that the dynamics of the interactions defining the melt properties should not be defined by statistical systems which are the single macromolecules. The failure of the reptation model also implies re-considering the concept of entanglement, the corner stone of polymer physics which, in our opinion, is not understood by the current paradigm of polymer physics.

2.4. Shear-Refinement and Sustained Orientation: The Lack of Understanding by the Current Paradigm

2.4.1. Shear-Refinement

"Shear-Refinement" is the observed influence on subsequent viscoelastic behavior (e.g., viscosity) of a pre-shearing treatment of a polymeric melt. Cogswell mentions the influence of thermo-mechanical history on viscosity in his book [51], p. 53:

> *"Intense working, producing high shear, will usually lead to a reduction in viscosity and also a decrease in the elastic response".*

Note that the viscosity reduction discussed by Cogswell is not due to a decrease in molecular weight, which is known to occur concomitantly, to a variable degree depending on the polymer and the experimental processing conditions.

Pre-Treatment on Branched Polymers

Most of the pioneering work was conducted 20 years ago on branched polymers (PE,PP) by such authors as D. E. Hanson [52], M. Rokudai [53], B. Maxwell [54], J.-F. Agassant [55], H. P. Schreiber [56] (who wrote a review of the subject up to 1966), G. Ritzau [57,58], who provides details of a shear-refinement apparatus, J.R. Leblans and Bastiaansen [59], Van Prooyen et al [60], Munstedt [61], who studied the effect of thermal elongational history, and A. Ram and L. Izailov [62]. Hanson [52] showed that the Melt Flow Index of a branched PE could be modified by shear-refinement from 0.28 to 0.66 and that the MFI returned to the initial value 0.27 after solution and re-precipitation of the pre-sheared sample. Cogswell [51] comments as follows on the results obtained by Hanson and others [52–54]:

> *"The change is seen to be reversible by solution treatment. Molecular weight characterization indicated that all these samples were identical. . . [Shear-refinement effects] "might at first appear to be the result of degrading the polymer, are frequently reversed by cooking the melt, though the time for which the melt may need to be cooked to achieve reversion may be much longer than the natural time of the material (viscosity/modulus at zero shear)".*

J.-F. Agassant et al. [55] show that the effects of shear-refinement are most obvious, and most commonly exploited, in the case of PVC which is known to have a morphology very sensitive to thermo-mechanical history.

No clear explanation was ever given to the origins of shear-refinement by these authors, which remained empirical until Bourrigaud [39] published a possible reptation-based interpretation in the case of branched polymers.

Bourrigaud [63], and Berger [64] have recently investigated the shear-refinement of long-chain branched ("LCB") polyolefins in their thesis. Bourrigaud focused on several well-characterized low-density branched polyethylene grades and obtained proof of the influence of the strain amplitude of shear deformation on the degree of viscosity reduction during subsequent processing. Bourrigaud suggested that molecular topology is critical, and his results support the view that molecules with very long-chain branches are highly affected by shear refinement, whereas linear polyethylene seems to undergo much smaller changes (if any), under the experimental shear refinement conditions he used. Bourrigaud and co-workers [65] concluded that the degree of long-chain branching or ramification qualifies or disqualifies, for the most part, the degree of viscosity reduction observed by shear refinement. In other words, controlled alteration by branching of the molecular weight distribution leads to the optimization of shear-refinement and of its benefits, according to these authors. Furthermore, Bourrigaud et al. showed that refinement by elongation is more effective than refinement by shear for the same flow strength [63,65]. Berger [64] and Berger et al. [66], worked with a long-chain-branched polypropylene under very high shear strain rates and found similar results. Additionally, Berger and coworkers [66] confirmed that the MFI of branched PP, collected as pellets, could be increased by shear-refinement, and that solvent dissolution would reverse the effect; after evaporation of the solvent, the

MFI returning to its original value. These authors concluded that disentanglement was responsible for the decrease of viscosity and die swell [66]:

> *The pre-treatment of the LCB-PP in the capillary rheometer at the highest shear stress applied causes a significant reduction of the tensile stress, which can be referred to the reduction of the mass-average molar mass. However, the significant decrease of the extrudate swell after the pre-treatment cannot be explained by the change of the molar mass, as the elastic behavior of polymer melts is known to be independent of the mass-average molar mass. Therefore, the reduction of the extrudate swell is an indication of a change of the entanglement network during the pre-treatment.*

Pre-Treatment on Linear Polymers

We published a series of papers and patents during the last two decades [67–69] to explain how the combination of shear rate and controlled strain mechanical treatments applied prior to or during processing of linear polymers (not branched) could result in substantial viscosity reduction benefits that allow, for instance, to work in extrusion at lower temperatures or under lower pressures at the same throughput. We invented, designed and ran "Rheo-Fluidizers", processing equipment making use of vibrational methods during melt extrusion to induce shear-refinement by shear strain energy coupled with extensional flow [67–69]. The emphasis of this "dynamic shear strain refinement" process was on the improved processability of **linear** high-molecular-weight polymer melts, such as polycarbonate and Plexiglas (PMMA), i.e., polymers without branches. We showed [68,69] that to induce the shear refinement benefits, a combination of shear stress and superposed oscillation could raise the elasticity of the melt to a level identical or perhaps even superior to what branching could do. In other words, we proposed that, at least under dynamic conditions, both linear polymers and branched polymers could qualify for "disentanglement" by shear strain refinement. Furthermore, we drew attention to the requirement of rheological criteria to be fulfilled for shear refinement to occur [Ref. [2] pp. 100, 110, 229], and pointed out the importance of the shear strain amplitude of the oscillation to operate the melt in the non-linear time-dependent viscoelastic range. We suggested that the combination of shear-thinning and strain softening during the pre-treatment, which we designated "Rheo-Fluidification", could produce either shear-refinement benefits [Ref. [2] Section 4.6], or Sustained-Orientation ("disentanglement") depending on certain conditions [67–69]. Sustained-Orientation is explained in the next Section 2.4.2.

Shear-refinement work has remained largely empirical because of the lack of its understanding by the current models. The viscosity reduction is temporary and rheological properties can be restored, which can occur in various ways and was not very well understood until now. Most of the comprehension necessary for its generalization and extrapolation to all macromolecules was lacking because the current models remained speechless about the shear-refinement results. For instance, for linear polymers, the current paradigm could not understand how it could be possible that shear-refinement effects could happen since the chains were linear and not branched. In addition, the Rheo-Fluidified melts had relaxation times calculated from their cross-over frequency much shorter than those with the same molecular weight without treatment, and this was as if they had been "disentangled", sometimes by a factor of 1000 or even 10 times that. The claim by Munstedt [70] that shear-refinement can only exist for branched polymer structures and not for linear chains is debated in Section 2.4.3 below and in [15].

It is clear that the lack of comprehension of shear-refinement for linear polymers by the current models poses a threat to the whole foundation of the existing paradigm in polymer science. The situation is different for branched polymers for which Bourrigaud's theoretical explanation has the merit to search for a classical interpretation [63]. Bourrigaud modified the McLeish and Larson's pom-pom model [12] to account for the increase, due to branching, in value of the tube renewal relaxation time and explained, at least partially, some of the shear-refinement results for its branched PE samples. For linear polymers, however, "disentangled" polymers present a real challenge to existing models of flow.

The positioning of the science community with respect to the "disentanglement" results remains confused and hesitant based on the claim of the reptationists' gate keepers that those results must be artifacts since they disprove their theory. Properties of melts brought out of equilibrium are largely ignored. Yet, many plastic industries are directly concerned and will benefit from the fundamental understanding of what causes shear refinement viscosity drops in linear or branched polymer, and how this can be applied to processing of polymer resins, branched or not. The ability to process plastic melt at much lower temperatures (50–80 °C below normal), because of reduced viscosity due to shear-refinement or disentanglement, opens up new boundaries not just in processing but also in blending, such as in nanoparticle dispersion, or for the processing of high-temperature sensitive additives (wood flour, instable additives such as peroxides, etc.). Details are given elsewhere [Ch. 8 of Ref. [2]].

2.4.2. Sustained Orientation

Shear-refinement can occur with unentangled polymers, linear or branched, and therefore shear-refinement should not always be called "disentanglement", like we did in our early publications (when we were not even aware of the work of others on shear-refinement). It is true that we only applied our Rheo-Fluidification pre-treatments on entangled melts, because of the commercial applications of reducing their viscosity, and this was one of the reasons to designate the results "disentanglement". When entangled polymer melts are submitted to Rheo-Fluidification treatments, the result produced is at least shear-refinement, at best Sustained-Orientation, and the distinction means that the Sustained-Orientation is more difficult to achieve, requiring a dual-phase model understanding of the differences between unentangled and entangled melts, in particular their stability under stress.

In simple terms, by manipulation of the stability of entanglements, it is possible to create and maintain quasi-stable at high temperatures in an amorphous polymeric melt (say 120 °C above T_g) a certain state of orientation that was induced by a mechanical deformation. The manipulation of entanglements was achieved by coupling two Rheo-Fluidification processors Section 2.2, Figures 2.1–2.4 in Ref. [2]. The "sustained-orientation" discovery describes the possibility to obtain non-equilibrium entanglement states for polymeric melts which can be preserved in a pellet formed after the treatment. This pellet displays a melt flow index (MFI) that can be 100% larger than the original (virgin) pellet before the treatment, after correction for any molecular degradation present due to the process. This new state of polymer matter challenges the current established models of polymer physics, because such "oriented" melts can remain oriented for hours at temperatures below their T_{LL} transition temperature, yet can slowly recover in time their initial un-oriented equilibrium state (the MFI of the treated pellet then slowly reverses to its original MFI). This esoteric behavior can be understood by the Dual-Phase model of the interactions that explains entanglements as a split of the statistical system of interactions yielding a set of cross-dual-phases [20].

The experiments of "sustained-orientation" could be interpreted qualitatively using the classical terminology by a change in M_e, the molecular weight between entanglement (thus the wording which was used, "disentanglement" or "re-entanglement"), except that there is no classical explanation to why M_e could vary so slowly in time, $M_e(t)$, independently of the terminal relaxation time, and be increased or decreased by relatively low shear forces. For instance, using the classical language, sustained-orientation would produce a melt with an M_e value twice as big as the virgin pellet, M_{eo}. That value can be frozen in the new pellet and stay stable as the pellet is reheated above the T_g, say at $T = T_g + 120$ °C, at least for a certain time that could be equal to a million times the value of the reptation time. The $M_e(t)$ can then start to decrease towards its original equilibrium value M_{eo}, the time to control the return to equilibrium being controlled by pressure. There is no explanation in the current theories for an unstable entanglement network res

ulting in an unstable liquid state for polymers, and on how the instability dynamics could be correlated to non-linear viscoelastic effects.

What sustained-orientation suggests is that the classical concept of M_e to describe entanglements is overly simplistic and its usefulness is, at best, limited to the linear range of viscoelasticity. The whole foundation of polymer physics, based on its understanding of entanglements, appears to be challenged, perhaps even overhauled, by the type of experimental results resulting in Sustained-Orientation.

Figure 26 below (similar to Figures 4–9 for PC and Figure 4.74 for PMMA in Ref. [2]) demonstrates the benefits of Sustained-Orientation, sometimes designated "disentanglement in a pellet" in contrast to "disentanglement in-line" which refers to the shear-refinement reductions in viscosity and melt elasticity while the melt is being processed after the pre-treatment.

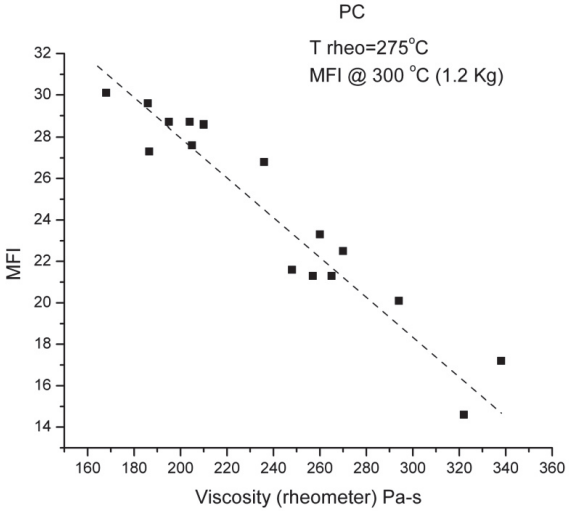

Figure 26. Signature of "Sustained-Orientation": MFI value found for pellets made out of a melt prepared by Rheo-Fluidification treatment are linearly correlated to the value of viscosity measured by the in-line viscometer at the exit of the Rheo-Fluidizer.

Figure 26 applies to a linear PC grade. One compares the MFI value found for pellets made from a melt prepared by the twin Rheo-Fluidification treatment stations of Figure 5a,b of Ref. [2] with the value of viscosity measured by the in-line viscometer (shown in Figure 4.8 of [2]) at the exit of the strand die. Although the two temperatures are different (300 °C for the MFI measurement, 275 °C for the in-line measurement), the correlation is validated: when the in-line viscosity drops, the pellet has a higher MFI than the reference pellet (11.3). In other words, the viscosity benefits obtained from the manipulation of the melt stability can be frozen into a state in a pellet that will survive subsequent heating periods, about 20,000 times its terminal relaxation time value at 150 °C above its T_g. This "Sustained-Orientation" behavior shambles completely the current understanding of viscoelasticity in polymer melts.

Ever since we were able to produce hundreds of pounds of linear polymers (PC, PMMA, LLDPE) exhibiting the Sustained-Orientation behavior and understood that this new property contradicted the current paradigm of polymer physics, we knew that a different explanation of "entanglements" was required and that polymer physics had to be reconstructed from a different understanding of the coupling between the covalent and inter-molecular interactions.

We conclude this section by claiming that the reptation tube model, as it stands now, cannot explain the challenging results obtained by "shear-refinement", and by "Sustained-

Orientation". If a model cannot comprehend a phenomenon that we can reproduce to produce batches of hundreds of pounds of pellets demonstrating the benefits of the phenomenon at a time, then this model should be abandoned. This is the way science works.

2.4.3. The Munstedt's Exclusive Requisite That the Polymer Must Be an LCB (with Long Chain Branches) to Be Able to Obtain Shear-Refinement

Munstedt [70] recently claimed that only branched polymers could demonstrate shear-refinement benefits, not linear polymers. According to him, linear polymers could only show artifacts or unreported degradation [70]. We offered a rebuttal to Munstedt's paper and his allegations [15]. These two publications should be read to illustrate how the gate keepers of an existing paradigm practice their censorship power to eliminate any possible existential threat. The rebuttal, for instance, was rejected by the Journal which published the paper by Munstedt (Journal of Rheology). Also, Munstedt misquoted and mischaracterized—intentionally or not is debatable—some parts of Ref. [2] to denigrate the results. Let us stay on course and only concentrate on excerpts from Ref. [15] relevant to the present discussion.

Münstedt's Critical Condition That Branching Must Be Present to Observe Shear-Refinement Is Wrong

In Ref. [2], we introduce new equations to analyze the rheology of melts (shear-thinning, strain-softening) in terms of the Dual-Phase model and show that they also explain the origin of the rheological instability. The long-term retention of the lower viscosity in the Rheo-fluidified pellets when re-heated to a melt state, sometimes for times several hundred thousand times greater than the reptation time at that temperature, represents an immense challenge to the currently admitted models of chain dynamics such as reptation. This challenge is not acknowledged by the community of rheologists, except swept away as artifact, such as in the paper by Münstedt [70]. However, how could this be an artifact when produced several lots of 150 lbs of **sustained-oriented pellets**, the product of the "artifact", which could regain in time their original viscosity after re-melting!

We concluded in [2] that this "Sustained Orientation" paradox is linked to a new concept: the instability of the Dual-Phase of the interactions. A first degree instability can be induced by a combination of shear-thinning and strain softening that may result in shear-refinement effects. Sustained-Orientation requires certain conditions in addition to the 1st degree instability criteria to trigger an instability of the 2nd kind: the instability of the Cross-Dual-Phase entanglement structure.

There are two types of sources to trigger the rheological instabilities of polymer melts: one is controlled by the recoverable dynamic free volume variations, the other by the modification of the entanglement network structure, by entropic dissipation (orientation of the network). This competition between these 2 mechanisms of instability is different for a given polymer and represents the true debate to have regarding the shear-refinement results, as we emphasized to Münstedt, during our intensive discussions [15]. For instance, the Dual-Phase model of the interactions that we have introduced in Ch. 1 of Ref. [2], a book reviewed by Munstedt, explains the dynamic source of the free volume, which is also influenced by the topology of the chains, in particular whether long chain branching, short chain branching or no branching is present. Both the **amount** and the **structure** of the dynamic free volume are influenced by branching. However, and this is missing in Munstedt's analysis, they are also influenced by other rheological factors, the orientation of the chains, the frequency and the amplitude of a vibration of the coherent interactive medium, the pressure in the melt, etc., all these parameters influence the local density of the melt and the frequency of the elastic dissipative wave that compensates for the local packing density inhomogeneity. In turn, they also influence the melt modulus (the famous $G_N = \rho RT/M$ correlation), and thus influence shear-thinning and strain softening. Münstedt focused on the presence of the long chain branches to determine a criterion for shear-refinement [70]. We argued that to understand why shear-refinement can occur in both branched and linear polymers one needed crucial information that are never

provided by the molecular models: 1. the determination of the local packing density and of the localization of the free volume in the structure, and 2. the influence of branching on these two variables. The Dual-Phase model is easily applicable to this situation [2] because of the local cross-duality between the F/b dissipative states and the conformational states (trans ,cis, gauche). This (F/b $\leftrightarrow$ (c,g,t)) local cross-duality also predicts the influence of vibration, shear rate and shear strain on the free volume amount and its distribution, in particular how to increase it, whether the basic polymer is branched or linear. Therefore, the topological criteria by Münstedt that branching **must be** present to observe the conditions for shear-refinement is simply wrong.

2.5. Strain-Induced Time Dependence of Rheological Functions

The conditions to achieve linear viscoelasticity are obtained at low strain amplitude for dynamic rheological experiments, where an oscillating strain is applied to a molten melt with frequency ω at temperature T. Under such conditions, the elastic and loss moduli, $G'(\omega,T)$ and $G''(\omega,T)$, respectively, are independent of the value of the strain, that could be 1%, 3%, 5%, etc., up to the limit of linear viscoelasticity. The limit of linear rheology is reached when the value of the moduli become strain dependent, i.e., when the stress is no longer proportional to the strain (non-affine deformation). The determination of this limit is compulsory before running any other tests in the linear region of viscoelasticity; it is done by running a strain sweep at given T and ω. The value of the strain is increased continuously and slowly until a deviation from the horizontality of the modulus appears that marks the beginning of non-linearity. In the following we are interested in the "stability" of the non-linear solution, meaning once we have reached the value of strain for non-linearity are the moduli values stable in time or starting to drift to make them time dependent?

1. Does a non-linear state obtained by increasing strain become *immediately* instable: time dependency starts as soon as its modulus differs from its linear value?
2. Is the strain value for the end of linear viscoelasticity different from the strain value for the start of the time dependency of the non-linear modulus?
3. Is the rate of the time dependency of modulus a function of the strain?

The general affirmative response for polymer melts answers question #2, adding in complement that the response is function of the chemical nature of the polymer, the value of ω, of $(T - T_g)$ and of the strain.

In other publications (Ch. I.7 and II.9 of [20]), we address the issue of determining the critical strain at which the instability of the non-linear rheology is triggered (question #2) and the influence of strain on the rate of the moduli decay (question #3).

When we say "instable", we are **not** talking about a chemical instability of some sort (degradation, esterification, cross-linking) or a surface instability (cracks, edge fracture, surface contact loss) that would alter the measurement, we are talking about the possibility to re-organize the interactions inside the material under stress that results in the time dependency of the moduli. For instance, using the language of the Dual-Phase model, we want to know if the dynamic free volume restructures (i.e., the (b/F $\leftrightarrow$ (c,g,t) kinetics evolves), or, for entangled melts, whether there is an enthalpic or entropic modification of the compensation between the two dual-phases, when the strain brings the system in the time-dependent non-linear range ("disentanglement").

It is clear that we need to ensure that the chemical instabilities or surface instabilities are not responsible for the time dependency observations. This point is crucial to consider in detail (see [71] section 4.4.2 "Challenging Interpretations": 4.4.2.1 "Viscous Heating. 4.4.2.2 "Shear Degradation. 4.4.2.3 "Drooling of the Melt outside the Rheometer Plates. 4.4.2.4 "Plastification Due to the Monomer Concentration Increase by the Shear Stress. 4.4.2.5 "Shear-Thinning. 4.4.2.6 "Edge Fracture Explanation. 4.4.2.6.1 "Melt Fracture Initiation: Vinogradov's Criteria. 4.4.2.6.2 "Simultaneous Dielectric and Dynamic Mechasnical Measurements in the Molten State. 4.4.2.6.3 "Effect of the Nature of the Surface Melt Contact"), because certain testing configurations are more inclined to create artifacts than others and we need to cross-reference those doubtful results with results that can be trusted 100%.

This dedication to scrutinize each experiment details to eliminate any potential artifact pitfalls is the absolute norm when dealing with the experiments exhibiting a strain induced time dependence of the rheological functions. This takes extra dedicated time [15,71] but is necessary to counter the artifact reflex of the deniers of such results by the gate keepers of the existing paradigm [70].

2.5.1. First Example of Strain Induced Transient of Viscosity (Inducement)

Figure 27a,b concern a PS melt studied with a dynamic rheometer (AR 2000, TA Instruments) in the time-sweep mode. The temperature is 165 °C (65° above the T_g of PS) and the frequency remains equal to 20 Hz (ω = 125 rad/s). The cross-over frequency for this PS at that temperature is 0.1 rad/s, so the Rouse time is 10 s. The initial strain is 5%, known to be in the linear viscoelastic range. The strain remains constant to this value for 3 min, then it is automatically increased to a new value, 10%, where it stays constant for 3 min; this action is repeated until the final strain is 23%. In other words, the strain varies step wisely every 3 min from 5% to 23%, the sample undergoing time-sweep steps lasting 3 min between each increase of the strain. Figure 27a displays the viscosity η*(ω) vs. Time for each time sweep for strain equal to: 5%, 10%, 15.2%, 17.5%, 20% and 23%. We record the value of G′ and G″ during each of the 3 min steps. Figure 27b provides the variation of G′(t) and G″(t) for the last step, corresponding to 23% of strain (ω is still 125 rad/s).

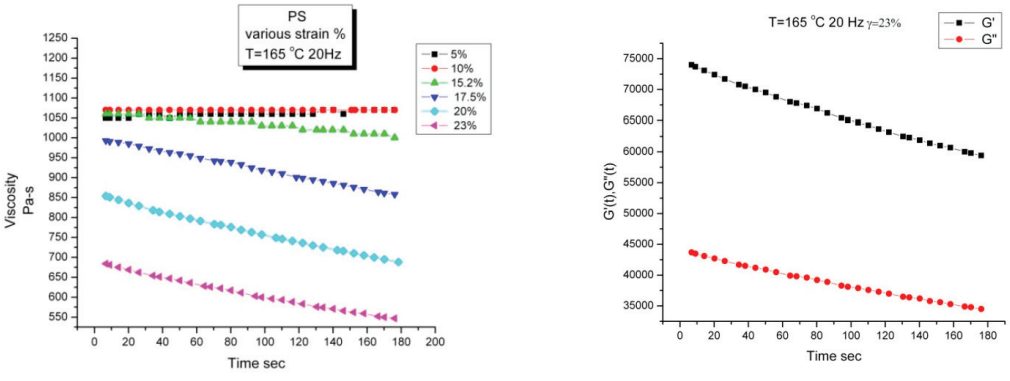

(**a**) (**b**)

Figure 27. (**a**) Viscosity (Pa-s) vs. Time (s) during successive time sweep sequences of 3 min each at 165 °C, 20 Hz for a PS sample in a dynamic rheometer. The strain is increased at the beginning of each sequence as shown in the inset. Viscosity is calculated from G′(t) and G″(t). (**b**) Details of Figure 27a regarding the strain = 23% sequence. This graph shows the decay of G′ and G″ with time.

It is apparent in Figure 27a that a time dependent (transient) behavior is triggered by the increase of strain at 15.2%. For 5% and 10% strain, the viscosity remains constant, but at 15.2% in Figure 27a, the viscosity starts to decay. The magnitude of the effect increases with strain, the rate of the decay does too (compare the viscosity curves for 15.2% strain (green triangles up) and 17.5% (green triangles down): the increase of the slope is proportional to the rate increase. As the strain increases, the apparent straight line decay becomes an exponential decay visible by the convex curvature. This is particularly visible for the 23% strain time sweep. Note that the decay of the moduli in Figure 27b is not over and has not reached a plateau after 3 min, which contrasts with a terminal relaxation time of 10 s for this melt. The time scale involved in the transient decay is very different from the molecular time scale. There is a classical "engineer" description of this phenomenon in terms of shear-thinning and strain softening: at ω = 125 rad/s T = 165 °C, the melt shear-thins, i.e., its viscosity drops from the Newtonian value at that temperature to a lower value, 1075 Pa-s in Figure 27a (@ 5% strain). The effect of strain on the modulus, a non-linear

effect, is called "strain-softening", which is quantified by the ratio, h, of the non-linear modulus to the linear modulus (h < 1). Shear-thinning is controlled by the value of ω, strain-softening by the value of the strain, γ, so it is expected that the strain rate maximum per cycle, ωγ, play a role to determine the onset of the time dependence behavior which we can designate by either "the instability of strain softening by the frequency ω" or "the instability of shear-thinning by the strain γ". Criteria of melt instability based on the value of the strain rate and/or the strain have been used to study non-linear effects such as melt fracture or melt flow non laminar decohesion [72,73]. It is important to verify [71] that none of these critical values for melt inhomogeneity is reached to explain the triggering, at such a low γ (15%), of the transient behavior observed in Figure 27a,b.

Wang [73] has established that two criteria must be met simultaneously to trigger a non-laminar structure of the melt in a gap: one of these criteria relates to the strain rate, the other to the strain. The strain criterion of Wang (γ > 100%) is not met, by far, in Figure 27 since the transient occurs for γ = 15.2%. The possibility that melt fracture occurred at the edge of the sample to explain the stress and viscosity decay in Figure 27 has also been considered and contradicted [72]. A simple experimental way to eliminate such an explanation for the strain induced triggering of a rheological transient is to consider if the phenomenon is reversible. This is shown in the next example on another polymer, a linear low density PE.

2.5.2. Second Example of Strain Induced Transient of Viscosity (Inducement and Recovery)

Figure 28a,b summarize schematically the frequency and strain experimental profile to create a transient with a laboratory dynamic rheometer, and demonstrate that the phenomenon is reversible upon cessation of the cause of the effect.

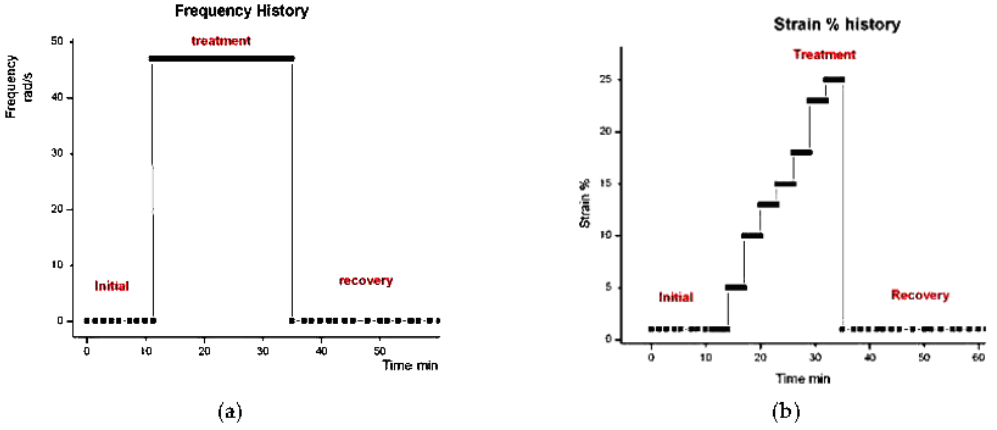

Figure 28. (**a**) Frequency history steps (plotted against time) for the sample in the dynamic rheometer. (**b**) Strain % history steps (plotted against time) for the sample in the dynamic rheometer of Figure 28a.

The data were obtained with a dynamic rheometer, the ARES from Rheometrics, using a parallel plate configuration, but a cone and plate combination was also used, providing essentially the same results. The resin was a LLDPE from Dupont-Dow Elastomers (Engage 8180), the temperature was 155 °C, and the gap was chosen between 1.2 and 2 mm.

Figure 28a,b describe the frequency and % strain history. Figure 29 plots dynamic viscosity against time. The first and last segment, called "initial" and "recovery" in Figure 28a,b represent the baseline, the value of viscosity under linear viscoelastic conditions, i.e., under very low frequency and amplitude (here 1 rad/s, 1% strain). The so-called «**treatment zone**» in Figures 28 and 29 was initiated by a jump of the frequency, from 1 to 47 rad/s, which created, in Figure 29, an "instantaneous" drop of viscosity from 57,000 Pa-s to 10,000 Pa-s, due to shear-thinning. The jump was then followed by a gradual stepwise increase of the

strain amplitude, from 1% to 25%. Figure 29 shows that for the first 2 steps of increase of strain, the viscosity held constant at 10,000 Pa-s, its shear-thinned value at that temperature and frequency, but that starting at strain = 13%, the viscosity started to become transient declining from 10,000 to a steady state value of 3100 Pa-s. The decay of the viscosity took about 25 min. The frequency and strain amplitude were then changed back to their low values of the linear range (1%, 1 rad/s), and one observes an "instantaneous" partial loss of the effect of shear-thinning combined with strain softening, i.e., the viscosity jumped back to 38,000 Pa-s. Further recovery of viscosity occurred over the following 20 min, viscosity increasing slowly and finally regaining its original Newtonian value, 57,000 Pa-s. In other words, the state of the melt produced by the transient treatment was unstable when the energy that produced the transient behavior was released: this is why viscosity slowly increased in time and returned back to the original value for the melt. Nevertheless, it took 20 min for recovery, and this time is 60 times longer than the terminal time at that temperature, making it possible to exploit the benefits of a smaller viscosity during recovery if the melt were to be processed at that stage. One can define the viscosity benefit by comparing the initial Newtonian viscosity (57,000) and the Newtonian viscosity before recovery after the shear-thinning elastic loss (38,000), a ratio of 1.5 in this treatment **(«50% viscosity drop»).** Notice that a processor could still benefit from shear-thinning of the treated resin (Figure 28), and work under much greater viscosity reduction (3100 Pa-s versus 57,000 Pa-s, an improvement of over 1700% !).

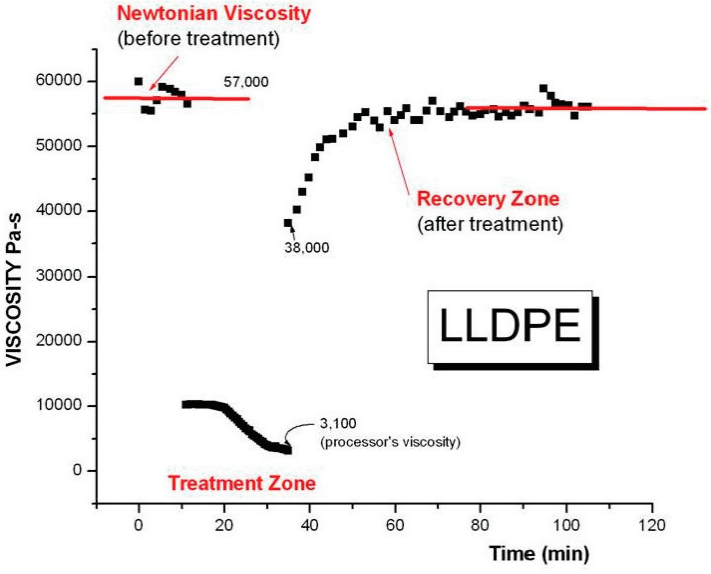

Figure 29. Dynamic viscosity vs. time for the 3 steps of Figure 28a,b.

The experimental procedure described in Figure 28 has many variations: the time duration between strain amplitude step-ups can vary, the strain amplitude increment itself can be changed as can the temperature of the melt and the frequency of operation during treatment. The treatment could also be done differently, by increasing at low frequency the strain to 25%, say, and step wisely increasing the frequency from 1 rad/s to 47 rad/s. All these changes contribute to the final % viscosity reduction, which can be as small as 20%, to as large as 3000%. The wrong procedure can also produce artifacts or surface effects, as is explained in [71].

2.5.3. Conclusions on the Strain-Induced Time Dependence of Rheological Variables
The "Process Engineer" Interpretation of the Results

Strain softening, known to decrease the modulus at higher strain, combines with shear-thinning due to the effect of frequency to render the melt unstable in its original entanglement network configuration; thus the transient behavior occurs. In a step strain experiment conducted in the molten state, a softening factor is defined, h = G(strain)/G(LVE), where G(strain) is the melt modulus for a given strain and G(LVE) refers to the strain independent Linear Viscoelastic Value (h < 1). At low strain, the modulus is only time dependent, and an increase of strain produces an increase of stress proportionally. Pure viscometry experiments have demonstrated that above certain strain rates, corresponding to a certain stress level, a transient decay towards steady state released the elastic energy stored during initialization. It was suggested in earlier publications dedicated to more engineering audiences [12,67–76] that the dynamics of this process could be viewed as a recursive effect of the stress on relaxation times. As stress continues to grow, due to increased strain, strain softening is the first revealing sign of the modification of the structure due to the stress dependence of the relaxation time. Figure 29 reveals that under dynamic conditions, the softening factor h can become time dependent, which translates into a transient behavior. The advantage of producing transient behavior with a dynamic viscometer is that G' and G'' become time dependent, so it is possible to analyze these curves individually and also follow how $(G'/G^*)^2$ varies during transient stress decay. The transient decay can be produced in-situ in the rheometer, and a frequency sweep performed before the transient and after it, allowing an easy way to analyze the differences due to the stay in the non-linear regime. This type of experiments allows us to analyze the influence of strain and frequency during time sweep ("the treatment"). Additionally, the fact that a frequency sweep in the linear regime can be performed on the sample after it has been treated non-linearly, proves the integrity of the sample and its surfaces, in contradiction to the claims by Munstedt [70] that the treatment conditions degraded the sample integrity.

The Theoretical Physicist Interpretation of the Results

We have studied many curves like those in Figures 27 and 29, obtained using a parallel plate configuration, a cone and plate and a Couette configuration, using many different polymers, using different temperatures, different molecular weights, under pressure in a confined environment with no edges, superposed to extrusion flow, under cross-lateral vibration etc.(Ref. [2] is dedicated to report in details those experiments and results), and the same conclusion imposes itself: the rheological phenomenon observed that is triggered by strain has a kinetic origin which makes it vary with frequency and temperature but **does not work at the same scale as the terminal time**, $\tau_p = 1/\omega_x$: it refers to a different phenomenon that is not accounted for in any previous model of viscoelasticity: the dissipative aspect of the interactions. In our theoretical work on the Grain-Field Statistics of open dissipative systems [21], this concept is embedded in the equations regulating the interactions between the dual-conformers, and these assumptions are applied to polymers in [19]. The "dissipative aspect" means, in essence, that beyond enthalpic and entropic changes occurring to constrained systems brought out of equilibrium, the size of the systems may restructure, rendering the statistical frame definition to become part of the dynamics. This fundamentally different statistical approach is what fuels the new paradigm of the interactions that we introduce which, in many ways, explains the shortcomings of the current paradigm to be able to correctly address the experimental results presented in this paper. One could say, to simplify, that the new paradigm fuses with the current paradigm, which may then regain some merit, when the system of interactions is in a state above the T_{LL} transition, a typical "dissipative transition" resulting from the dissipative nature of the interactions [19,24,34].

3. Conclusions

The deformation of a polymer melt in shear mode represents the main subject of interest in the science of rheology of such materials. It is a crucial topic for successfully processing these materials. In the above examples that dealt with linear viscoelastic rheological conditions with no effect of strain, in Sections 1–3, we saw that even in these simple conditions the Rouse model failed to satisfactorily describe the data of unentangled melts when carefully comparing experiments and theoretical predictions. The same failure of the reptation model was also demonstrated when comparing the calculated projections of the affine and non-affine hypotheses suggested by the reptation model of entangled melts with the experimental results obtained by Rheo-SANS. In summary, even in the linear range of viscoelasticity the acclaimed Rouse and de Gennes models are challenged by experimental evidence. In the non-linear range, at a high strain rate and strain, the subject of the other examples presented in this paper (Sections 2.4 and 2.5), it is generally admitted that the current theoretical developments that successfully predict the main characteristics of polymer melts in the linear range fall short, but merely need improving and tweaking of the parameters. The extrapolation to the non-linear behavior generally consist of adding some terms to the mathematical formulation of the linear viscoelastic model. As we stated at the beginning of this paper, all the current models in polymer physics are based on "chain dynamics statistics" [6–12]. The aura these polymer dynamic models have reached among the polymer scientific community makes them the current standard references that control the field of plastic engineering that relies on the understanding of viscoelasticity and rubber elasticity. Yet, as we suggest, it is possible that the experiments described in this work challenge the current paradigm to its limits, to the edge of its usefulness.

The present understanding of the physics of macromolecules is based on an analysis of the properties of a single chain. The presence of the other chains is perceived as a mean field influence on the properties of that chain. The reptation school considers that this mean field can be looked at as a topology, a homogeneous field of obstacles restricting the motion of the single chain, which is claimed to explain the extra molecular weight dependence of viscosity at M_c and beyond. We explain in this paper that, in our opinion, this assumption (which is also present in Rouse) is the origin of the failures of these models to describe the data correctly. The irony is that de Gennes [6] used the term "scaling concepts" in the title of his book on polymer physics [6], which resonates, but in a different context, with our definition of a scale of the basic unit that participates in the deformation process in our dissipative statistical approach. The difference is that our model not only defines the scale, in fact several "dynamic scales", but also determines the coupling and the modulation between these cooperative scales [20]. For instance, in our Cross-Dual-Phase explanation of entanglements, we make reference to a "network of strands" to describe the cooperative interactive process resulting in the "entanglement phase". We refer to a basic unit of deformation, the Dual-conformer, that participates in the evolving cooperative motion of a phase-wave responding to deformation as an open dissipative system [20]. We must define mathematically what "evolving cooperation" means, how many dual-conformers dynamically cooperate in an active strand at any instant, how many strands are active and how many relax, and where the cooperative dual-conformers are located: on a single chain or on several chains. The physics of dealing with all the chains at once in the statistics, redefining the coupling between the covalent and the inter-molecular interactions, is the model that we have adopted to describe the deformation of polymer melts and solids, above T_g and below T_g [2,19,20]. The theory not only addresses the interaction between the conformers of a single chain to assume the shape of a macro-coil (which can be deformed), but also defines why entangled macro-coils exhibit the response of a network of active strands when all the chains participate cooperatively in the deformation process. The dissipative dynamic coupling between the deformation of a conformer, of a macro-coil, and of a network of strands is quantitatively described. The new model explains the influence of chain molecular weight to predict a change in behavior below and above a critical molecular weight (M_e), in other words it proposes a new understanding of "entanglements" and their

influence on the dynamic melt properties G′(ω,T) and G″(ω,T) and the normal stresses. It predicts shear-thinning and strain softening in shear mode, and strain-hardening in extensional mode. It also successfully describes the transitional behavior at T_g, from a solid-like to a liquid-like behavior, also predicting the existence and the characteristics of the Boyer's T_{LL} upper melt transition temperature (the end of dissipative modulation). Finally, the theory addresses the stability (or the strain-induced lack of stability) of the Cross-Dual Phase entanglement network [20].

The theoretical assumptions of the new model and the quantitative descriptions it generates constitute a whole new understanding of the viscoelastic properties of polymers that could be considered the premises of a new paradigm in that field of physics. We would like to close by quoting Buckminster Fuller who once said:

> *"In order to change an existing paradigm you do not struggle to try and change the problematic model. You create a new model and make the old one obsolete."*
>
> —Richard Buckminster Fuller

Funding: This research received no external funding.

Conflicts of Interest: The authors declare no conflict of interest.

References

1. Staudinger, H. *Makromoleculare Chemie und Biologie*; Wepf & Co.: Bale, Switzerland, 1947.
2. Ibar, J.P. *The Physics of Polymer Interactions—A Novel Approach to Rheology and Processing*; Hanser Publishers: Munich, Germany, 2019.
3. Flory, P.J. Spatial Configuration of Macromolecular Chains. Nobel Lecture. Available online: https://www.google.co.uk/url?sa=t&rct=j&q=&esrc=s&source=web&cd=&ved=2ahUKEwiHnuCy3uiBAxVWVN4KHaLXCqwQFnoECAEQAQ&url=https%3A%2F%2Fwww.nobelprize.org%2Fuploads%2F2018%2F06%2Fflory-lecture.pdf&usg=AOvVaw3357NM8tA3uiBA966iScGM&opi=89978449 (accessed on 11 December 1974).
4. de Gennes, P.G. Soft Matter. Nobel Lecture. Available online: https://www.nobelprize.org/uploads/2018/06/gennes-lecture.pdf (accessed on 9 December 1991).
5. Flory, P.J. *Statistical Mechanics of Chain Molecules*; Interscience Press: New York, NY, USA, 1969; 308p.
6. de Gennes, P.G. *Scaling Concepts in Polymer Physics*; Cornell University Press: Ithaca, NY, USA, 1979.
7. Rouse, P.E. A theory of the linear viscoelastic properties of dilute solutions of coiling polymers. *J. Chem. Phys.* **1953**, *21*, 1272–1280. [CrossRef]
8. de Gennes, P.G. Reptation of a Polymer Chain in the Presence of Fixed Obstacles. *J. Chem. Phys.* **1971**, *55*, 572–579. [CrossRef]
9. Marrucci, G. Dynamics of Entanglements: A nonlinear model consistent with the Cox-Merz rule. *J. Non-Newton. Fluid. Mech.* **1996**, *62*, 279–289. [CrossRef]
10. Marrucci, G.; Ianniruberto, G. Interchain pressure effect in extensional flows of entangled polymer melts. *Macromolecules* **2004**, *37*, 3934–3942. [CrossRef]
11. Wagner, M.H.; Rubio, P.; Bastian, H. The molecular stress function model for polydisperse polymer melts with dissipative convective constraint release. *J. Rheol.* **2001**, *45*, 1387–1412. [CrossRef]
12. McLeish, T.C.B.; Larson, R.G. Molecular constitutive equations for a class of branched polymers: The pom-pom polymer. *J. Rheol.* **1998**, *42*, 81–110. [CrossRef]
13. Ibar, J.P. The Great Myths of Polymer Melt Rheology, Part I: Comparison of Experiment and Current Theory. *J. Macromol. Sci. Part. B Phys.* **2009**, *48*, 1143–1189. [CrossRef]
14. Ibar, J.P. The Great Myths of Rheology, Part II: Transient and Steady-State Melt Deformation: The Question of Melt Entanglement Stability. *J. Macromol. Sci. Part B Phys.* **2010**, *49*, 1148–1258. [CrossRef]
15. Ibar, J.P. Rebuttal to H. Munstedt's article " Mechanical Pretreatment of Polymer Melts. Critical Aspects and new rheological investigations on a linear and a long-chain branched Polypropylene", J.O.R, 65.5(2021):871-885, DOI: 10.1122/8.0000237". *Glob. J. Sci. Front. Res.* **2022**, *22*, 21–31.
16. Ibar, J.P. Trouble with Polymer Physics: Development of "Sustained Orientation" Contradicts the Current Understanding of the Liquid State of Polymers. *J. Macromol. Sci. Part. B* **2015**, *54*, 722–748. [CrossRef]
17. Ibar, J.P. Shear-Thinning of Polymeric Melts: The Failure of the Reptation Model. In *The Physics of Polymer Interactions—A Novel Approach to Rheology and Processing*; Hanser Publishers: Munich, Germany, 2019.
18. Ibar, J.P. Do we need a new theory in polymer physics? *J. Macromol. Sci. Part C Polym. Rev.* **1997**, *37*, 389–458. [CrossRef]
19. Ibar, J.P. A Dual and Cross-Dual interpretation of interactive coupling of conformers applied to thermally activated polarization and depolarization of polymers. In *Dual-Phase Depolarization Analysis*; Interactive Coupling in the Amorphous State of Polymers; De GRUYTER Publisher: Berlin, Germany, 2021.

20. Ibar, J.P. The Dual-Phase Model of Polymer Interactions and the Cross-Dual-Phase Model of Entanglements. In *Dual-Phase Rheology*; De GRUYTER Publisher: Berlin, Germany, 2024.
21. Ibar, J.P. *Grain-Field Statistics of Open Dissipative Systems. Application to Polymer Conformers in Interactions*; DE GRUYTER Publisher: Berlin, Germany, *in preparation*.
22. Matsumiya, Y.; Watanabe, H. NonLinear Elongational Rheology of Unentangled Polystyrene and Poly(p-tert-butylstyrene) Melts. *Macromolecules* **2018**, *51*, 9710–9729. [CrossRef]
23. Majeste, J.-C. Propriétés Viscoélastiques de Polymères Linéaires à Très Large Distribution de Masses Molaires. Ph.D. Thesis, Université de Pau et Pays de l'Adour, Pyrénées-Atlantiques, France, 1998.
24. Ibar, J.P. A Dual-Phase Approach to reveal the presence and the impact of the T_{LL} transition in Polymer Melts. Part I: Predicting the existence of Boyer's T_{LL} transition from the Vogel-Fulcher equation. *J. Macromol. Sci. B. Phys.* **2021**, *60*, 727–791. [CrossRef]
25. Montfort, J.P. Dynamique Moleculaire et Comportement Rheologique des Polymers Enchevetres en Phase Fondue et en Solution Concentree. p. 75. Ph.D. Thesis, Université de Pau et Pays de l'Adour, Pyrénées-Atlantiques, France, 1984.
26. Williams, M.L.; Landel, R.F.; Ferry, J.D. The temperature dependence of relaxation mechanisms in amorphous polymers and other glass-forming liquids. *J. Am. Chem. Soc.* **1955**, *77*, 3701. [CrossRef]
27. Ibar, J.P. The Great Myths of Rheology Part III: Elasticity of the Network of Entanglements. *J. Macromol. Sci. Part B Phys.* **2013**, *52*, 223–309. [CrossRef]
28. Gray, R.W.; Harrison, G.; Lamb, J. Dynamic viscoelastic behaviour of low-molecular-mass polystyrene melts. *Proc. Roy. Soc.* **1977**, *A 356*, 77.
29. Davidson, D.W.; Cole, R.H. Dispersion and absorption in dielectrics I. Alternating current characteristics. *J. Chem. Phys.* **1941**, *9*, 341.
30. Benallal, A.; Marin, G.; Montfort, J.P.; Derail, C. Linear viscoelasticity revisited: The relaxation function of monodisperse polymer melts. *Macromolecules* **1993**, *26*, 7229. [CrossRef]
31. Leonardi, F. Determination de la Distribution des Masses Molaires D'Homopolymeres Lineaaires par Spectroscopie Mecanique. Table III-1 p. 146. Ph.D. Thesis, Universite de Pau et Pays de l'Adour, Pyrénées-Atlantiques, France, 1999.
32. Ferry, J.D. *Viscoelastic Properties of Polymers*; John Wiley & Sons: Hoboken, NJ, USA, 1970.
33. Ibar, J.P. Non-Newtonian Flow Behavior of Amorphous Polymers in the $T > T_g$ Temperature Range: A New Analysis of the Data According to the "Double-Shift" Procedure. *J. Macromol. Sci. Phys.* **1981**, *B19*, 269–308. [CrossRef]
34. Ibar, J.P. A Dual-Phase Approach to reveal the presence and the impact of the T_{LL} transition in Polymer Melts. Part II: The theoretical and practical relevance of the T_{LL} existence and characteristics on the understanding of the melt thermal analysis and rheological properties of polymers: Duality and Cross-Duality of the interactions. *J. Macromol. Sci. B. Phys.* **2021**, *60*, 792–838.
35. Ibar, J.P. The Great Myths of Polymer Rheology: Elasticity of the Network of Entanglements. In *The Physics of Polymer Interactions—A Novel Approach to Rheology and Processing*; Hanser Publishers: Munich, Germany, 2019; pp. 307–311.
36. Doi, M. Molecular Rheology of Concentrated Polymer Systems I. *J. Polym. Sci. Polym. Phys. Ed.* **1980**, *18*, 1005. [CrossRef]
37. Milner, S.T.; McLeish, T.C.B. Reptation and Contour Length Fluctuations in Melts of Linear Polymers. *Phys. Rev. Lett.* **1998**, *81*, 725. [CrossRef]
38. Likhtman, A.E.; McLeish, T.C.B. Quantitative Theory for Linear Dynamics of Linear Entangled Polymers. *Macromolecules* **2002**, *35*, 6332. [CrossRef]
39. Daoud, M.; de Gennes, P.G. Some Remarks on the Dynamics of Polymer Melts. *J. Polym. Sci., Polym. Phys. Ed.* **1979**, *17*, 1971. [CrossRef]
40. Klein, J. Dynamics of Entangled Linear, Branched, and Cyclic Polymers. *Macromolecules* **1986**, *19*, 105. [CrossRef]
41. Mead, D.W.; Larson, R.G.; Doi, M. A Molecular Theory for Fast Flows of Entangled Polymers. *Macromolecules* **1998**, *31*, 7895. [CrossRef]
42. Milner, S.T.; McLeish, T.C.B.; Likhtman, A.E. Reptation and Contour-Length Fluctuations in Melts of Linear Polymers. *J. Rheol.* **2001**, *45*, 539. [CrossRef]
43. Marrucci, G.; Grizzuti, N. Fast Flows of Concentrated Polymers—Predictions of the Tube Model on Chain Stretching. *Gazz. Chim. Ital.* **1988**, *118*, 179.
44. Pearson, D.; Herbolzheimer, E.; Grizzuti, N.; Marrucci, G. Transient Behavior of Entangled Polymers at High Shear Rates. *J. Polym. Sci. B* **1991**, *29*, 1589. [CrossRef]
45. Graham, R.G.; Likhtman, A.E.; McLeish, T.C.B.; Milner, S.T. Microscopic Theory of Linear, Entangled Polymer Chains under Rapid Deformation Including Chain Stretch and Convective Constraint Release. *J. Rheol.* **2003**, *47*, 1171. [CrossRef]
46. Doi, M.; Edwards, S.F. Dynamics of Concentrated Polymer Systems Part 2.—Molecular Motion under Flow. *J. Chem. Soc., Faraday Trans.* **1978**, *2*, 1802. [CrossRef]
47. Larson, R.G. *Constitutive Equations for Polymer Melts and Solutions*; Butterworth-Heinemann: Oxford, UK, 2013.
48. Watanabe, H.; Kanaya, T.; Takahashi, Y. Rheo-SANS behavior of Entangled Polymer Chains with Local Label Under Fast Shear Flow. In *Activity Report on Neutron Scattering Research: Experimental Reports 14 (2007)*; Report Number: 146; Neutron Science Laboratory: Neutron Science Laboratory, Institute for Solid State Physics, University of Tokyo: Tokyo, Japan, 2007.
49. Noirez, L.; Mendil-Jakani, H.; Baroni, P. New light on old wisdoms on molten polymers: Conformation, slippage and shear banding in sheared entangled and unentangled melts. *Macromol. Rapid Commun.* **2009**, *30*, 1709–1714. [CrossRef] [PubMed]

50. Wang, Z.; Lam, C.N.; Chen, W.-R.; Wang, W.; Liu, J.; Liu, Y.; Porcar, L.; Stanley, C.B.; Zhao, Z.; Hong, K.; et al. Fingerprinting Molecular Relaxation in Deformed Polymers. *Phys. Rev. X* **2017**, *7*, 031003. [CrossRef]
51. Cogswell, F.N. Polymer Melt Rheology, a Guide for Industrial Practice. Woodhead Publishing Ltd.: Sawston, UK, 1997; p. 57.
52. Hanson, D.E. Shear Modification of Polyethylene. *Polym. Eng. Sci.* **1969**, *9*, 405–414. [CrossRef]
53. Rokudai, M. Influence of shearing history on the rheological properties and processability of branched polymers. I. *J. Appl. Polym. Sci.* **1979**, *23*, 463–471. [CrossRef]
54. Maxwell, B. Controlled Shear Modification of Low Density Polyethylene. In Proceedings of the 50th Anniversary Conference of the Society of Rheology, Boston, MA, USA, 28 October–1 November 1979.
55. Agassant, J.F.; Avenas, P.; Sergent, J.-P.; Vergnes, B.; Vincent, M. La Mise en Forme des Matières Plastiques. Lavoisier Tec et Doc, 1996. Available online: https://www.paprec.com/fr/comprendre-le-recyclage/tout-savoir-sur-les-matieres-recyclables/plastiques/la-mise-en-oeuvre-des-matieres-plastiques/ (accessed on 8 October 2023).
56. Schreiber, H.P. Cause and effect in time dependent flow of thermoplastics melts—A review. *Polym. Eng. Sci.* **1966**, 317–323. [CrossRef]
57. Ritzau, G. Shear modification of polyolefins and its integration on polymer processing. *Int. Polym. Process.* **1987**, *1*, 188–197. [CrossRef]
58. Ritzau, G.; Ram, A.; Izrailov, L. Effect of shear modification on the rheological behaviour of two LDPE grades. *Polym. Eng. Sci.* **1989**, *29*, 214. [CrossRef]
59. Leblans, P.J.R.; Bastiaansen, C. Shear modification of low density polyethylene: Its origin and its effect on the basic rheological functions of the melt. *Macromolecules* **1989**, *22*, 3312–3317. [CrossRef]
60. Van Prooyen, M.; Bremner, T.; Rudin, A. Mechanism of shear modification of low density polyethylene. *Polym. Eng. Sci.* **1994**, *34*, 570–579. [CrossRef]
61. Münstedt, H. The influence of various deformation histories on elongational properties of LDPE. *Colloid. Polim. Sci.* **1981**, *259*, 966–972. [CrossRef]
62. Ram, A.; Izailov, L. Shear modification of polyethylene. *J. Appl. Polym. Sci.* **1986**, *31*, 85–100. [CrossRef]
63. Bourrigaud, S. Etude de la Modification des Propriétés Rhéologiques Induite par L'écoulement: Application à L'extrusion-couchage. Ph.D. Thesis, Universite de Pau et Pays del'Adour, Pyrénées-Atlantiques, France, 2004.
64. Berger, S. Einfluss der Mechanischen Vorgeschichte aud das Rheologische Verhalten von Langkettenierzweigtem Polypropylen. Ph.D. Thesis, University of Erlanden, Erlangen, Germany, 2005.
65. Bourrigaud, S.; Marin, G.; Poitou, A. Shear-Modification of Long-Chain branched Polymers: A Theoretical Approach using the Pom-Pom Model. *Macromolecules* **2003**, *36*, 1388–1394. [CrossRef]
66. Stange, J.; Berger, S.; Munsted, H. *Influence of Flow History in the Rheological Properties of a Long-Chain Branched Polypropylene*; ESR AERC Grenoble: Grenoble, France, 2005.
67. Ibar, J.P. Extrusion of Polymer Melts under Intensive Shear-Thinning Inducing Lower Pressure and Temperature Requirements. In *ANTEC Proceedings 2001*; ANTEC: Danbury, CT, USA, 2001; p. 481.
68. Ibar, J.P. Control of Pseudo-Plasticity of Polymer Melts by Disentanglement Methods. In Proceedings of the 2nd Annual European Rheology Conference (AERC), Grenoble, France, 21–23 April 2005.
69. Ibar, J.P. Process for the Control of Flow Properties of Polymers. U.S. Patent US2005/0267289A1, 1 December 2005.
70. Munstedt, H. Mechanical pretreatment of polymer melts: Critical aspects and new rheological investigations on a linear and a long-chain branched polypropylene. *J. Rheol.* **2021**, *65*, 871–885. [CrossRef]
71. Ibar, J.P. The Great Myths of Polymer Rheology: Transient and Steady State. The Question of Melt Entanglement Stability. In *The Physics of Polymer Interactions—A Novel Approach to Rheology and Processing*; Hanser Publishers: Munich, Germany, 2019; pp. 211–232.
72. Vinogradov, G.V.; Malkin, A.Y.; Plotnikova, E.P.; Kargin, V.A. Thixotropy of polymers in the visco-fluid state. *Dokl. Akad. Nauk.* **1964**, *154*, 1421.
73. Wang, S.-Q. Molecular transitions and dynamics at polymer/wall interfaces: Origins of flow instabilities and wall slip. *Adv. Polym. Sci.* **1999**, *138*, 227–275.
74. Edwards, S.F.; Doi, M. *The Theory of Polymer Dynamics*; Clarendon: Oxford, UK, 1986.
75. Rokudai, M.; Mihara, S.; Fujiki, T. Influence of shearing history on the rheological properties and processability of branched polymers. II. Optical properties of low-density polyethylene blown films. *J. Appl. Polym. Sci.* **1979**, *23*, 3289–3294. [CrossRef]
76. Ibar, J.P. Control of Thixotropicity of Polymer Melts by Disentanglement Processing. In *ANTEC Proceedings 2005*; ANTEC: Danbury, CT, USA, 2005; p. 10370.

Disclaimer/Publisher's Note: The statements, opinions and data contained in all publications are solely those of the individual author(s) and contributor(s) and not of MDPI and/or the editor(s). MDPI and/or the editor(s) disclaim responsibility for any injury to people or property resulting from any ideas, methods, instructions or products referred to in the content.

polymers

MDPI

Article

Effect of Hydrothermal Aging on the Tribological Performance of Nitrile Butadiene Rubber Seals

Gege Huang [1,2], Zhihao Chen [1], Jian Wu [1,3,*], Ange Lin [1], Qinxiu Liu [1], Shouyao Liu [1,3], Benlong Su [1,3] and Youshan Wang [1,3]

[1] Center for Rubber Composite Materials and Structures, Harbin Institute of Technology, Weihai 264209, China; huanggege@gtc.com.cn (G.H.); 22b908093@stu.hit.edu.cn (Z.C.); 17554179361@163.com (A.L.); 17603881396@163.com (Q.L.); liushouyaoemail@sina.com (S.L.); subenlong@hit.edu.cn (B.S.); wangys@hit.edu.cn (Y.W.)
[2] Guizhou Tire Co., Ltd., Guiyang 550201, China
[3] National Key Laboratory of Science and Technology on Advanced Composites in Special Environments, Harbin Institute of Technology, Harbin 150090, China
* Correspondence: wujian@hitwh.edu.cn

Abstract: High temperature and humidity affect the tribological performance of nitrile butadiene rubber (NBR) seals, which affects the precise positioning of cylinder systems. Therefore, it is crucial to study the effect of hydrothermal aging on the tribological performance of the NBR seals. In this study, the changes in the tribological performance of the NBR seals under hydrothermal aging conditions were investigated. The results show that the volatilization of additives and the increase in crosslink density of the NBR seals occurs in the hydrothermal aging environment, leading to the deterioration of their surface quality, elastic deformability, and tribological performance. The formation of surface micropores due to additive volatilization is the main factor in the degradation of tribological performance.

Keywords: hydrothermal aging; NBR seals; tribological performance; finite element simulation

Citation: Huang, G.; Chen, Z.; Wu, J.; Lin, A.; Liu, Q.; Liu, S.; Su, B.; Wang, Y. Effect of Hydrothermal Aging on the Tribological Performance of Nitrile Butadiene Rubber Seals. *Polymers* **2024**, *16*, 81. https://doi.org/10.3390/polym16010081

Academic Editors: Ulrich Maschke, Matthias Ballauff, Rufina G. Alamo and Fahmi Zaïri

Received: 28 November 2023
Revised: 23 December 2023
Accepted: 25 December 2023
Published: 26 December 2023

Copyright: © 2023 by the authors. Licensee MDPI, Basel, Switzerland. This article is an open access article distributed under the terms and conditions of the Creative Commons Attribution (CC BY) license (https://creativecommons.org/licenses/by/4.0/).

1. Introduction

Pneumatic systems are widely used in robotics, aerospace, and medical devices due to their low cost, high efficiency, and light pollution [1–3]. The sealing structure is an essential part of realizing the precise positioning control of the cylinder in pneumatic systems, and the variation of the sealing material performance has an important impact on the service performance of the cylinder [4], and in addition, this variation is closely related to the overall efficiency and energy loss of the machine [5,6]. Nitrile butadiene rubber (NBR) is widely used as a sealing material in aerospace, automotive, robotics, etc. due to its high heat resistance, chemical stability, and wear resistance [7].

The rubber materials are subjected to thermal, electrical, optical, and mechanical stresses during service, which leads to rubber aging [8–10]. This means that the structure and properties of the rubber have changed, resulting in the deterioration of service performance [11–13]. At present, the structure and properties of rubber materials under aging conditions such as thermo-oxidative, prestressed, and marine have been extensively studied [14–19]. Moon et al. [20] investigated the aging behavior of rubber materials with a natural rubber/butadiene rubber (NR/BR) system and showed that there are differences in the changes in the structure of natural rubber at different aging stages. At the beginning of the aging process, the aging of rubber materials is dominated by crosslink aging. In contrast, at the later stage of the aging process, its aging mode changes to being dominated by main chain breakage. Hydrogenated nitrile butadiene rubber (HNBR) undergoes similar structural changes during high-temperature aging. The crosslink density on the surface increases after aging, leading to an increase in tensile stiffness and a decrease in failure

strain [21]. Liu et al. [22] observed, by swept surface electron microscopy (SEM), that the number of tiny pores appearing on the surface of NBR increased with increasing aging time, accompanied by an increase in the size of the pores. During the aging process, the interior additives of rubber migrate from its interior to the surface [23–25]. The research results of Liu et al. [26] on the high-temperature aging of NBR under compression conditions showed that the structural change of NBR during the aging process was mainly cross-linking, while the tensile strength and elongation at the break of nitrile rubber also changed significantly.

The NBR seals in cylinders are subject to complex environmental conditions of service, characterized by high temperature (up to 80 °C) and condensation, resulting in a variety of factors in the process of service by the common influence that inevitably will occur during the hydrothermal aging phenomenon. There are inevitably differences in the tribological performance of the NBR seals due to the hydrothermal aging phenomenon. Researchers have studied the hydrothermal aging of rubber materials to some extent. Choi et al. [27] studied the aging process of sulfur-cured ethylene propylene diene monomer (EPDM) under hydrothermal conditions. They showed that, under hydrothermal conditions, stearic acid in sulfur-cured EPDM reacts with Ca^{2+} in air or water to produce calcium stearate and causes EPDM surface to appear white. Patel et al. [28] investigated the permanent compression deformation of silicone rubber as a function of aging temperature and showed that the silicone rubber aged in a closed system softened with time.

The tribological behavior of rubber materials is a focus of attention [29,30], and the tribological performance after aging is crucial for rubber sealing materials. Dong et al. [31] investigated the dry sliding friction of NBR after aging. The results showed that its wear was dominated by fatigue wear and that aging caused a decrease in tribological performance. Han et al. [32] found that CeO_2 with a certain amount of graphene could protect the rubber matrix during thermal-oxidative aging and frictional heating. He et al. [33] investigated the tribological performance of CeO_2 blended rubber after aging and showed that the increase in crosslink density at the beginning of thermal aging could effectively improve its tribological performance. Luo et al. [34] found that the friction and contact pressure of NBR seals increased with the increase in temperature during hydrothermal aging.

However, the effect of hydrothermal aging on the tribological performance of the NBR seals is not fully understood. Therefore, it is particularly important to investigate the effect of hydrothermal aging on the tribological performance of the NBR seals for the practical application of cylinder seal structures. In this work, we investigated the effects of hydrothermal aging times on the mechanical properties and tribological performance of the NBR seals through experimental and finite element simulations to provide theoretical guidance for the subsequent implementation of accurate servo control of cylinders.

2. Experimental Methods

2.1. Materials

Two types of samples were tested: the NBR cylindrical samples and the NBR seals (PSD-20 from Osaka Co., Ltd., Osaka, Japan). The NBR cylindrical samples were prepared by vulcanizing the raw NBR material. The preparation process is as follows: the raw NBR material was cut into the cylindrical vulcanization mold and placed in the flat plate vulcanizer heated to 160 °C. The vulcanization conditions were 160 °C × 35 min and maintaining the loading pressure of 12 MPa during vulcanization. The specific preparation process is shown in Figure S1. The dimensions of the NBR cylindrical samples were 10 mm in diameter and 10 mm in height, and the NBR seals were tested as a finished part. The specific dimensions of the chosen NBR seals were 20 mm × 14 mm × 2.24 mm (outer diameter × inner diameter × wire diameter).

2.2. Hydrothermal Aging Test

The samples were subjected to hydrothermal aging tests. The test method refers to ISO 188-2023 [35]; a TZW-150UVA type Harris environment testing chamber (Wuxi Harris environment equipment Co., Ltd., Wuxi, China) was used for the hydrothermal aging test.

The accelerated aging temperature used was 80 °C, the humidity was 85%, and the duration of accelerated aging was 16 days (16 d), which produced the NBR seals with properties similar to those under actual service conditions. The mechanical properties and tribological performance of the samples with different hydrothermal aging times (0 d, 2 d, 4 d, 8 d, and 16 d) were tested.

The NBR seals were tested for tensile permanent deformation under hydrothermal aging conditions, and the test method refers to ISO 2285-2019 [36]. The NBR seals were inserted into cylindrical tensile test devices of different diameters. The tensile rates of the NBR seals were 10%, 20%, 30%, and 40% of the inner diameter, respectively, and the corresponding tensile die diameters were 15.4 mm, 16.8 mm, 18.2 mm, and 19.6 mm. The tensile permanent deformation rates of the NBR seals with different hydrothermal aging times were calculated by Equation (1).

$$K_1 = \frac{A_1 - A_0}{A_S - A_0} \times 100\% \quad (1)$$

where A_0 is the original inner diameter length (mm), A_1 is the recovered inner diameter length (mm), and A_S is the tensile inner diameter length (mm). Each sample was measured three times, and the average value was taken.

The NBR cylindrical samples were tested for compression permanent deformation under hydrothermal aging conditions, and the test method refers to ISO 815-1:2019 [37]. The NBR cylindrical samples were compressed by 20% using a compression restrictor. The compressive permanent deformation rates of the NBR cylindrical samples with different hydrothermal aging times were obtained by Equation (2).

$$K_2 = \frac{h_0 - h_2}{h_0 - h_1} \times 100\% \quad (2)$$

where h_0 is the height of the sample before compression (mm), h_1 is the height of the restrictor (mm), and h_2 is the height of the sample recovery after compression (mm). Each sample was measured three times, and the average value was taken.

2.3. Hydrothermal Aged NBR Characterization

The NBR seals with different hydrothermal aging times were intercepted as strips and tensile tests were performed using the uniaxial tensile testing machine (ZQ-990B-5, Zhiqu Precision Instrument Co., Ltd., Dongguan, China). The tests were carried out at a scale distance of 20 mm and a tensile rate of 100 mm/min. The NBR cylindrical samples with different hydrothermal aging times were compressed by the universal testing machine (WDW-02, Sida Testing Technology Co., Ltd., Jinan, China) at a rate of 20 mm/min, and the test method refers to ISO 7743-2017 [38].

The mass of the NBR cylindrical samples and the NBR seals were measured by electronic balance, and each sample was measured four times. The Shore hardness of the NBR cylindrical samples was tested using the LX-A instrument; each sample was measured four times, and the average value was taken as the Shore hardness value of the sample.

The infrared spectra of the NBR cylindrical samples were obtained using a Nicolet 380 Fourier transform infrared spectrometer (FTIR), which was used to compare the functional group composition of the rubber material before and after hydrothermal aging. The spectral range was selected from 800 cm^{-1} to 4000 cm^{-1} in the mid-infrared region with a resolution of 4 cm^{-1}, and the number of scans was set to 32. The background was first scanned and then the samples were tested afterward to remove the background. The surface micromorphology of the NBR cylindrical samples after aging was observed by the optical digital microscope (DSX 510, OLYMPUS Co., Ltd., Japan). The surface of the samples was cleaned with anhydrous ethanol before observation.

2.4. Friction Experiment

The tribological tests of the NBR cylindrical samples (0 d–16 d) with different conditions (lubrication and un-lubrication) were tested by the modified friction testing machine shown in Figure S2. The 6061 Aluminum alloy plate was used as the counterpart material, and 612 grease was applied to the surface during the lubrication test. By controlling the normal displacement of the friction testing machine, a load of 5 N was applied to the contact surface of the friction material, and the relative sliding velocity was 20 mm/min. Test the NBR cylindrical samples of 0 d, 1 d, 2 d, 4 d, 8 d, and 16 d, repeat five times for each group of tests, and take the average value.

The cylinder friction experiment machine was used to test the tribological performance of the NBR seals with different hydrothermal aging times and loading air pressures; the test parameters are shown in Table 1.

Table 1. The test parameters of the cylinder friction experiment.

Aging Time (Day)	Loading Air Pressure (MPa)	Piston Velocity (mm/s)
0 1 2 4 8 16	0, 0.05, 0.1, 0.15, 0.2, 0.25, 0.3, 0.35	10, 15, 20, 25, 30, 35, 40, 45, 50, 55, 60, 65, 70, 75, 80, 85, 90

The cylinder friction experiment machine was modified according to the universal testing machine WDW-02 (Sida Testing Technology Co., Ltd., Jinan, China), and the cylinder type was CDG1BN20-300 (SMC CORPORATION Co., Ltd., Tokyo, Japan). Its structure is shown in Figure S3. The lower chamber of the cylinder was connected to the air pump. The air pressure is provided by the air pump and controlled by the precision regulator (accuracy of 0.001 MPa) to stabilize the loading air pressure. The upper chamber is connected with air to create a pressure difference between the two chambers. The displacement and the change of the external force on the cylinder piston during the test were collected by the displacement sensor and the force sensor at the lower end of the test device, respectively. The test was conducted at room temperature (25 °C ± 2 °C), and the cylinder piston was subjected to uniform reciprocating motion. Each test was performed three times.

The LuGre model is widely used for the description of friction phenomena [39–41]. Therefore, the LuGre model was used to describe the dynamic friction of the cylinder, and the state variable A was used to characterize the average deformation of its deflection. The composition of the entire cylinder LuGre model primarily includes the cylinder nonlinear equation of state and the cylinder frictional force equation; the specific form is shown in Equations (3) and (4).

$$\frac{d_A}{d_t} = v_0 - k\frac{|v_0|}{g(v_0)}A \tag{3}$$

$$F_f = v_0 A + \sigma\frac{d_A}{d_t} + b_0 v_0 \tag{4}$$

where v_0 is the piston motion velocity in the cylinder (mm/s); k is the axial stiffness of the seal in the cylinder (N/mm); b_0 is the coefficient of viscous friction (N·s/mm^2); and σ is the axial damping coefficient of the seal in the cylinder (N/(mm/s)).

The steady-state form of the LuGre model was mainly determined by the function $g(v_0)$; the Stribeck velocity of the cylinder friction is described by Equation (5).

$$g(v_0) = F_C + (F_S - F_C)\exp(-(v_0/v_1)^2) \tag{5}$$

where F_C is the dynamic frictional force of the cylinder (N); F_S is the maximum static frictional force of the cylinder (N); and v_1 is the Stribeck speed of the cylinder (mm/s).

The LuGre model assumes that the cylinder is moving at a constant speed, and the deformation of the elastic mane between the two friction contact surfaces reaches a steady state, which means the state variable A is equal to 0. The average deformation value of the model is $g(v_0)\mathrm{sgn}(v_0)/k$ at this time. The cylinder frictional force in the steady state is obtained by Equation (6).

$$F_w = \left[F_C + (F_S - F_C)\exp(-(v_0/v_1)^2)\right]\mathrm{sgn}(v_0) + b_0 v_0 \quad (6)$$

According to Equation (6), the cylinder frictional force curve under different piston velocities obtained from the cylinder friction experiment was fitted by the least square method, and the values of four static parameter variables of the LuGre model in the steady state were obtained, which are F_C, F_S, v_1, and viscous friction ($b_0 v_0$). The cylinder friction experiment machine dragged the piston to move at a constant velocity; the frictional force of the cylinder friction experiment can be obtained by Equation (7).

$$F_f = F_1 - (P_1 A_1 - P_2 A_2) \quad (7)$$

where F_1 is the cylinder piston by all the external force (N), P_1 is the air pressure of the high-pressure chamber (MPa), P_2 is the air pressure of the low-pressure chamber (MPa), A_1 is the area of the piston rod on the high-pressure side (mm^2), and A_2 is the area of the piston rod on the low-pressure side (mm^2).

3. Finite Element Analysis of the NBR Seals Friction Process

The finite element simulation was conducted using ABAQUS software (Type 6.13). The material parameters were obtained by fitting the results of compression tests. Based on the compressive stress-strain relationship curves of the NBR cylindrical samples at different hydrothermal aging times, the parameters of the Mooney–Rivlin model were obtained, which are shown in Table S1. The mesh seed was set to 0.1 mm, and the encrypted mesh seed for the contact area at both ends was set to 0.05 mm, using a quadrilateral dominant mesh type. Three analysis steps were set up; the first one was pre-compression of the cylinder wall in contact with the seal, the second one was air pressure through the upper end of the seal, and the third one was the upward movement of the cylinder wall. Restrict the cylinder wall and the inner groove of the cylinder to be rigid bodies. The compression force between the NBR seals and the cylinder wall is reduced due to aging relaxation, and the simulation between the NBR seals and the cylinder wall at different aging times can be achieved by reducing the compression amount of the NBR seals. According to the compression rate of the NBR seals in the cylinder, which is 10% of the inner diameter and the tensile permanent deformation rates of the NBR seals, the equivalent simulation compressions of the NBR seals with different aging times were obtained as 0.050 mm (0 d), 0.042 mm (1 d), 0.034 mm (2 d), 0.031 mm (4 d), 0.026 mm (8 d), and 0.025 mm (16 d).

The simulation model of the NBR seals in the cylinder was established as shown in Figure S4. The cylinder wall and the piston rod were set as analytic rigid with smooth planar, and the NBR seals were set as deformable with Young's modulus obtained from the compression test of the NBR cylindrical sample and Poisson's ratio of 0.49. The step type was set as static general. The tangential and normal behaviors are defined in the contact properties. In the tangential behavior, the coefficient of friction (COF) was determined based on the lubrication friction test of the NBR cylindrical samples. In normal behavior, "hard" contact was set. Three analysis steps were set; the first step was the pre-compression of the cylinder wall in contact with the NBR seals, the second step was the air pressure passed to the upper end of the NBR seals, and the third step was the upward movement of the cylinder wall. The specific working parameters for the dynamic friction simulation are shown in Table 2.

Table 2. Finite element simulation conditions.

Aging Time (Day)	Loading Air Pressure (MPa)
0 1 2 4 8 16	0, 0.05, 0.1, 0.15, 0.2, 0.25, 0.3, 0.35

4. Results and Discussions

4.1. Mechanical Properties

Figure 1a,b show the recovered diameters and the tensile permanent deformation rates of the NBR seals with different hydrothermal aging times, respectively. As shown in Figure 1a, the un-tensile NBR seals shrink due to the increase of crosslink and the decrease of molecular chain length in the hydrothermal aging environment. Moreover, the shrinkage of the un-tensile NBR seals is more obvious with the increase of hydrothermal aging time, and the recovered diameter shrank from 20 mm to 19.85 mm when the aging time reached 16 days. The recovered diameters of the NBR seals under different tensile ratios increase with the hydrothermal aging time, which implies that the elastic recovery capacity of the NBR seals under the hydrothermal aging condition is weakened. Moreover, it is found that the difference in recovered diameters between the NBR seals with different tensile rates increased with the hydrothermal aging time, which further proves that the hydrothermal aging condition causes the deterioration of the elastic recovery capacity of the NBR seals.

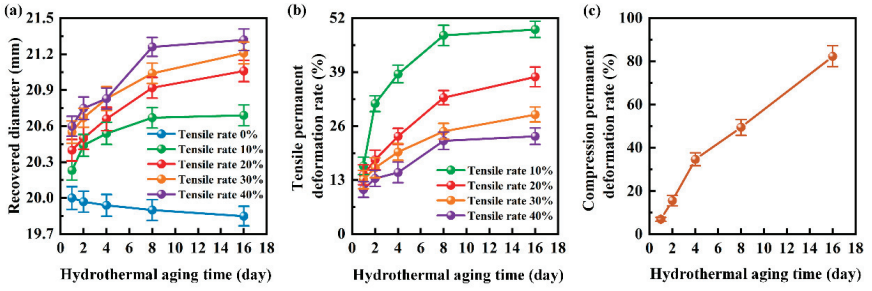

Figure 1. (**a**) The recovered diameters, (**b**) tensile permanent deformation rates of the NBR seals, and (**c**) the compression permanent deformation rates of the NBR cylindrical samples with different hydrothermal aging times.

The tensile permanent deformation rates of the NBR seals in Figure 1b show a monotonically increasing trend with the increase of hydrothermal aging time, which is consistent with the trend in Figure 1a. However, the NBR seals with lower tensile rates have greater tensile permanent deformation rates, which is due to the difference between the recovered diameters of the NBR seals with different tensile rates being smaller than the difference between tensile rates. In addition, it can be found that with the increase of hydrothermal aging time, the increased trend of recovered diameter and permanent deformation rate slows down, indicating that the aging process of NBR slows down with time. Figure 1c shows the variation curve of the compression permanent deformation rates of the NBR cylindrical samples with the hydrothermal aging time. The curve shows an overall trend consistent with that in Figure 1b. When the hydrothermal aging time is 16 d, the compression permanent deformation rate reaches the maximum value of 82.375.

Figure 2a shows the variation curves of the mass of the NBR cylindrical samples and the NBR seals with the hydrothermal aging time. The mass of both samples showed a significant increasing trend, and this trend decreases with the increase of the hydrothermal aging time. The increase in the mass of the NBR under the hydrothermal aging environment

is due to the water absorption and moisture absorption reaction. However, small molecular groups, volatile organic compounds, fillers, and additives within the rubber will gradually migrate from the interior to the surface and volatilize under hydrothermal aging conditions [23–25], which leads to a small decrease in the mass of the samples. This phenomenon was exhibited in the NBR cylindrical samples of 2 d. Figure 2b shows the variation curves of the hardness of the two samples with the hydrothermal aging time. The hardness of the two rubber material samples exhibits a monotonically increasing trend with the increase of the hydrothermal aging time, and the hardness of the samples exhibits a more obvious increase at the beginning of the hydrothermal aging (0 d–2 d), with an increase of 3.50 HA and 4.58 HA for the rubber cylindrical parts and the NBR seals, respectively. During the hydrothermal aging process, the crosslink density of NBR rubber increased and the internal structure became more compact, which led to an increase in the hardness of the samples.

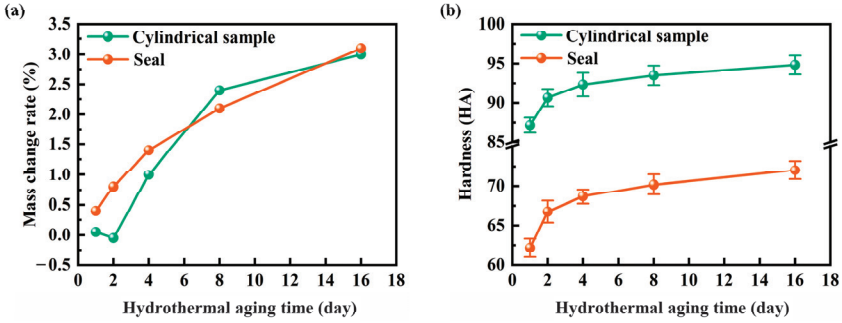

Figure 2. The variation curves of (**a**) mass and (**b**) hardness of the NBR cylindrical samples and the NBR seals with different hydrothermal aging times.

Figure 3 shows the compression stress-strain curves of the NBR cylindrical samples and the tensile force-deformation curves of the NBR seals with different hydrothermal aging times. As shown in Figure 3, the two samples showed similar trends in the compression test and tensile test; the NBR cylindrical samples and the NBR seals exhibited enhanced compressive strength and tensile strength, respectively, with the hydrothermal aging time increased. This enhanced trend became more obvious with the increase of hydrothermal aging time. The increase in the compressive strength and tensile strength of the samples is due to the increase in the crosslink density of NBR in the hydrothermal aging environment [21,26]. The degree of connection between the molecular network chains is enhanced, and more molecular chains bear stress during compression or stretching. In addition, the increase in the degree of crosslink between molecules leads to the shortening of the molecular chain and the deformation amount of the NBR decreases when subjected to stress. The other test data are shown in Figure S5.

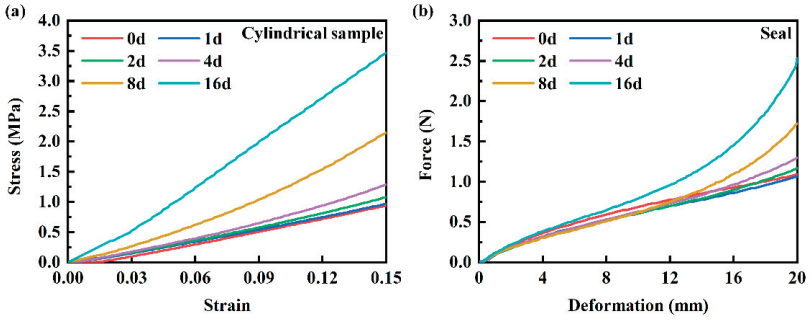

Figure 3. (**a**) Stress-strain curves of the NBR cylindrical samples and (**b**) force-deformation curves of the NBR seals with different hydrothermal aging times.

4.2. Tribological Behavior of Hydrothermal Aging

Figure 4 shows the surface morphology of NBR cylindrical samples with different hydrothermal aging times. The surface quality of the NBR cylindrical samples deteriorated due to hydrothermal aging, and obvious microporous structures appeared. Moreover, the number and size of these micropores increase significantly with the increase of hydrothermal aging time, which means that the deterioration of its surface quality is positively correlated with the hydrothermal aging time. This deterioration is mainly due to the migration of fillers, small molecular groups, and volatile organic compounds, etc., in the rubber material from internal to surface and volatilization [23–25], which is consistent with the results in Figures 2 and 4. The deterioration of the frictional surface quality is an important factor leading to the reduction of the tribological performance of the rubber material [42].

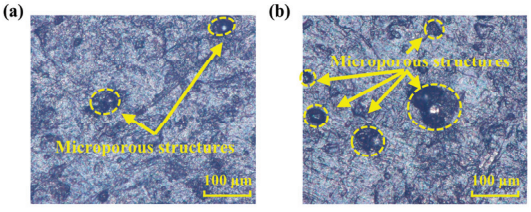

Figure 4. The surface morphology of the (**a**) 1 d and (**b**) 16 d NBR cylindrical samples.

During the service of cylinder seals, the loading air pressure in the cylinder is an important environmental condition; therefore, the tribological performance of cylinder seals under different loading air pressure is studied first. The cylinder friction experiment was conducted to further investigate the actual effect of hydrothermal aging on the tribological performance of the NBR seals in the cylinder. The cylinder friction experiment needs to be tested from the highest velocity and then reduced to the experimental velocity. In the low-velocity cylinder friction experiment, the cylinder needs to be stared at high velocity three times, which ensures the internal grease distribution is uniform.

The influence of the 0 d NBR seals on the static parameters of the cylinder was investigated. As shown in Figure 5a, the F_f-piston velocity variation curves and fitted curves are shown for the cylinder equipped with the 0 d NBR seals. Based on Equation (6), the squared difference between the curve obtained by least squares fitting and the mean value of the experimental results and the fitting coefficient is 0.9974, which has a good fitting effect. According to Figure 5b, which shows the effect of the loading air pressure on the F_C of the cylinder equipped with the 0 d NBR seals, it can be seen that with the increase of the loading air pressure, the static parameters in the friction model changed accordingly, and the F_C showed a monotonically increasing trend. When the loading air pressure increases from 0 MPa to 0.35 Ma, the F_C increases from 6.7 N to 10.5 N (with a total increase of about 56.72%). This indicates a linear relationship between increasing loading air pressure and the dynamic tribological performance of the cylinder. After investigating the kinetic tribological performance of the cylinder with different loading air pressure and the tribological performance of the 0 d NBR seals, the kinetic tribological performance of the cylinder with the aged NBR seal was further investigated.

The friction tests were conducted on cylinders equipped with the aged NBR seals at different velocities in 0 MPa, and the results are shown in Figure S6. The curves were fitted by the least squares method, using Equation (6), in order to obtain the variation curve of F_C with the hydrothermal aging times, as shown in Figure 6a. It can be observed that the F_C increases not linearly with the increase of hydrothermal aging time at the loading air pressure of 0 MPa. According to the extension line, the incremental rate of F_C increases gradually with the increase of hydrothermal aging time, which indicates that the relationship between hydrothermal aging time and F_C shows an exponential change, and the increase of hydrothermal aging time leads to a faster decrease of tribological performance of the NBR seals. As shown in Figure 6b, the F_C increases with the loading air

pressure, which does not change due to hydrothermal aging. Moreover, the variation trend of F_C with hydrothermal aging time does not change with the loading air pressure. This indicates that the loading air pressure does not affect the effect of hydrothermal aging on the tribological performance of the NBR seals in the cylinder during service, which only generates greater friction during the cylinder motion.

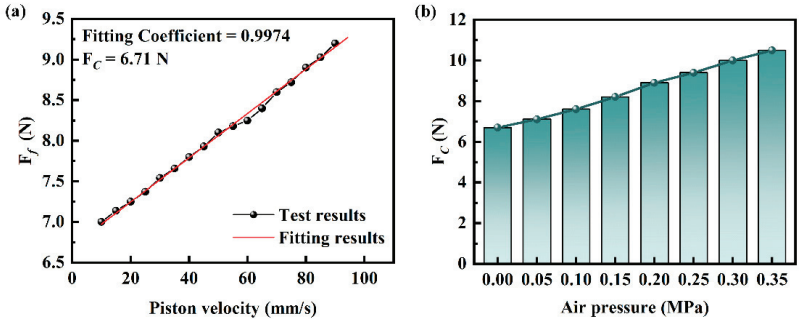

Figure 5. (**a**) The F_f-piston velocity variation curves and fitted curves of the cylinder equipped with the 0 d NBR seals; (**b**) the F_C of the cylinder equipped with the 0 d NBR seals with different loading air pressure.

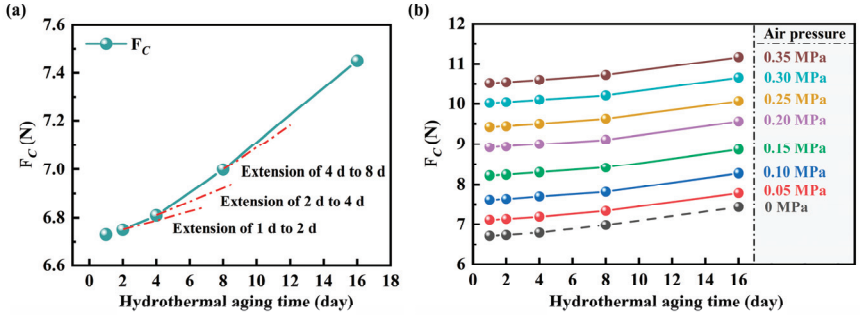

Figure 6. The F_C of the cylinder equipped with the aged NBR seals under loading air pressure of (**a**) 0 MPa and (**b**) 0–0.35 MPa.

The mechanical test proved that the mechanical properties of the NBR cylindrical samples and NBR seals vary in a consistent manner, and their compositions are both NBR. In order to further investigate the influence of loading air pressure on the tribological performance of the NBR seals, the frictional force and the contact area of the NBR seals under different simulation conditions were first analyzed by finite element simulation.

Figure 7 shows the frictional force and the contact area of 0 d NBR seals. Figure 7a shows the frictional force of the 0 d NBR seals under different loading air pressures. The frictional force shows a monotonic increasing trend with the increase of loading air pressure and is consistent with the trend of F_C variation in the cylinder friction experiment. The frictional force of the NBR seals increases by 1.54 N when the loading pressure increases from 0 MPa to 0.35 MPa. Figure 7b shows the contact areas between the 0 d NBR seals and the cylinder wall under different loading air pressures. The contact areas increase with the loading air pressure, and this increasing trend is phased. The contact areas increase rapidly at the loading air pressure of 0.05 MPa, 0.2 MPa, and 0.3 MPa, the loading air pressure increased from 0 MPa to 0.35 Ma, and the contact area increased from 22.1 mm^2 to 31.4 mm^2, which is a total increase of about 42.1%. This indicates that the variation of the frictional force of the NBR seals with the loading air pressure is not completely determined by the contact area. In order to further investigate the variation of the tribological performance, the variation of the stress at different loading air pressures was analyzed.

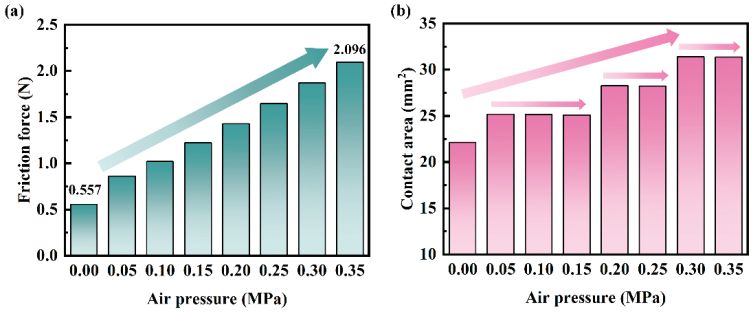

Figure 7. (**a**) The frictional force and (**b**) the contact area of the 0 d NBR seals under different loading air pressures.

Figure 8 shows the Mises stress distribution cloud and shear stress (CSHEAR1) distribution at the frictional contact interface of the 0 d NBR seals. The maximum Mises stress of the seal gradually shifts to the lower right side of the NBR seal with the increase of the loading air pressure and gradually increases. Meanwhile, the NBR seals move downward and deform significantly as the loading air pressure increases and their contact position with the cylinder wall shifts from the middle region to the lower region. The shear stress of the NBR seals presents a parabolic shape and reaches the maximum value at the center of the frictional contact interface. The change of shear stress of the NBR seals increases significantly with the increase of the loading air pressure. The maximum shear stress increases from 0.037 MPa to 0.084 MPa when the air pressure increases from 0 MPa to 0.35 MPa. This is mainly due to the increased loading air pressure causing the NBR seals to have a greater tendency to deform and therefore generate greater contact pressure at the frictional contact interface, which can be seen in the Mises stress distribution cloud.

Meanwhile, according to the distribution of shear stress, it is found that the value is smaller at the edge of the contact interface, and the frictional force does not show a phased increase when the contact area phase increases, which indicates the change of contact area does not determine the frictional force of the NBR seals under different loading air pressure. Moreover, the change of maximum shear stress shows the same trend as the change of frictional force, and it can be judged that the effect of loading air pressure on the frictional force of the NBR seals in the cylinder is mainly through the increase of contact pressure at the contact interface, not the increase of contact area. Figure S7 show the shear stress distribution of the NBR seals under different hydrothermal aging times. Hydrothermal aging has no obvious effect on the distribution pattern of shear stress at the friction contact interface of the NBR seals. The effect of hydrothermal aging on the shear stress is mainly reflected in the distribution area and size of the shear stress. This change is mainly due to the hydrothermal aging caused by the elastic modulus of the NBR seals increasing, thus reducing the friction process of the contact area, and is caused by the increase in shear stress.

Figure 9 shows the variation of frictional force and contact area of the NBR seals with different loading air pressures for different hydrothermal aging times. According to Figure 9a, the variation trend of aging NBR seals obtained by finite element simulation at different loading air pressures is generally consistent with the F_C results of the cylinder friction experiment. However, there are some differences, which will be analyzed later. According to Figure 9b, the contact area of the aged NBR seals during the friction process exhibits a phased increase with the increase of loading air pressure (specific values are shown in Table S2), which is consistent with the trend of the 0 d NBR seals. This indicates that hydrothermal aging does not change the influence of loading air pressure on the tribological performance of the NBR seals, which is consistent with that of the cylinder friction experiment. The frictional force of the NBR seals obtained in the finite element simulation showed a certain degree of decrease within 0 d–2 d. This decreasing trend

disappeared with the increase of the loading air pressure, and when the loading air pressure increased to 0.3 MPa, the trend of its frictional force was basically the same as that of the F_C in the cylinder friction experiment. The NBR seals inevitably shrink due to the increase of cross-link density in the hydrothermal aging environment; its compression in the cylinder decreases and leads to the decrease of contact pressure, which decreases the frictional force in 0 d–2 d. However, the COF of the NBR seals increases with the hydrothermal aging time, and, after 2 d, the frictional force shows a trend of increasing with the hydrothermal aging time. Meanwhile, the frictional contact area of the NBR seals increases with the loading air pressure increases, which implies that the contact pressure increases, and effectively reduces the reduction of the contact pressure between the NBR seals and the cylinder wall due to hydrothermal aging. Therefore, the decreasing trend of the frictional force decreases with the increase of loading air pressure within 0 d–2 d. This can be further confirmed by comparing the multiplication of the increase in COF in Figure S8 and the increase in frictional force in Figure 9 with hydrothermal aging time, revealing that the multiplication of the increase in COF is greater than the increase in frictional force. The shrinkage of the inner diameter of the NBR seals caused by hydrothermal aging reduces its contact pressure with the cylinder wall and suppress the decrease of its tribological performance, which is known by combining the above analysis and Figure 1.

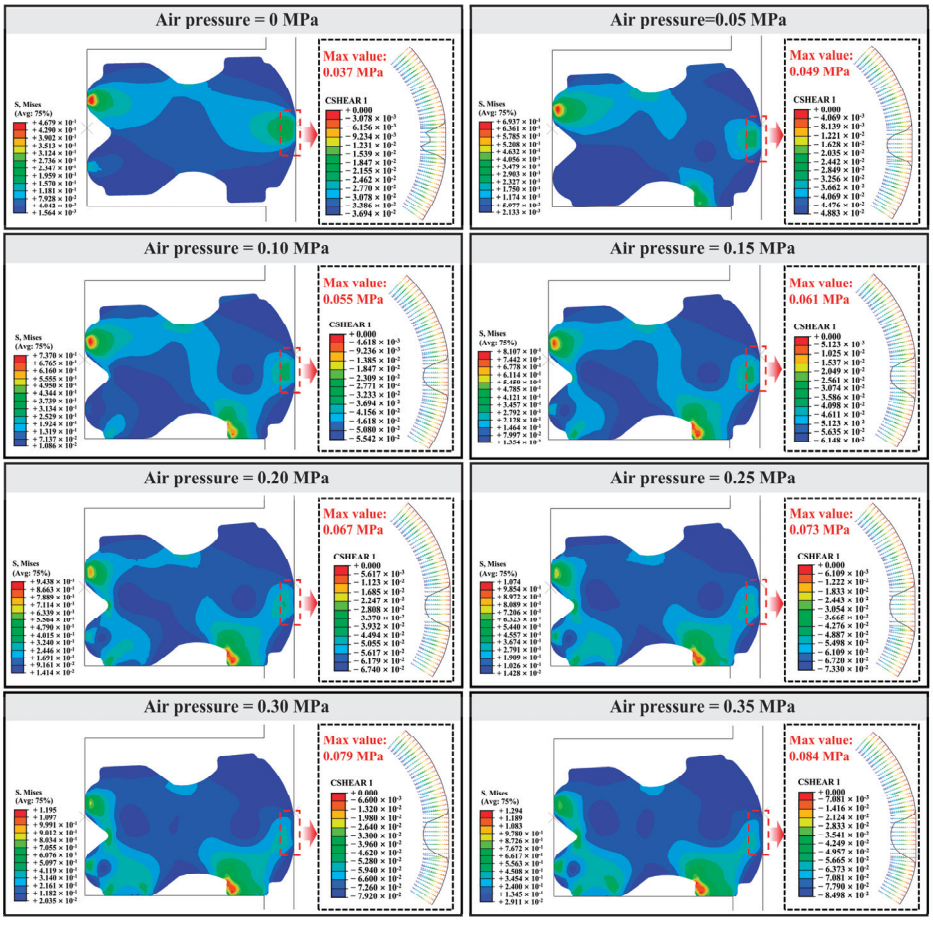

Figure 8. The Mises stress clouds and shear stress (CSHEAR1) distribution of the 0 d NBR seals under different loading air pressures.

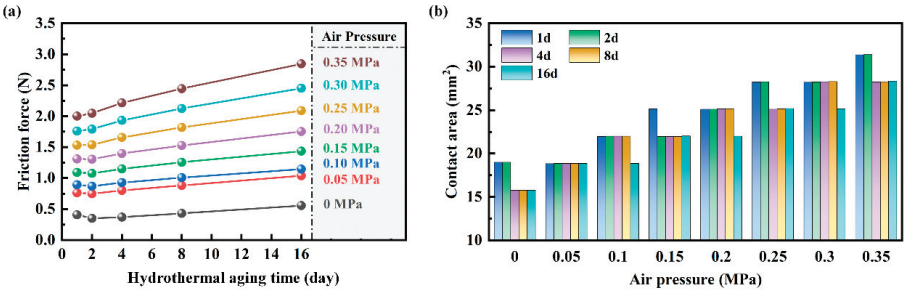

Figure 9. (**a**) The frictional force and (**b**) the contact area of the aged NBR seals under different loading air pressures.

In addition, it was found that the main difference between the cylinder friction experiment and the finite element simulations is the surface quality of the NBR seals. According to the friction test of the NBR cylindrical samples and previous studies [42], the surface quality of the rubber material is closely related to its tribological properties. Moreover, the frictional contact area is not the main factor affecting the tribological performance according to the cylinder friction experiment and the finite element simulation results, and the shrinkage of NBR seals in the hydrothermal aging environment reduces the contact pressure with the cylinder wall. Therefore, the effect of damp aging on the surface quality of NBR seals leads to the main factor of its tribological performance change. The evaporation of additives inside the NBR in the hydrothermal aging environment causes the deterioration of the surface quality and leads to a faster deterioration of the tribological performance with increasing hydrothermal aging time.

5. Conclusions

The influence law of hydrothermal aging conditions on the mechanical properties and tribological performance of rubber sealing materials was investigated through experiments and finite element simulation. This has an important theoretical value and significance for the subsequent realization of servo control of pneumatic servo systems under hydrothermal aging conditions and the development of pneumatic technology. The main conclusions are summarized as follows:

- NBR undergoes oxidation, cross-linking, chain-breaking, etc. in the hydrothermal aging environment, which leads to changes in the chemical structure. Moreover, the internal additives precipitate out onto its surface, which causes the appearance of surface micropores. The number and size of these micropores increase with the hydrothermal aging time.
- The cross-link density between molecules of NBR increases in the hydrothermal aging environment, and the strength of the connection between molecular chains is enhanced, resulting in increased hardness, tensile and compressive resistance, and weakened elastic deformation. Therefore, the NBR seals shrink in the hydrothermal aging environment, which reduces the contact pressure between them and the cylinder wall.
- The increase in loading air pressure in the cylinder causes an increase in dynamic friction and does not affect the effect of hydrothermal aging time on the tribological performance of NBR seals. The dynamic friction of the NBR seals in the cylinder gradually increases with the increase of the hydrothermal aging time, which is mainly due to the increase in the number and size of surface micropores caused by the volatilization of additives inside the NBR in the damp aging environment. The deterioration of the surface quality leads to the degradation of the tribological performance of the NBR seals, and shrinkage of the NBR seals due to hydrothermal aging suppresses the degradation of the tribological performance.

Supplementary Materials: The following supporting information can be downloaded at: https://www.mdpi.com/article/10.3390/polym16010081/s1, Figure S1: Schematic diagram of the NBR cylindrical samples preparation; Figure S2: Schematic diagram of the modified friction testing machine; Figure S3: Schematic diagram of the cylinder dynamic friction test machine; Figure S4: The simulation model of the NBR seals in the cylinder; Figure S5: (a) Stress-strain curves of the NBR cylindrical samples and (b) force-deformation curves of the NBR seals with different hydrothermal aging times; Figure S6: The F_f-piston velocity variation curves of the cylinder equipped with the aged NBR seals; Figure S7: The shear stress distribution of the NBR seals under different hydrothermal aging times (Air pressure = 0.35 MPa); Figure S8: The variation curves of the COF of the rubber cylindrical samples with the hydrothermal aging time under lubrication conditions; Table S1: Parameters of Mooney-Rivlin model for rubber under different hydrothermal aging times; Table S2: The specific contact areas of the aged COP-type seals during sliding under different loading air pressures.

Author Contributions: G.H.: Conceptualization (lead); Investigation (lead); Visualization (lead); Writing—original draft (lead). Z.C.: Conceptualization (supporting); Investigation (supporting); Software (lead); Writing—original draft (supporting); Writing—review and editing (supporting). J.W.: Conceptualization (lead); Funding acquisition (lead); Investigation (supporting); Methodology (lead); Supervision (lead); Writing—original draft (supporting); Writing—review and editing (supporting). A.L.: Data curation (lead); Investigation (lead). Q.L.: Data curation (supporting); Investigation (supporting). S.L.: Conceptualization (supporting); Methodology (supporting); Software (supporting). B.S.: Conceptualization (supporting); Methodology (supporting). Y.W.: Conceptualization (supporting). All authors have read and agreed to the published version of the manuscript.

Funding: This research is supported by the Science Foundation of National Key Laboratory of Science and Technology on Advanced Composites in Special Environments (JCKYS2023603C021).

Data Availability Statement: Data are contained within the article and Supplementary Materials.

Conflicts of Interest: Author Gege Huang was employed by the Guizhou Tire Co., Ltd. The remaining authors declare that the research was conducted in the absence of any commercial or financial relationships that could be construed as a potential conflict of interest.

References

1. Saravanakumar, D.; Mohan, B.; Muthuramalingam, T.; Sakthivel, G. Performance evaluation of interconnected pneumatic cylinders positioning system. *Sens. Actuat. A Phys.* **2018**, *274*, 155–164.
2. Taghizadeh, M.; Ghaffari, A.; Najafi, F. Improving dynamic performances of PWM-driven servo-pneumatic systems via a novel pneumatic circuit. *ISA Trans.* **2009**, *48*, 512–518. [CrossRef] [PubMed]
3. Shi, Y.; Cai, M.; Xu, W.; Wang, Y.J. Methods to Evaluate and Measure Power of Pneumatic System and Their Applications. *Chin. J. Mech. Eng.* **2019**, *32*, 322019.
4. Shen, M.X.; Peng, X.D.; Meng, X.K.; Zheng, J.P.; Zhu, M.H. Fretting wear behavior of acrylonitrile–butadiene rubber (NBR) for mechanical seal applications. *Tribol. Int.* **2016**, *93*, 419–428. [CrossRef]
5. Bai, C.; Gong, Z.; An, L.; Qiang, L.; Zhang, J.; Yushkov, G.; Nikolaev, A.; Shandrikov, M.; Zhang, B. Adhesion and friction performance of DLC/rubber: The influence of plasma pretreatment. *Friction* **2021**, *9*, 627–641. [CrossRef]
6. Bai, C.; Qiang, L.; Zhang, B.; Gao, K.; Zhang, J. Optimizing the tribological performance of DLC-coated NBR rubber: The role of hydrogen in films. *Friction* **2021**, *10*, 866–877. [CrossRef]
7. Qu, C.; Zhang, N.; Wang, C.; Wang, T.; Wang, Q.; Li, S.; Chen, S. MoS2/CF synergistic reinforcement on tribological properties of NBR/PU/EP interpenetrating polymer networks. *Tribol. Int.* **2022**, *167*, 107384. [CrossRef]
8. Bauer, D.R.; Baldwin, J.M.; Ellwood, K.R. Rubber aging in tires. Part 2: Accelerated oven aging tests. *Polym. Degrad. Stabil.* **2007**, *92*, 110–117. [CrossRef]
9. Sridharan, H.; Chanda, J.; Ghosh, P.; Mukhopadhyay, R. Rubber blend and filler effects on damage mechanisms under monotonic and fatigue loading. *Rubber. Chem. Tech.* **2019**, *92*, 415–430. [CrossRef]
10. Lucas, P.; Baba, M.; Lacoste, J.; Gardette, J.L. Crosslinking of dienic elastomers resulting from ageing: X-ray diffraction and refractometry measurements. *Polym. Degrad. Stabil.* **2002**, *76*, 449–453. [CrossRef]
11. Woo, C.S.; Ki, W.D.; Kwon, J.D. A study on the material properties and fatigue life prediction of natural rubber component. *Mat. Sci. Eng. A* **2008**, *376*, 483–484. [CrossRef]
12. Wu, J.; Dong, J.; Wang, Y.; Gond, B.K. Thermal oxidation ageing effects on silicone rubber sealing performance. *Polym. Degrad. Stabil.* **2017**, *135*, 43–53. [CrossRef]
13. Le Huy, M.; Evrard, G. Methodologies for lifetime predictions of rubber using Arrhenius and WLF models. *Angew. Makromol. Chem.* **1998**, *261*, 135–142. [CrossRef]
14. Bernstein, R.; Gillen, K.T. Predicting the lifetime of fluorosilicone o-rings. *Polym. Degrad. Stabil.* **2009**, *94*, 2107–2113. [CrossRef]

15. Woo, C.S.; Park, H.S. Useful lifetime prediction of rubber component. *Eng. Fail. Anal.* **2011**, *18*, 1645–1651. [CrossRef]
16. Woo, C.S.; Kim, W.D.; Lee, S.H.; Choi, B.I.; Park, H.S. Fatigue life prediction of vulcanized natural rubber subjected to heat-aging. *Procedia Eng.* **2009**, *1*, 9–12. [CrossRef]
17. He, S.; Bai, F.; Liu, S.; Ma, H.; Hu, J.; Chen, L.; Lin, J.; Wei, G.; Du, X. Aging properties of styrene-butadiene rubber nanocomposites filled with carbon black and rectorite. *Polym. Test.* **2017**, *64*, 92–100. [CrossRef]
18. Roland, C.M.; Mott, P.H. Aging of Natural Rubber in Air and Seawater. *Rubber. Chem. Techn* **2001**, *74*, 79.
19. Woo, C.S.; Choi, S.S.; Lee, S.B.; Kim, H.S. Useful lifetime prediction of rubber components using accelerated testing. *IEEE. Trans. Reliab.* **2010**, *59*, 11–17. [CrossRef]
20. Moon, B.; Lee, J.; Park, S.; Seok, C.-S. Study on the Aging Behavior of Natural Rubber/Butadiene Rubber (NR/BR) Blends Using a Parallel Spring Model. *Polymers* **2018**, *10*, 658. [CrossRef]
21. Alcock, B.; Jørgensen, J.K. The mechanical properties of a model hydrogenated nitrile butadiene rubber (HNBR) following simulated sweet oil exposure at elevated temperature and pressure. *Polym. Test.* **2015**, *46*, 50–58. [CrossRef]
22. Liu, J.; Li, X.; Xu, L.; Zhang, P. Investigation of aging behavior and mechanism of nitrile-butadiene rubber (NBR) in the accelerated thermal aging environment. *Polym. Test.* **2016**, *54*, 59–66. [CrossRef]
23. Zou, Y.; Sun, Y.; Zhang, Y.; He, J.; Tang, Z.; Zhu, L.; Luo, Y.; Liu, F. Antioxidative behavior of a novel samarium complex in styrene-butadiene rubber/silica composites. *Polym. Degrad. Stabil.* **2016**, *133*, 201–210. [CrossRef]
24. Nabil, H.; Ismail, H.; Azura, A.R. Comparison of thermo-oxidative ageing and thermal analysis of carbon black-filled NR/Virgin EPDM and NR/Recycled EPDM blends. *Polym. Test.* **2013**, *32*, 631–639. [CrossRef]
25. Choudhury, A.; Bhowmick, A.K.; Soddemann, M. Effect of organo-modified clay on accelerated aging resistance of hydrogenated nitrile rubber nanocomposites and their life time prediction. *Polym. Degrad. Stabil.* **2010**, *95*, 2555–2562. [CrossRef]
26. Liu, X.R.; Zhang, W.F.; Lou, W.T.; Huang, Y.X.; Dai, W. Investigation on thermal oxidative aging of nitrile rubber (NBR) O-rings under compression stress. *IOP. Conf. Ser. Mater. Sci. Eng.* **2017**, *265*, 012003. [CrossRef]
27. Choi, S.S.; Chung, H.S.; Joo, Y.T.; Yang, K.M.; Lee, S.H. Analysis of whitening phenomenon of EPDM article by humid aging. *J. Appl. Polym. Sci.* **2012**, *123*, 2451–2457. [CrossRef]
28. Patel, M.; Skinner, A.R. Thermal ageing studies on room-temperature vulcanised polysiloxane rubbers. *Polym. Degrad. Stabil.* **2001**, *73*, 399–402. [CrossRef]
29. Liu, S.; Cui, Z.; Su, Z.; Zhu, B.; He, S.; Su, B.; Wu, J.; Wang, Y. Sliding characteristics of bioinspired polydimethylsiloxane micropillars under bending states. *Tribol. Int.* **2022**, *175*, 107808. [CrossRef]
30. Teng, F.; Wu, J.; Su, B.; Wang, Y. High-speed tribological properties of Eucommia ulmoides gum/natural rubber blends: Experimental and molecular dynamics simulation study. *Tribol. Int.* **2022**, *171*, 107542. [CrossRef]
31. Dong, C.L.; Yuan, C.Q.; Bai, X.Q.; Yan, X.P.; Peng, Z. Tribological properties of aged nitrile butadiene rubber under dry sliding conditions. *Wear* **2015**, *322*, 226–237. [CrossRef]
32. Han, R.; Quan, X.; Shao, Y.; Niu, K. Tribological properties of phenyl-silicone rubber composites with nano-CeO_2 and graphene under thermal-oxidative aging. *Appl. Nanosci.* **2020**, *10*, 2129–2138. [CrossRef]
33. He, Q.; Wang, G.; Zhang, Y.; Li, Z.; Kong, L.; Zhou, W. Thermo-oxidative ageing behavior of cerium oxide/silicone rubber. *J. Rare Earths* **2020**, *38*, 436–444. [CrossRef]
34. Luo, H.; Wu, J.; Teng, F.; Su, B.; Li, H.; Lin, A.; Li, Z.; Wang, Y. Multiscale simulation on dynamic friction behavior of cylinder sealing rings under hydrothermal aging. *J. Appl. Polym. Sci.* **2021**, *138*, 50453. [CrossRef]
35. *ISO 188:2023*; Rubber, Vulcanized or Thermoplastic—Accelerated Ageing and Heat Resistance Tests. ISO: Geneva, Switzerland, 2023.
36. *ISO 2285:2019*; Rubber, Vulcanized or Thermoplastic—Determination of Tension Set under Constant Elongation, and of Tension Set, Elongation and Creep under Constant Tensile Load. ISO: Geneva, Switzerland, 2019.
37. *ISO 815-1:2019*; Rubber, Vulcanized or Thermoplastic: Determination of Compression Set—Part 1: At Ambient or Elevated Temperatures. ISO: Geneva, Switzerland, 2019.
38. *ISO 7743:2017*; Rubber, Vulcanized or Thermoplastic: Determination of Compression Stress-Strain Properties. ISO: Geneva, Switzerland, 2017.
39. Bazaei, A.; Moallem, M. Presticition friction modeling and position control in an actuated rotary arm. *IEEE. Trans. Instrum. Meas.* **2010**, *59*, 131–139. [CrossRef]
40. Jiménez, R.; Álvarez-Icaza, L. LuGre friction model for a magnetorheological damper. *Struct. Control. Health Monitor.* **2005**, *12*, 91–116. [CrossRef]
41. Muvengei, O.; Kihiu, J.; Ikua, B. Dynamic analysis of planar multi-body systems with LuGre friction at differently located revolute clearance joints. *Multibody Syst. Dyn.* **2012**, *28*, 369–393. [CrossRef]
42. Li, B.; Li, S.X.; Shen, M.X.; Xiao, Y.L.; Zhang, J.; Xiong, G.Y.; Zhang, Z.N. Tribological behaviour of acrylonitrile-butadiene rubber under thermal oxidation ageing. *Polym. Test.* **2021**, *93*, 106954. [CrossRef]

Disclaimer/Publisher's Note: The statements, opinions and data contained in all publications are solely those of the individual author(s) and contributor(s) and not of MDPI and/or the editor(s). MDPI and/or the editor(s) disclaim responsibility for any injury to people or property resulting from any ideas, methods, instructions or products referred to in the content.

MDPI AG
Grosspeteranlage 5
4052 Basel
Switzerland
Tel.: +41 61 683 77 34

Polymers Editorial Office
E-mail: polymers@mdpi.com
www.mdpi.com/journal/polymers

Disclaimer/Publisher's Note: The statements, opinions and data contained in all publications are solely those of the individual author(s) and contributor(s) and not of MDPI and/or the editor(s). MDPI and/or the editor(s) disclaim responsibility for any injury to people or property resulting from any ideas, methods, instructions or products referred to in the content.

Academic Open
Access Publishing

mdpi.com

ISBN 978-3-7258-1420-6